35th conference with international participation

COMPUTATIONAL MECHANICS 2019

PROCEEDINGS OF COMPUTATIONAL MECHANICS 2019

November 4 - 6, 2019

HOTEL SRNÍ AND ŠUMAVA, SRNÍ
CZECH REPUBLIC

FACULTY OF APPLIED SCIENCES
UNIVERSITY OF WEST BOHEMIA

PILSEN REGION

ČSM

IFToMM

cea cm
Central European Association for Computational Mechanics

PROCEEDINGS OF COMPUTATIONAL MECHANICS 2019

ISBN 978-80-261-0889-4

Published by
University of West Bohemia, Univerzitní 8, 301 00 Plzeň, Czech Republic, IC 49777513

Edited by
Vítězslav Adámek
Alena Jonášová
Stanislav Plánička
Martin Zajíček

Conference secretariat
Monika Grätschová
Department of Mechanics
Faculty of Applied Sciences
University of West Bohemia
Univerzitní 8
301 00 Plzeň
Czech Republic

phone: +420 377 632 301
e-mail: vm@kme.zcu.cz

PREFACE

The proceedings contain 80 conference papers presented at the 35th conference **Computational Mechanics 2019**, which was held at the Hotel Srní and Šumava in Srní, Czech Republic, on November 4 – 6, 2019. This annual conference, which was attended by over one hundred participants from the Czech Republic, Slovakia and from abroad, was organised by the Department of Mechanics, Faculty of Applied Sciences of the University of West Bohemia under the auspices of

- Vlasta Radová, the Dean of the Faculty of Applied Sciences,
- Ivana Bartošová, the Vice-President of the Pilsen Region for Education and Tourism,
- Czech Society for Mechanics,
- Czech National Committee of IFToMM,
- Central European Association for Computational Mechanics.

The main objective of this traditional conference is to bring together academicians, researchers and industrial partners interested in relevant disciplines of mechanics including

- solid mechanics,
- dynamics of mechanical systems,
- mechatronics and vibrations,
- reliability and durability of structures,
- fracture mechanics,
- mechanics in civil engineering,
- fluid mechanics and fluid-structure interaction,
- thermodynamics,
- biomechanics,
- heterogeneous media and multiscale problems,
- experimental methods in mechanics,

to create an opportunity for meeting, discussion and collaboration among the participants. As in the previous years, the three best papers presented at this conference were awarded the Czech Society for Mechanics Award for young researchers under 35 years of age.

To all conference participants, we offer the possibility to publish their peer-reviewed full papers in the international journal **Applied and Computational Mechanics** indexed by Scopus. This journal has been published by the University of West Bohemia since 2007 (see https://www.kme.zcu.cz/acm/).

We would like to express our gratitude to all the invited speakers for their significant contribution to the conference and the time and effort they put. Considerable acknowledgement belongs also to the members of the Organising Committee for their important work.

We strongly believe that all participants of the CM2019 enjoyed their stay in the beautiful nature of the Šumava region in a meaningful way. Finally, we would like to invite you all to come to the next conference CM2020.

Jan Vimmr
University of West Bohemia
Chairman of the Scientific Committee

Vítězslav Adámek
University of West Bohemia
Chairman of the Organising Committee

SCIENTIFIC COMMITTEE

Chairman:

Jan Vimmr
University of West Bohemia, Faculty of Applied Sciences, Czech Republic

Members:

Miroslav Balda
Research and Testing Institute Plzeň, Czech Republic

Jiří Burša
Brno University of Technology, Faculty of Mechanical Engineering, Czech Republic

Jan Dupal
University of West Bohemia, Faculty of Applied Sciences, Czech Republic

Václav Dvořák
Technical University of Liberec, Faculty of Mechanical Engineering, Czech Republic

Jiří Fürst
Czech Technical University in Prague, Faculty of Mechanical Engineering, Czech Republic

Miroslav Holeček
University of West Bohemia, Czech Republic

Jaromír Horáček
Institute of Thermomechanics, Czech Academy of Sciences, Czech Republic

Michal Kotoul
Brno University of Technology, Faculty of Mechanical Engineering, Czech Republic

Jiří Křen
University of West Bohemia, Faculty of Applied Sciences, Czech Republic

Vladislav Laš
University of West Bohemia, Faculty of Applied Sciences, Czech Republic

Justín Murín
Slovak University of Technology in Bratislava, Faculty of Mechanical Engineering, Slovak Republic

Milan Naď
Slovak University of Technology in Bratislava, Faculty of Materials Science and Technology in Trnava, Slovak Republic

Jiří Náprstek
Institute of Theoretical and Applied Mechanics, Czech Academy of Sciences, Czech Republic

Miloslav Okrouhlík
Institute of Thermomechanics, Czech Academy of Sciences, Czech Republic

Luděk Pešek
Institute of Thermomechanics, Czech Academy of Sciences, Czech Republic

Jindřich Petruška
Brno University of Technology, Faculty of Mechanical Engineering, Czech Republic

Jiří Plešek
Institute of Thermomechanics, Czech Academy of Sciences, Czech Republic

František Pochylý
Brno University of Technology, Faculty of Mechanical Engineering, Czech Republic

Pavel Polach
Research and Testing Institute Plzeň, Czech Republic

Eduard Rohan
University of West Bohemia, Faculty of Applied Sciences, Czech Republic
Josef Rosenberg
University of West Bohemia, Faculty of Applied Sciences, Czech Republic
Milan Růžička
Czech Technical University in Prague, Faculty of Mechanical Engineering, Czech Republic
Milan Sága
University of Žilina, Faculty of Mechanical Engineering, Slovak Republic
Petr Sváček
Czech Technical University in Prague, Faculty of Mechanical Engineering, Czech Republic
Zbyněk Šika
Czech Technical University in Prague, Faculty of Mechanical Engineering, Czech Republic
Michael Valášek
Czech Technical University in Prague, Faculty of Mechanical Engineering, Czech Republic
Jaroslav Zapoměl
VŠB – Technical University of Ostrava, Faculty of Mechanical Engineering, Czech Republic
Vladimír Zeman
University of West Bohemia, Faculty of Applied Sciences, Czech Republic

Table of Contents

COMPUTATIONAL MECHANICS 2019
35th conference with international participation
Srní
November 4 - 6, 2019

Optimization and control of mechatronic tensegrity for robotics

A. Balon[a], Z. Šika[a]

[a] *Department of Mechanics, Biomechanics and Mechatronics, Faculty of Mechanical Engineering, Czech Technical University in Prague, Technicka 4, Praha 6, Czech Republic*

1. Introduction

Tensegrities are stable structures consisting of discontinuous compressive members and continuous tensile members. In engineering applications compressive members are often rods that do not touch each other, while tensile members are often pretensioned cables. The word *tensegrity* comes from conjugation of words *tension* and *integrity* [4]. Active tensegrities are gaining popularity in applications regarding mobile robots and deployable structures (Fig. 1). Our goal is to explore possibilities of active tensegrity application in robotic manipulators.

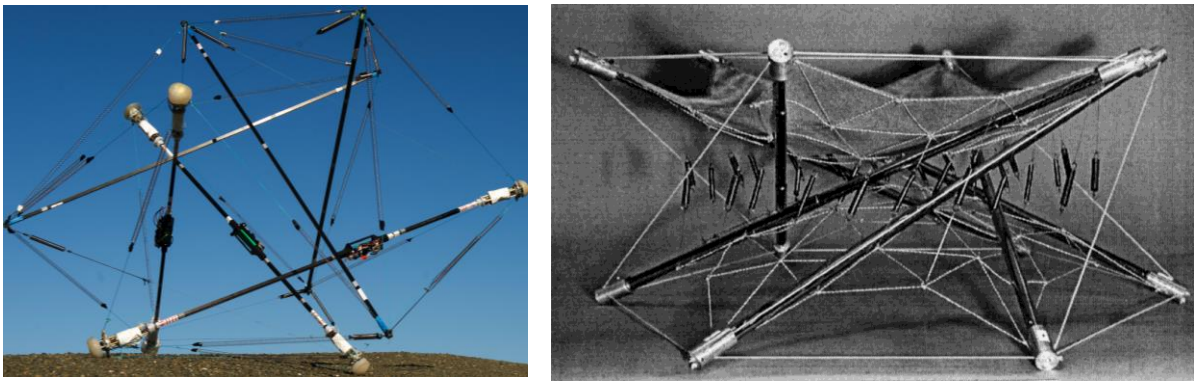

Fig. 1. (Left) mobile tensegrity robot "Super Ball Bot", (right) deployable antenna using tensegrity structure

2. Dynamic model of planar tensegrity

Dynamic model is derived using Lagrange Equations of Second Kind with following assumptions. Individual rods are considered as perfectly rigid bodies, friction in joints is ignored, mass of cables is ignored, and cables are modelled as parallel combination of tension spring and linear viscous damper. However dynamic model alone does not provide stability of tensegrity.

3. Form-finding optimization

Form-finding is a process of searching for such pretension in cables that stabilizes the tensegrity structure. Static form-finding method, called *Force Density Method*, is used to stabilize the dynamic model. Advantage of this method is that only topology describing the connection of cables and rods needs to be known. Force density method analyses so called *Stress Matrix* which describes force densities between individual nodes of a tensegrity [1]. Genetic algorithm is used to solve the form-finding problem as presented in [2]. This

approach also allows to use the symmetric nature of tensegrity structures to reduce the number of optimization parameters significantly.

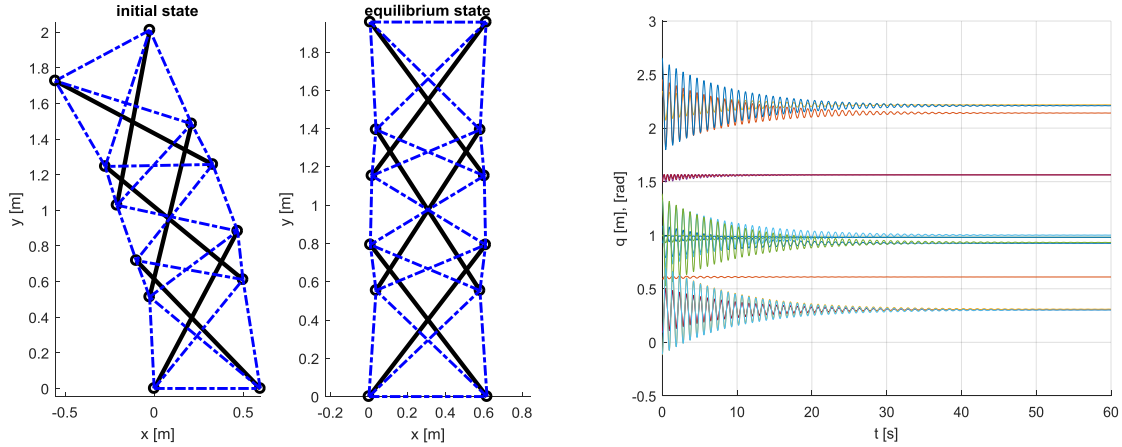

Fig. 2. (Left) initial state of 15 DOF tensegrity and its equilibrium state. (Right) plot showing the evolution of individual coordinates of the dynamic model from the initial state to the equilibrium state

4. Motion control

Motion control of stable planar tensegrity is achieved by varying free lengths of pretensioned cables. For this purpose, *Computed Torque Control* method is applied to the dynamic model of planar tensegrity with 15 DOF (Fig. 2). Since this method involves solving inverse dynamics problem and it is assumed that each of total 22 cables are active, an undetermined system of equations needs to be solved. This allows to optimize the result in such way that all cables are pretensioned and no force exceeds specified limit given by the cable properties.

5. Eigenmotion

To plan the motion of the 15 DOF tensegrity a concept called Eigenmotion is used. Characteristic of Eigenmotion is that total mechanical energy is constant during motion [3]. This concept allows to control the motion of the tensegrity so that control inputs only compensate the energy dissipation in the system. Furthermore, Eigenmotion of tensegrity can be varied by adjusting mass of individual rods or stiffness of cables to match the Eigenmotion with desired motion. Adjusting of these parameters is solved as an optimization problem. This optimization is solved in a model without energy dissipation. Applying optimization results to a model with active control and energy dissipation leads to an energy efficient control.

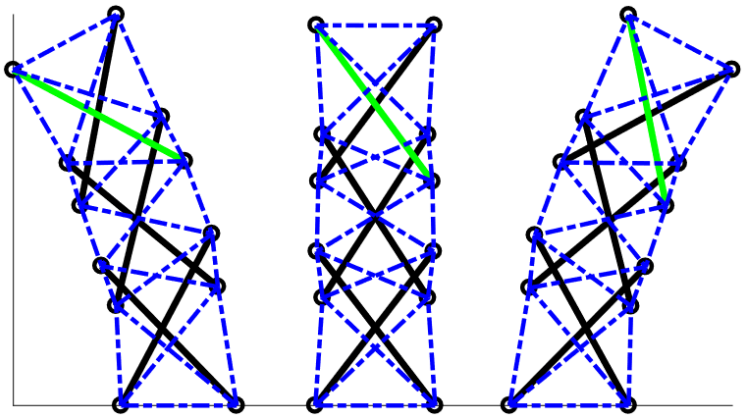

Fig. 3. Desired positions of rod 6 at time t = 0 s, t = 0.4 s, and t = 0.8 s for Eigenmotion optimization

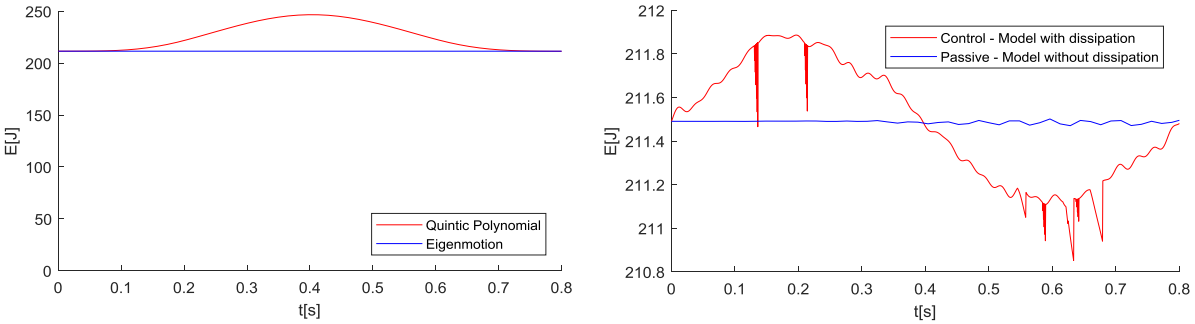

Fig. 4. (Left) comparison of total mechanical energy between trajectory generated with quintic polynomials (red) and trajectory obtained from Eigenmotion optimization (blue). (Right) comparison between total mechanical energy of passive tensegrity in a model without dissipation (blue) and total mechanical energy of controlled tensegrity in a model with dissipation (red)

6. Conclusion

To explore the possibilities of use of active tensegrities in robotic manipulators a dynamic model of planar tensegrity was derived. This model was then stabilized using genetic algorithm to solve the form-finding problem. Computed torque control was then applied to the model to control motion of tensegrity. Lastly, Eigenmotion concept was applied to control the tensegrity in energy efficient manner.

Acknowledgements

The work has been supported by the project SGS19/156/OHK2/3T/12 "Mechatronics and adaptronics 2019" of Czech Technical University in Prague.

References

[1] Connely, R., Tensegrity structures: Why are they stable?, Rigidity Theory and Applications (1999) 47-54.
[2] Koohestani, K., Form-finding of tensegrity structures via genetic algorithm, International Journal of Solids and Structures 49 (2012) 47 – 54.
[3] Schwarzfischer, F., The dynamic synthesis of an energy-efficient slider-crank-mechanism, Proceedings of the International Symposium of Mechanism and Machine Science, 2017, pp. 156 – 163.
[4] Skelton, R. E., Oliveira, M. C., Tensegrity systems, 2009.

COMPUTATIONAL MECHANICS 2019
35th conference with international participation
Srní
November 4 - 6, 2019

SHAVO control of a morphing wing

P. Beneš[a], Z. Šika[a], M. Hromčík[b], F. Svoboda[b], A. Balon[a]

[a] Faculty of Mechanical Engineering, CTU in Prague, Technická 4,160 00 Praha 6, Czech Republic
[b] Faculty of Electrical Engineering, CTU in Prague, Technická 2,166 27 Praha 6, Czech Republic

Conventional wings are usually designed for a single typical flight condition, or for a balanced combination of multiple flight conditions. Therefore, they cannot be fully optimal for a wide range of flight modes simultaneously. Continuously variable profile geometries promise significantly increased efficiency, minimized drag, and low noise levels compared to wings with conventional flaps with necessary constructional gaps. The use of smart materials eliminates the large and heavy traditional actuators. The associated reduction in weight and air resistance also means significant fuel savings and therefore cost savings. Moreover, the usage of smart materials reduces energy conversions and related losses (classical servomechanisms with electrical to mechanical or hydraulic forces). Reducing the number of individual parts also provides better system reliability.

The morphing wing technology appears as feasible and very promising way for near future air transportation and wind power generation systems. The airfoil fabricated from smart materials and equipped with a vast number of integrated actuators and sensors can be used for active damping, increased resistance to flutter, higher lift-to-drag ratio of air vehicles or better efficiency of wind power generators in various operational regimes. Finding the right control concept is key to achieve the desired features. The SHAVO control approach combines advantages of the feedforward command shaping and the feedback control. The command shaping part based on the model of the system is capable to quickly and efficiently eliminate residual vibration while the feedback part ensures the stability and robustness to unmodeled disturbances and deviations. The structure of SHAVO control is in Fig. 1.

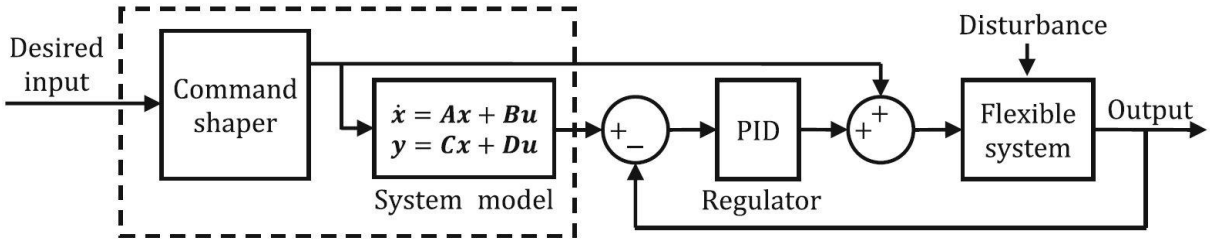

Fig. 1. Structure of SHAVO control, [1]

The system model is used not only to design the shaper itself, but also to predict the behaviour of the controlled system. The feedback part then compensates only differences between the expected and the actual state.

Command shaper used in the SHAVO structure is based on an optimized control curve that is converted into the form of a dynamic shaper with re-entry property [2]. Unlike traditional approaches to command/shaping control the length of the shaper is not determined by the system natural frequency and thus can be set arbitrarily (with respect to limits of the actuator).

The simulation model is based on state space representation of the wing dynamics [3]. We considered small displacements and linear elastic material, thus the Hooks law is valid. Some of the first simulation results are in Fig. 2. The desired input was a step signal. The model error has been introduced in the form of 10% change of mass. The external disturbance was represented by randomly added noise. The performance of SHAVO control was compared to command shaping without feedback.

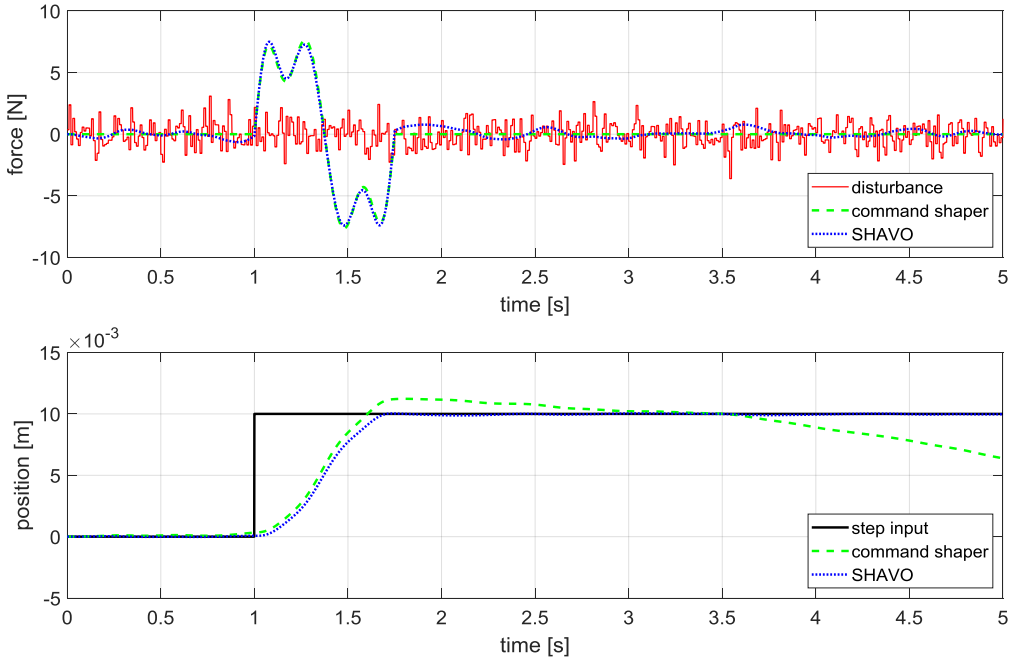

Fig. 2. Simulations: model error and external disturbance

Simulation experiments proved that SHAVO approach is capable to deal with both model error and unpredicted external disturbance. Actuator requirements remain practically the same as in the case of the pure command shaper. The next step will be the application to the smooth morphing trailing edge demonstrator [4].

Acknowledgements

The work has been supported by the Czech Science Foundation project GA19-16772S - Aerodynamic bodies with actively controlled morphing.

References

[1] Beneš, P., Valášek, M., Šika, Z., SHAVO control: the combination of the adjusted command shaping and feedback control for vibration suppression, Acta Mechanica 230 (5) (2019) 1891-1905.
[2] Beneš, P., Valášek, M., Optimized re-entry input shapers, Journal of Theoretical and Applied Mechanics 54 (2) (2016) 353-368.
[3] Svoboda, F., Hromčík, M., Finite element method based modeling of a flexible wing structure, Proceedings of the 21st International Conference on Process Control, 2017, pp. 222–227.
[4] Svoboda, F., Hromčík, M., Construction of the smooth morphing trailing edge demonstrator, Proceedings of the 22nd International Conference on Process Control, Piscataway, 2019, pp. 136-139.

COMPUTATIONAL MECHANICS 2019
35th conference with international participation
Srní
November 4 - 6, 2019

Comparison of two numerical approaches for simulation of fire with radiative heat transfer into solid walls

V. Bělák[a]

[a] Czech Aerospace Research Centre, Department of Engines, Beranovych 130, 199 05 Prague, Czech Republic

1. Introduction

Mathematical modeling of fluid flow is important in modern engineering. It allows us to improve performance characteristics and increase the lifetime of modern products due to the prediction of drag, lift, pressure and thermal load, pollutant emission or study of highly unsteady transition phenomena. Mathematical modeling is often used in cases where the application of the experimental method is limited such as in the case of combustion. Based on the length scale, these simulations can be divided into three areas. The smallest one relates to the simulation of combustion in the combustion chamber of gas turbines [1]. The middle one relates to modeling combustion in industrial chambers such as glass melting furnace [2]. The great one is focused on fire modeling in buildings and exteriors. Part of this topic will be discussed in the following paper.

There are two possibilities for fire modeling. The first one is based on an empirical approach and does not include any additional equation connected with combustion modeling. The second approach is based on combustion modeling and it is suitable for complex geometries.

To evaluate the fire resistance, the heat load of the wall must be overstated. The wall can be heated by direct contact with the hot gases or by radiation. The radiation model and its dependence on the combustion model will be presented in this paper.

2. Mathematical model

The fire modeling is based on the following system of equations

$$\frac{\partial \rho}{\partial t} + \frac{\partial}{\partial x_j}(\rho u_j) = 0, \tag{1}$$

$$\frac{\partial}{\partial t}(\rho u_i) + \frac{\partial}{\partial x_j}(\rho u_i u_j) = -\frac{\partial p}{\partial x_i} + \frac{\partial}{\partial x_j}[(\mu + \mu_t)(\frac{\partial u_i}{\partial x_j} + \frac{\partial u_j}{\partial x_i} - \frac{2}{3}\frac{\partial u_k}{\partial x_k}\delta_{ij})], \tag{2}$$

$$\frac{\partial}{\partial t}(\rho h) + \frac{\partial}{\partial x_j}(\rho h u_j) = \frac{\partial}{\partial x_j}\left[\left(\alpha + \frac{\mu_t}{Pr_t}\right)\frac{\partial h}{\partial x_j}\right] + S_h, \tag{3}$$

where ρ is density, u_i is a component of the velocity vector, p is pressure, μ is a dynamic viscosity, h is enthalpy, α is a coefficient of heat diffusion and μ_t is a turbulent viscosity. Source terms in enthalpy equations represent via S_h.

The empirical model is based on the combustion heat $\dot{Q}$ of fuel and relationship defined in [3,5] especially length of flames which is based on the diameter of the fire pool

$$L_f = -1.02D + 0{,}0148\dot{Q}^{\frac{2}{5}}. \tag{4}$$

These parameters define a cell zone where is prescribed source term in enthalpy equations.

If the combustion model is included, then the system of equations (1) – (3) is extended by transport equation for mass fraction Y_i

$$\frac{\partial}{\partial t}(\rho Y_i) + \frac{\partial}{\partial x_j}(\rho Y_i) = \frac{\partial}{\partial x_j}[(\mu + \mu_t)\frac{\partial Y_i}{\partial x_j}] + S_{Y_i}, \quad (5)$$

where S_{Y_i}represent source terms.

The Number of additional PDE and ODE equations is depended on the complexity of the combustion model. In this case is used the simplest one equation combustion model called "infinitelyFastChemistry" [6] which is used one constant $C$for tuning heat release rate.

The radiative model has to be included in fire simulation. The P1 radiation model [7] was chosen first but had to be replaced by DO(discrete-ordinates) radiative model [4].

In order to capture the heat flux into the wall correctly, the energy equation in solid region has to be solved. This equation is described by following partial differential equation

$$\frac{\partial h}{\partial t} + \frac{\partial}{\partial x_j}[(\alpha)\frac{\partial h}{\partial x_j}] = 0\,. \quad (6)$$

Based on required properties a suitable solver has to been chosen. ChtMultiRegion from OpenFOAM [6] library is used. This solver is based on PISO algorithm and allow to solve coupled problem of fluid flow with heat transfer through solid region.

3. Results

Fire simulation is tested on simplified geometry with a defined pool (1x1 m) which is 1.5 m away from the wall as is shown in Fig. 1. The rate of fuel (kerosene) vaporization from the pool is prescribed as 0.022 kg s^{-1} m^{-2} at temperature 480 K. This amount of fuel corresponding to firepower 0,96 MW. The ambient boundary conditions (300 K, 101325 Pa) is prescribed at free stream boundaries.

The simulation model is shown in Fig. 1 where the pool is located at a given distance from the wall. The computational domain is constructed by hexa-dominant algorithm and consist from 488k cells.

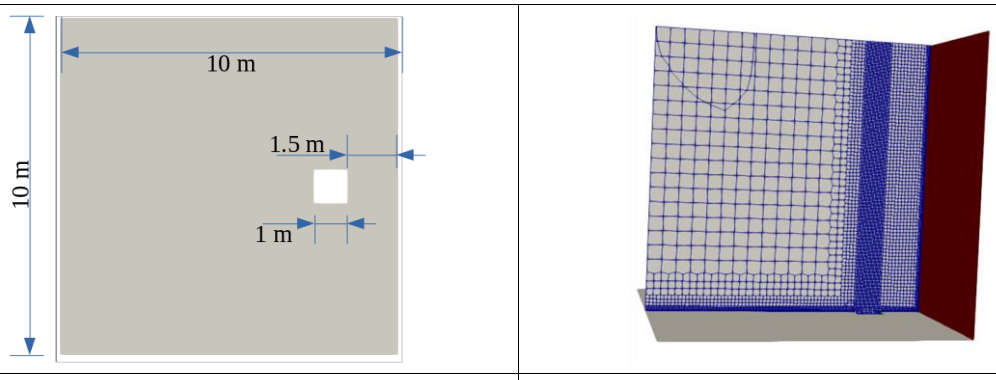

a) geometry description | b) example of computational domain

Fig. 1. The computational domain

Determining radiative heat flux is the goal of the simulation. There are compared three models. The first one is based on empirical approach and RANS turbulence model (*"case1"*). The second and third one is based on a simplified combustion model which is used with different turbulence model. The first one is based on RANS approach (*"case2"*) and the second one is based on DES approach (*"case3"*). The results are shown in Figs. 2 and 3. It is possible to see that the model based on a simplified chemical model predicting about three times greater radiative heat flux. This is caused by the application of the combustion model and modeling of radiative heat flux from three atomic molecules of H_2O and CO_2. The difference between the

turbulent model is at a height above 3 m where the higher radiative heat flux and wall temperature are predicted by simulation based on DES turbulence model.

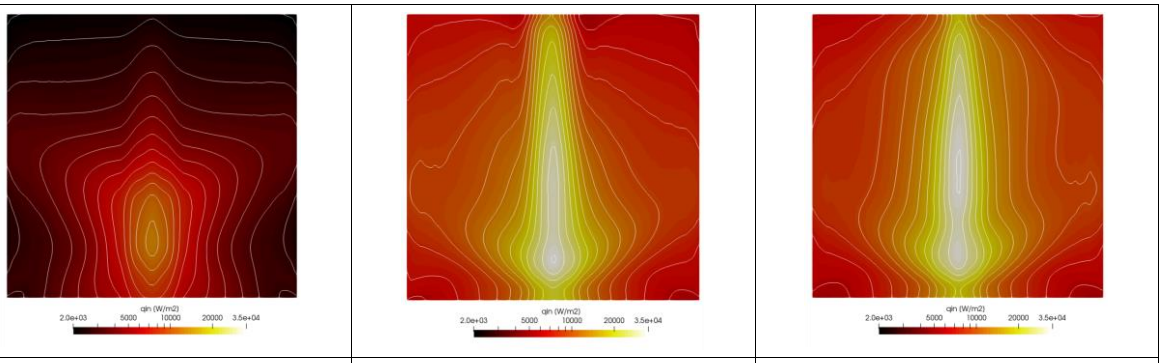

a) case1 | b) case2 | c) case3

Fig. 2. Comparison of prediction radiative heat flux into wall by diferent model

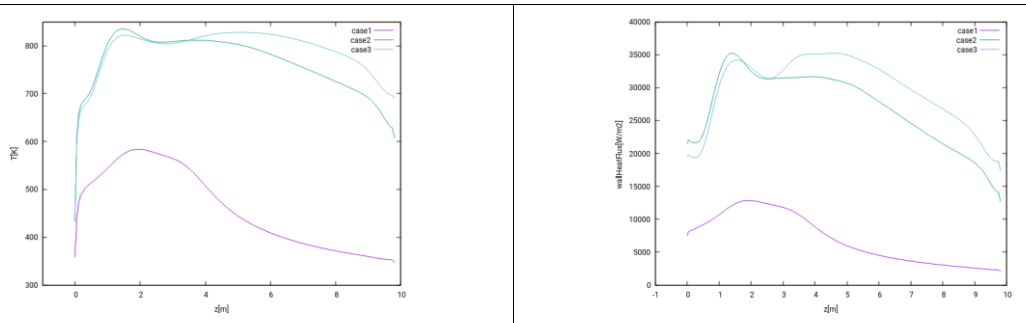

a) temperature | b) wall heat flux

Fig. 3. Profile of selected variables along wall symmetry axis

The radiative heat flux intensity can be influenced by setting the combustion model constant C. If the value is reduced, then radiative heat flux and wall temperature increased. If, on the other hand, the value is increased then radiative heat flux decreased. To achieve a similar flame temperature as in the case of the empirical model, it is necessary to select a constant in the range from 20 to 50 as is possible to see in Table 1.

Table 1. Overview of simulations

	Combustion	**Turbulence**	**C**	**Wall heat flux [MW]**	**Wall average temperature [K]**	**Wall maximum temperature [K]**	**Flame maximum temperature [K]**
Case 1	Emp.	RANS		0.394	392	583	1405
Case 2	Inf.Fast	RANS	5	1.088	533	835	1597
Case 3	Inf.Fast	DES	5	1.183	552	829	1631
Case 4	Inf.Fast	DES	2	1.186	558	840	1711
Case 5	Inf.Fast	DES	1	1.215	556	840	1739
Case 6	Inf.Fast	DES	0.5	1.251	556	843	2269
Case 7	Inf.Fast	DES	0.1	2.283	709	1059	>2500
Case 8	Inf.Fast	DES	10	1.201	547	823	1584
Case 9	Inf.Fast	DES	20	1.174	546	814	1589
Case 10	Inf.Fast	DES	50	0.855	498	709	1320
Case 11	Inf.Fast	DES	100	0.744	460	640	1208

4. Conclusion

Validation and calibration of a simplified combustion model is shown in this paper. This model is designed to simulate fire and temperature flux into a building wall for a study fire and structural safety of buildings. It is necessary to choose a combustion model that works with three and more atomic gases. These gases have a significant influence on the determination of the radiation heat flux. Their neglect reduces the radiation flow to 1/3.

The calibrated model is used to simulate large fires near and inside buildings.

Acknowledgments

This work has been supported by the grant project Of the Ministry of the Interior of the Czech Republic no. VI20172020092 and by The Ministry of Education, Youth and Sports from the Large Infrastructures for Research, Experimental Development and Innovations project „IT4Innovations National Supercomputing Center – LM2015070“

References

[1] Betak, V., Numerical simulation of combustion in small aero engines by using segregated algorithm,Proceedings of the 12th conference on Power System Engineering, Thermodynamics & Fluid Flow, Pilsen, 2019.

[2] Betak, V., Advanced DES simulations of oxy-gas burner located into model of real melting chamber, Proceedings of the 14th international seminar on furnace design, operations and processes simulation, Velke Karlovice, 2017.

[3] ČSN EN 1991-1-2.

[4] Fiveland, W. A., Three-dimensional radiative heat-transfer solutions by the discrete-ordinates method. Journal of Thermophysics and Heat Transfer 2 (4) (1988) 309-316.

[5] Kucera, P., Pokorny, J., Fire dynamics, VŠB-TUO, 2014. (in Czech)

[6] OpenFOAM, www.openfoam.com

[7] Sazhin, S.S., Sazhina, E.M., Faltsi-Saravelou, O., Wild. P., The P-1model for thermal radiation transfer: advantages and limitations, Fuel 75 (3) (1996) 289-294.

COMPUTATIONAL MECHANICS 2019
35th conference with international participation
Srní
November 4 - 6, 2019

Mathematical model for determining the viscoelastic properties of soft tissues using indentation tests

V. Bittner[a], F. Maršík[b]

[a]Faculty of Science, Humanities and Education, Technical University of Liberec, Czech Republic
[b]Institute of Thermomechanics of the CAS, v. v. i., Prague, Czech Republic

1. Introduction

Indenting is a mechanical stress test where a very hard indentor is pressed into the material under investigation. It takes use of a hard tip whose geometrical and mechanical properties are known. In a measurement, load placed on the indenter tip is progressively increased, until it reaches a user defined value F_{max}. This load may be held constant for a period and is then gradually removed again. The periods of loading, holding and unloading the sample are user defined and recorded along with measured data. The course of the load curve for the viscoelastic material is shown in Fig. 1.

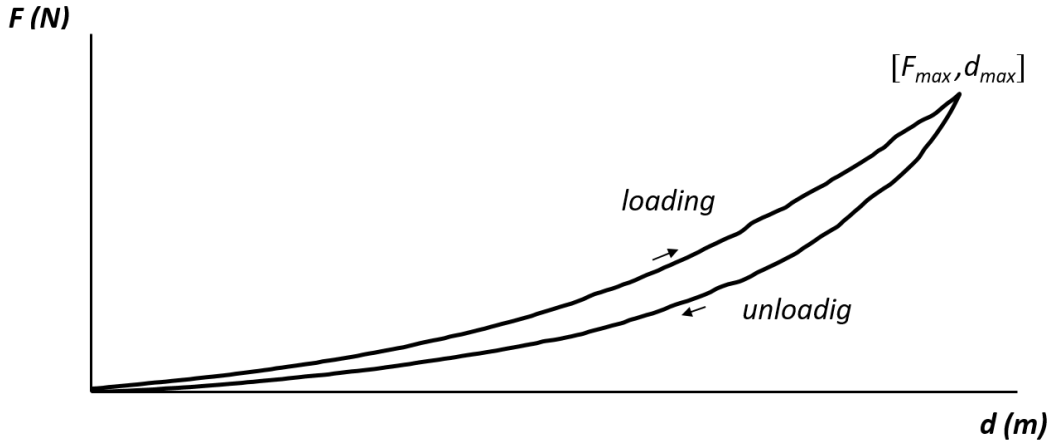

Fig. 1. A typical course of the load curve when indenting a viscoelastic material by a cylindrical indentor

The method is used especially for the testing of mechanical properties of materials at micro and nano scale. According to available sources, mathematical models are based on the theory of small deformations and developed especially to determine the hardness of the material. The question is whether it is possible to extend this reflection to a macroscopic scale and examine the viscoelasticity of materials? Such a concept could be used in medicine to objectify palpation examination of soft tissues, especially muscles. Instruments based on this principle already exist. They are called myotonometers.

2. Aim

The aim of the thesis was to create a mathematical model for the determination of viscoelastic properties of soft tissues using indentation stress tests.

3. Methods

Problem is formulated for indentation of a solid cylinder penetrating into an infinite half-space of viscoelastic material. The task is solved first, provided that the material is only elastic and with small deformations. The found shape of the deformation is used in the next step to formulate the tensor of deformation for the Neo-Hooke's hyperelastic material. The geometry of the task is shown in Fig. 2.

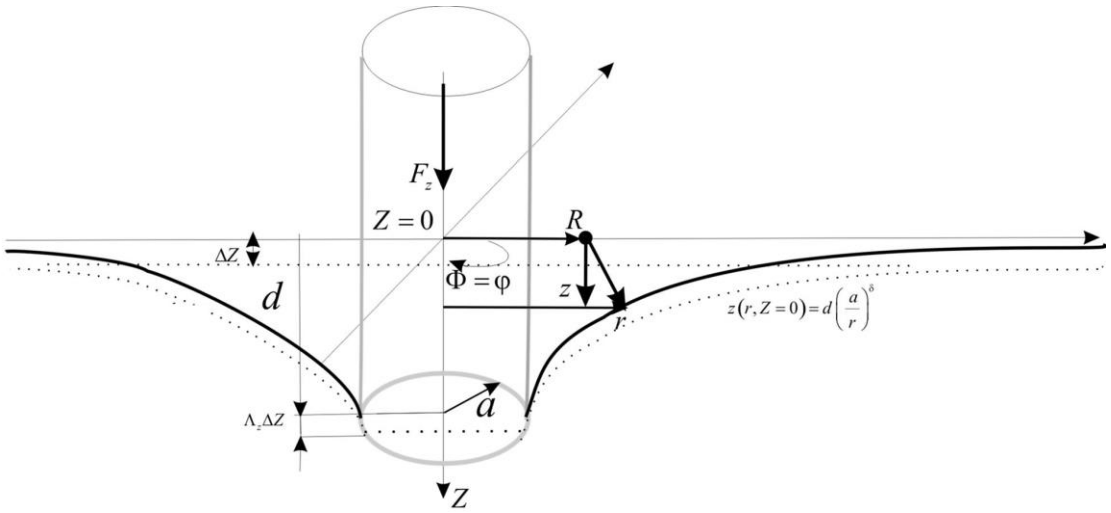

Fig. 2. Penetration of the solid cylinder into half-space by the action of point surface forces $\boldsymbol{F}$ = (0; 0; F_z)

4. Solution and results

During each deformation the weight is retained. Deformation gradient $F^i{}_I$ is used to determine deformation tensor. The change in density ρ is related to the change in volume (1-*j*). The volume change is proportional to the pressure *p*, *K* is the compressibility modulus (1)

$$\begin{aligned} &\rho_o = j\rho, \quad j = \det\left|F^i{}_I\right|, \quad F^i{}_I = \frac{\partial x^i}{\partial X^I}, \\ &p = K\left(1-j\right) = K\left(1-\frac{\rho_o}{\rho}\right). \end{aligned} \tag{1}$$

The constitutive equation for the homogeneous elastic material (2a) can be generalized to the viscoelastic material (2b), [3]. In loading tests is typically measured elastic modulus *E* and Poisson's ratio σ

$$\begin{aligned} &a) \quad t^{ij} = Ke_{(1)}\delta^{ij} + 2\hat{\mu}\overset{(o)}{e}{}^{ij} && K = \frac{E}{3\left(1-2\sigma\right)}, \quad \hat{\mu} = \frac{E}{2\left(1+\sigma\right)} \\ &b) \quad t^{ij} = Ke_{(1)}\delta^{ij} + 2\hat{\mu}\overset{(o)}{e}{}^{ij} + 2\mu\overset{(o)}{d}{}^{ij} && K\left[\frac{\mathrm{J}}{\mathrm{m}^3}\right],\ \hat{\mu}\left[\frac{\mathrm{J}}{\mathrm{m}^3}\right],\ \mu\left[\mathrm{Pa}\cdot\mathrm{s}\right] \end{aligned} \tag{2}$$

Another generalization is the hyperelastic material (Neo-Hook's). It is especially suitable for low compressible materials [4] and is also useful for describing biological tissues [1]. For the geometry of Fig. 2, it can be shown that the main components of Green's stress tensor are

$$t_{zz} = \frac{\hat{\mu}}{j^{5/3}}\left(\lambda^2 - \frac{j}{\lambda}\right), \qquad t_{xx} = t_{yy} = 0, \tag{3}$$

where λ is the elongation in the main direction of deformation. For small deformations ($d \sim 2a / 3$) can be used equation

$$(1-2\sigma)\Delta\mathbf{u} + \operatorname{grad}\operatorname{div}\mathbf{u} = 0\,, \tag{4}$$

where $\boldsymbol{u}$ = (u_x; u_y; u_z) is the displacement vector. Assuming the force under the cylindrical surface generates pressure

$$p(R) = p(0)\left(1 - \frac{R^2}{a^2}\right)^{-1/2} \quad \text{for} \quad R \le a\,. \tag{5}$$

Analytical solution can be found using the Green function method [2]. It can be shown that the only non-zero displacement is in the z-direction (for $R \in (0, a)$) and is equal to

$$u_z = \frac{\pi\left(1-\sigma^2\right) a\, p(0)}{E} = d\,. \tag{6}$$

The indentation size is the same under the entire indentor area and corresponds to the depth of indentation d (Fig. 1 and Fig. 2).

$$F_z = \frac{2aE}{\left(1-\sigma^2\right)} d \tag{7}$$

Equation (7) is essential for determining the elastic material constants from the indentation test.

For large deformations, it is necessary to find Green's tensor of deformation $\boldsymbol{C}$ (10) and its own numbers (in cylindrical coordinates)

$$\begin{aligned} C_r &= \frac{a_{11} + \Lambda_z^2}{2} + \sqrt{\left(a_{11} - \Lambda_z^2\right)^2 + 4a_{31}^2}, \\ C_\varphi &= \left(\frac{r}{R}\right)^2, \\ C_z &= \frac{a_{11} + \Lambda_z^2}{2} - \sqrt{\left(a_{11} - \Lambda_z^2\right)^2 + 4a_{31}^2} \end{aligned} \quad \text{where} \quad \begin{aligned} a_{11} &= \left[1 + \left(\delta \frac{d}{r}\left(\frac{a}{r}\right)^{\delta}\right)^2\right]\left(\frac{\partial r}{\partial R}\right)^2, \\ a_{31} &= -\left(\delta\Lambda_z \frac{d}{r}\left(\frac{a}{r}\right)^{\delta}\right)\left(\frac{\partial r}{\partial R}\right). \end{aligned} \tag{8}$$

Variable Λ_z represents compression of material in the z direction and δ is the surface curvature parameter. Next can be used (3).

To determine the viscosity of the material can use the (2b) and the Oldquist equation (4). For unidirectional load can be written

$$\begin{aligned} t^{ij} &= t_{\text{el}}^{ij} + t_{\text{dis}}^{ij}, \qquad \text{where} \qquad t_{\text{el}}^{ij} = Ke_{(1)}\delta^{ij} + 2\hat{\mu}\overset{(o)}{e}{}^{ij}, \quad t_{\text{dis}}^{ij} = 2\mu\overset{(o)}{d}{}^{ij}, \\ t_{\text{dis}}^{zz} &= 2\mu\overset{(o)}{d}{}^{zz} = \frac{4}{3}\mu_0\left(\frac{2}{3}\right)^n d_{zz}^{2n-1}, \qquad n \in \langle 0.5; 1\rangle \end{aligned} \tag{9}$$

where μ_0 [Pa.s] is the coefficient of viscosity. The velocity deformation tensor d_{ij} can be obtained from the tensor of large deformations

$$2d_{ij} = \mathbf{F}^{-T}\dot{\mathbf{C}}\mathbf{F}^{-1}, \qquad \mathbf{C} = \mathbf{F}^{T}\mathbf{F} \tag{10}$$

for small deformations, then

$$d_{zz} = \dot{e}_{zz} = -\frac{8\dot{d}}{3\pi a} \approx \left(-\frac{8}{\pi}\frac{d}{a^2}\dot{d}\right) \tag{11}$$

5. Discussion

From the experimental point of view, it is difficult to determine the coefficients j, Λ_z, n and δ. The coefficient μ_0 can be determined from the velocity of indentation $\dot{d}$ at the corresponding stress.

6. Conclusion

The present study offers a theoretical analysis of indentation tests to determine the viscoelastic properties of soft tissues. The results can be used to objectify palpation examinations of the locomotor system by myotonometry.

The proposed concept can be further developed for FEM and layered composite materials. Can be used to study the mechanical properties of 3D structures (nonwovens, fibrous, nanofibrous and composite structures, or foam materials).

Acknowledgements

The work has been supported by the grants projects TG01010117 – PROSYKO and SGS Technical University of Liberec.

References

[1] Humphrey, J.D., Cardiovascular solid mechanics: cells, tissues, and organs, Springer, New York, 2002.
[2] Landau, L.D., Lifschitz, E.M., Theoretical physics, vol. 7: Theory of elasticity, Oxford, 1999.
[3] Maršík, F., Termodynamika kontinua, Praha, 1999.
[4] Taber, L.A., Nonlinear theory of elasticity: applications in biomechanics, River Edge, 2004.

COMPUTATIONAL MECHANICS 2019
35th conference with international participation
Srní
November 4 - 6, 2019

Structural elements of multifloor frames

P. Brož[a]

[a] *Faculty of Applied Sciences, University of West Bohemia in Pilsen, Univerzitní 8, 301 00 Plzeň, Czech Republic*

1. Space supporting systems

In compliance with the vertical structural elements composition we divide systems into skeletals, bearing-walls, and combined ones. In principle, we divide structural elements into two groups: the first said are bar elements and the second form flat ones. Walls are the flat plane structural elements loaded primarily in the middle-plane level that can be shaped like web girders and shear walls. The web girders exploit a load-bearing web of the higher floor to release the lower floor layout. Shear walls represent the basic components of the three-dimensional stiffening of a building, these walls transfer the horizontal even vertical loads to foundation construction.

2. Stiffening elements under horizontal loading

As a rule, stiffening elements are made up of shear walls and communication cores, transferring not only the horizontal loadings but they represent even the vertical loading carry-over. [2] It is possible to determine the vertical loading magnitude from the issues analysis of floor plates or approximately from load areas of the adjacent floor structures. The horizontal loadings of the elements tackled are stipulated by both the building position and its structural design. Horizontal loading usually acting on buildings, apart from other things, are represented by eg

- extraordinary horizontal loading
- geotechnics load
- seismicity loading

2.1 Earth pressure loading

This pressure can range whatever values between the active and passive pressure subject to the magnitude and strain direction, and displacement of both, the construction or its part. For very small (virtually negligible) strains of the structure, a soil acts for the most part in an elastic state, for bigger deformations, the structure under earth pressure gain importance the plastic (irreversible) deformation constituents gradually earth pressure ranges the increased active pressure values, and when squeezing into the soil more, plastic deformation constituents gradually gain importance and the earth pressure ranges magnitudes of the reduced passive pressure.

2.2 Earth pressure at a standstill

This pressure is expressed by a magnitude of the initial pressure at a standstill before building works are commenced which will be then influenced by technological processes when building up the supporting structure. The pressure at a standstill represents region of the predominant elastic deformation without almost significant strains. The limit values of the

earth pressure at a standstill are “active earth pressure” (the least value) and “passive earth pressure” (the highest value).

$$\sigma_0 = \sigma_z \,.\, K_0 ,$$

where

$$K_0 = (1 - \sin \varphi')\sqrt{OCR},$$

φ' effective coefficient of soil internal friction, for cohesive soils it is possible instead φ' introduce $\operatorname{tg} \varphi_c = \operatorname{tg} \varphi + c/\sigma_z$,

φ soil internal friction angle,

c soil cohesion,

σ_z vertical pressure at depth z,

OCR coefficient of overcondolidation.

2.3 Extraordinary loading

Eg the gas explosion loading is in question, or the vehicle impacts (such as at the garages, car parks) or the high-lift trucks (in the halls and storage structures).

2.4 Gas explosion loading

The design pressure is contemplated as larger from among quantities

$$p_{Ed} = 3.0 + p_v \ [\mathrm{kN/m^2}] \ \text{and} \ p_{Ed} = 3.0 + 0.5 \,.\, p_v + 0.04 \,/\, (A_v/V)\ 2 \ [\mathrm{kN/m^2}],$$

where p_v is an evenly distributed statical pressure in kN/m2 when the infilling elements are damaged.

For glass walls is considered $p_v = 3\mathrm{kN/m^2}$,

A_v area of exhaust elements in $\mathrm{m^2}$,

V space volume in $\mathrm{m^3}$.

The relations hold good for $V \leq 1000\ \mathrm{m^3}$ and A_v/V ranges from 0.05 to 0.15 $\mathrm{m^{-1}}$.

2.5 Seismic effects

In a simplified fashion, this loading can be transferred to the horizontal forces loading applied in floor plate planes. In is necessary to consider the seismic loads if those are larger than the 1.5 multiple of wind loading. When performing a reduced calculation of equivalent horizontal forces, we determine the first natural frequency of the building.

2.6 Dynamic structural characteristics:

Magnitude	X direction	Y direction
Stiffness constant to calculate natural frequency	$K_x = 3EI_x/h_i^3$	$K_y = 3EI_y/h_i^3$
Natural frequency	$\omega_x = \sqrt{K_x/M}$	$\omega_y = \sqrt{K_y/M}$
Vibration period	$T_{1x} = 2\pi/\omega_x$	$T_{1y} = 2\pi/\omega_y$
Design value of spectrum acceleration corresponding to vibration period	$S_{dx} = S_d(T_{1x})$	$S_{dy} = S_d(T_{1y})$
Total equivalent horizontal force	$F_{bx} = S_{dx} \cdot M \cdot \lambda_x$	$F_{bx} = S_{dx} \cdot M \cdot \lambda_x$

In the event of reduced method of equivalent horizontal forces determination, the biggest value of the spectrum acceleration is usually considered (B – C region).

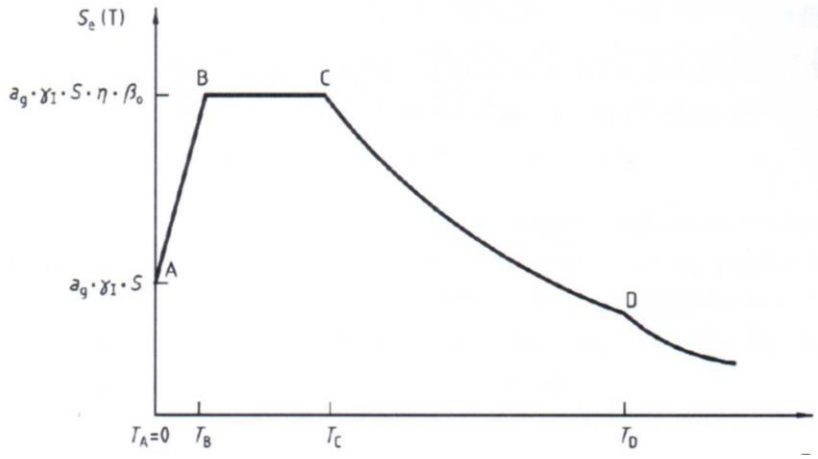

Fig. 1. Spectrum acceleration belonging to the construction work location, [1]

3. Design documentation

Within the bounds of program documentation of a multifloor structure there is chiefly important to determine the loading on its walls and columns. Concurrently, load-bearing reinforced concrete elements are dimensioned above all with respect to the horizontal reinforcement, and further the load-carrying capacity for masonry, steel connections, and timber plates is checked.

Eg, according to [3], program problems can embrace: wind loading determination; design walls and columns; global loading division of both floor slabs and bed-plate foundations; control of both actions and loading stages; imperfect loadings determination (earthquake loading, response forces, buckling resistance coefficients); determination of the extreme loads for walls and columns; vertical loadings summarisation; verification dependent on material; presentation of results.

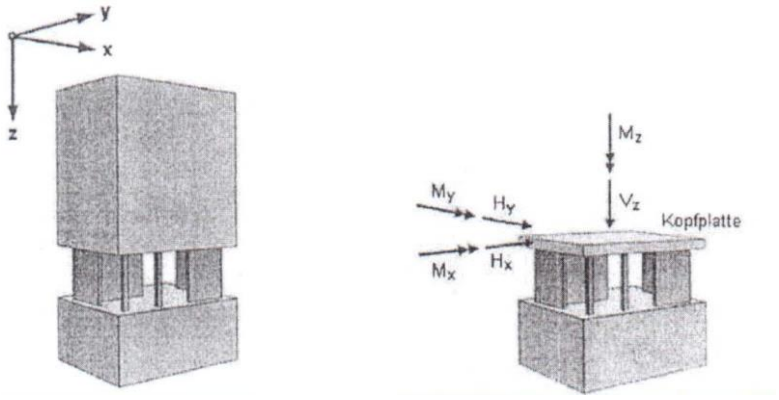

Fig. 2. Top building being load himself, [3]

Problem algorithm is illustrated in Fig. 2. A top part of the building originates loading in the form of both the dead load and imposed one. It is subjected to further loadings (eg snow) and primarily also to horizontal wind loads and aptly as loading or imperfect one.

Loadings can be summarized and transferred to a floor slab in the top edge height of the monitored storey. Now, it is necessary to prove that the walls and columns can jointly catch these loadings when applying safety defined concepts. In order to a necessity is to divide loadings into individual load – bearing elements. This division is performed in a ratio of walls to columns taking into account the facts in this way, that supporting elements react by diverse

response forces to a displacement (rotation) of the plates. It is assumed that the walls are subject in the wall direction only. Possible wall loadings scheme is fully described by the quantities qa_i, qe_i and H_i. This approach will be a success all the time, at least, if three walls are defined which do not lie on line, its basic lines do not intersect in the same point and some of whom one wall has not located parallel to the other one.

4. Conclusions

In the paper presented, important problems of both the design and assessment of multi-storey structures are laid down, particularly horizontal stiffness guarantee, coupling and analysis of shape factors of structural elements, what is connected with requirements for their layout and systematization of horizontal loadings. In next part, the guidelines for operating sequence in the points concerning, apart from other things, eg material properties and dimensioning reinforced concrete and columns.

Acknowledgements

The account of Department of Mechanics (Faculty of Applied Sciences) for overheads was credited with outgoings of the presented research. It is highly appreciated.

References

[1] Albert, A., Bautabelle für Ingenieure mit Berechnungshinweisen und Beispielen, Köln, 2014.
[2] Procházka, J., Šmejkal, J., Concrete multiple-storey and hall construction, CTU Prague, 2018. (in Czech)
[3] 4H-HORA Horizontale Aussteifung, Hannover, 2016.

COMPUTATIONAL MECHANICS 2019
35th conference with international participation
Srní
November 4 - 6, 2019

Vibration analysis of a turbine blading with frictional inter-blade couplings

J. Brůha[a], V. Zeman[a]

[a] *Department of Mechanics, Faculty of Applied Sciences, University of West Bohemia, Univerzitní 8, 301 00 Plzeň, Czech Republic*

Vibration analysis of interacting blades is an essential part in steam turbine design. However, modern large-scale finite-element-based computational models with a considerable number of degrees of freedom constitute challenges when used in dynamic simulations due to their complexity and time-consuming computations. Thus, various model reduction techniques are employed to lower the computational costs [1, 3]. In this contribution, a new generalized modal reduction method based on the complex modal values of the linearized nonconservative system is utilized.

Let us consider a rotating turbine blading with frictional inter-blade couplings (see Fig. 1). The corresponding equations of motion can be written in the form

$$\boldsymbol{M}\ddot{\boldsymbol{q}} + (\boldsymbol{B} + \omega_0 \boldsymbol{G})\,\dot{\boldsymbol{q}} + \left[\boldsymbol{K}_S + \omega_0^2\,(\boldsymbol{K}_\omega - \boldsymbol{K}_{\mathrm{so}}) + \boldsymbol{K}_C\right]\boldsymbol{q} = \boldsymbol{f}_F\,(\boldsymbol{q}, \dot{\boldsymbol{q}}) + \boldsymbol{f}_E\,(t)\,, \qquad (1)$$

where $\boldsymbol{q}$ is the global vector of the generalized coordinates of all blades, $\boldsymbol{M}$, $\boldsymbol{B}$, $\omega_0\boldsymbol{G}$, $\boldsymbol{K}_S$, $\omega_0^2\boldsymbol{K}_\omega$ and $-\omega_0^2\boldsymbol{K}_{\mathrm{so}}$ are the block-diagonal matrices of mass, internal damping, gyroscopic effects, static stiffness, centrifugal stiffening and softening due to modelling in the rotating frame, respectively, $\boldsymbol{K}_C$ is the stiffness matrix corresponding to the linearized normal contact forces in couplings, $\boldsymbol{f}_F\,(\boldsymbol{q}, \dot{\boldsymbol{q}})$ is the vector of the nonlinear frictional forces and $\boldsymbol{f}_E\,(t)$ is the

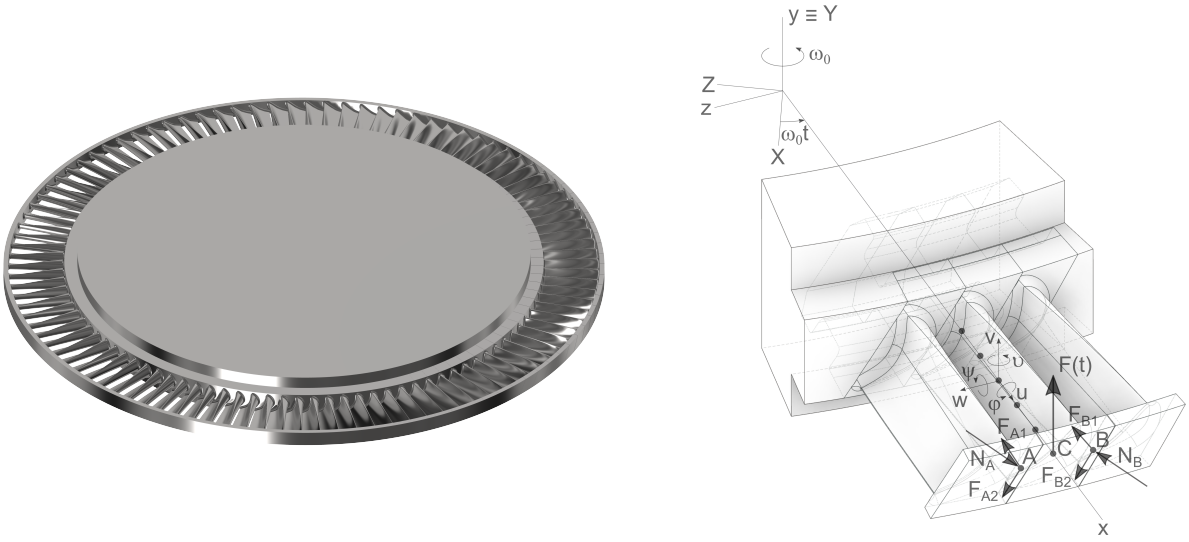

Fig. 1. (*Left*) Bladed turbine disk consisting of one hundred MTD30-HP15 blades; (*right*) drawing of a segment of the disk with contact forces

vector of the harmonic excitation forces. Eq. (1) may then be expanded to the state-space form

$$\boldsymbol{N}\dot{\boldsymbol{u}} + \boldsymbol{P}\boldsymbol{u} = \boldsymbol{p}, \tag{2}$$

where

$$\boldsymbol{u} = \begin{bmatrix} \dot{\boldsymbol{q}} \\ \boldsymbol{q} \end{bmatrix}, \quad \boldsymbol{N} = \begin{bmatrix} \boldsymbol{0} & \boldsymbol{M} \\ \boldsymbol{M} & \boldsymbol{B} + \omega_0 \boldsymbol{G} \end{bmatrix},$$
$$\boldsymbol{P} = \begin{bmatrix} -\boldsymbol{M} & \boldsymbol{0} \\ \boldsymbol{0} & \boldsymbol{K}_S + \omega_0^2 \left(\boldsymbol{K}_\omega - \boldsymbol{K}_{\text{so}}\right) + \boldsymbol{K}_C \end{bmatrix}, \quad \boldsymbol{p} = \begin{bmatrix} \boldsymbol{0} \\ \boldsymbol{f}_F\left(\boldsymbol{q}, \dot{\boldsymbol{q}}\right) + \boldsymbol{f}_E\left(t\right) \end{bmatrix}. \tag{3}$$

In the first step, modal analysis of the linearized homogenous system

$$\boldsymbol{N}\dot{\boldsymbol{u}} + \boldsymbol{P}\boldsymbol{u} = \boldsymbol{0} \tag{4}$$

is performed. Complex right $\boldsymbol{U}$ and left $\boldsymbol{W}$ modal matrices (in the state space) can be written as

$$\boldsymbol{U} = \begin{bmatrix} \boldsymbol{Q}\boldsymbol{\Lambda} \\ \boldsymbol{Q} \end{bmatrix}, \qquad \boldsymbol{W} = \begin{bmatrix} \boldsymbol{R}\boldsymbol{\Lambda} \\ \boldsymbol{R} \end{bmatrix}, \tag{5}$$

where $\boldsymbol{Q}$ and $\boldsymbol{R}$, corresponding to complex spectral matrix $\boldsymbol{\Lambda}$, represent complex right and left modal matrices in generalized coordinates, respectively. Nevertheless, we consider only the reduced spectral matrix

$$\boldsymbol{\Lambda}_{\text{red}} = \text{diag}[\lambda_1, \ldots, \lambda_R, \lambda_1^*, \ldots, \lambda_R^*] = \text{diag}[\boldsymbol{\Lambda}_{\text{sub}}, \boldsymbol{\Lambda}_{\text{sub}}^*], \tag{6}$$

where λ_i, $i = 1, 2, \ldots, R$, are selected (master) complex eigenvalues with positive imaginary parts and λ_i^* are their complex conjugates. Potential real eigenvalues are excluded. Corresponding right $\boldsymbol{U}_{\text{red}}$ and left $\boldsymbol{W}_{\text{red}}$ reduced modal matrices in the form

$$\boldsymbol{U}_{\text{red}} = \begin{bmatrix} \boldsymbol{Q}_{\text{red}}\boldsymbol{\Lambda}_{\text{red}} \\ \boldsymbol{Q}_{\text{red}} \end{bmatrix}, \qquad \boldsymbol{W}_{\text{red}} = \begin{bmatrix} \boldsymbol{R}_{\text{red}}\boldsymbol{\Lambda}_{\text{red}} \\ \boldsymbol{R}_{\text{red}} \end{bmatrix} \tag{7}$$

are composed of the matrices

$$\boldsymbol{Q}_{\text{red}} = \left[\boldsymbol{Q}_{\text{sub}}, \boldsymbol{Q}_{\text{sub}}^*\right], \qquad \boldsymbol{R}_{\text{red}} = \left[\boldsymbol{R}_{\text{sub}}, \boldsymbol{R}_{\text{sub}}^*\right], \tag{8}$$

where the submatrices $\boldsymbol{Q}_{\text{sub}}$ and $\boldsymbol{R}_{\text{sub}}$ contain master complex eigenvectors corresponding to the eigenvalues λ_i and the submatrices $\boldsymbol{Q}_{\text{sub}}^*$ and $\boldsymbol{R}_{\text{sub}}^*$ contain their corresponding complex conjugates.

In the second step, applying modal transformation

$$\boldsymbol{u} = \boldsymbol{U}_{\text{red}}\, \boldsymbol{x}, \tag{9}$$

where

$$\boldsymbol{x} = [x_1, \ldots, x_R, x_1^*, \ldots, x_R^*]^T = \begin{bmatrix} \boldsymbol{x}_{\text{sub}} \\ \boldsymbol{x}_{\text{sub}}^* \end{bmatrix} \tag{10}$$

is the vector of the master complex modal coordinates x_i, $i = 1, 2, \ldots, R$, and their complex conjugates x_i^*, and with regard to the biorthonormality conditions

$$\boldsymbol{W}_{\text{red}}^T \boldsymbol{N} \boldsymbol{U}_{\text{red}} = \boldsymbol{E}, \qquad \boldsymbol{W}_{\text{red}}^T \boldsymbol{P} \boldsymbol{U}_{\text{red}} = -\boldsymbol{\Lambda}_{\text{red}}, \tag{11}$$

where $\boldsymbol{E}$ is the identity matrix, Eq. (2) leads to

$$\begin{bmatrix} \dot{\boldsymbol{x}}_{\text{sub}} \\ \dot{\boldsymbol{x}}_{\text{sub}}^* \end{bmatrix} - \begin{bmatrix} \boldsymbol{\Lambda}_{\text{sub}} & \boldsymbol{0} \\ \boldsymbol{0} & \boldsymbol{\Lambda}_{\text{sub}}^* \end{bmatrix} \begin{bmatrix} \boldsymbol{x}_{\text{sub}} \\ \boldsymbol{x}_{\text{sub}}^* \end{bmatrix} = \begin{bmatrix} \boldsymbol{R}_{\text{sub}}^T \\ \boldsymbol{R}_{\text{sub}}^H \end{bmatrix} \left[\boldsymbol{f}_F \left(\boldsymbol{q}, \dot{\boldsymbol{q}} \right) + \boldsymbol{f}_E \left(t \right) \right]. \tag{12}$$

Finally, the dynamic response in the generalized coordinates is, according to relations (3), (7), (8), (9) and (10), given by

$$\boldsymbol{q} = \boldsymbol{Q}_{\text{sub}} \boldsymbol{x}_{\text{sub}} + \boldsymbol{Q}_{\text{sub}}^* \boldsymbol{x}_{\text{sub}}^* = 2\,\text{Re}\left(\boldsymbol{Q}_{\text{sub}} \boldsymbol{x}_{\text{sub}} \right), \tag{13}$$

$$\dot{\boldsymbol{q}} = \boldsymbol{Q}_{\text{sub}} \boldsymbol{\Lambda}_{\text{sub}} \boldsymbol{x}_{\text{sub}} + \boldsymbol{Q}_{\text{sub}}^* \boldsymbol{\Lambda}_{\text{sub}}^* \boldsymbol{x}_{\text{sub}}^* = 2\,\text{Re}\left(\boldsymbol{Q}_{\text{sub}} \boldsymbol{\Lambda}_{\text{sub}} \boldsymbol{x}_{\text{sub}} \right). \tag{14}$$

The presented methodology was used to perform vibration analysis of the high-pressure turbine blading consisting of one hundred MTD30-HP15 blades [2] (see Fig. 1), where three different values of the coefficient of friction f were compared (see Fig. 2). It proved to be a valuable tool and provided a computationally cheap approach without incurring significant loss of accuracy.

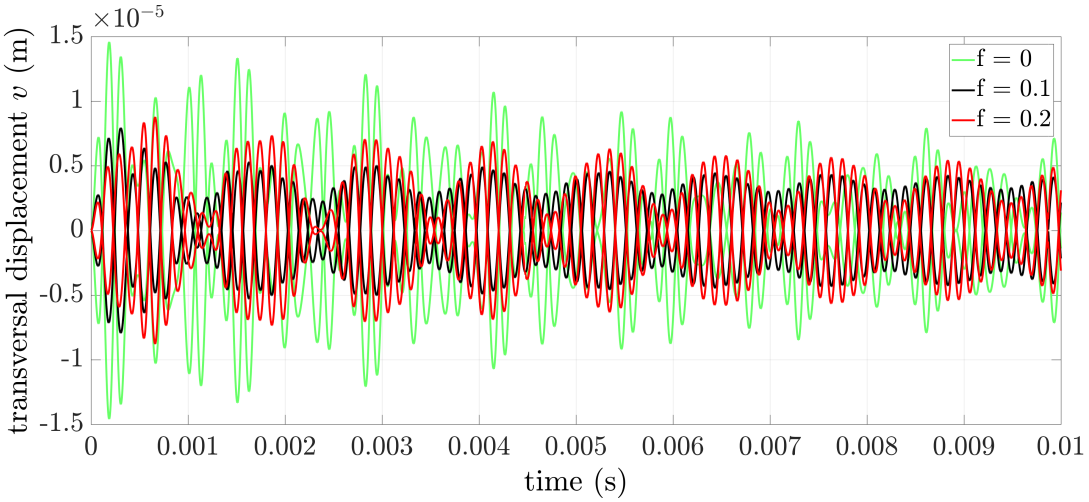

Fig. 2. Dynamic response of the blades to harmonic excitation for three different values of the coefficient of friction f

Acknowledgements

This work was supported by the internal student grant project SGS-2019-009 of the University of West Bohemia and by the project TE01020068 "Centre of research and experimental development of reliable energy production" of the Technology Agency of the Czech Republic.

References

[1] Besselink, B., Tabak, U., Lutowska, A., Wouw, N., Nijmeijer, H., Rixen, D. J., Hochstenbach, M. E., Schilders, W. H. A., A comparison of model reduction techniques from structural dynamics, numerical mathematics and systems and control, Journal of Sound and Vibration 332 (2013) 4403-4422.

[2] Kubín, Z., Hlous, J., Measurement of a rhombic bladed disk, Technical Report, Doosan Škoda Power, 2013.

[3] Lozovskiy, A., The modal reduction method for multi-body dynamics with non-smooth contact, International Journal for Numerical Methods in Engineering 98 (2014) 937-959.

COMPUTATIONAL MECHANICS 2019
35th conference with international participation
Srní
November 4 - 6, 2019

Fast pressure prediction along the NACA airfoil using the convolution neural network

O. Bublík[a]

[a] *NTIS – New Technologies for the Information Society, Faculty of Applied Sciences, University of West Bohemia, Univerzitní 8, 301 00 Plzeň, Czech Republic*

Convolution neural network (CNN) is a class of neural networks developed for image processing. The common use of CNN lies in objects classification or image segmentation, see Fig. 1. A typical CNN architecture consists of a sequence of convolution and pooling layers, see Fig. 1 (left). The convolution layers provide the convolution using a selected kernel function, while the pooling layers reduce the data dimensions. At the output of the CNN is fully connected (dense) neural network, which can make an object classification, see Fig. 1 (left). In the case of image segmentation (Fig. 1 (right)), the additional layers are connected to the output of dense neural network to recover the original shape of the input data. The additional layers are created using convolution and up-sampling (reversed to pooling) layers. The resulting CNN is usually called autoencoder or U-net, see Fig. 2. The autoencoder (U-net) is the base architecture for the use of CNN in physical modelling.

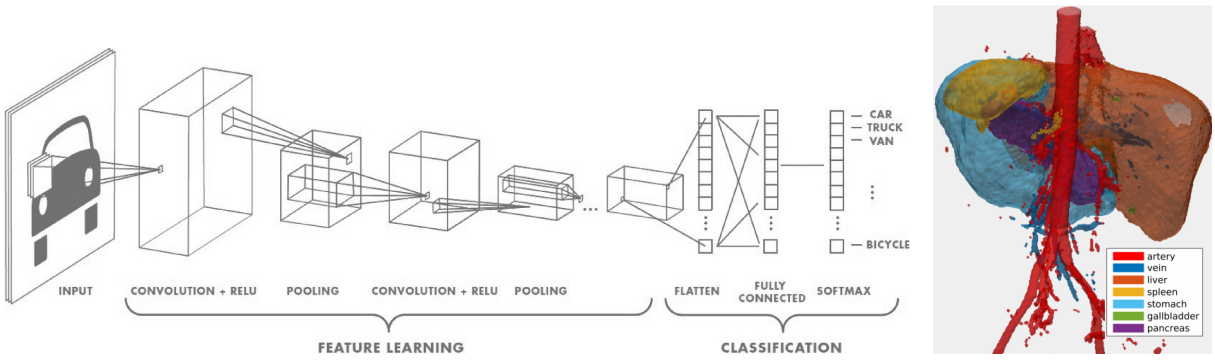

Fig. 1. (*Left*) The use of the CNN for the cars classification. The image was taken from the web site [7]. (*Right*) The use of the CNN for the organ segmentation in the human body [6].

The pioneering use of the CNN for the steady fluid flow simulation was published in the paper [4], where the input image, which contains the boundary information, was transformed to the velocity field. The CNN was trained on the set of solutions, for various boundaries, solved by the lattice Boltzmann method. The results show good accuracy of the generated velocity field. The use of CNN for the unsteady fluid flow simulation was described in [5].

This work aims to use CNN for the pressure prediction along the NACA airfoil and establish the lift and drag coefficients. The knowledge of the lift and drag coefficients in dependence on the angle of attack is the most important airfoil characteristic. The determination of the lift and drag coefficients by the classical CFD methods, such as finite volume or finite element methods, is very time-demanding. This is inappropriate when a new profile is being designed

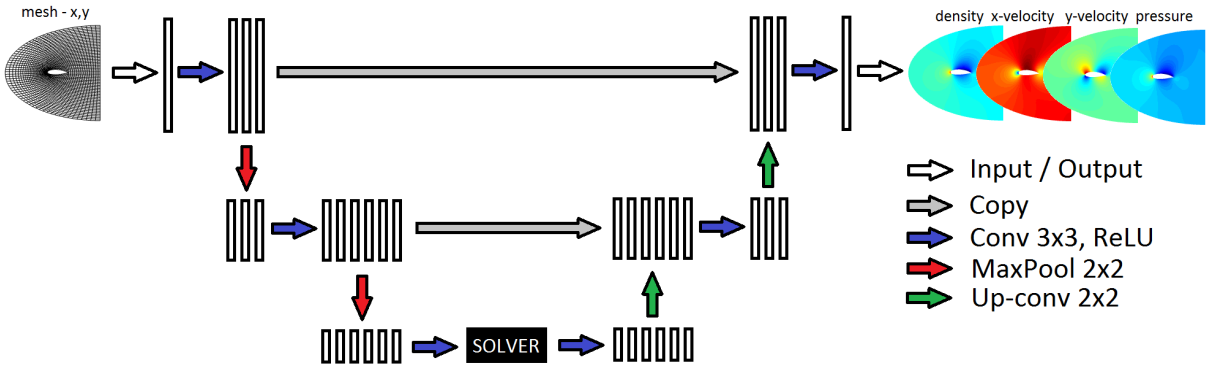

Fig. 2. Architecture of the U-net CNN used for the pressure prediction around a NACA airfoil

using the optimisation techniques, where the calculation of the pressure field for many different variations of the geometry is necessary. The use of CNN aims to utilize the fast prediction of the flow field, from which the pressure distribution around NACA airfoil could be extracted.

For the prediction of the flow field the U-net architecture described above was considered. The x and y coordinates of the structured C-mesh with 64×32 points was set as a CNN input, see Fig. 3. At the output the flow field, which includes density, pressure and velocity in x and y directions, is generated. The CNN include two decoding and encoding convolution layers with ReLU (Rectified Linear Unit) activation function. The dense neural network (basically fluid flow solver) between decoder and encoder has four layers. The CNN contains 106 324 trainable parameters in total.

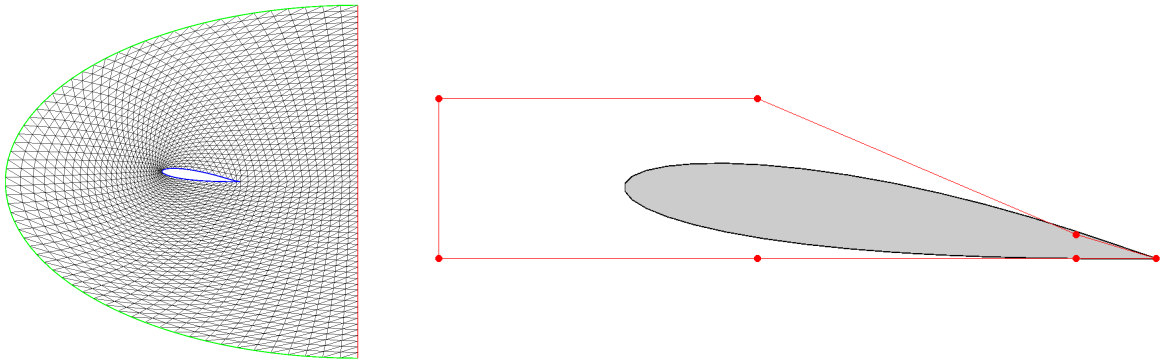

Fig. 3. (*Left*) C-mesh around an airfoil generated using the elliptic mesh generator. (*Right*) Airfoil generated by Bezier curve with eight control points (red dots).

The input C-mesh is generated using the elliptic mesh generator. The airfoil body in the center of the C-mesh is described using the Bezier curves with eight control points $X_p = [x_p, y_p]$, $p = 1, 2, ..., 8$, where the first and the last control points are the same at the tail of the airfoil. For the simplicity, the x_p coordinates of the control points were fixed and y_p coordinates were varying in the interval $[-0.25, 0.25]$. The airfoil was consequently parametrized by six free parameters. The choice of five division per interval for each y_p leads to $6^5 = 7776$ variants of the airfoils. After filtering the inappropriate airfoils, for example with a negative area, the set of 1866 airfoils were left. The simulation of fluid flow around each of airfoils was performed using the open-source CFD software FlowPro [2]. The nonlinear system of Euler equations was chosen for the simulation of inviscid fluid flow. The angle of attack was set to $\alpha = 0$ and Mach number to $M_\infty = 0.4$. For the speed-up of the calculation, only the first order of spatial accuracy was utilised. The numerical simulation of all the 1866 airfoil variants took 7.4 hours of the

Table 1. The relative error of the generated lift coefficient for different angles of attack α and NACA four digit airfoils

α / profile	0012	2412	4412	6615	8607	9210	0020	0030
5°	2.57	3.45	0.24	6.12	2.07	4.76	2.63	2.60
10°	2.89	2.71	2.39	6.29	0.75	0.56	0.93	5.30
20°	4.50	4.11	3.32	3.52	3.88	1.92	3.00	4.54

CPU time (intel i7, 4-cores), where pure computation took 4.5 hours and the mesh generation with the preliminary phase took the rest of the CPU time.

The implementation of CNN was done using the open-source software Keras [3] through the python interface. The Keras software provides an interface to a TensorFlow [1] library, which is an open-source software library for dataflow used for machine learning. The designed neural network was trained on the full set of 1866 airfoils, with RMSProp (Root Mean Square Prop) optimiser. The evaluation of all the airfoils with the CNN took 10.7 s of CPU time, which is approximately 1500 times faster than computation by traditional computation methods.

The precision of CNN generated solution was tested on the set of NACA profiles, which were not presented in the training set. Table 1 shows the relative error between the CFD solution and the generated CNN solution computed as

$$\text{error} = 100\,\frac{|c_L^{CFD} - c_L^{CNN}|}{c_L^{CFD}}\,[\%].$$

The relative error is below five percent in most cases, which is a good result. Together with the speed of generation, CNN can be used as a powerful tool in the optimisation process. Fig. 4 shows the NACA 4412 airfoil and the corresponding CFD and CNN pressure fields around the airfoil body for different angles of attack.

Acknowledgement

This research is supported by the project "Centre of research and experimental development of reliable energy production" TE01020068 of the Technology Agency of the Czech Republic.

References

[1] Abadi, M., Agarwal, A., Barham, P., Brevdo, E., Chen, Z., Citro, C., Corrado, G. S., Davis, A., Dean, J., Devin, M. et al., TensorFlow: Large-scale machine learning on heterogeneous systems, software, 2015, https://tensorflow.org

[2] Bublík, O., Pecka, A., Vimmr, J., FlowPro – multipurpose CFD software written in Java, Proceedings of the 33rd conference Computational Mechanics, University of West Bohemia, Špičák, 2017, pp. 13-14.

[3] Chollet, F. et al., Keras: The Python deep learning library, 2015, https://keras.io

[4] Guo, X., Li, W., Iorio, F., Convolutional neural networks for steady flow approximation, Proceedings of the ACM SIGKDD International Conference on Knowledge Discovery and Data Mining, 2016, doi: 10.1145/2939672.2939738.

[5] Hennigh, O., Lat-Net: Compressing lattice Boltzmann flow simulations using deep neural networks, 2017, arXiv:1705.09036. (preprint)

[6] Roth, H. R., Oda, H., Zhou, X., Shimizu, N., Yang, Y., Hayashi, Y., Oda, M., Fujiwara, M., Misawa, K., Mori, K., An application of cascaded 3D fully convolutional networks for medical image segmentation, Computerized Medical Imaging and Graphics 66 (2018) 90-99.

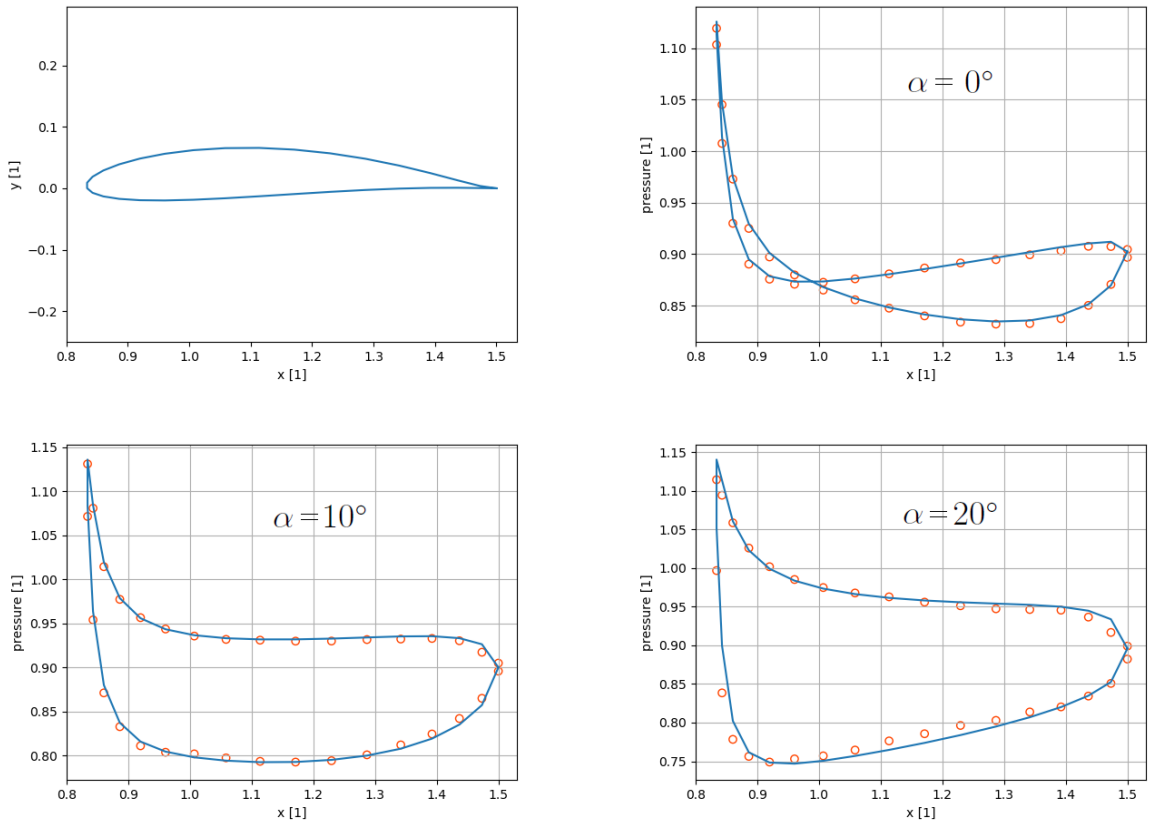

Fig. 4. Pressure field around NACA 4412 airfoil. The blue line represents pressure field obtained by CFD simulation, while red circles represent pressure field generated by CNN.

[7] Saha, S., A comprehensive guide to convolutional neural networks — The ELI5 way, 2018, https://towardsdatascience.com/a-comprehensive-guide-to-convolutional-neural-networks-the-eli5-way-3bd2b1164a53

COMPUTATIONAL MECHANICS 2019
35th conference with international participation
Srní
November 4 - 6, 2019

Overview of absolute nodal coordinate formulation and usage of recently formulated finite elements

R. Bulín[a]

[a] *NTIS – New Technologies for the Information Society, Faculty of Applied Sciences, University of West Bohemia, Technická 8, 301 00 Pilsen, Czech Republic*

This paper is dedicated to a description of finite elements defined using the absolute nodal coordinate formulation (ANCF). The ANCF is a modern finite element formulation which is suitable for modelling of flexible bodies that are parts of multibody systems. The main advantage of these elements is their ability to describe large displacements and rotations of flexible bodies. As it is mentioned in [3, 5], the ANCF elements can exactly describe an arbitrary rigid body motion of a discretized flexible body. This ability is achieved by using absolute position vectors of nodes and their gradients (slopes) with respect to local element coordinates as nodal coordinates. Unlike the ANCF method, classical finite element formulations of beams and shells use infinitesimal rotations instead of slopes as nodal coordinates which leads to a nonzero element elastic forces in case of an arbitrary rigid body motion [5] and thus these classical finite elements are not suitable for large motion problems.

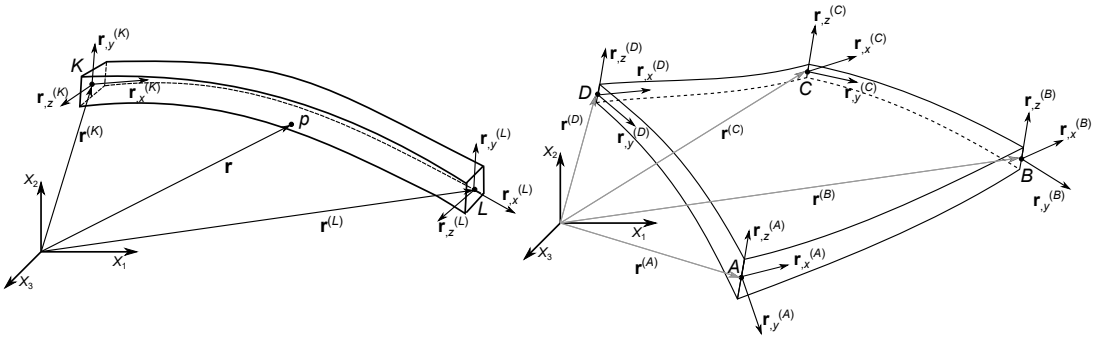

Fig. 1. Deformed fully parameterized ANCF beam element and ANCF plate element with vectors which defining the nodal coordinates (absolute positions of nodes and gradients in nodes)

In Fig. 1, a deformed fully parameterized original ANCF beam element and ANCF plate element are shown. In this picture, coordinates $X_1X_2X_3$ represent the global (absolute) coordinate system and xyz is a local element coordinate system. For the beam element, coordinate $x \in \langle 0,\ l_e \rangle$ is the axial parameter of the beam centerline and l_e is the beam element length. Coordinates y and z are cross-sectional beam coordinates. In case of the plate element, coordinates $x \in \langle 0,\ a_e \rangle$ and $y \in \langle 0,\ b_e \rangle$ are plate mid-surface coordinates and $z \in \langle -\frac{t_e}{2},\ \frac{t_e}{2} \rangle$ represents the coordinate perpendicular to plate mid-surface. Parameters a_e, b_e and t_e are the plate element length, width and thickness.

The absolute position vector of node i is denoted as $\mathbf{r}^{(i)}$, where $i = \{A,\ B,\ C,\ D,\ K,\ L\}$. In Fig. 1, and in further text of this paper, following symbolic notation for partial derivatives of

node position vector is used

$$\mathbf{r}_{,j}^{(i)} = \frac{\partial \mathbf{r}^{(i)}}{\partial j}, \qquad j = \{x,\ y,\ z\}\,. \tag{1}$$

These partial derivatives represent slope vectors or gradients of node position vector with respect to local coordinates.

The nodal coordinates of chosen node i can be written as

$$\mathbf{e}^{(i)} = \left[\mathbf{r}^{(i)T},\ \mathbf{r}_{,x}^{(i)T},\ \mathbf{r}_{,y}^{(i)T},\ \mathbf{r}_{,z}^{(i)T}\right]^T. \tag{2}$$

From Eq. (2), it is apparent, that each node has three positional degrees of freedom and nine degrees of freedom related to the components of three gradients. The ANCF beam element has 24 degrees of freedom because it uses two nodes – K and L. Its resultant vector of nodal coordinates can be expressed as

$$\mathbf{e} = \left[\mathbf{e}^{(K)T},\ \mathbf{e}^{(L)T}\right]^T. \tag{3}$$

The vector of nodal coordinates of the ANCF plate element can be expressed in the similar way with a difference in number of nodes – it uses four nodes (A, B, C and D). The resultant element has 48 degrees of freedom and its vector of nodal coordinates is

$$\mathbf{e} = \left[\mathbf{e}^{(A)T},\ \mathbf{e}^{(B)T},\ \mathbf{e}^{(C)T},\ \mathbf{e}^{(D)T}\right]^T. \tag{4}$$

It must be noted here that the vector $\mathbf{r}_{,z}^{(i)T}$ (plate element) or vectors $\mathbf{r}_{,z}^{(i)T}$ and $\mathbf{r}_{,y}^{(i)T}$ (beam element) can be omitted from the Eq. (2). The resultant element is called gradient-deficient ANCF element [2], its element elastic forces are derived in another manner than it is described later in this paper and these elements are suitable mainly for thin structures.

In case of the original ANCF beam element, the position vector $\mathbf{r}$ of arbitrary beam point p is approximated using cubic polynomials in x and linear polynomials in y and z, which is written in following form [2]

$$\mathbf{r} = \begin{bmatrix} a_0 + a_1x + a_2y + a_3z + a_4xy + a_5xz + a_6x^2 + a_7x^3 \\ b_0 + b_1x + b_2y + b_3z + b_4xy + b_5xz + b_6x^2 + b_7x^3 \\ c_0 + c_1x + c_2y + c_3z + c_4xy + c_5xz + c_6x^2 + c_7x^3 \end{bmatrix}, \tag{5}$$

where coefficients a, b and c can be expressed using known local coordinates of nodes. In case of plate elements it is similar with the difference that a cubic approximation is used in y. Then the interpolation uses following set of basis polynomials

$$\left[1,\ x,\ y,\ z,\ xy,\ xz,\ yz,\ x^2,\ y^2,\ x^3,\ y^3,\ x^2y,\ xy^2,\ xyz,\ x^3y,\ xy^3\right]. \tag{6}$$

After several operations, the global position vector of arbitrary beam/plate point p can be expressed as

$$\mathbf{r} = \mathbf{S}\left(x,\ y,\ z\right)\mathbf{e}, \tag{7}$$

where $\mathbf{S}$ is the matrix of shape functions of a chosen element (differs for beam and plate elements).

After the kinematic description of ANCF elements, the element kinetic energy is

$$E_{ke} = \frac{1}{2}\int_{V_e} \rho \dot{\mathbf{r}}^T \dot{\mathbf{r}} \mathrm{d}V_e, \tag{8}$$

where V_e is the element volume and ρ is material density. With the use of (7), the resultant constant mass matrix has a form

$$\mathbf{M}_e = \int_{V_e} \rho \mathbf{S}^T \mathbf{S} \mathrm{d}V_e. \tag{9}$$

There are several procedures for ANCF element elastic force derivation. The original ANCF elements use the *continuum mechanics approach*. In this formulation, the Saint Venant–Kirchhoff material model is used and the strain energy is

$$U_e = \frac{1}{2} \int_{V_e} \boldsymbol{\varepsilon}^T \mathbf{E} \boldsymbol{\varepsilon} \mathrm{d}V_e, \tag{10}$$

where $\mathbf{E}$ is the matrix of the elastic constants of the material and $\boldsymbol{\varepsilon}$ is the vector of components of Lagrange–Green strain tensor written as

$$\boldsymbol{\varepsilon} = \left[\varepsilon_x,\ \varepsilon_y,\ \varepsilon_z,\ 2\varepsilon_{xy},\ 2\varepsilon_{xz},\ 2\varepsilon_{yz}\right], \tag{11}$$

where

$$\begin{aligned} &\varepsilon_x = \tfrac{1}{2}(\mathbf{r}_{,x}^T \mathbf{r}_{,x} - 1), \quad \varepsilon_y = \tfrac{1}{2}(\mathbf{r}_{,y}^T \mathbf{r}_{,y} - 1), \quad \varepsilon_z = \tfrac{1}{2}(\mathbf{r}_{,z}^T \mathbf{r}_{,z} - 1), \\ &\varepsilon_{xy} = \tfrac{1}{2}\mathbf{r}_{,x}^T \mathbf{r}_{,y}, \qquad \varepsilon_{xz} = \tfrac{1}{2}\mathbf{r}_{,x}^T \mathbf{r}_{,z}, \qquad \varepsilon_{yz} = \tfrac{1}{2}\mathbf{r}_{,y}^T \mathbf{r}_{,z}. \end{aligned} \tag{12}$$

The resultant nonlinear vector of element elastic forces is

$$\mathbf{Q}_e = \frac{\partial U_e}{\partial \mathbf{e}}. \tag{13}$$

Based on the described formulation an in-house software in Matlab that uses ANCF beam and plate elements was created and was used in several applications. The typical benchmark simulation for ANCF beam elements is the simulation of a motion of a flexible pendulum. This benchmark problem is used to demonstrate the ability to describe large motions of the flexible bodies. In Fig. 2, the snapshots of the pendulum motion in discrete time steps are shown. The pendulum is 2 m long, has a square cross-section with the edge length of 0.01 m, material density is 4000 kg.m^{-3}, Young's modulus is 10^8 Pa, Poisson's ratio is 0.3 and 10 ANCF beam elements are used.

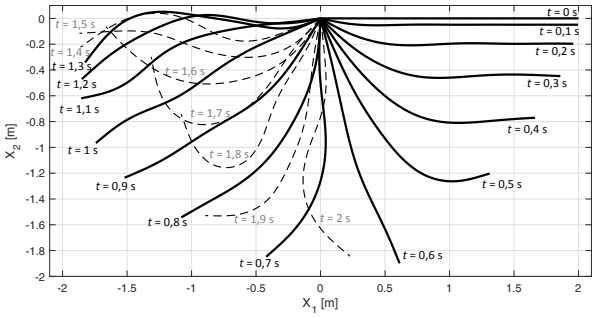

Fig. 2. Visualisation of the flexible pendulum in discrete time steps

Similar benchmark problem is typical for plate elements testing and demonstration – flexible plate pendulum. The tested flexible plate length is 1 m, width is 1 m and thickness is 0.02 m. The plate is connected to the ground by spherical joint in one plate corner. The chosen material density is 1000 kg.m^{-3}, Young's modulus is 10^5 Pa, Poisson's ratio is 0.3 and 8×8 plate elements are used. The snapshots of the flexible plate motion in discrete time steps are shown in Fig. 3.

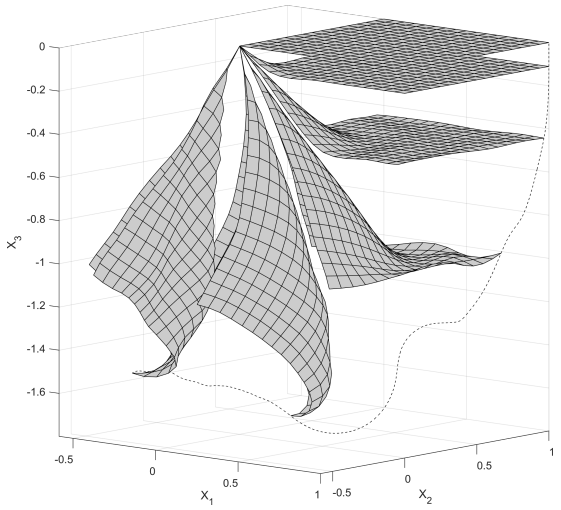

Fig. 3. Visualisation of the flexible plate in discrete time steps

There are a lot of practical use of various ANCF elements. In paper [1] ANCF beam elements were used for cable modelling and the cable–pulley interaction model is investigated and verified by experiment. The ANCF beam and plate elements were successfully used for nonlinear dynamic analysis of parabolic leaf springs in paper [6]. In fact, the ANCF method can be used anywhere, where the flexibility of bodies of multibody systems is not negligible, such as detailed tire modelling, dynamics of thin membrane structures used in aerospace or modelling of railway catenary. For completeness it is necessary to mention that also solid ANCF elements were developed recently [4] and they can be used, e.g., for rubber structures modelling. The main disadvantage of ANCF method is, that the resultant dynamic simulations are relatively time consuming which is caused by nonlinearity of the elastic forces and higher number of element degrees of freedom.

Acknowledgement

This publication was supported by the project LO1506 of the Czech Ministry of Education, Youth and Sports under the program NPU I.

References

[1] Bulín, R., Hajžman, M., Polach, P., Nonlinear dynamics of a cable-pulley system using the absolute nodal coordinate formulation, Mechanics Research Communications 82 (2017) 21-28.

[2] Gerstmayr, J., Shabana, A. A., Analysis of thin beams and cables using absolute nodal co-ordinate formulation, Nonlinear Dynamics 45 (2006) 109-130.

[3] Mikkola, A.M., Shabana, A.A., A Non-incremental finite element procedure for the analysis of large deformation of plates and shells in mechanical system applications, Multibody System Dynamics 9 (2003) 283-309.

[4] Olshevskiy, A., Dmitrochenko, O., Kim, C.-W., Three-dimensional solid brick element using slopes in the absolute nodal coordinate formulation, Journal of Computational and Nonlinear Dynamics 9 (2014) 1-10.

[5] Shabana, A. A., Dynamics of multibody systems, 3rd edition, Cambridge University Press, Cambridge, 2005.

[6] Wang, T., Tinsley, B., Patel, M. D., Shabana, A. A., Nonlinear dynamic analysis of parabolic leaf springs using ANCF geometry and data acquisition, Nonlinear Dynamics 93 (2018) 2487-2515.

COMPUTATIONAL MECHANICS 2019
35th conference with international participation
Srní
November 4 - 6, 2019

Whirl flutter-related certification of turboprop aircraft

J. Čečrdle[a]

[a] Czech Aerospace Research Centre (VZLU), Beranových 130, 199 05 Praha Letňany, Czech Republic

Whirl flutter is aeroelastic flutter instability that may appear on turboprop aircraft. It is driven by motion-induced unsteady aerodynamic propeller forces and moments acting on the propeller plane and it may cause unstable vibration of a propeller mounting, leading to the failure of an engine installation or an entire wing. Therefore, airworthiness regulation standards include also requirements related to the whirl flutter; however, these requirements are specified just generally without any detailed description of the acceptable means and methodologies of compliance. This paper describes the methodology of compliance with the requirements of FAR / CS 23 and 25 regulation standards applicable for utility, commuter and for larger transport aircraft.

The principle of the whirl flutter phenomenon is outlined on a simple mechanical system with two degrees of freedom. A flexible engine mounting is represented by two rotational springs of stiffnesses K_Ψ and K_Θ, as illustrated in Fig. 1.

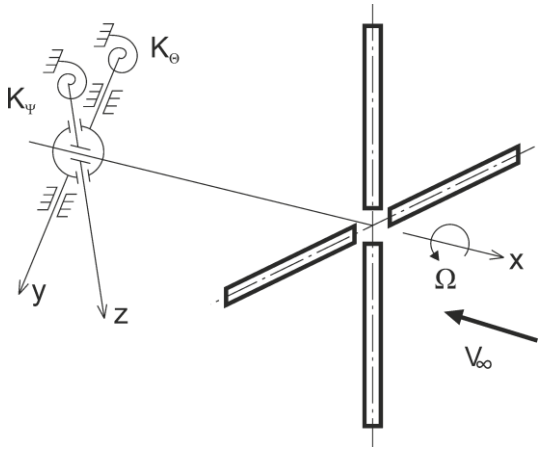

Fig. 1. Gyroscopic system with propeller

Such a system has two independent mode shapes (yaw and pitch) with angular frequencies ω_Ψ and ω_Θ. For a propeller rotation with angular velocity Ω, the gyroscopic effect causes both independent mode shapes to merge into a whirl motion. The axis of rotation of the propeller exhibits an elliptical movement. The orientation is backward relative to the propeller rotation for the mode with the lower frequency (backward whirl mode) and forward relative to the propeller rotation for the mode with the higher frequency (forward whirl mode). The gyroscopic motion results in changes in the propeller blades' angles of attack, consequently leading to unsteady aerodynamic forces. These forces may induce whirl flutter instability. The flutter state is defined as the neutrally stable state with no damping of the system, and the corresponding airflow ($V_\infty = V_{FL}$) is called the critical flutter speed. If the air velocity is lower than flutter speed ($V_\infty < V_{FL}$), the system is stable and the gyroscopic motion is damped

(Fig. 2a). If the airspeed exceeds the flutter speed ($V_\infty > V_{FL}$), the system becomes unstable, and the gyroscopic motion is divergent (Fig. 2b).

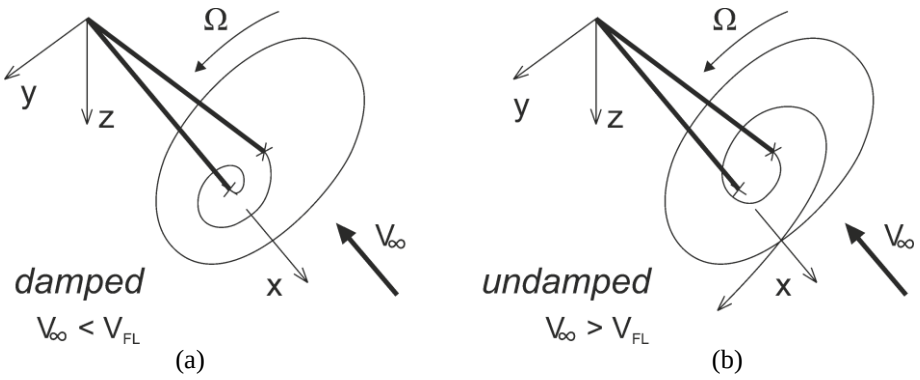

Fig. 2. Stable (a) and unstable (b) states of gyroscopic vibrations for the backward flutter mode

For whirl flutter analysis, two approaches may be employed: 1) Standard approach in which the input data are parameters of a structure and the outputs of the analysis are whirl flutter characteristics, i.e., V-g-f diagrams, and flutter speed and flutter frequency. The solution is performed for multiple velocities and the state with the zero damping represents the critical flutter state. 2) Optimisation-based approach employing gradient-based algorithms. In this case, the flutter speed is set as an input parameter (certification speed), and the results are critical values of structural parameters. This solution, which is performed only for a single velocity, enables to obtain the stability margin for the specified certification speed. The analysed states are then compared with respect to the stability margin only. Such an approach can save large amount of time because the number of analyses required by the regulations is dramatically reduced.

FAR / CS 23 represent the simpler category of standards, applicable to the smaller turboprop aircraft. The whirl flutter-related requirement included in §629(e) is applicable for all configurations of aircraft regardless the number and placement of engine(s). §629(e)(1) includes the main requirement to evidence the stability within the required V-H envelope, while §629(e)(2) requires the variation of structural parameters such as the stiffness and damping of the power plant attachment. The latter represents the influence of the variance of the power plant mount structural parameters when simulating the possible changes due to structural damage (e.g., deterioration of engine mount-isolators). Analysis must include all wing mass configurations, especially fuel load variation. Contrary to that the payload does not have a significant influence. Analyses are performed just for the certification altitude, which is the most critical with respect to both whirl flutter and the value of certification speed ($1.2*V_{DTAS}$). Inertia characteristics of rotating parts must be considered with respect to the directions of rotation of a particular part (generator, turbine, propeller), revolutions are usually normalised to a propeller revolutions. For the purpose of certification analysis, the most critical mode of the propeller and engine revolutions are considered, i.e. the mode that produce the maximal normalised moment of inertia of the rotating parts. To comply with the main requirement (§629(e)(1)), the nominal state analyses are performed. For this purpose, the standard approach is employed. Fig. 3 shows an example of a V-g-f diagram of such a calculation for a single mass configuration. No flutter instability is indicated up to the certification velocity (191.4 m/s), and therefore, the regulation requirement is fulfilled.

To comply with the parameter variation requirement (§629(e)(2)), parametric studies that may include huge numbers of analyses would be necessary and such an approach would become ineffective. Therefore, the analysis of stability margins using optimisation-based approach is good for this purpose. In this approach, the flutter speed is set equal to the

certification speed, and the results are margin values of structural parameters. Fig. 4 shows an example of a V-g-f diagram of optimisation-based calculation in which flutter speed is equal to the certification velocity (191.4 m/s). Flutter mode (#2) is the engine pitch vibration mode.

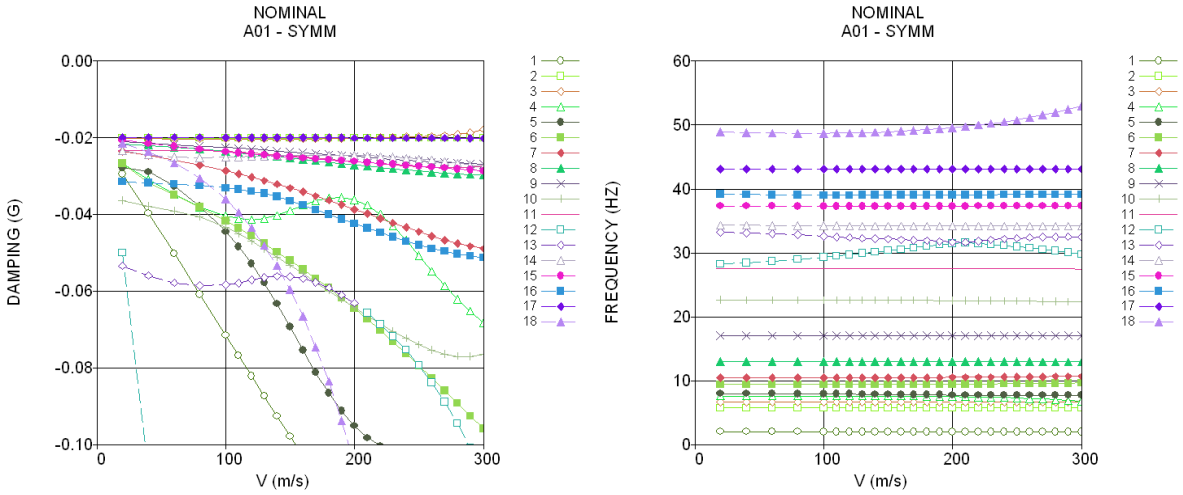

(a) (b)

Fig. 3. Whirl flutter calculation (V-g-f) diagram, (a) damping, (b) frequency, nominal state

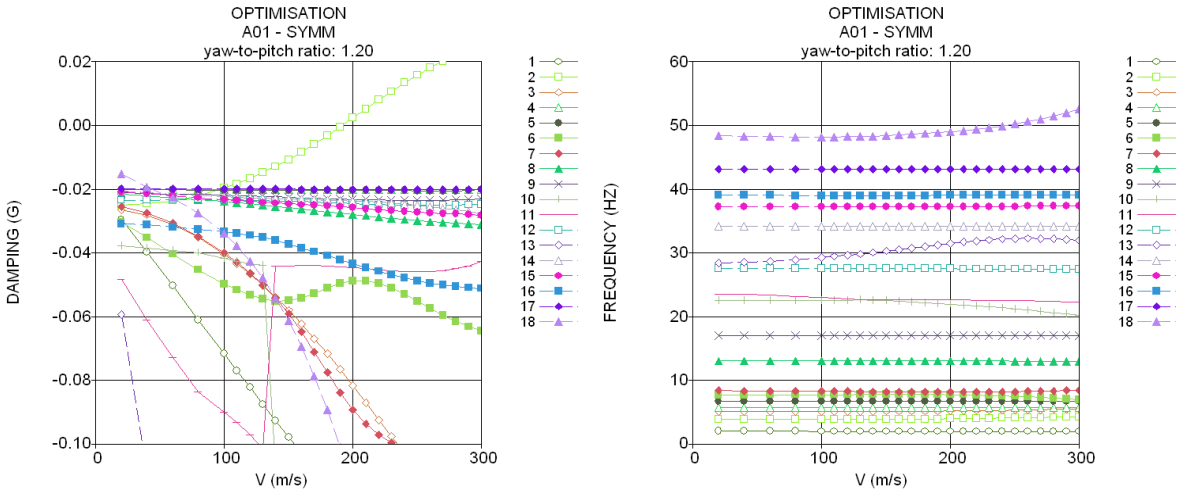

(a) (b)

Fig. 4. Whirl flutter calculation (V-g-f) diagram, (a) damping, (b) frequency, optimisation-based calculation

Calculations are performed for several values of the yaw-to-pitch frequency ratio to construct a stability margin curve with respect to the engine yaw and pitch vibration frequency. Stability margins are then constructed for all applicable mass configurations. The frequency-based margin may be then compared with the engine vibration frequencies, obtained by the GVT or analytically, to evaluate the rate of reserve as shown in Fig. 5. The dashed line represents the (+/-) 30% variance margin in engine attachment stiffness. Another parameter to be evaluated is the damping. This is provided using the calculation with very low structural damping, represented by the damping of $g = 0.005$, while the standard structural damping included in the analyses is $g = 0.02$. As obvious from Fig. 5, there is sufficient reserve in stability of the nominal state (including parameter variations) with respect to the stability margin, and therefore, the regulation requirements are fulfilled.

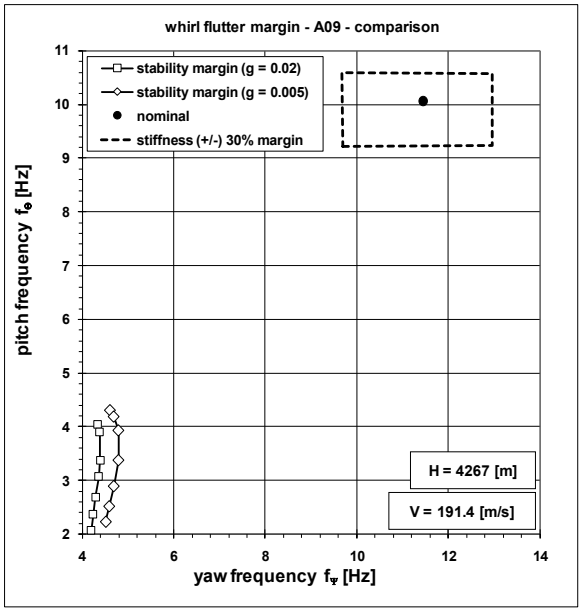

Fig. 5. Whirl flutter stability margin evaluation

FAR / CS 25 is the standard applicable to larger turboprops. In addition to the requirements similar to those of the previous case, some specific states of failure, malfunctions and adverse conditions are required to be analysed as well. These states are: 1) Critical fuel load conditions. This requirement includes the analysis of unsymmetrical conditions of the fuel loading that may come from the mismanagement of the fuel. In this case, fuel model is modified while the power plants model shows the nominal conditions. 2) Failure of any single element supporting any engine. This requirement includes in particular the failure of any single engine bed truss. The failure conditions are introduced into a single power plant mount system while other power plant mount systems use a nominal condition. All engines show the nominal condition. 3) Failure of any single element of the engine. This requirement includes, in particular, the failure of any single engine mount-isolator. The failure conditions are introduced into a single power plant mount system while other ones show nominal conditions. All engine mounts were used under nominal conditions. 4) Absence of aerodynamic and gyroscopic forces due to feathered propellers. The failure states defined in this section represent the states of a nonrotating engine and a nonrotating feathered propeller. The power plant system under such conditions generates no aerodynamic or gyroscopic forces. In addition, the single feathered propeller or rotating device failure must be coupled with the failures of the engine mount and the engine. 5) Any single propeller overspeed. The power plant system under such conditions generates maximal aerodynamic and gyroscopic forces. The condition of overspeed must include the highest likely overspeed of both engine and propeller. The state of overspeed is applied to any single propeller while the other ones are under the nominal conditions. 6) Other failure states coming from the damage-tolerance analysis, from bird strike damages and from damages of the control systems, the stability augmentation systems and other equipment systems and installations.

References

[1] Čečrdle, J., Whirl flutter of turboprop aircraft structures, Elsevier Science, Oxford, 2015.
[2] Forsching, H.W., Grundlagen der Aeroelastik, Springer – Verlag, 1974.
[3] Houbolt, J.C., Reed, W.H., Propeller – nacelle whirl flutter, Journal of the Aerospace Sciences 29 (3) (1962) 333-346.
[4] Ribner, H.S., Propellers in yaw, NACA Report 820, 1945.

COMPUTATIONAL MECHANICS 2019
35th conference with international participation
Srní
November 4 - 6, 2019

Optimization of pseudopotentials for electronic structure calculations

R. Cimrman[a], J. Vackář[b], M. Novák[b,c]

[a] New Technologies Research Centre, University of West Bohemia, Univerzitní 8, 301 00 Plzeň, Czech Republic
[b] Institute of Physics, Academy of Sciences of the Czech Republic, Na Slovance 2, 182 21 Praha 8, Czech Republic
[c] Faculty of Applied Sciences, University of West Bohemia, Univerzitní 8, 301 00 Plzeň, Czech Republic

The electronic structure calculations represent a rigorous tool for predicting and understanding the properties of materials from first principles. In our research devoted to understanding crack propagation in iron we have developed a new software [2] for electronic structure calculations that is based on the pseudopotential approach [5, 7] within the context of the density functional theory [4]. A properly constructed pseudopotential can be used both to reduce numerical difficulties by hiding the core singularity as well as to substantially reduce the number of the electrons (degrees of freedom) required to calculate with by hiding non-valence electrons. However, designing an accurate and efficient pseudopotential is a non-trivial task as there are many, often contradictory, criteria on the pseudopotential optimality, such as smoothness, softness (no strongly oscillating pseudo-wavefunctions), transferability (validity in different neighboring atom configurations, reproduction of scattering properties in a wide range of energies), computational efficiency, etc.

Our approach to generating and optimizing pseudopotentials is based on the algorithm proposed in the dissertation work [6], where so called environment-reflecting all-electron pseudopotentials were introduced. The original fortran77 implementation, while still working very well, started to be a maintenance burden over the years, which motivated us to begin with the development of a new, easily maintainable and extensible implementation using Python as the top-level programming language. In this contribution we describe the new implementation and present preliminary numerical examples.

In our approach [6], a pseudopotential is generated for the given energy E and orbital quantum number l, and is assumed to be a linear combination of basis functions $F_i(r)$, $i = 0, \ldots, 4$

$$V_{E,l}^{\mathrm{PS}}(r) = \sum_{j=0}^{4} a_j F_j(r) \ , \tag{1}$$

where

$$\begin{aligned} F_0(r) = 1 \ , \quad F_1(r) = e^{-(\rho_1 r)^2} - 1 \ , \quad F_2(r) = (\rho_2 r)^2 e^{-(\rho_2 r)^2} \ , \\ F_3(r) = e^{-(\rho_3 r)^2} - 1 \ , \quad F_4(r) = (\rho_4 r)^2 e^{-(\rho_4 r)^2} \ . \end{aligned} \tag{2}$$

Pseudopotentials are generated for individual atoms by repeatedly solving the Schrödinger equation numerically in spherical coordinates: for this purpose we can use either our test implementation in Python (mainly for debugging), or a very fast and accurate implementation

of dftatom [1]. We denote the resulting all-electron wavefunctions by $\psi^{\mathrm{AE}}_{E,l}(r)$ and the corresponding energy by E, when solving with the original all-electron potential $V^{\mathrm{AE}}(r)$, and the pseudofunctions by $\psi^{\mathrm{PS}}_{E,l}(r)$ for the calculation with $V^{\mathrm{PS}}_{E,l}(r)$. For a given cut-off radius R_c, the following conditions have to hold

$$V^{\mathrm{PS}}_{E,l}(r) = V^{\mathrm{AE}}(r) \ , \qquad r \geq R_c \ , \tag{3}$$

$$\frac{\partial^i}{\partial r^i} V^{\mathrm{PS}}_{E,l}(r) = \frac{\partial^i}{\partial r^i} V^{\mathrm{AE}}(r) \ , \qquad r = R_c \ , \quad i = 1, 2 \ . \tag{4}$$

Using normalization constants such that $\psi^{\mathrm{PS}}_{E,l}(R_c) = \psi^{\mathrm{AE}}_{E,l}(R_c)$, the following conditions are required to hold

$$\tfrac{\partial}{\partial r}\psi^{\mathrm{PS}}_{E,l}(r) = \tfrac{\partial}{\partial r}\psi^{\mathrm{AE}}_{E,l}(r) \ , \quad r = R_c \ , \tag{5}$$

$$\int_0^{R_c} \left|\psi^{\mathrm{PS}}_{E,l}(r)\right|^2 r^2 \, \mathrm{d}r = \int_0^{R_c} \left|\psi^{\mathrm{AE}}_{E,l}(r)\right|^2 r^2 \, \mathrm{d}r \ . \tag{6}$$

The condition (6) corresponds to the charge conservation and makes the resulting pseudopotentials "norm-conserving", which implies transferability, i.e., use at different energies.

The pseudopotential basis functions $F_j(r)$ in (2) have free parameters $\boldsymbol{\rho} \equiv [\rho_1, \rho_2, \rho_3, \rho_4]^T$. Those parameters can be chosen in a way that is optimal w.r.t. some selected criterion Θ — an optimization problem is defined as follows: Find $\hat{\boldsymbol{\rho}}$ such that

$$[\hat{\boldsymbol{a}}, \hat{\boldsymbol{\rho}}] = \mathrm{argmin}_{\boldsymbol{\rho}} \{\Theta(V^{\mathrm{PS}}_{E,l}(\boldsymbol{a}, \boldsymbol{\rho}, r))\} \ , \tag{7}$$

where the linear combination (1) parameters $\hat{\boldsymbol{a}} \equiv [\hat{a}_0, \ldots, \hat{a}_4]^T$ follow from (3) – (6). Many optimization criteria are possible, for instance:

- minimizing the "length" of Fourier image of the pseudopotential;
- minimizing the integrated curvature;
- minimizing the depth of the pseudopotential.

As an example we show results of pseudopotential optimization for the nitrogen atom and minimize the initial pseudopotential curvature

$$\Theta_0(V^{\mathrm{PS}}_{E,l}(\boldsymbol{a}, \boldsymbol{\rho}, r)) \equiv |\frac{\partial^2}{\partial r^2}(V^{\mathrm{PS}}_{E,l})(\boldsymbol{a}, \boldsymbol{\rho}, 0))| \ . \tag{8}$$

This atom has 7 electrons in three sub-shells 1s: 2, 2s: 2, 2p: 3, with energies $E_{1s2} \approx -14.01$, $E_{2s2} \approx -0.676$, $E_{2p3} \approx -0.266$ (in atomic units). The pseudopotentials were generated for the valence states 2s ($l = 0$), 2p ($l = 1$) as well as for the first unoccupied state 3d ($l = 2$) with $E_{3d0} \approx 0.018$. The initial parameters were $\boldsymbol{\rho} = [0.5, 0.7, 1.4, 1.3]^T$. For the optimization, the L-BFGS-B solver from SciPy [3] was used: it allowed specifying additional box constraints: $0.001 < \{\rho_1, \rho_2\} < 1.1$, $1.11 < \{\rho_3, \rho_4\} < 2$ to prevent linearly dependent basis functions. The results are summarized in Fig. 1. Adhering (3) – (6), the pseudofunctions are equal to the all-electron wavefunctions outside the cut-off radius $R_c = 1.5$ (Fig. 1a). The optimized pseudopotentials (orange curves in Fig. 1b-d) are equal to all-electron potentials (green curves) outside R_c and are shallower and smoother than the ones obtained for the initial setting of parameters (blue curves), and thus more numerically suitable for electronic structure calculations.

Acknowledgement

The work was supported by the Czech Science Foundation, grant project GA17-12925S.

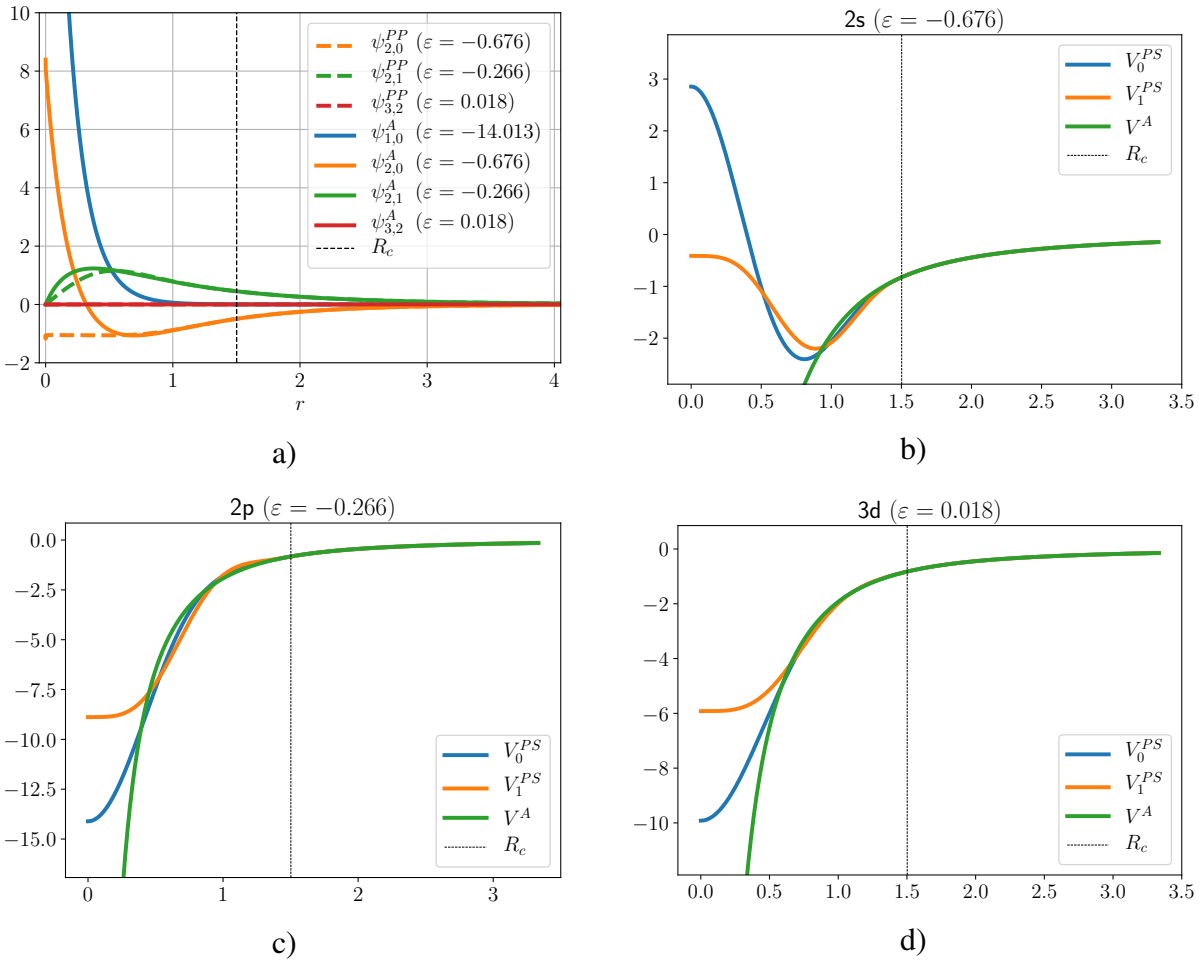

Fig. 1. The pseudopotential optimization results: a) comparison of the all-electron wavefunctions (solid) and the corresponding pseudofunctions (dashed); b) the initial (blue) and optimized (orange) pseudopotentials compared with the all-electron potential (green) for the state 2s, c) for the state 2p and d) for the state 3d. The cut-off radius $R_c = 1.5$ is denoted by the vertical line.

References

[1] Čertík, O., Pask, J. E., Vackář, J., dftatom: A robust and general Schrödinger and Dirac solver for atomic structure calculations, Computer Physics Communications 184 (7) (2013) 1777-1791.

[2] Cimrman, R., Novák, M., Kolman, R., Tůma, M., Plešek, J., Vackář, J., Convergence study of isogeometric analysis based on Bézier extraction in electronic structure calculations, Applied Mathematics and Computation 319 (2018) 138-152.

[3] Jones, E., Oliphant, T., Peterson, P., et al., SciPy: Open source scientific tools for Python, 2001–2019. (Online; accessed 2019-02-14).

[4] Martin, R. M., Electronic structure: Basic theory and practical methods, Cambridge University Press, 2005.

[5] Pickett, W. E., Pseudopotential methods in condensed matter applications, Computer Physics Reports 9 (3) (1989) 115-198.

[6] Vackář, J., Construction of generalized semilocal norm-preserving pseudopotentials by direct method, Ph.D. thesis, Institute of Physics of the Czechoslovak Academy of Sciences, 1992. (in Czech)

[7] Vackář, J., Šimůnek, A., Adaptability and accuracy of all-electron pseudopotentials, Physical Review B 67 (12) (2003) No. 125113, doi: 10.1103/PhysRevB.67.125113.

COMPUTATIONAL MECHANICS 2019
35th conference with international participation
Srní
November 4 - 6, 2019

The optimization of the driving power distribution between power units of the HEV powertrain based on the velocity profile

P. Denk[a], Z. Šika[a], P. Steinbauer[a], J. Macek[b], J. Morkus[b]

[a] *Czech Technical University in Prague, Faculty of Mechanical Engineering, Department of Mechanics, Biomechanics and Mechatronics, Technická 4, Praha 6, Czech Republic*
[b] *Czech Technical University in Prague, Faculty of Mechanical Engineering, Department of Automotive, Combustion Engine and Railway Engineering, Technická 4, Praha 6, Czech Republic*

One of the main advantages of a Hybrid Electric Vehicle (HEV) is the possibility to control flow of the power distribution between vehicle power units especially in case of recuperation energy mode. In general, the power distribution can be controlled independently on the vehicle velocity and current state of the other vehicle power units, but with respect to physical limits and other boundaries. The HEV is designed from two main power circuits – driving power circuit and the thermal power circuit [1]. Both of mentioned circuits can be in general independent from energy flow point of view and the same from the control point of view, but the specific and most important advantage of HEV is also connecting driving power circuit and thermal power circuit on both points of view. By the energy connecting of both circuits is possible to recuperate the waste thermal energy especially from ICE cooling circuit to the cabin heating. The cabin heating requirement or vehicle engine and battery preheating requirement can be also powered directly from recuperation electric energy. The presented heating and preheating requirements open the new way for smart control all type of energy flow between each energy units, especially if it is vehicle velocity profile known in advance.

The presented control process can be provided by ordinary type of controller for example by PID controller in feedback control, it can be provided by the higher level of controller, for example by the predictive control strategy with chosen value of predictive horizon and in the highest level, it can be provided by the previous optimization of the energy flows for all considered route. The task defined by this idea can be one part of the whole optimization problem focused on the optimization the total energy consumption on the primary energy sources (vehicle battery and fuel tank). The presented whole optimization problem may be designed for example in two steps. In the first step is optimized the vehicle velocity profile and subsequently in the second step will be optimize the internal energy flows. The value of total energy consumption is calculated in the objective function for lower optimization level with respect to define velocity profile obtained from higher optimization level. The contribution presented on the next lines is focused on the concept for optimization energy flow between vehicle power unit with respect to given vehicle velocity profile.

The basis for optimization task is define the possibilities how to control energy flows between each power units based on individual concept of the vehicle powertrain and in the second line the possible energy inputs and its distribution control. The first presented category is directly fixed on the vehicle powertrain concept. For example for the parallel hybrid powertrain concept is possible to considered energy flow into the motors controlled independently. The vehicle energy inputs also directly depends on vehicle powertrain design, for example for plug-in hybrid powertrain (PHEV) is possible to considered two external

inputs – electric energy and gasoline and the additional source can be considered recuperation possibilities depends on specific route properties. The vehicle battery is possible charged from external and internal sources, whereas for basic type hybrid powertrain (HEV) without external charging connection is possible battery charging only from internal sources. This introduced properties is most important for energy flow control, because the battery state of charge have to be kept on requires level in both cases, but in the case of PHEV is possible to powered the vehicle only on ICE without forced charging and in second one it is not possible [2]. If it will be considered the case of PHEV powertrain, the most important energy flow for optimization is power dividing between each vehicle motors. The power ratio between each motors can be define by parameter *U* based on the power requirement on the vehicle wheels. The *U*-parameter is given by following power equilibrium equation

$$P_{source}\left(U_{(t)}, t\right) = P_w + P_{HVAC\ ICE} + P_{loss\ EM} + P_{HVAC\ el} + P_{aux}$$
$$= \frac{1}{\eta_{gear}} \cdot [(1-U) \cdot P_W + U \cdot P_W] + \frac{1}{\eta_{ICE}} \cdot (1-U) \cdot P_W + \frac{1}{\eta_{EM}} \cdot U \cdot P_W$$
$$+ P_{HVAC\ el} + P_{aux}$$

where P_W represents driving power on the vehicle wheels, $P_{HVAC\ ICE}$ represents the loss power from ICE, $P_{loss\ EM}$ represents loss power from electric motor, $P_{HVAC\ el}$ represents the electric power input to the cabin heating, if it is considered and P_{aux} represents the power of auxiliary units, like vehicle lights etc.

The other energy flows is controlled with respect to introduced parameter *U* by the conventional controllers with respects to following preferences.

a) The temperature of ICE have to be achieved in the shortest time (the cabin heating is possible only by electric heating unit)
b) The cabin is primarily heating by energy losses from ICE to the cooling system

The presented method have been used for optimization the *U*-parameter at the testing route and chosen velocity profile and the result of this test is shown in following Fig. 1.

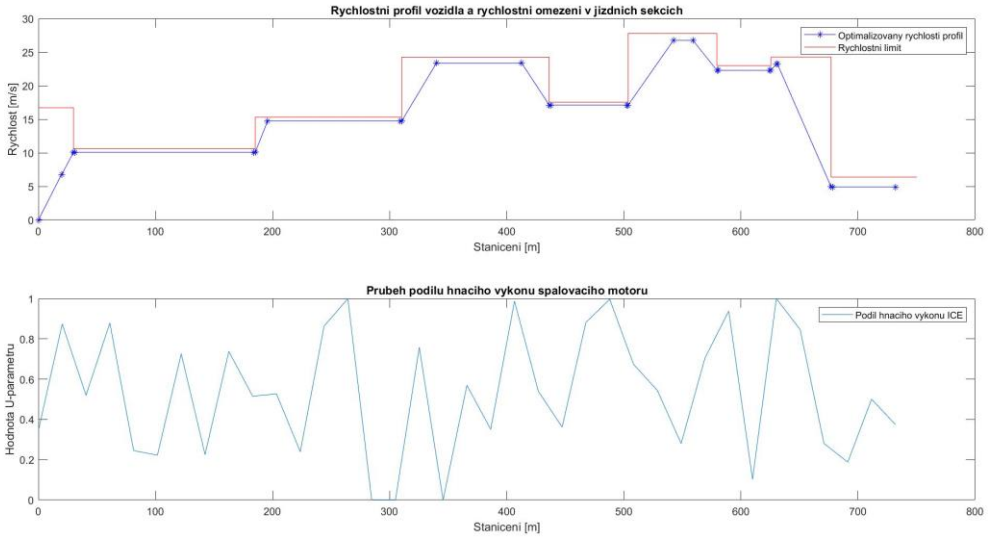

Fig. 1. Optimal velocity profile (above) and *U* parameter result (below)

The cabin heating has been controlled by basic PID controller that the controller constants have been settings by MATLAB control settings tool.

Acknowledgements

The work has been supported by the grant EU project "ADVICE" (ADvancing user acceptance of general purpose hybridized Vehicles by Improved Cost and Efficiency) number 724095 and the word of thanks bellows also to support program for young researchers and Ph.D. students named Mechatronika a adaptronika 2019 SGS19/156/OHK2/3T/12.

References

[1] Denk, P., Šika, Z., Steinbauer, P., Macek, J., Morkus, J., Mathematical model of the Hybrid Electric Vehicle for driving consumption optimization, Proceedings of the 33rd conference Computational Mechanics, Špičák, 2017.

[2] Denk, P., Šika, Z., Steinbauer, P., Macek, J., Morkus, J., The study of possibilities towards to extending the Hybrid Electric Vehicle mathematical, Proceedings of the 34th conference Computational Mechanics, Srní, 2018.

COMPUTATIONAL MECHANICS 2019
35th conference with international participation
Srní
November 4 - 6, 2019

Fracture mechanics description of the defect in rolling cylinder

P. Dlhý[a,b], J. Poduška[a], L. Náhlík[c], M. Berer[d], A. Gosch[e], G. Pinter[e], P. Hutař[a]

[a] Institute of Physics of Materials, Academy of Sciences of Czech Republic, Žižkova 22, 616 62 Brno, Czech Republic
[b] Central European Institute of Technology - Brno University of Technology, Purkyňova 656/123, 612 00, Brno, Czech Republic
[c] Central European Institute of Technology - Institute of Physics of Materials, Purkyňova 656/123, 612 00, Brno, Czech Republic
[d] Polymer Competence Center Leoben GmbH, Roseggerstrasse 12, 8700 Leoben, Austria
[e] Material Science and Testing of Polymers, Montanuniversitaet Leoben, Otto Gloeckel-Straße 2, 8700 Leoben, Austria

Bearing elements (e.g. cylinders) made of polymer materials are very common in a wide variety of engineering applications. These elements are typically made of semi-crystalline thermoplastics like polyamide (PA), polyoxymethylene (POM) or polyetheretherketone (PEEK). It is typical for these thermoplastics to shrink significantly when cooling down [2] and develop internal stresses after solidifying from the melt. A widely used manufacturing process for this type of parts is injection moulding. The injection moulding offers high production rate while maintaining low production cost. However, shrinkage defects occur frequently in the injection moulding production of bearing elements. Although the manufacturers put effort into removing these defects by the so-called holding pressure applied after filling the cavity however, inside defects keep appearing. This contribution deals with a case of a bearing cylinder with a crack that initiated from a shrinkage defect. The conditions of the crack growth are assessed, simulation is carried out and fracture mechanics parameters are calculated in order to calculate lifetime predictions for these elements later on.

The component in question is a rolling cylinder compressed between two planes. A crack is considered in the middle of the cylinder. When the element is rolling, the orientation of the crack to the load direction changes gradually. Pure mode I (crack opening) in compression loaded cracked cylinder only occurs when the plane of a 2-dimensional crack and the load are aligned [1] (rolling angle 0°, see Fig. 1 on the left). During the rotation the situation changes from pure mode I to distinct mixed-mode conditions (all three modes are present at rolling angle 45°, see Fig. 1 on the right). Thus, the contribution of mode II and mode III cannot be neglected in this case. However, mixed mode conditions in bulk polymeric components are usually ignored. Hence, little information about the material characterization under shear crack opening (mode II and mode III) is available.

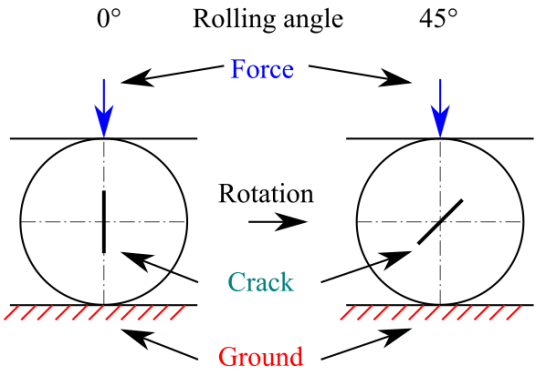

Fig. 1. Schematic illustration of rotation of cylinder and boundary conditions

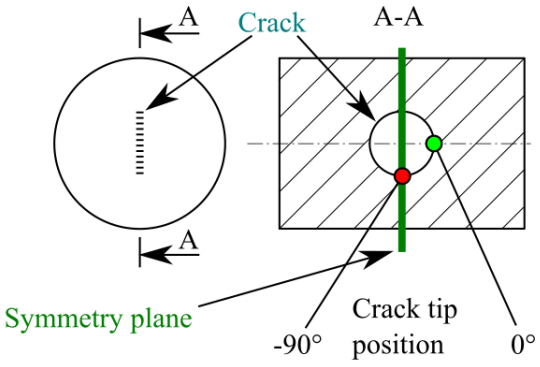

Fig. 2. Schematic illustration of cross-section of cylinder with internal central crack

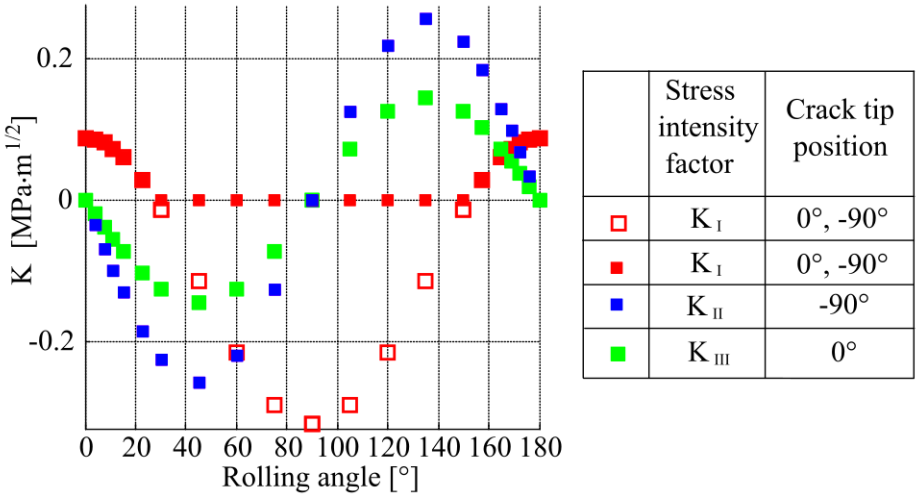

Fig. 3. Stress intensity factor for two different positions at crack tip, crack length 0.25mm, force 350N

Parametrical finite element model was developed in order to simulate different combinations of crack lengths, rolling angles, dimensions of cylinder and forces. ANSYS software was used, taking advantage of APDL and its capability of programming macros. Model was created with one possible symmetry plane (showed in Fig. 2) to reduce number of elements as well as computing time. Nevertheless, the whole model contains about from 40000 up to 325000 elements, depending on crack length.

The model consisted of three solid parts all represented by linear elastic isotropic material –two steel plates (Young's modulus of 210 GPa and Poisson's ratio of 0.3) and a cylinder between them with a flat crack (Young's modulus of 3.6 GPa and Poisson's ratio of 0.45). Dimensions of simulated cylinder are 6 mm for both diameter and length. The crack length was considered 0.25 mm (a/W = 0,083) to 1.75 mm (*a/W* = 0.583). Rolling was assessed by changing the angle between the crack plane and the applied force from 0° to 180°. Force 350 N was applied at the top of upper steel plate and the bottom plate was fixed (Fig. 1). Parts was connected by contacts for mutual interaction. Contact between crack faces was also considered. Stress intensity factors K_I, K_{II}, K_{III} for the rotating part were calculated.

Results from the model with the contact between crack faces are shown in Fig. 3 (filled points). In order to identify the cycle asymmetry, variants without contact on the crack faces were also solved. In Fig. 3, these values of K_I are shown using empty points. Stress asymmetry is close to -3.5, in the case of mode I loading. Asymmetry for loading modes II and III is equal to -1. However, shear modes are in out-of-phase loading with opening mode I. Minimal and maximal values for shear modes are observed in 45° and 135° of rolling angle respectively however in different crack tip position.

Acknowledgements

This research has been supported by Polymer Competence Center Leoben GmbH (PCCL, Austria) and the Ministry of Education, Youth and Sports of the Czech Republic under the project m- IPMinfra (CZ.02.1.01/0.0/0.0/16_013/0001823) and the equipment and the base of research infrastructure IPMinfra were used during the research activities.

References

[1] Berer, M., Mitev, I., Pinter, G., Finite element study of mode I crack opening effects in compression-loaded cracked cylinders, Engineering Fracture Mechanics 175 (2017) 1-14.

[2] Painter, P.C., Coleman, M.M., Fundamentals of polymer science: An introductory text, Technomic Pub. Co., Lancaster, 1997.

COMPUTATIONAL MECHANICS 2019
35th conference with international participation
Srní
November 4 - 6, 2019

Split Hopkinson bar technique in a tensile test

M. Dohnal[a], M. Šebík[a], T. Sedlář[a]

[a] SVS FEM s.r.o., Škrochova 42, 615 00, Brno, Czech Republic

1. Tensile test arrangement

1.1 Impactor device

The Hopkinson Split Bar is generally a test of the material properties of a sample tested at a fast dynamic problem. The base of the test is based on a one-dimensional theory of elastic pulse propagation. The source of the pressure pulse extending longitudinally in the measuring rods in the Hopkinson test is the impact of the small elastic bar ("impactor") to the front of the first rod.

The value of the longitudinal strain (amplitude) on the first bar at the first passage of the pressure waveform to the strain gauge is directly proportional to the impact velocity of the impactor. The length of this first pulse depends on the length of the impactor, i.e. the time over which the kinetic energy of the pound acts on the face of the first rod. This corresponds to the length of the first input pulse of approximately 60 microseconds.

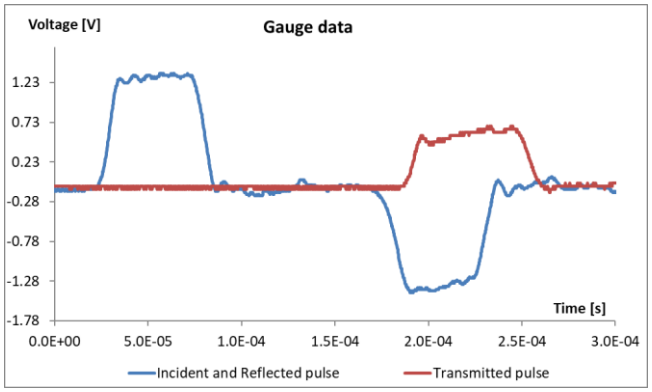

Fig. 1. Typical strain gauge recording of the Hopkinson test in pressure

The impact of the majority of similar devices is caused by the punching of the impactor from the gun with compressed air. Pulse energy is obtained by releasing compressed air from a cylinder, such as a diving or cylinder, as part of a compressor station. The device for Hopkinson's test in SVSFEM uses the energy of a small cartridge that fires a piston from the pulse generator and the end of that piston hits the rear face of the impactor. On a track of approximately 40 mm, it will give this impactor a speed of 20 to 60 m/s depending on the set size of the cartridge chamber. This speed is higher than similar equipment using compressed air. The pulse generator is based on the ANTREG pistol adapted for mounting on the proposed device. The source of the piston's energy in this pistol is a standard 9x16 mm industrial cartridge, for example from Sellier-Bellot.

1.2 Measuring rods

The new measuring device (TSHB Tri Split Hopkinson Bar) differs from conventional Hopkinson test equipment by dividing the measuring rods into three parallel bars. This solution creates a significantly larger space for the sample to be measured and at the same time it is possible to assemble the rods so that the sample is subjected to tension and pressure.

In the first variant, the numerical simulation showed that with the assumed magnitude of the input force pulse generated by an impactor hit, stress about approximately 50 MPa is generated on the specimen. This value is sufficient, for example, to measure samples of concrete and similar materials.

The disadvantage of this solution is the occurrence of bending stress on the measuring rods. More variants of the connecting part were analyzed.

In a final variant, the functional part of the measuring device has been adjusted by inserting another front and rear rod on the axis of the whole device. The force pulse in front of and behind the sample is thus always transmitted by only one rod in the axis of the device, which is not stressed by unwanted bending.

For the tensile testing variant, it is possible to replace the rear three parallel bars by simply anchoring the one rear measuring rod. This anchorage can be easily used to position a load cell that can directly verify the value of the force pulse obtained from the rear measuring rod.

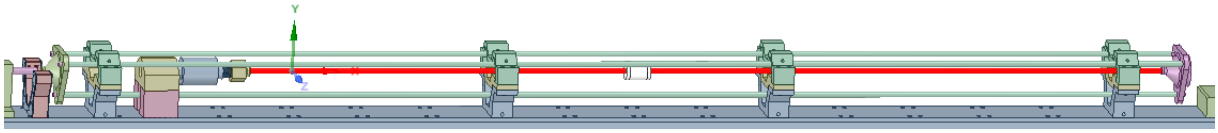

Fig. 2. Final CAD model of measurement device

2. Measurement evaluation

2.1 Capacity analysis

The exact record of deformation of the test sample in the Hopkinson test is one of the key problems of this method. The entire test time, in the order of tens of microseconds, places great demands on the write speed of the entire device while maintaining the high quality of the recorded data. The deformation of the sample is usually evaluated indirectly from the deformation of measuring rods. Assuming elastic deformation of the measuring rod and the constant cross-section, it is possible to quantify the time course of forces acting on the measured sample and thus also the deformation of the sample. The deformation of the measuring rods is usually evaluated by means of strain gauges located at half length. In some cases, the deformation is evaluated by means of capacitive sensors, which evaluate their longitudinal deformation on the basis of a change in the cross-section of the rod. Capacitive sensors record the change in electromagnetic field between two surface electrodes. The distortion of the sample in the Hopkinson test is basically also a change in the position of the two surface electrodes (sample-to-probe interface). If a voltage difference is applied to these surfaces, it would be possible to evaluate the deformation of the sample directly from the position change of the two surfaces. Most measurements are made with steel measuring rods. An electromagnetic field analysis was performed between two measuring rods.

We start from the capacitance of a plate capacitor consisting of two electrodes and a dielectric between them. The capacitance of capacitor can be calculated from geometric properties and material properties - permittivity. The relationship between these properties is apparent from the following equation

$$C = \frac{\varepsilon \cdot S}{d},$$

where C is the capacitance of the plate capacitor, ε is the dielectric permittivity, S is the electrode area above the dielectric, d is the dielectric thickness between the electrodes.

The measured sample, together with the bars, forms a plate capacitor which changes its capacity during deformation depending on the change in the dielectric thickness. By measuring the change in capacity over time during the deformation phenomenon, it is possible to determine the strain over time. The hypothesis applies only to dielectric (non-conductive) samples of course.

The deformation of the measured specimen is approximately 10-20%. Typical specimens are made of materials, wood, plastics or fabrics. Their relative permittivity is very low in the range of 1 - 10. This makes the ambient air permittivity negligible for the electric field. The thickness of the wood specimen is usually approximately 8 mm.

The relative permittivity of the specimen is selected with a value of 2. The analysis is calculated as electrostatic with a potential of 12 V between the electrodes. By analytical calculation we can determine the approximate capacity.

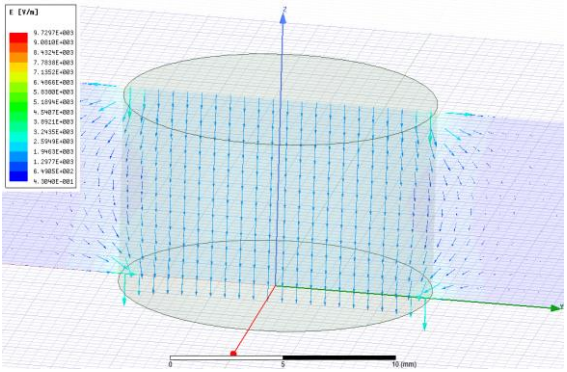

Fig. 3. Electric intensity field

$$C = \frac{\varepsilon_0 \cdot \varepsilon_r \cdot S}{d} = \frac{8.854 \cdot 10^{-12} \cdot 2 \cdot 1.54 \cdot 10^{-4}}{8 \cdot 10^{-3}} = 340.74fF$$

The capacity of a capacitor with a specimen thickness of 8 mm is determined from the finite element model through the electrostatic field energy. Due to the environmental impact, the capacity value has changed by more than 30%.

$$C = \frac{2W}{U^2} = \frac{2 \cdot 3.2239737 \cdot 10^{-11}}{12^2} = 447.7fF$$

Next figure shows a very small change in capacity at 15% strain of the capacitor. For mm units, the capacity changes only in tens of fF. The evaluation of the deformation of the sample by means of the electromagnetic field between the measuring rods is therefore theoretically possible, but it is practicaly difficult to implement due to the very small measured values. This method was not used in final device assembly.

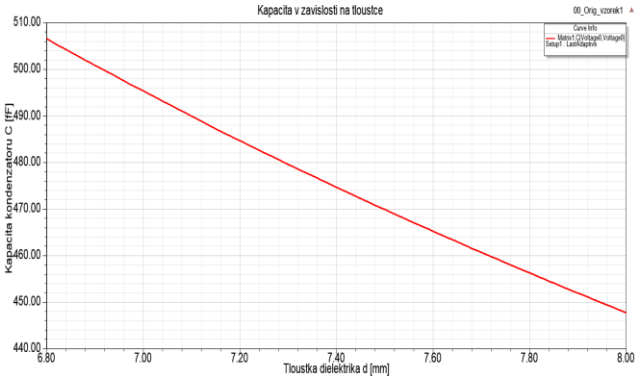

Fig. 4. Capacity versus specimen thickness

2.2 Stress-strain analysis

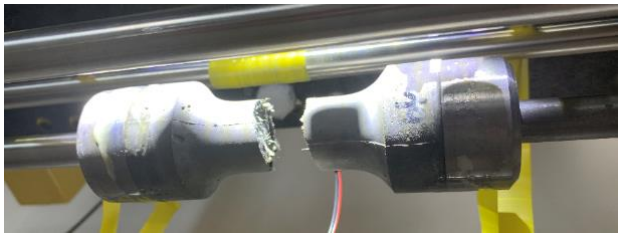

Fig. 5. Concrete specimen after test

The new measuring device (TSHB Tri Split Hopkinson Bar) was tested by the first set of measurements. The specimen was made from UHPC concrete including 6 mm length Aramid fibers.

Gauge sensors were placed on the front and back measurement rods. There was found a good agreement with the previous numerical simulations. The strain history of the specimen was measured directly by the videoextensometr Model 200XR from H.-D. Rudolph GmbH company. The stress-strain curve of the specimen evaluated from combination of the gauges and the videoextensometr is presented in next picture.

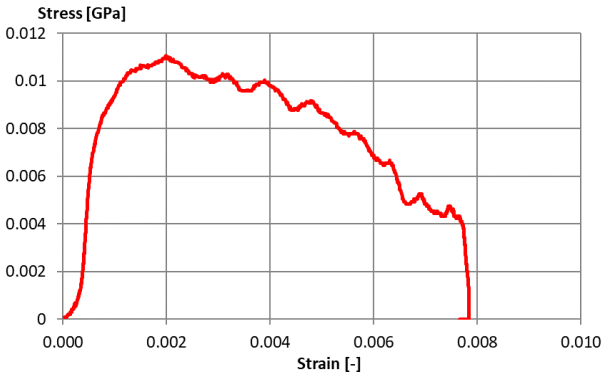

Fig. 6. Stress-Strain curve of the UHPC specimen

3. Conclusion

The tensile test of the UHPC specimen was performed on the new measurement device Tri-Split Hopkinson Bar (TSHB). The specimen deformation was caused by a hit of the impactor to pair of measurements rods. The impact velocity was about 50 m/s. Stress-Strain history of the specimen was evaluated by a combination of gauge measurement and optical measurement.

Acknowledgements

The authors wish to express their gratitude and sincere appreciation to the authority of The Technology Agency of the Czech Republic, project No. TJ01000257 for financial support.

COMPUTATIONAL MECHANICS 2019
35th conference with international participation
Srní
November 4 - 6, 2019

Experimental investigation of fan for personal protection equipment – influence of number of blades

V. Dvořák[a], G. Moro[a], J. Lampa[a],

[a] *Faculty of Mechanical Engineering, Technical University of Liberec, Studentská 2, 461 17 Liberec, Czech Republic*

1. Introduction

The aim of research is development of new generation of powered air purifying respirators designed to filtrate contaminants in the form of gases, vapours and particles. These high performance units guarantee sufficient protection of the wearer even in heavy industrial environments, the chemical industry, laboratories and the pharmaceutical industry [4].

To help people while breathing through filter, a fan is used to propel air flowing in personal respiratory protection systems and units. Because, the reliability and efficiency are crucial for operation of these systems, our work is focused on improvement and optimization of a centrifugal fan used.

2. Methods

An example of the geometry of the impellers examined can be seen in Fig. 1. Two types of wheels were examined: with radial vanes with an inlet blade angle $\beta_1 = 90°$ and an exit blade angle $\beta_2 = 90°$, and backward curved vanes with various inlet and outlet angles. Around 15 variants with different numbers of various blades were investigated by experimental, numerical and theoretical methods. All wheels fort testing with diameter $d_2 = 60mm$ and width $b_2 = 4mm$ were produced by 3D printing technology [1].

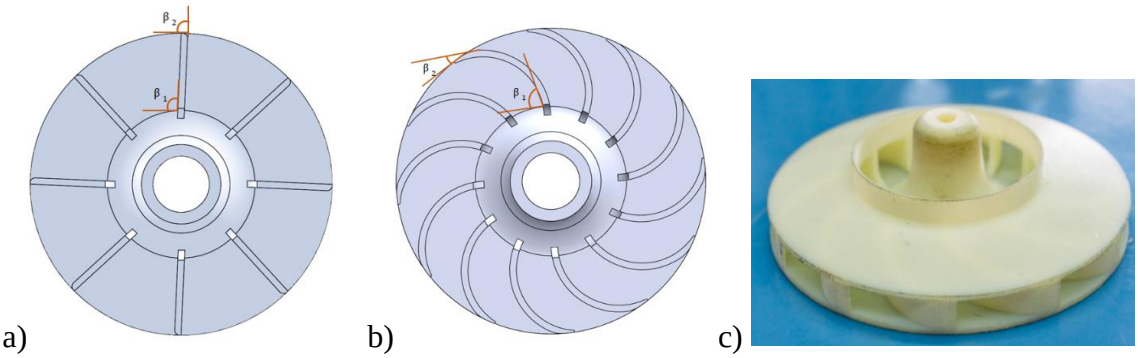

Fig. 1. Investigated wheels – a) radial blades, b) backward blades, c) a wheel manufactured by 3D printing technology

2.1 Theoretical Background

The theoretical increase of the total pressure Δp_{th} in a radial fan is described by the Euler equation

$$\Delta p_{th} = \rho(c_{2u}u_2 - c_{1u}u_1), \tag{1}$$

where c_u is a component of the total velocity in the direction of the peripheral velocity u, where indices 1 and 2 denote an input and an output point, respectively. As can be seen from the above relationship, it does not affect the number of blades in any way. However, the number of blades affects the individual losses that occur and which reduce the total achieved pressure Δp_{th} to the actual Δp. These losses include impeller inlet and outlet losses, directional input loss, pre-swirl loss or internal volumetric leakage. Among the most significant losses is the so-called inter blade circulation loss, which is caused by the finite number of blades z and the only one affects their number. The swirl loss between the blades is expressed by the formula

$$\Delta p_{blade} = \rho(u_2) r \omega, \tag{2}$$

where ω is the rotational speed of the impeller is r the radius of the imaginary circle between two blades, which can be expressed from the blades output angle β_2 as

$$r = \frac{\pi d_2 \sin \beta_2}{2z}, \tag{3}$$

in which d_2 is the impeller diameter and z is the number of blades. The resulting relationship for inter blade circulation loss is given by the relationship

$$\Delta p_{blade} = \rho u_2^2 \frac{\pi \sin \beta_2}{z}. \tag{4}$$

It is clear from the above relationship that loss by the finite number of blades is very significant and grows strongly with a small number of blades. Nevertheless, it should not be forgotten that with the increasing number of blades there are other losses, which, however, are often not taken into account: more blades cause a reduction in flow cross section and hence reduce flow volume and friction losses in the inter-bladder channel increase. The resulting power fan characteristic is shown in Fig. 2 on the left.

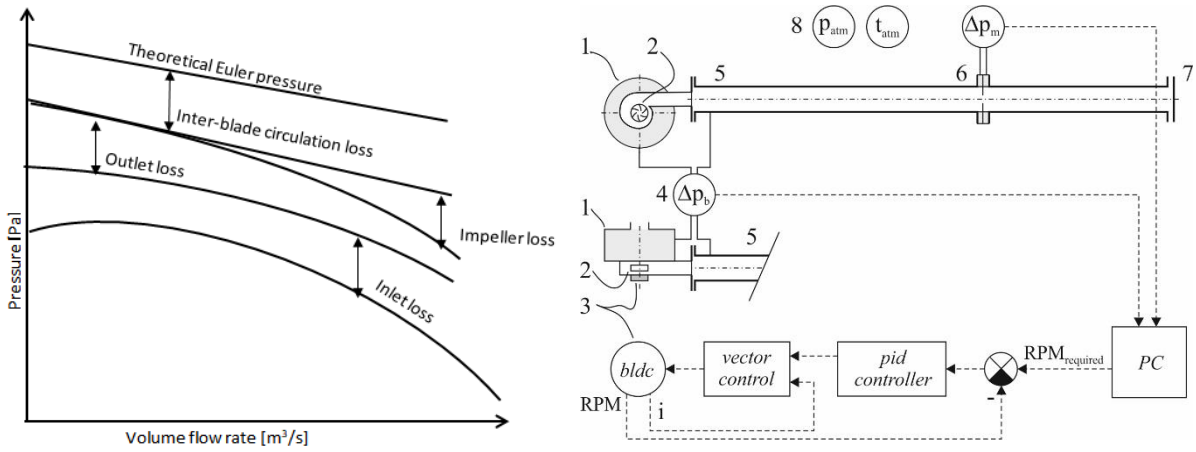

Fig. 2. (on the left) power curve of centrifugal fan, (on the right), testing stand: 1 – suction chamber with filter assembling, 2 – fan wheel, 3 – brushless DC motor, 4 – working pressure measuring (Δp_b), 5 – outflow tube, 6 – differential pressure Δp_m measuring for mass flow specification, 7 – chocking, 8 – measuring of atmospheric pressure and temperature

2.2 Experimental Investigation

The testing stand is visible in Fig. 2 on the right. The fan wheel (2) was propelled by electronically controlled brushless DC motor (3). To obtained power curves of a fan, rotations were specified directly and kept constant during measurements [1].

The air was sucked through suction chamber (1), which allowed assembling of filters, and was compressed and transported into the outflow tube (5). The back pressure and thus the

working pressure Δp_b of the fan was controlled manually by chocking (7) at the tube exit and measured by differential pressure transducer. The mass flow rate was measured by orifice (6), where differential pressure Δp_m is measured.

3. Results

The curves obtained experimentally and predicted for the radial blade wheels are plotted in the diagram in Fig. 3 on the left. As can be seen from the results, the experimentally found deviations between the measured data for a different number of blades are almost negligible. With a small difference, the twelve-blade wheel, which exhibits a higher pressure, especially for higher flow rates, is optimal. The worst case is the 8-blade wheel, while the 16-blade wheel lies somewhere in between. In contrast, the results obtained theoretically differ considerably for a wheel with a different number of blades, see relation (4). The 8-blade wheel is the worst, while the 16-blade is the best. It is also evident that further increases in the number of blades will have less and less influence. Comparison of theoretically obtained and experimentally measured data shows the best match for a twelve blade wheel, while the results for the 8 and 16 blades differ considerably.

Similarly, the results for a wheel with 8 and 12 backward curved blades with blade angles $\beta_1 = 80°$ and $\beta_2 = 85°$ are shown in Fig. 3 on the right. Here too, the differences between the two wheels found experimentally are negligible and we can see good agreement with the theoretical calculation for the 12 blades, but the high mismatch for the 8-blade wheel.

Very similar results were obtained for backward curved blades with angles $\beta_1 = 60°$, $\beta_2 = 76°$ and also for angles $\beta_1 = 40°$, $\beta_2 = 68°$ (not presented in diagrams). Also with these wheels there is a relatively good match between the predicted and measured characteristics for the 12-blade wheel, the influence of the number of blades on the measured curves is negligible and the predicted curve for 8 blades is significantly underestimated.

The results of the research on the influence of the number of blades on a rear-angled low angle blade ($\beta_1 = 45°$, $\beta_2 = 30°$) are presented in Fig. 4, where we can observe the results of testing for 10, 12 and 14 blade wheels and numerical calculations for the wheels with 8 to 16 blades. Here, too, we see that the effect of the number of blades is minimal, but wheels with a lower number of blades seem to be advantageous for high flow rates, while a higher number of blades is more favourable for high back pressure. Nevertheless, the differences between the wheels are negligible.

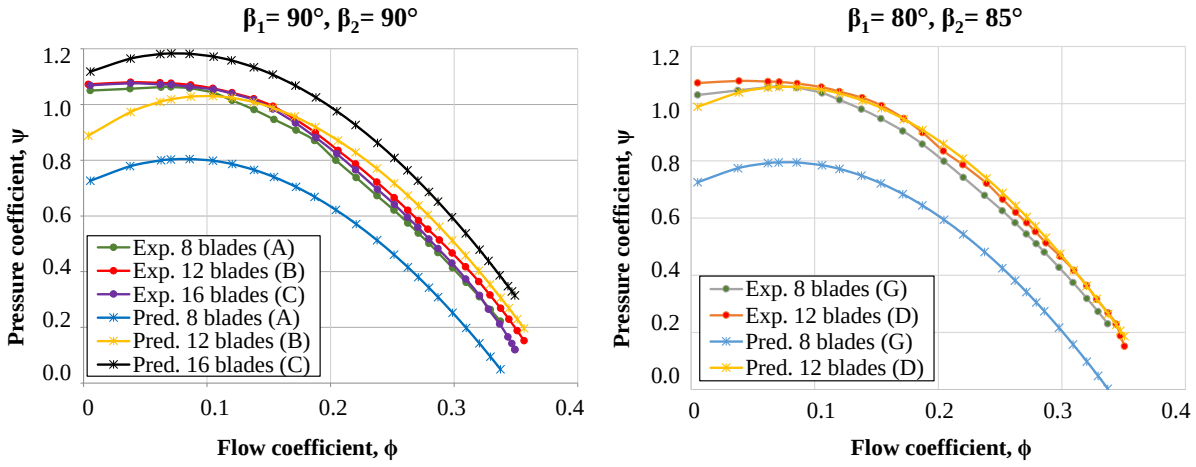

Fig. 3. Results for wheels with 8, 12 and 16 radial blades (on the left), results for wheels with 8 and 12 backward curved blades (on the right), $\beta_1 = 80°$, $\beta_2 = 85°$ [3]

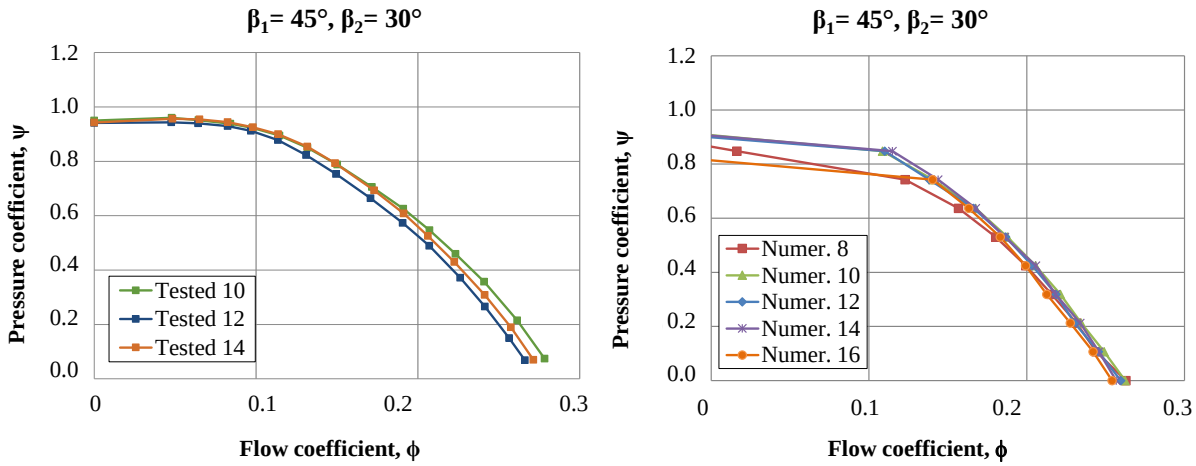

Fig. 4. Results for wheels with 8 to 16 backward blades with angles $\beta_1 = 45°$, $\beta_2 = 30°$ obtained experimentally (on the left) and numerically (on the right) [2]

4. Discussions

The results show that the influence of the number of blades on the characteristics of the fan is very small, sometimes almost negligible. The ideal number of blades appears to be 12 for the wheel under investigation, but neither the number 8 nor the 16 shows too much difference in the achieved values. The results show that theoretically determined influence of the number of blades on pressure loss due to inter blade circulation loss is considerably overestimated. Apparently this is due to the fact that in the calculations the number of blades is included only in this loss, which perceives the increase in the number of blades only positively and does not include accompanying influences – e.g. reduction of the characteristic dimension of the inter-blade channel.

5. Conclusions

Research into the influence of the number of blades on the characteristics of a radial fan has shown that the number of blades only slightly influences the performance of the fan. According to the test results, 12 blades seem to be optimal regardless of their shape. Numerical calculations show similar results. The predicted curves visibly overestimate the effect of inter blade circulation loss and do not count on additional losses at a higher number of blades. In order to optimize and predict the appropriate number of blades, the fan flow analysis model will need to be further modified.

Acknowledgements

This paper was created in the framework of project “Applied research in the field of the new generation of personal protective equipment for the demands of joint rescue service” no. VI20172020052, supported by Ministry of Interior of the Czech Republic.

References

[1] Dvořák, V., Votrubec, R., Šafka, J., Kracík, J., Experimental investigation of centrifugal fans for personal protection equipment – effect of used 3D printing technologies, EPJ web of Conferences, 2018.
[2] Lampa, J., Design of a fan for personal protective equipment, Technical University of Liberec, Czech Republic, 2019.
[3] Moro, G., Experimental investigation of fans for personal protective equipment, Technical University of Liberec, Czech Republic, 2019.
[4] https://www.clean-air.cz

COMPUTATIONAL MECHANICS 2019
35th conference with international participation
Srní
November 4 - 6, 2019

Methods for linearized analysis of floating ring bearings

Š. Dyk[a], J. Rendl[a], L. Smolík[a]

[a] *Faculty of Applied Sciences, University of West Bohemia, Univerzitní 8, 301 00 Plzeň, Czech Republic*

Automotive turbochargers [1] are typically supported by floating ring bearings (FRBs), where a rotor journal is held by two oil films separated by a rotating ring. This construction brings the advantage of high damping capacity, however, the rotor tends to behave in the nonlinear way—during the operation, oil whirl/whip instabilities [3] occur in the inner or outer oil film or in both at the same time. This leads to *jump phenomena* [2, 5] in the rotor response during runup/rundown.

Although the rotors with the FRBs are by nature nonlinear, linear analysis can also provide important insight into the dynamical behaviour of such a system. Using the linear approach, the nonlinear forces generated in the fluid films are approximated by linear or linearized spring-damper couplings. If the modelling is done precisely enough, it can show the possible regions of instability and predict operation modes of the rotor in these regions. There are several methods to create the linear model, that are discussed in this contribution. In order from the simpliest to the most complex, the bearing model can be considered as follows: (i) constant isotropic approximation of the whole FRB, (ii) constant orthotropic approximation of the whole FRB, (iii) FRB with linearized outer oil film only [4], (iv) constant isotropic approximation of the inner and outer fluid film with neglected ring mass, (v) constant isotropic approximaiton of the inner and outer fluid film with ring mass considered, (vi) ring mass considered and both fluid films linearized. Moreover, the last method can be performed in several ways:

- (a) separated linearization for the inner and the outer fluid film,
- (b) coupled linearization for both fluid films,
- (c) same as (b) with ring speed ratio (RSR) variable with eccentricity,
- (d) same as (b) with RSR calculated based on its own degree of freedom in the static equilibrium (algebraic) equations.

In general and not distinguishing between the methods with and without ring degrees of freedom, the turbocharger with two floating ring bearings can be described by the matrix equation

$$\boldsymbol{M}\ddot{\boldsymbol{q}} + \left[\boldsymbol{B} + \boldsymbol{G}(\omega_R) + \boldsymbol{B}_B^{(M)}\right]\dot{\boldsymbol{q}} + \left[\boldsymbol{K} + \boldsymbol{K}_B^{(M)}\right]\boldsymbol{q}_R = \boldsymbol{0}, \tag{1}$$

where $\boldsymbol{M}, \boldsymbol{B}, \boldsymbol{G}, \boldsymbol{K} \in \mathbb{R}^{n,n}$ are global mass, damping, gyroscopic and stiffness matrices, respectively, without bearing couplings. Bearing couplings are expressed using coupling bearing matrices $\boldsymbol{K}_B^{(M)}, \boldsymbol{B}_B^{(M)} \in \mathbb{R}^{n,n}$. The particular form of these matrices depends on the chosen method $M = i, ii, \ldots vi$. For the methods with $M = i, ii, iv, v$, these matrices are constant and for $M = iii, vi$ (in all the considered variants), they are a product of linearization process and hence they are speed dependent, i.e. $\boldsymbol{K}_B^{(M)} = \boldsymbol{K}_B^{(M)}(\omega_R, \omega_{FR})$, $\boldsymbol{B}_B^{(M)} = \boldsymbol{B}_B^{(M)}(\omega_R, \omega_{FR})$. Number of degrees of freedom is also dependent on the chosen method – for the methods with

neglected ring mass $n = n_R$ (number of degrees of freedom of the rotor) and for the methods with FRBs considered $n = n_R + 4$ (a,b,c) and $n = n_R + 6$ (d). Since the stability of the turbocharger is analysed using Campbell diagrams, right-hand side of Eq. (1) equals zero for modal analysis purposes.

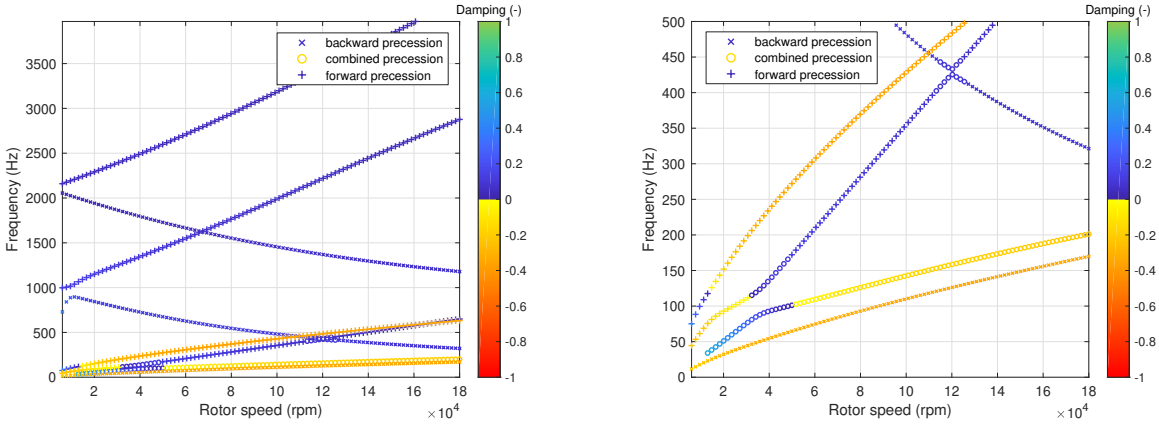

Figure 1. Campbell diagram of the turbocharger considering separated static solution for both fluid films – the diagram up to 3000 Hz (*left*) and the detail of unstable branches (*right*)

The results are analysed using the Campbell diagrams depicting together all important information about the system: they show change of natural frequencies with angular speed of the rotor, the precession (forward, backward and combined) is distinguished by different markers and the damping is shown using a carefully designed colormap. The results show significant differences between proposed methods with respect to the measure of abstraction. Slight differences in Campbell diagrams are obtained in case of method (vi) with all the considered subcases (a)-(d). However, the computational time is strongly affected by the chosen method. The contribution also shows a comparison of resulting Campbell diagrams with nonlinear run-up simulations.

Acknowledgements

This publication was supported by the project of the Czech Science Foundation No. 17-15915S entitled *Nonlinear dynamics of rotating systems considering fluid film instabilities with the emphasis on local effects* and by the Motivation system of the University of West Bohemia – Part POSTDOC.

References

[1] Nguyen-Schäffer, H., Rotordynamics of automotive turbochargers, Springer-Verlag, Berlin, 2012.

[2] Schweizer, B., Dynamics and stability of turbocharger rotors, Archive of Applied Mechanics 80 (9) (2010) 1017-1043.

[3] Schweizer, B., Oil whirl, oil whip and whirl/whip synchronization occurring in rotor systems with full-floating ring bearings, Nonlinear Dynamics 57 (4) (2009) 509-532.

[4] Tian, L., Wang, W. J., Peng, Z. J., Effects of bearing outer clearance on the dynamic behaviours of the full floating ring bearings upported turbocharger rotor, Mechanical Systems and Signal Processing 31 (2012) 155-175.

[5] Wang, J. K., Khonsari, M. M., Bifurcation analysis of a flexible rotor supported by two fluid-film journal bearings, Journal of Tribology 128 (3) (2006) 594-603.

COMPUTATIONAL MECHANICS 2019
35th conference with international participation
Srní
November 4 - 6, 2019

Sensitivity of the generalized van der Pol equation to sub- or super-harmonic resonance

C. Fischer[a], J. Náprstek[a]

[a] *Institute of Theoretical and Applied Mechanics of the Czech Academy of Sciences, Prosecká 76, 190 00 Prague, Czech Republic*

1. Introduction

The flow-induced vibration causes very interesting effects namely in the case of slender engineering structures. The airflow around the structure induces a wide spectrum of the non-linear aero-elastic processes. The beating effects which emerge due to vortex shedding may represent (almost) periodic load. This type of excitation is dangerous to the functionality and safety of structures. When the vortex frequency becomes close to the structure eigenfrequency, i.e., when the lock-in regime occurs, the quasiperiodic beatings constitute regular load and possibly cause significant fatigue in the material of the structure. Unfortunately, the non-linear character of slender or soft structures is often neglected in the engineering practice. This could lead to a significant underestimation of the overall response properties because the non-linear physical systems of such type are prone to the effect of the sub- or super-harmonic synchronization.

The sub- or super-harmonic synchronization effect represent cases when the driving frequency is close to integer multiples or fractions of the eigenfrequency of the structure. Due to non-linear effects, such load can induce significant vibration of the structure in the dominant eigenmode and can cause undesired or even dangerous effects.

The quasiperiodic phenomena of the resonance which occurs in the basic aero-elastic model and its stability properties were theoretically investigated by the authors in the past [3]. The recent study of the authors [4] concentrates on the stability assessments of the sub- or super-harmonic synchronization and its effect on the free component of the system response. The both works use the harmonic balance method for analytical investigation and their results depend on the fulfilment of the relevant assumptions. The authors also tried to illustrate some properties of the system using the numerical study in [1]. On the analysis of numerically obtained resonance curves, the authors shown dependence of the sub- and super-harmonic synchronization effect on the value of the excitation amplitude. It has been shown that due to the synchronization effect loses the response its beating character in a vicinity of integer multiples of the eigenfrequency of the structure and exhibits stationary response. The effect was better visible for lower excitation amplitudes, where the width of affected frequency interval was wider than it was for higher amplitudes. The super-harmonic synchronization effect (for driving frequency close to integer fractions of the dominant eigenfrequency) was much lower than the sub-harmonic one.

The present contribution studies numerically effect of the sub-harmonic, resonant and super-harmonic excitation on the frequency content of the response. This way it tries to measure effects of individual excitation modes on the character of the response, namely the influence of the sub- and super-harmonic excitation on the dominant eigenmode vibration.

The commonly used Single-Degree-of-Freedom (SDOF) or the more complicated Two-Degree-of-Freedom (TDOF) section models of a structure in the air stream represent a reasonable compromise between complexity and ability to characterise the dynamic processes. Such type of models is used often in the aerodynamic wind tunnel experiments and well serve their purpose. However, it appears that in many cases when the TDOF model is used, one of the components is dominant and, thus, the second one can be neglected. It reveals that majority of the resulting SDOF systems can be modelled by the van der Pol-Duffing or generalized van der Pol type equations or their combination adjusting degree of individual non-linear terms or their coefficients. This hypothesis is generally accepted, see, e.g., [2].

The paper is organized as follows. First, the generalized van der Pol model is described and modified to separate the forced and induced parts of the response. Then the resonance properties of the model are discussed. In Section 3, the individual sub- and super-harmonic cases are briefly mentioned. Results are summarized in the last section.

2. Mathematical model

Vibration of a slender structure in an airflow is usually modelled using the generalized van der Pol equation with a harmonic right hand side. The inclusion of the fourth order term in the description of the damping allows to better describe the lock-in regime and the corresponding most important limit cycles, from whose one is stable (attractive) and the other is unstable (repulsive). Consequently, the governing equation reads

$$\ddot{u} - (\eta - \nu u^2 + \vartheta u^4)\dot{u} + \omega_0^2 u = \omega_0^2 P \cos \omega t, \tag{1}$$

where u is the response of the system, $\omega_0^2 = K/m$ is the eigenfrequency of the associated linear system with stiffness K and concentrated mass m, η, ν, ϑ are positive coefficients of linear viscous and non-linear damping, $\omega_0^2 P$ is the amplitude of the harmonic excitation (excitation force per unit mass, frequency ω). P can be interpreted as an amplitude of the air pressure variation during vortex shedding.

Following [4], the solution in the sub- or super-harmonic cases can be written in the form

$$u = v + F_n \cos \omega t\,, \qquad F_n = P/(1 - n^2), \tag{2}$$

where $n = 2, 3, \ldots$ for sub-harmonic cases and $n = 1/2, 1/3, \ldots$ for super-harmonic cases. The solution u consists from a harmonic forced term ($F_n \cos \omega t$) and an auto-oscillation component v which represents the (possible) sub- or super-harmonic effects induced by the equation. The auto-oscillation part does not occur in a linear case. This approach neglects the damping, however, the introduced inaccuracy is acceptable, see the discussion in [4].

Introduction of Eq. (2) into (1) results in the following differential relation for the complementing auto-oscillation component v:

$$\ddot{v} + \omega_0^2 v(t) = \left(\eta - \nu(v + F\cos\omega t)^2 + \vartheta(v + F\cos\omega t)^4\right)(\dot{v} - F\omega \sin \omega t) + \left(\omega^2 - n^2\omega_0^2\right) F \cos \omega t\,. \tag{3}$$

3. Numerical analysis

A thorough analysis was conducted to illustrate the general properties of the theoretical system. Results obtained for particular setting of system parameters ($\eta = 1$, $\nu = 0.5$, $\gamma = 0.1$, $\vartheta = 0.025$) are described in this paragraph. The natural frequency of the oscillator is set as $\omega_0 = 1$ and thus the integer fractions and multiples of the natural frequency are easy to follow.

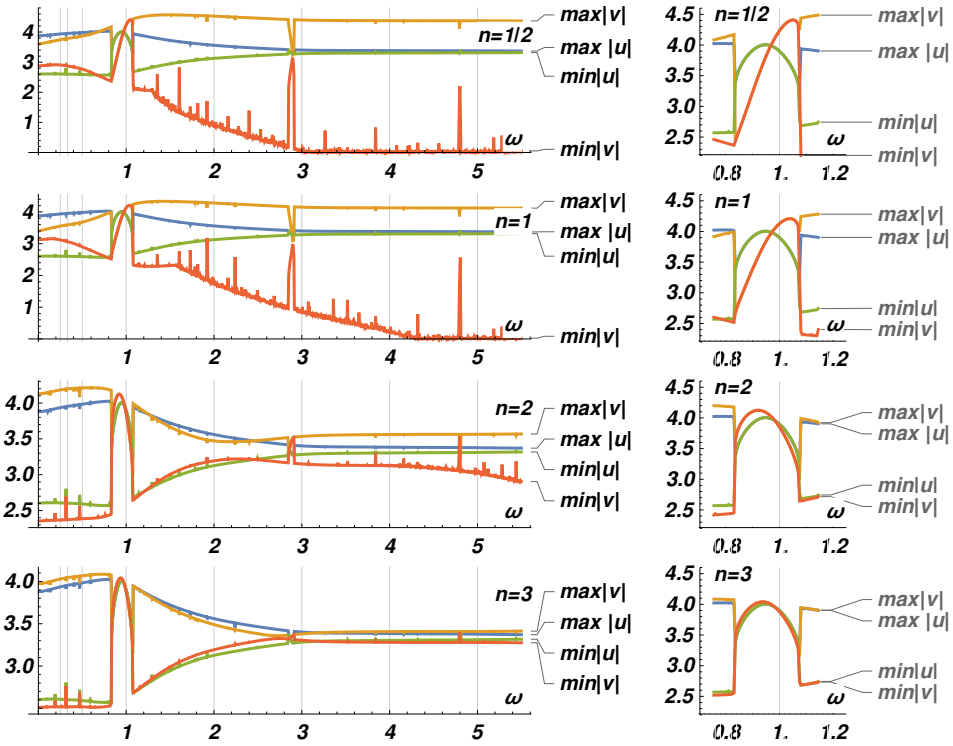

Fig. 1. Numerically obtained resonance curves of the generalized van der Pol equation response u, Eq. (1), and the corresponding auto-oscillation component v, Eq. (3), for the excitation amplitude $P = 0.75$ and $n = {}^1\!/_2, 1, 2, 3$; $\eta = 1$, $\nu = 0.5$, $\gamma = 0.1$, $\vartheta = 0.025$, $\omega_0 = 1$

The resonance curves for the selected example are depicted in Fig 1. Each row shows the complete plot on the left and a detailed view of interval $(0.7, 1.3)$ on the right hand side. Four curves are shown in individual graphs. For each excitation frequency ω they represent the maximal and minimal values of the solution envelope curves for u and v separately. When both minimal and maximal envelope curves coincide, the response is stationary. The response u does not change within individual plots, as it is apparent from Eq. (1), however, character of the part v varies significantly with increasing value of n. Fig. 2 shows dependence of the frequency content of the response (vertical axis, ω_1) on the excitation frequency (horizontal axis, ω). The heat map in the logarithmic scale shows amplified responses for $\omega_1 \approx 1$ and 3 for almost all excitation frequencies (horizontal), and also narrow peaks corresponding to selected excitation frequencies (vertical lines).

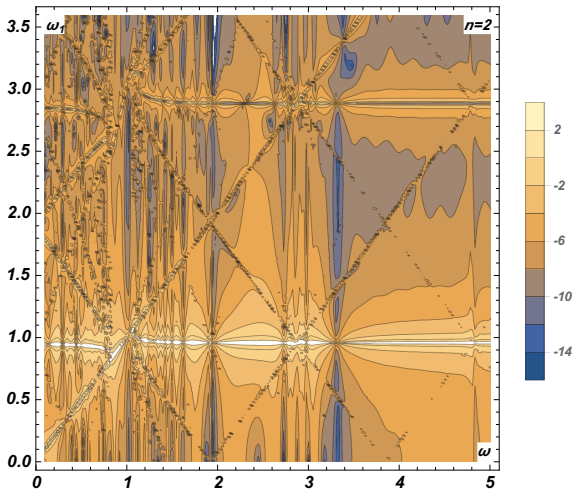

Fig. 2. Frequency properties of the auto-oscillatory part v for $n = 2$.

The most important results of the paper measure the influence of the sub- or super-harmonic excitation to individual frequency components of the response. These characteristics are shown in Fig. 3. The excitation intervals surrounding $2\omega_0$ and $3\omega_0$, $\omega_0 = 1\ \mathrm{s}^{-1}$, are considered in the

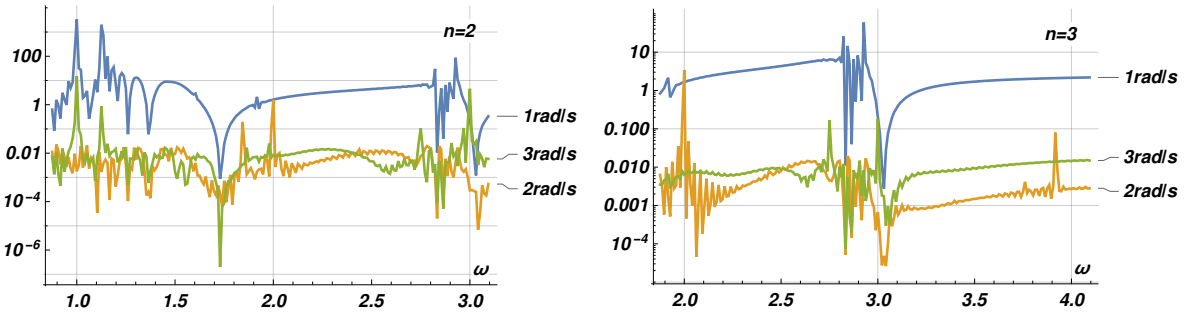

Fig. 3. Contributions of the individual frequency components 1, 2, 3 rad.s^{-1} in to the total auto-oscillation part of the response to the sub-harmonic excitation

left and right hand plots, respectively. The curves show amplitudes of the frequency components $\omega = 1, 2, 3$ rad^{-1} of the auto-oscillation response in dependence on excitation frequencies. In both plots is the component of the response in the eigenfrequency $\omega_0 = 1$ dominant (blue curves). In the left plot for $n = 2$, the response component "2rad/s" (brown curve) exhibits resonance for excitation $\omega = 2$, however, the system is apparently not very sensitive. Similar results are predicted also in [4]. More interesting is the case $n = 3$. The effect of the sub-harmonic excitation is clearly visible in all three component curves in the right hand plot. Note that the curves in Fig. 3 are approximative only because the actual resonance frequency is generally shifted down from the nominal values due to non-linear effects.

Results for $\omega = {}^1\!/_2, {}^1\!/_3, \ldots$ rad^{-1} are less apparent and are omitted due to space limitation.

4. Conclusions

The generalized van der Pol equation describes the state when the linear damping component becomes negative and the stability of the system is maintained due to non-linear effects only. Its selected resonance properties are identified numerically in the present contribution as a supplement to the approximate analytical results by the authors published in the past. The quantitative results support those theoretical, however, only a single value set was used and thus they serve for illustrative purposes only.

Acknowledgements

The kind support of the Czech Science Foundation project No. 19-21817S and of the RVO 68378297 institutional support are gratefully acknowledged.

References

[1] Fischer, C., Náprstek, J., Local stabilization of the quasiperiodic response of the generalized van der Pol oscillator, Proceedings of the conference Engineering Mechanics 2019, Institute of Thermomechanics of the Czech Academy of Sciences, Svratka, 2019, pp. 105-108.

[2] Koloušek, V., Pirner, M., Fischer, O., Náprstek, J., Wind effects on civil engineering structures, Elsevier, Amsterdam, 1984.

[3] Náprstek, J., Fischer, C., Analysis of the quasiperiodic response of a generalized van der Pol nonlinear system in the resonance zone, Computers and Structures 207 (2018) 59-74.

[4] Náprstek, J., Fischer, C., Super and sub-harmonic synchronization in generalized van der Pol oscillator, Computers and Structures 224 (2019) No. 106103, doi: 10.1016/j.compstruc.2019.106103.

COMPUTATIONAL MECHANICS 2019
35th conference with international participation
Srní
November 4 - 6, 2019

Numerical simulation of non-equilibrium wet steam flow in a turbine cascade

J. Fürst[a], J. Halama[a], V. Hric[a]

[a] *Faculty of Mechanical Engineering, Czech Technical University in Prague, Karlovo nám. 13, 121 35, Praha, Czech Republic*

The work deals with numerical simulation of non-equilibrium wet steam flows. The non-equilibrium steam is described by the system of Navier-Stokes equations. Thermophysical properties of the steam are calculated according to IAPWS IF97 formulation [3] and the non-equilibrium condensation is described by an additional two-equation model for liquid phase mass fraction and specific number of droplets (the so called mono-dispersion no-slip model, see e.g. [2] or [6]).

The system of Navier-Stokes equations describing the movement of the gas-liquid mixture is

$$\begin{aligned} \rho_t + \nabla \cdot (\rho \vec{v}) &= 0, & (1)\\ (\rho \vec{v})_t + \nabla \cdot (\rho \vec{v} \otimes \vec{v}) + \nabla p &= \nabla \cdot \vec{\vec{\tau}}, & (2)\\ (\rho E) + \nabla \cdot (\rho H \vec{v}) &= \nabla \cdot (\vec{\vec{\tau}} \cdot \vec{v}) - \nabla \cdot \vec{q}. & (3) \end{aligned}$$

Here ρ is the density, $\vec{v}$ is the common velocity, p is the pressure, $\vec{\vec{\tau}}$ is the effective deviatoric stress tensor, $E = e + v^2/2$ is the specific total energy where e is the specific internal energy, $H = h + v^2/2$ is the specific total enthalpy, and q is the effective heat flux. The system is coupled to standard two equation $k-\omega$ SST turbulence model.

The non-equilibrium condensation is described by the classical nucleation theory using the wetness w defined as the mass fraction of the liquid phase in the mixture and the specific number of droplets Q_0. These quantities are described by the following system of equations

$$\begin{aligned} (\rho w)_t + \nabla \cdot (\rho w \vec{v}) &= \frac{4}{3}\pi r_c^3 \rho_l J + 4\pi r_{30}^2 \rho_l \rho Q_0 \dot{r}, & (4)\\ (\rho Q_0)_t + \nabla \cdot (\rho Q_0 \vec{v}) &= J, & (5) \end{aligned}$$

where r_c is the critical droplet radius, $r_{30} = \sqrt[3]{3w/4Q_0\pi\rho_l}$ is the average droplet radius, $\dot{r}$ is the droplet growth ratio, ρ_l is the liquid phase density, and J is the nucleation rate. For details see, e.g., [2].

Thermophysical properties of the mixture are calculated using IAPWS IF97 equation of state for gaseous phase (denoted by subscript g) and combined with polynomial properties of liquid phase (subscript l) at the saturation line in the following way

$$\begin{aligned} \frac{1}{\rho} &= \frac{w}{\rho_l} + \frac{1-w}{\rho_g} \approx \frac{1-w}{\rho_g}, & (6)\\ h &= w h_l + (1-w) h_g = h_g - wL, & (7)\\ p &= p_g, & (8)\\ T &= T_g = T_l, & (9) \end{aligned}$$

where $L = h_g - h_l$ is the specific latent heat of evaporation.

The whole system of 9 partial differential equations is solved with an in-house finite volume solver based on the OpenFOAM framework [4]. The time dependent solution is of coupled system of equations is obtained using a modified version of sequential pressure correction method for compressible flows. The basic structure of the algorithm is described in the following listing for one time-step:

Algorithm 1: Pressure correction loop structure

input : State at the time t^n
output: State at the time t^{n+1}

```
1  update ρ using continuity eq. (1)
2  for outer corrector = 1, ... do
3  |  update v⃗ using momentum eq.(1) with actual pressure
4  |  update h using energy eq. (1) formulated in terms of enthalpy
5  |  correct condensation model by solving eq. (4) and (5)
6  |  calculate h_g using current L and w using eq. (7)
7  |  calculate gas phase properties from p and h_g using IF97
8  |  calculate mixture properties using eqns. (6-9)
9  |  for piso corrector = 1, ... do
10 |  |  correct the pressure in order to satisfy continuity
11 |  |  update velocity from the pressure correction; update turbulence model;
12 |  end
13 end
```

For most of calculations we use 2 PISO correctors (line 9) and 5-10 outer correctors (line 2), although the actual number of outer correctors depends on the setup of convergence criteria.

The solver is validated using 2D flows through a transonic nozzle. The nozzle inflow is characterized by the value of total pressure $p_{tot} = 78.39\,\text{kPa}$ and total temperature $T_{tot} = 373.15\,\text{K}$. The outflow is supersonic. The simulation is performed using a structured mesh with 500×100 hexahedral cells with near-wall refinement corresponding $y^+ \approx 1$.

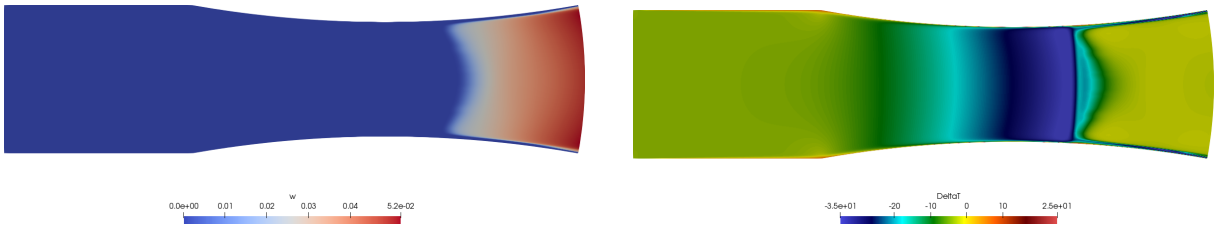

Fig. 1. Wet steam flow through a transonic nozzle: (*left*) wetness w, (*right*) sub-cooling $T - T_{sat}$

Fig. 1 shows the distribution of the wetness w (on the left) and the subcooling defined as the difference of T and the saturation temperature $T_{sat}(p)$. One can see that the condensation starts approximately at $T - T_{sat} \approx -35\,\text{K}$, whereas the equilibrium condensation would start at $T = T_{sat}$.

Fig. 2 shows the distribution of the pressure, wetness, and droplet radius along the axis of the nozzle. The pressure is compared to experimental data taken from [1]. One can see that the current calculation overpredicts the strength of the condensation shock, although the position of the shock corresponds very well to the experimental data. Similar behavior was found also

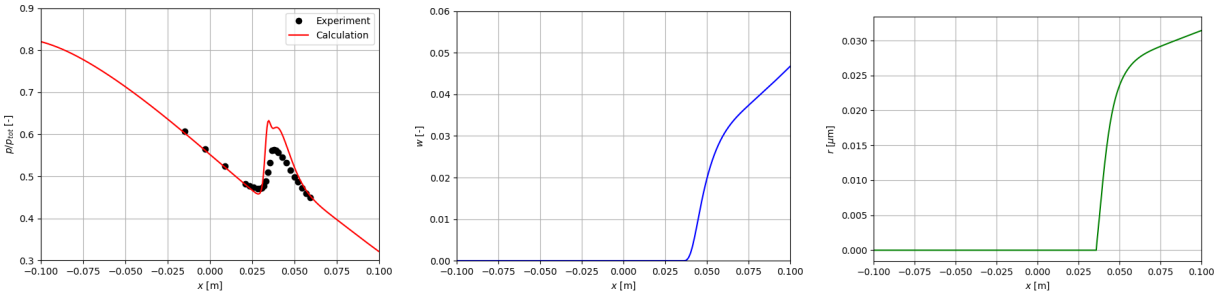

Fig. 2. Distribution of the pressure (*left*), wetness (*middle*), and droplet radius (*right*) along the nozzle axis

for completely different numerical method based on advanced Riemann solvers in [2] with very fine meshes. The wetness and the droplet radius correspond to results published in [2].

Fig. 3 shows the results of simulation of flows through a 2D model of turbine cascade. The simulation is done using an unstructured mesh with approximately 25 000 cells. The mesh is refined in the vicinity of the blade with $y^+ \approx 50$ and the near wall treatment with standard wall functions is used. The regime is characterized by the inlet total pressure $p_{tot} = 40.3\,\text{kPa}$, total temperature $T_{tot} = 354\,\text{K}$ and axial flow direction. The outlet pressure is $p_2 = 16.3\,\text{kPa}$. Fig. 3 shows the distribution of the pressure, wetness, and the entropy in the form if is-lines. One can recognize an entropy production in the zone of condensation indicating the energy losses due to phase transition. The distribution of the wetness documents that the model predicts also evaporation at the shock wave cased by the temperature jump across the shock. The distribution of the pressure along the blade shows quite good agreement with experimental data [5].

The presented results show that the solver is able to simulate wet steam flows with non-equilibrium condensation model. The method is based on a very simple two-equation model which usually does not predict very well droplet sizes. Nevertheless, the wetness as well as the flow field is predicted with reasonable accuracy. The use of real gas equation of state naturally slows down the execution speed of the solver, although this slowdown is not prohibitive for pressure correction family of schemes where on spends a large portion of time in the solution of the Helmholtz equation for the pressure.

Acknowledgements

The work was supported by TACR, project no. TK01020029. We also thank Doosan Škoda Power for allowing us to present the results of the calculations.

References

[1] Barschdorf, D., Course of state variables and gas-dynamic correlations in the spontaneous condensation of pure water vapor in Laval nozzles, Forschung im Ingenieurwesen 37 (5) (1971) 146-157. (in German)

[2] Halama, J., Hric, V., Numerical solution of steam flow in a nozzle using different non-equilibrium condensation models, Applied Mathematics and Computation 272 (2016) 657-669.

[3] Wagner, W., Cooper, J. R., Dittmann, A., Kijima, J., Kretzschmar, H.-J., Kruse, A., Mareš, R. Oguchi, K., Sato, H., Stöcker, I. Šifner, O., Takaishi, Y., Tanishita, I., Trübenbach, J., Willkommen, T., The IAPWS industrial formulation 1997 for the thermodynamic properties of water and steam, Journal of Engineering for Gas Turbines and Power 122 (1) (2000) 150-184.

[4] Weller, H. G., Tabor, G., Jasak, H., Fureby, C., A tensorial approach to computational continuum mechanics using object-oriented techniques, Computers in Physics 12 (6) (1998) 620-631.

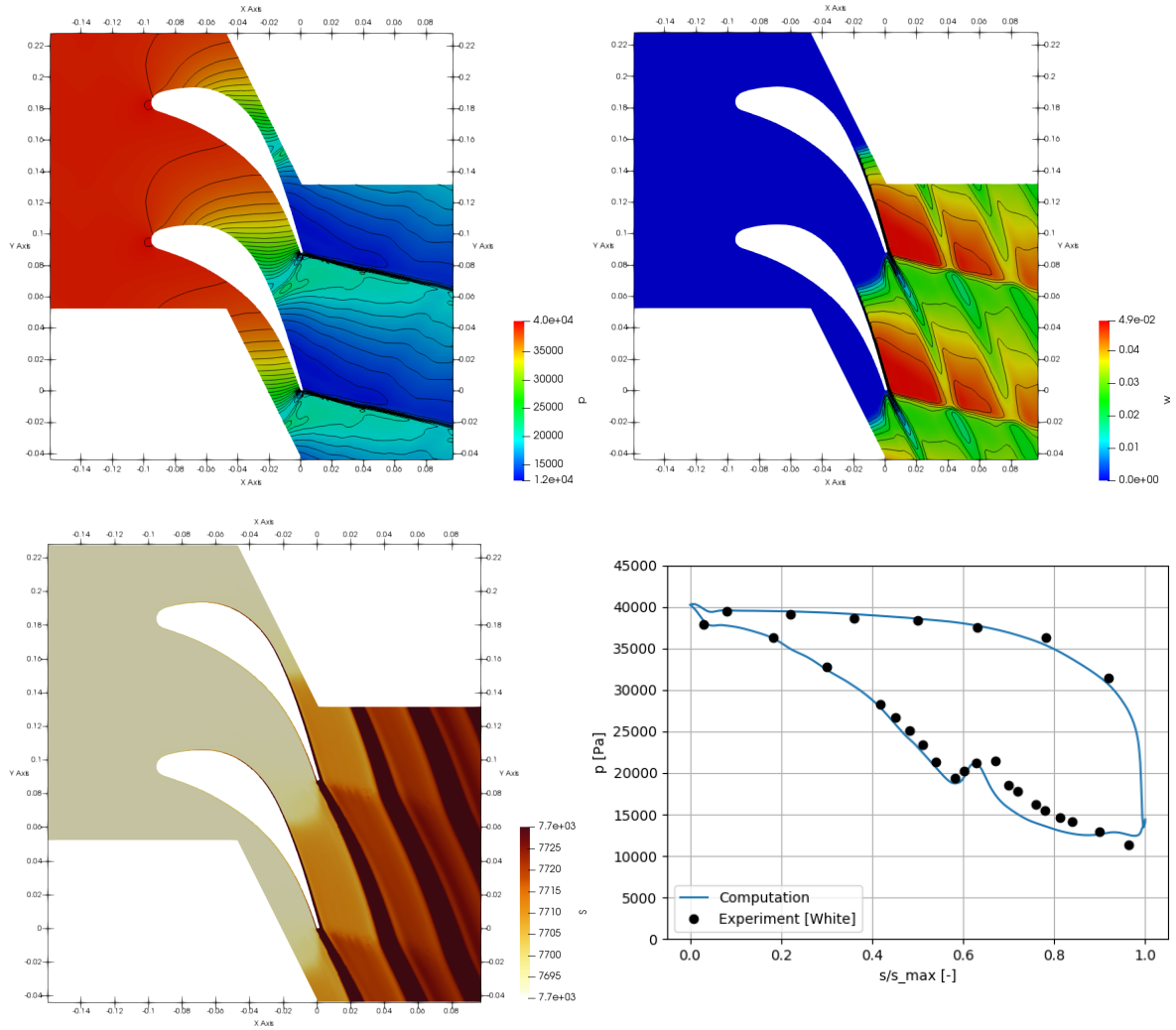

Fig. 3. Wet steam flow through a turbine cascade, the isolines of the pressure, wetness, and entropy, and the distripution of the pressure along the blade

[5] White, A. J., Young, J. B., Walters, P. T., Experimental validation of condensing flow theory for a stationary cascade of steam turbine blades, Philosophical Transactions of the Royal Society A: Mathematical, Physical and Engineering Sciences 354 (1704) (1996) 59-88.

[6] Wróblewski, W., Dykas, S., Chmielniak, T., Models for water steam condensing flows, Archives of Thermodynamics 33 (1) (2012) 67-86.

COMPUTATIONAL MECHANICS 2019
35th conference with international participation
Srní
November 4 - 6, 2019

Multibody modelling and numerical simulations in drive train dynamics of road vehicles

M. Hajžman[a], R. Bulín[a], Š. Dyk[a]

[a] *NTIS – New Technologies for the Information Society, Faculty of Applied Sciences, University of West Bohemia, Univerzitní 8, 301 00 Plzeň, Czech Republic*

Multibody approaches are very powerful tools for the modelling and analysis of real mechanical systems. Design elements of drive trains perform large motion with both rotations and translations and there are many force interactions between particular parts. Therefore the modelling methodology based on the multibody dynamics is suitable for the analysis and optimization of drive trains. This paper introduces the methodology for the creation of particular models and for performing numerical simulations of various operational vehicle states. It addresses two solved case studies of real rally car drive train problems including experimental verification and validation.

The approach used in this work is based on generalized (Cartesian) coordinates, which lead to the mathematical model in the form of a set of differential-algebraic equations (DAEs). Holonomic rheonomic constraints between the coordinates described by vector $\mathbf{q}$ can be written using the vector notation $\mathbf{\Phi}(\mathbf{q}, t) = \mathbf{0}$ and after their differentiation Jacobian matrix $\mathbf{\Phi}_q$ is obtained. Common mathematical model can be expressed as the set of differential-algebraic equations of index one in the form

$$\begin{bmatrix} \mathbf{M} & \mathbf{\Phi}_q^T \\ \mathbf{\Phi}_q & \mathbf{0} \end{bmatrix} \begin{bmatrix} \ddot{\mathbf{q}} \\ -\boldsymbol{\lambda} \end{bmatrix} = \begin{bmatrix} \mathbf{g}(\mathbf{q}, \dot{\mathbf{q}}, t) \\ \boldsymbol{\gamma}(\mathbf{q}, \dot{\mathbf{q}}, t) \end{bmatrix} \tag{1}$$

by the double differentiation of the constraint equations with respect to time. Vector $\boldsymbol{\gamma}(\mathbf{q}, \dot{\mathbf{q}}, t)$ represents the remaining terms after the constraints differentiation. Solution of equations of motion (1) can be based e.g. on elimination of Lagrange multipliers [2] and further direct integration of the underlying ordinary differential equation. Vector of Lagrange multipliers λ is introduced in Eq. (1). Matrix $\mathbf{M}$ is the global mass matrix of the multibody system and vector $\mathbf{g}(\mathbf{q}, \dot{\mathbf{q}}, t)$ contains centrifugal and Coriolis inertia forces, elastic and damping forces and other externally applied forces including the gravity.

The first solved problem is aimed at sequential manual transmissions which are common sources of impacts and contacts that impose time varying excitation. Design engineers need sufficient computational methodologies and tools in order to predict dynamic behaviour of developing systems. The computational model of the particular driving system with a sequential gearbox was built up in MSC.Adams. The model visual representation is shown in Fig. 1 on the left. The purpose of the model is to simulate shifting between the third and the fourth gear stage because it is the most common maneuvre during a rally car race.

At the input of the driving chain, all the engine parts are modelled using a body with reduced inertia properties (see position 1 in Fig. 1), which include inertia of all relevant rotating parts of the engine. Using torsional elastic coupling of the clutch, body 1 is connected to the inner

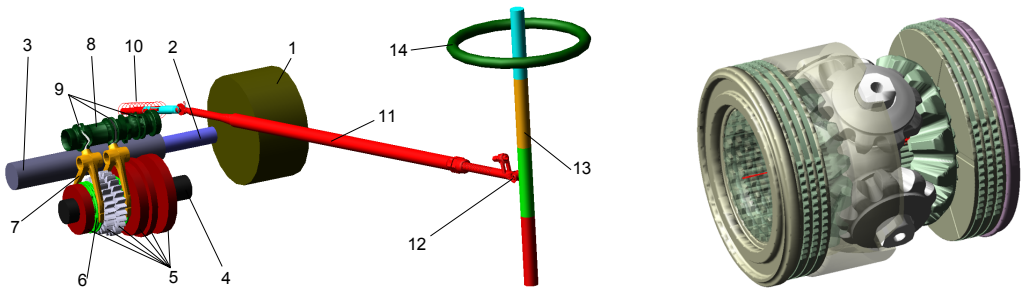

Fig. 1. Visualization of the gearbox model (*left*) and the differential model (*right*)

primary shaft (position 2 in Fig. 1), which goes through whole body of outer primary shaft (position 3) and at the end, both shafts are coupled by gear coupling. Body 3 – outer primary shaft – includes reduced mass properties of all primary gears. Torque flow is transmitted through the third or the fourth gear stage to the secondary shaft by means of a claw clutch between dog-rings (position 6) and secondary gears (position 5). Gear shifting is performed by moving a flexible gear-shift lever (position 13). The translational motion of the rod is transformed by gear coupling to the rotation of a selector (position 8) with guide curves (position 9), which translate corresponding forks (position 7) with dog-rings along the axis of the selector. In this manner, the desired gear stage is chosen. Model's input characteristics are engine angular velocity, engine driving torque and shifting force, which is measured by sensor located between the gear-shift lever and the rod. The aim of the model is to simulate the shifting process and to evaluate the overall shifting time. The results obtained using the computational model were compared to experimental data. The comparison of computed and experimental data for the ideal case (correct shifting without collision), that the presented model of the state dependent shifting force is in good compliance with the experimental data. The resultant driving torque also corresponds to the experimental data.

The second topic deals with approaches to the modelling and dynamical analysis of a special class of automotive differentials called limited-slip differentials. It is also the problem characterized by large motion and contact and friction interactions. The differential is modelled in complex manner with detailed interior structure (see Fig. 1 on the right) and with other elements of the whole drive train. The developed multibody differential model can be utilized in wide range of simulation tasks. In order to generate typical locking characteristics the model was employed in nonlinear dynamical analyses with prescribed input torque and output revolutions, which are motivated by typical experimental tests. The locking characteristics are composed of total torque transmitted by both semi-axles, which is plotted on the horizontal axis, and the difference of theses torques, which is plotted on the vertical axis. The resulting characteristics were successfully compared with experimental results.

Acknowledgement

The research was supported by the project LO1506 of the Czech Ministry of Education, Youth and Sports under the program NPU I.

References

[1] Bulín, R., Hajžman, M., On the modelling of contact forces in the framework of rigid body dynamics, Manufacturing Technology 14 (2014) 136-141.

[2] Hajžman, M., Polach, P., Application of stabilization techniques in the dynamic analysis of multibody systems, Applied and Computational Mechanics 1 (2007) 479-488.

COMPUTATIONAL MECHANICS 2019
35th conference with international participation
Srní
November 4 - 6, 2019

Optimization of velocity feedback control parameters of machine tools drive axis

V. Halamka[a], Z. Šika[a], J. Moravec[a], P. Beneš[a]

[a] *Faculty of Mechanical Engineering, Czech Technical University in Prague, Technická 4, 166 07 Praha, Czech Republic*

Machine tool control has evolved over the years. The original mechanical principle was replaced by electric and then electronic. Modern machines use control software to control individual drive axes. The most commonly used method of driving axis control is cascade control (Fig. 1). This method consists of position, velocity and current feedback, which are nested. Each feedback includes a regulator. The parameters of these regulators are subject of optimization, [7].

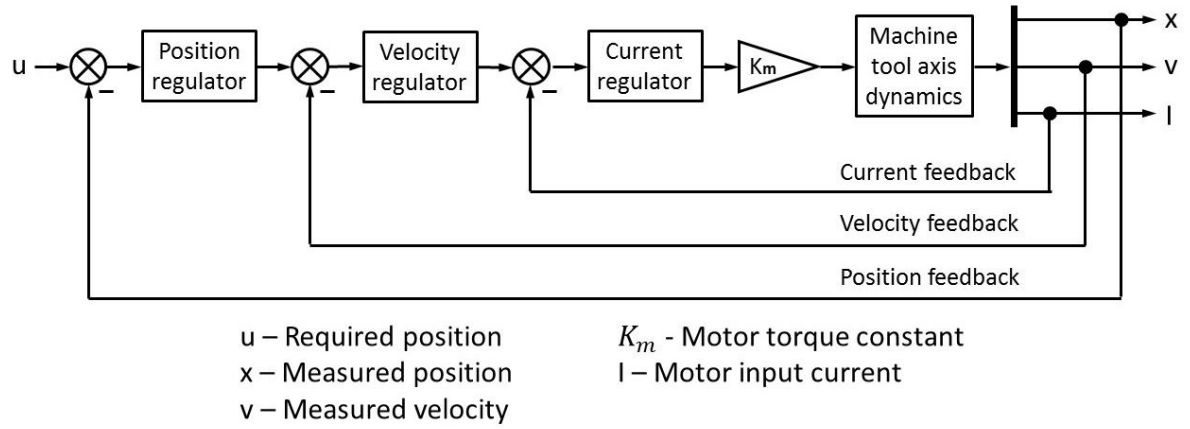

Fig. 1. Cascade control scheme, [7]

Optimizing these parameters is very demanding and requires a high level of expertise from the operator who performs the process. For this reason, there was a need to develop a general methodology. Development of this methodology and its subsequent application to the identified model of the real machine is the subject of this lecture.

The development itself can be divided into three phases: formulation of the optimization task, creation of the user interface (instructions for working with the program) and testing the methodology functionality.

First, a velocity feedback model (Fig. 2) in form of state-space was built. The velocity feedback was chosen because its tuning is the most difficult and usually brings the most problems. The model consists of two higher units (velocity regulator and mechanical system with current feedback) and negative feedback. The velocity regulator consists of a PI regulator, a series of notch filter and low-pass filter. A state-space description of mechanical system with current feedback can be obtained by modelling or identifying, [4], [1].

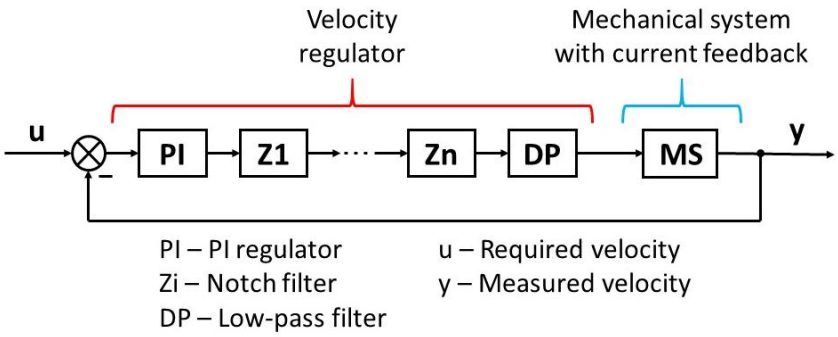

Fig. 2. Model of velocity feedback

Thereafter, the criteria of control optimization were selected. These criteria include the course of the amplitude Bode characteristic and the system response to the unit step. The distance of the system from the stability border was also considered. Based on these criteria, the target function was compiled as an input of the optimization algorithm. For the methodology two optimization methods were used: fminsearch [5] (local optimization) and the genetic algorithm [3] (global optimization).

The methodology was applied to the identified models of the real machine tool at different loads. Based on the results of the optimization, it can be said that the methodology is functional and can be used as an alternative to manual tuning by the operator.

Acknowledgements

The work has been supported by the project SGS19/156/OHK2/3T/12 "Mechatronics and adaptronics 2019" of Czech Technical University in Prague.

References

[1] Callafon, R. D., Moaveni, B., General realization algorithm for modal identification of linear dynamic system, Journal of Engineering Mechanics 134 (9) (2008) 712-722.
[2] Gawronski, W.K., Advanced structural dynamics and activ control of structures, Springer-Verlag, New York, 2004.
[3] Houck, C., Joines, J., Kay, A., A genetic algorithm for function optimization: A MATLAB implementation, North California State University, 1994.
[4] Katayma, T., Subspace methods for system identification, Springer- Verlag, London, 2005.
[5] Lederer, P., Theory and optimization of mechanical systems I, Prague, 1988. (in Czech)
[6] Preumont, A., Vibration control of active structures an introduction, Solid Mechanics and its Application 96 (2002).
[7] Souček, P., Servomechanisms in production machines, CTU, Prague, 2004.
[8] Šika, Z., Zavřel, J., Valášek, M., Residual modes for structure reduction and efficient coupling of substructures, Bulletin of Applied Mechanics 5 (19) (2009) 54-59.

COMPUTATIONAL MECHANICS 2019
35th conference with international participation
Srní
November 4 - 6, 2019

Structural analysis of parts made by 3D printing reinforced by long fibers

M. Handrik[a], M. Vaško[a], M. Ságа[a], J. Majko[a]

[a] *Faculty of Mechanical Engineering, University of Žilina, Univerzitní 8215/1, 010 26 Žilina, Slovak Republic*

1. Introduction to composites and modelling of CFRTP composites

The composites are attractive materials for many sectors of industry, but their working principle limits faster extension in the manufacturing process. In recent time, additive manufacturing becomes an alternative to the traditional production methods and 3D printing is one of the methods, which are involved in additive manufacturing. Although there are many production limitations, the production variability of printed composites is better than offer conventional methods. The production limitations significantly relate to fibre addition into a printed structure. This is the case for solely two 3D printing methods allow printing of continuous fibre reinforced thermoplastic (CFRTP) composite. The parts produced by additive manufacturing achieve a tensile strength of approximately 700 MPa. The development of 3D printing and composite production is still ongoing, thus there is an expectation of a continued increase in the production [4].

The most of applications require reliable prediction of composite behaviour under loading. Stress and deformation analysis of reinforced composites can be done at three different levels. The microscopic level examines deformations and stresses at the level of composite constituents. Attributes, which affect results, are fibre shape, geometric distribution and properties of composite components. At the macroscopic level, a composite is considered as homogeneous equivalent material, but solely deformation, buckling and vibration frequencies could be predicted. Simulation at the microscopic level is limited by a computational capacity and the macroscopic level cannot calculate stress distribution in a laminate. The mesoscale approach gets over these limitations and allows prediction of stresses and strains in every lamina, but elastic properties, fibre orientation and layer thickness of each lamina must be given into the program [3].

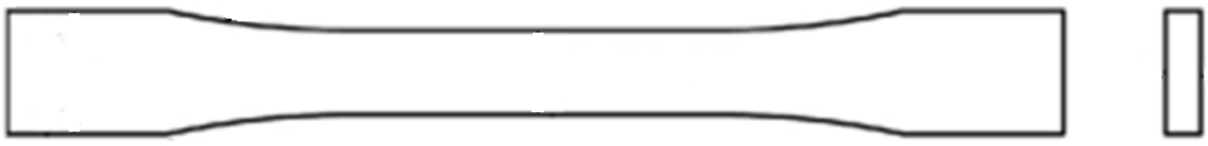

Fig. 1. Specimen shape

The simulation of CFRTP composite specimen loaded to the tension was performed using two methods - rebar and geometry distribution approaches. Assessed dogbone shaped specimen (Fig. 1) was designed in the CAD program and imported to the slicing software developed by the printer manufacturer.

The models of the specimen were created using scripts in MATLAB, which help with model generation in program ADINA. Both modelling approaches are described, analysed and compared in the next chapter.

2. Modelling of CFRTP composites – description and analysis

2.1 Embedded reinforcement method

The method initially proposed for modelling of reinforced concrete; currently exploited for composite modelling. The model is based on the virtual work principle. The reinforcement could be modelled as smearded or discrete rebar.

The discrete rebar models each fibre separately. This method is appropriate to modelling of structures, which consist of sparsely deposited fibres with inconsistent attitudes, for instance, fibre orientation, material, cross-section etc. The reinforcement start point and curved trajectory of the fibre in the structure do not represent complications, because each fibre in this method is modelled separately as a beam with uniaxial stiffness. The widespread problem is the bonding between fibre and matrix. Therefore representing elements, such as REINF 264 (Fig. 2), do not allow relative movement between composite components [2].

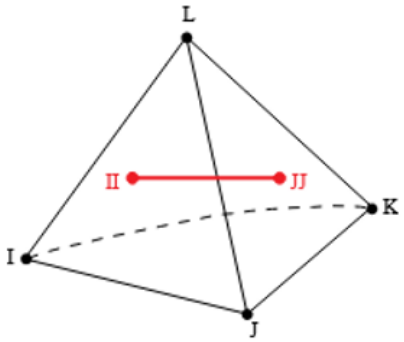

Fig. 2. Element REINF 264, [2]

The discrete rebar element was the first assessed modelling method of CFRTP composite. The modelling process of the composites in program ADINA is realised in the following steps. Rebar line representing designed reinforcements in the composite structure intersects faces of generated 3D solid elements (Fig. 3, left). In this intersections are created nodes, which are subsequently connected utilizing truss elements. The constraint equations define connections between the rebar truss elements and generated mesh of the matrix. The connection is prepared between the nodes and the three closest nodes of the mesh (Fig. 3, right) [1].

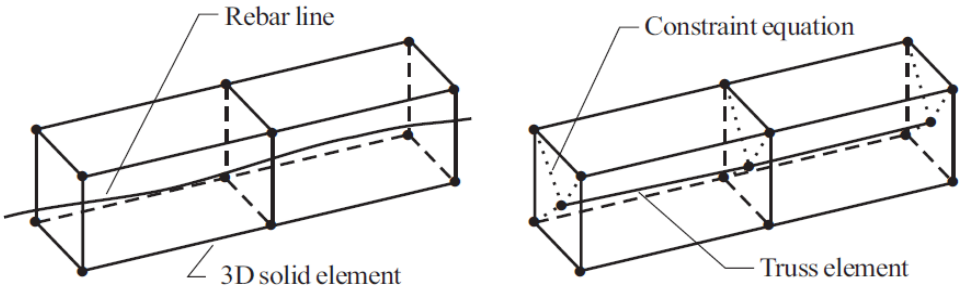

Fig. 3. Generation process of rebar elements, [1]

The constraint equations are added to the system of equations, that models simulated tension test. The addition effects to raising matrix density, therefore computation becomes more difficult at time consumption and computational resources.

In terms of mesh convergence criterion, usage of the rebar elements affects solution accuracy because finite element program divides the rebar lines into the truss elements of various lengths (Fig. 4).

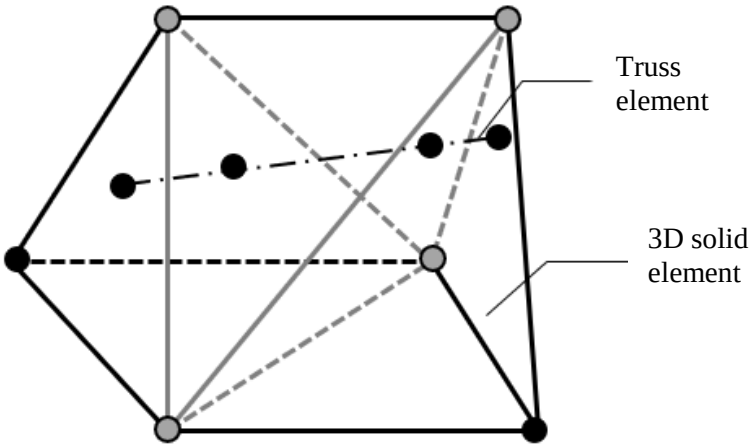

Fig. 4. Different length of truss elements

Sizing variability of the truss rebar elements requires the application of direct solvers. Various lengths of the truss elements affect the computational precision. In comparison to longer truss elements, relatively negligible computational error in deformations of small truss element can cause a large error in strains and stresses. This feature of the rebar modelling influences the occurrence of significant variations of stresses on fibres (Fig. 5).

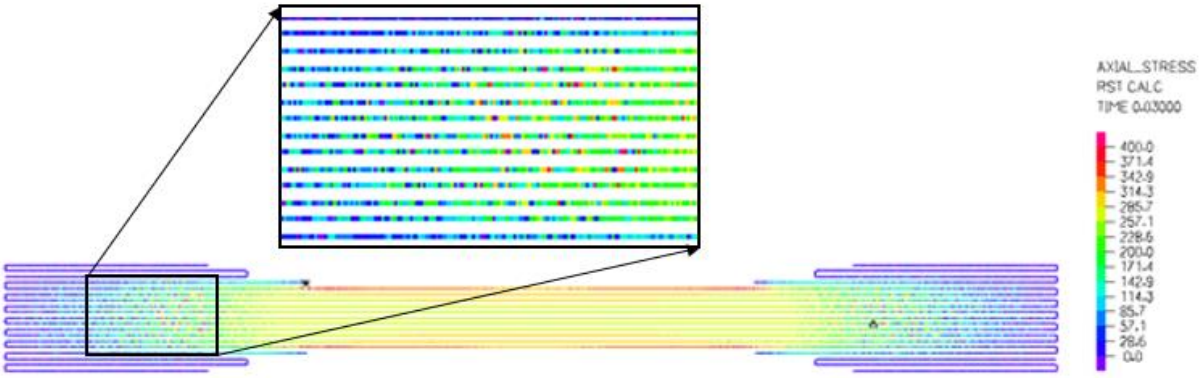

Fig. 5. Stress distribution in fibers of CFRTP composite specimen modelled using rebar elements

2.2 Geometry distribution approach

The second assessed modelling method was geometry distribution of the composite model. As a result, the location of the truss element representing fibre reinforcement in the structure is on the edge of the matrix element (Fig. 6). The connections between the truss elements and the solid elements are generated without constraint equations. Thus stiffnesses of fibres are added to some elements in matrix stiffness. This type of modelling reduces computational time consumption.

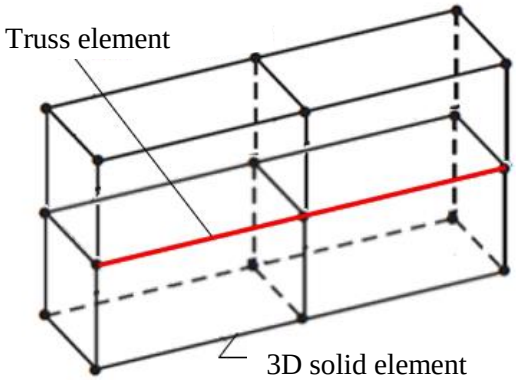

Fig. 6. Truss element located on edge of matrix element

The main advantage of the method is equal sizing of the truss elements because there is a relatively small difference between the largest and the smallest elements on diagonal. Therefore iterative solvers are efficient. Compared to the rebar elements, solution accuracy is higher and computed stress distributions fluently change without significant gaps (Fig. 7).

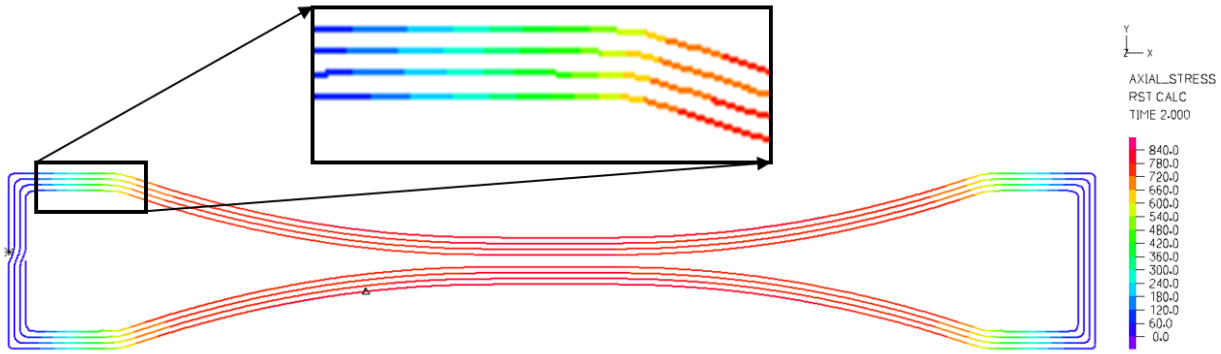

Fig. 7. Stress distribution in fibers of CFRTP composite specimen modelled using geometry distribution

3. Conclusion

Both presented methods are appropriate to modelling of CFRTP composites in program ADINA, but geometry distribution modelling approach offers more benefits than rebar elements method. These benefits are: stress computation in fibres is more precise, a matrix of the system has smaller bandwidth and display of stresses on fibre layers is better.

Acknowledgements

The work has been supported by the grant project KEGA No. 037ŽU-4/2018 and APVV 14-0096.

References

[1] ADINA, Theory and Modelling guide, Vol. I, Adina structure, help manual, 2017.
[2] ANSYS, Reinf 264 element description, In: mm.bme.hu [online], available at: http://www.mm.bme.hu/~gyebro/files/ans_help_v182/ans_elem/Hlp_E_REINF264.html
[3] Barbero, J.E., Finite element analysis of composite materials using ANSYS®, CRC Press, Boca Raton, 2014.
[4] Goh, G.D., Yap, Y.L., Agarwala, S., Yeong, W.Y., Recent progress in additive manufacturing of fiber reinforced polymer composite, Advanced Materials Technologies 4 (1) (2018).

COMPUTATIONAL MECHANICS 2019
35th conference with international participation
Srní
November 4 - 6, 2019

Rubber ageing at elevated temperature – model calibration

J. Heczko[a], R. Kottner[b]

[a] Department of Mechanics, Faculty of Applied Sciences, University of West Bohemia, Univerzitní 8, 301 00 Plzeň, Czech Republic
[b] NTIS – New Technologies for the Information Society, Faculty of Applied Sciences, University of West Bohemia, Technicka 8, 301 00 Plzeň, Czech Republic

1. Introduction

The dynamic network model by Naumann and Ihlemann [4] is considered in order to capture mechanical behavior of rubber subjected to mechanical and thermal loading. The model has been adapted to account for fatigue damage instead of Mullins effect [3].

The model is based on a kinematic split such that the deformation gradient

$$\mathbf{F} = \mathbf{F}_2 \, \mathbf{F}_1 \,, \tag{1}$$

where $\mathbf{F}_1$ corresponds to a stress-free state of deformation and $\mathbf{F}_2$ is the elastic deformation. In its simplest form (neo-hookean), the strain energy density is

$$W = C_{10} \, (1 - D) \, \mu \, \nu \, \left(\mathbf{C}_2 : \mathbf{I} - 3 \right) , \tag{2}$$

where $\mathbf{C}_2 = \mathbf{F}_2^{\mathrm{T}} \, \mathbf{F}_2$ is the right Cauchy-Green deformation tensor corresponding to the elastic part of deformation. The internal variables μ and ν reflect increase and decrease in material stiffness due to chemical ageing respectively and under the assumption of homogeneous oxygen distribution, valid, e.g., in thin rubber samples, are driven by the following evolution equations:

$$\dot{\mu} = k_{\mathrm{R}} \, \mu \,, \quad \dot{\nu} = -k_{\mathrm{S}} \, \nu \,, \quad \mu(0) = \nu(0) = 1 \,, \tag{3}$$

where the coefficients are usually assumed to behave according to the Arrhenius law

$$k_{\{\mathrm{R,S}\}} = k_{\{\mathrm{R,S}\}_0} \exp \left[- \frac{E_{\{\mathrm{R,S}\}}}{R \, T} \right] , \tag{4}$$

$k_{\{\mathrm{R,S}\}_0}$ and $E_{\{\mathrm{R,S}\}}$ being material parameters, $R = 8.314 \, \mathrm{J \, mol^{-1} \, kg^{-1}}$ the gas constant, and T absolute temperature. In the case of thick samples, the diffusion equation with an added reaction term would be used to model oxygen transport and both k_{R} and k_{S} would depend on oxygen concentration.

Fatigue damage is described by a power law [1]

$$\dot{D} = (-A \, Y)^a \,, \quad Y = \frac{\partial W}{\partial D} \,, \tag{5}$$

A and a being its parameters.

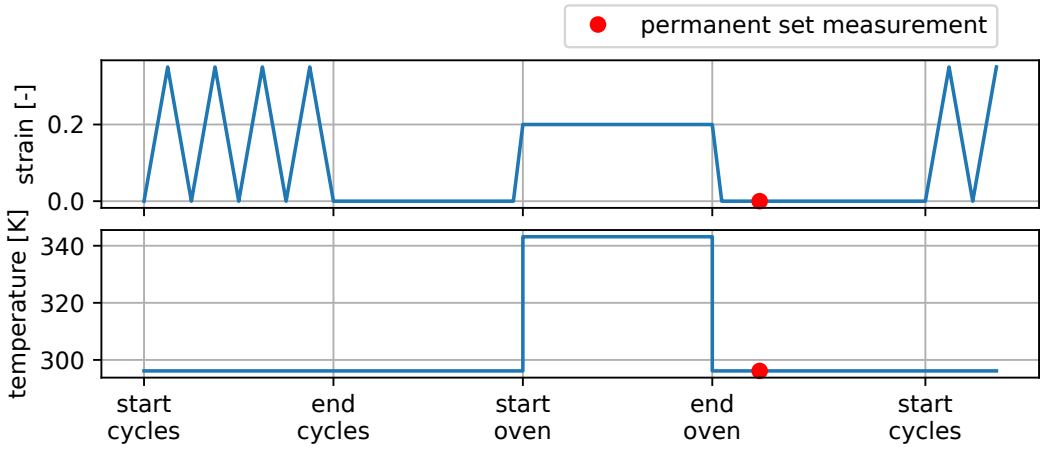

Fig. 1. Single block of prescribed strain and temperature

2. Experimental procedure

The test sequence, used for calibration of the model, consists of repeated cyclic loading and an ageing period of constant deformation at elevated temperature, see Fig. 1. The measured data contain both stress-strain curves from the cyclic loading and permanent set measured before and after each ageing period. All cycles were performed up to $35\,\%$ nominal deformation in compression whereas the constant deformation during the ageing periods was one of 0, $15\,\%$ or $25\,\%$. The ageing temperature was either $23 \pm 2\,^{\circ}\mathrm{C}$ or $70 \pm 2\,^{\circ}\mathrm{C}$.

3. Numerical modeling and model calibration

The numerical simulations were implemented with the assumption of uniaxial stress and homogeneous distribution of oxygen and temperature. The system of partial differential equations therefore changes into ordinary differential equations. Moreover, the ageing variables μ and ν become independent of strain history.

The calibration procedure was formulated as a nonlinear least squares problem with the objective function to be minimized

$$f(\mathbf{x}) = \sum_i \frac{\sum_j \left(\sigma_{ij} - \sigma_i(t_j)\right)^2}{\sum_j \sigma_{ij}^2}\,, \tag{6}$$

where i denotes different experiments (e.g., cyclic stretch, permanent set, different stretch values), t_j are values of the independent variable (i.e., time), σ_{ij} are measured values, and $\sigma_i(\cdot)$ is the numerical simulation of the i-th experiment, and the vector $\mathbf{x} = [C_{10}, k_{\mathrm{R}}, E_{\mathrm{R}}, k_{\mathrm{S}}, \ldots]^{\mathrm{T}}$ contains the unknown parameters of the model.

It is known that calibration of the Arrhenius-type relation might lead to multicollinearity, but several techniques exist that overcome this issue [5]. However, in the case of the experimental data considered here, the principal obstacle is insufficient data regarding temperature, i.e. only two temperature values being measured. The solution to this problem is to discard relation (4) completely and consider separate reaction rates for each temperature: k_{R23}, k_{R70}, k_{S23}, and k_{S70}. Should sufficient temperature-data be available, the parameters of (4) may be fitted to the values of the independent reaction rates.

Based on numerical examples [2], a combination of relaxation and permanent-set measurements is suggested in order to identify the time- and history-related parameters of the dynamic network model under constant temperature. The data available here (Section 2) contain cyclic

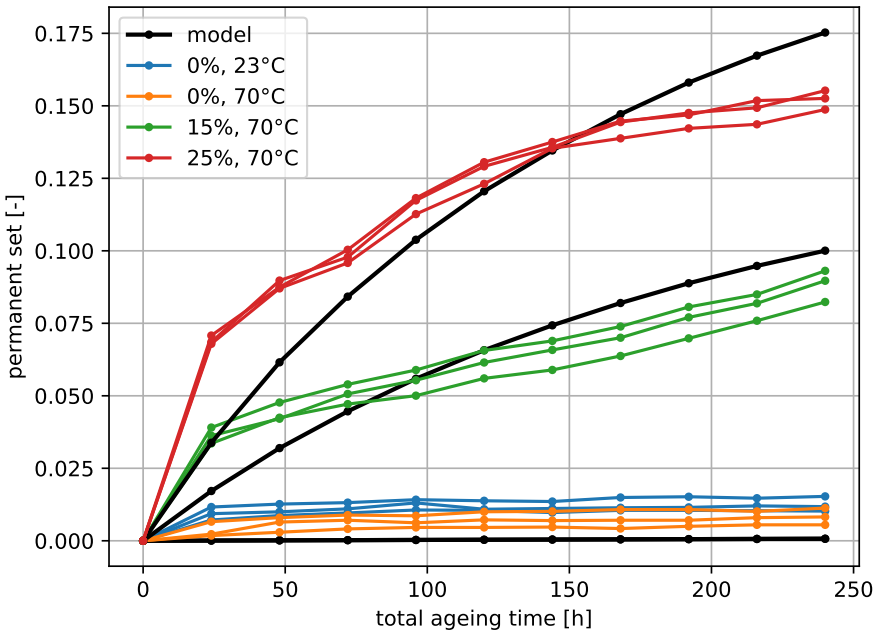

Fig. 2. Comparison of measured and predicted permanent-set

stretch instead of relaxation. Similar numerical examples with these data used here suggest that the reaction rates are identifiable in the absence of damage. The effects of damage compete with those of network-scission, which might lead to non-uniqueness of model calibration.

Nevertheless, an attempt to calibrate the model to real-world data was made. The identified parameters are:

$$C_{10} = 6.69\,\mathrm{MPa}\,, \qquad k_{\mathrm{R23}} = 6.36 \cdot 10^{-7}\,\mathrm{s}^{-1}\,, \qquad k_{\mathrm{R70}} = 1.12 \cdot 10^{-6}\,\mathrm{s}^{-1}\,,$$
$$k_{\mathrm{S23}} = 5.90 \cdot 10^{-7}\,\mathrm{s}^{-1}\,, \qquad k_{\mathrm{S70}} = 8.32 \cdot 10^{-7}\,\mathrm{s}^{-1}\,, \qquad A = 1.18 \cdot 10^{-10}\,\mathrm{Pa}^{-1}\,,$$
$$a = 2.25\,.$$

A comparison of measured and predicted permanent-set is shown in Fig. 2. Comparison of stress-strain curves is shown in Fig. 3.

4. Summary and conclusions

Results of the calibration clearly show several discrepancies between the model and real-world data. The simplifications considered of lesser importance are uniaxial stress assumption and neglecting of oxygen diffusion.

One of the most obvious (and expected) source of disagreement is that only the simplest form of the dynamic network model was used, i.e., only the neo-hookean term with the coefficient C_{10}. Should other terms be included, better description of the stress-strain curves would be expected.

Another shortcoming of the model, when compared to the real-world data, is probably omission of mechanisms other than chemical ageing. This can be shown from the histories of permanent-set, where the blocks of cyclic stretch induce some permanent deformation in the experimental data, as opposed to the numerical model where the impact of cyclic stretch

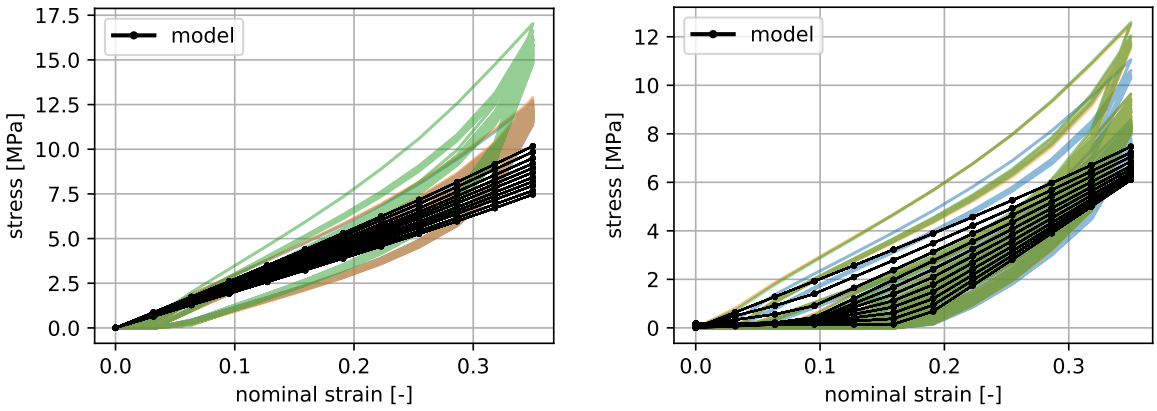

Fig. 3. Stress-strain curves at 0 % (*left*) and 25 % (*right*) strain during the ageing blocks

blocks on permanent-set seems to be negligible. This behavior might be corrected by adding mechanisms such as plasticity, viscoelasticity or physical ageing to the model.

Finally there is the issue of sufficient data and proper selection of loading histories that would enable the identification of a unique combination of parameters. This is already subject of an ongoing research [2], however, the results of this work are essential regarding further modifications of the material model, as discussed above.

Acknowledgements

The work was supported by the students grant system SGS-2019-009 and from European Regional Development Fund-Project „Research and Development of Intelligent Components of Advanced Technologies for the Pilsen Metropolitan Area (InteCom)" (No. CZ.02.1.01/0.0/0.0/17_048/0007267).

References

[1] Ayoub, G., Naït-Abdelaziz, M., Zaïri, F., Gloaguen, M., Charrier, P., A continuum damage model for the high-cycle fatigue life prediction of styrene-butadiene rubber under multiaxial loading, International Journal of Solids and Structures 48 (18) (2011) 2458-2466.

[2] Heczko, J., Kottner, R., Identification of parameters in the case of material model of chemical ageing and damage, Proceedings of the 11th European Conference on Constitutive Models for Rubber – Constitutive Models for Rubber XI, Nantes, CRC Press/Balkema, 2019, pp. 593-598.

[3] Heczko, J., Kottner, R., Modelling of ageing and fatigue under large strains, Proceedings of the conference Computational Mechanics 2017, University of West Bohemia, Špičák, 2017, pp. 31-32.

[4] Naumann, C., Ihlemann, J., A dynamic network model to simulate chemical aging processes in elastomers, Proceedings of the 9th European Conference on Constitutive Models for Rubber – Constitutive Models for Rubber IX, Prague, CRC Press/Balkema, 2015, pp. 39-45.

[5] Rodionova, O. E., Pomerantsev, A. L., Estimating the parameters of the Arrhenius equation, Kinetics and Catalysis 46 (3) (2005) 305-308.

COMPUTATIONAL MECHANICS 2019
35th conference with international participation
Srní
November 4 - 6, 2019

Interpolation of suspension kinematics for the purpose of vehicle dynamics simulation

V. Houdek[a], O. Verlinden[b], M. Hajžman[a]

[a] *Faculty of Applied Sciences, University of West Bohemia, Univerzitní 8, 301 00 Plzeň, Czech Republic*
[b] *Faculty of Engineering, University of Mons, Rue de Houdain 9, 7000 Mons, Belgium*

Suspensions (for example, see Fig. 1 on the left) are usually 1 DOF systems. The expression of the position of the wheel support in terms of some parameter can be obtained by solving the constraints imposed by the joints present in the system. But this is not efficient as the same equations are solved several times. This paper explains another strategy consisting in solving the kinematic problem (at position and velocity level) for particular points and using these points to calculate all other positions by interpolation. The proposed interpolation is C^1 continuous in translation and rotation.

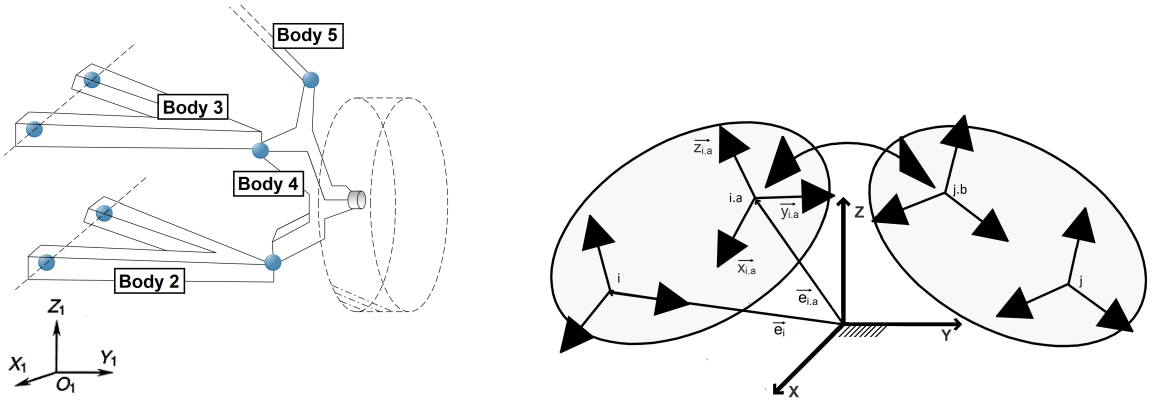

Figure 1. Double wishbone suspension (*left*) and main coordinate system, principal frames of the bodies and secondary frames of the bodies (*right*) [2]

The homogeneous transformation matrix giving the situation of the principal frame of body *i* can be written as

$$\mathbf{T}_{0,i} = \begin{pmatrix} & \mathbf{R}_{0,i} & & \{\mathbf{e}_i\}_0 \\ 0 & 0 & 0 & 1 \end{pmatrix}, \tag{1}$$

where the columns of $\mathbf{R}_{0,i} = [\boldsymbol{x}_i \ \boldsymbol{y}_i \ \boldsymbol{z}_i]$ give the orientation of the axes of the principal frame of body *i* in the main coordinate system and $\{\mathbf{e}_i\}_0$ gives the position of the principal frame of the body i in the main coordinate system $\{\}_0$ (see Fig. 1 on the right) .

The transformation matrix between the main coordinate system and the secondary coordinate system of body *i* is given by the dot product

$$\mathbf{T}_{0,i.a} = \mathbf{T}_{0,i} \cdot \mathbf{T}_{i,i.a} = \begin{pmatrix} \mathbf{x}_{i.a} & \mathbf{y}_{i.a} & \mathbf{z}_{i.a} & \mathbf{e}_{i.a} \\ 0 & 0 & 0 & 1 \end{pmatrix}, \tag{2}$$

where $\mathbf{x}_{i.a}$, $\mathbf{y}_{i.a}$ and $\mathbf{z}_{i.a}$ are the unit vectors of the axes of secondary frame and $\mathbf{e}_{i.a}$ is the position of the secondary frame. All vectors are considered with respect to the main coordinate system.

Constraint equations allow to set joints between two arbitrary bodies (body *i* and body *j*) of the mechanical system. The joints are defined between the frames of two different bodies. The main frame of the body is usually placed into the mass center of the body so there is the need to define secondary frames on the bodies (frame *a* of body *i* = *i.a* and frame *b* of body *j* = *j.b*) between which are defined the joints.

Set of constraint equations ${}^1b$, ${}^2b$ ... ${}^6b$ is defined as

$$
\begin{aligned}
{}^1b &\equiv \mathbf{x}_{i.a} \cdot (\mathbf{e}_{i.a} - \mathbf{e}_{j.b}) = 0, && (3)\\
{}^2b &\equiv \mathbf{y}_{i.a} \cdot (\mathbf{e}_{i.a} - \mathbf{e}_{j.b}) = 0, && (4)\\
{}^3b &\equiv \mathbf{z}_{i.a} \cdot (\mathbf{e}_{i.a} - \mathbf{e}_{j.b}) = 0, && (5)\\
{}^4b &\equiv \mathbf{y}_{i.a} \cdot \mathbf{z}_{j.b} = 0, && (6)\\
{}^5b &\equiv \mathbf{z}_{i.a} \cdot \mathbf{x}_{j.b} = 0, && (7)\\
{}^6b &\equiv \mathbf{x}_{i.a} \cdot \mathbf{y}_{j.b} = 0. && (8)
\end{aligned}
$$

The constraint equations relative to each classical joint can be presented as a subset of the six previous generic equations (e.g., spherical joint is represented by ${}^1b$, ${}^2b$ and ${}^3b$).

The system of the constraint (non-linear) equations could be expressed as

$$\mathbf{F}(\mathbf{q}) = \left(b_1, b_2, \ldots, b_{n_C}\right)^T = \mathbf{0}, \tag{9}$$

where n_C is the number of constraints (${}^jb \neq b_j$). The vector of unknown variables is defined as

$$\mathbf{q} = \left(x_1,\ y_1,\ z_1,\ \phi_1,\ \ldots,\ \psi_{n_B}\right)^T = \left(q_1,\ q_2,\ q_3,\ q_4,\ \ldots,\ q_{6n_B}\right)^T, \tag{10}$$

where n_B is number of all bodies.

All types of suspensions correspond to a one degree of freedom mechanism (assuming the rotation and the steering of the wheel are locked), so one variable in the system of equations has to be given (e.g., the vertical coordinate of a wheel support denoted as u). For a given value of u, the equations are solved in terms of $\mathbf{q}$ by the Newton-Raphson method.

For the interpolation it is important to define velocity $\mathbf{v}_i$ and angular velocity $\boldsymbol{\omega}_i$ of body *i*. Motion of body 1 depends on q_1 to q_6, so motion of body i depends on q_{6i-5} to q_{6i}. Then it is possible to consider

$$\mathbf{T}_{0,i}(\mathbf{q}_i) = \begin{pmatrix} & \mathbf{R}(q_{6i-2}, q_{6i-1}, q_{6i}) & & \begin{matrix} q_{6i-5} \\ q_{6i-4} \\ q_{6i-3} \end{matrix} \\ 0 & 0 & 0 & 1 \end{pmatrix}. \tag{11}$$

For the velocity of principal frame of body *i* is possible to write

$$\{\mathbf{v}_i\}_0 = \begin{pmatrix} 1 & 0 & 0 & 0 & 0 & 0 \\ 0 & 1 & 0 & 0 & 0 & 0 \\ 0 & \underbrace{0}_{\mathbf{d}_{i,6i-4}} & 1 & 0 & 0 & 0 \end{pmatrix} \cdot \begin{pmatrix} \dot{q}_{6i-5} \\ \dot{q}_{6i-4} \\ \dot{q}_{6i-3} \\ \dot{q}_{6i-2} \\ \dot{q}_{6i-1} \\ \dot{q}_{6i} \end{pmatrix}, \tag{12}$$

where $\mathbf{d}_{i,k}$ can be written as $\mathbf{d}_{i,k} = \frac{\partial \mathbf{v}_i}{\partial \dot{q}_k}$. It is also possible to write [2]

$$\boldsymbol{\omega}_i = \begin{pmatrix} 0 & 0 & 0 & \cos q_6 \cos q_5 & -\sin q_6 & 0 \\ 0 & 0 & 0 & \sin q_6 \cos q_5 & \cos q_6 & 0 \\ 0 & 0 & 0 & \underbrace{-\sin q_5}_{\boldsymbol{\delta}_{i,6i-2}} & 0 & 1 \end{pmatrix} \cdot \begin{pmatrix} \dot{q}_{6i-5} \\ \dot{q}_{6i-4} \\ \dot{q}_{6i-3} \\ \dot{q}_{6i-2} \\ \dot{q}_{6i-1} \\ \dot{q}_{6i} \end{pmatrix}, \tag{13}$$

where $\boldsymbol{\delta}_{i,k}$ can be written as $\boldsymbol{\delta}_{i,k} = \frac{\partial \boldsymbol{\omega}_i}{\partial \dot{q}_k}$.

Kinematic quantities, which are calculated using presented approach, are important for the interpolation. The interpolation assumes that the evolution of a homogeneous transformation matrix $\mathbf{T}_{0,A}$ of an arbitrary body A and derivatives $\mathbf{d}_{A,u}$ and $\boldsymbol{\delta}_{A,u}$ (obtained from the constraints at the velocity level) have been calculated for particular values of parameter u, where vectors $\mathbf{d}_{A,u}$ and $\boldsymbol{\delta}_{A,u}$ are defined as [2]

$$\mathbf{d}_{A,u} = \frac{\partial \mathbf{e}_A}{\partial u} = \frac{\partial \mathbf{v}_A}{\partial \dot{u}}, \quad \boldsymbol{\delta}_{A,u} = \frac{\partial \boldsymbol{\omega}_A}{\partial \dot{u}}. \tag{14}$$

It is useful to store the data into the table in terms of a series of values u (u_0, u_1, u_2, ..., u_N)

$$\begin{array}{cccc} u_0 & \mathbf{T}_{0,A}(u_0) & \{\mathbf{d}_{A,u}(u_0)\}_0 & \{\boldsymbol{\delta}_{A,u}(u_0)\}_0 \\ u_1 & \mathbf{T}_{0,A}(u_1) & \{\mathbf{d}_{A,u}(u_1)\}_0 & \{\boldsymbol{\delta}_{A,u}(u_1)\}_0 \\ u_2 & \mathbf{T}_{0,A}(u_2) & \{\mathbf{d}_{A,u}(u_2)\}_0 & \{\boldsymbol{\delta}_{A,u}(u_2)\}_0 \\ \vdots & \vdots & \vdots & \vdots \\ u_N & \mathbf{T}_{0,A}(u_N) & \{\mathbf{d}_{A,u}(u_N)\}_0 & \{\boldsymbol{\delta}_{A,u}(u_N)\}_0, \end{array}$$

where $\mathbf{T}_{0,A}$ consists of $\mathbf{R}_{0,A}$ and $\mathbf{e}_{0,A}$. The interpolation is now a matter of finding continuous functions between each row of previous table. For this Cubic Hermite splines are typically used. The functions are

$$h_{00}(\xi) = 2\xi^3 - 3\xi^2 + 1, \quad h_{01}(\xi) = -2\xi^3 + 3\xi^2, \tag{15}$$

$$h_{10}(\xi) = \xi^3 - 2\xi^2 + \xi, \quad h_{11}(\xi) = \xi^3 - \xi^2. \tag{16}$$

With respect to boundary conditions ($f(x_0) = f_0,\ f(x_1) = f_1,\ f'(x_0) = m_0,\ f'(x_1) = m_1$) is the interpolation of an arbirary function given by

$$\begin{aligned} f(x) = f_0 h_{00}\left(\frac{x - x_0}{x_1 - x_0}\right) + f_1 h_{01}\left(\frac{x - x_0}{x_1 - x_0}\right) + \\ + m_0 h_{10}\left(\frac{x - x_0}{x_1 - x_0}\right) \cdot (x_1 - x_0) + m_1 h_{11}\left(\frac{x - x_0}{x_1 - x_0}\right) \cdot (x_1 - x_0), \end{aligned} \tag{17}$$

which can be used in a straightforward way to interpolate the position as

$$\begin{aligned} \mathbf{e}_A(u) = \mathbf{e}_A(u_i) h_{00}(\xi) + \mathbf{e}_A(u_{i+1}) h_{01}(\xi) + \mathbf{d}_{A,u}(u_i) h_{10}(\xi) \cdot (u_{i+1} - u_i) \\ + \mathbf{d}_{A,u}(u_{i+1}) h_{11}(\xi) \cdot (u_{i+1} - u_i), \end{aligned} \tag{18}$$

where $\xi = \frac{u - u_i}{u_{i+1} - u_i}$ and u_i ($i = 1, \ldots, N$) are chosen values of independent suspension parameter u from the table. The velocity and the acceleration can be found in the same way. For the interpolation of rotation it is important to obtain relative rotation matrix $\mathbf{R}_{0,A}^{i,i+1}$ which is given by

$$\mathbf{R}_{0,A}^{i,i+1} = \mathbf{R}_{0,A}^{-1}(u_i) \cdot \mathbf{R}_{0,A}(u_{i+1}) = \mathbf{R}_{0,A}^{T}(u_i) \cdot \mathbf{R}_{0,A}(u_{i+1}). \tag{19}$$

It is possible to express every spatial rotation as the rotation of the angle θ around the unit vector $\mathbf{n}$ which define $\mathbf{R_{ra}}(\mathbf{n},\theta)$ that is given by

$$\mathbf{R_{ra}}(\mathbf{n},\theta) = \begin{pmatrix} n_x^2V + C & n_xn_yV - n_zS & N_xn_zV + n_yS \\ n_xn_yV + n_zS & n_y^2V + C & n_yn_zV - n_xS \\ n_xn_zV - n_yS & n_yn_zV + n_xS & n_z^2V + C \end{pmatrix}, \tag{20}$$

where $C = \cos(\theta)$, $S = \sin(\theta)$ and $V = 1 - \cos(\theta)$. It is possible for any rotation matrix $\mathbf{R}_{0,A}^{i,i+1}$ to determine the axis and the angle to which it corresponds. The angle is given directly by

$$\theta^{i,i+1} = \arccos\left(\frac{r_{11} + r_{22} + r_{33} - 1}{2}\right), \tag{21}$$

where $r_{11},\ r_{12},\ r_{13},\ r_{21},\ r_{22},\ r_{23},\ r_{31},\ r_{32},\ r_{33}$ are elements of matrix $\mathbf{R}_{0,A}^{i,i+1}$ and it is assumed that $0 < \theta < \pi$.

The unit vector parallel to the axis can then be obtained by (if $\sin\theta \neq 0$)

$$\{\mathbf{n}^{i,i+1}\}_i = \frac{1}{2\sin\theta} \cdot \begin{Bmatrix} r_{32} - r_{23} \\ r_{13} - r_{31} \\ r_{21} - r_{12} \end{Bmatrix}. \tag{22}$$

The full orientation matrix will then be calculated from

$$\mathbf{R}_{0,A}(u) = \mathbf{R}_{0,A}(u_i) \cdot \mathbf{R}_{0,A}^{int}(u) = \mathbf{R}_{0,A}(u_i) \cdot \mathbf{R}^1(u) \cdot \mathbf{R}^2(u) \cdot \mathbf{R}^3(u), \tag{23}$$

where matrices $\mathbf{R}^1(u)$, $\mathbf{R}^2(u)$ and $\mathbf{R}^3(u)$ correspond to

$$\mathbf{R}^1(u) = \mathbf{R_{ra}}\left(\frac{\{\boldsymbol{\delta}_{A,u}(u_i)\}_i}{\|\boldsymbol{\delta}_{A,u}(u_i)\|},\ \|\boldsymbol{\delta}_{A,u}(u_i)\| \cdot h_{10}(\xi(u)) \cdot (u_{i+1} - u_i)\right), \tag{24}$$

$$\mathbf{R}^2(u) = \mathbf{R_{ra}}(\{\mathbf{n}_{A,u}^{i,i+1}\}_i,\ \theta^{i,i+1} \cdot h_{01}(\xi(u))), \tag{25}$$

$$\mathbf{R}^3(u) = \mathbf{R_{ra}}\left(\frac{\{\boldsymbol{\delta}_{A,u}(u_{i+1})\}_{i+1}}{\|\boldsymbol{\delta}_{A,u}(u_{i+1})\|},\ \|\boldsymbol{\delta}_{A,u}(u_{i+1})\| \cdot h_{11}(\xi(u)) \cdot (u_{i+1} - u_i)\right). \tag{26}$$

The proposed methodology was implemented in MATLAB and tested on the double wishbone suspension (Fig. 1 on the left). The exact position and orientation (of a wheel or a sample for verifying the interpolation method) were compared with the calculated values obtained from the interpolation. It applies $\mathbf{R}_{i,e} = \mathbf{R}_i^T \cdot \mathbf{R}_e$, for the error in rotation, where $\mathbf{R}_{i,e}$ is the relative rotation matrix between interpolated and exact position, $\mathbf{R}_i$ and $\mathbf{R}_e$ are interpolated and exact rotation matrices. Error in rotation is then given by formula (21), applied to $\mathbf{R}_{i,e}$. The error in translation was evaluated as norm of the distance vector between the two versions (exact and interpolated). For the position the highest norm is smaller than 4×10^{-3} mm and for the rotation the biggest difference is smaller than 4×10^{-3} rad (0.03°).

Acknowledgement

This publication was supported by project SGS-2019-009 of Czech Ministry of Education, Young and Sport.

References

[1] Blundell, M., Harty, D., Multibody systems approach to vehicle dynamics, Oxford, Elsevier, 2004.

[2] Verlinden, O., Computer-aided analysis of mechanical systems, Lecture Notes, Faculté Polytechnique de Mons, Service de Mécanique Rationnelle, 2016.

COMPUTATIONAL MECHANICS 2019
35th conference with international participation
Srní
November 4 - 6, 2019

Study of aeroelastic interference effect among four cylinders arranged in rectangular configuration

S. Hračov[a], M. Macháček[a], P. Michálek[a]

[a] *Institute of Theoretical and Applied Mechanics, Czech Academy of Sciences, Prosecká 76, 19000 Prague,, Czech Republic*

1. Introduction

The hangers used for supporting the large civil engineering structures as, e.g., roofs or bridge decks represent the flexible structural elements susceptible to excessive vibration due to wind excitation. In the case of closely-spaced individual hangers, the significant wake-induced oscillations leading to significant reduction of their lifetime can occur, see [1-5].

This abstract deals with an analysis of the aerodynamic vibration of a group of four existing hangers supporting the hangar roof and creating in cross-section the rectangular array, see Fig. 1. It is especially concentrated upon the determination of the cause of the violent vibration of one of the hangers. In particular, the excessive vibration of the bottom downwind hanger in the across wind direction was observed, while the rest of hangers remained nearly stationary. The dominant vibration mode of the hanger was characterized by a one node in the middle of the length and by frequency $f = 5.85$ Hz. It corresponds to the second resonant frequency identified from the spectrum of the response related to hammer impact test. All four hangers in the form of tension rods have the same diameter, $D = 84.1$ mm, mass per unit length $\mu = 43.6$ kgm^{-1} and almost identical length 21 m and modal properties. The normalized distance between hangers in horizontal and vertical directions is equal to 3.15 D, and 3.8 D, respectively. The relatively high Scruton number of the hanger, $Sc = 59.2$, was determined for the expected very low logarithmic decrement of structural damping, $\vartheta = 0.006$.

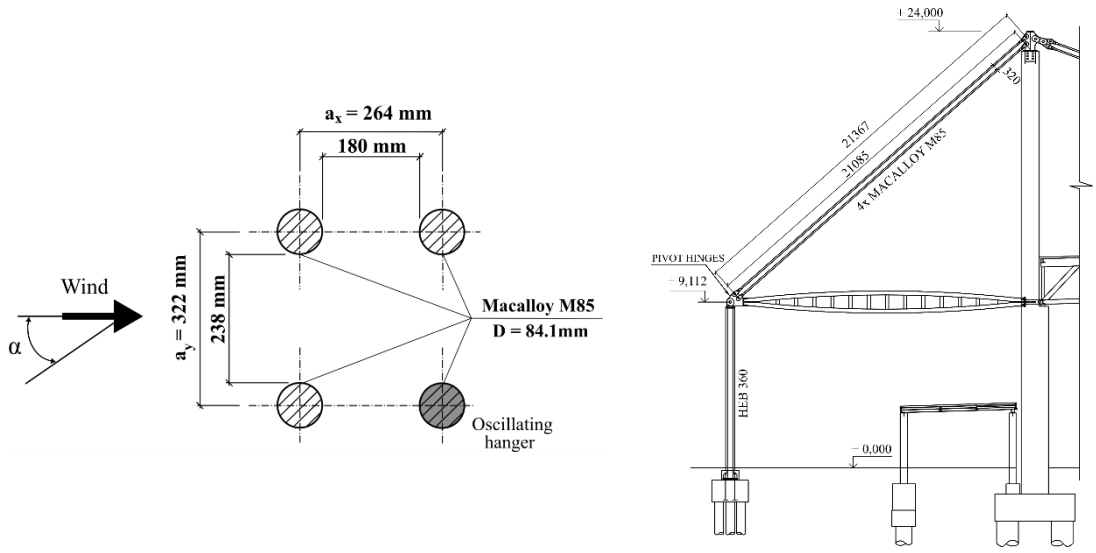

Fig. 1. Layout of hangers (left) and scheme of the part of roof supporting structure with hangers (right)

2. Theoretical analysis of wind-induced vibration

At first, the theoretical analysis of possible causes of the violent vibrations of the hanger was carried out. The calculations of critical wind speeds for vortex shedding and galloping of isolated one hanger according to Eurocode [2] confirmed the assumption of origin of excessive vibration in the wake induced vibration. In addition, the analysis of a pair of hangers did not reveal the significant increase in the response of the downwind hanger due vortex shedding effect on the upwind hanger. The theoretical analysis identifies the interference galloping as one of the possible causes of the serious vibrations. The formula for calculation of critical wind speed related to this type of aero-elastic instability can be found in the code [2] in the form:

$$v_{CIG} = 3.5 \cdot f \cdot D \cdot \sqrt{\frac{\frac{a}{D} \cdot S_c}{a_{IG}}}, \tag{1}$$

where f is natural frequency of hanger; D is diameter of hanger; a is distance between hangers; Sc is Scruton number and a_{IG} is a combined stability parameter with a value of 3. In our case, the formula (1) gives for the observed resonant frequency the estimations of critical wind speed equal to 13.6 m/s, which is realistic to be present at site. It must be noted, that this formula is related to only a pair of hangers and can be adopted only up to ratio $a/D = 3$. Nevertheless, the code [2] does not provide the solution for both, the higher ratios, a/D, even though the interference galloping can occur for ratio up to 4 [1] as well as for more complex arrangements of hangers as, e.g., analyzed tetrad of hangers. Thus, in our case, where the ratio in the wind direction is very close to the boundary value in [2] the above mentioned formula was used only for rough estimate of critical wind speed and the real interaction effect among four hangers needed to be investigated experimentally.

3. Procedure of wind tunnel testing

Aero-elastic stability and dynamic behavior of the bottom downwind hanger as a vibrating member of the tetrad of the rods were investigated experimentally in the wind tunnel of ITAM AS CR in Telč in the Czech Republic. The experimental model of each hanger was represented by 1.3-meter long plastic cylinder with the real cross section. Thus identical flow conditions around the cylinder as in reality i.e. same Reynolds number was reached. The cylinders were fixed horizontally to a specially designed experimental stand, see Fig. 2.

Fig. 2. Experimental set-up with mounted cylinders represented a real configuration of hangers

The bottom downwind hanger was placed into the special mechanism of this set-up allowing only the vertical (cross wind direction) movement. The stand enabled to analyze the influence of two values of Scruton number (*Sc = 44* and *Sc = 79*) on aeroelastic instability of the cylinder, while its natural frequency (*f = 2.6 Hz*) and the damping ratio (*ζ = 1.5 %*) remained fixed. The lower natural frequency than in the real case was chosen due to mechanical restrictions of the stand. The low value selected in this way allows also to reduce the influence of vortex shedding emerging at wind velocity below 3 ms^{-1} on the instabilities occurring at higher wind speeds. The other three cylinders from tetrad were assumed as stationary, i.e. non-vibrating and were fixed between two plastic end-plates of the stand. Two positions of these fixed hangers were investigated in order to simulate two basic wind direction, i.e. $\alpha = 0°$ and $\alpha = 10°$, respectively, see Fig. 1. The latter case represents the critical wind incidence angle for the interference galloping [2]. In addition, behavior of an isolated hanger and a pair of hangers in the horizontal row were tested to compare the susceptibility to the aero-elastic instability with the full rectangular array configuration.

All tests were performed in the smooth flow conditions and consisted from incremental increases of the wind velocity from 2 ms^{-1} with the step approximately equal to 0.7 ms^{-1}. The maximum reached velocity was determined by the mechanical vibration limit of the set-up. Subsequently, the wind speed was decreased by the same step in order to identify the expected hysteresis effect. The steady-state response of the bottom downwind cylinder was measured for each velocity step using the rotary transducer connected to one of the moving lower arms of the set-up.

4. Results of experimental testing

At first, the hanger in rectangular array, in a pair of hangers and as an isolated element was tested in the smooth flow for angle of attack $\alpha = 0°$. The results of the dynamic response in all did not indicate any loss of the dynamic stability of the cylinder or an occurrence of high level oscillations as observed in reality. In particular, the RMS value of the vertical displacement did not exceed the value of *0.06 D*.

The experiments of all analyzed groups of hangers under the wind flow incidence angle $\alpha = 10°$ revealed sudden and significant increase of the cross-wind vibration response of the bottom downwind hanger at certain critical wind speed. By reaching the critical velocity, the harmonic response with high amplitudes was observed. Increase of the velocity above the critical one leads to the further increase of the response amplitude. It is documented in Fig. 3 in terms of RMS value of measured relative displacement for both the pair and the tetrad of hangers possessing the same and different Scruton numbers, *Sc*. For identical *Sc*, the outset of vibrations with high amplitudes for the rectangular array was detected at approximately two times lower reduced wind speed than for the pair of hangers. This implies on a significant influence of the upper row of hangers on interference galloping of downwind hanger in the bottom row. When comparing two groups of 4 hangers for different *Sc*, the initiation of instability for the higher *Sc* is becoming as expected at higher reduced wind velocity than for smaller *Sc*. The ratio between reduced critical wind speeds for these cases with different *Sc* equal to 1.34. It is a slightly higher than the square root of ratio of corresponding *Sc* equal to 1.84, which is relation between both critical velocities when applying formula (1). It should be also noted, that the level of vibration for higher *Sc* was lower than for smaller *Sc* as expected.

Strong hysteresis behavior was observed during whole testing process. The bottom downwind cylinder in the rectangular array as well as the downwind cylinder in a pair were oscillating with high amplitudes not only above the critical wind velocity, but also when the wind velocity was decreased below the critical one, see the dashed lines in Fig. 3. However, with further decrease in wind velocity at some moment a sudden significant reduction in the response occurred. This holds for all of the analyzed configurations.

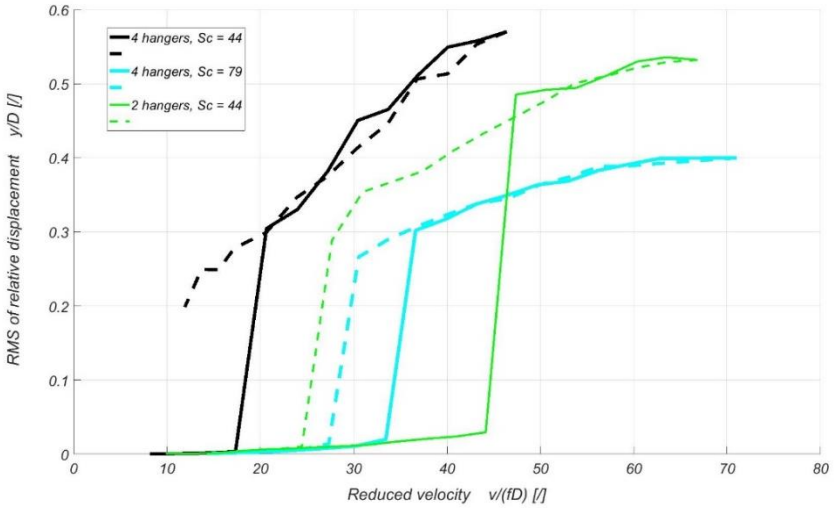

Fig. 3. Root Mean Square (RMS) value of relative displacement of the oscillating cylinder as a function of reduced velocity (solid line – increasing velocity branch, dashed line – decreasing velocity branch)

The estimations of critical wind speed for interference galloping of real bottom downwind hanger on site based on combination of experimental results and formula (1) was done. In the case of the rectangular array of the hangers, the critical wind speeds determined for both values of *Sc* are not too much apart from the value determined according the code [2] corresponding to the pair of hangers. In particular, the critical wind speed equal to 10.9 ms^{-1} and 15.1 ms^{-1} were determined for smaller *Sc* and higher *Sc*, respectively. The wind speeds in this range can occur on-site and can cause serious vibrations and damages as already observed at the real structure. In case of a pair of the hangers, the critical wind velocity equal to 26.4 ms^{-1} obtained from the wind tunnel results is significantly higher than its counterpart calculated according formula (1). It is because we consider the code value is representing very conservative estimate that secures the highest level of the safety comprising large amount of cases of the geometrical arrangement. It must be also noted, that the estimated critical values can be affected by prerequisites and limitations of the experiment, e.g., only cross-wind vibration of the bottom downwind hanger was allowed, the rest of hangers were assumed as static, etc.

The aforementioned conclusions can be of interest of specialist dealing with similar problems in engineering practice and also be a motivation for further investigation of the influence, e.g., the spacing among the hangers in the rectangular array on the instability and the whole character of flow around such bundle of individual structural elements.

Acknowledgements

The work has been supported by the project No. 19-21817S of the Czech Science Foundation (GAČR).

References

[1] de Sá Caetano, E., Cable vibrations in cable-stayed bridges, IABSE, 2007
[2] Eurocode 1: Actions on structures - Part 1-4: General actions - wind actions, 2005.
[3] Sumner, D., Two circular cylinders in cross-flow: A review, Journal of Fluids and Structures 26 (6) (2010) 849-899.
[4] Yoshimura, T., Savage, M.G., Tanaka, H., Urano, D., Wind-induced oscillations of groups of bridge stay-cables, Journal of Wind Engineering and Industrial Aerodynamics 54-55 (1995) 251-262.
[5] Zdravkovich, M.M., The effects of interference between circular cylinders in cross flow, Journal of Fluids and Structures 1 (2) (1987) 239–261.

COMPUTATIONAL MECHANICS 2019
35th conference with international participation
Srní
November 4 - 6, 2019

A comparative analysis of four implants used to treat a supracondylar periprosthetic fracture of ostheoporotic femur

M. Jansová[a], T. Malotín[b], J. Křen[a], P. Votápek[c], L. Lobovský[a], L. Hynčík[d]

[a] *NTIS - New Technologies for the Information Society, Faculty of Applied Sciences, University of West Bohemia, Univerzitní 8, 301 00 Plzeň, Czech Republic*
[b] *Department of Orthopaedics and Traumatology, Faculty of Medicine of Charles University and Faculty Hospital in Plzeň, alej Svobody 80, 304 60 Plzeň, Czech Republic*
[c] *Department of Machine Design, Faculty of Mechanical Engineering, University of West Bohemia, Univerzitní 8, 301 00 Plzeň, Czech Republic*
[d] *New Technologies – Research Centre, University of West Bohemia, Univerzitní 8, 301 00 Plzeň, Czech Republic*

A total knee arthroplasty (TKA) is in rare cases followed by an extra-articular fracture of distal femur. It happens mostly in elderly patients with ostheoporosis and can be stabilized only by a surgical treatment. Several implant types are used by orthopedic surgeons for its management. In this study we compare a response to axial load and torque for four implants: Distal Femoral Nail (DFN), Locking Compression Plate (LCP), Angled Blade Plate (ABP) and Dynamic Compression Screw (DCS).

The geometry of femur with fracture and the implants is the same one as in the previous studies [2, 3]. Both compact and spongy bone are modelled by 3D elements. The gap of a simple extra-articular fracture is 2 mm wide. There is no callus formed. The finite element models with the implants are shown in Fig. 1.

Fig. 1. The frontal (left) and lateral (right) view of model of femur with TKA (green), fracture (black) and implants from left to right: DFN (red), LCP (dark blue), ABP (pink) and DCS (light blue)

The material parameters of ostheoporotic bone were taken from Jimenez-Cruz et al. [4]. The screws, the spiral blade and the implants are made of titanium alloy.

Two types of load were used as in the previous study [3] – the uniaxial load on the femoral head and the torque. The loading conditions correspond to those of Brinkman et al. [1]. For both loads, a rigid body was formed at the surface of the femoral head and the greater trochanter and all degrees of freedom of the distal part of the femoral component were fixed. In case of the uniaxial load, a force corresponding to the body mass of 80 kg was applied on the center of femoral head in the direction of mechanical axis and all other degrees of freedom were fixed. For torque, a moment of 5 Nm was applied on the center of femoral head about the mechanical axis and all other degrees of freedom except the movement in axial direction were fixed.

The von Mises stress distribution in the implants and the displacement of femur in all three main directions were analyzed for the four implants and the two loading conditions.

The results of uniaxial load are similar to those of the previous studies [2, 3]. In case of DFN there is an increased stress in the middle of the spiral blade in the area in contact with the nail and in the nail in the area around and above the fracture location. Von Mises stress in the three external implants is the highest in the area below the lowest nail in the diaphysis. The screws are loaded mainly in the area of their intersection with compact bone. The displacement in all cases is the most prominent in the sagittal plane, the femoral mid-shaft bends ventrally in all cases. The medio-lateral movement and the compression in the direction of axial load is significantly lower.

With torque about mechanical axis, the greater trochanter rotates dorsally for all implants. The femoral mid-shaft undergoes at least twice as large rotation along the mechanical axis in case of LCP over the remaining three implants. Also the stress reaches significantly higher values in LCP implant, especially below the level of the screws in the diaphysis and at the level of upper three screws on the condyle.

The most important difference among the four implants is in the rotation along the mechanical axis in case of LPC under torque consequently causing notably higher stress in the implant.

Acknowledgements

The work was supported by the project LO1506 of the Czech Ministry of Education, Youth and Sports under the program NPU I., by the project SGS-2019-001 of the University of West Bohemia and from European Regional Development Fund-Project „Application of Modern Technologies in Medicine and Industry" (No. CZ.02.1.01/0.0/0.0/17_048/0007280).

References

[1] Brinkman, J.M., et al., Biomechanical testing of distal femur osteotomy plate fixation techniques: the role of simulated physiological loading, Journal of Experimental Orthopaedics 1 (2014).

[2] Jansová, M., Malotín, T., Křen, J., Votápek, P., Lobovský, L., Hynčík, L., Finite element analysis of supracondylar periprosthetic femoral fracture treatment, Proceedings of the 32nd conference Computational Mechanics, Špičák, 2016, pp. 45-46.

[3] Jansová, M., Malotín, T., Křen, J., Votápek, P., Lobovský, L., Hynčík, L., A comparative analysis of treatment of a supracondylar periprosthetic femoral fracture under axial load and torque, Proceedings of the 33rd conference Computational Mechanics, Srní, 2018, pp 33-34.

[4] Jimenez-Cruz, D., Alonso Rasgado, T., Bailey, C., Board, T., Failure analysis following osteochondroplasty for hip impingement in osteoporotic and non-osteoporotic bones, Journal of Osteoporosis and Physical Activity 4 (2016).

COMPUTATIONAL MECHANICS 2019
35th conference with international participation
Srní
November 4 - 6, 2019

Application of semi-analytical solution for transient wave propagation in 1D layered medium to various optimisation problems

O. Kába[a], V. Adámek[b], R. Kroft[b]

[a] Faculty of Applied Sciences, University of West Bohemia, Univerzitní 8, 301 00 Plzeň, Czech Republic
[b] NTIS - New Technologies for the Information Society, Faculty of Applied Sciences, University of West Bohemia, Technická 8, 301 00 Plzeň, Czech Republic

The main aim of this work is to solve the problem of transient waves propagated through a 1D layered elastic medium and to find an effective tool for solving optimisation problems for such type of heterogeneous medium. First, the semi-analytical solution for waves induced in a layered elastic thin rod by an axial impact is presented. Then, using the experimental data, three selected optimisation problems are solved by using an in-house Matlab code. Specifically, the inverse problems of material and geometrical properties and of loading pulse identification are solved followed by the problem of optimal design of layers to reduce the effect of impact.

The investigation of non-stationary response of a 1D layered medium made of n homogeneous elastic layers (see Fig. 1) can be handled by different methods. Probably the simplest way is to apply the existing solution for homogeneous thin rod (see e.g. [3]) to each ith layer ($i = 1, \ldots, n$) and to use the "stick" boundary conditions defined at each of $n-1$ rods' interfaces. Using the Laplace transform and taking into account zero initial conditions of the problem, the wave equation for each ith homogeneous 1D rod leads to a simple ordinary differential equation. Introducing the Laplace transform of the axial displacement $U_i(x,p)$ and the transform of the axial stress $\Sigma_i(x,p)$, one can write the solution of such ith equation as

$$U_i(x_i,p) = A_i(p)\sinh\left(\frac{px_i}{c_{0,i}}\right) + B_i(p)\cosh\left(\frac{px_i}{c_{0,i}}\right), \tag{1}$$

$$\Sigma_i(x_i,p) = \frac{E_i p}{c_{0,i}}\left[A_i(p)\cosh\left(\frac{px_i}{c_{0,i}}\right) + B_i(p)\sinh\left(\frac{px_i}{c_{0,i}}\right)\right], \tag{2}$$

where x_i denotes the local coordinate (see Fig. 1), E_i is the Young's modulus, $c_{0,i}$ represents the wave speed, p is the complex variable and $A_i(p)$ and $B_i(p)$ are complex functions dependent on boundary conditions. These conditions can be formulated for the free (or fixed) end at $x_n = 0$ and for the excited end at $x_1 = l_1$ in a standard way (see e.g. [3]). The remaining $2(n-1)$

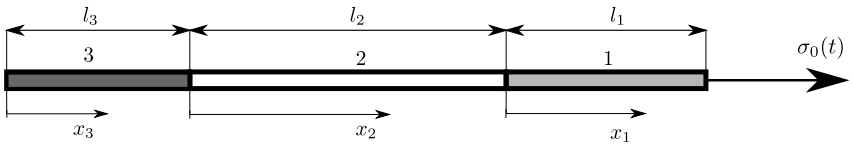

Fig. 1. Layered 1D media composed of three homogeneous mediums ($n = 3$)

conditions for the interfaces can be defined in Laplace domain as follows:

$$U_i(l_i, p) = U_{i-1}(0, p) \quad \text{and} \quad \Sigma_i(l_i, p) = \Sigma_{i-1}(0, p) \quad \text{for} \quad i = 2, \ldots, n. \tag{3}$$

Introducing the Laplace transforms (1) - (2) into the mentioned conditions, a system of $2n$ complex equations for the unknowns $A_i(p)$ and $B_i(p)$ is obtained. Basically, this system can be solved exactly only for very simple cases, so the numerical approach needs to be used for a general case. Once the values of $A_i(p)$ and $B_i(p)$ are determined, the problem of inverse Laplace transform has to be resolved. In this work, numerical inverse Laplace transform based on fast Fourier transform and Wynn's ε-algorithm (see [2]) are used. This approach delivers very precise results with low computational demands (see [1]), which makes it suitable for solving optimisation problems.

There are three optimisation problems solved in this work. Two of them are the inverse problems based on the acceleration response measured at free end of an excited rod made of three layers. The side layers were identical from the geometrical and material point of view while the central one was made of a different material and has different length. The identification of Young's modulus of all three layers is the first optimisation problem considered. This problem was solved using the standard Matlab function *fmincon* to very satisfying and accurate results. More than forty optimisations have been run for different lengths of the center layer and for different shapes of the loading pulse with a relative deviation of identified moduli under 5%.

The identification of the loading pulse is the second inverse problem solved. For this purpose, the pulse was approximated by Fourier sine series and its coefficients and base frequency were then the optimised parameters. Using more complex procedures based on the particle swarm optimisation (PSO) and on the genetic algorithm (GA), it was possible to obtain very accurate results already for 14 terms of the Fourier series. It is obvious from Fig. 2, where the identified pulse is compared to the measured one.

The last optimisation problem consists in the minimisation of stress amplitude at free end of the layered rod by designing the material parameters (material densities ρ_i and moduli E_i) and the lengths l_i of the layers. This problem was also solved using PSO and GA in Matlab

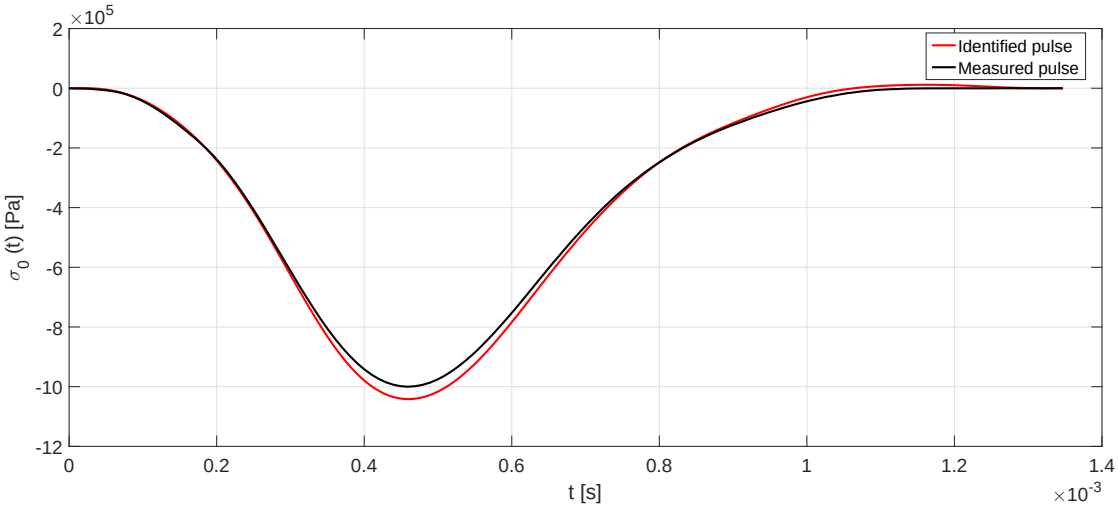

Fig. 2. Comparison of measured and identified pulse

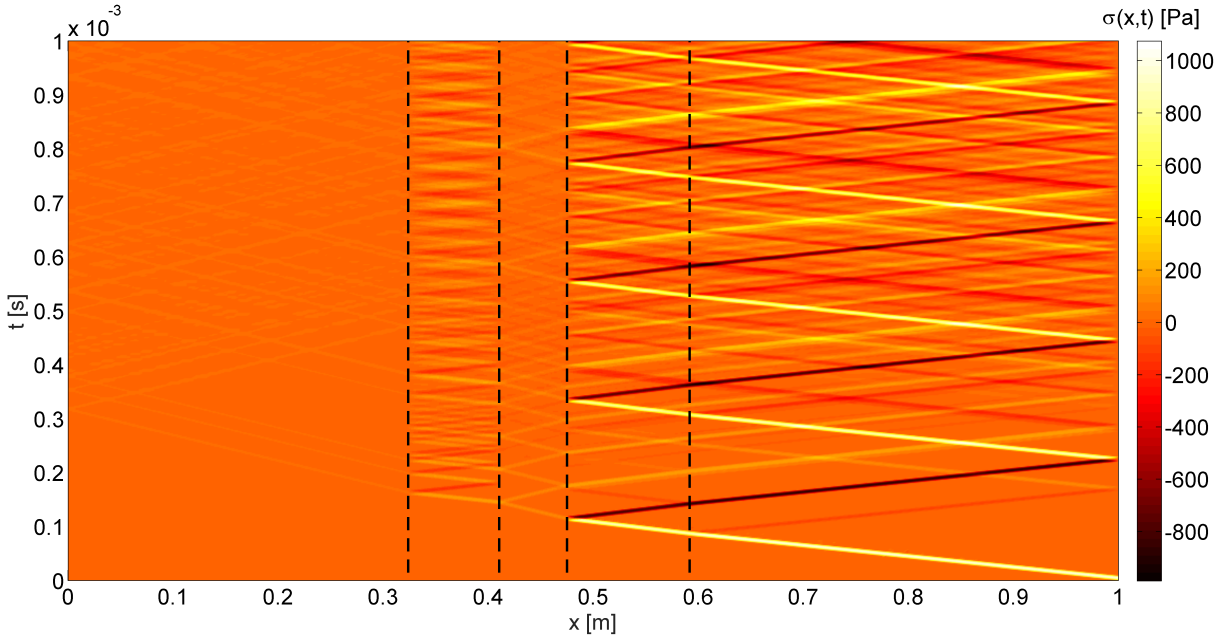

Fig. 3. Spatio-temporal distribution of axial stress $\sigma(x,t)$ in optimised rod composed of 5 layers

environment. Optimisations running over the same intervals of optimised parameters led to similar measure of initial pulse reduction but with different layer properties and composition. This problem, as formulated, has a lot of local minima and it was not possible to find one optimal solution by using mentioned procedures. The value of axial stress at free end of the rod was reduced to 1% - 30% of the initial pulse amplitude depending on the pulse duration. One example of a five-layered rod with optimised composition is presented in Fig. 3. This spatio-temporal distribution of axial stress $\sigma(x,t)$ in the rod clearly shows the primary tensile pulse propagating from the right excited end, interacting with the layer's boundaries (dashed lines) and reaching the free end of the rod with the amplitude about 3.6% of its initial value.

This work gives an overview of the fast solver developed for problems of non-stationary wave propagation in a 1D layered elastic media based on the semi-analytical approach. Using the experimental data, the solver is then effectively used for solving selected optimisation problems and the advantages and disadvantages of the proposed procedure are shown. Presented technique can also be used for the approximate solution of more general 1D heterogeneous problems, e.g. for the investigation of transient waves in functional graded materials.

Acknowledgements

This publication was supported by the student project SGS-2019-009, by the grant GA 19-04956S and by the project LO1506 of the Czech Ministry of Education, Youth and Sports under the program NPU I.

References

[1] Adámek, V., Valeš, F., Červ, J., Numerical Laplace inversion in problems of elastodynamics: Comparison of four algorithms, Advances in Engineering Software 113 (2017) 120-129.

[2] Brančík, L., Programs for fast numerical inversion of Laplace transforms in Matlab language environment, Proceedings of the 7th MATLAB Conference, Prague, 1999, pp. 27-39.

[3] Graff, K.F., Wave motion in elastic solids, Dover Publications, Inc., New York, 1991.

COMPUTATIONAL MECHANICS 2019
35th conference with international participation
Srní
November 4 - 6, 2019

Influence of elevated temperature on motorcyclist protective equipment

S. Kaňáková[a], R. Kottner[a], T. Bońkowski[b]

[a] Faculty of Applied Sciences, University of West Bohemia, Univerzitní 8, 301 00 Pilsen, Czech Republic
[b] New Technologies Research Centre, University of West Bohemia, Univerzitní 8, 301 00 Pilsen, Czech Republic

1. Introduction

Motorcycle transportation is becoming more popular nowadays and therefore it is really important to use a qualitative protective equipment. Simulations of the protective equipment such as [2] and [3] are becoming a common matter and their main purpose is to improve the protector and its designing process. Unfortunately, many aspects influence the ability to absorb energy during the accident. One of the key aspect is the temperature.

Joint protectors should satisfy requirements of the standard EN 1621-1. However, the higher temperatures are common matter in the motorcycle transportation, the part of this standard concerning a temperature influence is optional [1].

This work deals with a different mechanical response of commercially available joint protectors exposed to a variety of temperatures during an impact test. These temperatures were selected to reflect obligatory 23 ± 2 °C and optional 40 ± 2 °C according the standard, and moreover 50 ± 2 °C. The temperature influence proved to be an important factor that marginally affected ability of protectors to absorb energy. Since in addition to transmitted forces, displacements of an impactor were measured during the compression of the protectors, the measured data will be used to model the protectors.

2. Experiment

An impact test was chosen to demonstrate the influence of elevated temperature on the motorcyclist protective equipment.

A serie of impact tests was realized to obtain source data. A drop tower was designed to reflect the geometry of the standard test [1]. An impactor with flat steel head weighted 5 kg. The impactor was released from 1 m height over a spherical anvil.

The maximal transmitted forces and the impactor displacements were measured. The experiment was carried out for three temperatures, namely 23 ± 2 °C, optional 40 ± 2 °C, and above standard 50 ± 2 °C. The protectors were left in the respective temperature for one hour prior the testing. The impact tests were carried out within 30 s after taking out the protector from a heating chamber, which meets the requirements of the standard.

Three types of joint protectors were examined, see Fig. 1: (a) SAS-TEC SCL-2, (b) perforated BETAC, and (c) compound BETAC protector. Both, SAS-TEC SCL-2 and perforated BETAC, consist of one type of a different energy absorbing foam. The compound BETAC protector has complicated structure and consists of two main firmly connected layers. The bottom layer is made of a softer foam. The upper layer is made of a denser foam, similar to the

materials of previous protectors. Both SAS-TEC SCL-2 and compound BETAC are protectors with protection level 2, therefore, the maximal transmitted force during the standard test cannot overcome 20 kN. The perforated BETAC is level 1 protector, its limit for maximal transmitted force is 35 kN.

The chosen protectors are commercially available and were recommended for the research by czech manufacturer of motorcycle clothing PSÍ Hubík.

Fig. 1. Joint protectors: (a) SAS-TEC SCL-2, (b) BETAC with perforations, (c) compound BETAC

The obtained data are displayed in Fig. 2. The temperature has a negative influence on both the maximal compressions and the maximal transmitted forces. The transmitted force increases its value with increasing temperature.

The perforated BETAC protector satisfies the level 1 protection requirements for all three temperatures. This protector satisfies level 2 protection limit for 23 °C.

The SAS-TEC SCL-2 meets the requirements of the level 2 protection limit, however, its response is on the verge of the level 2 protection limit for 40 °C. The level 2 limit is overcome in case of 50 °C.

The compound BETAC protector satisfies this limit for all measured temperatures. Its compressions reach significantly lesser values for 23 °C and 40 °C than SAS-TEC SCL-2.

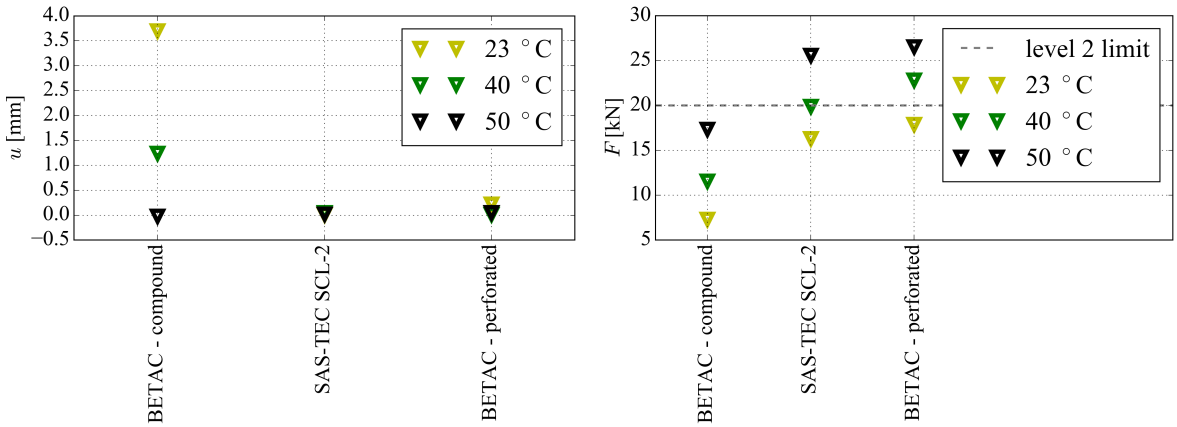

Fig. 2. Obtained data: (a) maximal compressions, (b) maximal transmitted forces

3. Simulation

The simulation of the carried out test was created in ABAQUS software. The model uses the symmetry of the geometry, boundary conditions and load, therefore, only the half of the problem was simulated (see Fig. 3). The impactor head and the anvil were simulated using shell elements. The geometry of the SAS-TEC SCL-2 protector was created in Rhinoceros software. The protector consisted of 5151 solid elements. The impactor displacement and the transmitted force were evaluated.

This simulation will be further used for a calibration of a material model previously researched in [4] and [5]. The simulation will be also extend with the compound BETAC protector geometry and its material models identification.

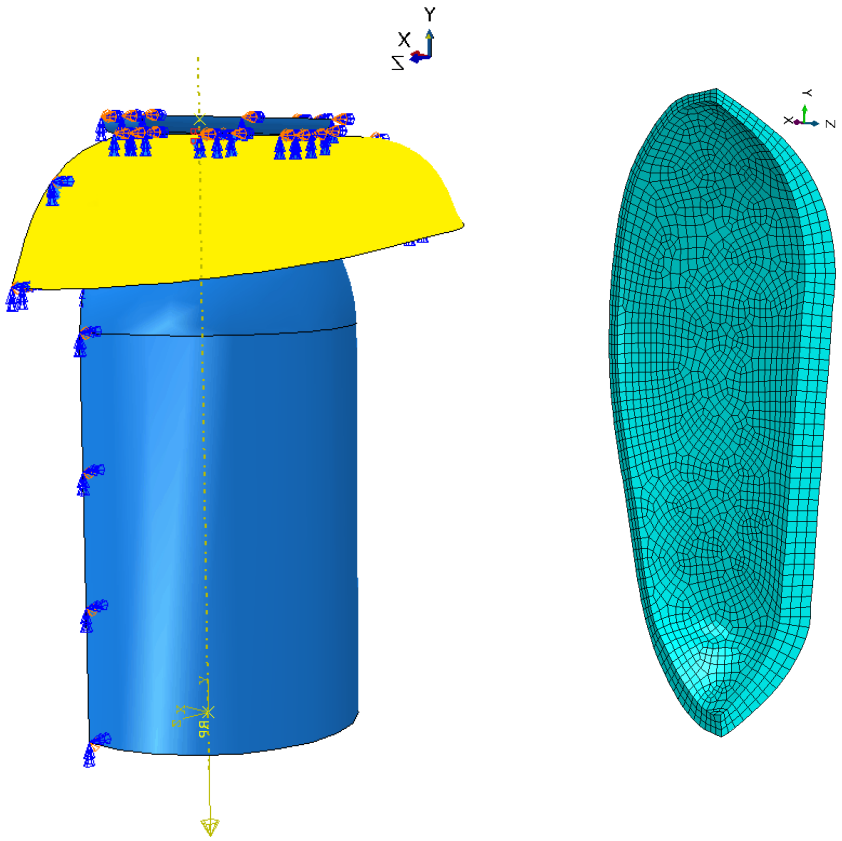

Fig. 3. Simulation: (a) assembly, (b) protector mesh

4. Conclusions

Elevated temperature has a negative influence on the foam protectors. The values of the maximal transferred forces are rising with increasing temperature. Omitting the optional part of the standard [1] can favour the protector and grade it as the level 2. The SAS-TEC SCL-2 and the perforated BETAC reach comparable values of the maximal transmitted forces and the maximal compressions, despite their different protection levels. The compound BETAC protector was the best of the tested protectors.

The simulation of the experiment will be further used for the identification of material model parameters of the compound BETAC protector and the calibration of SAS-TEC SCL-2 material model.

Acknowledgements

The work was supported by the internal grant project SGS-2019-002 *Biomechanical models of human body, biological tissues and biomechanical processes with application in industry and medicine* and from European Regional Development Fund-Project *Application of Modern Technologies in Medicine and Industry* (No. CZ.02.1.01/0.0/0.0/17_048/0007280). The authors would like to thank PSÍ Hubík for providing researched protectors.

References

[1] ČSN EN 1621-1, Motorcyclists' protective clothing against mechanical impact Part 1: Requirements and test methods for impact protectors, Prague, Czech Office for Standards, Metrology and Testing, 2013. (in Czech)

[2] Fornells, A., Parera, N., Azpeitia, J. A., Ferris, S., Alba, J. J., Kid-shell: Safety system protection for child passengers travelling on powered two-wheeled vehicles, Proceedings of the 6th Transport Research Arena, Warsaw, Poland: Elsevier, 2016, vol. 14, pp. 3886-3894.

[3] Hynčík, L., Bońkowski, T., Kottner, R., Virtual assessment of motorcycle helmet contribution to decreasing injury risk in impact, Proceedings of the 37th Fisita World Automotive Congress, Chennai, India, 2018, pp. 1-6.

[4] Kaňáková, S., Above-standard tests of motorcycle protective equipment, Thesis, University of West Bohemia, Pilsen, 2019. (in Czech)

[5] Kottner, R., Kaňáková, S., Bońkowski, T., Yeung, R., Pukaro, R., Improvement of impact protection by Kordcarbon-Cpreg-200- T-3k-Ep1-42-A composite, Proceedings of the 36th Danubia Adria Symposium on Advances in Experimental Mechanics, University of West Bohemia, Pilsen, 2019.

COMPUTATIONAL MECHANICS 2019
35th conference with international participation
Srní
November 4 - 6, 2019

3-DOF planar manipulator utilizing compliant joints with variable stiffness

J. Karlíček[a], Z. Šika[a]

[a] *Faculty of Mechanical Engineering, Czech Technical University in Prague, Technická 4, 166 07 Prague, Czech Republic*

On the way to more productive manufacturing, principle of human-robot collaboration is often mentioned. Compared to heavy industrial robots, which perform their tasks behind safety fences, requirements for collaborative robots (cobots) differ. They should be small, light and powerful enough to help humans but not to hurt them. In other words, their design is mainly determined by current safety standards. Overview of safety measures used in industrial plants is presented in [2]. One of the drawbacks of cobots in today's design is their payload. Due to higher inertia of heavy load, they are not allowed to carry too much. One option, how to deal with this fact, is incorporating intrinsic compliant systems into their structure, to prevent potential collision damage. Such a system could be a variable impedance actuator, which allows controlling its position and stiffness simultaneously. Reviews on their types and design could be found in e.g. [4, 5]. Our goal is therefore to study and develop structures with intrinsic safety, which comply with safety standards and are able to assist during collaborative human-robot production tasks.

Firstly in presented work, one type of a variable stiffness actuator was adopted, namely VSA-II (Fig. 1 left) described in [3]. It consists of two motors in antagonistic setup and nonlinear transmission connecting each motor to the controlled link. The nonlinear transmission is made of 4-bar mechanism (Fig. 1 right) with specific dimensions, which makes the relationship between motor input angle θ and output angle β nonlinear and thus the stiffness seen at O is nonlinear too.

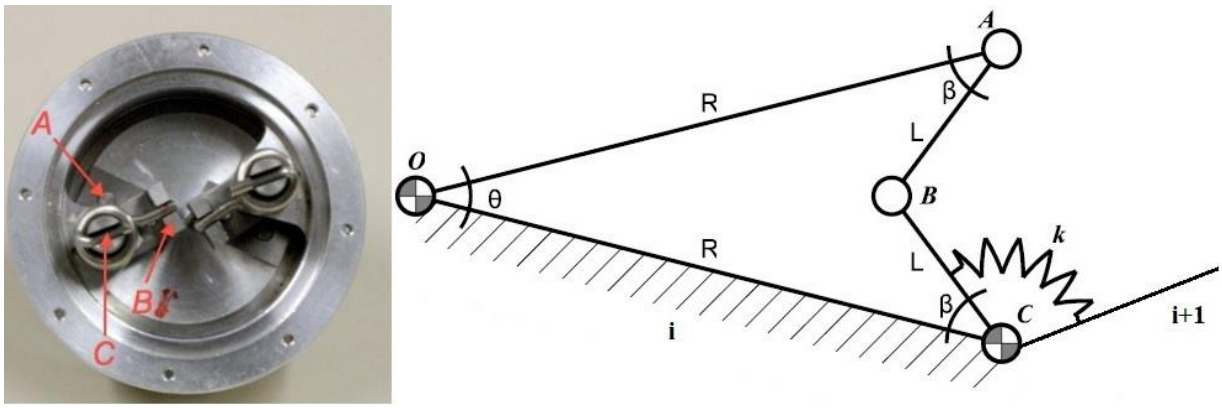

Fig. 1. VSA-II prototype (left) and 4-bar mechanism (right) used as nonlinear spring (modified from [4, 5])

Based on description in [3] simulation model of VSA-II connected to the output shaft was created and simple PD control scheme was used to control shaft position and it´s stiffness. First simulation was performed under simplifying assumptions, where no load torque and gravity is considered and steady state equilibrium is assumed, which permit us to define shaft

position as motors mean position. Fig. 2 shows results of these simulations, where trajectory of the output shaft is seen on the left and tracking of angle corresponding to output stiffness could be seen in the right picture.

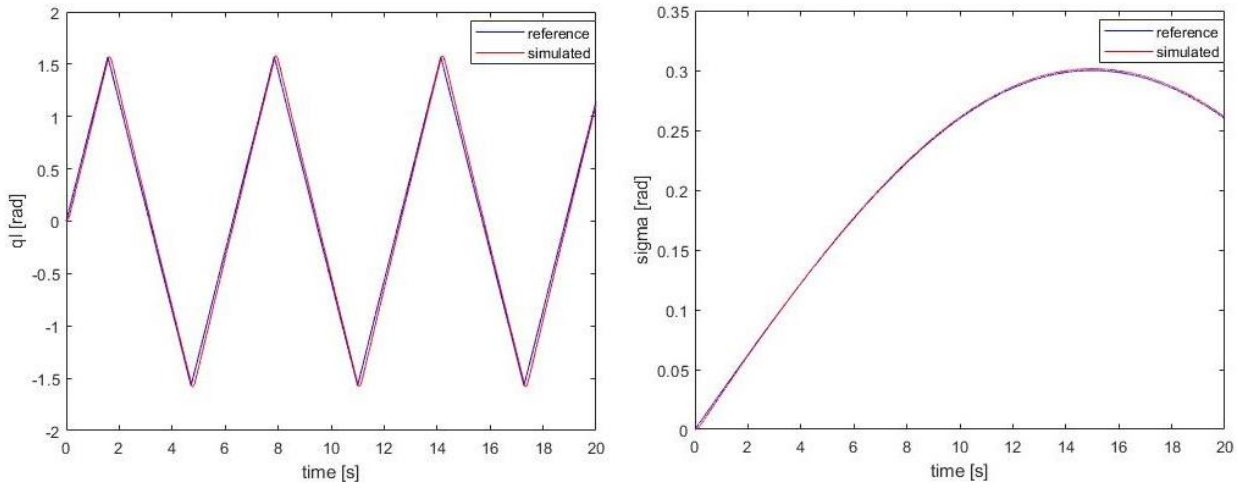

Fig. 2. Position (left) and angle corresponding to stiffness (right) tracking by 1-DOF rod controlled by VSA-II using PD regulator

As mentioned above this model was simplified, which in fact means that the dynamics of the link was ignored. Therefore next simulations with presence of load torque external disturbances and gravity for the output shaft were performed. Increased complexity of the system and especially the control algorithms were observed. The principles of state feedback linearization or feedback linearization (as mentioned in [1]) seem to be the promising solution.

Finally, the model of planar manipulator arm with three revolute joints equipped with one VSA-II in each joint was created. Four-bar mechanism is attached on link *i* with output shaft *i+1*connected to revolute pair C and linear spring with stiffness *k*, as described in Fig. 1 (right). The whole structure with 9-DOF together with efficient control scheme is studied with emphasis to the precise end-effector position tracking, stiffness adjusting and undesirable collision effect reduction.

Acknowledgements

This work has been supported by Student Grant Competition of CTU under project Modelling, control and design of mechanical systems 2019 No. SGS19/157/OHK2/3T/12.

References

[1] Flacco, F., Modelling and control of robots with compliant actuation, Ph.D. thesis, Sapienza University of Rome, 2012.
[2] Robla-Gómez, S., Becerra, V.M., et al., Working together: A review on safe human-robot collaboration in industrial environments, IEEE, 2017.
[3] Schiavi, R., Grioli, G., Sen, S., Bicchi, A., VSA-II: a novel prototype of variable stiffness actuator for safe and performing robots interacting with humans, Proceedings of the International Conference on Robotics and Automation, Pasadena, 2008, pp. 2171-2176.
[4] Vanderborght, B., et al., Variable impedance actuators: A review, Robotics and Autonomous Systems 61 (12) (2013) 1601-1614.
[5] Wolf, S., et al., Variable stiffness actuators: Review on design and components, IEEE/ASME Transactions on Mechatronics 21 (5) (2016) 2418-2430.

COMPUTATIONAL MECHANICS 2019
35th conference with international participation
Srní
November 4 - 6, 2019

Influence of distributed electrical propulsion (DEP) on wing airfoil characteristics

J. Klesa[a]

[a] *Faculty of Mechanical Engineering, Czech Technical University, Karlovo náměstí 13, 121 35 Praha 2, Czech Republic*

Distributed electrical propulsion (DEP) represents modern and promising development trend in aircraft design. Main advantage of this concept should be lower energy consumption due to higher lift to drag ratio in cruise flight regime and smaller wing area needed. However, DEP itself brings new problems and challenges to aircraft design. DEP is based on the increase of flow velocity on the wing by propellers. So, the lift is increased and smaller wing area is needed for given landing velocity. The influence of DEP is analysed on the generic wing for single engine turboprop aircraft with two common NASA airfoils with relative thickness 17%: LS(1)-0417 and MS(1)-0317. Various propeller diameters are tested and airfoil drag, pitching moment and required power are compared. Results can be used for detailed design of aircraft with DEP system.

Classical DEP system consisting of many smaller propeller in front of the wing leading edge is assumed. This increases dynamic pressure on the wing and thus can be used for lift increase during take off and landing. It is analyzed for generic general aviation aircraft (i.e., aircrafts of the class like Pilatus PC-12 or Daher TBM 940). Assumed aircraft configatation is similar to EcoPulse project [1]. Following input parametrs are used:

- wing load $\frac{m}{A} = 200\,\mathrm{kg.m^{-2}}$,
- wing aspect ratio $\lambda = 10$,
- wing chord $c = 1.6\,\mathrm{m}$,
- flight level $0\,\mathrm{m}$ ISA.

The starting point of the analysis is the fact that thrust is equal to the drag in steady horizontal flight. Only wing drag is assumed, i.e., drag coefficient c_D is determined as the sum of airfoil and induced drag

$$c_D = c_{Dprof} + c_{Di}. \tag{1}$$

Airfoil drag is computed by xFoil software [2]. Mach and Reynolds numbers corresponding to the real flight conditions are used, i.e., flight velocity is computed for every lift coefficient c_L and then used for determination of Reynolds and Mach numbers. Induced drag is computed by simple formula [3]

$$c_{Di} = \frac{c_L^2}{\pi\lambda}. \tag{2}$$

Power required for the aircraft propulsion is determined as induced power of the propulsion system, i.e., power required to the acceleration of the air from flight velocity v_0 to v_2. It is computer for one meter wingspan

$$\frac{P}{l} = \frac{1}{2}\dot{m}(v_2^2 - v_0^2), \tag{3}$$

where the propulsion system exit velocity is $v_2 = v_0 + 2\Delta v$. Δv can be determined for given DEP system heighth (represents DEP propeller diameter) from the equation

$$\Delta v = \frac{v_2}{2}(1 - \sqrt{1 - \frac{cc_D}{D}}). \tag{4}$$

Sample comparison of DEP with standard propulsion system (e.g., propeller) can be seen in Fig. 1. Dependence of required thrust on flight velocity shows clearly difference in the stall velocity. Distributed propulsion causes lower stall velocity with identical wing area and airfoil. However, for higher velocity, DEP wing has higher drag and thus lower lift to drag ratio in the cruise regime.

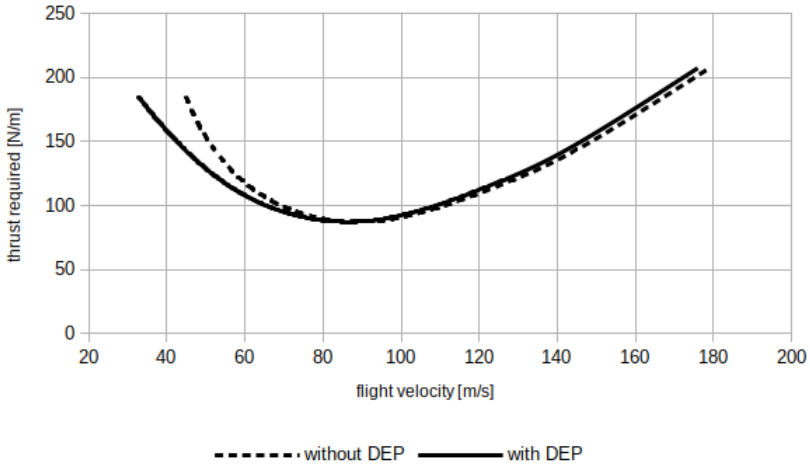

Fig. 1. Influence of DEP on required thrust, propulsor height equals to 20% of wing chord, Airfoil MS(1)-0317

This paper presents analysis of the DEP propulsion for the wing of generic general aviation category aircraft. Wing airfoils MS(1)-0317 (i.e., medium speed airfoil) and LS(1)-0417 (i.e., low speed airfoil) with relative thickness 17% are studied. Some trade-offs are necessary during design of this propulsion system. Decrease of minimal flight speed is connected with slight drag increase in cruise regime. Detailed computational fluid dynamics (CFD) simulations will be done in order to verify analytical results. Results will be used as input data for higher fidelity methods for the design and optimization of the DEP system so that advantages are fully used and disavantages eliminated as much as possible.

References

[1] Daher, Airbus and Safran team up to develop EcoPulseTM, a distributed hybrid propulsion aircraft demonstrator, https://www.airbus.com/newsroom/press-releases/en/2019/06/daher-airbus-and-safran-team-up-to-develop-ecopulsetm-a-distributed-hybrid-propulsion-aircraft-demonstrator.html (retrieved 6 September 2019)

[2] Drela, M., Youngren, H., XFOIL 6.9 User Guide, 2001.

[3] McCormick, B. W., Aerodynamics, aeronautics, and flight mechanics, Wiley, 1995.

COMPUTATIONAL MECHANICS 2019
35th conference with international participation
Srní
November 4 - 6, 2019

Utilization of virtual human body model Virthuman in the mountaineering safety

A. Kolínková[a], J. Špička[a,b]

[a] Faculty of Applied Sciences, University of West Bohemia, Univerzitní 8, 301 00 Plzeň, Czech Republic
[b] New Technologies - Research Centre, University of West Bohemia, Univerzitní 8, 301 00 Plzeň, Czech Republic

1. Introduction

Human safety and security are currently main topics of the research in many fields. The primarily area is an automotive safety, followed by other way of transport industry (trains, trams, aircraft etc). Currently, there is a big effort of the human safety in the sports, mainly in contact sports. There is a massive investment in the american football research, since there is a high risk of the injury and there is a very strong economical background beyond this sport. However, the biomechanical research focused on human safety starts to play a role in more and more different kind of sports (ice hockey, cycling, martial arts, etc.).

This work is a preliminary research of a student's project utilizing a very new field of the safety focused on the rock climber/mountaineers. Nowadays, the rock climbing become very popular between the people of all ages, especially in Europe. The number of climbers, the number of new climbing routes as well as number of climbing gyms dramatically increased in last few years. Moreover, the professional climbers are still pushing the limits of human skills further and further. Such effort is followed by higher number of falls. However, the numbers of athletes death because of the fall is very low, the loading which human body have to sustained is significant. The climbing gear is still enhancing, to be more safe but also to be more user friendly. In this case, to be light enough to minimize the disturbance of the athlete. The climbing rope become thinner (from 20 mm in the past, to 8 mm nowadays) with even better dynamics behavior. Similarly the harness, slings and so on dramatically decrease their diameter and mass. Decreasing of the mass results in the lower lifetime of the gear and it can lead up to decreasing of the comfort or even the safety of the athletes.

Purpose of this work is to use Virthuman (validated human body model successfully used in the traffic safety purposes [3, 6, 7, 8]) and utilized it in the rock climbing fall scenario. The main aim is to understand the mechanism of the fall, to build an appropriate numerical model of the climbing harness and the rope and to simulate the athlete fall in the rope-harness protection chain. The model developed here can be further used as a tool to predict the loading of the human body (mainly the head, neck, abdomen and the spine) and can be used in the development of the new protection gear. There are several published papers focused on the climbing fall [4, 5] or modeling of the rope, harness and belaying devices [1, 2]. However, the evaluation of the athlete's injury risk and level of the dynamic loading of the body has not been accessed.

This work firstly deals with the modeling of the harness and the rope and together with the model of the athlete prepare some falling configurations in order to understand the mechanism

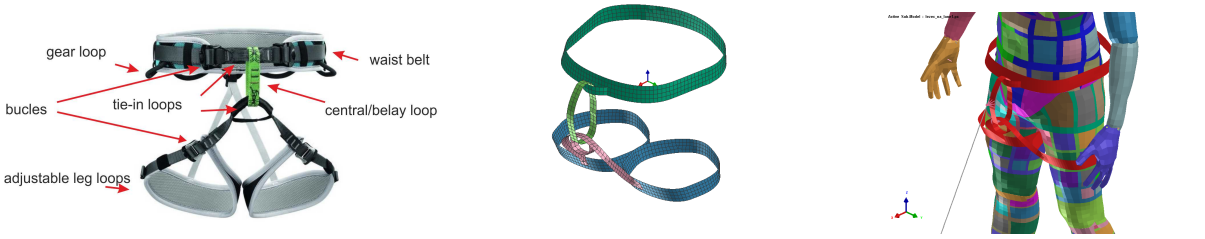

(a) Rock climber harness (b) FEM model of the harness (c) Virthuman with the harness

Fig. 1. Climbing harness and its FEM model

of all fall stages and to understand how to body reacts with the harness. Fig. 1a, 1b and 1c show the climbing harness, model of the harness and athlete (Virthuman) wearing the harness, respectively.

2. Results and future work

Since this is an ongoing student's project, the authors present only a preliminary results, consisting basic athlete's fall into the harness-rope. Free fall of the athlete into the protection devices (harness and rope) from the initial height and laterally shifted, are used for testing robustness and capability of the model in such scenarios. The material models used here are standard materials used in car seat belt (flat slings and rope). Due to the lack of the material data and experimental tests, the further work includes also material testing and material model fitting.

Acknowledgement

The result was financially supported with internal research project of University of West Bohemia SGS-2019-002: Computer modelling and monitoring of human body used for medicine.

References

[1] Bedogni, V., Computer mathematical models in belaying techniques, Proceedings of the conference Nylon and Ropes for Mountaineering and Caving, Club Alpino Italiano, Turin, 2002, pp. 8-9.

[2] Bedogni, V., Manes, A., A constitutive equation for the behaviour of a mountaineering rope under stretching during a climber's fall, Procedia Engineering 10 (2011) 3353-3358.

[3] Hynčík, L., Špička, J., Maňas, J., Vychytil, J., Stature based approach towards vehicle safety, SAE Technical Paper, 2015, doi: 10.4271/2015-26-0209.

[4] Pavier, M., Experimental and theoretical simulations of climbing falls, Sports engineering 1 (2) (1998) 79-91.

[5] Spörri, M., Numerical simulation of a climbers fall, Sports Engineering 17 (1) (2014) 61-72.

[6] Vychytil, J., Manas, J., Cechova, H., Spirk, S., Hyncik, L., Kovar, L., Scalable multi-purpose virtual human model for future safety assessment, SAE Technical Paper, 2014, doi: 10.4271/2014-01-0534.

[7] Vychytil, J., Manas, J., Pavlata, P., Striegler, R., Moser, T., Valasek, R., Prediction of injury risk in pedestrian accidents using virtual human model VIRTHUMAN: Real case and parametric study, SAE Technical Paper, 2016, doi: 10.4271/2016-01-1511.

[8] Vychytil, J., Spicka, J., Hyncik, L., Manas, J., Pavlata, P., Striegler, R., Moser, T., Valasek, R., Novel approach in vehicle front-end modeling for numerical analyses of pedestrian impact scenarios, SAE Technical Paper, 2017, doi: 10.4271/2017-01-1451.

COMPUTATIONAL MECHANICS 2019
35th conference with international participation
Srní
November 4 - 6, 2019

Flutter problems of electrically powered aircraft

A. Kratochvíl[a]

[a]*Department of Aerospace Engineering, Faculty of Mechanical Engineering, Center of Advanced Aerospace Technology, Czech Technical University in Prague, Technicka Street 4, 16607, Prague 6, Czech Republic*

The aircraft flutter is self-excited harmonic oscillation of structure. It occur without any warning and leads to destruction within a second. Flutter is cause by interaction of inertia, stiffness and aerodynamic forces. There have to be considered the feedback between force and deformation of structure during mathematical analysis of problem. A producer of airplane have to proof that each prototype of airplane is free from flutter up to certain velocity given by airworthiness requirements.

There have to be carried out a ground vibration test (next as GVT) [1] of an airplane for obtaining input data to flutter analysis in form of modal parameters. Any analytical methods for evaluation modal parameters of complex structure such as airplane fail. The GVT is based on excitation of aircraft structure by electromagnetic exciter with force meters and sensing a response by accelerometers. The measured data are process by Fast Fourier Transformation and Frequency response Function is subsequently determined for the purpose of modal parameters evaluation. The flutter analysis can be carry out on a finite element model tuned at the modal parameters from GVT [2] and [1]. Alternatively, by mathematical model derived directly in modal coordinates where eigen-vectors are not calculate on behalf of tuned finite element model, but directly imported from GVT measured data [3]. There were used the second method in this paper.

An electrical propulsion of an aircraft becoming more and more popular in last few years. A companies focused at aircraft production are experimenting with installation an electrical propulsion unit (next as EPU) to their aircraft. There is also a company aimed on developing and certification of such as propulsion unit, for serial production as an alternative to Rotax engine, which is popular among sports aircraft producer. In these days, a thrust produced by electrical engine installed in such as airplane is enough for safety take-off and fast enough to cruise. Nevertheless, a maximum velocity or endurance of airplane with EPU is far less than for combustion engine. In addition, the EPU installation can quite affect a flutter velocity of an airplane in negative way.

The subject of presented work is two-seater all-metal low-wing sports airplane with wingspan 9m. A fuel stores are situating in wings. A luggage compartment is situate in wings and fuselage. The airplane is certified according CS-23, thus a minimal flutter velocity has to be higher than 1,2 multiple of design velocity of airplane (next as V_D). The airplane has standard combustion engine Rotax. Moreover, there was did a modification of this airplane in sense of installing an EPU. There were performed the GVTs with 94 measuring points and 13 excitations locations together with flutter analysis for both version of airplane.

The flutter analysis for airplane with Rotax engine was carried out for light (one light pilot, no fuel, no luggage) and heavy (two heavy pilots, full fuel tanks, full luggage compartment) mass configuration with free and blocked control. On behalf of CS-23

Table 1. Flutter summary for Rotax version (light mass configuration, altitude 0m); A1: 1st Anti. wing bending; 1.AR-KR: 1st Anti. aileron rotation; 1.TT: 1st Fuselage torsion; 1.R-SK: 1st Rudder rotation

Flutter type	Modes involved	Flutter velocity	Flutter frequency	Control
Aileron flutter	A1 (Node in 48%) + 1.AR-KR	$1{,}48V_D$	19,3 Hz	Free
Rudder flutter	1.TT + 1.R-SK	$1{,}35V_D$	15,8 Hz	Blocked

requirement, the limits of all variables that can affect the flutter velocity have been examine. Analysed flutter velocities for nominal state are present in Table 1. All flutter velocities are above $1{,}2V_D$, thus the airplane meets the requirement to flutter resistance for nominal state.

The modification of airplane for a purpose of EPU installations is based on removing combustion engine and installing the electrical one, which is lighter and smaller than combustion one. The batteries are install in the wing. The fuel storage and wing luggage compartment were replace by battery bed structure. Each half-wing contains three battery segments, distributed from root rib up to 55% of wingspan. The mass of all batteries installed is 185kg, which is about 45% more than for mass of maximum fuel and luggage in wing compartments. The structure of airplane gets heavier due to installation of EPU by 40kg e.g. 9,5%, without considering the mass of batteries.

The result of nominal state flutter analysis for modified airplane with EPU is present in Table 2. All flutter velocities are above $1{,}2V_D$, except first Aileron flutter for Free control, where the flutter velocity is inside a flight envelope at $0{,}88\ V_D$. This flutter does not occur for Rotax version of airplane and is cause by battery installation. There are two symmetric and two antisymmetric 1st wing bending modes for EPU version. The Rotax version of airplane has only one mode for each, as usual airplanes have. See Fig. 1 for first wing bending modes comparison. The second wing bending modes for both airplane versions have no such as anomaly and they are similar in frequency and eigen-shape. The installation of battery bed have to be well stiff to battery will not stress by bending moment, together with add mass of battery it cause that new modes similar to first bending modes appear. They differ from standard structural modes in position of node point. Symmetric battery mode is not a problem because even that it have eigen-frequency higher than structural one it is still quite far away from eigen-frequency of symmetrical aileron rotation, which is about 30Hz, for free and blocked control. Unfortunately, eigen-frequency of antisymmetric battery mode is about half of structural one, and thus gets closer to antisymmetric aileron rotation mode, which is 7,5Hz for free control. Those two modes pairs together at certain velocity and causing the flutter occurrence in flight envelope.

Table 2. Flutter summary for EPU version (light mass configuration, altitude 0m); A1: 1st Anti. wing bending; 1.AR-KR: 1st Anti. aileron rotation; S2: 2nd Sym. wing bending; 1.SR-KR: 1st Sym. aileron rotation; 1.TT 1st Fuselage torsion; 2.R-SK: 2nd Rudder rotation; 1.SOT 1st Fuselage side bending

Flutter type	Modes involved	Flutter velocity	Flutter frequency	Control
Aileron flutter (Battery mode)	A1(Node in 26%) + 1.AR-KR	$0{,}88V_D$	13Hz	Free
Aileron flutter	S2 + 1.SR-KR	$1{,}48V_D$	42 Hz	Free & Blocked
Rudder flutter	1.TT + 2.R-SK + 1.SOT	Free: $1{,}29V_D$ Blocked: $1{,}27V_D$	Free: 20,5Hz Blocked: 19,8Hz	Free & Blocked

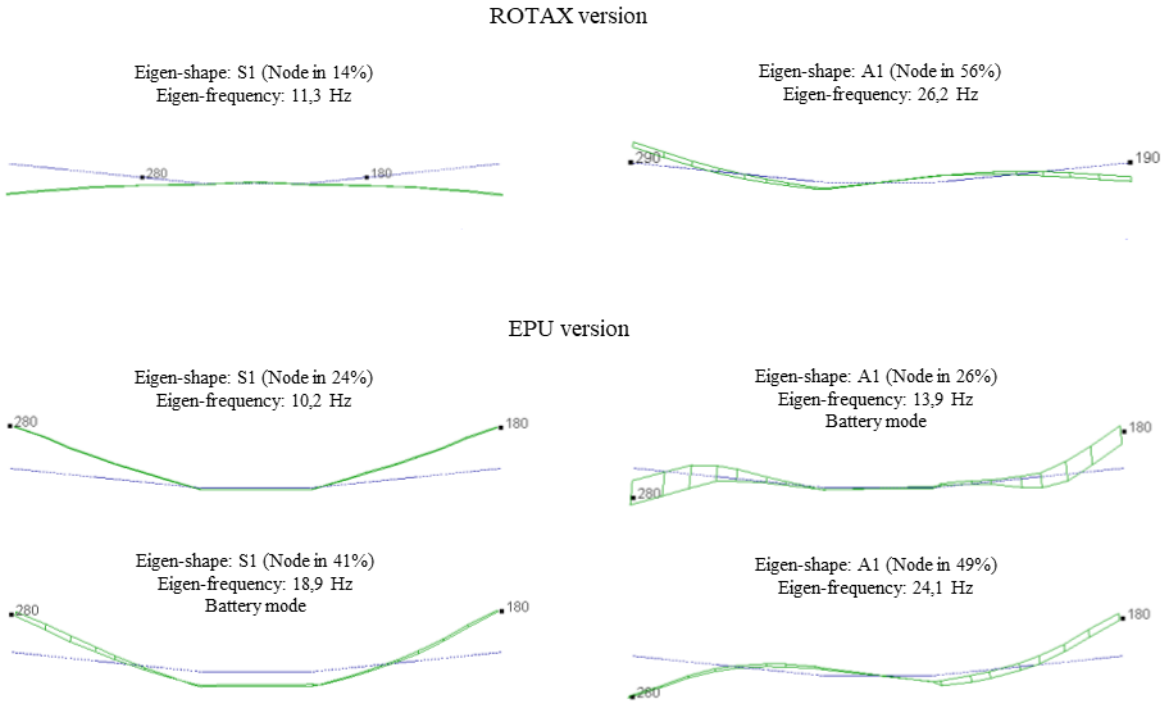

Fig. 1. First wing bending modes comparison. Symmetric modes – left column. Antisymmetric – right column

The installation of large amount of battery to wing can negatively affect the flutter velocity of aircraft. The presence of battery mass together with stiff battery bed will cause appearance of battery eigen-modes in bending. It was observed that the frequency of symmetric shape of battery mode get higher than structural 1st wing bending, and for antisymmetric shape of battery mode the frequency get lower than structural one. The exact frequency shift will depend on total mass of battery and stiffness of battery bed. In this case, it was about double for symmetric and half for antisymmetric shape. However, there is high

Table 3. Statistic of selected eigen-modes, for two seats sports airplane with combustion engine

Eigen-frequencies of antisymmetric modes [Hz]			
Airplane	**1st Aileron rotation Free control**	**1st Aileron rotation Blocked control**	**1st Wing bending Light mass config.**
NG5	3,9	24,0	25,5
Magic	4,9	12,0	30,7
Faeta NG	5,3	22,1	16,1
Rotax version	6,2	23,0	26,2
SkyLane	6,7	10,8	19,4
Lambada	7,1	13,2	10,5
EPU version	*7,5*	*24,6*	*24,1*
Sting	8,2	9,2	17,2
Sparrow	8,5	15,8	18,7
Piper Sport	10,5	14,4	23,7
Vampire	14,6	14,6	15,0
Minisport	15,0	24,2	21,7
SkyLane NG	12,2	15,3	21,7
VIA	16,2	16,3	27,6
GP-ONE	17,4	21,5	15,8
Legend	16,2	18,0	12,5
Viper	20,4	21,4	13,4
Average value	*10,6*	*17,7*	*20,0*

probability that eigen-frequency of antisymmetric battery mode will get close to 1st antisymmetric aileron rotation in free control configuration. This mode act as kinematic mechanism thus the eigen-frequency is low. Based on statistic of 17-measured two seats sports airplane with combustion engine, presented in Table 3, the average antisymmetric aileron eigen-frequency is about 10,6 Hz. Meanwhile average antisymmetric wing bending eigen-frequency is about 20,0 Hz, which will be reduce by battery installation. With increasing velocity of flight, the aileron eigen-frequency will rise and can easily meet the antisymmetric battery mode, coupled each other and cause the flutter at low velocities. Thus, the installation of EPU with large mass of batteries in the wing can be quite dangerous from flutter point of view.

Acknowledgements

Authors acknowledge support from the ESIF, EU Operational Programme Research, Development and Education, and from the Center of Advanced Aerospace Technology (CZ.02.1.01/0.0/0.0/16_019/0000826), Faculty of Mechanical Engineering, Czech Technical University in Prague.

References

[1] Čečrdle, J., Hlavatý, V., Aeroelastic analysis of light sport aircraft using ground vibration test data, Proceedings of the Institution of Mechanical Engineers, Part G: Journal of Aerospace Engineering, Vol. 229, Issue 12, 2015, pp. 2282-2296.

[2] Čečrdle, J., Updating of finite element model of aircraft structure according results of ground vibration test, Proceedings of the Institution of Mechanical Engineers, Part G: Journal of Aerospace Engineering, Vol. 230, Issue 7, 2016, pp. 1348-1356.

[3] Slavík, S., Weigl, K., Flutter calculation model with isolated modal characteristics of control surfaces for small sport airplanes, Czech Aerospace Proceedings, No. 2/2008, 2008, pp. 44-49.

COMPUTATIONAL MECHANICS 2019
35th conference with international participation
Srní
November 4 - 6, 2019

LQR control of multi-DoF absorber for planar robots

K. Kraus[a], Z. Šika[a]

[a] *Department of Mechanics, Biomechanics and Mechatronics, Faculty of Mechanical Engineering, Czech Technical University in Prague, Technická 4, Praha 6, 160 00 Prague, Czech republic*

Vibration suppression takes place in many applications, including robotics. The serial robots are one of the examples of robots, which can serve large workspace, but also have large mass/stiffness ratio, which leads to low accuracy of the end-effector during high dynamic operations, e.g. drilling [2]. In such cases, serial robot needs to be more precise, even when externally excited by the drilling harmonic force or other disturbances. Attaching an additional absorber mass to the primary structure is one of the approaches to suppress vibrations among many others and will be discussed in this paper.

Firstly, the single-mass multi-degrees-of-freedom absorber is used to manage the task rather than many single-axis absorbers combined. It has the advantage of smaller mass with same effect in multiple axes, which leads to lower spatial and power requirements. Secondly, an active approach is chosen to cover more configurations of primary system. Passive tuning is still important as a base design, since it is supposed to handle the major forces, leaving the active part of the solution to do the rest with smallest possible power requirements. There are various algorithms (mostly centralized) that can be used to drive absorber's actuators, such as PID regulation, H-inf, LQR [3], Delayed resonator [1], etc.

In this paper, LQR algorithm is considered as initial control design, which controls three voice-coil actuators placed perpendicularly to each other (Fig.1a) along with springs of the planar absorber. This attached actuated spring-single-mass multi-DoF system is used to suppress vibrations of flexible planar simulated serial robot (Fig. 1b) in various positions of workspace. Such a system should be able to work while following the trajectory of the robot, along which the properties of the primary structure varies significantly. The LQR algorithm always needs to be aware of the current position of the robot and use appropriate linearized model of the structure. There are three basic questions to be answered.

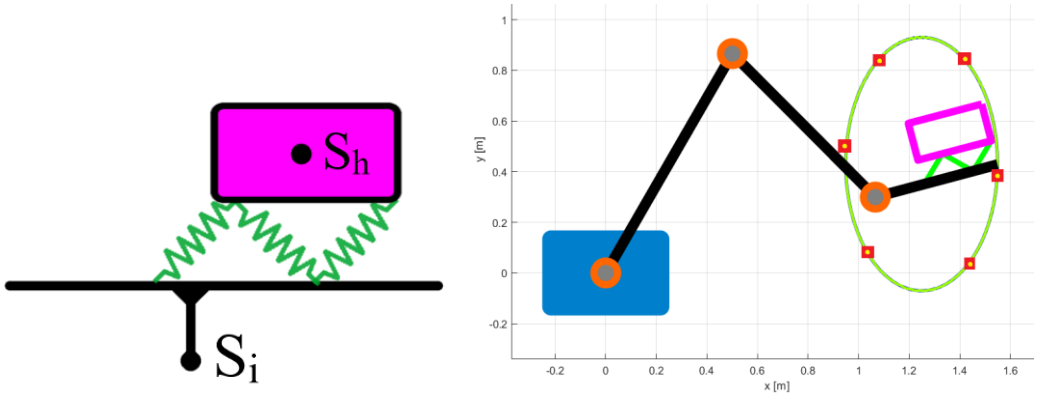

a) Planar absorber attached to arm b) Planar robot with trajectory

Fig. 1. Planar absorber design and its attachment to planar serial robot following specific trajectory

Mainly, linearized models need to be known in advance. A grid of ABCD matrices has to exist through workspace of the system with sufficient density (red squares in Fig. 1b), so there are small enough differences from the real state in every position. Gain scheduling is then applied to combine results from neighbors linearized model. After that, linearized models must be precise enough to be able to observe the whole system. Observation could be performed using any built-in sensors of the robot and few extra attached sensors, that has to be robust and relative (e.g. absolute position measurement can be challenging in industrial environment), so absorber's actuator's encoders, conveniently located accelerometers or velocity measurement through geophones would be first to join the observation. Finally, an efficient cost function of the LQR algorithm needs to be designed, which aims to as low vibrations of the end-effector as possible. That can be achieved through velocity or acceleration amplitudes of the observed end-effector, since position observation is more prone to errors when sliding between grid points of known linearized models.

Fig. 2a compares amplitude characteristics of the robot itself to robot with attached passive absorber (tuned to first eigenfrequency of the robot) and to active absorber controlled by LQR algorithm (using full state feedback so far). Observation of the primary system using unperfect linearized models makes the results little bit hazier and is in process of evaluation. Fig. 2b then compares same cases, only in time domain, when external force impulse acts on the end-effector every 2 seconds through whole 12 seconds trajectory shown in Fig. 1b.

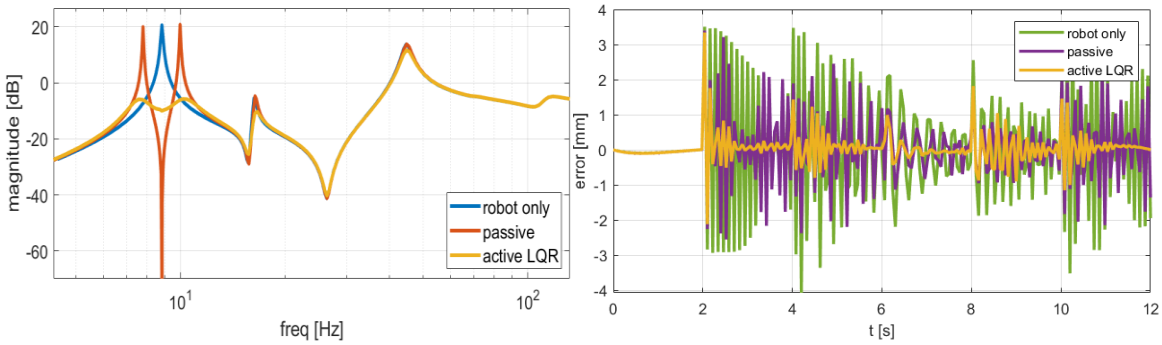

a) Amplitude characteristics b) Time impulse responses

Fig. 2. Responses of the robot's end-effector with or without passive/active absorber

Acknowledgements

The work has been supported by the Czech Science Foundation project GA17-20943S "Active multidimensional vibration absorbers for complex mechanical structures based on delayed resonator method".

References

[1] Olgac, N., Elmali, H., Hosek, M., Renzulli, M., Active vibration control of distributed systems using delayed resonator with acceleration feedback, Journal of Dynamic Systems, measurement, and control 119 (3) (1997) 380-389.

[2] Olsson, T., Haage, M., Kihlman H., et al., Cost-efficient drilling using industrial robots with high-bandwidth force feedback, Robotics and Computer-Integrating Manufacturing 26 (1) (2010) 24-38.

[3] Šika, Z., Kraus, K., Beneš, P., Vyhlídal, T., Valášek, M., Active multidimensional vibration absorbers for light robots, Proceedings of the 5th Joint International Conference on Multibody System Dynamics, Lisbon, 2018, pp. 1-12.

COMPUTATIONAL MECHANICS 2019
35th conference with international participation
Srní
November 4 - 6, 2019

Feedback control of myosin head

M. Krejčová[a], P. Světlík[c]

[a] Faculty of Applied Sciences, University of West Bohemia, Univerzitní 8, 301 00 Plzeň, Czech Republic
[c] Faculty of Electrical Engineering, University of West Bohemia, Univerzitní 8, 301 00 Plzeň, Czech Republic

1. Introduction

Myosin is a molecular motor responsible for muscle contraction. To do so, it hydrolysed molecule of adenosine triphosphate (ATP) to adenosine diphosphate (ADP) and free phosphorus (P). The proper function of muscle is controlled by the concentration of several ions. In this contribution, we control the myosin velocity by ATP concentration with a PD (proportional-derivative) regulator system.

2. Mathematical model

Myosin movement characteristic size is in nanometers, so it is influenced by thermal fluctuations. Due to it, myosin moves chaotically. We limit our mathematical model to catching the movement of myosin head only. We describe its movement by the Fokker-Planck equation [5]

$$\frac{\partial \rho_i}{\partial t} = D\frac{\partial}{\partial x}\left[\frac{1}{k_B T}\left(\frac{\partial V_i(x)}{\partial x} + F_{Load}\right)\rho_i\right] + D\frac{\partial^2 \rho_i}{\partial x^2} + \sum_{j=1}^{N} k_{ij}\rho_j - \sum_{j=1}^{N} k_{ji}\rho_i, \tag{1}$$

where the indexes i and j denote the state of the myosin head. The equation is solved for ρ_i, which stands for the probability density of the presence of head in state i, given time t and space x. The other parameters are variables which influence the movement. The parameters are diffusion D, and the product of Boltzmann's constant k_B and thermodynamics temperature T. The potential $V_i(x)$ is produced by chemical reactions and F_{Load} is the external load. The potential dependences on x are as follows

$$V_2 = \Delta G\left(\sin\left(\frac{2\pi x}{L}\right) - \frac{1}{2}\sin\left(\frac{4\pi x}{L}\right) + \frac{1}{3}\sin\left(\frac{6\pi x}{L}\right)\right) + E, \tag{2}$$

$$V_3 = -\Delta G\left(\sin\left(\frac{2\pi x}{L}\right) - \frac{1}{2}\sin\left(\frac{4\pi x}{L}\right) + \frac{1}{3}\sin\left(\frac{6\pi x}{L}\right)\right) + E, \tag{3}$$

$$V_1 = E, \tag{4}$$

where E is spring energy. The spring corresponds with the myosin neck – the connector between myosin filament and the head. The amplitude of the Fourier series ΔG is free energy amount. It expresses in $\mathrm{k_B T}$ units according to [3] as

$$\Delta G = \frac{\Delta G_0}{k_B T} - \log\frac{[ATP]}{[ADP]\,[P]}\,. \tag{5}$$

The square brackets stand for the concentration of the chemical composition inside.

Parameters k are rates constants to switching between chemical states. The states are as follows: unbound (further numbered as 1), weakly-bound (2) and post-power stroke (3). The cycle is not reversible – the transition from unbound state to post-power stroke is forbidden.

2.1 Transition rates

The transition rates are modified from the article [5], where the five-state model was simplified to two-state one. The modification procedure to the tree-state model was based on the same paper.

The transition states recount in this way

$$\frac{1}{k_{12}} \approx \frac{1}{k_1} + \frac{1}{k_5}, \tag{6}$$

$$\frac{1}{k_{21}} \approx \frac{1}{k_1^-} + \frac{1}{k_5^-}, \tag{7}$$

$$\frac{1}{k_{31}} \approx \frac{1}{k_3} + \frac{1}{k_4} - \left(\frac{1}{k_3^-} + \frac{1}{k_4^-}\right), \tag{8}$$

$$\frac{1}{k_{23}} \approx \frac{1}{k_2}, \tag{9}$$

$$\frac{1}{k_{32}} \approx \frac{1}{k_2^-}. \tag{10}$$

The transition rates on the right side are the original one. Its numbering was kept. The rates k_l ($l = 1, 2, 3, 4, 5$) denote the transition rate outcoming from the state l. The rates k_l^- states for the rates going to the state l. According to the paper [5], the transition rate k_3 is a function of the ATP concentration.

Transition rates on the left side belong the three-state model. They have two indexes each. The first one is the original one, the second the ending one.

The structure of the transition rate k_{31} is different from the others. It is caused due to one-way direction transition between unbound and post-power stroke state.

2.2 Myosin velocity

One of the important parameters of the molecular motors is their velocity ν. In this model, it is possible to count it as

$$\nu = \frac{1}{3}\sum_{i=1}^{N} L J_i, \tag{11}$$

where J_i is the flux given by

$$J_i = D\left[\frac{1}{k_B T}\left(\frac{\partial V_i(x)}{\partial x} + F_{Load}\right)\rho_i\right] + D\frac{\partial \rho_i}{\partial x}. \tag{12}$$

Data, shown in Fig. 1, are quality correct, not quantitative, see Fig. 2. In the case of values from that figure, there is no influence of concentration of ADP neither P.

The concentrations for Fig 1 are taken from [3] and shown in Table 1.

3. PD regulator

To correct velocity values, we need to influence (or control) some of the model parameters. The chosen one is the ATP concentration. Other concentrations are kept. The most common

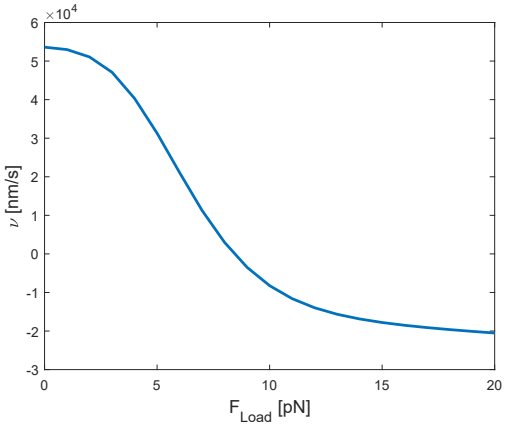

Fig. 1. Velocity with no interference of the feedback controller

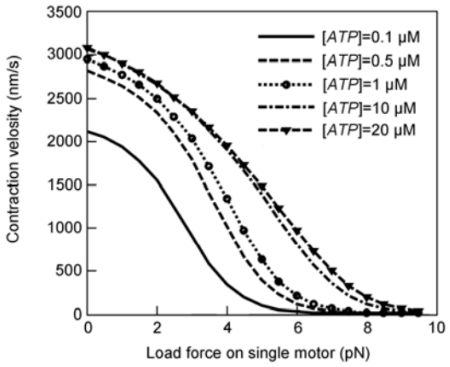

Fig. 2. Velocity dependence on an external load for different ATP concentrations, taken from [5]

Table 1. Adenosine triphosphate (ATP), adenosine diphosphate (ADP) and free phosphate (P) initial concentration taken from [3]

Molecule	ATP	ADP	P
Concentration [Mols]	4e-3	20e-6	2e-3

controller is the PID (Proportional, Integral, Derivative) one. The function u(t) which governed the regulator is

$$u(t) = K_p e(t) + K_i \int_0^t e(t')\mathrm{d}t' + K_d \frac{\mathrm{e(t)}}{\mathrm{t}}\,, \tag{13}$$

where e is the error. Constants K_p, K_i and K_d are coefficients of the proportional (index p), integral (index i) and derivative (index d), respectively.

The model describes the Markov process (the future state is influenced only by the present situation, not the past). Since the integral component needs the past for its functionality [1], only the PD controller is used.

The goal velocity is chosen to 3000 nms^{-1}. Parameters values were obtained by numerical experiments. Results are shown in Table 2.

Table 2. Found values of the PD regulator for the desired value of 3000 nms^{-1}. The values of concentration ATP are in a time when the velocity reaches the desired value.

F_{Load} [pN]	0	10	20
K_p	3.3e-04	3.3e-04	3.3e-04
K_d	1.8e-15	1.0e-18	9.0e-18
[ATP]	2.1e-13	1.2e-16	1.1e-15

4. Conclusions

The regulator constant K_p is constant for all studied loads. The constant K_d varies between the order of e-15 to e-18. The opposite signs of contraction velocities cause the big difference of the orders. The next research will be focused on the meaning of the ATP concentration provided by the PD regulator and on the controlling ADP and P concentrations.

Acknowledgements

M. Krejčová was supported by project SGS-2019-002. She also wishes to express her big thanks to Mr Rosenberg and Mr Holeček for their valuable advice.

References

[1] Åström, K.J., Hägglund, T., The future of PID control, IFAC Proceedings Volumes 33 (4) (2000) 19-30.

[2] Chen, J., Zhang, X. Lin, S., Wan, H., Gu, L., Multiscale modeling of skeletal muscle active contraction in relation to mechanochemical coupling of molecular motors, Micromachines 6 (2015) 902-914.

[3] Howard, J., Mechanics of motor proteins and the cytoskeleton, Sinauer Associates, Inc., Sunderland, Massachusetts, 2018.

[4] Krejčová, M., Holeček, M., Chełminiak, P., The measurement of single myosin head in Fokker-Planck framework and information gain, Proceedings of the 20th international conference Applied Mechanics 2018, Myslovice, University of West Bohemia, 2018, pp. 63-68.

[5] Yin, Y.-H., Guo, Z., Collective mechanism of molecular motors and a dynamic mechanical model for sarcomere, Science China Technological Sciences 54 (8) (2011) 2130-2137.

COMPUTATIONAL MECHANICS 2019
35th conference with international participation
Srní
November 4 - 6, 2019

Dispersion errors for wave propagation in thin plate due to the finite element method

A. Kruisová[a], R. Kolman[a], M. Mračko[a]

[a] *Institute of Thermomechanics, Czech Academy of Sciences, Dolejškova 5, 182 00 Prague 8, Czech Republic*

Widespread use of ultrasonic guided waves in non-destructive testing increases demand for the efficient and reliable numerical modeling of this phenomena [4]. Here the effect of spatial and temporal discretisation in finite element modeling on the accuracy of the numerical predictions is illustrated.

In former works [1, 2] the analytical solution for dispersion errors estimation in finite element modeling of wave propagation was derived. These works include the solution of the regular mesh and the plane strain elements. Here these relations are illustrated by the example of modeling of Lamb's waves propagating in a plate.

Lamb's wave is an elastic wave which propagates through a solid thin plate with free boundaries. In a homogeneous isotropic plate of a finite thickness two set of waves propagates with finite speed, these sets are called symmetric and antisymmetric waves, according to its shape, Fig. 1. Their velocities depends on the relationship between the thickness of the plate and the wavelength of the wave. These waves are highly dispersive, but their phase and group velocities can be stated analytically [3]. Their small wavelengths in higher frequency range and only a small loss of amplitude magnitude make them very popular for nondestructive testing. Thus, the properties of the finite element method modeling are desirable, see [4, 5].

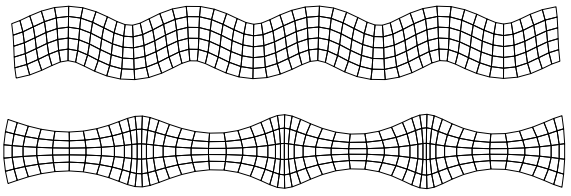

Fig. 1. Antisymmetric (*top*) and symmetric (*bottom*) mode of the Lamb's wave in thin plane

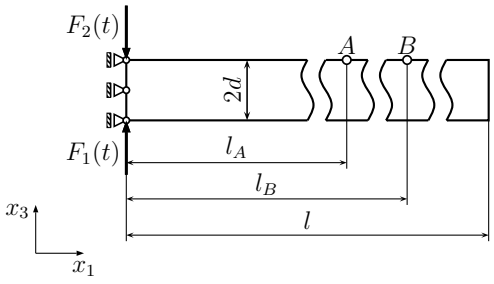

Fig. 2. Model of the plate

Both the spatial and temporal discretisation in finite element modeling lead to numerical dispersion errors. This means that the phase velocity of the numerical solution of the wave propagation is frequency dependent even in the absence of any dispersion in the actual media. When a dispersive waves are modeled, the dispersion error caused the difference between the analytical and numerical solution.

Characteristic equations determining the relation between the wave number $k = 2\pi/\lambda$, λ is the wavelength, and the angular velocity $\omega = 2\pi f$, f denoting frequency, of Lamb's wave are

$$\frac{\tan(\beta\, d/2)}{\tan(\alpha\, d/2)} = -\frac{4\alpha\beta k^2}{\left(k^2-\beta^2\right)^2} \tag{1}$$

and

$$\frac{\tan(\beta\, d/2)}{\tan(\alpha\, d/2)} = -\frac{\left(k^2-\beta^2\right)^2}{4\alpha\beta k^2}, \tag{2}$$

where

$$\alpha^2 = \frac{\omega^2}{c_{\mathrm{L}}^2} - k^2 \qquad \text{and} \qquad \beta^2 = \frac{\omega^2}{c_{\mathrm{T}}^2} - k^2. \tag{3}$$

c_{L}, c_{T} are the velocities of the longitudinal and shear waves, respectively.

Numerical methods are used to find phase velocity $c_{\mathrm{p}} = \omega/k$ and the group velocity $c_{\mathrm{g}} = \mathrm{d}\omega/\mathrm{d}k$. Solutions of Eq. (1) are waves with a symmetric shape and solution of Eq. (2) are waves with an antisymmetric shape. See Fig. 1.

The dispersion curves were calculated from (1) and (2), see Fig. 3.

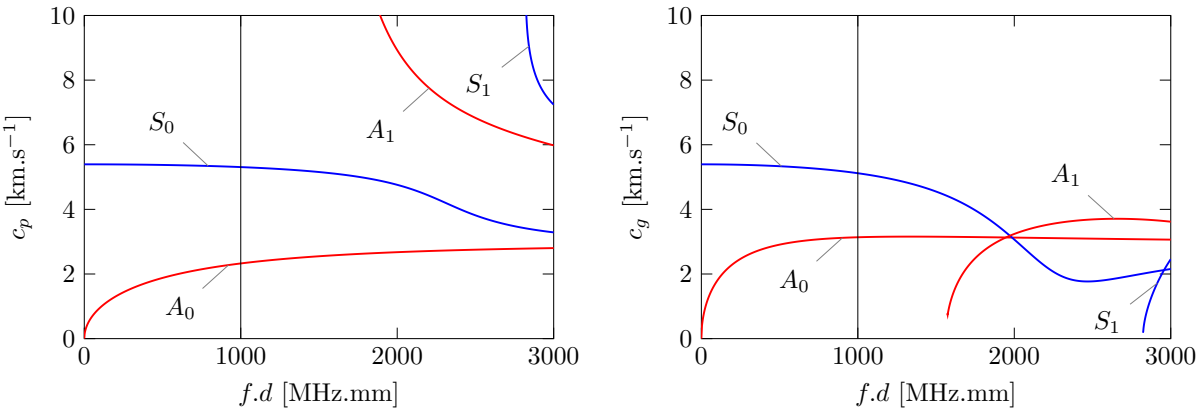

Fig. 3. Dispersion curves of Lamb's wave. The phase velocity vs. frequency (*left*) and the group velocity vs. frequency (*right*). Red lines show the first and second wave with an antisymmetric mode, the blue lines show the first and second wave with the symmetric mode. Black line shows the velocities of waves used in the example with frequency f of 0.5 MHz and the plate thickness d of 2 mm.

Since the Lamb's wave propagation suppose the plain strain problem, the plain strain 2D elements can be used. The thickness of the plate $2d$ is 2 mm and the modelled plate's length l is 500 mm, see Fig. 2. The plate is made from aluminium with Young's modulus of elasticity $E = 70$ GPa, $\nu = 0.33$, $\rho = 2.7$ g.cm^{-3}. Then shear modulus G is 26.3 GPa.

The Lamb's wave in the plate can be excited by applying forces

$$F_1(t) = \hat{F}\sin(\omega t)\sin^2\left(\frac{\omega t}{2n}\right), \tag{4}$$

where $\omega = 2\pi f$ at two points at the opposite sides of the plate, as is shown in Fig. 2. The loading frequency f is 500 000 Hz and $n = 16$ is the number of cycles and it determines the width of the signal around the central frequency. For the symmetric mode force amplitudes are $F_2 = -F_1$ and for the antisymmetric mode $F_2 = F_1$. The signal is shown on the left side in Fig. 4.

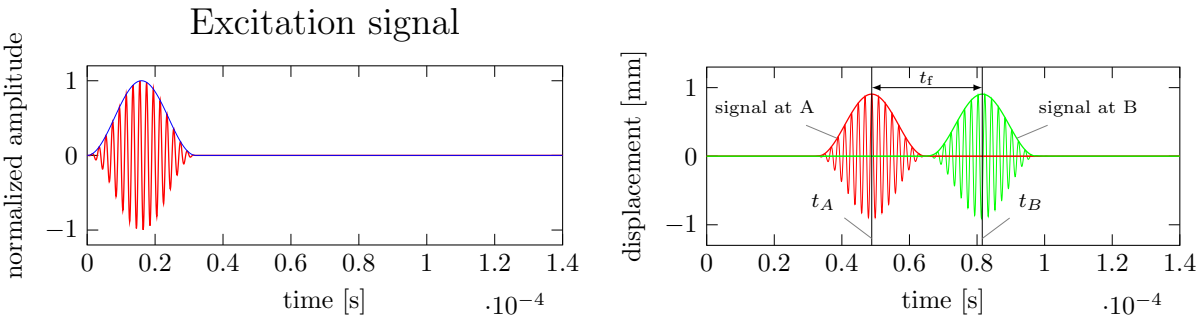

Fig. 4. (*Left*) Time history of applied force F. (*Right*) Calculated displacement at points A and B, plotted with the red and green line, respectively. The envelope of the signal. The centroid of both envelopes defines the time when the wave reach point A and B, denoted t_A and t_B, respectively. The flight time of the wave is then $t_\mathrm{f} = t_B - t_A$.

The signal is read as a displacement in two points, point A in distance of $l_A = 0.1\,\mathrm{m}$ from the loading force and point B in distance of $l_B = 0.2\,\mathrm{m}$ of the loading force, see Fig. 2. The plane is long enough that no reflections of the free end of the plane occur.

The loading is supposed to be in the middle of the plane, so the displacement in the direction of the wave propagation of all nodes of the cross section of the plane on one side (loading side) is prescribed to be zero.

For wave propagation modeling, three different finite element meshes were used. All of them contain square 4-node plain strain elements with the element size H equal to 0.67 mm, 0.4 mm and 0.2 mm, respectively, thus we have 3, 5 and 10 elements for the thickness of the plate. Part of the mesh with 5 elements to thickness are shown in Fig. 1.

The time integration method used in our example was the Newmark method with parameters $\gamma = 1/2$ and $\beta = 1/4$ and consistent mass matrix. Here only the results for antisymmetric mode, when for given frequency f the theoretical value of phase and group velocities are $c_{p\,\mathrm{A}} = 2.3266\,\mathrm{km.s^{-1}}$ and $c_{g\,\mathrm{A}} = 3.1371\ \mathrm{km.s^{-1}}$. The time step used in finite element simulation was for prescribed Courant number $C = \Delta t\, c_{g\,\mathrm{A}}/H$ calculated from $\Delta t = C_\mathrm{L} H/c_{g\,\mathrm{A}}$, it differs for different element size H.

For frequency $f = 0.5\,\mathrm{MHz}$, the wave number $k = 2\pi f/c_{p\,\mathrm{A}}$ is 1350 and the product $k.H/\pi$ is equal to 0.29, 0.17 and 0.086, respectively. This corresponds to 7, 11.6 and 23 elements modeling the whole wavelength.

A group velocity of FEM model was determined from displacement signal in point A and B using Hilbert transform to obtain the envelope of the signal and the speed of the centroid of the signal is the group velocity in the model, see the right side of Fig. 4.

The table with calculated group velocities for different Courant number and different k is given (in $\mathrm{km.s^{-1}}$) as:

Courant number C	0.1	0.5	1	2
$kH/\pi = 0.29$	3.6301	3.5406	3.2692	2.3285
$kH/\pi = 0.17$	3.1311	3.1017	3.0103	2.6650
$kH/\pi = 0.09$	3.1354	3.1281	3.1054	3.0145

The relative error can be calculated as a ratio of the calculated group velocity and theoretical group velocity $c_{g\,\mathrm{A}} = 3.1371\ \mathrm{km.s^{-1}}$, see Fig. 3. Since the antisymmetric mode in plate corresponds with its shape more to the shear mode of the wave propagating in space, in Fig. 5 the relative error is shown together with theoretical dispersive errors of the shear wave in FEM model of space, see [2].

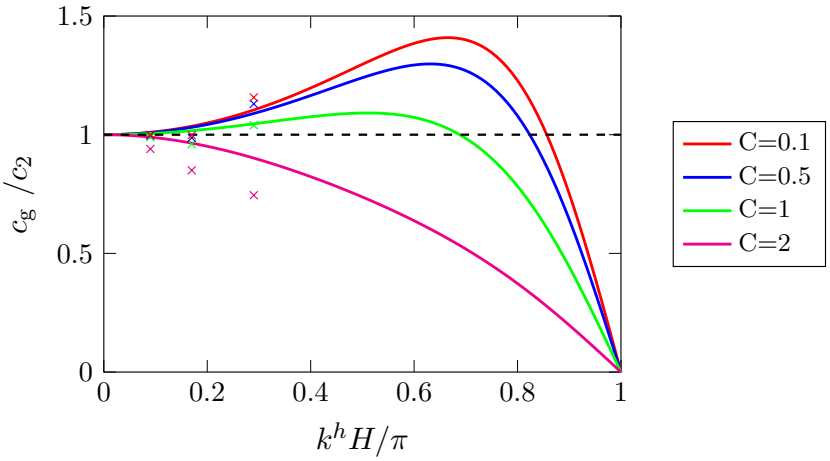

Fig. 5. The comparison of dispersion errors of finite element models in space (solid lines) and in plate ($\times$ mark). Different values of Courant number denoted by different colors.

In Fig. 5, the non-dispersive relative group velocity with dashed line is plotted together with the theoretical relative dispersive group velocities of a shear wave in space with solid lines (different colors for different Courant number). The size of the dispersive error is given by the deviation of the curve to the horizontal dashed line.

From the ratio of the calculated and theoretical value of group velocity of the antisymmetric mode of a Lamb's wave the relative dispersive errors were calculated and plotted in the same graph by cross mark. The relative error is here the distance between the horizontal line and the cross for particular values of kH/π and C.

Here it is verified that the theoretical expression for dispersion errors in space [2] serves well for the estimation of dispersion errors in other example, when the plain strain element can be used.

Acknowledgement

The outcome of this work has been achieved with the financial support of the Grant Agency of the Czech Republic, project No. 19-14237S. The financial support is gratefully acknowledged.

References

[1] Kolman, R., Plešek, J., Červ, J., Okrouhlík, M., Pařík, P., Temporal-spatial dispersion and stability analysis of finite element method in explicit elastodynamics, International Journal for Numerical Methods in Engineering 106 (2016) 113-128.

[2] Kruisová, A., Kolman, R., Mračko, M., Okrouhlík, M., Temporal-spatial dispersion analysis of finite element method in implicit time integration, Proceedings of the 25th conference Engineering Mechanics 2019, Svratka, Institute of Thermomechanics of the Czech Academy of Sciences, 2019, pp. 215-218.

[3] Rose, J. L., Ultrasonic guided waves in solid media, Cambridge University Press, 2014.

[4] Wan, X., Xu, G., Zhang, Q., Tse, P. W., Tan, H., A quantitative method for evaluating numerical simulation accuracy of time-transient Lamb wave propagation with its application to selecting appropriate element size and time step, Ultrasonics 64 (2016) 25-42.

[5] Willberg, C., Duczek S., Vivar Perez J. M., Schmicker D., Gabbert, U., Comparison of different higher order finite element schemes for the simulation of Lamb waves, Computer Methods in Applied Mechanics and Engineering 241-244 (2012) 246-261.

COMPUTATIONAL MECHANICS 2019
35th conference with international participation
Srní
November 4 - 6, 2019

Fire ladder test simulation

J. Kuželka[a], M. Španiel[a], K. Doubrava[a]

[a] *Faculty of Mechanival Engineering, Czech Technical University in Prague, Technická 4, 160 00 Praha 6, Czech Republic*

1. Introduction

The fire ladders could be exposed to high temperatures during their service. The exposure leads to mechanical properties degradation and a ladder could become unsafe for further use. According to regulations the fire ladders must be continuously tested to prove their capability. The test is based on ladder bending. Assembled ladder is supported on the ends and loaded in the middle by defined weight. The capability is assessed on the base of deflections under load and residual deflections. The regulation does not include the basis for assessment (material properties and ladder design) so it is probably arise from experience. Thus there is need to get better insight to ladder stress during service, relation between this stress and described test results according to material failure and the influence of mechanical properties degradation on limit loading.

2. Material data calibration

There were performed material tests on specimens cut out of ladder. There was tested the base material and material exposed to defined temperatures and defined periods of time as is shown in Table 1.

Table 1. Temperatures and exposure times of specimens and calibrated material parameters

temperature [°C]	time [min]	A [MPa]	B [MPa]	n [-]
20	-	200	153	0.3
200	120	190	147	0.28
200	240	185	150	0.28
200	480	180	162	0.33
300	5	120	232	0.48
300	30	80	328	0.57
300	120	77	267	0.55
400	5	120	232	0.48
400	30	30	200	0.41

The Johnson – Cook plasticity model [1] was considered, thus actual yield stress can be expressed as

$$\sigma_y = A + B\left(\varepsilon_{pl}\right)^n .$$

The experimental data were used for material parameters *A*, *B* and *n* calibration employing Levenberg-Marquardt nonlinear least square algorithm. The calibrated values can be seen in Table 1. The material model also includes a ductile damage cummulation [1] in the form

$$\varepsilon^f = d_1 + d_2 e^{(-d_3 \eta)},$$

where ε^f is fracture locus, η is stress triaxiality and $d_{1\text{-}3}$ are material parameters. Due to lack of experimental data only parameter d_1 was calibrated considering tensile tests and d_2 = 0.089 and d_3 = 2.44 were adopted from [2].

3. Ladder testing

Three assembled ladders were tested in total. The supports were placed 200 mm from the ladder ends thus their distance was 3815 mm. One support was fixed and the second was movable in horizontal direction. In the middle was installed weight carrier connected with IBC container which was gradually filled by water during the test. Force gauge HBM S9M with 10 kN range connected to container was used for applied load monitoring. The deflection was monitored by potentiometric gauge with range 900 mm. Also strain gauges were installed in one case. All gauges where connected to universal measuring amplifier module HBM Quantum 840 which was connected with PC. For data recording with sampling frequency 10 Hz was used software HBM Catman Easy. The results are shown in Fig. 1. On the base of the measurements was estimated limit load as Flim = 3482 N.

4. Numerical simulation

The FE model of ladder was created. It consists of four instances (ladder segments) coupled by tie constrain. All parts of ladder are modeled as continuum solids. FE model contains about 230 000 linear elements with full integration. In the first step the ladder is loaded by own weight and by weight of empty container. In the second step only weight of container increases. The simulations were done for all cases when whole ladder had degraded mechanical properties Since whole ladder is not exposed to higher temperatures in reality the simulation of this case was made. There was focus on two cases. In the first the exposed part is on the end of ladder and in second the exposed part is in the middle. For simulations was used commercial software Abaqus.

5. Results

In Fig. 1. are shown computed and measured dependencies of load on deflection. The magnitude of ductile damage parameter for load corresponding to measured limit load was obtained. On the base of this value were estimated limit loads and limit deflections for cases of ladders with degraded mechanical properties. Quite interesting are results of partially degraded ladders. It demonstrates high sensitivity on the ladder assemblage. The case with degraded material of the end of the ladder shows relatively high limit force as well as high deflections in comparison of the case with degraded middle.

6. Conclusions

The material parameters of Johnson – Cook plasticity model were calibrated. The limit load was experimentally measured and was used for limit loads of degraded ladder estimation employing numerical simulations considering ductile damage cummulation. There was shown significant dependency between limit loads and deflections on the ladder assemblage. This aspect in not included in current regulations.

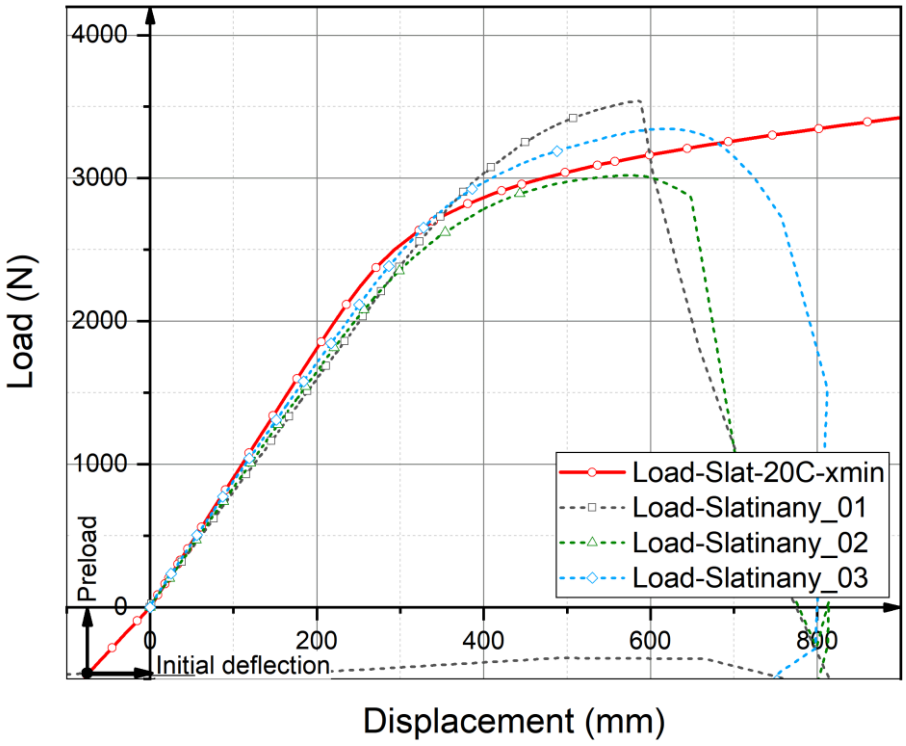

Fig. 1. Load vs. displacement. Dotted lines are experimental results. Full line is computed response for unexposed basic material

Acknowledgements

The work has been supported by the research project BVIII/1-VS VI20162020021.

References

[1] Johnson, G.R., Cook, W.H., Fracture characteristics of three metals subjected to various strains, strain rates, temperatures and pressures, Engineering Fracture Mechanic 21 (1) (1985) 31–48.

[2] Zhenyu, W., Yang, Z., Xu, L., Zhiguo, H., Analysis of the dynamic response in blast-loaded CFRP-strengthened metallic beams, Advances in Materials Science and Engineering (2013) 13.

COMPUTATIONAL MECHANICS 2019
35th conference with international participation
Srní
November 4 - 6, 2019

Computational aeroacoustics in a human vocal tract

M. Lasota[a], P. Šidlof[a,b]

[a] Technical University of Liberec, NTI FM, Studentska 2, 461 17 Liberec, Czech Republic
[b] Institute of Thermodynamics, Academy of Sciences of the Czech Republic, Dolejskova 5, 182 00 Prague 8, Czech Republic

1. Introduction

The usage of computational analyses in the research of human voice generation have a justified reason, because of the restricted access in a larynx just during phonation. The voice research allows merely visual tools to study a vibration of vocal folds (VFs) such as stroboscopy and videoendoscopy.

2. Mathematical model

Mathematical models of turbulence add up to some limitations regarding a capture of a physical phenomenon. This contribution tackles a laryngeal flow through the domain, the used parametres are taken over from the Scherer's M5 model [3] of a human larynx. The used CFD grids are built up with tetrahedral control volumes (CVs) by Šidlof et al. [4] for cases (A1, A2) and with hexahedral CVs by Lasota and Šidlof [2] for a case (A4). The computational aeroacoustic (CAA) simulation was performed on a domain consisting of the CFD domain (larynx) and a vocal tract model with a propagation region and perfectly matched layer (PMLs), see Fig. 1. The acoustic grid was made by Zörner et al. [6] via geometrical parameters from the study of Story [5]. The fine CFD meshes are used for computation of the laryngeal flow at first, then the results is used for the aeroacoustic sources and afterwards the right-hand side (RHS) is interpolated to the coarser CAA mesh for a decrease of computational costs, see Hüppe [1]. The transient aeroacoustic simulation is solved in a last step.

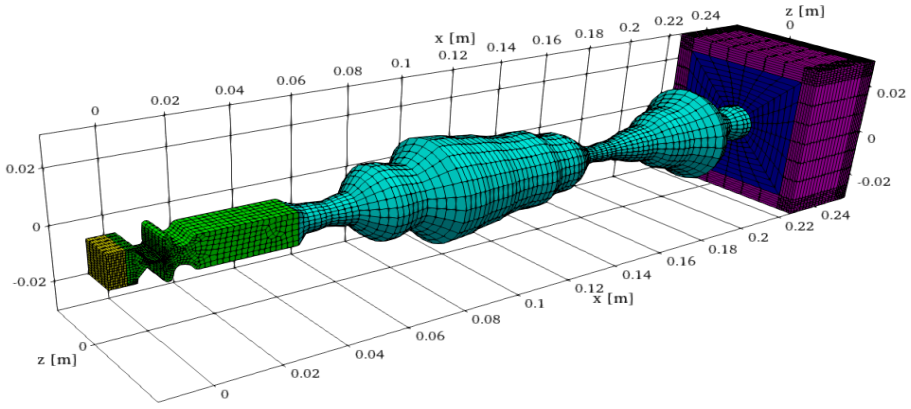

Fig. 1. Mesh for acoustic simulation: a) PML at inlet (yellow), b) larynx (green), c) vocal tract (light blue), d) propagation field (dark blue), e) PML at outlet (purple)

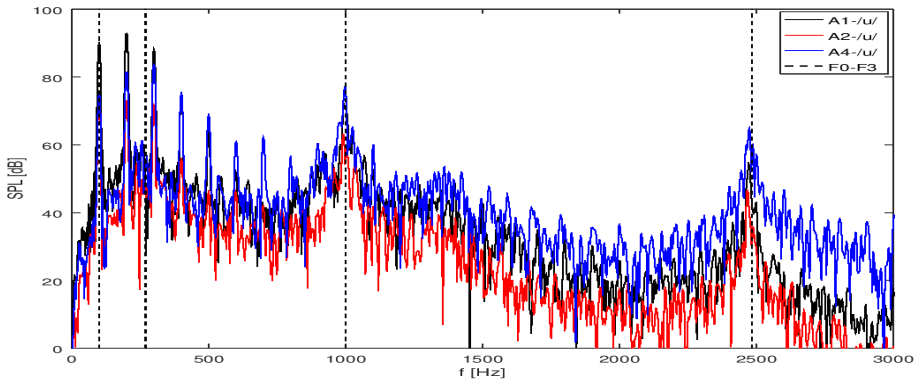

Fig. 2. Acoustic sound spectrum at monitoring point; dashed vertical lines: formants, A1: laminar model, A2: Smagorinsky model, A4: WALE model

3. Results

Fig. 2 presents a frequency spectrum for the three cases with the same prescribed kinematic pressure drop $dP = 300\ \mathrm{m^2\,s^{-2}}$ and the laryngeal flow externally forced by oscillating VFs, but for different turbulent LES models: A2-Smagorinsky model, A4-WALE model. The spectrum is computed from the probe, which is located 1 cm at the propagation zone (1 cm from mouth). The shape of the vocal tract refers to the vowel [u:], hence the dashed lines are positions of formants in accordance with a magnetic resonance imaging (MRI) study carried out by Story [5]. The acoustic sources are computed with the Lighthill tensor on the RHS. The transient simulation is done with $\Delta t = 1.10^{-5}$ s, the resolution $\Delta f = \pm 2.5$ Hz. The oscillation of the VFs accounts for the fundamental frequency 100 Hz. The amplitudes of higher harmonic frequencies (blue) are stronger, owing to the property of the WALE model, it is caused by y^3 near-wall scaling considering the eddy-viscosity behaviour with no additional damping in equations and its ability to predict the transition from laminar to turbulent regime.

Acknowledgements

The computational results presented have been achieved using the finite element software CFS++ and OpenFOAM. This work was supported by the Ministry of Education of the Czech Republic through the SGS project no. *21333/115* of the Technical University of Liberec

References

[1] Hüppe, A., Kaltenbacher, M., Investigation of interpolation strategies for hybrid schemes in computational aeroacoustics, Proceedings of the conference DAGA 2015 (41. Deutsche Jahrestagung für Akustik), Nürnberg, 2015, pp. 872-875.

[2] Lasota, M., Šidlof, P., Large-eddy simulation of flow through human larynx with a turbulence grid at inlet, Proceedings of the conference Topical Problems of Fluid Mechanics, Prague, 2019.

[3] Scherer, R., Shinwari, D., De Witt, J., Zhang, C., Kucinschi, R., Afjeh, A., Intraglottal pressure profiles for a symmetric and oblique glottis with a divergence angle of 10 degrees, The Journal of the Acoustical Society of America 109 (4) (2001) 1616-1630.

[4] Šidlof, P., Zörner, S., Hüppe, A., A hybrid approach to the computational aeroacoustics of human voice production, Biomechanics and Modeling in Mechanobiology 14 (3) (2015) 473-488.

[5] Story, B. H., Titze, I. R., Hoffman, E. A., Vocal tract area functions from magnetic resonance imaging, The Journal of the Acoustical Society of America 100 (1) (1996) 537-554.

[6] Zörner, S., Šidlof, P., Hüppe, A., Kaltenbacher, M., Flow and acoustic effects in the larynx for varying geometries, Acta Acustica united with Acustica 102 (2) (2016) 257-267.

COMPUTATIONAL MECHANICS 2019
35th conference with international participation
Srní
November 4 - 6, 2019

Finite element analysis of composite tubes with integrated loop connections

A. Malá[a], V. Kulíšek[b], N. Schmidová[a], T. Zámečníková[a], T. Ponížil[b], T. Mareš[a]

[a] *Faculty of Mechanical Engineering, Czech Technical University in Prague, Technická 4, 160 07 Prague 6, Czech Republic*
[b] *Compo Tech PLUS, spol. s r.o., Nová 1316, 342 01 Sušice, Czech Republic*

The paper deals with the modelling of integrated loop connections of composite tubes by finite element (FE) analysis. Composite beams have been employed in many structural applications during the last decades as the composite materials benefit in their light-weight properties with a great strength and stiffness. However, their application is sometimes limited due to difficult designing of connection interfaces, which would enable to transfer loads into the composites. The currently used connection interfaces of composite tubes (bonded joints, mechanical joints) are demanding in terms of manufacturing and often offer only limited load transfer in comparison with the strength of the composite tube. That is the reason for development of a less problematic connection, where the stress transfer will be continuous and also the connection will be sufficiently strength and stiff. Therefore, a project dealing with connections of tubes has been started with aim to develop integrated loop connections, which are made directly from the composite tube endings. One of the goals of the project is to build a reliable numerical model of the tube and its connection interface with aim to predict the joint strength and to obtain a tool for the joint design.

Coupons with integrated loops were manufactured by fibre winding and placement technology. Simultaneously, their FE models were created. The first type of the investigated coupon was designed, manufactured and tested (see Fig. 1 below left). The basic test of the coupon was in loading by the tension force. In the FE model, the loading of the tube by tensional force was applied by a steel cylinder inserted into a pair of the loops on one side of the coupon. In the second ending, an identical cylinder was inserted as the fixed support (see Fig. 1).

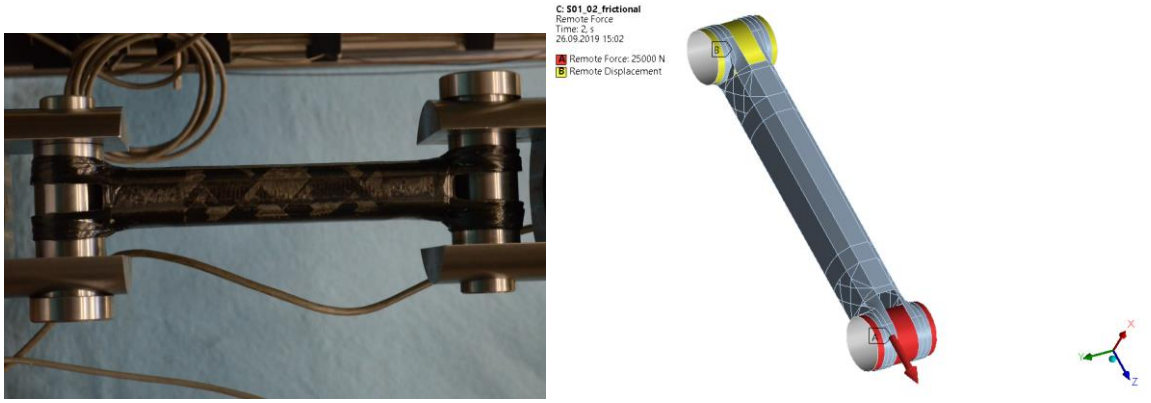

Fig. 1. Composite coupon with integrated loops and its model

The FE model of coupon was created to develop the connection interface and the tube lay-up with the required mechanical properties of tube near the integrated loop joints The FE

model was built up in ANSYS version 19.2 and the definition of laminate was set up using the ANSYS Composite Prep/Post (ACP) package. During preparation of the model, it was important to specify the lay-up stacking sequence and connections between tube and cylinders in the best accordance with reality. The basic stacking sequence and material properties were provided by the coupon supplier. The aim was to build the model as close to reality as possible, to test the model response and compare it with the experimental results. And if the predicted strength would match the experimental results, to optimize the composite lay-up of the tube and integrated loops to maximize the coupon strength and stiffness.

The specification of loops layer thicknesses was problematic, because in the real coupons, the fibre layers tend to change thickness together with their width, while keeping the constant fibre amount in the layer. To deal with this problem, the specification of layers thicknesses for the most critical parts of the model was made using linear functions, because there was a linear dependence between the thickness and the width of layer.

The basic FE model was made from shell elements; to input all the layers, the model was divided into sections and all the layers of fibre tows were input as close as they were made in the reality (see Fig. 2 for the demonstration of one fibre tow loop specification in the model).

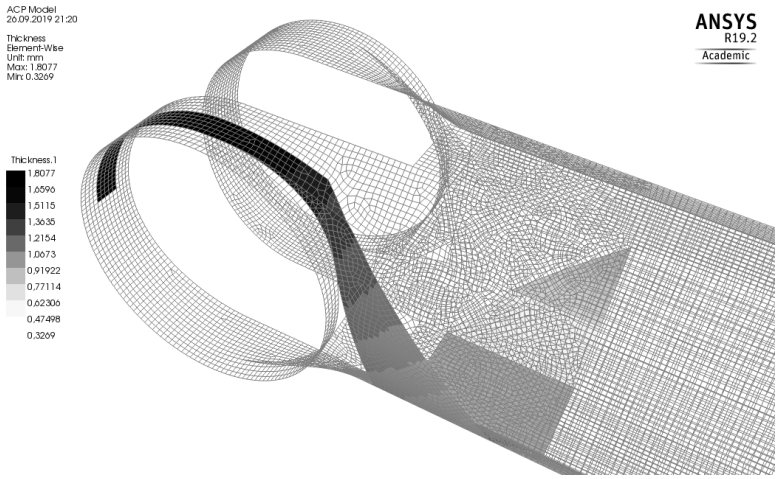

Fig. 2. Specification of 1 layer in the tube and loop

An experimental testing was carried out performing tensile tests of the coupons and evaluating the force-displacement behaviour of the coupon together with a digital image correlation in the critical parts of the coupons. The similar type of loading was performed using the FE model with aim to perform a comparison between the experimental and numerical results. Damage has been represented by the Inverse Reverse Factor (IRF) in the numerical model and by the Digital image correlation results from the experimental tests. The strength failure in the FEA was presented by three failure criteria: Tsai-Wu, Tsai-Hill and Maximum Stress. All three criteria were used to evaluate the failure parameter of the model given the full lay-up and nominal strength values of the composite layers.

The critical places of the construction were found by the FEA. The first deformations are initialized on the roving which sets up the loops. Next deformations are initialized on the square, placed near to the loops. Subsequently the critical areas are getting bigger with the increasing force value. The analysis is linear, which is the reason why the deformed places still retains the same mechanical properties (a progressive damage model has not been used) even after the ply-failure is detected. Damage of the composite coupon, interpreted by a failure index, during the increasing loading is shown in Fig. 3.

In the experiment, the first cracking was visible in the tube body and this was captured with FE precisely. This is corresponding to the tube damage, which is visible for load 0.4*Fmax. The developed FE model is consistent with the experimental testing in finding of

the initial failure. However, the final strength from the FE prediction was much lower than the final strength from the experimental specimen. There, the maximal failure from experiment exceed the predicted critical load almost five times, which clearly show the limitation of the first-ply failure criteria for the final strength prediction.

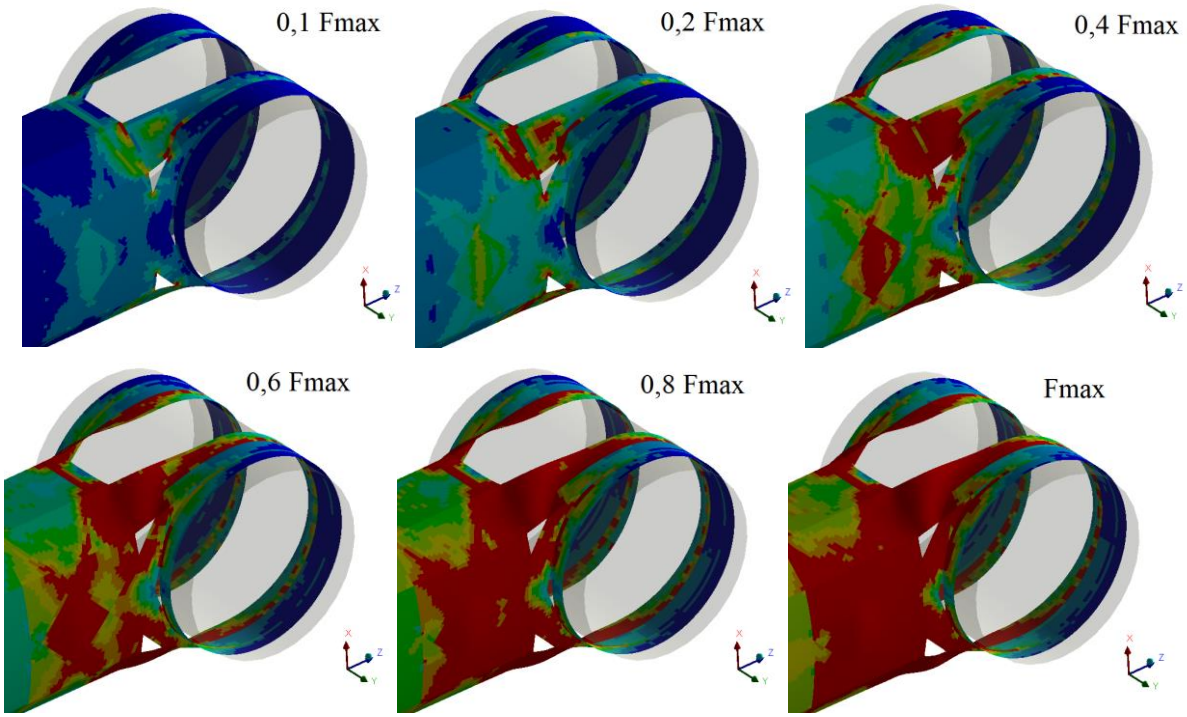

Fig. 3. Damage spreading (rupture in red)

The critical places of design were found by the proposed FE model and modelling approach. The current model is able to provide a tool in improving the tube strength and increasing the initial failure, as the body failure happened in the first coupons at load five times smaller than the critical one. On the other hand, failure criteria must be developed to predict the critical load in the fibre tow loops, which will be aim of the future work.

Acknowledgements

This work has been supported by project No. SGS18/175/OHK2/3T/12 of the Grant Agency of the Czech Technical University in Prague and by project No. TJ02000252 of the Technology Agency of the Czech Republic. Support of the Compo Tech PLUS company in development, manufacturing and testing of composite parts is also greatly acknowledged.

References

[1] ANSYS 19.2 Help.
[2] Quintelier, J., Samyn, P., de Baets, P., Ost, W., van Paepegem, W, Wear of steel against carbon fibre reinforced PPS, Tribology in Industry 27 (2005) 29-35.
[3] Yi, X., et al., The effective friction coefficient of a laminate composite, and analysis of pin-loaded plates, Journal of Composite Materials 34 (1) (2000) 69-87.

COMPUTATIONAL MECHANICS 2019
35th conference with international participation
Srní
November 4 - 6, 2019

Protective helmet behavior under dynamic load

O. Medůna[a], J. Kult[a], P. Hisem[a], N. Pomp[b], P. Klouček[b]

[a] R&D Department of Computations and Modelling, VUTS, a. s., Svárovská 619, Liberec XI- Růžodol I, 460 01 Liberec, Czech Republic
[b] R&D Department of Measurements, VUTS, a. s., Svárovská 619, Liberec XI- Růžodol I, 460 01 Liberec, Czech Republic

The article deals with the analysis of the foam part of the protective helmet under dynamic load. Protective helmets are tested by drop tests to meet technical standards [2]. During them, the helmet is subjected to impact by a heavy rigid punch while being mounted on the head model. The standards specify the minimum value of energy that a helmet must absorb, while not exceeding the maximum permissible force transferred to the helmet user's head. For possibility to improve these helmet properties by changing its geometry [1], a drop test simulation model is being created. The result of the drop test simulation of the helmet foam part is then compared with the measured stiffness characteristics.

The drop test is simulated using explicit FEM analysis in Ansys software (Fig. 1). For simulation purposes, a compression test of the foam samples is performed. Foam properties are represented by porosity-crushable foam material model in the simulation.

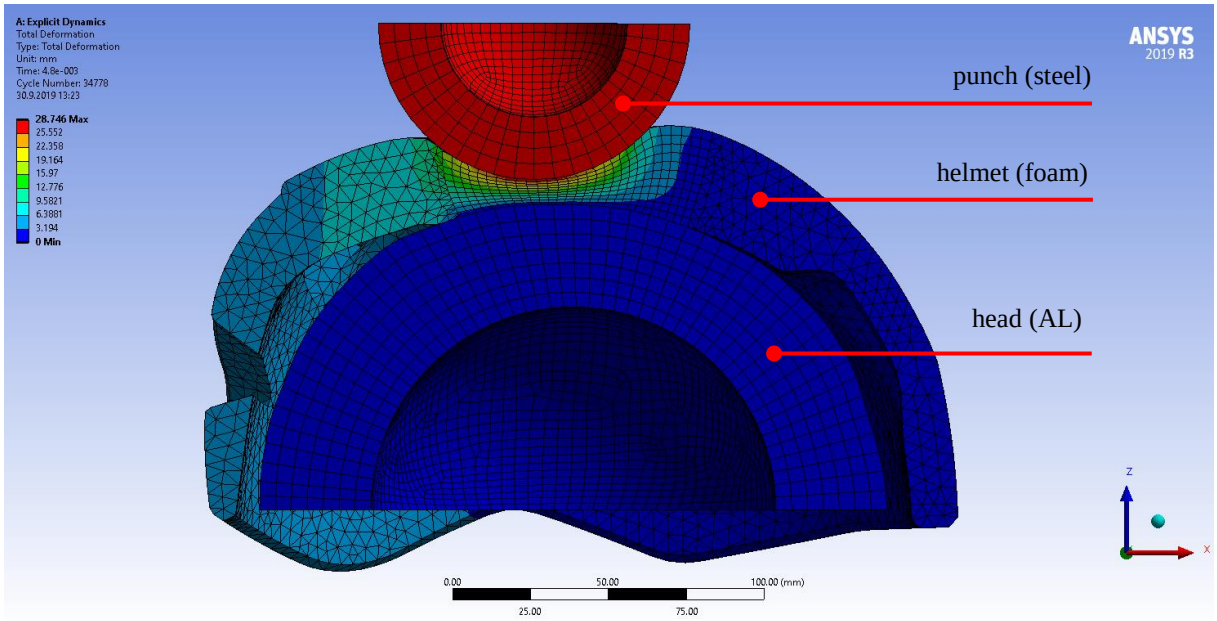

Fig. 1. Explicit FEM analysis of a drop test

Real drop tests are performed on a test machine that is commonly used by a helmet manufacturer. As standard, the test machine is equipped with a strain gauge force sensor placed in the base, on which the head model with the tested helmet is attached. In some cases, the obtained record of force did not match the assumptions because of the unexpected waves. Therefore, the testing machine is supplemented with other sensors (Fig. 2) - dynamometer consisting of piezoelectric force sensors (ForceZ), acceleration sensors (AccFront, AccBack) and laser distance sensors (DispL, DispR). The aim is to obtain independent signals of the

force [3]. In addition, two high-speed cameras are used to monitor the stability of the punch and helmet movement during impact.

By evaluating the measured data considering the dynamic properties of all used sensors, it is possible to explain the differences in the results obtained by different methods of force measurement. The cause of the unexpected waves in the force record obtained by a strain gauge force sensor is the low natural frequency of the sensor and the attached masses. Similarly, the results from a plate dynamometer with piezoelectric force sensors are negatively affected too, because it lies on the oscillating force sensor.

The most accurate method for obtaining a force curve in a drop test is to use an acceleration sensors (AccFront, AccBack) verified by displacement signals (DispL, DispR). The resulting acceleration is then converted to the force by applying Newton's law of force.

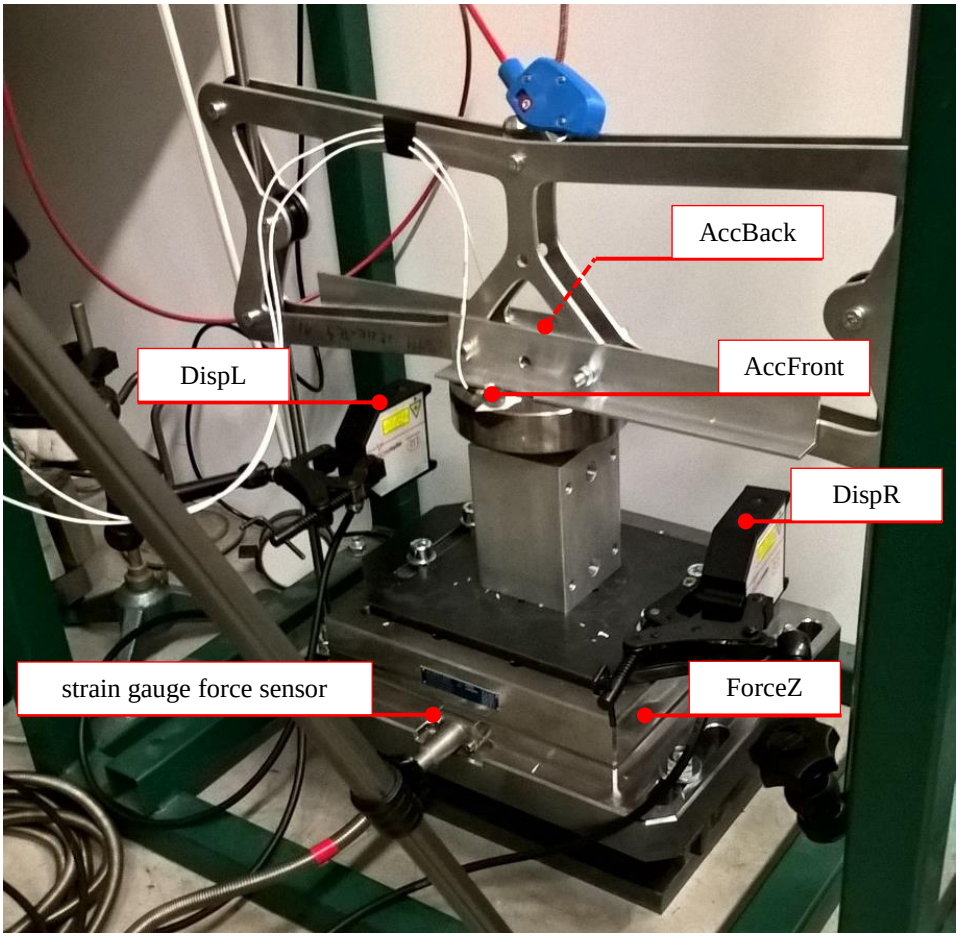

Fig. 2. Drop tower with all used sensors

Acknowledgements

The publication was created with the financial support of the Ministry of Industry and Trade within the institutional support for long-term conceptual development of the research organization: the grantor - the Ministry of Industry and Trade, beneficiary - VÚTS, a.s.

References

[1] Medůna, O., Optimization of helmet geometry using FEM stiffness analysis, VÚTS, a. s., Liberec, 2019.
[2] Mountaineering equipment – Helmets for mountaineers – Safety requirements and test methods, EN 12492, 2012.
[3] Pomp, N., Klouček, P., Force measurement during drop tests of helmets, VÚTS, a. s., Liberec, 2019.

COMPUTATIONAL MECHANICS 2019
35th conference with international participation
Srní
November 4 - 6, 2019

Demonstration of the developed procedure for the computation of the nonlinear steady-state response on practical examples

M. Molčan[a], P. Ferfecki[a,b], J. Zapoměl[b]

[a] IT4Innovations, VSB - Technical University of Ostrava, 17. listopadu 15/2172, Ostrava-Poruba, 708 00, Czech Republic
[b] Department of Applied Mechanics, VSB - Technical University of Ostrava, 17. listopadu 15/2172, Ostrava-Poruba, 708 00, Czech Republic

1. Introduction

In the rotor dynamics, complex behaviour occurs due to nonlinear properties of the rolling elements, rubbing contact between disc and stator, crack breathing, fluid effects of bearings and dampers, the development of efficient numerical methods for prediction of nonlinear steady-state periodic response [1, 2] and its stability [3] is needed.

The nonlinear equations of motion of a rotor dynamic system with the discs, rotor shaft, different types of bearings, dampers, and supports elements, can be stated in the following form

$$\mathbf{M}\ddot{\mathbf{x}}(t) + \mathbf{B}(\omega)\dot{\mathbf{x}}(t) + \mathbf{K}(\omega)\mathbf{x}(t) = \mathbf{f}_{\mathbf{NL}}(\mathbf{x}, \dot{\mathbf{x}}, \ddot{\mathbf{x}}, \omega) + \mathbf{f}_{\mathbf{P}}(t, \omega) + \mathbf{f}_{\mathbf{S}}. \tag{1}$$

$\mathbf{M}$, $\mathbf{B}(\omega)$, $\mathbf{K}(\omega)$ denote the $n \times n$ matrices of mass, damping, and stiffness, respectively, which depend on the excitation frequency ω due to the rotational effect, $\ddot{\mathbf{x}}$, $\dot{\mathbf{x}}$, and $\mathbf{x}$ are the vectors of generalized accelerations, velocities, and displacements, respectively, $\mathbf{f}_{\mathbf{NL}}$, $\mathbf{f}_{\mathbf{P}}$, and $\mathbf{f}_{\mathbf{S}}$ are the vectors of the nonlinear forces, periodic external excitation forces, and static load, respectively, t is time, and $(\cdot)$ denotes time derivation.

The paper shows the application of the computational procedure for the determination of the steady-state response of the nonlinear motion equations. The created procedure is based on the harmonic balance method with the utilization of the arc-length parametrization and Floquet's theory. In addition, the selected steady-state responses were verified by direct integration of the motion equations and the solution shows a good agreement.

2. Approximation of the periodic response by the harmonic balance method

The periodic response of the motion equation (1) can be approximated by Fourier series [1]

$$\mathbf{x}(t) = \mathbf{q}_0 + \sum_{k=1}^{n_{\mathrm{H}}} \mathbf{q}_{\mathbf{C}k} \cos(k\omega t) + \mathbf{q}_{\mathbf{S}k} \sin(k\omega t), \tag{2}$$

where n_{H} stands for the number of the harmonic terms. For convenience, the Fourier coefficients can be arranged into $(2n_{\mathrm{H}} + 1)n \times 1$ vector

$$\mathbf{q} = \begin{bmatrix} \mathbf{q_0} & \mathbf{q_{C1}} & \mathbf{q_{S1}} & \cdots & \mathbf{q}_{\mathbf{C}k} & \mathbf{q}_{\mathbf{S}k} & \cdots & \mathbf{q}_{\mathbf{C}n_{\mathrm{H}}} & \mathbf{q}_{\mathbf{S}n_{\mathrm{H}}} \end{bmatrix}^{\mathrm{T}}, \tag{3}$$

the trigonometric Fourier basis can be arranged into $n \times (2n_{\mathrm{H}} + 1)n$ transformation matrix [4]

$$\mathbf{T} = [\mathbf{I}\ \cos(\omega t)\mathbf{I}\ \sin(\omega t)\mathbf{I}\ \ldots\ \cos(k\omega t)\mathbf{I}\ \sin(k\omega t)\mathbf{I}\ \ldots\ \cos(n_{\mathrm{H}}\omega t)\mathbf{I}\ \sin(n_{\mathrm{H}}\omega t)\mathbf{I}], \tag{4}$$

which is often called inverse discrete Fourier transform (DFT) matrix and where $\mathbf{I}$ is $n \times n$ identity matrix. Now, instantaneous displacement values can obtained in a compact form

$$\mathbf{x}(t) = \mathbf{T}(\omega t)\mathbf{q}. \tag{5}$$

For the derivatives with respect to time, $(2n_{\mathrm{H}}+1)n \times (2n_{\mathrm{H}}+1)n$ frequential derivative operator matrix

$$\nabla = \mathrm{diag}\left(\mathbf{0}_{n\times n}\nabla_1 \ldots \nabla_k \ldots \nabla_{n_{\mathrm{H}}}\right), \quad \text{where} \quad \nabla_k = k\begin{bmatrix}\mathbf{0} & \mathbf{I}\\ -\mathbf{I} & \mathbf{0}\end{bmatrix}, \tag{6}$$

can be assembled. The matrix deals with chain rule products (ω is intentionally omitted) and modification of DFT transformation matrix. Therefore, the r-th derivatives can be obtained as

$$\mathbf{x}^{(r)} = \omega^r \mathbf{T}(\omega t)\nabla^r\, \mathbf{q}\,. \tag{7}$$

Substituting (5) and (7) into (1), one can obtain the nonlinear algebraic residual equation

$$\mathbf{h}(\omega, \mathbf{q}) = \mathbf{P}(\omega)\mathbf{q} - \mathbf{T}^{+}\mathbf{f}_{\mathbf{NL}}(\mathbf{T}\mathbf{q}, \omega\mathbf{T}\nabla\mathbf{q}, \omega^2\mathbf{T}\nabla^2\mathbf{q}, \omega) - \mathbf{u}_{\mathbf{P}}(\omega) - \mathbf{g}_{\mathbf{S}}, \tag{8}$$

where $\mathbf{P}(\omega) = \omega^2(\mathbf{I}\otimes\mathbf{M})\nabla^2 + \omega(\mathbf{I}\otimes\mathbf{B})\nabla + \mathbf{I}\otimes\mathbf{K}$ is the dynamical stiffness matrix, $\mathbf{I}$ is the identity matrix of order $2n_{\mathrm{H}}+1$, and the vectors $\mathbf{u}_{\mathbf{P}}$, $\mathbf{g}_{\mathbf{S}}$ contain amplitudes of the periodic unbalance forces and the static forces. The $\mathbf{T}^{+}\mathbf{f}_{\mathbf{NL}}(\mathbf{T}\mathbf{q}, \omega\mathbf{T}\nabla\mathbf{q}, \omega^2\mathbf{T}\nabla^2\mathbf{q}, \omega)$ term represents so called alternating frequency-time (AFT) technique [1]. The $(^{+})$ stands for Moore-Penrose pseudoinverse and the $\otimes$ denotes the Kronecker product.

For obtaining the response of a nonlinear systems, it is often mandatory to use a continuation technique [1]. In general, the continuation consists of predictor and corrector steps. The predictor was based on secant, which passed through previous solutions and determined the direction of the next initial guess. The length of this predictor vector was normalised to appropriate arc length value s. For the corrector phase, Crisfield's arc-length parametrization [1] was used in the form of the additional residual equation

$$\mathbf{p}(\omega, \mathbf{q}) = (\mathbf{q} - \mathbf{q}_{\text{prev}})^{\mathrm{T}}(\mathbf{q} - \mathbf{q}_{\text{prev}}) + (\omega - \omega_{\text{prev}})^2 - s^2, \tag{9}$$

where $\mathbf{q}_{\text{prev}}$ and ω_{prev} denote values acquired at the previous continuation step.

The harmonic balance method procedure with the utilisation of the arc-length parametrization can be described in the following steps:

1. Choose the initial Fourier coefficients vector and angular velocity.
2. Apply the inverse DFT on the Fourier coefficients vector and evaluate the $\mathbf{f}_{\mathbf{NL}}$.
3. Transform the nonlinear forces from the time-domain to the frequency-domain by DFT and assemble the dynamical stiffness matrix $\mathbf{P}$.
4. Solve the system given by nonlinear algebraic equations (8) and (9).
5. Compute the predictor and go to step 2.

3. Determination of the vibration stability by Floquet's theory

The vibration stability of the periodic response (2) was evaluated by Floquet theory [1] applied in the time domain. Therefore, the stability of a periodic solution is determined by the eigenvalues of the transition matrix [3], assembled over time of one period.

In the proposed procedure the transition matrix is obtained by a repeated solution of initial value problems for differently chosen initial conditions. It is known that with regard to either accuracy or computational time the transition matrix can be approximated by the product of exponential matrices, by the relationships of Newmark integration technique [3], and others.

4. Test cases

The first test case was the Duffing oscillator with nonlinear restoring force [2]. The equation of motion can be expressed as

$$\ddot{x}(t) + 2\xi\dot{x}(t) + \omega_0^2 x(t) + \alpha[x(t)]^3 = p_0 \cos(\omega t)\,. \tag{10}$$

Numerical simulations were carried out with parameters: the damping coefficient $\xi = 0.05\,\mathrm{s}^{-1}$, the natural frequency $\omega_0 = 1\,\mathrm{rad\,s}^{-1}$, the amplitude $p_0 = 0.1\,\mathrm{mm\,s}^{-2}$, and the nonlinear coefficient $\alpha = 0.02\,\mathrm{mm}^{-2}\,\mathrm{s}^{-2}$ orange or $\alpha = 10\,\mathrm{mm}^{-2}\,\mathrm{s}^{-2}$ blue color curve, respectively, see Fig. 1.

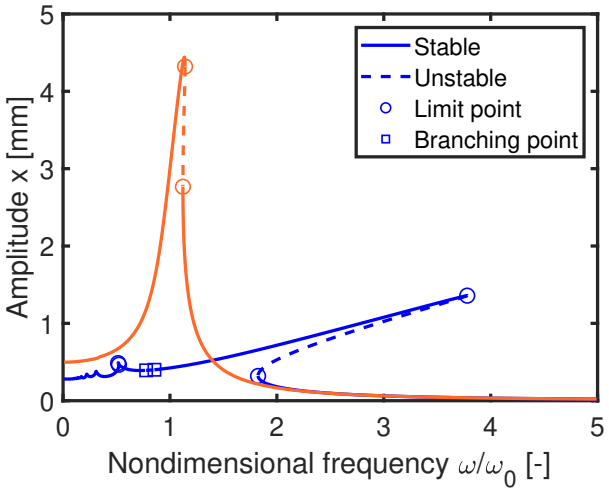

Fig. 1. Response curves of Duffing oscillator

To ensure good accuracy agreement with the time integration the $n_\mathrm{H} = 19$ harmonic terms were used to the approximation of the periodic response (2). Fig. 1 shows that the nonlinear effect is stronger for the higher value of the nonlinearity coefficient and that the limit and branching points on the response curve were detected.

Modified Jeffcott rotor according to the article [2] was employed as the second example, where different type of nonlinearity was tested. Due to the unbalance forces, the rotor can exceed clearance and interact with the stator modeled by stiffness. The equations of motion of the rotor system with contact between the disc and stator can be written as

$$m\ddot{x} + d\dot{x} + kx + k_\mathrm{c}\left(1 - \frac{h}{r}\right)[x - \mu y\,\mathrm{sign}(v_\mathrm{rel})] = p_\mathrm{b}\,\omega^2\cos(\omega t), \tag{11}$$

$$m\ddot{y} + d\dot{y} + ky + k_\mathrm{c}\left(1 - \frac{h}{r}\right)[y + \mu x\,\mathrm{sign}(v_\mathrm{rel})] = p_\mathrm{b}\,\omega^2\sin(\omega t), \tag{12}$$

where $r = \sqrt{x^2 + y^2}$ is the radial displacement and $v_\mathrm{rel} = \frac{x}{r}\dot{y} - \frac{y}{r}\dot{x} + R_\mathrm{disc}\omega$ is the relative velocity between the disc and stator surfaces.

The simulations were performed with parameters: the mass $m = 1\,\mathrm{kg}$, the damping coefficient $d = 5\,\mathrm{kg\,s}^{-1}$, the rotor stiffness $k = 100\,\mathrm{N\,m}^{-1}$, the stator stiffness $k_\mathrm{c} = 2500\,\mathrm{N\,m}^{-1}$, the clearance $h = 0.105\,\mathrm{mm}$, the unbalance $p_\mathrm{b} = 0.1\,\mathrm{kg\,m}$, the disc radius $R_\mathrm{disc} = 2.1\,\mathrm{mm}$, the natural frequency $\omega_0 = \sqrt{\frac{k_\mathrm{c}}{m}} = 50\,\mathrm{rad\,s}^{-1}$, and μ is the friction coefficient.

Simulation of the Jeffcott rotor was carried out with the $n_\mathrm{H} = 15$ harmonic terms and the resulting response curves are plotted in Fig. 2, where one can observe the influence of the friction coefficient value to the rotor response and locations of identified limit and Neimark-Sacker bifurcation points.

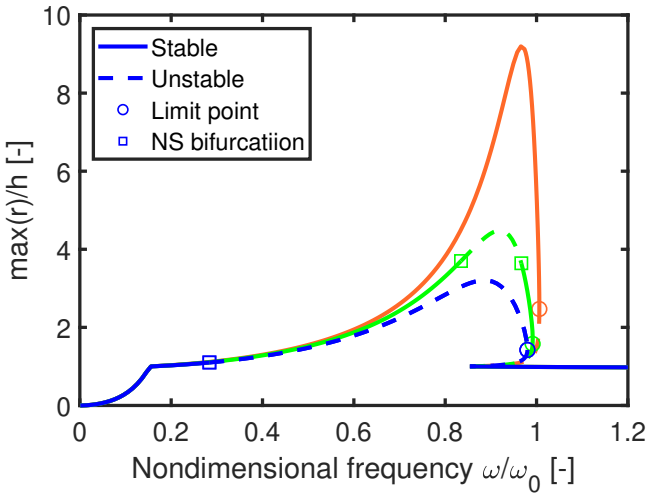

Fig. 2. Response curves of the modified Jeffcott rotor ($\mu = 0$, $\mu = 0.11$, and $\mu = 0.2$, orange, green, and blue color curve, respectively)

5. Conclusions

Procedure for the computing response curves of the nonlinear rotor dynamic models based on the harmonic balance method combined with the arc-length parametrization and Floquet's theory has been investigated. Numerical examples of Duffing oscillator and the modified Jeffcott rotor with enabled contact between the disc and stator are used for testing the developed procedure. The computed frequency responses, the vibration stability, and the locations of the limit and branch points are identical with the results presented in the article [2]. The results of the carried out study show the validity and capability of the created procedure for the computing whole frequency response curve and the determination of the vibration stability.

Acknowledgements

This work has been supported by the Ministry of Education, Youth and Sports from the National Programme of Sustainability (NPU II) project "IT4Innovations excellence in science - LQ1602", by the Student's Grant Competition project SP2019/97", and by the grant project 19-06666S of the Czech Science Foundation.

References

[1] Krack, M., Gross, J., Harmonic balance for nonlinear vibration problems, New York, Springer Berlin Heidelberg, 2019.

[2] Xie, L., Baguet, S., Prabel, B., Dufour, R., Numerical tracking of limit points for direct parametric analysis in nonlinear rotordynamics, ASME Journal of Vibration and Acoustics 138 (2) (2016) No. 021007, doi: 10.1115/1.4032182.

[3] Zaoral, F., Ferfecki, P., Application of Floquet theory to investigation of motion stability of parametrically excited rotor systems, Proceedings of the Applied Mechanics 2019, Ostrava, VSB – Technical University of Ostrava, 2019, pp. 235-240.

[4] Zhou, B., Thouverez, F., Lenoir, D., A variable-coefficient harmonic balance method for the prediction of quasi-periodic response in nonlinear systems, Mechanical Systems and Signal Processing 64–65 (2015) 233-244.

COMPUTATIONAL MECHANICS 2017
33rd conference with international participation
Špičák
November 6 - 8, 2017

Sensitivity analysis for an almost periodic unsteady flow problem; application to turbo-machinery modelling

F. Moravcová[a], V. Lukeš[a], E. Rohan[a]

[a] *NTIS – New Technologies for Information Society, Faculty of Applied Sciences, University of West Bohemia, Univerzitní 8, 301 00 Plzeň Czech Republic*

1. Introduction

The shape optimization in both the compressible and incompressible flow problems still belongs to areas of intensive research due to its high applicability on one hand and the complicated mathematical structure of the problem on the other hand. The present contribution is a continuation of our previous work [2], where the shape optimization of a turbine blade was reported for the incompressible 2D flows with the aim to minimize the dissipation power. There the steady incompressible Navier-Stokes (N-S) system of equations was discretized using the finite volume method and the continuous version of the adjoint system method was employed to compute total shape gradients of the objective function.

In the present work, we are concerned with compressible 2D flows in channels whose the geometries vary periodically with time. Such a situation arises in the stator-rotor configuration of turbines where the mutual position of the blades commutes periodically. Obviously, the steady motion the rotor blades which are arranged periodically induces the unsteady flows which can be considered as quasi-periodic. Our study relies on this hypothesis, we assume the existence of T-periodic solutions. The time period $T = H/U$ is given by the circumferential geometric period H and the circumferential speed U associated with a given radius of the rectification plane where the 2D flow problem is defined.

As the new contribution, for a general shape optimization problem we introduce the state problem with an implicitly stated T-periodic condition and propose an iterative algorithm of the sensitivity analysis. In contrast with the standard evolutionary problems, the sensitivity analysis (SA) of a time periodic problem leads to a more complicated computational scheme. For efficiency of the SA computations, we propose an iterative algorithm which is constructed for the discretized state problem. We developed two versions of the SA algorithm according to the two commonly used approaches, the Direct Differentiation and the Adjoint System methods [3, 4]. Numerical solutions of the state problem are obtained using the in-house developed CFD software FlowPro [1] based on the Discontinuous Galerkin Method whereby the first-order approximation is used, thus, actually yielding the discretization scheme of the Finite Volume Method.

2. The flow problem

The flow in the stator-rotor channels is represented by a reduced two-dimensional model. Its geometrical configuration reflects the periodic arrangement of the blades, see Fig. 1. The problem is imposed in a domain constituted by two subdomains associated with the stator and rotor

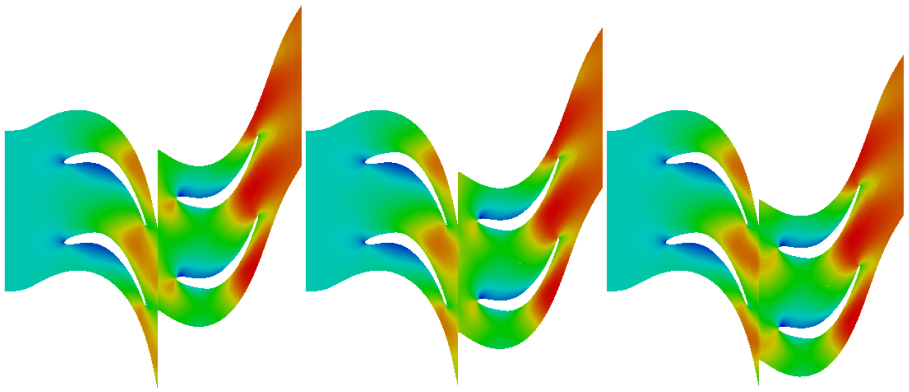

Fig. 1. Mach distribution in the flow domain at various time steps of the simulation with $\alpha = 0$ (attack angle), $p^{out} = 0.75$ (out pressure) and $U = 0.05$ (rotor velocity), the Mach number values range the interval [0.025, 0.41]

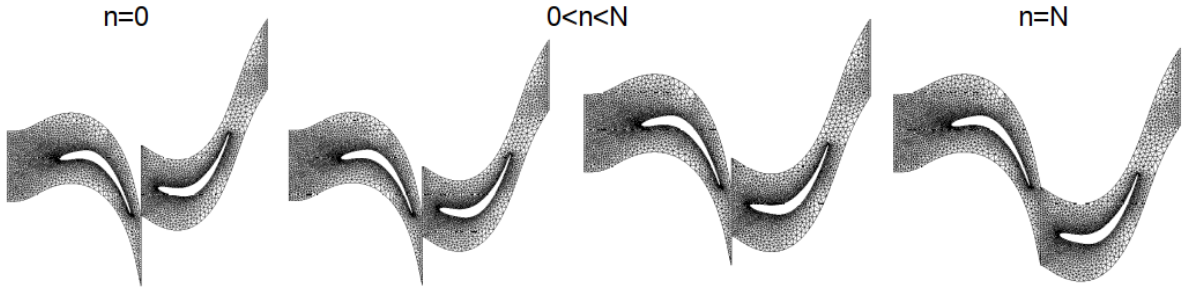

Fig. 2. An illustration of the time sequence of the stator-rotor geometric configurations. For $n = 0$, the meshes of the two subdomains are joint at one node, while at $n = N$ the meshes share all nodes on the discretized stator-rotor interface. Obviously, the configuration $n = 0$ can be released due to the assumed quasi-T-periodicity of the state problem solutions.

channels, respectively, each embedding a single turbine blade profile, as shown in Fig. 2. These subdomains have a common interface on which the coupling conditions are prescribed according to the actual instantaneous position of the rotor. The viscous compressible fluid obeys the Navier-Stokes equations which can be expressed in a compact dimensionless form, as follows

$$\frac{\partial \boldsymbol{w}}{\partial t} + \nabla \cdot \boldsymbol{F} = 0 \,, \quad \text{i.e.} \quad \frac{\partial w_j}{\partial t} + \sum_i \frac{\partial F_{ji}}{\partial x_i} = 0 \,, \tag{1}$$

$$\boldsymbol{w} = \begin{pmatrix} \rho \\ \rho v_1 \\ \rho v_2 \\ \rho e \end{pmatrix}, \quad \boldsymbol{f}_i^E = \begin{pmatrix} \rho v_i \\ \rho v_1 v_i + p\delta_{1i} \\ \rho v_2 v_i + p\delta_{2i} \\ v_i(\rho e + p) \end{pmatrix}, \quad \boldsymbol{f}_i^V = \frac{1}{Re} \begin{pmatrix} 0 \\ \tau_{1i} \\ \tau_{2i} \\ \sum(\tau_{ij} v_j) - \frac{\gamma}{Pr} \nabla (e - \frac{v^2}{2}) \end{pmatrix},$$

where $\boldsymbol{f}_i^E$ and $\boldsymbol{f}_i^V$, are the columns of $\boldsymbol{F}^E$ and $\boldsymbol{F}^V$, respectively, and $\boldsymbol{F} = \boldsymbol{F}^E(\boldsymbol{w}) - \boldsymbol{F}^V(\boldsymbol{w}, \nabla \boldsymbol{w})$. The state variable $\boldsymbol{w}$ involves the density ρ, velocity (v_1, v_2) and the internal energy e. The viscous part of the stress is denoted by τ_{ij}. We consider laminar subsonic flows and the boundary conditions are classically defined by the flow direction at the inlet (the angle of attack α) and a pressure at the outlet p^{out}, while the value 1 is assigned to the inlet stagnation density and pressure. The initial conditions can be chosen almost arbitrarily, since the state problem solution is defined as a steadily periodic solution. Although an exact periodic solution is not enforced

and, thus not guaranteed, we assume the existence of time t_0 such that the solutions $\boldsymbol{w}(t)$ of the initial value problem satisfy an approximate periodicity condition

$$\|\boldsymbol{w}(t) - \boldsymbol{w}(t+T)| < \epsilon \ , \quad \text{for all } t \geq t_0 \ , \tag{2}$$

where ϵ is a given precision and the norm $\|\boldsymbol{w}\|$ is represented by the Euclidean norm of the space-discretized state vector $\boldsymbol{w}$. Adhering to the assumption (2), we consider only the time steps $n \in [1, N]$ such that $t^n = t^0 + n\Delta t$. Thus, the quasi-T-periodic solutions of the state problem are represented by the N-tuples $\{\boldsymbol{w}^n\}_{n=1}^N$, whereby $\boldsymbol{w}^0 \approx \boldsymbol{w}^N$ in the sense of (2)

To capture the motion of the rotor part domain, we consider a decomposition of the velocity field $\boldsymbol{v}$ involved in (1) into the mesh velocity $\boldsymbol{v}^{msh}$, and the relative velocity $\boldsymbol{v}^{rel}$, so that $\boldsymbol{v} = \boldsymbol{v}^{rel} + \boldsymbol{v}^{msh}$. For the stator-rotor system, $\boldsymbol{v}^{msh}$ is defined piecewise constant; while it vanishes in the stator subdomain, in the rotor subdomain, $\boldsymbol{v}^{msh}$ equals a constant vector $\boldsymbol{U}$ which describes the revolution speed $U = |\boldsymbol{U}|$ of the rotor. Therefore, $\boldsymbol{U}$ is involved in the convective acceleration terms of the flow equations in the rotor domain only. The discontinuity of $\boldsymbol{v}^{msh}$ on the stator-rotor interface requires updating the position of the mesh nodes of the rotor mesh. Consequently, pairs of the homologous nodes on the interface commute with subsequent time levels. One time period T is subdivided into N steps $\Delta t = U\delta d$ according to the interface discretization δd which defines the shift of the rotor mesh position with respect to the stator ones, see Fig. 2, where the sequence of N relevant geometric configurations is displayed. Thus, for a given time level, this shift provides a particular coupling scheme for the nodal values of the discretized quantities along the matching interfaces of the subdomains.

3. Shape sensitivity of an objective function

The shape sensitivity analysis is needed to allow for using gradient based optimization methods. In this context, we consider a general objective functional

$$\Phi = \int_{t^0}^{t^0+T} \varphi(\boldsymbol{w}(t), t) \mathrm{d}\, t \ , \tag{3}$$

where φ evaluates a criterion of the flow optimality at time t. For instance φ can express the loss of stagnation pressure relative to the inlet kinetic energy. In general, we assume Φ is bounded below over the set of all admissible solutions of the State Problem (SP) given by (1) – (2). Since the sensitivity has been derived for the fully discretized SP, we introduce the shape Optimization Problem (OP) in terms of the discretized SP; by $\boldsymbol{W}^n$ we refer to the discretized state $\boldsymbol{w}^n$. The shape of the blades profiles is described the non-uniform rational basis spline functions involving m^P control points P^i. By $\boldsymbol{Y}$ we denote the vector of $m = 2m^P$ coordinates of the control points P^i; in Fig. 3, locations of P^i in the reference configuration is depicted. Below we consider the set $\mathcal{Y}$ of all admissible blades designs restricting the shape geometry with respect to criteria independent of the state $\boldsymbol{W}$.

We consider the general OP: Find $\boldsymbol{Y}^* \in \mathcal{Y}$ and the state $\boldsymbol{W}^* = \boldsymbol{W}(\boldsymbol{Y}^*)$, such that

$$\begin{aligned} &\Phi(\boldsymbol{Y}^*, \boldsymbol{W}(\boldsymbol{Y}^*)) \leq \Phi(\boldsymbol{Y}, \boldsymbol{W}(\boldsymbol{Y})) \quad \forall \boldsymbol{Y} \in \mathcal{Y} \ , \text{ where } \quad \Phi := \sum_{n=1}^{N} \phi^n(\boldsymbol{Y}, \boldsymbol{W}^n) \ , \\ &\text{subject to: } \boldsymbol{\mathcal{F}}^n(\boldsymbol{Y}, \boldsymbol{W}^n, \boldsymbol{W}^{n-1}) = 0 \ , n = 1, \ldots, N \ , \quad \text{and } \boldsymbol{W}^N \approx \boldsymbol{W}^0 \ , \end{aligned} \tag{4}$$

where $\boldsymbol{\mathcal{F}}^n = \boldsymbol{0}$ represents the space-time discretized approximation of Problem (1) – (2), and $\boldsymbol{W} = \{\boldsymbol{W}^n\}_{n=1}^N$ involves the state vectors at all relevant time levels. The admissible states $\boldsymbol{W}(\boldsymbol{Y})$ are defined as an implicit function constituted by the constraint $(4)_2$.

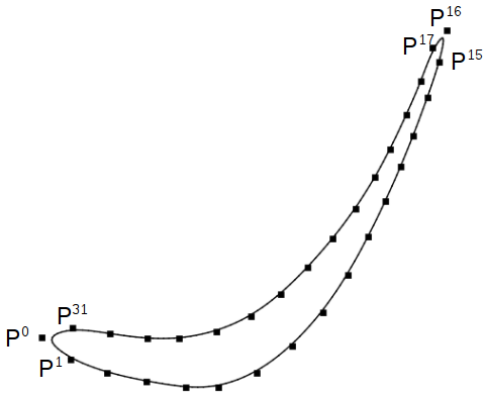

Fig. 3. The rotor blade profile and positions of 32 control points in the reference configuration.

Within the design-state space of any $(\boldsymbol{Y}.\boldsymbol{W})$, the sensitivity analysis provides the total design gradient $\mathrm{d}^{\mathrm{tot}}\,\Phi(\boldsymbol{Y},\boldsymbol{W}(\boldsymbol{Y}))/\mathrm{d}\,\boldsymbol{Y}$ on a manifold of admissible states $\boldsymbol{W}(\boldsymbol{Y})$,

$$\frac{\mathrm{d}^{\mathrm{tot}}\,\Phi}{\mathrm{d}\,\boldsymbol{Y}} = \sum_{n=1}^{N}\left(\frac{\partial\phi^n}{\partial\boldsymbol{Y}} + \frac{\partial\phi^n}{\partial\boldsymbol{W}^n}\boldsymbol{G}^n\right)\,, \tag{5}$$

where the matrix $\boldsymbol{G}^n = \partial\boldsymbol{W}^n/\partial\boldsymbol{Y}$ is the design gradient of the state $\boldsymbol{W}^n$. To evaluate total design gradient, we pursue the Direct Differentiation (DDM) and the Adjoint System (ASM) methods, the latter one allows to avoid computing matrices $\boldsymbol{G}^n$, however, the adjoint vectors $\boldsymbol{\lambda}^n$ must be solved for. In contrast with the standard transient problems, the initial condition $\boldsymbol{W}^0$ is not known, as explained above. Instead, the time periodicity conditions must be handled. Computing $\boldsymbol{\lambda}^n$ rigorously would require solving a set of coupled linear equations for all $\{\boldsymbol{\lambda}^n\}_{n=1}^N$. In the case of the DDM, a similar difficulty is encountered. Therefore, we propose iterative DDM and ASM algorithms. The dimension of $\boldsymbol{\lambda}^n$ is independent of the number of design variables. Consequently, when the number of the design variables is large, the ASM is preferred to the DDM, cf. [3]. Both these methods have been implemented to our application. Numerical tests and verifications have been performed.

Acknowledgments

This research is supported by the project "Centre of research and experimental development of reliable energy production" TE01020068 of the Technology Agency of the Czech Republic. The authors also thank O. Bublík for his assistance in the numerical implementation of algorithms.

References

[1] Bublík, O., Pecka, A., Vimmr, J., FlowPro documentation, University of West Bohemia, 2017. https://www.kme.zcu.cz/flowpro/index.php

[2] Moravcová, F., Lukeš, V., Rohan, E., Surface sensitivities computation for turbine blades using OpenFOAM, Proceedings of the conference Computational Mechanics 2016, Špičák, 2016, pp. 79-80.

[3] Rohan, E., Cimrman, R., Sensitivity analysis and material identification for activated smooth muscle, Computer Assisted Mechanics and Engineering Sciences 9 (4) (2002) 519-541.

[4] Rohan, E., Whiteman, J., Shape optimization of elasto-plastic structures and continua, Computer Methods in Applied Mechanics and Engineering 187 (2000) 261-288.

COMPUTATIONAL MECHANICS 2019
35th conference with international participation
Srní
November 4 - 6, 2019

Tuning of position control loop of machine tools based on experimentally identified mechanical model

J. Moravec[a], Z. Šika[a]

[a] *Faculty of Mechanical Engineering, Czech Technical University in Prague, Technická 4, 166 07 Praha, Czech Republic*

Feedback control of machine tool feed drive axes is highly demanding in the accuracy point of view. Overshot only micrometers can worse machined surface with impact on workpiece, for example on mould surface. Surface quality is not only reason for demands on smooth and accurate movement. There are other aims like productivity of machining and ability to track highly curvature shapes. It illustrates the wide field for complex views on machine tool cascade servo control.

Desired input for position control, or position setpoint, is derived from the workpiece dimension and desired machining speed (given for example by technology and workpiece material). But no machine is capable to ideally track the desired inputs. One significant influence that limits the tracking accuracy are vibrations caused by interaction of flexible machine mechanics with the machine feedback control system [1]. Manufacturers of commercial control systems implement to their product some tools which enables to supress unwanted vibrations. Such functions are for example current and speed filters. Thus beside the setting of P and PI controllers in feedback loops there are an extended possibilities to increase the loop gain and consequently to reach higher dynamic stiffness and wider bandwidth in frequency response.

Optimization via these functions is usually done in the level of speed and position feedback. However, resulting vibrations can also be lowered by shaping the input command. This can be easily done by setting the value of jerk [1]. Higher values of jerk tends to excite higher oscillations. But from the pure kinematical point of view higher values of jerk enables to reach acceleration in shorter time and hence higher curvature can be machined. That indicates requirement on finding its proper value. Finding the appropriate value of jerk together with the setting of position controller gain known as Kv factor is the key task in the optimizing position feedback loop of machine tool axis.

This article is focused on the automatic tuning of position control loop. Kv factor and jerk value are taken into consideration. Tests were carried out on the experimentally identified mechanical model of machine tool feed drive axis. The inner velocity control loop was set to suitable dynamics and this setting was held during the experiments with position control. The model order of mechanics was set to accurate describe mechanics in high as well as low frequencies.

The influence of jerk and Kv factor on the accuracy will be evaluated on the shape of position error. Its steady state part has a zero mean due to the active velocity feedforward and transient part is nonzero due to the limited dynamical stiffness. Two criteria were used as a measurement for the evaluation of position error. Maximal overshot of position error Δ and ITAEn integral criteria with the enhanced meaning of time. First criteria is the natural measure of maximal deflection from the desired trajectory. This criteria does not catch time

duration or settling time of the overshot. The second one evaluate the surface of position error with strong emphasis on its time progress. For this reason time exponent n = 5 was chosen.

$$ITAEn = min \int_0^{\infty} t^n |\Delta(t)|\, dt, \qquad n = 5$$

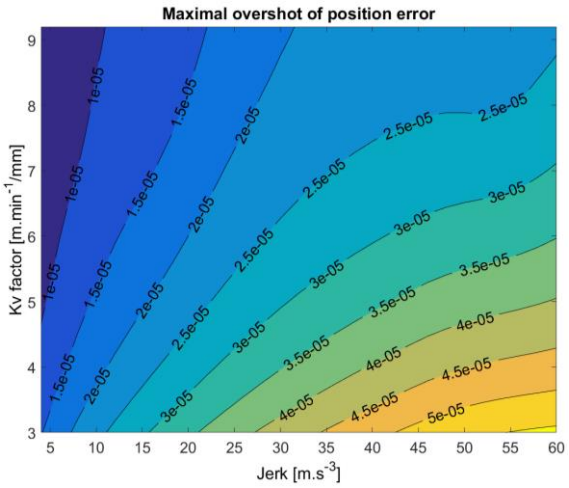

Fig. 1. Maximal overshot of position error

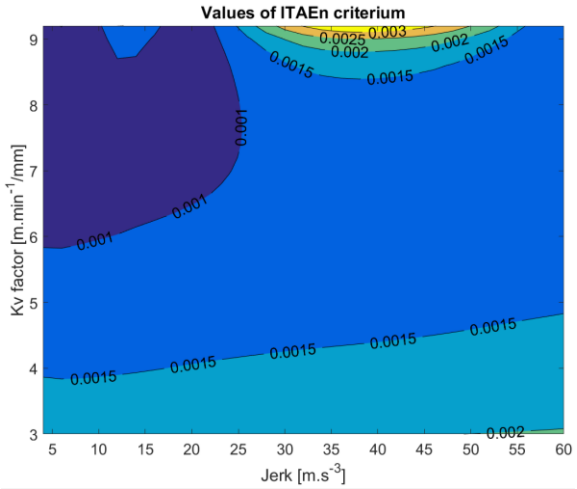

Fig. 2. Values of ITAEn criteria

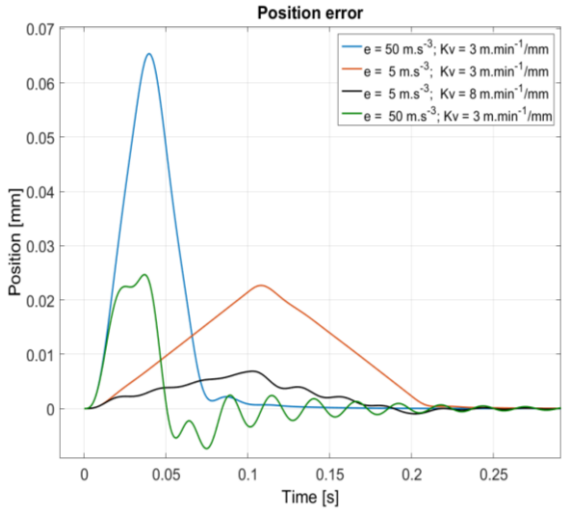

Fig. 3. Overshots in position error

Simulations were carried out in Matlab-Simulink environment. Values of both criteria for several combinations of jerk and Kv factors are shown in Fig. 1 and Fig. 2. Dark blue regions distinguishes areas with the low overshot and also with low ITAEn criteria. Such regions are defined by low position error and are valid for higher Kv factor and lower jerk. Fig. 3 shows that lower Kv factor and higher jerk can result in higher overshot but without oscillations, case e = 50 m.s^{-3} and Kv = 3 m.min^{-1}/mm, whilst higher Kv factor with higher jerk, case e = 50 m.s^{-3} and Kv = 8 m.min^{-1}/mm, have both criteria low but significant number of unwanted oscillating periods are present.

We can conclude that the low value of integral criteria and low overshot in position deviation at the same time need necessarily not lead to satisfactory behaviour of feed drive axis. Higher number of oscillating periods can decrease the machining accuracy and surface smoothness. Computer simulations can be carry out for finding the appropriate values of jerk and Kv factor. When adjusting the machine in practice, it is necessary to be careful with possible transfer of parameters into the control system. Some effects such as friction are not included in the model so real oscillations may differ from the modelled ones.

References

[1] Souček, P., Servomechanisms, CTU, Prague, 2004. (in Czech)

COMPUTATIONAL MECHANICS 2019
35th conference with international participation
Srní
November 4 - 6, 2019

Influence of longitudinal variability of material properties in non-uniform torsion of FGM beams

J. Murín[a], M. Aminbaghai[b], J. Hrabovský[a], V. Kutiš[a]

[a] *Faculty of Electrical Engineering and Information Technology, Slovak University of Technology in Bratislava, Department of Applied Mechanics and Mechatronics of IAMT, Ilkovičova 3, 812 19 Bratislava, Slovakia*
[b] *Vienna University of Technology, Institute of Mechanics of Materials and Structures, Karlsplatz 13, A-1040 Vienna, Austria*

1. Introduction

The effect of non-uniform torsion may be significant in structural elastostatic and elastodynamic analysis of thin-walled beams with open as well as closed cross-sections and with constant material properties. The maximum normal stress resulting from the bimoment occurs at the points of action of the external torques (except for free ends of beams) and at cross-sections of restrained warping (e.g. clamped cross-sections). A comprehensive overview of the literature dealing with the issue of non-uniform torsion of thin-walled beams made of homogeneous material can be found, e.g., in [1, 5]. Structures with spatially inhomogeneous material properties are of a great practical importance in modern product and system design. Functionally Graded Materials (FGMs) are formed mainly by a continuous gradation of two or more constituents over the physical volume of a material body. In the literature, a huge amount of papers can be found, which deal with modelling and simulation of static and dynamic problems of FGM beams. In [4], a review of the principal developments in FGM structures is processed. A common feature of the cited articles is that constant material properties of the beams are assumed in longitudinal direction and Saint-Venant torsion is considered. According to our knowledge, especially for torsion of the FGM beams with longitudinally or spatially varying material properties, the warping effect has not yet been considered. In [6], an effect of longitudinally varying material properties on the warping torsion eigenmodes was studied originally. Significant effect of the material properties variation has been detected.

In the presentation to this conference contribution, an advance in solution of non-uniform torsion of the FGM beams will be presented that is a result of our research on this area. A theoretical background of our approach to solution of non-uniform torsion of the FGM beams with doubly symmetric open and closed cross-section, [2], will be shortly presented. Results of numerical experiments, performed by our warping torsion beam finite element (FGM-WT) that is based on the above mentioned theoretical backgrounds, will be introduced. The FGM-WT is a two-node straight finite element, which we have assembled by a direct stiffness method taking into account the Secondary Torsion Moment Deformation Effect (STDME). In addition to the angle of twist of the cross-section, a further degree of freedom is considered. It is the part of the bicurvature caused by the bimoment. The stiffness matrix in the local coordinate system has a dimension (4x4) [2]. The solution results for torsion of the clamped thin walled beams will be evaluated and compared with the ones obtained by the standard solid and shell finite elements. The polynomial and parabolic longitudinal variations of the effective material properties along the length of the beam is considered that can be obtained by homogenization of the spatially varying material properties in three directions (symmetrically in the lateral *y*-axis and transversal *z*-axis, and polynomial in the longitudinal *x*-axis of the beam). The effect

of longitudinally varying material properties on the twist angle and the bimoment will be evaluated.

2. Numerical simulations

In this section, the results from elastostatic analysis of cantilever FGM beams with I-cross-sections are presented. The length of the beams, L, is equal to 0.1m. The FGM consists of a mixture of aluminum (denoted with the index m) and tungsten (denoted with the index f). The material properties are listed in Table 1.

Table 1. Material properties of the FGM constituents

Material properties		
Young's modulus	$E_f = 4.8 \cdot 10^{11}$, $E_m = 0.69 \cdot 10^{11}$	Pa
Poisson's ratio	$\nu_f = 0.2$, $\nu_m = 0.33$	-
Shear modulus	$G_f = 2.0 \cdot 10^{11}$, $G_m = 0.26 \cdot 10^{11}$	Pa

The variable Young's and shear modulus, and the Poisson's ratio are chosen for Case 1 as

$$E(x) = E_f + (E_m - E_f)\left(\frac{x}{L}\right)^n, \nu(x) = \nu_f + (\nu_m - \nu_f)\left(\frac{x}{L}\right)^n, G(x) = \frac{E(x)}{2(1+\nu(x))},$$

where n denotes the power of (x/L). The axial variation of the material properties is drawn in Fig. 1 for $n \in \langle 1, 5 \rangle$.

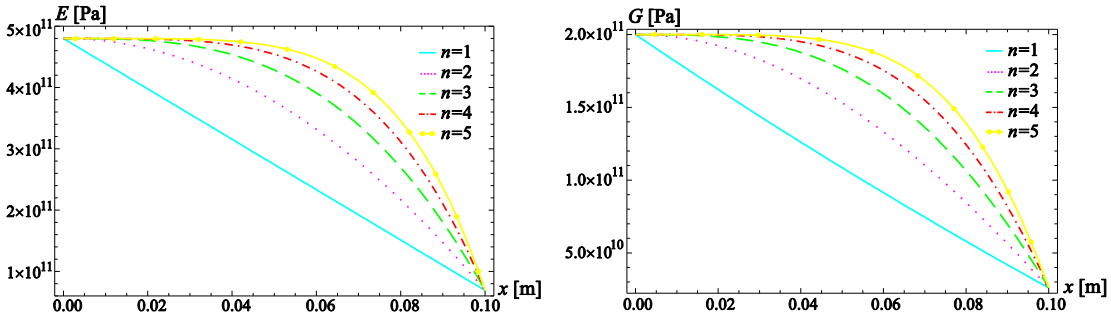

Fig. 1. Variation of the Young's and shear modulus for different values of n

For the Case 2, from the chosen parabolic longitudinal variation of the volume fractions of tungsten, $v_f(x) = -400x^2 + 40x$, and the aluminium, $v_m(x) = 1 - v_f(x) = 400x^2 - 40x + 1$, the effective elasticity modules and the Poison ratio are obtained as follows: $E(x) = E_f v_f(x) + E_m v_m(x) = 6.9 \times 10^{10} + 1.644 \times 10^{10} x - 1.644 \times 10^{11} x^2$,

$\nu(x) = \nu_f v_v(x) + \nu_m v_m(x) = 0.33 + 5.2x + 52x^2$, $G(x) = \frac{E(x)}{2(1+\nu(x))}$. Physical dimension of the elastic modules is [Pa]. The axial variation of the elasticity modules is shown in Fig. 2.

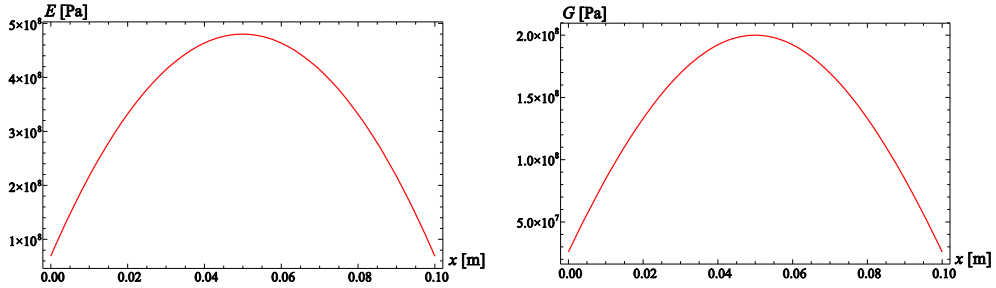

Fig. 2. Variation of the Young's and the shear modulus

The cross-sectional dimensions of the cantilever beam, shown in Fig. 3, are given as follows: $b = 0.005\,\text{m}$, $h_1 = 0.01\,\text{m}$, $h = h_1 - t = 0.00875\,\text{m}$, $t = s = 0.00125\,\text{m}$. In Table 2, the cross-sectional parameters required for the analysis are listed. The beam is loaded at point *k* by the torsional moment $M_T = Fh = 1\,\text{Nm}$ .The elastostatic non-uniform torsional analysis of the considered cantilever beam were performed with the material properties for the Case 1 and 2.

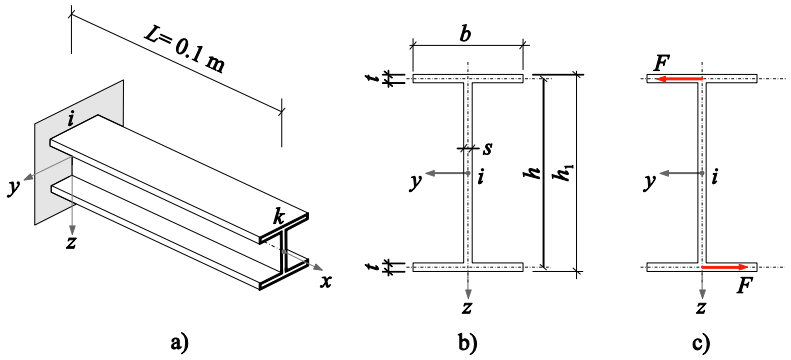

Fig. 3. Cantilever beam with an I cross-section: a) system, b) cross-section, c) applied forces (*F* = 114.3 N)

Table 2. Cross-sectional parameters for warping torsion

Cross-sectional parameters		
Cross-sectional area	$A = 0.21875 \cdot 10^{-4}$	m^2
Second moment of area about the y-axis	$I_y = 0.28483 \cdot 10^{-9}$	m^4
Second moment of area about the z-axis	$I_z = 0.27262 \cdot 10^{-10}$	m^4
Polar moment of area	$I_p = I_y + I_z = 0.31212 \cdot 10^{-9}$	m^4
Torsion constant	$I_T = 0.1119 \cdot 10^{-10}$	m^4
Secondary torsion constant	$I_{Ts} = 0.19938 \cdot 10^{-9}$	m^4
Warping constant	$I_\omega = 0.498 \cdot 10^{-15}$	m^6

Plots of the longitudinal distribution of the angle of twist, ψ [rad], for the both cases of non-uniform torsion of the investigated cantilever are shown in Fig 4. Fig. 5 shows the longitudinal variation of the bimoment, M_ω [kNm^2], for the cantilever beam with an I cross-section. These quantities were computed by only one FGM-WT beam element with STMDE and by very fine mesh of the SOLID186 finite elements [3]. The curves in Figs. 4 and 5 for $n = 0$ show the distributions for the beam made from tungsten only. The normal bimoment stresses can be further computed by the thin tube theory.

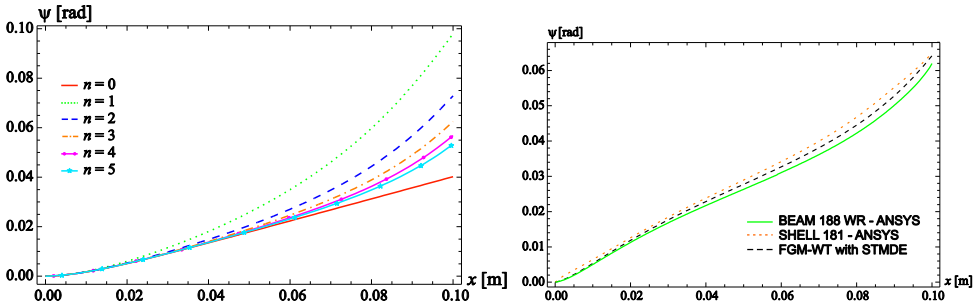

Fig. 4. Angle of twist, ψ [rad], for non-uniform torsion of the cantilever beam with an I cross-section, Case 1 - left figure, Case 2 - right figure

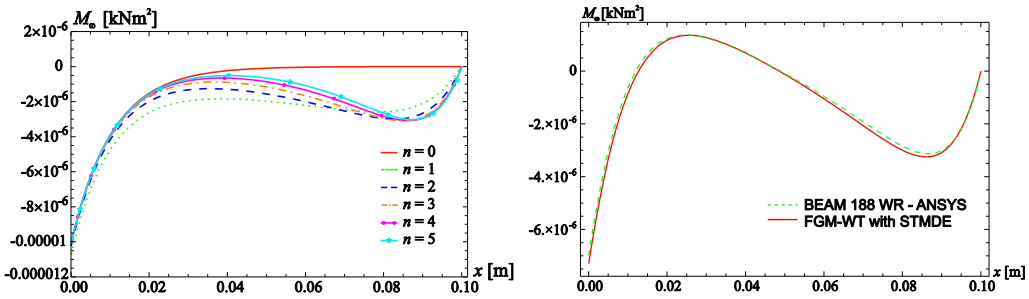

Fig. 5. Bimoment, M_ω [kNm^2], for the cantilever beam with, Case 1 - left figure, Case 2 - right figure

3. Conclusions

The Figs. 4 and 5 show significant impact of the material properties variation not only at the clamped end of the beam but also in the field of the beam. This is the new original knowledge that may be very important for the designers of the FGM structures made of thin walled beams. As will be shown in the presentation, this effect will also results in an occurrence of the large bimoment normal stresses caused by warping torsion. It is also shown a very good agreement of the results obtained by only one FGM -WT beam finite element with the ones obtained by the standart beam, shell and solid finite elements [3]. Similar results were obtained also for the hollow cross-section beams [2].

Acknowledgements

The authors gratefully acknowledge financial support by the Slovak Grant Agencies: VEGA No. 1/0102/18.

References

[1] Aminbaghai, M., Murin, J., Hrabovsky, J., Mang, H.A., Torsional warping eigenmodes including the effect of the secondary torsion moment on the deformations, Engineering Structures 106 (2016) 299-316.
[2] Aminbaghai, M., Murin, J., Kutis, V., Hrabovsky, J., Kostolani, M., Mang, H.A., Torsion warping elastostatic analysis of FGM beams with longitudinally varying material properties, Engineering Structures 2019. (in press)
[3] ANSYS Swanson Analysis System, Inc., Houston.
[4] Attenshamudin, S.S., Yuvaraj, M.G., Modeling and analysis of functionally graded sandwich structures, Mechanics of Advanced Materials and Structures 26 (21) (2019) 1776-1795.
[5] Dikaros, I.C., Sapountzakis, E.J., Argyridi, A.K., Generalized warping effect in the dynamic analysis of beams of arbitrary cross section, Sound and Vibrations 369 (2016) 119-146.
[6] Murin, J., Aminbaghai, M., Hrabovsky, J., Balduzzi, G., Dorn, M., Mang, H.A., Torsional warping eigenmodes of FGM beams with longitudinally varying material properties. Engineering Structures 175 (2018) 912-9725.

COMPUTATIONAL MECHANICS 2019
35th conference with international participation
Srní
November 4 - 6, 2019

Effect of various boundary conditions on the supersonic flow through the tip-section turbine blade cascade with a flat profile

J. Musil[a], J. Příhoda[a,b], J. Fürst[b]

[a] *Institute of Thermomechanics, Czech Academy of Sciences, Dolejškova 5, 182 00 Praha 8, Czech Republic*
[b] *Faculty of Mechanical Engineering, Czech Technical University in Prague, Karlovo nám. 13, 121 35 Praha, Czech Republic*

Transonic flows through turbine blade cascades are usually connected with the shock-wave/boundary-layer interaction. This interaction mostly leads to the laminar/turbulent transition in separated flow. The flow through the tip-section turbine blade cascades is mainly supersonic due to a very high circumferential velocity. The stagger angle of the blade is large and so flow in the cascade is characterized by the supersonic inlet and outlet (see Synáč et al. [1]). In case of the tip-section turbine blade cascades with the inlet supersonic flow there are some further problems connected with numerical simulations. Partly it is necessary to modify the inlet part of the computational domain because of the suppression of parasitic shock waves arising by the reflection from boundaries of the domain. Further there is a relation between of the inlet Mach number and the inlet angle given by the unique incidence rule (see Lakshminarayana [2]). The inlet flow angle is prescribed in numerical simulations and corresponding inflow conditions are established in the distance about one chord upstream of the leading edge plane. The tip-section blade cascade was designed for two nominal regimes with the inlet Mach number $M_1 = 1.2$ and isentropic outlet Mach numbers $M_{2is} = 1.7$ and 1.9. Numerical simulations of 2D compressible flow through the tip-section turbine blade cascade with a flat profile were carried out at free-stream turbulence $Tu = 1.5\%$ for three regimes including nominal regimes. Further, the effect of inlet free-stream turbulence was studied. The Reynolds number related to the isentropic exit Mach number and the profile chord was $Re_c = 2\times10^6$.

The OpenFOAM code was used for simulations based on the Favre-averaged Navier-Stokes equations completed by the two-equation SST turbulence model and the γ-$Re_{\theta t}$ transition model proposed by Langtry and Menter [3]. The transport equation for the intermittency coefficient γ is given by the equation

$$\frac{\partial(\rho\gamma)}{\partial t}+\frac{\partial\left(\rho U_j\gamma\right)}{\partial x_j}=P_\gamma-E_\gamma+\frac{\partial}{\partial x_j}\left[\left(\mu+\frac{\mu_t}{\sigma_\gamma}\right)\frac{\partial\gamma}{\partial x_j}\right]$$

with production term P_γ and the destruction term E_γ. The onset and length of the transition region are expressed by means of the local Reynolds number given by the transport equation as well. The model is switched over to a simple algebraic transition model for the transition in separated flow. The only two-equation SST turbulence model was used for comparison.

The computational domain takes up one spacing of the blade cascade and it is extended up to 2.4t upstream of the leading edge plane. Similarly the outlet part is shifted downstream of trailing edges. The inlet boundary conditions are prescribed by the constant total pressure, total temperature and inlet flow angle. The outlet boundary condition is defined by the

constant static pressure determined according to the outlet isentropic Mach number. Periodicity conditions were used on side boundaries of the computation domain. As the inlet Mach number is very sensitive to small changes of the inlet angle, the variation of M_1 with α_1 was studied. The presented numerical results were obtained for the inlet angle $\alpha_1 = 82.82^o$ and the corresponding inlet Mach number $M_1 = 1.135$. Some numerical results for $M_{2is} = 1.817$ are described by Musil et al. [5]. Due to the geometrical configuration of blades and to inlet boundary conditions pressure and suction sides are on the inverse blade sides than usually. The evaluation of numerical results was carried out using the data reduction method proposed by Amecke and Šafařík [1]. Numerical results were compared with results of optical and pressure measurements, see Luxa et al. [4].

The field of Mach number isolines obtained by numerical simulation for the $M_{2is} = 1.747$ is compared in Fig. 1 with the interferometric picture for corresponding boundary conditions. The flow structure in the blade cascade is influenced particularly by the inner branch of the exit shock wave of the neighbouring blade and its interaction with the laminar boundary layer on the suction side of the blade resulting in the flow separation and the transition in separated flow. The separation on the blade suction side induced by the interaction begins at x/b ≈ 0.54. The length of the separation is $\Delta(x(b)_{sep} \approx 0.05$ for the $M_{2is} = 1.817$ and slightly reduces with increasing free-stream turbulence. With diminishing entropic outlet Mach number the separation onset moves upstream equally as the position of the shock-wave interaction.

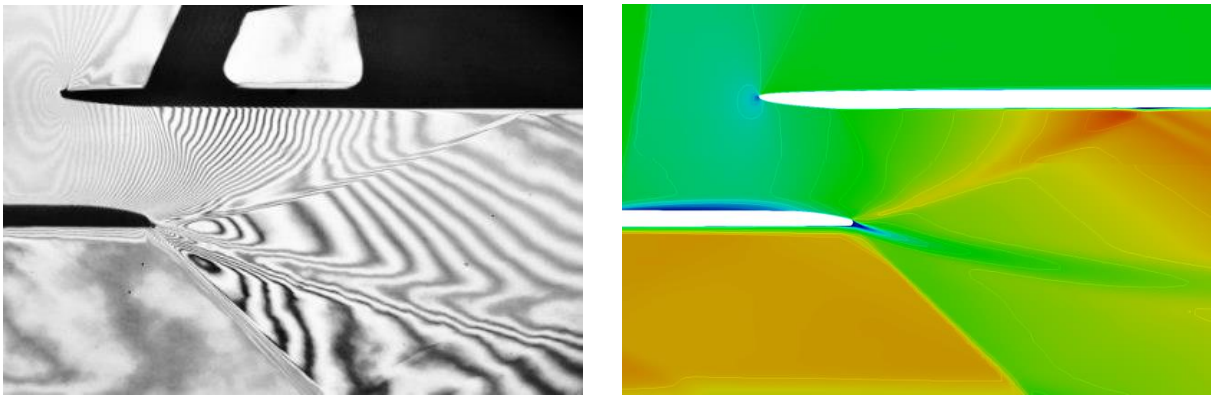

a) Interferometric picture b) Mach number isolines

Fig. 1. Flow field in the blade cascade

Due to the asymmetric blade trailing edge the supersonic expansion comes up on the pressure side leading to flow separation and to shifting of the near wake in the suction side direction with a very thick exit shock wave. Through different outlet isentropic Mach numbers at same boundary conditions due to the supersonic inlet the agreement of numerical simulations with experimental results is acceptable.

Acknowledgements

The work was supported by the Technology Agency of the Czech Republic under the National Centre for Power Engineering TH1000072. Institutional support RVO 61388998 is also gratefully acknowledged.

References

[1] Amecke, J., Šafařík, P., Date reduction of wake flow measurements with injection of another gas, DLR-Forschungsbericht, Göttingen, 1995.

[2] Lakshminarayana, B., Fluid dynamics and heat transfer of turbomachinery, Wiley Interscience Publication, New York, 1996.

[3] Langtry, R.B., Menter, F.R., Correlation-based transition modeling for unstructured parallelized computational fluid dynamics codes, AIAA Journal, 47 (12) (2009) 2894-2906.
[4] Luxa, M., Šimurda, D., Optical and pneumatic measurements on TR-U-8 cascade, Czech Academy of Sciences, Institute of Thermomechanics, Research Report Z-1558/18, 2018.
[5] Musil, J., Příhoda, J., Fürst, J., Simulation of supersonic flow through the tip-section turbine blade cascade with a flat profile, Proceedings of the conference Topical Problems of Fluid Mechanics, Praha, 2019, pp. 169-174.
[6] Synáč, J., Rudas, B., Luxa, M., Fürst, J., Nominal regimes of supersonic profile cascade, Proceedings of the AIP Conference 2118:030044, 2019.

COMPUTATIONAL MECHANICS 2019
35th conference with international participation
Srní
November 4 - 6, 2019

Ultrasonic stepped horn design with adaptive modal properties

M. Naď[a], L. Kolíková[a], Š. Šimon[a], L. Rolník[a]

[a] *Faculty of Materials Science and Technology in Trnava, Slovak University of Technology in Bratislva, J. Bottu 25, 917 24 Trnava, Slovak Republic*

High demands on performance, quality and reliability in the development and production of modern technical equipment result in the development of qualitatively new materials and material structures. These new modern materials (ceramics, composites and others) are generally characterized by improved physico-mechanical properties, with the result that this situation leads to relatively large problems in their technological processing [3]. For this reason, the hybrid technology processes are used to process these materials - e.g. combination of conventional technological processes with vibrations (ultrasound). The transmission of vibrations into the technological process is performed by means of the so-called ultrasonic horn, which must be operated in resonant mode. However, during the technological process, ultrasonic horn resonance properties change under load [1]. Design and analysis of stepped ultrasonic horn with adaptive change of modal properties is solved in this paper. Modification of modal properties is carried out using an embedded core which changes distribution of the spatial properties of horn structure.

The structural design of ultrasonic stepped horn with adaptive modal properties is shown in Fig. 1. The stepped horn starting radius is R_0 and the steppped change to radius r is at length L_s. The fundamental part of the ultrasonic stepped horn body has a drilled hole (radius r_c) for insertion of core with a length L_{lc}. The different material properties can be used for body of stepped horn and movable core. The longitudinal displacements of interacting points between the stepped horn body and the core are the same, i.e. perfect adhesion is assumed for the corresponding points.

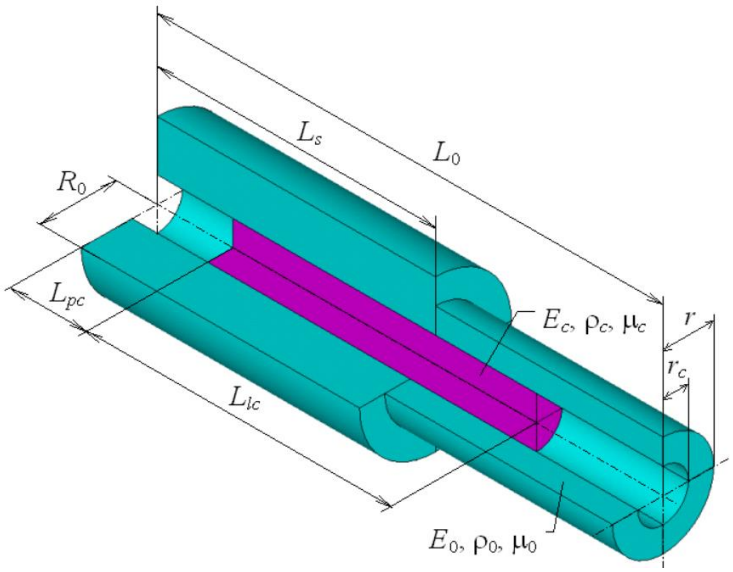

Fig. 1. Structural model of stepped horn

Generally, the partial differential equation (PDE) describing the free longitudinal vibration of *k*-th segment of horn structure is defined [2] in the following form

$$\frac{\partial}{\partial x_k}\left((ES)_k \frac{\partial u_k(x_k,t)}{\partial x_k}\right)-(\rho S)_k \frac{\partial^2 u_k(x_k,t)}{\partial t}=0, \tag{1}$$

where $(ES)_k$ is the longitudinal stifness and $(\rho S)_k$ is the unit mass parameter of the *k*-th segment of horn structure, $u_k(x_k,t)$ is the longitudinal displacement of cross-section (contained in *k*-th segment) in positon x_k, *k* is the number of segments (*k* = 4).

By solving the PDE (1) in the form $u_k(x_k,t)=U_k(x_k)T(t)$ [4] and introducing dimensionless parameters, the following ODE is obtained

$$\frac{d^2\bar{u}_k(\xi_k)}{d\xi_k^2}+\beta_k^2\bar{u}_k(\xi_k)=0, \tag{2}$$

and the frequency parameter β_k is formulated

$$\beta_k=\omega_{0,m}L_0\sqrt{\frac{\rho_0 S_0}{E_0 S_0}}\sqrt{\frac{\delta_S+\kappa_S(1-\delta_S)+\kappa_{Sc}(\delta_k\kappa_\rho-1)}{\delta_S+\kappa_S(1-\delta_S)+\kappa_{Sc}(\delta_k\kappa_E-1)}}, \tag{3}$$

where dimensionless geometrical and material parameters are $\bar{u}_k(\xi_k)=U_k(x_k)/L_0$, $\kappa_S=S/S_0$, $\kappa_{Sc}=S_c/S_0$, $\kappa_E=E_c/E_0$, $\kappa_\rho=\rho_c/\rho_0$, $\xi_k=x_k/L_0$, $\delta_S\langle{}^{=1;\ x\in\langle 0;L_S\rangle}_{=0;\ x\in\langle L_S;L_0\rangle}$, $\delta_{k=1\div4}\langle{}^{=1;\ S_k=S_0+S_c}_{=0;\ S_k=S_0}$, and cross-sections S_0, S_c, S are defined by

$$S_0=\pi R_0^2, \qquad S_c=\pi r_c^2, \qquad S=\pi r^2. \tag{4}$$

By the formulation of relevant boundary conditions, the frequency determinant is created from which the modified natural angular frequency for stepped ultrasonic horn with adaptive modal properties is determined by

$$\omega_{0,m,j}=\omega_{0,j}\,f_m(\kappa_S,\kappa_{Sc},\kappa_E,\kappa_\rho,\delta_S,\delta_{k=1\div4}), \tag{5}$$

where modified function is expressed by

$$f_m(\kappa_S,\kappa_{Sc},\kappa_E,\kappa_\rho,\delta_S,\delta_{k=1\div4})=\sqrt{\frac{\delta_S+\kappa_S(1-\delta_S)+\kappa_{Sc}(\delta_k\kappa_E-1)}{\delta_S+\kappa_S(1-\delta_S)+\kappa_{Sc}(\delta_k\kappa_\rho-1)}}. \tag{6}$$

and $\omega_{0,j}=\frac{\beta_j}{L_0}\sqrt{\frac{E_0 S_0}{\rho_0 S_0}}$ is *j*-th natural angular frequency for unstepped horn shape with radius R_0 and length L_0.

Acknowledgements

The work has been supported by the research project VEGA-1/1010/16 and by the "Young researcher project" MTF-1343.

References

[1] Dekýš, V., Sága, M., Žmindák, M., Dynamics and reliability of mechanical systems, VTS ZU, Žilina, 2004.

[2] Meirovitch, L., Analytical methods in vibrations, McMillan Comp., London, 1987.

[3] Naď, M., Kolíková, L., Rolník, L., Ďuriš, R., Investigation of vibration effects and tool shape on edge chipping phenomenon occurring during rotary ultrasonic drilling, Journal of Sound and Vibration 439 (2019) 251-259.

[4] Timoshenko, S.P., Young, D.H., Weawer, W., Vibration problems in engineering, John Wiley & Sons, New York, 1985.

COMPUTATIONAL MECHANICS 2019
35th conference with international participation
Srní
November 4 - 6, 2019

System response with random imperfections in coefficients on the space of realizations

J. Náprstek[a], C. Fischer[a]

[a] *Institute of Theoretical and Applied Mechanics of the Czech Academy of Sciences, Prosecká 76, 190 00 Prague, Czech Republic*

Parameters of dynamic systems are usually disturbed by a random noise, which emerges due to an imperfect function of the system, due to external influences, etc. These noises are random functions of time. The task assignment, however, may require determination of response statistics when the parameters of the system have indefinite values due to scattering of production, aging, wear or degradation of the system, etc. It turns out that the nature of the formulated task where the statistical set consists of individual realizations of the system is quite different from the case when parameters are influenced by random variables in time.

Therefore, a different assignment of the task is presented. Parameters of the system response statistics are looked for, when items of an initial statistical set are individual cases of the system itself. In other words, the coefficients have two sources of perturbation. Random noises, usually introduced as the Gaussian white noises, which are functions of time, and the random imperfection, which represents statistics in the set of implementations of the system described by a certain probability density.

From this point of view, it is crucial if, for instance, the material density is limited on both sides of the phase variables. If it is not limited (it is driven, e.g., by the normal distribution), the system will lose stochastic stability immediately or after a certain period of time. Therefore, the width of the band containing admissible cases should be strictly limited, see, e.g., [6]. Furthermore, many more papers can be cited investigating specific attributes of stochastic stability phenomena related with the topic dealt in this study, see, e.g. [1, 5] or [7]. The adequate limitations strongly depend in each parameter on the intensity of the parametric noise applied, correlation with an additive excitation noise and type of probability density of structural parameters.

Let us consider a simple system the function of which can be described by a stochastic differential equation of the first order

$$\dot{u}(t) = -(C + p + w(t))u(t) \; + \; f(t) \; + \; \varphi(t)\,, \tag{1}$$

where:

C	– constant, nominal value of a system parameter;
p	– deviation (imperfections) of the parameter from its nominal value; discrete set of values in realisations with zero mathematical mean value and known probability density;
$f(t)$	– useful signal (deterministic part of excitation);
$w(t)$, $\varphi(t)$	– time variable parametric perturbation or additive perturbation of excitation; Gaussian white noises of constant intensities $s_w, s_\varphi, s_{w\varphi}$.

The initial condition of the response $u(0) = u_\circ$ is a random quantity of probability density $h_\circ(u_\circ)$. The imperfection p can be considered as a constant. Within every individual realization of the system or time period of its service, the parameter is not subjected to differentiation or integration in time.

For every value of p we can consider in Eq. (1) the processes $w(t), \varphi(t), u(t)$ as Markov processes in time. With respect to Eq. (1), the Fokker-Planck equation can be deduced. Using the Ito white noise definition, see [2, 3, 8] and other monographs, the relevant equation can be written as

$$\begin{aligned}\frac{\partial h(u,t)}{\partial t} =& \frac{\partial}{\partial u}\left[\left(\left(C + p - \frac{1}{2}s_{ww}\right)u(t) + \frac{1}{2}s_{w\varphi} - f(t)\right)h(u,t)\right] \\ &+ \frac{1}{2}\frac{\partial^2}{\partial u^2}\left[\left(s_{ww}u^2(t) - 2s_{w\varphi}u(t) + s_{\varphi\varphi}\right)h(u,t)\right], \end{aligned} \tag{2}$$

where:
$h = h(u,t)$ – probability density function of the system response;
s_{ww}, $s_{w\varphi}$, $s_{\varphi\varphi}$ – intensity or cross-intensity of parametric and additive noises $w(t)$, $\varphi(t)$.

Using Eq. (2) for the construction of the equations for the first and second unknown stochastic moments of the response, it can be obtained

$$\dot{u}_s^i(t) = -(C + p^i - \frac{1}{2}s_w)u_s^i(t) \; - \; \frac{1}{2}s_{w\varphi} \; + \; f(t); \quad u_s^i(0) = u_{s\circ}^i\,, \tag{3}$$

$$\dot{D}_u^i(t) = -2(C + p^i - s_w)D_u^i(t) \; - \; 2s_{w\varphi}u_s^i(t) \; + \; s_\varphi; \quad D_u^i(0) = D_{u\circ}^i\,, \tag{4}$$

where:
$u_s^i(t)$ – mathematical mean value of the response for the i-th realization of the parameter imperfection;
$D_u^i(t)$ – variance of the response for the i-th realization of the parameter imperfection;
$u_{s\circ}^i$, $D_{u\circ}^i$ – random initial conditions (we will introduce the assumption of the statistical independence of initial conditions and parameter imperfections).

The solution of these equations can be expressed by means of Green functions in the form of

$$u_s^i(t) = u_{sg}^i(t,0,p^i)\cdot u_{s\circ}^i \; + \; \int_0^t u_{sg}^i(t,\tau,p^i)(f(\tau) - \frac{1}{2}s_{w\varphi})\mathrm{d}\tau\,, \tag{5}$$

$$D_u^i(t) = D_{ug}^i(t,0,p^i)\cdot D_{u\circ}^i \; + \; \int_0^t D_{ug}^i(t,\tau,p^i)(s_\varphi - 2s_{w\varphi}u_s^i(\tau))\mathrm{d}\tau\,, \tag{6}$$

where $u_{sg}^i(t,\tau,p^i)$ and $D_{ug}^i(t,\tau,p^i)$ are Green functions arising from Eqs. (3) and (4) for annulled right-hand sides and initial conditions of $u_{sg}^i(\tau,\tau,p^i) = 1$, $D_{ug}^i(\tau,\tau,p^i) = 0$ or $u_{sg}^i(\tau,\tau,p^i) = 0$, $D_{ug}^i(\tau,\tau,p^i) = 1$, respectively,

$$u_{sg}^i(t,\tau,p^i) = \exp\left[-\left(C + p^i - \frac{1}{2}s_w\right)(t-\tau)\right], \tag{7}$$

$$D_{ug}^i(t,\tau,p^i) = \exp\left[-2\left(C + p^i - s_w\right)(t-\tau)\right]. \tag{8}$$

To determine the mathematical mean value $u_s(t)$ and variance of the response $D_u(t)$ on the set of realizations, we will apply the mathematical mean value operator $\mathbf{E}\{\cdot\}$ to Eqs. (5) and

(6), making use of the fact that in the given case the operators of mathematical mean value and integration are mutually commutable, and of the statistical independence of initial conditions from imperfections. That means

$$u_s(t) = u_{sg}(t,0) \cdot u_{s\circ} \; + \; \int\limits_0^t u_{sg}(t,\tau)(f(\tau) - \frac{1}{2}s_{w\varphi})\mathrm{d}\tau \,, \tag{9}$$

$$D_u(t) = D_{ug}(t,0) \cdot D_{u\circ} \; + \; \int\limits_0^t D_{ug}(t,\tau)(s_\varphi - 2s_{w\varphi}u_s(\tau))\mathrm{d}\tau \,, \tag{10}$$

$$u_{sg}(t,\tau) = \mathbf{E}\{u^i_{sg}(t,\tau,p^i)\} \; ; \quad D_{ug}(t,\tau) = \mathbf{E}\{D^i_{ug}(t,\tau,p^i)\} \,. \tag{11}$$

The kernels of integrals in Eqs. (9) and (10) implicitly depend, in the meaning of Eq. (11), on the probability density of the imperfection p, while the influence of particularly the additive noise $\varphi(t)$ is expressed in Eqs. (9) and (10) relatively distinctly.

Let us pay attention to some special cases of imperfection probability density distribution:

(i) Normal distribution of imperfections. The uncertainty of the quality of the individual parts of the system is commonly characterized by the normal distribution or its mean value and by variance D_p, see [4] and many others,

$$h(p) = \frac{1}{\sqrt{2\pi D_p}} \cdot \exp\left(-\frac{p^2}{2D_p}\right). \tag{12}$$

Let us assume that the useful signal $f(t) = \text{const}$. If $C > s_w/2$, then $0 < t < t_m = 2(C - \frac{1}{2}s_w)/D_p$, i.e., within a finite time interval, the system is stochastically stable in probability. Provided that $C \leq s_w/2$, the system is unstable from the very beginning, i.e., for all $t > 0$. These conclusions would not change even if $f(t) \neq \text{const}$. The initial or "deferred" loss of stability in both cases results from the dispersal of imperfections D_p different from zero.

(ii) Uniform distribution of imperfections. The parameter imperfection should be obviously limited on both sides within a finite interval $-\Delta \leq p \leq \Delta$. The simplest distribution of probability complying with this requirement is the uniform distribution, see [2, 3] and others,

$$h(p) = \begin{cases} \frac{1}{2d} & ; \quad -\Delta < p < \Delta, \\ 0 & ; \quad p < -\Delta \; ; \; p > \Delta. \end{cases} \tag{13}$$

It can be shown that for $t \to \infty$ the mathematical mean value equals

$$\lim_{t\to\infty} u_s(t) = u_{sn} = \frac{f_\circ - \frac{1}{2}s_{w\varphi}}{2\Delta} \cdot lg\, \frac{C - \frac{1}{2}s_w + \Delta}{C - \frac{1}{2}s_w - \Delta}. \tag{14}$$

This limit exists, if the imperfection interval is limited by $C \; > \; \frac{1}{2}s_w \; + \; \Delta$.

(iii) Truncated normal distribution of imperfections. The probability density of imperfections p is described by the truncated Gaussian distribution for $|p| \leq \Delta$, see [4] and a number of additional papers cited herein,

$$h(p) \; = \; \begin{cases} 0 & ; \; p \leq C - \Delta, \\ \frac{\mu}{\sqrt{2\pi D_p}} \cdot \exp\left(-\frac{(p-C)^2}{2D_p}\right) & ; \; C - \Delta < p < C + \Delta, \\ 0 & ; \; p \geq C + \Delta, \end{cases} \tag{15}$$

$$\mu^{-1} \;=\; 2\Phi\left(\frac{\Delta}{\sqrt{2D_p}}\right) \;=\; \frac{2}{\sqrt{2\pi}} \int_0^{\Delta/\sqrt{D_p}} e^{-\xi^2/2}\, d\xi. \tag{16}$$

If Δ is finite and $C > s_w/2 + \Delta$, the influence of initial conditions successively disappears with growing t and the system reveals to be stable in the mathematical mean value. The permissible width Δ of the zone of imperfections is determined by the white noise intensity s_w. It is decreasing with the increasing noise intensity and vice versa. The permissible zone is wider for the truncated normal distribution than for the uniform distribution.

Acknowledgements

The kind support of the Czech Science Foundation project No. 19-21817S and of the RVO 68378297 institutional support are gratefully acknowledged.

References

[1] Ariaratnam, S. T., W.-C. Xie, Lyapunov exponents and stochastic stability of two-dimensional parametrically excited random systems, Journal of Applied Mechanics 60 (3) (1993) 677-682.

[2] Arnold, L., Stochastic differential equations: Theory and applications, Wiley, New York-London, 1974.

[3] Bolotin, V. V., Random vibrations of elastic systems, Nauka, Moscow, 1979. (in Russian)

[4] Bolshev, L. N., Smirnov, N. V., Tables of mathematical statistics, Nauka, Moscow, 1983. (in Russian)

[5] Khasminski, R. Z., Stability of differential systems with perturbations of their parameters, Nauka, Moscow, 1969. (in Russian)

[6] Náprstek, J., Correlation analysis of a first order system with random perturbations, Proceedings of the conference Dynamics of Machines '96, Institute of Thermomechanics of the Czech Academy of Sciences, Prague, 1996, pp. 113-120.

[7] Náprstek, J., Stochastic exponential and asymptotic stability of simple non-linear systems, International Journal of Non-Linear Mechanics 31 (5) (1996) 693-705.

[8] Pugachev, V. S., Sinitsyn, I. N., Stochastic differential systems: Analysis and filtering, J. Wiley, Chichester, 1987.

COMPUTATIONAL MECHANICS 2019
35th conference with international participation
Srní
November 4 - 6, 2019

Fatigue crack front curvature due to the plasticity induced crack closure

T. Oplt[a,b], P. Hutař[b,c], P. Pokorný[b], L. Náhlík[c], F. Berto[d]

[a] *Faculty of Mechanical Engineering, Brno University of Technology, Technická 2896/2, Brno, Czech Republic*
[b] *Institute of Physics of Materials of the Academy of Sciences of the Czech Republic, Žižkova 22, Brno, Czech Republic Czech Republic*
[c] *CEITEC IPM, Institute of Physics of Materials of the Academy of Sciences of the Czech Republic, Žižkova 22, Brno, Czech Republic*
[d] *Norwegian University of Science and Technology, NO-7491 Trondheim, Norway*

Numerical modelling of cracked bodies is required for many research and engineering applications. Majority of cases is satisfied with two-dimensional (2D) modelling assuming plane strain or plane stress conditions. When three-dimensional (3D) model is created, it contains mostly only straight crack front. For the purpose of most of the applications it seems to be good enough. However in reality, fatigue crack front doesn't propagate as a straight line, but it is always curved. Basic reason for the crack front curvature is the presence of so called vertex point singularity, which is appears at the intersection of the crack front with free surface. Vertex point singularity affects stress distribution close to the free surface, resulting in the curvature of fatigue crack front. This effect might be observed at high asymmetry loadings, description may be found in [2]. It seems that additional curvature is caused when plasticity induced crack closure effect is present. Elber [1] was the first describing this phenomenom, which is caused by residual plastic strains left behind propagating fatigue crack. Residual strains form plastic wake and causing the crack faces come to the contact before the crack is actually closed. Advanced computational possibilities enable closer insight into the closure mechanics, leading to improving the physical background and ability to develop accurate models for fatigue life prediction.

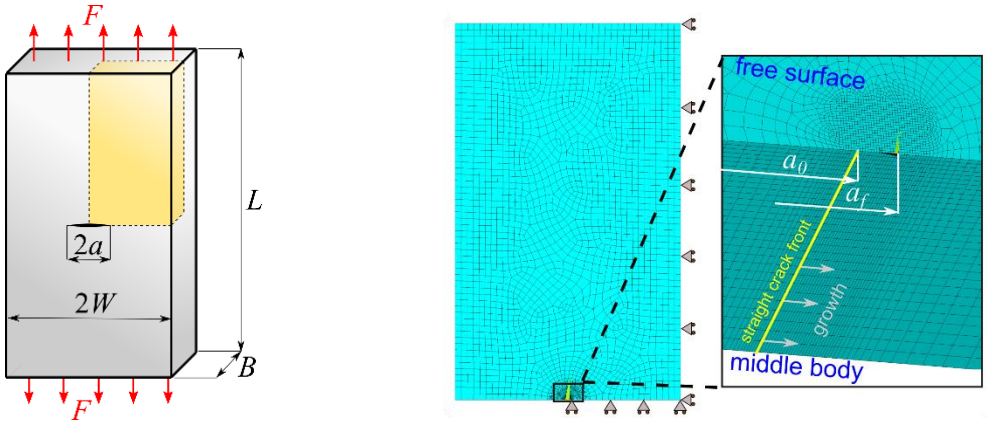

Fig. 1. Middle tension specimen geometry a) and numerical model b)

The methodology of numerical modelling of plasticity infuced crack closure was adopted from previous studies [3]. For the purpose of the study, MT specimen with dimensions 2L = 200 mm, 2W = 60 mm, B = 10 mm was used (Fig. 1). In order to compare the results, 2D finite model was created by using PLANE182 finite elements, while 3D finite element was build with SOLID185 finite elements. Material model assumed elastic-plastic behaviour according to the

cyclic curve of steel EA4T (σ_Y = 611 MPa and σ_{UTS} = 727 MPa, σ_{YC} = 470 MPa). Specimen was cyclically loaded with constant stress intensity factor range ΔK = 20 MPa$\sqrt{m}$ and load range R = 0. Crack growth was simulated by debonding nodes of the crack front when maximum load was reached, specimen was subjected in total to 10 cycles with 10 crack increments in order to reach final crack length 2a = 15 mm.

Contact elements were required in order to simulate premature crack faces contact. Therefore contact elements were prescribed on the crack face, while the opposite stationary crack face was substituted by creating horizontal line or surface and meshed with target elements. Crack closure determination was performed by monitoring of displacement of the 1st node behind the crack tip. Change of the displacement u_y to a negative value signalized that crack was closed and corresponding K_{cl} was determined.

3D numerical model was assumed with straight crack front only in order to compare 2D and 3D results. Crack closure values, determined after the 10 cycles of loading, agree very well between 2D and 3D. In the middle of the body, where plain strain conditions prevails, closure values correspond to the 2D model assuming plane strain conditions and furthermore, it agrees also with Newman+Wanhill empirical equation and Pokorny [4] experimental results. Crack closure values at the free surface are also very similar with 2D results, assuming plane stress conditions.

Since the effect of residual plastic strains is the deciding factor on crack closure appearance, it would be appropriate to take a look at plastic zones (Fig. 2a). Thick lines reffers to the plastic zone shapes through the 3D crack front. It can be found that plastic zone shape is moreless constant from the middle of the body almost the the free surface (Fig. 2b). There can be found a pop-up inside the body close to free surface, but it goes back to stabilized cylindrical shape . Plane strain result is very similar to the plastic zone at the middle of the body. In contrary, plane stress assumption provides significantly different shape of plastic zone than the plastic zone \at the free surface of 3D body.

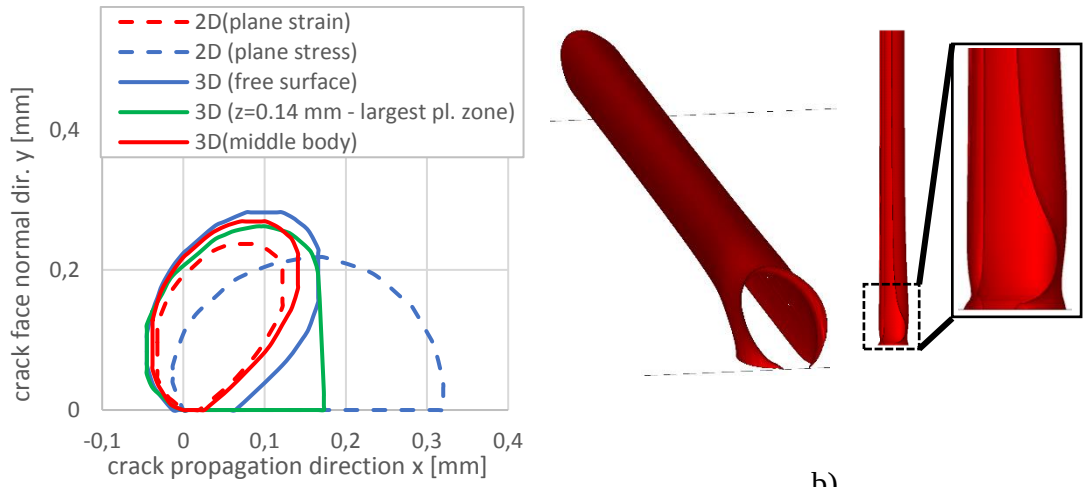

Fig. 2. Plastic zone shapes comparison between 2D and 3D model after monotonic loading a) and 3D plastic zone shape envelope b)

It is generally assumed that when the crack closure is present, the determinitive factor in the crack growth is not whole range of the loading cycle ΔK, but only its effective part ΔK without the rest of the cycle where the crack has been already closed

$$\Delta K_{eff} = \Delta K - K_{cl} \tag{1}$$

Fig. 3 presents plotted distributions of elastic K_{max}, closure value K_{cl} and determined effective part of the cycle ΔK_{eff} through the specimen thickness for case of the straight crack. At the free surface, elastic K_{max} decreases due to the vertex point singularity. In the paper [2] was presented that the crack front curvature caused due to the free surface effect is found when constant horizontal Kmax distribution is obtained. For the MT specimen, horizontal K_{max} distribution was found for crack front curvature with angle 7.5°. However, crack closure values K_{cl} didn't decrease, but increase. Finally, the effective part of the loading ΔK_{eff} remains more or less similar as for the straight crack front.

It seems that curvature of the crack front doesn't affect ΔK_{eff} distribution in numerical model, although in experimental results there is a difference between pure free surface effect and cyclic loading with plasticity induced crack closure involved. Therefore, further research must be devoted to this topic in order to prove or disprove the validity of effective stress intensity factor range ΔK_{eff}.

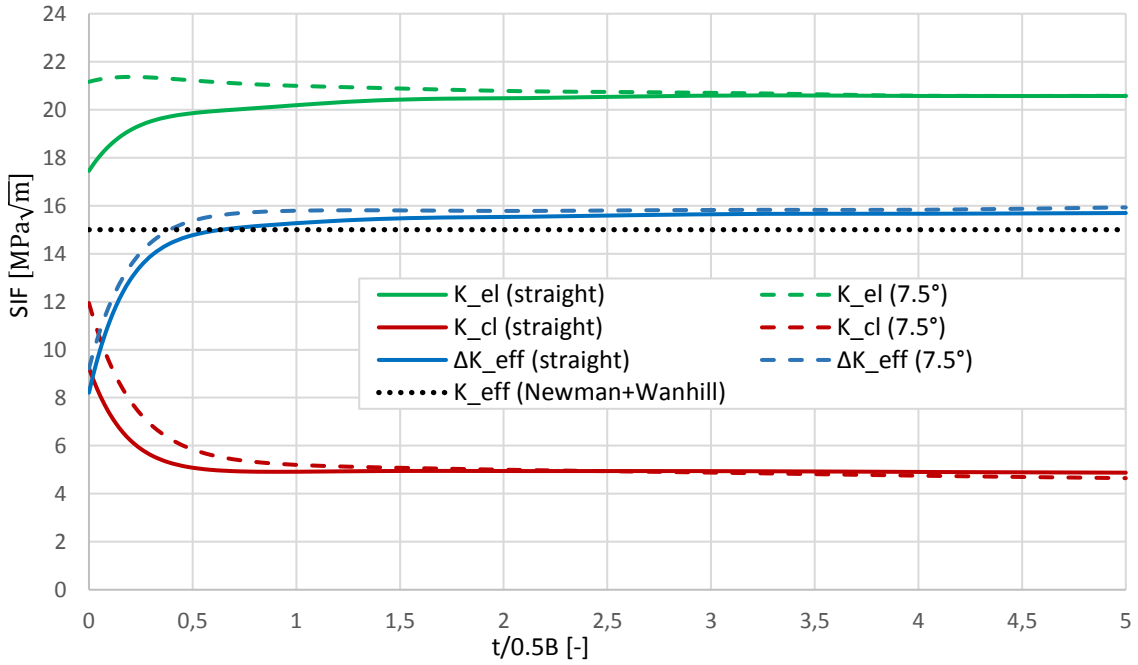

Fig. 3. Elastic SIF (Kmax), closure SIF (Kcl) and effective SIF (Keff) for the specimen with straight crack front

Acknowledgements

This research has been supported by the Ministry of Education, Youth and Sports of the Czech Republic under the project m-IPMinfra (CZ.02.1.01/0.0/0.0/16_013/0001823) and specific research project FSI-S-17-4386 of the Faculty of Mechanical Engineering, BUT.

References

[1] Elber, W., Fatigue crack closure under cyclic tension. Engineering Fracture Mechanics 2 (1) (1970) 37–45.
[2] Oplt, T., Hutař, P., Pokorný, P., Náhlík, L., Chlup, Z., Berto, F., Effect of the free surface on the fatigue crack front curvature at high stress asymmetry. International Journal of Fatigue 118 (2018) 249–261.
[3] Oplt, T., Šebík, M., Berto, F., Náhlík, L., Pokorný, P., Hutař, P., Strategy of plasticity induced crack closure numerical evaluation. Theoretical and Applied Fracture Mechanics 102 (2019).
[4] Pokorný, P., Vojtek, T., Náhlík, L., Hutař, P., Crack closure in near-threshold fatigue crack propagation in railway axle steel EA4T. Engineering Fracture Mechanics 185 (2017) 2–19.

COMPUTATIONAL MECHANICS 2019
35th conference with international participation
Srní
November 4 - 6, 2019

Experimental and numerical evaluation of composite part strength

Z. Padovec[a], R. Sedláček[a], T. Zámečníková[a]

[a] *CTU in Prague, Faculty of Mechanical Engineering, Department of Mechanics, Biomechanics and Mechatronics, Technická 4, 160 00, Prague, Czech Republic*

Presented work deals with the design, stress/strain analysis and testing of composite element for aircraft construction. Main idea of the work is replacement of titanium part with composite manufactured from C/PPS 5H satin fabric [1, 2] by thermoforming technology. At first loading of the composite was simulated in FE software Abaqus and it was proved, that it should withstand the load without failure.

Experiment was done after the manufacturing of testing specimens. Tests were done on TIRA 2300 universal testing machine with loading speed of 1 mm/min (respectively 2 mm/min). Tensile load was realized through the screws in the web of the element jointed with the jaws of the machine. Relationship between loading force and displacement for three tested specimens can be seen in Fig. 1. Comparison of failed specimen with FE prediction of failure index (according to maximal stress theory [3]) can be seen in Fig. 2.

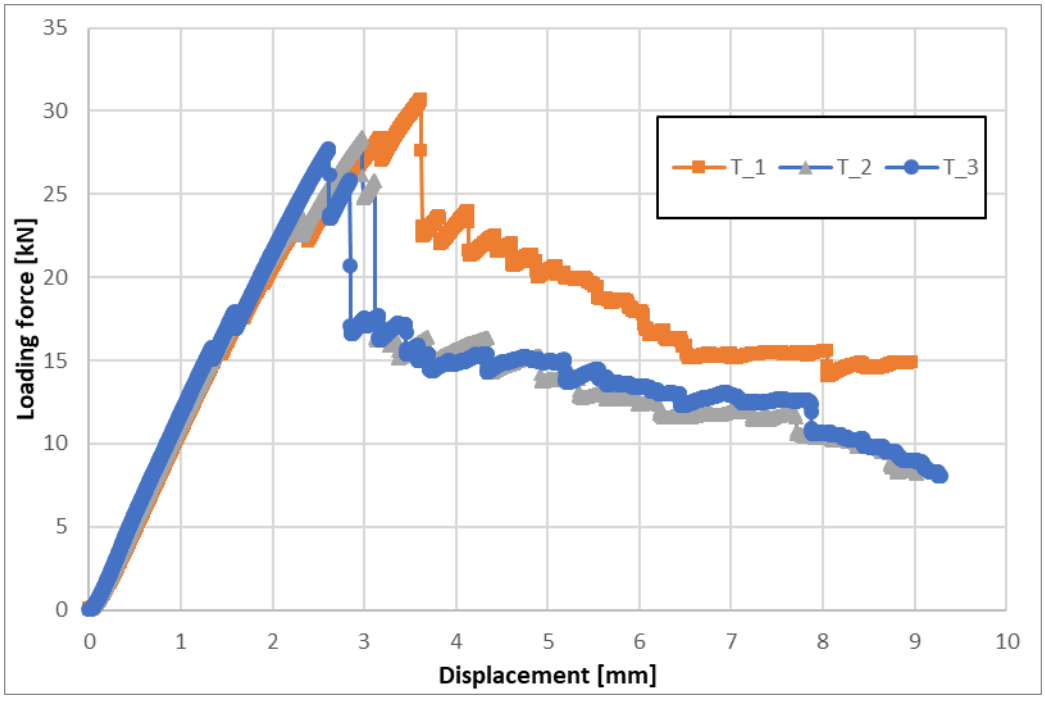

Fig. 1. Relationship between loading force and displacement for three tested specimens

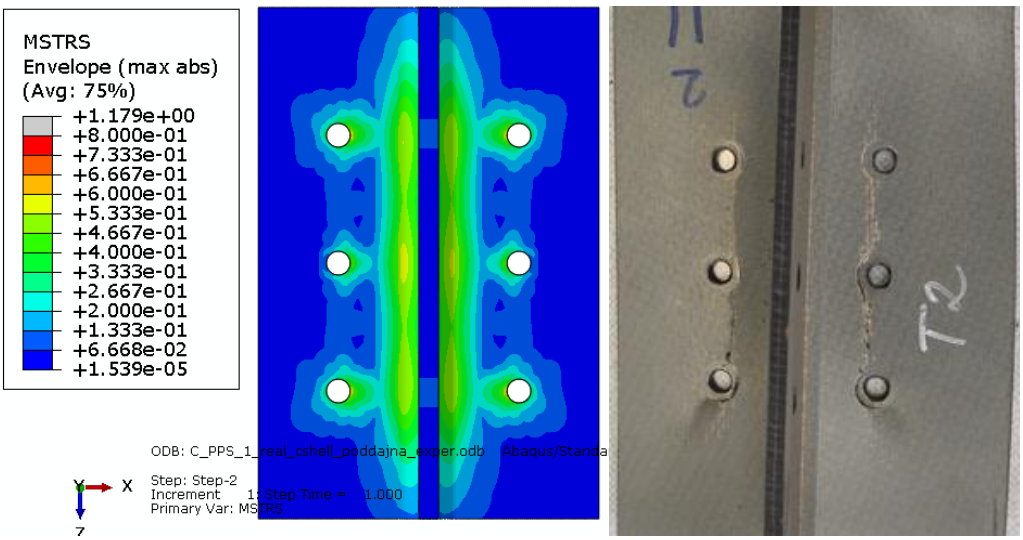

Fig. 2. Comparison of predicted failure index with real failure of the specimen

Next part of the work is comparison of interlaminar shear strength of our part (which is consolidated from two plates with 8 layers of fabric) with properties of plate manufactured from 16 layers of fabric. One set of specimens cut from 16 layers plate and two sets of specimens cut from profile with 2x8 layers were prepared for tests. Experiment and its evaluation is like single lap joint testing (according to ČSN EN 1465 standard for example). Tests were done on TIRA 2300 machine with loading speed 1 mm/min. Tested specimens can be seen in Fig. 3. Results can be seen in Table 1.

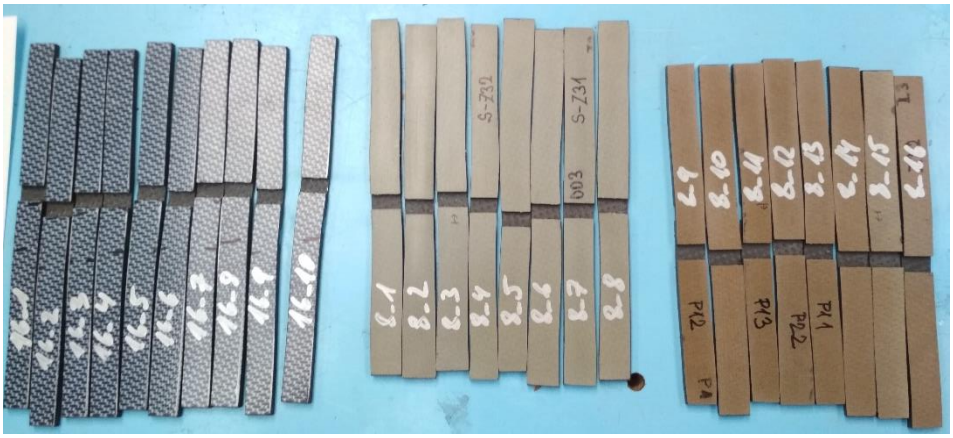

Fig. 3. Tested specimens

Table 1. Comparison of deflection/rotation for designed versions

	Average interlaminar shear strength [MPa]	**Standard deviation [MPa]**
Specimens 8_1 -8_8	22,63	0,86
Specimens 8_9 -8_16	20,17	0,66
Specimens 16_1 -16_10	19,01	1,49

Conclusions

Three specimens of composite bracket were tested with achieving average maximal force 28,94 ± 1,25 kN. Comparison of FE and experimental results shows that FE model predicts well areas of failure which are around the bolt holes and on transition radius between lower flange and web of the profile.

From the Table 1 can be seen that specimens cut from plate with 16 layers have lower average interlaminar shear strength and higher standard deviation then specimens cut from consolidated profile (2x8 layers). It means that the consolidated profile from 2x8 layers has similar or even better interlaminar shear properties then profile made from 16 layers.

Acknowledgements

This work has been supported by project FV30033 of the Ministry of Industry and Trade of the Czech Republic and by the Grant Agency of the Czech Technical University in Prague, under grant No. SGS18/175/OHK2/3T/12.

References

[1] ABS5045, Aerospace series, carbon fibre fabrics reinforced PPS, laminates w/ or w/o lightning protection, w/ or w/o anti-corrosion protection, structural material.
[2] AIMS05-09-002, Airbus material specification carbon fabric, 285 g/m2 fibre area mass with 43% PPS resin or equivalent resin material specification.
[3] https://classes.engineering.wustl.edu/2009/spring/mase5513/abaqus/docs/v6.6/books/usb/default.htm?start at=pt05ch17s02abm04.html

COMPUTATIONAL MECHANICS 2019
35th conference with international participation
Srní
November 4 - 6, 2019

Use of FEM in traffic accident analyses

P. Pavlata[a]

[a] *Vision Consulting Automotive s.r.o.*

Since the 1950s, in traffic accident analysis, forensic experts have been using simple trigonometric methods of force triangles solved only with a pencil, a plastic ruler and a logarithmic ruler. Later, with the massive expansion of pocket calculators in the 1970s and 1980s, calculations accelerated, but procedures remained the same. It was only with the boom of desktop PCs that simple computer programs began to be created from the beginning of the 1990s, which were algorithmically based on the methods used so far. With the wide rise of Windows OS, faster processors and powerful graphics cards, several successful programs have gradually developed since the beginning of the new millennium. Some of these programs were probably based on algorithmic engines of racing car game simulators. These engines at that time were increasingly worked with the true vehicle dynamics based on mechanical multi-body-systems (MBS). Among such programs, which have achieved commercial use, it is necessary to mention especially PC-crash and later also Virtual-crash, with much easier and intuitive control. Gradual variants of this software from version 1.0, which solved ground plan tasks only in 2D, through version 2.0 and especially very successful version 2.2, which worked excellently since 2005 even in 3D space, further versions 3.0 and 4.0 focused mainly on improving real graphics even with rendering and also modeling realistic terrain using Google orthophotomaps, which make it easy to model a road elevation and realistic relief of the surrounding terrain.

However, MBS algorithms generally work with non-deformable models defined only by the simple outer envelope of the modeled object. However, such models usually do not contain any deformation zone elements by demanding procedures tuned in the development of real vehicles or other elements hidden under the hood (engine, transmission, cooling system components and many others). Usually, the stiffness of the individual vehicle body parts is also not known.

In the case of vehicles, only the outer contours of their shape and, in some cases, their interior contours are entered. The whole vehicle model is then composed of several hundred or several thousand usually triangular faces of various sizes so that the simplified shapes of the vehicle are sufficiently modeled.

A range of vehicle damage in these models is implemented by simplifying special procedures working only with estimating the depth of overlap of vehicles at the moment of collision (in milliseconds), estimating the impact restitution coefficient and estimating the so-called equivalent energy speed (EES). Other simplifications envisaged in MBS programs include a linear relationship between vehicle deformation and contact force. In addition, movement after impact is extremely sensitive to contact parameters, which is typical for non-linear systems. This cause differences between the results of the experiment and the simulation. Despite of these facts, the procedures described above give relatively convincing results for most traffic accidents. It should be noted, however, that the expert by the application of these procedures always obtains “some” result, which does not always mean a

technically acceptable solution to the task. Although experts must have sufficient experience in entering individual task input parameters, many other important physical inputs are only predefined in the software implicitly and often do not even change them by experts. The expert can then be satisfied with the result of his simulation, which at first view makes some sense, but in fact does not fully correspond to the physical conditions. Consequently, the expert can prepare an inaccurate technical report, which can subsequently affect life fates of the road accident participants. Thus, in many other cases, the above procedures can fail.

MBS algorithms on mechanical systems of usually only a few hundred or thousand degrees of freedom, with relatively large time steps of individual iterations of solutions (0.001 to 0.01s), give fast results and thus allow a large number of different solution variants to be processed in a short time, for instance when some input parameters of the task are varied.

This paper deals with the use of nonlinear finite element (FEM) algorithms solving generally fast dynamic processes. These algorithms work with deformable models of vehicles or their components, the achieved results can in some cases bring to the task much more realistic look of the deformation process and behavior of the objects involved comparing to MBS.

Further considered procedures require much more sophisticated models requiring knowledge of a much larger range of input parameters, including a description of the mechanical properties of all structural materials. The results of such computer simulations today give a very realistic view of the deformation behavior of individual vehicles or objects during a traffic accident. Suitable complete vehicle models are now available to vehicle manufacturers, who use them in the virtual development cycle of new vehicle generations. Such models now have several tens of millions of degrees of freedom, the time step of each solution iteration is around 1μs to be good numerical convergence.

Unfortunately, such vehicle models are generally not currently available for use in forensic practice, and the vast majority of current experts do not have enough expertise, experience and equipment to apply these methods in practice. However, even today, it is possible to solve with the use of FEM methods a number of more complex tasks where standard approaches of forensic experts fail.

The author of this paper will demonstrate several examples solved since the turn of the millennium using the software PAM-crash. The Virthuman as a scalable human body model will be introduced in some of these examples where the passengers or a vehicle crew were modelled.

Fig. 1. An example of traffic accident analysing by Virtual-crash

References

[1] Pavlata, P., A new approach in traffic accident analyses, MECAS user forum, 2006.
[2] Pavlata, P., BMW X5 trafic accident analysis using FEM, VPS user forum, Břasy, 2016.
[3] Pavlata, P., Computer simulation of the frontal collision of the articulated urban bus into the column of the traffic board portal, Proceedings of the conference Computational Mechanics, Srní, 2018.
[4] Pavlata, P., Examples of calculations for approval of vehicle seats using Virthuman, VPS conference, Nesuchyně, 2019.
[5] Pavlata, P., Heavy vehicle accident analysis, VPS user forum, Myslovice, 2017.
[6] Pavlata, P., Simulation of an articulated bus traffic accident with respect of passenger biomechanic load evaluation, Proceedings of the international conference ExFos, Brno, 2018.
[7] Pavlata, P., Small trailer accident analysis using FEM, International congress EVU, Bratislava, 2005.
[8] Pavlata, P., Using the biomechanical human model Virthuman in traffic accident analyses, Proceedings of the national congress Traffic accidents, Brno, 2019.

COMPUTATIONAL MECHANICS 2019
35th conference with international participation
Srní
November 4 - 6, 2019

Modelling of large plastic deformation of polyethylene for geomembranes

J. Poduška[a,b], P. Hutař[a], E. Nezbedová[c], F. Šebek[b], L. Náhlík[d]

[a] *Institute of Physics of Materials AS CR, Žižkova 22, 616 62 Brno, Czech Republic*
[b] *Institute of Solid Mechanics, Mechatronics and Biomechanics, FME, BUT, Technická 2896/2, 616 69 Brno, Czech Republic*
[c] *Unipetrol RPA, s.r.o. – Polymer Institute Brno, Tkalcovská 36/2, 602 00 Brno, Czech Republic*
[d] *CEITEC IPM, Žižkova 22, 616 62 Brno, Czech Republic*

Being a versatile material with many advantageous properties, polyethylene is used for making various structural parts in many applications. However, modelling the mechanical behavior of structural parts made of polyethylene is more demanding, as it often requires slightly more complicated material model that includes specific types of behavior like viscoelasticity or plasticity. This contribution is concerned with finite element simulations of tensile test specimens made of polyethylene for geomembranes.

The geomembranes (or geosynthetic barriers) are used as waterproofing elements in construction of civil structures like buildings, roads, railroads, tunnels, solid waste storage sites, reservoirs and many more. Among other tests, the geosynthetics are a subject to tensile tests of specimens directly cut out of the extruded membrane sheets. In these tests, the specimens must achieve a certain level of ductility, which is usually no problem for specimens cut out of smooth-surfaced membranes. However, the surface is often structured on one side or on both sides. The surface features cause the specimens perform worse in the tensile tests. The work described in this contribution is aimed at finding a method for prediction of the performance of real specimens in tensile tests. The prediction should be based on FEM simulations of tests of specimens with various combinations of surface features. The ability to predict the specimens would save substantial costs in developing new types of surface structures for the membranes.

FEM simulation of the specimen was carried out in ANSYS. The material model used in the simulation was based on the tensile test results of the smooth surfaced specimens. The force-deformation dependency obtained from the tests is shown in Fig. 1 (marked as *tensile test*). It has typical features of tensile test results of ductile semicrystaline polymers [3]. The first part is almost linear elastic, then there is the yield point, after which necking occurs. This is marked by a shear drop in

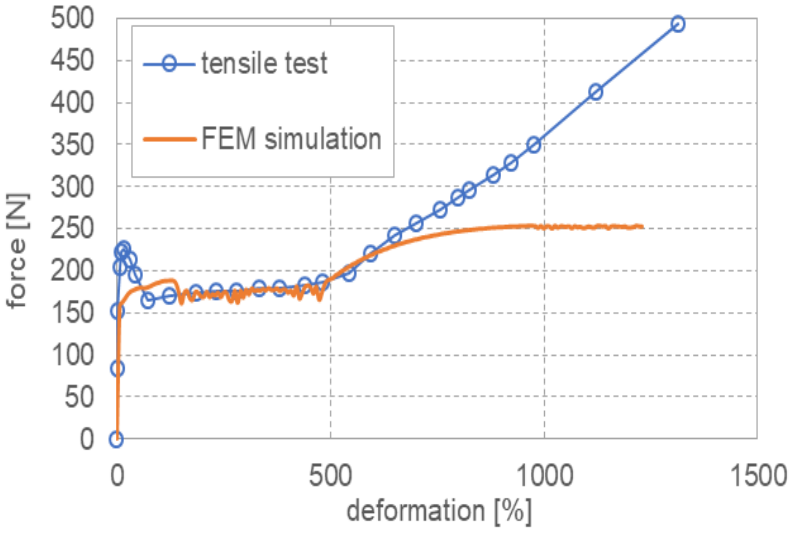

Fig. 1. Comparison of force-deformation dependancy from experiment and FEM simulation

the force. In the second part, the neck propagates until the chain molecules of the material become straight. After that, hardening occurs followed by ultimate failure. Note that the elongation at break goes up to 1200 %. This dependency was recalculated to form a true stress-true strain dependency which was used to define the multilinear material model in the simulation. Isotropic hardening rule was used. Other features of polyethylene material, like viscoelasticity and effect of strain rate, were neglected in the model. The strain rate of the tensile tests was 50 mm/min, which should not influence the results substantially [1, 2], and the viscoelasticity is not playing any significant role in this type of problem.

As a first step in the simulations, the tensile test of a smooth specimen was modelled. The ANSYS Autodyn explicit solver had to be used for the solution because of the very large deformations. The force-deformation dependency was obtained and compared to the dependency from the real tensile test (see Fig. 1). The simulated dependency lacks the force increase before the necking but then the necking propagation takes place at identical force as in the experiment and also the final hardening starts in the right moment. However, the hardening part is not described accurately at all in the area of very large deformations. This might be caused by the fact that only simple logarithmic relationships were used to calculate the true stress and strain for the model and their validity is limited to smaller deformations. This problem will be addressed in further work.

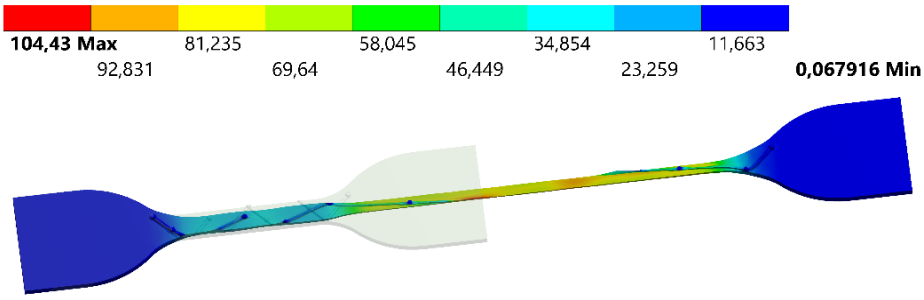

Fig. 2. Simulation of structure-surfaced specimen tensile test

The second step was modeling the structured-surfaced specimens (see Fig. 2). So far, it seems that the models can predict the place, where the necking starts in the tensile tests of structure-surfaced specimens. It can be observed in both the failed specimens and the simulation, that the necking starts in the area, where there is the largest space with no surface features. However, a criterion must be formed to assess where the specimens break and the ability of the specimens to achieve a certain deformation after necking.

Acknowledgements

Results were obtained using equipment from the Large Infrastructures for Research, Experimental Development and Innovation - project IPMinfra, LM2015069. The research was also funded from the Polymer Competence Center Leoben GmbH (PCCL, Austria) within the framework of the COMET-program of the Federal Ministry for Transport, Innovation and Technology and the Federal Ministry for Digital and Economic Affairs with contributions by the Department of Polymer Engineering and Science, Montanuniversität Leoben (Austria). The PCCL is funded by the Austrian Government and the State Governments of Styria, Lower Austria and Upper Austria.

References

[1] Dasari, A., Misra, R.D.K., On the strain rate sensitivity of high density polyethylene and polypropylenes, Journal of Materials Science and Engineering 358 (2003) 356–371.
[2] Kwon, H.J., Jar, P.Y.B., On the application of FEM to deformation of high-density polyethylene, International Journal of Solids and Structures 45 (2008) 3521–3543.
[3] Painter, P.C., Coleman, M.M., Fundamentals of polymer science: An introductory text, Technomic Publishing Company, Inc., Lancaster, 1994.

COMPUTATIONAL MECHANICS 2019
35th conference with international participation
Srní
November 4 - 6, 2019

Energy saving of bipedal walking mechanism

L. Poláček[a] , M. Valášek[a]

[a] *Faculty of machinery, Czech technical University in Prague, Technická 4, 166 07 Praha, Czech Republic*

1. Introduction

The analysis of passive dynamic walkers shows that walking mechanisms have different energy requirements. This logically raises the question of what mechanism is least energy efficient. From this point of view, it is clear, that the best is the wheel. On a flat surface, the center of gravity moves along a straight line, ensuring that energy is not wasted on vertical movement. Thus, the question arises as to how to minimize energy consumption of the walking bipedal mechanism, which has a periodic vertical movement. The solution could be a combination of straight-line mechanism and passive walker.

2. Straight-line mechanism

Generation of straight-line motion using linkage mechanisms has always been a common requirement in machine design practice. Although exact straight line cannot be generated using simple mechanisms though some simple mechanisms are designed such that they can produce approximate straight lines for short range of motion. These approximate straight-line mechanisms have wide applications in machine design. These mechanisms were used in classical machines such as steam engines. Perfect straight lines can also be generated using linkage mechanisms but those are relatively complex mechanisms, [3].

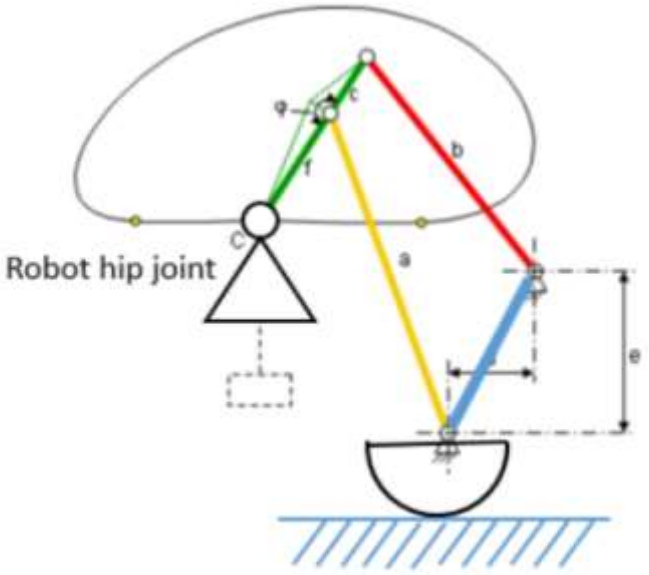

Fig. 1. Crane straight-line mechanism, [2]

3. Passive dynamic walker

Passive-dynamic walkers are simple mechanical devices, comprised of solid parts connected with joints, that can walk stably down a slope. They have no motors or controllers, although can have remarkably human-like motions. Here we present three new robots which extend passive-dynamic walking principles to walking on level ground by using an active power source. These robots use less control and less energy than other powered robots, yet walk more naturally. These results highlight the importance of the coupling between form and function in human and animal locomotion, [1].

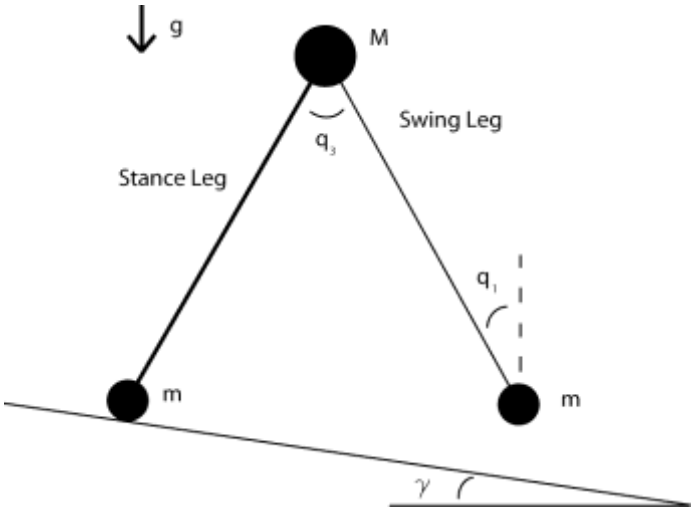

Fig. 2. Passive dynamic walker, [4]

First simulations support that these mechanisms works and that the walking consume relatively same amount of energy as human walking.

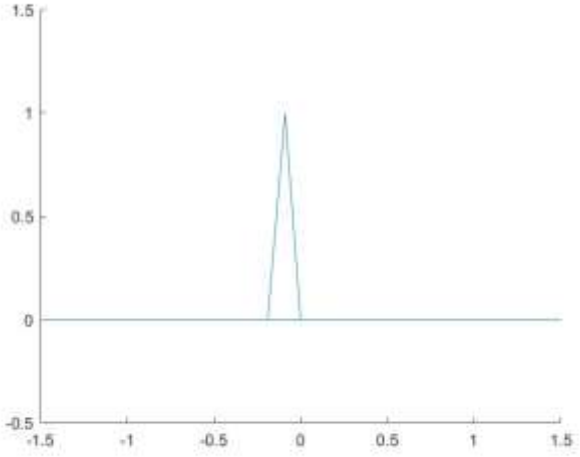

Fig. 3. Simulation of passive dynamic walker

Although these mechanisms move periodically and the hip joint, where center of mass is located, moves vertically in 2D. In 3D the movement is much more complex and involves periodical movement from side to side.

4. Combination of straight-line mechanism and passive dynamic walker

First experimental simulation suggests that it is possible to combine passive dynamic walking and straight-line mechanisms.

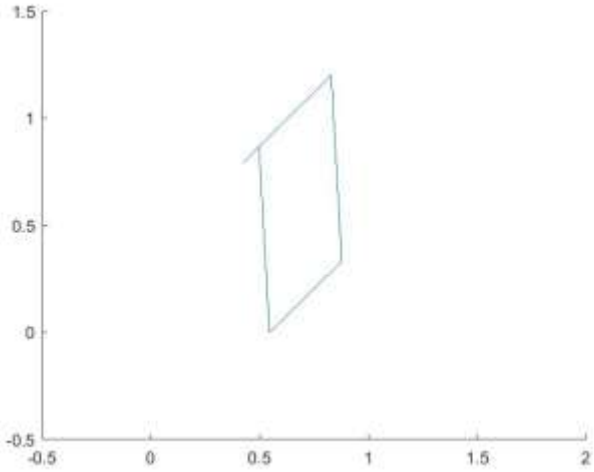

Fig. 4. Straight-line crane mechanism combination with passive dynamic walker

Although these kinds of mechanism are not passive so there have to be some kind of control system and actuation. In design of control it would be necessary to implement need of stable system but most of all low energy consumption. This approach leads to problem of optimal control of underactuated systems.

5. Conclusion

From this point of view and from observing movement of human movement is possible to say that human skeletal mechanism uses some kind of passive dynamic and straight-line mechanism that reduces movement of center of mass. And this way reduces energy consumption.

Acknowledgements

Presented work has been supported by Students Grant Competition of CTU under the project Modelling, control and design of mechanical systems 2019, No. SGS19/157/OHK2/3T/12.

References

[1] Collins, S., Efficient bipedal robots based on passive-dynamic walkers, Science 307 (5712) (20005) 1082-1085.
[2] https://mechmotion.blogspot.com
[3] Naveenagrawal. Kinematics – special mechanisms: Straight line mechanisms, available on: https://www.brighthubengineering.com/machine-design/10568-straight-line-mechanisms/
[4] Ruina, A., Petersen, J., Bhounsule, P., available on: http://ruina.tam.cornell.edu/research/topics/locomotion_and_robotics/ranger/ranger_paper/Reports/Ranger_Robot/control/simulator/simplestwalker.html
[5] Stejskal, V., Valášek, M., Kinematics and dynamics of machinery, Marcel Dekker, Inc., New York, 1996.

COMPUTATIONAL MECHANICS 2019
35th conference with international participation
Srní
November 4 - 6, 2019

Self-excited and flow-induced vibrations of a rotor supported on journal bearings

P. Polach[a], L. Smolík[a], J. Rendl[a], M. Hajžman[a]

[a] *New Technologies for the Information Society, European Centre of Excellence, Faculty of Applied Sciences, University of West Bohemia, Univerzitní 8, 301 00 Plzeň, Czech Republic*

A rotor supported on hydrodynamic journal bearings represents a complex dynamic system, whose vibrations are significantly influenced by fluid films in the journal bearings. Except for resonant frequencies, dangerous self-excited vibrations of the rotor due to oil-whirl and oil-whip instabilities can occur under certain conditions (e.g. [1], [4]). Flow-induced vibrations can occur when journal bearings are poorly lubricated. These vibrations are sub-synchronous and they do not pose a danger for the rotor (e.g. [2], [5]). Self-excited and flow-induced vibrations of the rotor can be predicted using computational models or they can be detected experimentally. Close understanding of behaviour of the journal bearing before, during and after the self-excited and the flow-induced vibrations is the main motivation for the complex research of dynamics and hydrodynamics of the rotor-bearing system. Deep knowledge of relations between the dynamics of a fluid film in journal bearings and the dynamic response of rotating systems of these types of vibration can help to improve designs of many modern rotating machines.

During last few years many aspects regarding the influence of the fluid film in journal bearings on the dynamics of rotor systems were introduced (e.g. [4], [5]). Recent development in numerical methods for nonlinear models and numerical continuation methods allowed the oil-induced instabilities and resulting bifurcations to be studied even deeper. E.g. De Castro et al. [1] implemented nonlinear hydrodynamic forces and predicted oil whirl and oil whip for a real vertical rotor train and for a horizontal test rig. Sub-synchronous fluid-induced vibrations were observed e.g. by DeCamillo in thrust bearings [2]. DeCamillo noted that such vibrations usually occur in poorly lubricated bearings but he was unable to identify all conditions that can lead to the reported sub-synchronous vibrations. The problem of the sub-synchronous fluid-induced vibrations is not commonly studied in available literature and, therefore, the investigation of this problem is a challenge.

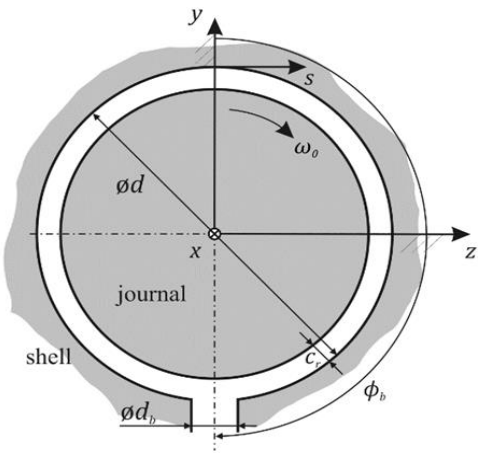

Fig. 1. Geometry of the journal bearing

There are several common methods for the modelling and dynamic analysis of rotating systems. The approaches are based on the finite element method (for the one-dimensional Euler-Bernoulli and/or Timoshenko continua) or on multibody dynamics. Journal bearings are represented by nonlinear forces acting at points corresponding to the bearing support. The oil film dynamic behaviour is described by the Reynolds equation. It has to be solved in each time integration step and the resultant pressure distribution is transformed into dynamic

forces, which are subsequently included into equations of motion.

Equations of motion for the rotor supported on journal bearings that are used in this work are derived based on a multi-body formalism. Motions of the rotor are decomposed to global (gross) motions and elastic motions (vibrations) in this approach. In order to simulate both types of the motion, the system of differential algebraic equations is employed, [3], (time t is omitted for a better clarity)

$$\mathbf{M}\,\ddot{\mathbf{q}} + \mathbf{f}^{rb}(\mathbf{z},\dot{\mathbf{z}}) = \mathbf{f}^{gyr}(\mathbf{z}) + \mathbf{f}^{j}(\mathbf{z},\boldsymbol{w}) + \mathbf{f}^{e}(\mathbf{z}) - \mathbf{D}\,\dot{\mathbf{q}} - \mathbf{K}\,\mathbf{q}, \tag{1}$$

$$\mathbf{S}(\boldsymbol{\theta}_B)\,\dot{\boldsymbol{\theta}}_B = \boldsymbol{\Omega}_B, \tag{2}$$

$$\boldsymbol{\theta}_B^{\top}\,\boldsymbol{\theta}_B = 1, \tag{3}$$

$$\mathbf{r}(\mathbf{q}) = \mathbf{0}. \tag{4}$$

The position, the orientation and the deformation of the rotor are included in state vector $\mathbf{z} = [\mathbf{x}_B^{\top}, \boldsymbol{\theta}_B^{\top}, \dot{\mathbf{x}}_B^{\top}, \boldsymbol{\Omega}_B^{\top}, \mathbf{q}^{\top}, \dot{\mathbf{q}}^{\top}]^{\top}$. Vector $\mathbf{x}_B$ and quaternion $\boldsymbol{\theta}_B$ characterize the position and the orientation of the rotor, respectively, and vector $\mathbf{q}$ contains elastic coordinates relative to a coordinate system whose position is defined by vector $\mathbf{x}_B$ and whose orientation is given by four Euler parameters in quaternion $\boldsymbol{\theta}_B$. Vector $\mathbf{w}$ is composed of state vectors of all bodies coupled to the rotor. $\mathbf{M}, \mathbf{D}, \mathbf{K}$ are constant matrices, which characterize mass, damping and stiffness of the rotor, respectively. $\mathbf{f}^{rb}, \mathbf{f}^{gyr}$ are vectors of forces, which result from the rigid body accelerations and gyroscopic effects, respectively. Vector $\mathbf{f}^{j}$ accommodates forces in couplings and $\mathbf{f}^{e}$ contains prescribed external forces and moments.

Equation (2) describes the relation between angular velocity $\boldsymbol{\Omega}_B$ of the global motion and quaternion $\boldsymbol{\theta}_B$, (3) is the normalization condition and (4) is introduced in order to obtain a unique separation of the global and the elastic coordinates. These additional equations are described in detail e.g. by Offner et al. [3].

The forces acting on the rotor in its journal bearings are obtained using the solution of the Reynolds equation. These so-called hydrodynamic forces can be evaluated by integrating a pressure in an oil film over the surface of the bearing. Here it is assumed, that the oil is an incompressible Newtonian fluid, the film is thin and the flow in the film is laminar. Furthermore, cavitation may occur and mass conservation in cavitated areas is considered. Pressure $p = p(s,x,t)$ is then governed by the Reynolds equation in the form (see e.g. [5]):

$$\frac{\partial}{\partial s}\left(\frac{\theta\,h^3}{12\,\mu}\,\frac{\partial p}{\partial s}\right) + \frac{\partial}{\partial x}\left(\frac{\theta\,h^3}{12\,\mu}\,\frac{\partial p}{\partial x}\right) = \frac{u_j+u_s}{2}\,\frac{\partial(\theta\,h)}{\partial s} + \frac{\partial(\theta\,h)}{\partial t}, \tag{5}$$

where s, x are the circumferential and axial coordinates, respectively. These coordinates are depicted in Fig. 1. Function $h = h(s,x,t)$ determines the gap between a journal and a shell, $\theta = \theta(s,x,t)$ is the percentage of the bearing gap that is filled with oil, $\mu = \mu(s,x,t)$ is the dynamic viscosity of the oil and u_j, u_s are the surface velocities of the journal and the shell, respectively. Note that there are two unknown variables in (5): p and θ. For $t = 0$, ratio θ is prescribed by initial conditions (usually $\theta = 1$) and (5) is solved for p. If p drops below the value of saturation pressure p_c at any node then the Gümbel condition (i.e. $p = p_c$) is applied and (5) is solved for θ.

Table 1. Nominal parameters of journal bearings (valid for both the rotors [4], [5])

Parameter	Symbol	Value	Parameter	Symbol	Value
bearing diameter	d	38.0 mm	ambient pressure	p_a	1.00 bar
bearing length	l	20.0 mm	saturation pressure	p_c	0.98 bar
radial clearance	c_r	40.5 μm	supply pressure	p_s	1.25 bar
lubricant viscosity	μ	28.3 mPa·s	supply bore diameter	d_b	5.00 mm

Different rotor-bearing systems were considered in order to investigate self-excited and flow-induced vibrations of the rotor. Geometry of the journal bearings was the same for the investigation of both vibration types, see Fig. 1. Parameters of the bearings are summarized in Table 1. The RENOLIN VG 46 lubricant is supplied to the bearings through a circular supply bore, which is located in the lower half of the bearing shell.

The proposed configuration of the test rig for the investigation of oil-whirl and oil-whip is shown in Fig. 2. The shaft in this configuration is rather slender and a massive disc is attached to the shaft.

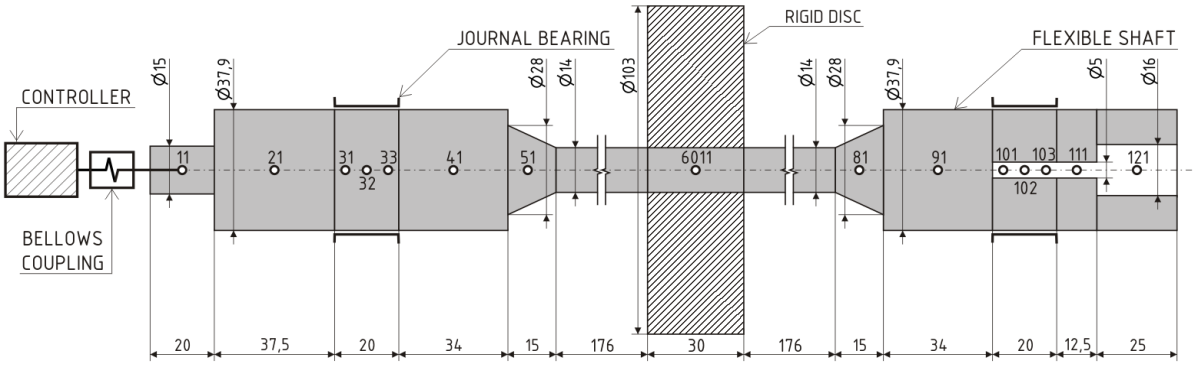

Fig. 2. Geometry and discretization of the rotor for the investigation of oil-whirl and oil-whip instabilities, [4]

The simulations suggest (Fig. 3b) that the oil-whip develops at frequency of rotation f_r in the range of 100–106 Hz (6,000–6,350 RPM) with a dominant response at 50–52 Hz, which corresponds with the first bending mode. Further simulations suggest that the threshold speed for the oil-whip is only little sensitive to the radial clearance or the lubricant dynamic viscosity. Furthermore, there is a short speed interval in which the oil-whirl takes place (92–98 Hz). Although the proposed test rig geometry is suitable for the investigation of both oil-whirl and oil-whip, a prolonged operation under oil-whip conditions is impossible because of a high level of vibrations of the disc, which exceed 1 mm peak-to-peak (Fig. 3a).

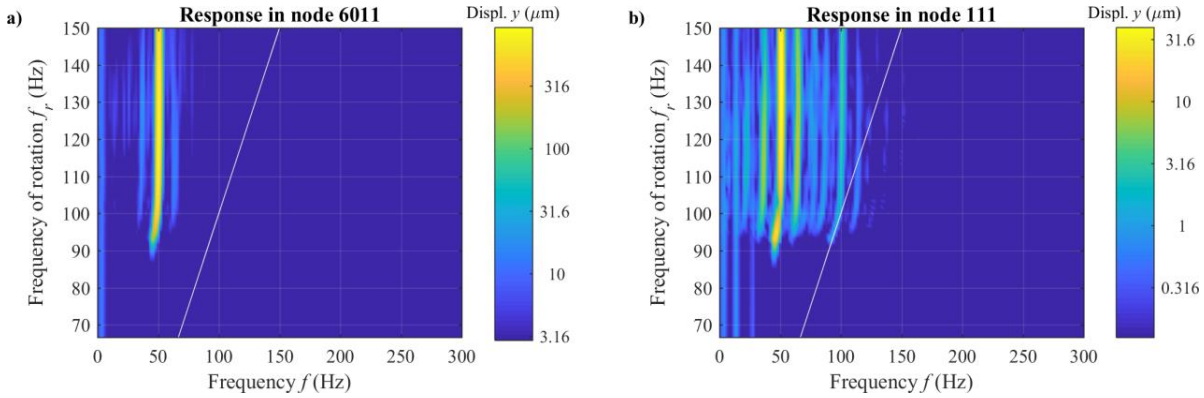

Fig. 3. Simulated steady state response of the perfectly balanced rotor from Fig. 2 (taken from [4]). Response of the rigid disc (a) and of the journal in the bearing at the non-drive end (b).

An arrangement and dimensions of the analysed system for the investigation of flow-induced vibrations are depicted in Fig. 4. The system consists of the rotor supported on two journal bearings and a controller, which controls the speed of the rotor.

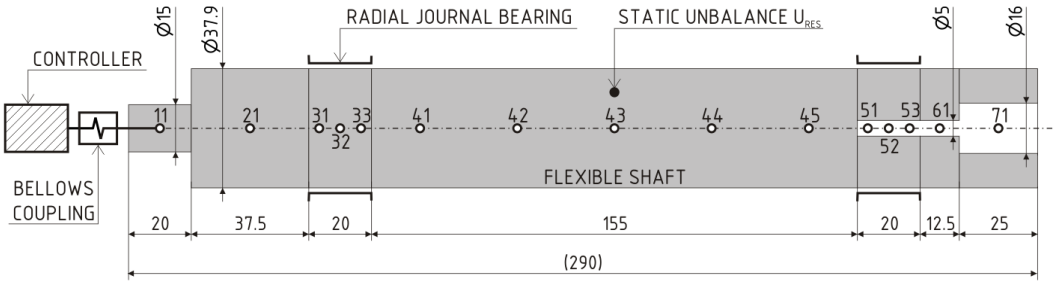

Fig. 4. Geometry and discretization of the rotor for the investigation of the sub-synchronous flow-induced vibrations, [5]

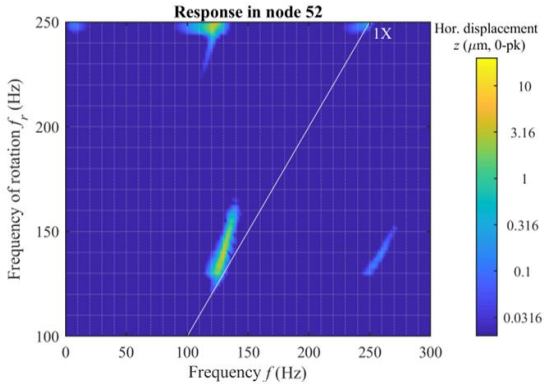

Fig. 5. Steady-state response of the perfectly balanced rotor for the investigation of the sub-synchronous flow-induced vibrations, [5]

The steady-state response of the perfectly balanced rotor was simulated for frequency of rotation f_r in the range of 100–250 Hz. The response was analysed in time interval 1–2 seconds and is depicted in Fig. 5. Flow-induced vibrations manifest themselves as a sub-synchronous component, which appears at $f_r \approx 130$ Hz and disappears at $f_r \approx 160$ Hz. Moreover, self-excited vibrations develop at $f_r \approx 245$ Hz at the frequency of $0.48 \times f_r$.

The reported sub-synchronous flow-induced vibrations can occur only if the rotor is well balanced (balance quality grade G1 or lower in accordance with ISO 21940-1), and if it is radially supported on poorly lubricated journal bearings, whose supply bores are located in the lower half of the bearings. These vibrations are stable and cover roughly 10 % of the bearing clearance and, therefore, they are not dangerous. However, they might be undesirable in precise machinery.

Acknowledgements

The paper has originated in the framework of solving No. 17-15915S project of the Czech Science Foundation entitled "Nonlinear dynamics of rotating systems considering fluid film instabilities with the emphasis on local effects". Simulations were performed in the AVL Excite software which is available in the framework of the University Partnership Program of AVL List GmbH and its usage is greatly acknowledged.

References

[1] De Castro, H.F., Cavalca, K.L., Nordmann, R., Whirl and whip instabilities in rotor-bearing system considering a nonlinear force model, Journal of Sound and Vibration 317 (1-2) (2008) 273-293.

[2] DeCamillo, S., Current issues regarding unusual conditions in high-speed turbomachinery, Proceedings of the 5th EDF & LMS Poitiers Workshop: Bearing Behavior Under Unusual Operating Conditions, Paris, 2006, pp. A.1-A.10.

[3] Offner, G., Eizenberger, T., Priebsch, H.H., Separation of reference motions and elastic deformations in an elastic multi-body system, Proceedings of the Institution of Mechanical Engineers, Part K: Journal of Multi-body Dynamics 220 (1) (2006) 63-75.

[4] Polach, P., Smolík, L., Rendl, J., Hartl, M., Omasta, M., Dyk, Š., Investigation of rotor dynamics with fluid film instabilities II, Proceedings of the 24th International Conference Engineering Mechanics, Svratka, 2018, pp. 689-692.

[5] Smolík, L., Polach, P., Rendl, J., Sub-synchronous vibrations of a rotor supported on poorly lubricated journal bearings, Book of full texts of the 25th International Conference Engineering Mechanics, Svratka, 2019, pp. 339-342.

COMPUTATIONAL MECHANICS 2019
35th conference with international participation
Srní
November 4 - 6, 2019

Numerical and experimental investigation of compressible viscous fluid flow in minichannels

H. Prausová[a], O. Bublík[a], J. Vimmr[a], J. Hála[b], M. Luxa[b]

[a] *NTIS – New Technologies for the Information Society, Faculty of Applied Sciences, University of West Bohemia, Technická 8, 301 00 Plzeň, Czech Republic*

[b] *Institute of Thermomechanics, Czech Academy of Sciences, Dolejškova 1402/5, 182 00 Praha 8, Czech Republic*

1. Introduction

The work deals with compressible viscous fluid flow in narrow channels with rectangular cross-section with high aspect ratio. The characteristic dimension is the height of the channel which is varied from 0.5 to 10 mm. The issue of fluid flow in a straight channel may appear very easy thanks to the simplicity of the geometry and many commonly known facts. The opposite is true in case of narrow channels and compressible fluid. The study is focused on the value of critical Reynolds number Re_c and also on suitable approaches to the measuring and modelling of such flows. The usually known value of $Re_c \approx 2\,300$ is derived for channels of ordinary dimensions. In microchannels (height to 200 μm) the laminar flow can be stable to the values of $Re_c \approx 10^4$. The study aims mostly at minichannels (height between 200 μm and 3 mm), where the situation is very poorly explored, especially in case of a compressible fluid. Fluid flow in narrow channels and gaps of various cross-sections is a phenomenon occuring in many technical applications, such as clearance gap flow in control valves of steam turbines, tip leakage flow in gas and steam turbines, clearance gaps in screw compressors etc., and it is therefore important to further develop knowledge in this area.

The experimental part of the study is taking place in the Institute of Thermomechanics of the CAS, v.v.i., where properties of air flow through the channels were measured. The air is sucked in the channel through the shaped inlet area, then it is accelerated thanks to the selected pressure drop and behind the channel the air flows into the free space represented by a settling chamber. The appropriate pressure is maintained in the settling chamber. Distribution of static and total pressure was measured in the channel axis together with wall shear stress. Interferograms were also obtained in several cases. Experiments are performed in a calibration channel of height 10 mm and sufficient length for the flow to get fully developed. This channel serves for calibration of mesurement techniques and for validation of numerical solver for this type of flow. Experiments and numerical simulations in minichannels are then carried out for heights from 0.5 to 4 mm and conclusions concerning critical Reynolds number are drawn from them.

2. Numerical discretization using discontinuous Galerkin method

Laminar and fully turbulent numerical simulations were performed to examine compressible fluid behaviour in minichannels. The in-house numerical solver based on the discontinuous Galerkin finite element method [1, 2] is used. Mathematical model of laminar compressible

viscous fluid flow is formed by the system of Navier-Stokes equations in 2D. In case of turbulent simulations the system is Favre averaged and closed by the two-equation k-ω turbulence model of Wilcox [4]. Spatial discretization of the mathematical model is accomplished by the discontinuous Galerkin method (DGM), using second order of accuracy and Langrange basis functions. Time discretization is realized with first order of accuracy using an implicit scheme and GMRES method.

Despite of many advantages of the discontinuous Galerkin method, discretization of the two-equation turbulence model by DGM causes serious problems with stability of numerical simulations. Modifications of the turbulence model are employed for this reason, namely the logarithmic formulation of the transport equation for specific dissipation rate ω [3] and restriction of turbulent kinetic energy k.

3. Validation of experimental and numerical methods in calibration channel

Geometry of the calibration channel computational domain and appropriate boundary conditions are shown in Fig. 1. The real channel is the thin middle part of length 1526 mm and the small inlet area of length 114 mm. The large added inlet and outlet areas are necessary to prevent boundary conditions to influence natural intake of air into the channel and free outflow into the settling chamber. The computational domain is discretized by a structured computational grid properly refined near the walls and in the outflow area, where shock waves occur in case of an over-critical pressure ratio. Considering the dimensions of the channel and velocity of the flow, the numerical simulation is performed as fully turbulent. There is a distribution of static and total pressure in channel axis for pressure ratio 0.3 shown in Fig. 2, numerical results are compared to the experimental ones. Similar results are obtained for two under-critical pressure ratios 0.6 and 0.8. Wall shear stress distribution for all pressure ratios is show in Fig. 3. Experimental and numerical values of the wall shear stress are in very good agreement except for the first three measured points, where the flow is not yet fully developed and the used measuring technique (sublayer fence probe) gives not quite reliable values. Despite small disagreement in the total pressure we consider the numerical solver suitable for use in minichannels.

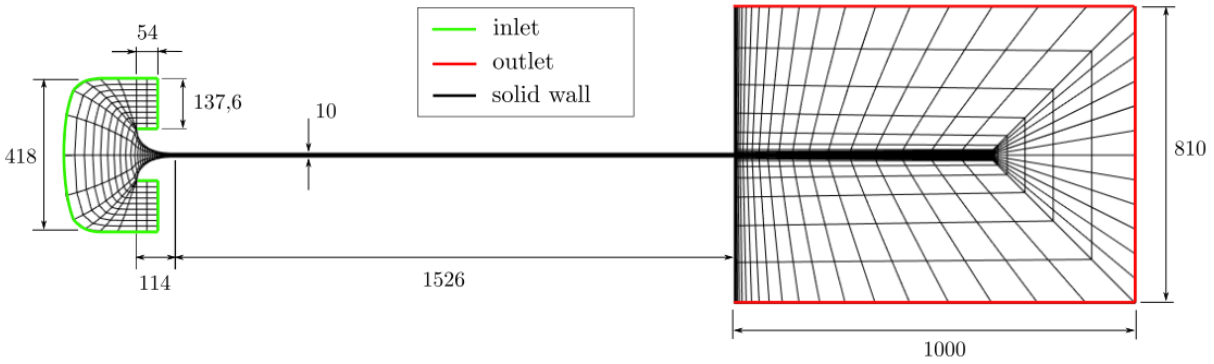

Fig. 1. Geometry of computational domain for the calibration channel with highlighted boundary conditions; dimensions are in millimetres, grid density is only illustrative

4. Compressible fluid flow in minichannels of height 0.5 to 4 mm

Geometry of the computational domain for minichannels is very similar to the one of the calibration channel. The height is set to 0.5, 2, 3 and 4 mm and the length is 92 mm. Only static pressure is measured in minichannels because of the small dimensions of the channel. Estimated Reynolds numbers for all minichannels lie above commonly recognized critical value,

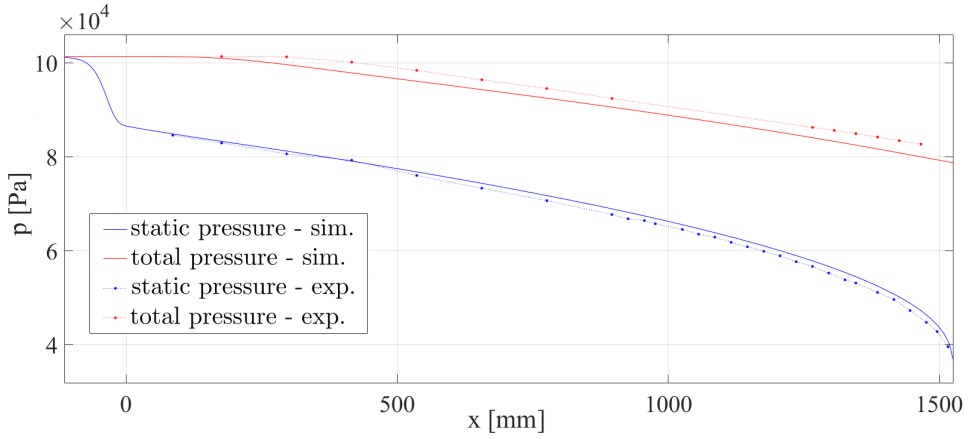

Fig. 2. Distribution of static and total pressure in calibration channel axis for pressure ratio 0.3

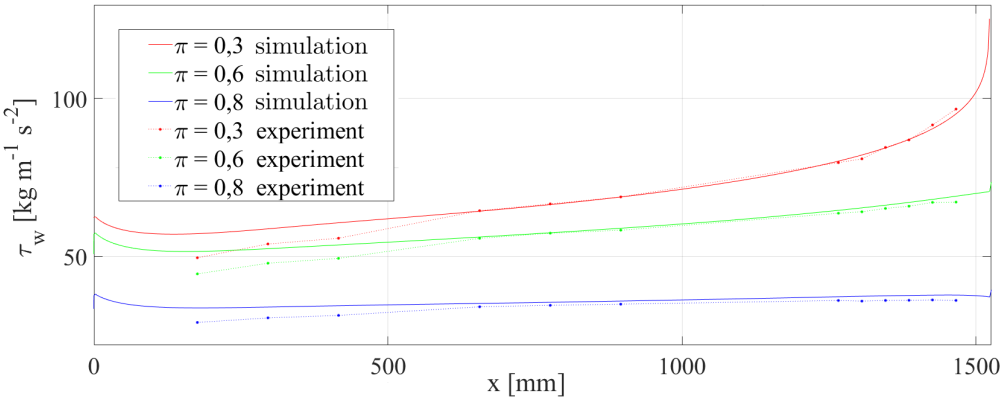

Fig. 3. Distribution of wall shear stress in calibration channel for all three pressure ratios

but due to many uncertainties in this area both laminar and fully turbulent simulations are performed. Numerical results in comparison with experimental data are shown in Fig. 4 for channel of height 3 mm. For all four channels we get similar numerical results. For channels of height up to 2 mm the experimental values fit very closely the laminar curve. From 3 mm we can observe clear deviation from laminar curve as in Fig. 4. Nevertheless the experimental values stay far from the turbulent curve. They come close to the turbulent curve only at the end of the channel. Reynolds number in the channel based on the height of the channel and approximate velocity in the vertical cross-section is at least $Re_c \approx 17\,000$ for the height 2 mm, which is far above the supposed critical values. In this case the flow turns out to be laminar in the whole channel.

5. Conclusions

The obtained results indicate that there starts a transition from laminar to turbulent flow in channel of height around 3 mm. An intermittent regime may occur in the channel. Where exactly in the channel and for which height the transition occures is a very difficult question. We must have a proper model of transition to answer this question. Since essentially almost all current models of transition are calibrated for flow around the body, there is a need to calibrate one of them for internal flows and broadly test it with help of experimental data.

The shift of the critical Reynolds number to the value of approximately $17\,000$ is an important result. It confirmes the assumption of the need to treat minichannels differently than

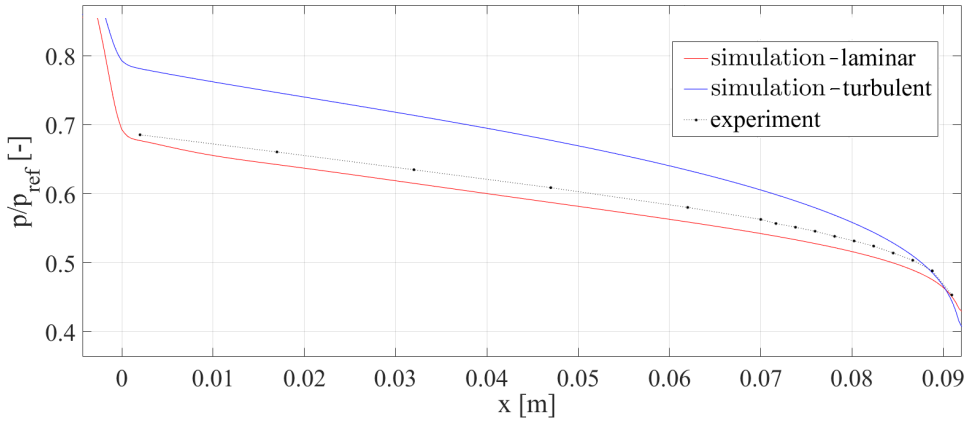

Fig. 4. Distribution of static pressure in channel of height 3 mm, pressure ratio 0.189

common channels or microchannels. The chosen approaches and numerical methods prove themselves to be suitable for investigation of the compressible viscous fluid flow in narrow channels and can be used for future research in this area.

Acknowledgements

This work was supported by the project LO1506 of the Czech Ministry of Education, Youth and Sports under the program NPU I, and by the project SGS-2019-009.

References

[1] Bassi, F., Crivellini, A., Rebay, S., Savini, M., Discontinuous Galerkin solution of the Reynolds-averaged Navier-Stokes and k-ω turbulence model equations, Computers & Fluids 34 (2005) 507-540.

[2] Bublík, O., Aplication of discontinuous Galerkin finite element method for the solution of flow problems, Ph.D. thesis, University of West Bohemia, 2014. (in Czech)

[3] Ilinca, F., Pelletier, D., Positivity preservation and adaptive solution for the k-ϵ model of turbulence, AIAA Journal 36 (1) (1998) 44-50.

[4] Wilcox, D. C., Turbulence modeling for CFD, DCW Industries, La Cañada, California, 2006.

COMPUTATIONAL MECHANICS 2019
35th conference with international participation
Srní
November 4 - 6, 2019

Galerkin method for approximate modelling of finite-length journal bearings

J. Rendl[a]

[a] NTIS – New Technologies for the Information Society, Faculty of Applied Sciences, University of West Bohemia, Univerzitní 8, 301 00 Plzeň, Czech Republic

Galerkin method as a weighted residual method is one of many possible approaches to solve a partial differential equation whose solution is approximated by combination of trial functions. These functions are mutually linearly independent and satisfy boundary conditions.

Pressure field in a circular journal bearing is governed by Reynolds equation in the dimensionless form [2]

$$\frac{\partial}{\partial\varphi}\left(\overline{h}^3\frac{\partial\overline{p}}{\partial\varphi}\right)+\left(\frac{R}{L}\right)^2\frac{\partial}{\partial\overline{Z}}\left(\overline{h}^3\frac{\partial\overline{p}}{\partial\overline{Z}}\right)=\left(2\frac{\dot{\gamma}}{\omega}-1\right)\varepsilon\sin\varphi+2\frac{\dot{\varepsilon}}{\omega}\cos\varphi, \tag{1}$$

where $\overline{p}(\varphi,\overline{Z})$ is the dimensionless pressure field, φ and $\overline{Z}$ are the circumferential and axial coordinates, respectively, ω is the angular speed, R is the radius of a bearing shell, L is the length of a bearing, $\overline{h}$ is the dimensionless height of thin oil film, ε is the relative eccentricity and $\dot{\varepsilon}$ and $\dot{\gamma}$ are the velocities of relative eccentricity and attitude angle, respectively.

Unknown pressure distribution in the circular journal bearing is approximated by Fourier series in circumferential direction and by goniometric sinus function in axial direction. Final form of the pressure field approximation [1] is written as

$$\overline{p}\approx\hat{p}\left(\varphi,\overline{Z},t\right)=\overline{p}_{amb}+\sum_{i=0}^{N_O}\sum_{j=1}^{N_A}\left[a_{i,j}\sin\left(i\varphi\right)+b_{i,j}\cos\left(i\varphi\right)\right]\sin\left(j\pi\overline{Z}\right), \tag{2}$$

where $\overline{p}_{amb}$ is the dimensionless ambient pressure, $a_{i,j}, b_{i,j}$ are unknown coefficients of Fourier series and $N_O, N_A \in \mathbb{N}$ are the numbers of trial functions in the circumferential and axial direction. Aim of weighted residual methods is to minimize a residuum [1]

$$r=\frac{\partial}{\partial\varphi}\left(\overline{h}^3\frac{\partial\hat{p}}{\partial\varphi}\right)+\left(\frac{R}{L}\right)^2\frac{\partial}{\partial\overline{Z}}\left(\overline{h}^3\frac{\partial\hat{p}}{\partial\overline{Z}}\right)-\left[\left(2\frac{\dot{\gamma}}{\omega}-1\right)\varepsilon\sin\varphi+2\frac{\dot{\varepsilon}}{\omega}\cos\varphi\right]. \tag{3}$$

In the case of the Galerkin method, weight functions are the same as the trial functions and final generalized scalar multiplication is defined as follows

$$\int_0^1\int_0^{2\pi} r\cdot\left[\sin\left(k\varphi\right)+\cos\left(k\varphi\right)\right]\sin\left(l\pi\overline{Z}\right)\,\mathrm{d}\varphi\,\mathrm{d}\overline{Z}=0. \tag{4}$$

After consecutive generalized scalar multiplication by all weight functions, final system of algebraic equations can be rewritten into matrix form [1]

$$\begin{bmatrix}\mathbf{A}&\mathbf{0}\\\mathbf{0}&\mathbf{B}\end{bmatrix}\begin{bmatrix}\mathbf{a}\\\mathbf{b}\end{bmatrix}=\begin{bmatrix}\mathbf{f_1}\\\mathbf{f_2}\end{bmatrix},\qquad \mathbf{A}^{(\mathrm{GAL})}\mathbf{x}^{(\mathrm{GAL})}=\mathbf{f}^{(\mathrm{GAL})}, \tag{5}$$

where all unknown coefficients $a_{i,j}, b_{i,j}$ from Eq. (2) are associated into corresponding subvectors $\mathbf{a} \in \mathbb{R}^{N_A N_O,1}$ and $\mathbf{b} \in \mathbb{R}^{N_A(N_O+1),1}$. Coefficients $a_{0,j} = 0$ for $j = 1, 2, \ldots, N_A$. Submatrices $\mathbf{A} \in \mathbb{R}^{N_A N_O, N_A N_O}$ and $\mathbf{B} \in \mathbb{R}^{N_A(N_O+1), N_A(N_O+1)}$ are sparse, diagonal and regular. Each element of submatrices results from solution of each integral (4) and similarly for right-hand side subvectors $\mathbf{f}_1 \in \mathbb{R}^{N_A N_O,1}$ a $\mathbf{f}_2 \in \mathbb{R}^{N_A(N_O+1),1}$. Based on mutual orthogonality of goniometric functions, the elements of submatrices and subvectors are analytically derivable.

Hydrodynamic force is determined by the hydrodynamic pressure and the force components are obtained from pressure integration

$$\begin{bmatrix} F_{rad}^{hd} \\ F_{tan}^{hd} \end{bmatrix} \approx RL \frac{6\mu R^2 \omega}{c^2} \int_{-\frac{1}{2}}^{\frac{1}{2}} \int_{0}^{\pi} \hat{p}(\varphi, \overline{Z}, t) \begin{bmatrix} \cos\varphi \\ \sin\varphi \end{bmatrix} \mathrm{d}\varphi \, \mathrm{d}\overline{Z}, \tag{6}$$

where μ is the dynamic viscosity, c is the radial clearance and pressure field $\hat{p}$ satisfies half-Sommerfeld boundary condition [2]. Components of the hydrodynamic force can be written in the closed form using previously calculated coefficients $a_{i,j}, b_{i,j}$ from Eq. (5). The hydrodynamic force can be expressed in Taylor series and linearized stiffness and damping coefficients of fluid film can be found. Stability of a rotor-bearing system is then determined based on Routh-Hourwitz stability criterion [2].

Presented Galerkin method (GAL) was applied on chosen bearing system with following parameters: $R = 50$ mm, $L = 100$ mm, $c = 0.8$ mm, $\mu = 0.04$ Pa.s, $p_{amb} = 0$ Pa and bearing load $F_0 = -147.15$ N. In-house software [3] with implemented solver based on finite difference method (FDM) was also used in order to perform comparison with obtained results. Comparison of journal trajectories and stability borderlines for both applied methods is depicted in Fig. 1. Intersection point of these two curves is a moment when system becomes unstable.

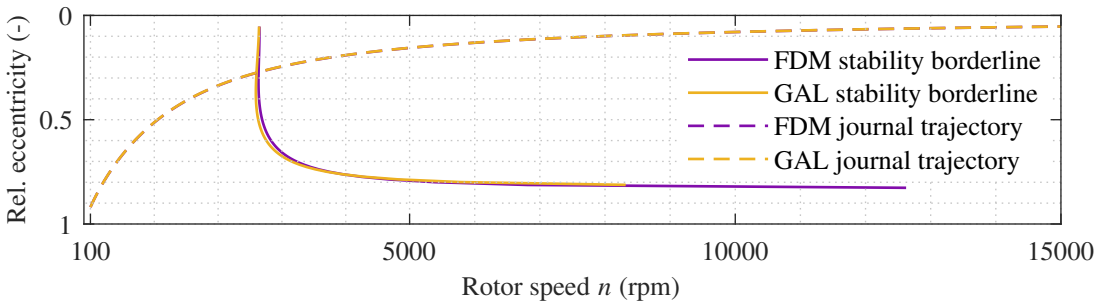

Fig. 1. Comparison of journal trajectories and stability borderlines

Acknowledgements

This publication was supported by project SGS-2019-009 and by project 17-15915S of Czech Science Foundation entitled Nonlinear dynamics of rotating systems considering fluid film instabilities with the emphasis on local effects.

References

[1] Chatzisavvas, I., Efficient thermohydrodynamic radial and thrust bearing modeling for transient rotor simulations, Ph.D. thesis, Darmstadt, TU Darmstadt, 2018.

[2] Chen, W. J., Practical rotordynamics and fluid film bearing design, Trafford Publishing, 2015.

[3] Rendl, J., Software for investigation of dynamic behaviour of rotating systems supported on journal bearings, Proceedings of the conference Applied Mechanics 2019, Ostrava, VSB – Technical University of Ostrava, 2019, pp. 184-188.

COMPUTATIONAL MECHANICS 2019
35th conference with international participation
Srní
November 4 - 6, 2019

Application of structural modification for beam vibration control

L. Rolník[a], M. Nad'[a], L. Kolíková[a] , R. Ďuriš[a]

[a] *Faculty of Materials Science and Technology in Trnava, Slovak University of Technology in Bratislva, J. Bottu 25, 917 24 Trnava, Slovak Republic*

The beam as one of the fundamental structural elements is very often used in the engineering application - mechanical and civil engineering. During operation, these structures may be subjected to periodic dynamic loading forces, which in certain adverse cases may cause their resonance state. The possibility of reducing the level of undesirable vibrations or preventing their occurrence should be one of the important objectives in the design of the structure. The design and analysis of the beam structure that will allow its spatial properties (mass and stiffness) to be redistributed using the displaceable core inserted into the beam structure is investigated in this paper. The change in the deflection of a beam loaded by the force effect that causes its resonance state, depending on the redistribution of spatial properties (based on the position of the reinforcement core), is studied.

The structural model enabling continuous modification of dynamic properties of the beam structure by inserting the reinforcement core is shown in Fig.1. The basic shape of beam body has a length L_0 and a rectangular cross-section - width b_0 and height h_0. In the longitudinal direction, a hole with a radius r_c for insertion reinforcing the core is drilled into the beam body. The top surface of the beam structure is loaded with time-varying pressure $p_y(t)$. The different material properties are considered for beam body and movable core. The following assumptions are considered in the mathematical model of beam composite structure modified by the reinforcing core - beam cross section is planar before and during deformation, isotropic and homogeneous material properties of beam structural parts are assumed, mutual displacements of interacting points between beam body and core are the same, i.e. perfect adhesion is assumed for the corresponding points perfect adhesion at the interfaces of beam structural parts is supposed.

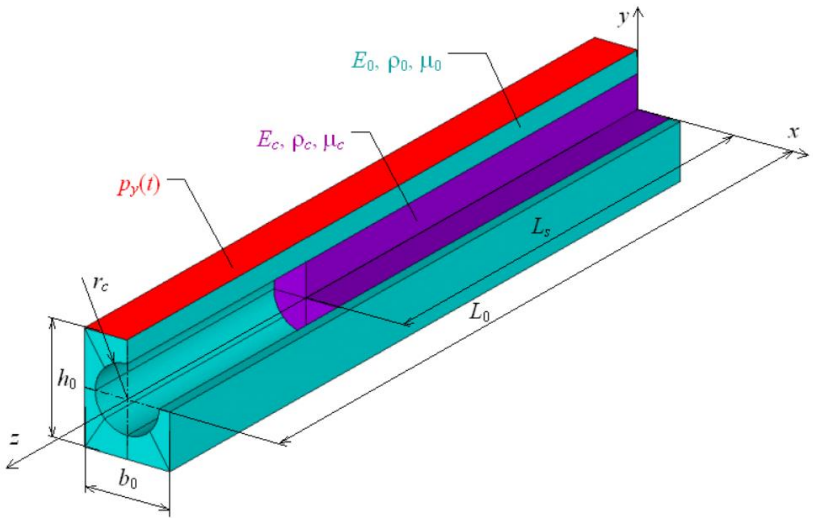

Fig. 1. Structural model of modified beam structure

The model of considered beam structure is divided into two segments with different cross-sections. The general equation of motion for forced bending vibration of *k*-th segment of considered beam structure [1,2] can be expressed in the following form

$$\frac{\partial^2}{\partial x_k^2}\left[(EJ)_k \frac{\partial^2 w_k(x_k,t)}{\partial x_k^2}\right] + (\rho S)_k \frac{\partial^2 w_k(x_k,t)}{\partial t^2} = p_y(t), \quad (k = 1,2), \tag{1}$$

where $w_k(x_k,t)$ - beam displacement in *k*-th segment, $p_y(t)$ - uniform pressure acting on top surface of beam and cross-section parameters of *k*-th segment of beam structure are

- bending stiffness $(EJ)_k = E_0 J_0[(1-\kappa_J) + \delta_k \kappa_E \kappa_J]$, (2)
- unit mass $(\rho J)_k = \rho_0 S_0[(1-\kappa_S) + \delta_k \kappa_\rho \kappa_S]$. (3)

The dimensionless parameters applied in (2), (3) are defined by $\kappa_S = S_c/S_0$, $\kappa_J = J_c/J_0$, $\kappa_E = E_c/E_0$, $\kappa_\rho = \rho_c/\rho_0$. The following is applied for $\delta_{k=1\div 2}\begin{cases}=1; & S_k = S_0 + S_c \text{ and } J_k = J_0 + J_c \\ =0; & S_k = S_0 \text{ and } J_k = J_0\end{cases}$, where *S* is cross-section area and *J* is quadratic moment of cross-section for full beam cross-section (subscript 0) and core (subscript *c*).

After application $w_k(x_k,t) = W_k(x_k)T(t)$ into (1) (for $p_y(t) = 0$), the differential equation of the *k*-th segment for determination of mode shapes and natural angular frequency for complete beam structure [2] has the following form

$$\overline{W}_k^{IV}(\xi_k) - \beta_k^4 \overline{W}_k(\xi_k) = 0, \tag{4}$$

where $\beta_j^4 = \omega_{0,m}^2 \left(\frac{\rho_0 S_0}{E_0 J_0} L_0^4\right) f_m(\delta_k, \kappa_S, \kappa_E, \kappa_J, \kappa_\rho)$ is a frequency parameter, $\overline{W}_k(\xi_k) = W_k(x_k)/L_0$, $\xi_k = x_k/L_0$ and x_k is position of cross-section in *k*-th segment.

The states of resonant behavior of the beam structure, which is caused e.g. by the action of harmonic pressure $p_y(t) = p_0 \sin(\omega t)$, can be eliminated by the insertion of a reinforcing core. During the core insertion process, the stiffness and mass parameters are redistributed and this new structural state leads to a change in the resonant frequency [2] and and this also causes a change in the deflection of the beam structure.

Acknowledgements

The work has been supported by the education research project KEGA 029STU-4/2018 and research project VEGA-1/1010/16.

References

[1] Meirovitch, L., Analytical methods in vibrations, McMillan Comp., London, 1987.

[2] Naď, M., Rolník, L., Čičmancová, L., Prediction of changes in modal properties of the Euler–Bernoulli beam structures due to the modification of its spatial properties, International Journal of Structural Stability and Dynamic 17 (9) (2017).

[3] Timoshenko, S.P., Young, D.H., Weawer, W., Vibration problems in engineering, John Wiley & Sons, New York, 1985.

COMPUTATIONAL MECHANICS 2019
35th conference with international participation
Srní
November 4 - 6, 2019

Application of the entropy based criteria on the ECG analysis

J. Rosenberg[a], M. Krejčová[a], L. Nalos[b,c], D. Jarkovská[b,c], M. Štengl[b,c]

[a] *NTIS – New Technologies for the Information Society, Faculty of Applied Sciences, University of West Bohemia, Technická 8, 301 00 Plzeň, Czech Republic*
[b] *Biomedical Center, Faculty of Medicine in Pilsen, Charles University, alej Svobody 1655/76, 323 00 Plzeň, Czech Republic*
[c] *Department of Physiology, Faculty of Medicine in Pilsen, Charles University, alej Svobody 1655/76, 323 00 Plzeň, Czech Republic*

This contribution follows up the paper [3] dealing with the finding of the best deterministic approximation of the Brownian motion using the known thermostatic oscillator. The purpose was to use this approximation in the model of the molecular motor dynein. We used different criteria like entropies, complexity, Lyapunov exponents etc. The developed program seems to be suitable also for the analysis of the ECG signal to predict the heart arrhythmia before they occur. It is an actual problem investigated on experimentally obtained rabbits' ECGs.

Some criteria exist, like index of cardiac electrophysiological balance (iCEB), or others which are more complicate. They need more leads and manual treating. Therefore, we have tried to use some of the criteria based on entropy mentioned above. As a basis seems to be useful the permutation entropy [2].

From all criteria, we chose after analysis two of them – new empirical amplitude aware permutation entropy [1] and information exergy index combining singular value decomposition (SVD) and information exergy [5]. The first criterion corresponds with the properties of the ECG signal in the one given time interval and the second one takes into account the changes during a longer time.

In the following, we try to explain both criteria very shortly:

Entropy (information entropy). Entropy is the measure of the disorder of a closed system. We suppose the rabbits' ECG signal with arrhythmia in comparison of the healthy rabbits has some irregularities. The criteria based on entropy seems to be the best suitable. A lot of possibilities to define the entropy of the time series exist, like the ECG signal. As a very simple and effective, we have chosen the permutation entropy, introduced in [2].

Permutation entropy. Let us have a one-dimensional time series $S = \{x_t;\ t = 1, 2, \ldots, N\}$. In the arbitrary time s, we introduce a D-dimensional vector $(s) \to (x_{s-(D-1)\tau}, x_{s-(D-2)\tau}, \ldots, x_{s-1\tau}, x_s)$, where τ is the delay (usually equal 1). To this vector, we assign the **ordinal pattern** which is permutation $\pi = (r_0, r_1, \ldots, r_{D-1})$ from the order number of the elements of the vector elements. It is defined with the inequality

$$x_{s-r_{D-1}} \leq x_{s-r_{D-2}} \leq \ldots \leq x_{s-r_1} \leq x_{s-r_0}. \tag{1}$$

The number of these permutations – patterns – is $D!$. For $N \gg D!$ we can write for the probability of π

$$p(\pi) = \frac{\text{number of patterns } \pi}{N - D + 1}\,. \tag{2}$$

The probability distribution is then $P = \{p(\pi)\}$. Putting these probabilities into the known formula of **Shannon entropy**

$$S(P) = -\sum_{j-1}^{N} p_j \ln p_j \,, \tag{3}$$

we obtain the permutation entropy.

Amplitude-aware permutation entropy (AAPE). Original permutation entropy has two weaknesses: First, it does not take into account the different absolute values and differences of vectors elements creating the same patterns (for example, (2,1,4) creates the same pattern as (20,1,40)). The second problem is that the vector has the same elements with the same values. Their in order of emergence is ranked (e.g., (2,4,4) can create the same pattern as (2,3,4)). Azami [1] tried to solve these problems in the following approach: To the probability, he added the probabilities

$$\frac{A}{D}\sum_{k=1}^{D}|x_{s-(k-1)\tau}| + \frac{1-A}{D-1}\sum_{k=2}^{D}|x_{s-(k-1)\tau} - x_{s-(k-2)\tau}|, \tag{4}$$

where A is chosen from the range [0,1]. In case of two or more vector elements having the same value, into account is taken only the corresponding part – for two same elements the half, for three the third etc.

Information exergy. Information exergy is equal the change (or transfer) of the Kullback information between the supposed state (the ECG of the healthy rabbits) and the actual state. Generally, it is given with formula

$$K(p_0, p) = \int p \log \frac{p}{p_0} \mathrm{d}t \,. \tag{5}$$

The actual state can be the function of time τ this can evaluate the change of state during the time

$$K(p_0, p(\tau)) = \int p(\tau) \log \frac{p(\tau)}{p_0} \mathrm{d}t \,. \tag{6}$$

The problem is how to express this change using only one variable. Zhang [5] calls this variable again information exergy and mentions that it is a "time cumulating function of information entropy"

$$\mathbf{Y}(\tau_2) = \int_{\tau_1}^{\tau_2} S(\tau) \mathrm{d}\tau, \tag{7}$$

where $S(\tau)$ is information entropy obtained in the time moment τ from the neighbouring part of the time series s.c. window WS. The discretised formula is

$$\mathbf{Y}(\mathbf{m-1}) = \sum_{i=1}^{m-1} \frac{S(i) + S(i+1)}{2} \,, \tag{8}$$

where $m = 1, 2, \ldots, M$ is a moment in the solved time interval. All these $\mathbf{Y}(\mathbf{m-1})$ can be arranged into a column vector Y. If we choose $\mathbf{K}$ different time intervals (τ_1, τ_2) from the time series (ECG), it is possible to create the information exergy matrix $\mathbf{F}((\mathbf{M-1}) \times \mathbf{K})$ from the corresponding vectors $\mathbf{Y}$:

$$\mathbf{F} = \begin{pmatrix} \frac{S(1,1)+S(2,1)}{2} & \frac{S(1,2)+S(2,2)}{2} & \cdots & \frac{S(1,K)+S(2,K)}{2} \\ \sum_{i=1}^{2} \frac{S(i,1)+S(i+1,1)}{2} & \sum_{i=1}^{2} \frac{S(i,2)+S(i+1,2)}{2} & \cdots & \sum_{i=1}^{2} \frac{S(i,K)+S(i+1,K)}{2} \\ \vdots & \vdots & \ddots & \vdots \\ \sum_{i=1}^{M-1} \frac{S(i,1)+S(i+1,1)}{2} & \sum_{i=1}^{M-1} \frac{S(i,2)+S(i+1,2)}{2} & \cdots & \sum_{i=1}^{M-1} \frac{S(i,K)+S(i+1,K)}{2} \end{pmatrix}. \tag{9}$$

It is necessary to mention that the different time intervals can be used as the different leads of ECG. Articles [4] and [5] suggest how to obtain from the information exergy matrix one parameter called information exergy index. For this purpose, it is necessary to use singular value decomposition. The decomposition of the matrix $\mathbf{F}$ in the product of three matrices

$$\mathbf{F} = \mathbf{U}\mathbf{\Sigma}\mathbf{V}^T, \tag{10}$$

where $\mathbf{\Sigma}$ is the diagonal matrix. The diagonal entries are the singular values. They are for the square matrices equal the square root of the eigenvalues of the matrix $\mathbf{F}\mathbf{F}^T$. The greatest singular value σ can be used as an indicator of entropy changes of the time series during the time.

As a most effective has been shown to use both parameters AAPE and σ. Both these criteria should distinguish two groups of ECG – ECG of the healthy rabbits and of the rabbits with both types of arrhythmia (Torsades de Pointes (TdP) and non TpD).

The first one characterises the basic ordering of the ECG signal and the second one its change during time. A time series is chosen the series the peaks of the ECG signal, which is a special type of the Poincare section (Fig. 1). Our code is called Rabbits_ExergyMES1.m.

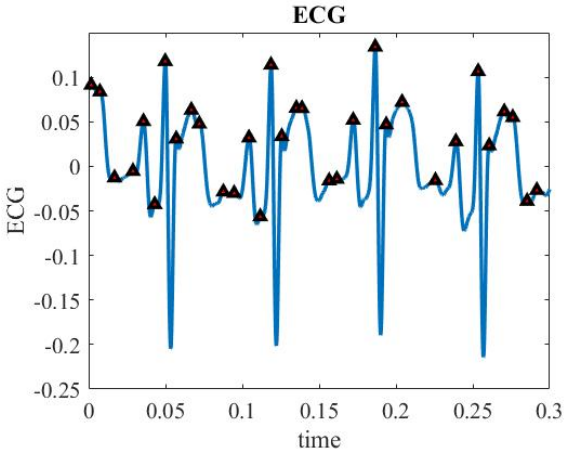

Fig. 1. Poincare section of the ECG signal

To verify the efficiency of this method, we have analysed 39 rabbits' one-lead ECG. They were divided into three groups healthy rabbits, rabbits with TdP arrhythmias and rabbits with non-TdP arrhythmias. The experiment is the result of the in vivo study realised in the Biomedicine Centre of the Faculty of Medicine in Pilsen. The result is shown in Fig. 2.

Conclusions. From the result, we can conclude:

1. AAPE allows distinguishing rabbits without arrhytmias and rabbits with (TdP) arrhythmias with good sensitivity and specificity.
2. The parameter σ cannot distinguish between healthy and non-healthy rabbits, but its value is in some boundary smaller for healthy rabbits.
3. The method does not allow to distinguish between TdP and non-TdP arrhythmias. Although, it can be seen the growing number of TdP arrhythmias with the growing σ. The tendency is opposite for the non-TdP. It can be a task for further research.

The introduced methods are very simple and offer the possibility to select the ECG of healthy rabbits. Further analysis and comparison with other published methods are needed. Also, it is necessary to apply to human ECG.

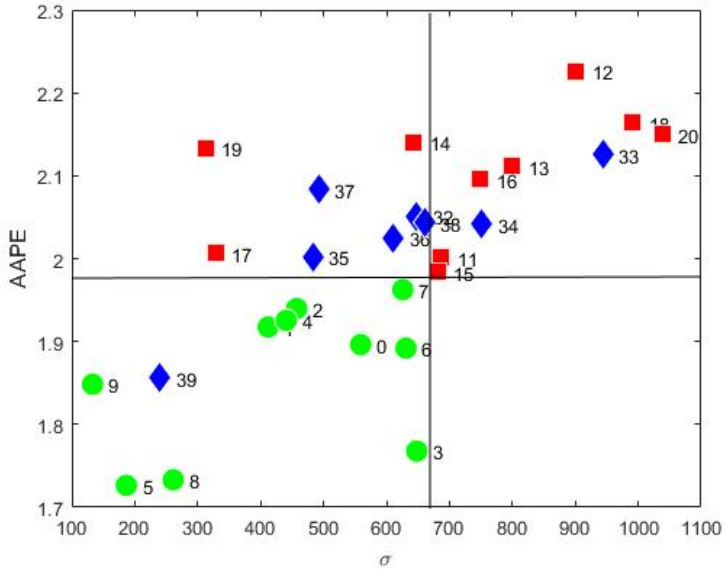

Fig. 2. Green-healthy rabbits, red-rabbits with TdP arrythmias and blue-rabbits with non-TdP arrythmias

Acknowledgements

Rosenberg and Krejčová were supported by European Regional Development Fund-Project "Application of Modern Technologies in Medicine and Industry" (No. CZ.02.1.01/0.0/0.0/17_048/0007280) and by the project LO1506 of the Czech Ministry of Education, Youth and Sports. Nalos, Jarkovská and Štengl were supported by the National Sustainability Program I (NPU I) Nr. LO1503 provided by the Ministry of Education Youth and Sports of the Czech Republic.

References

[1] Azami, H., Escudero, J., Amplitude-aware permutation entropy: Illustration in spike detection and signal segmentation, Computer methods and programs in Biomedicine 128 (2016) 40-51.

[2] Bandt, C., Pompe, B., Permutation entropy: A natural complexity measure for time series, Physical Review Letter 89 (2002) No. 174102, doi: 10.1103/PhysRevLett.88.174102.

[3] Rosenberg, J., Byrtus, M., Time-reversibly thermostatic oscillators in the modelling of dynein, Proceedings of the 33th conference Computational Mechanics 2017, Špičák, University of West Bohemia, 2017, Plzeň, pp. 115-116.

[4] Tian, J. et al., Fault diagnosis of intershaft bearings using fusion information exergy distance method, Shock and Vibration 2018 (2018) No. 7546128, doi: 10.1155/2018/7546128.

[5] Zhang, B., Zhang, L., Xu, J., Liu, J., Information exergy-based method for structural damage diagnosis, Journal of Vibroengineering 15 (3) (2013) 1606-1618.

COMPUTATIONAL MECHANICS 2019
35th conference with international participation
Srní
November 4 - 6, 2019

Lagrangian tracking of a cavitation bubble

P. Rudolf[a], A. Bossio[b]

[a] Viktor Kaplan Dept. of Fluid Engineering, Brno University of Technology, Technická 2, 616 99 Brno, Czech Republic
[b] Institute of Mathematics, Brno University of Technology, Technická 2, 616 99 Brno, Czech Republic

Cavitation is usually defined as the generation of vapor bubbles in a liquid flow due to a pressure drop under vapor pressure at corresponding liquid temperature [1]. It is a widely studied phenomenon in fluid mechanics, mainly because when the bubbles are exposed again to high pressures, condensation occurs and bubbles experience a violent compression, which releases a large amount of energy. For a very short time period temperature within bubble reaches thousands of Kelvins and dissociation of water molecules results in production of hydroxyl radicals. The effects of this collapse are well known by engineers, especially those involved with hydraulic devices, where a cavitating flow may cause losses in efficiency, high levels of noise and vibration and severe erosion of internal solid surfaces. However this phenomenon can also be exploited positively for elimination of pathogenic microorganisms or reduction of dangerous chemical residuals contained in water (volatile organic compounds, pharmaceuticals etc.). To design efficient devices for removal of undesired biological or chemical contamination it is necessary to understand the process of cavitation bubble collapse in flowing liquid, which is a combination of advection by the liquid stream and bubble dynamics induced by variable pressure field.

Dynamics of an isolated cavitation bubble submerged in a steady flow is studied numerically in present contribution. An Eulerian-Lagrangian approach is considered in which properties of the fluid are computed first, using a two-phase homogeneous mixture model, by means of a Eulerian method within commercial CFD code, and then the trajectory of the bubble is computed in a Lagrangian fashion, i.e., the bubble is considered as a small particle moving relative to the fluid, due to the effect of several forces depending on fluid's pressure and velocity fields previously computed. Important ingredient is change of the bubble's radius imposed by surrounding pressure field, which is modeled by Rayleigh-Plesset equation. In the end energy released by the successive collapses of the bubble is evaluated to estimate the energy available for damage of material surface or rupture of the cell membranes.

Newton's law of motion can be used to describe bubble's trajectory

$$m_b \frac{d\boldsymbol{u_b}}{dt} = \boldsymbol{F_D} + \boldsymbol{F_L} + \boldsymbol{F_P} + \boldsymbol{F_A} + \boldsymbol{F_g}, \tag{1}$$

where m_B is the mass of the bubble, $\boldsymbol{u_B}$ is the absolute velocity of the bubble. The terms on the R.H.S. represent respectively the drag force, the lift force, the force due to pressure gradient, added mass force and buoyancy/gravity effects. In addition, bold fonts imply vector quantities. Obviously the bubble/bubble and bubble/wall interactions are not included. The drag force $\boldsymbol{F_D}$ over a sphere is usually taken as

$$\boldsymbol{F_D} = -\frac{1}{2} C_D \pi R^2 \rho_l |\boldsymbol{u_s}| \boldsymbol{u_s}, \tag{2}$$

where R stands for the radius of the bubble, ρ_f is the surrounding fluid's density, $\boldsymbol{u_s}$ is the slip velocity defined as $\boldsymbol{u_s} = \boldsymbol{u_b} - \boldsymbol{u_f}$, with $\boldsymbol{u_f}$ being the absolute velocity of a fluid's particle located at bubble's center, and C_D is the drag coefficient, depending mostly on the Reynolds number of the flow, $\mathrm{Re} = \frac{2R\rho u_s}{\mu}$. Non-linear relation between drag coefficient C_D and Reynolds number is assumed according to formula proposed by Yang et al. [3].

The force $\boldsymbol{F_L}$ accounts for the lift force, a force usually represented by

$$\boldsymbol{F_L} = -C_L \rho_l V_b \boldsymbol{u_s} \times (\boldsymbol{\nabla} \times \boldsymbol{u_l}), \tag{3}$$

$\boldsymbol{F_P}$ is the force due to pressure gradient defined as

$$\boldsymbol{F_P} = V_b \boldsymbol{\nabla} p, \tag{4}$$

$\boldsymbol{F_A}$ is the so called added mass or virtual mass effect, and represents the additional inertia added to the system due to the need of accelerating the surrounding fluid in order to occupy a new position. It is usually implemented as

$$\begin{aligned} \boldsymbol{F_A} &= -C_A \rho_l \frac{D}{Dt} \left(V_b (\boldsymbol{u_b} - \boldsymbol{u_l}) \right) \\ &= -C_A \rho_l V_b \left(\frac{d\boldsymbol{u_b}}{dt} - \frac{D\boldsymbol{u_l}}{Dt} \right) - C_A \rho_l \frac{dV_b}{dt} \boldsymbol{u_s}. \end{aligned} \tag{5}$$

Finally, $\boldsymbol{F_g}$ represents a combined gravitational and buoyancy force and is therefore implemented as

$$\boldsymbol{F_g} = (m_b - \rho_l V_b) \boldsymbol{g}, \tag{6}$$

where $\boldsymbol{g}$ is the acceleration due to gravity. Since bubble is changing its diameter along its trajectory, it is clear that the change also has impact on magnitude of the respective forces (especially drag force, buoyancy force and added mass force). Bubble dynamics of a spherical isolated cavitation bubble was first described by Lord Rayleigh [2]. More accurate equations, which are extension of the original formulation appeared later (Rayleigh-Plesset, Gilmore, Herring, Keller, ...). Due to some stability problems basic formulation by Rayleigh and Plesset [1] is employed in present contribution

$$R\ddot{R} + \frac{3}{2}\dot{R}^2 = \frac{p_v - p_\infty}{\rho} + \frac{p_{g_0}}{\rho} \left(\frac{R_0}{R} \right)^{3k} - \frac{2S}{\rho R} - \frac{4\mu}{\rho R}\dot{R}, \tag{7}$$

where p_v is vapor pressure at liquid's temperature, p_∞ is the pressure in the liquid far from the bubble, p_{g_0} is the partial pressure of the air inside the bubble at a reference bubble size R_0, k is the polytropic coefficient, S is the surface tension and μ is the viscosity of the liquid. This equation assumes spherical shape of the bubble, incompressibility of the surrounding fluid and zero heat and mass transfer between the bubble and the surrounding fluid.

Venturi tube with dimensions according to Fig. 1 was used as an example for the bubble tracking.

Velocity and pressure fields were computed numerically using ANSYS Fluent 19.1, with Reynolds-averaged Navier-Stokes (RANS) equations accompanied by realizable k–ε model, the numerical method is finite volume method (FVM), using segregated approach with SIMPLE algorithm. The geometry and equations are adopted for axisymmetric assumption. Multiphase cavitating flow was implemented by homegeneous mixture approach with simplified Rayleigh-Plesset equation. See distribution of the phases for cavitation number $\sigma = 0.42$ in Fig. 2. These fields were used as an input for MATLAB code and its Adams-Bashforth-Moulton method,

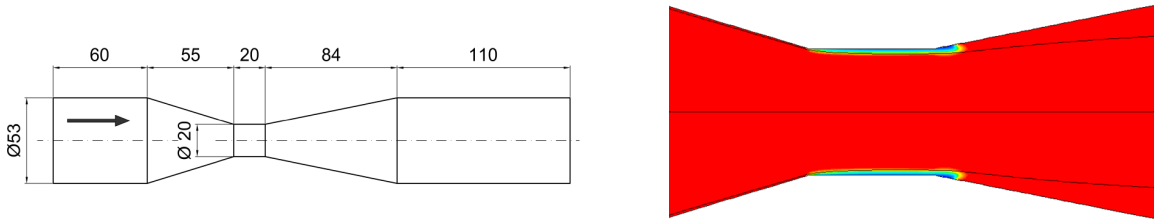

Fig. 1. Geometric description of the simulated Venturi tube (all dimensions in mm) (*left*), phase distribution for the Eulerian approach (*right*)

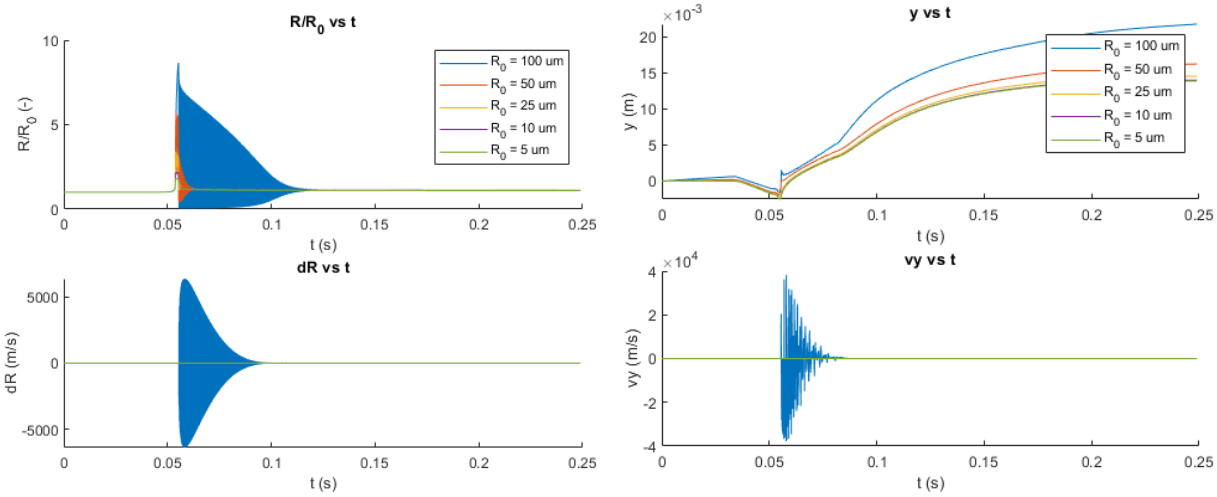

Fig. 2. Bubble dynamics along its trajectory (*left*), bubble position and velocity in the y-direction (*right*)

where the set of equations (1) – (7) was implemented. Results were computed for a range of different initial bubble radii and trajectory of the bubbles was depicted in Fig. 2.

Energy released by bubble collapse is computed according to [4] as work done by the pressure inside the bubble against the ambient pressure

$$W = \int_{R_{min}}^{R_{max}} 4\pi R_B^2 (p_\infty - p_B)\, \mathrm{d}R. \tag{8}$$

The energy is then determined by subtracting the values for two successive maxima of the radii. Generally, the energy released during the i-th collapse is given by

$$E_i = W\Big|_{R_{min_i}}^{R_{max_i}} - W\Big|_{R_{min_{i+1}}}^{R_{max_{i+1}}}. \tag{9}$$

Accompanied by correlation of material (or cell membrane) damage obtained from experimental investigations the presented approach can constitute a basis for cavitation erosion model or cell rupture model.

Acknowledgement

Research was supported by Czech Science Foundation grant project No. 19-10660S "Removal of estrogens from waste water using hydrodynamic cavitation in combination with advanced oxidation processes".

References

[1] Franc, J. P., Michel, J. M., Fundamentals of cavitation, Kluwer Academic Publishers, 2005.

[2] Lord Rayleigh, O.M. F.R.S., On the pressure developed in a liquid during the collapse of a spherical cavity, Philosophical Magazine Series 6 34 (200) (1917) 94–98.

[3] Yang, H., Fan, M., Liu, A., Dong, L., General formulas for drag coefficient and settling velocity of sphere based on theoretical law, International Journal of Mining Science and Technology 25 (2) (2015) 219–223.

[4] Zima, P., Sedlář, M., Müller, M., Modeling collapse aggressiveness of cavitation bubbles in hydromachinery, Proceedings of the 7th International Symposium on Cavitation, Ann Arbor, Michigan, 2009, pp. 1-7.

COMPUTATIONAL MECHANICS 2019
35th conference with international participation
Srní
November 4 - 6, 2019

Influence of notches on the mechanical properties of machine parts

M. Růžička[a], J. Papuga[a], M. Lutovinov[a], A. Karkulín[a]

[a] *Faculty of Mechanical Engineering, Czech Technical University in Prague, Technická 4, 160 00 Praha 6, Czech Republic*

1. Introduction

The design of machine parts and machines is associated with the use of appropriate types of materials and thus the determination of their physical and mechanical properties. Usually these are metallic materials (high-strength steels, pure alloys, etc.), in recent decades also other non-traditional materials, such as composites (particle or fiber composites, hybrid materials). Each real part is characterized by its geometric shape, which is adapted to the functionality of structure and also to operational loading and stresses. Each part is also made by a specific technology. This forms its future structural and mechanical properties including static, dynamic and fatigue resistance in relation to operational loads. Designers should be able to optimize and correctly design the so-called "notch effect" of a part. In this sense, a notch means a local stress and strain concentrator. Locations with high local stress concentration usually form critical points in mechanical structures where a static failure occurs or where a fatigue crack begins to spread. Notches can be categorized from different criteria. Let us mention here geometrical, structural or technological notches. The first group is unambiguously described by its geometric shape and dimension. Structural notches, such as inclusions or inhomogeneity in material, also create local deformation concentrations. Their real shape is usually replaced by a simplified geometry. Also, various technological treatments of materials can cause a notch effect, for example on the transition of two layers of material of different structural and mechanical properties, etc. Here we will focus on geometric notches and description of stress in the notch root as well as description of prediction methods to evaluate durability of notched parts using nominal stress approach or local stress approach by using of calculations with finite element method (FEM).

2. Stress concentration and the stress gradient effect in the notches

It is known that the concentration of nominal stress, σ_n, to the local elastic (virtual) stress, $\sigma_{\max}$, which are at the root of geometrical notches can be described using a stress concentration factor (also shape factor) defined as

$$K_t = \frac{\sigma_{\max}}{\sigma_n}. \tag{1}$$

The so-called exposed material volume in which a significant part of the local damage occurs, can be described using the relative stress gradient at the notch root, *G*, where

$$G = \left[\frac{\Delta\sigma_y}{\Delta x}\right]_{x\to 0} \cdot \frac{1}{\sigma_{\max}} \quad [\mathrm{mm}^{-1}]. \tag{2}$$

If the stress peaks occur along the entire L region (as, for example, in Fig. 1, where L represent the sample thickness), the L/G ratio characterized the exposed region. All these quantities can be determined in the notch locality from the results of the FEM calculations, also during complex loading conditions, when the condition of the multicomponent strain is usually assessed using equivalent stress values according to strength hypotheses, for example, σ_{HMH} .

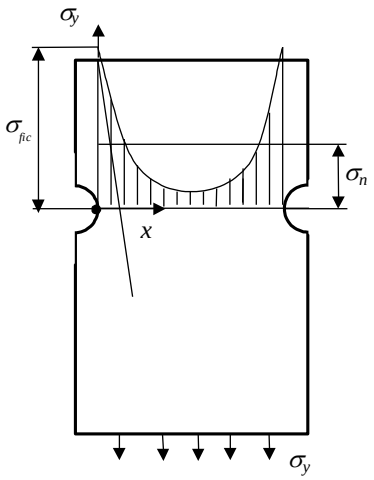

Fig. 1. Stress in the notch specimen

3. The effective notch effect on the fatigue strength

It is also known that the effect of the stress peaks on the notch fatigue strength is not as significant as it would correspond to the theoretical stress concentration. Experiments define the effective notch effect on the fatigue limit by a notch factor,

$$K_f = \frac{\sigma_C}{\sigma_C^*} . \tag{3}$$

In the past, several relations were proposed for the computational estimation of the notch factor, which are reviewed, for example, in Ref. [5]. Let us define the ratio of the shape and notch factor by the fatigue ratio, $n = \frac{K_t}{K_f}$. The methods for expressing the n quantity can be split into two major groups, see Table 1.

Table 1. Fatigue ratios calculated by different methods

Author	***Fatigue ratio n***	***Note***	***Eq.***
Neuber	$n_\rho = 1 + \frac{A}{\rho} \cdot \left(1 - \frac{1}{K_f}\right)$	where A=f(R_m) is the Neuber factor, see, *e.g.*, [5]	(2)
Peterson	$n_\rho = 1 + \sqrt{\frac{a}{\rho}} \cdot \left(1 - \frac{1}{K_f}\right)$	where a is the critical surface layer depth, see, *e.g.*, [5]	(3)
Heywood	$n_\rho = 1 + 2\sqrt{\frac{a'}{\rho}} \cdot \left(1 - \frac{1}{K_f}\right)$	empirical factor a' see, *e.g.*,. [5]	(4)
Siebel, Stiller	$n_G = 1 + \sqrt{c \cdot G}$	parameter c see, *e.g.*, [5]	(5)
Bäumel Seeger [1]	$n_G = 1 + \sqrt{G} \cdot 10^{-\left(\frac{R_e}{810} + 0{,}35\right)}$	where R_e is the yield strength	(6)
Eichelseder [2]	$n_G = 1 + \left(\frac{\sigma_{C,b}}{\sigma_C} - 1\right) \cdot \left(\frac{G}{2/d}\right)^k$	where $\sigma_{C,b}$ and σ_C are the bending and tensile fatigue limits, d is the diameter of the bending sample	(7)
Volejnik, Kogaev [7]	$n_G = 1 + \left(\frac{1}{\nu_\infty} - 1\right) \cdot \left(\frac{L/G}{L_0/G_0}\right)^\mu$	here ν_∞ is the magnitude factor for the homogeneous strength, μ is an exponent	(8)

The first group is formed by relations that are determined in dependence on the notch root radius, ρ. The second group involves expressions depending on the relative stress gradient, *G*. In Table 1, the values of the n_ρ and n_G ratio are compared for some most frequently used relations. For the FEM applications, the expression by means of the stress gradient, *G*, turns out to be more convenient. For the determination of the local fatigue limit in the notch root, $\sigma_{C,FEM}$, (*i.e.*, of the limit values of the elastic stress peaks in the FEM calculations), the following relation can be used:

$n_G = \frac{K_t}{K_f} = \frac{K_t \cdot \sigma_C^*}{\sigma_C} = \frac{\sigma_{C,FEM}}{\sigma_C}$, so that $\sigma_{C,FEM} = n_G \cdot \sigma_C$,

where σ_C is the material fatigue limit during a homogeneous uniaxial tensile stress.

Analogously to the K_f factor introduced in the region of the unlimited fatigue life, it is possible to define the notch factor, $K_{f,N} = \frac{\sigma_A}{\sigma_A^*}$, in the region of the limited life from the fatigue test results. The fatigue ratio is modified by the relation $n_{G,N} = \frac{K_t}{K_{f,N}}$. It is then possible to obtain the fatigue curve of virtual stress values at the notch root, $\sigma_{FEM} = \frac{K_t}{K_{f,N}} \cdot \sigma_C = n_{G,N} \cdot \sigma_C$, which must lie above the smooth sample curve (see Fig. 2). In practical calculations, we can also use an opposite procedure. During the damage calculation, we use the fatigue curve of a smooth sample and correct the local stress amplitudes by calculating the quantity

$$\sigma_{cor} = \sigma_{FEM} \cdot \frac{K_{f,N}}{K_t}. \tag{4}$$

Fig. 2 also shows the main difference between the Nominal Stress Approach (NSA), used by analytical fatigue calculations and Local Elastic Stress Approach (LESA), used by FEM analysis. While the fatigue curve is corrected in the downward direction in the nominal approach with respect to the notches, and the fatigue damage is determined from the nominal stress amplitude. The local approach uses the corrected stress peak at the notches and the initial fatigue curve of the sample without notches. Let us mention, however, that all the effects of the surface quality of the actual machine part should be projected into the curve and, as the case may be, its further technological modifications. The magnitude factor is taken into account in the above-indicated similarity criterion of the stress gradient effect and exposed volume.

The author of this paper proposed a modification of the Heywood expression (see [3]) for the description of the notch effect in the region of the limited life, *i.e.*, for the expression of the $K_{f,N}$ coefficient,

$$K_{f,N} = 1 + (1 - K_t) \cdot \mu(N), \tag{5}$$

in which the dependence on the relative stress gradient, *G*. It was expressed in the following form: $n_G = \frac{K_t}{K_f} = 1 + \sqrt{G} \cdot 10^{-\left(\frac{R_e}{K1} + K2\right)}$ and the time functions as $\mu(N) = \frac{(\log N)^{K3}}{K4 + (\log N)^{K3}}$.

Parameters *K1* up to *K4* were determined to describe best the experimental *S-N* curves of samples with a various shape factor. A bunch of the so-called synthetic fatigue curves can be generated for any general stress gradient and shape factor; these curves can represent the required areas of the structure in the NSA approach, see Fig. 3. The example of these curves

is indicated in Fig. 3 according to the results in Ref. [6]. The set of these equations can also be used for correcting the elastic stress peaks according to relation (4) in the LESA approach.

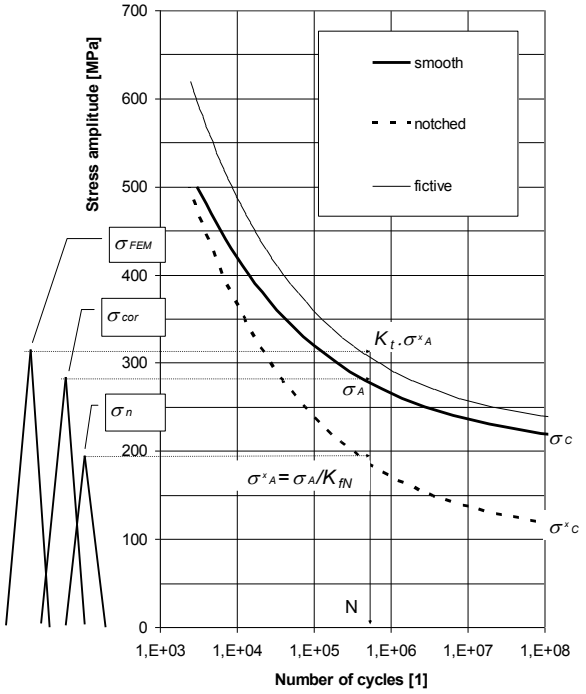

Fig. 2. Fatigue curves use for NSA and LESA

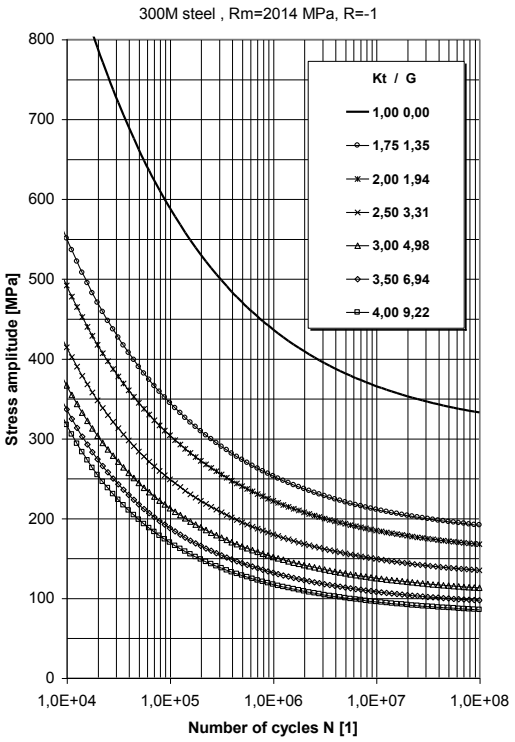

Fig. 3. Synthetic fatigue curves

Acknowledgements

Authors acknowledge support from the ESIF, EU Operational Programme Research, Development and Education, and from the Center of Advanced Aerospace Technology (CZ.02.1.01/0.0/0.0/16_019/0000826), Faculty of Mechanical Engineering, Czech Technical University in Prague. Further support for the research was provided within the project from the Grant Agency of the Czech Technical University in Prague (grant no. SGS17/175/OHK2/3T/12).

References

[1] Bäumel, A., Seeger, T., Material data for cyclic loading – Suppl. 1. Materials Science Monographs 61, Elsevier Sc. Publisher, Amsterdam 1990.
[2] Eichlseder, W., Fatigue analysis by local stress concept based on finite element results, Computers & Structures 80 (27-30) (2002) 2109–2113.
[3] Heywood, R.B, Design against fatigue, Pergamon Press, 1965.
[4] Neuber, H., Kerbspannungslehre: theorie der spannungskonzentration genaue berechnung der festigkeit, 4th ed., Springer, Berlin, Heidelberg, 2001.
[5] Růžička, M.; Hanke, M., Rost, M., Dynamic strength and service life, Lecture notes of the Faculty of mechanical Engineering, CTU in Prague, 1992. (in Czech)
[6] Růžička, M, Life prediction of machine parts using the local approach, In: Kolokvium dynamiky strojů 94. Prague, Institute of Thermomechanics AS CR, 1994, pp. 77-80. (in Czech)
[7] Volejnik, N.V., Carrying capacity of machine parts, Naukova Dumka, Moscow 1985. (in Russian)

COMPUTATIONAL MECHANICS 2019
35th conference with international participation
Srní
November 4 - 6, 2019

Contribution to computational analysis of tightness prediction of complex technical systems

M. Ságaa, M. Handrika, M. Vaškoa, P. Kopasa, A. Sapietováa, L. Jakubovičováa

a Department of Applied Mechanics, Faculty of Mechanical Engineering, University of Žilina, Univerzitná 1, 010 26 Žilina, Slovakia

1. Introduction

We are faced with the requirement to analyze the state of a technical device in the event of its fall from some height in technical practice. Special attention must be given to the various storage and transport containers intended for the transport of dangerous substances. The problem of loss of tightness of technical equipment during its fall is a complex computational problem. Therefore, it often has to include the following partial tasks:

- Solution the dynamic problem of continuum mechanics using implicit or explicit time integration.
- Solution with a relatively small time step, requiring the solution of a large number of time steps.
- Solution of geometrically nonlinear problem.
- Solution of material nonlinear problem.
- Solve contact problem.

2. Model of solved problem

The simulation of the fall of the transport container is solved in the FE program ADINA. The geometry of the transport container is formed by a large number of bodies (the model consists of almost 200 geometric bodies). A large number of geometric bodies have a significant effect on the number of defined contact pairs in the model. By considering all possibilities of contacting bodies we receive more than 200 contact pairs. The transport container consists of two cylindrical vessels, which are inserted into each other. In this case, there are large areas in contact with a large number of elements. A large number of contact pairs and large contact areas have a high demand for contact detection in the calculation process.

The complexity of the shape geometry requires the use of cubic elements in size from 0.25 mm to 2 mm in meshing. The geometric model is shown in Fig. 1. The finite element mesh has more than 20 million elements and the number of equations exceeds 14 million. Considering the size of the elements and the convergence criterion for explicit time integration, it is necessary to use a very small time step (of the order of 1×10^{-9} seconds). When solving the impact of the transport container we consider a solution time of 4×10^{-3} seconds. Body contact needs to be detected more than 4 million times using explicit time integration. By using implicit time integration, time step 1×10^{-5} and 400 time increments can be used for the solution to the desired time. The solution of 15 to 20 iterations of the non-linear solver is required at each time step.

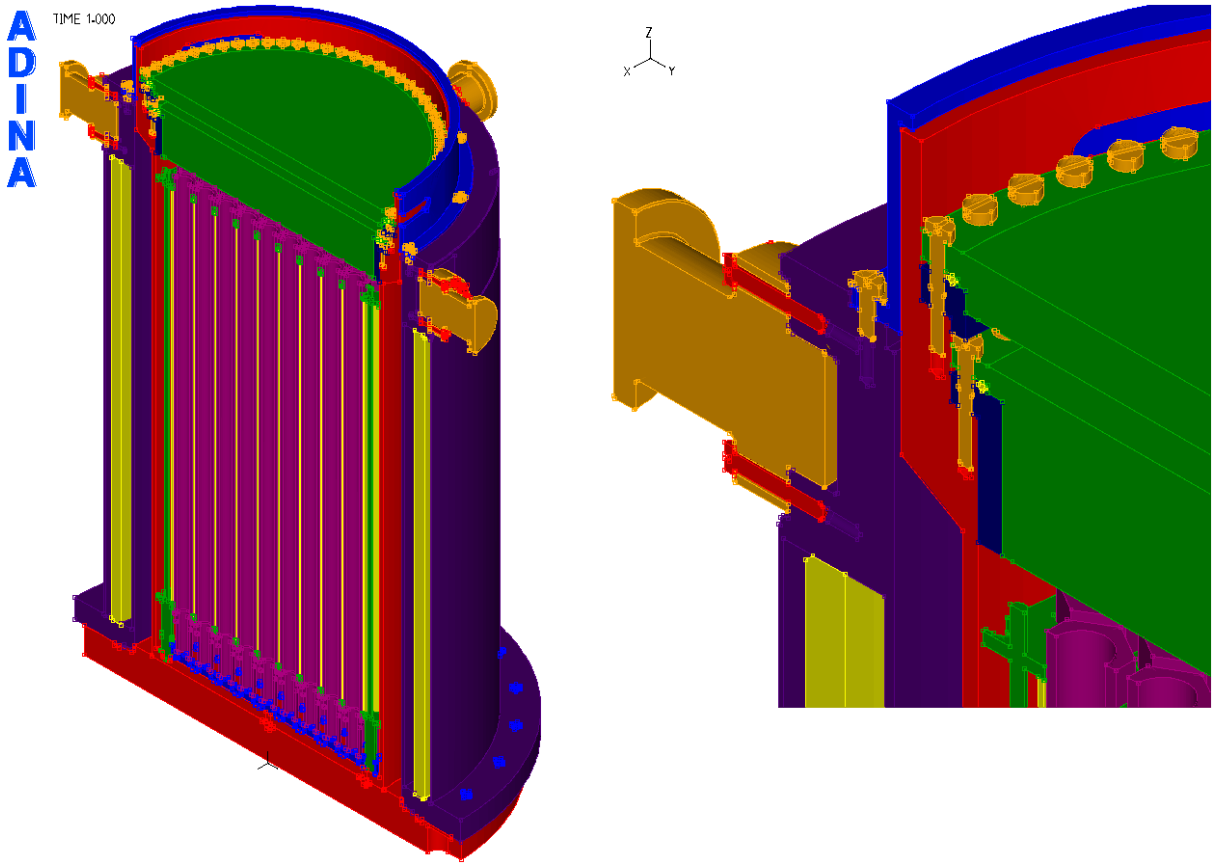

Fig. 1. The geometric model of transport container

Practical calculations have shown that using implicit time integration is significantly more efficient than using explicit time integration. Implicit time integration is more than five times faster than explicit time integration. Placing the body near the bottom and defining the initial velocity determined by the free fall relationship of the body allows a solution for a short period of time even when falling from a large height.

The following material models are used to define the material properties of the individual parts of the model:

- bilinear material model - for less important parts of the structure,
- multilinear material model - for parts of the structure that are directly related to the tightness of the transport container.

The elements switch-off criterion when reaching the material strength limit is used in a multilinear material model. Fall test simulations were performed for 20 positions of impact of the shipping container on the base.

3. Analysis of results

We focus on evaluating the following properties of the structure when analyzing the results:

- Breaking the casing tightness of the transport container, the formation of a crack - monitoring the switching off of elements in the casing of the transport container.
- Breaking the fastening screws of the transport container, breaking the screws - monitoring the switching off of the elements in the screws.
- Plastic deformation of screws of the transport container, permanent loosening of the gasket - loss of contact forces on the gasket or their significant decrease. The gasket release status is shown in Fig. 2.

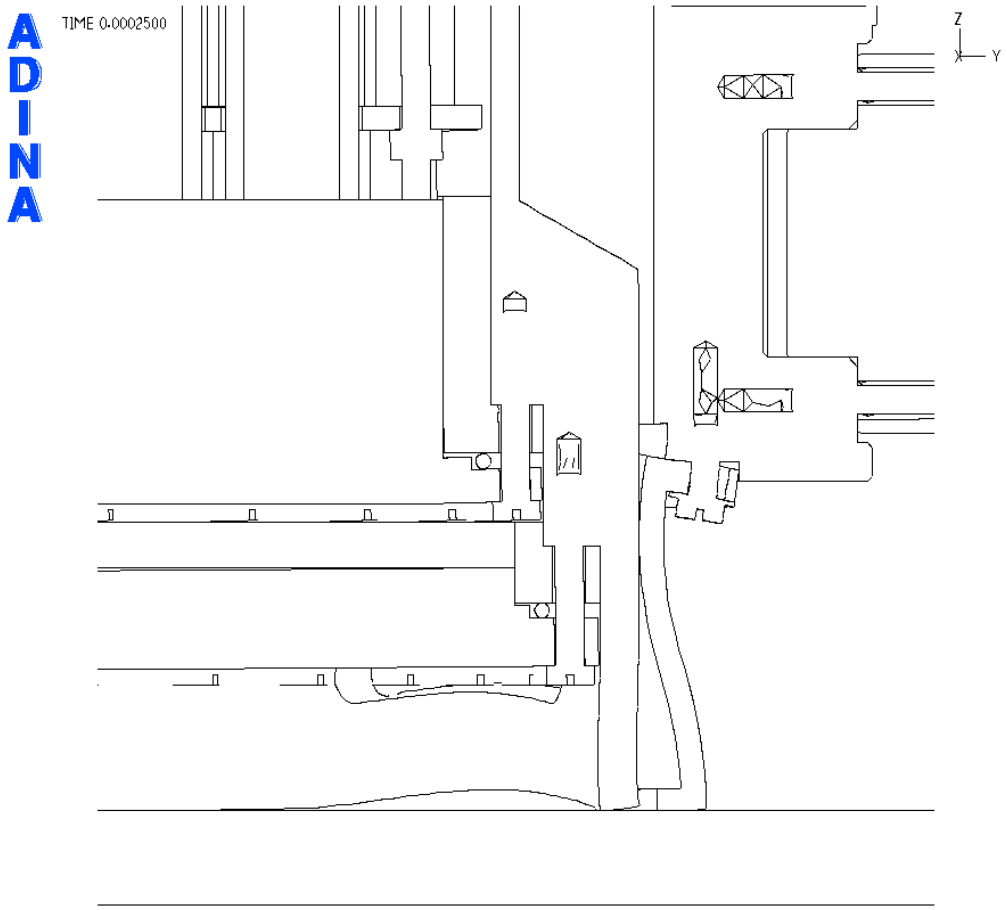

Fig. 2. The gasket release status after analysis

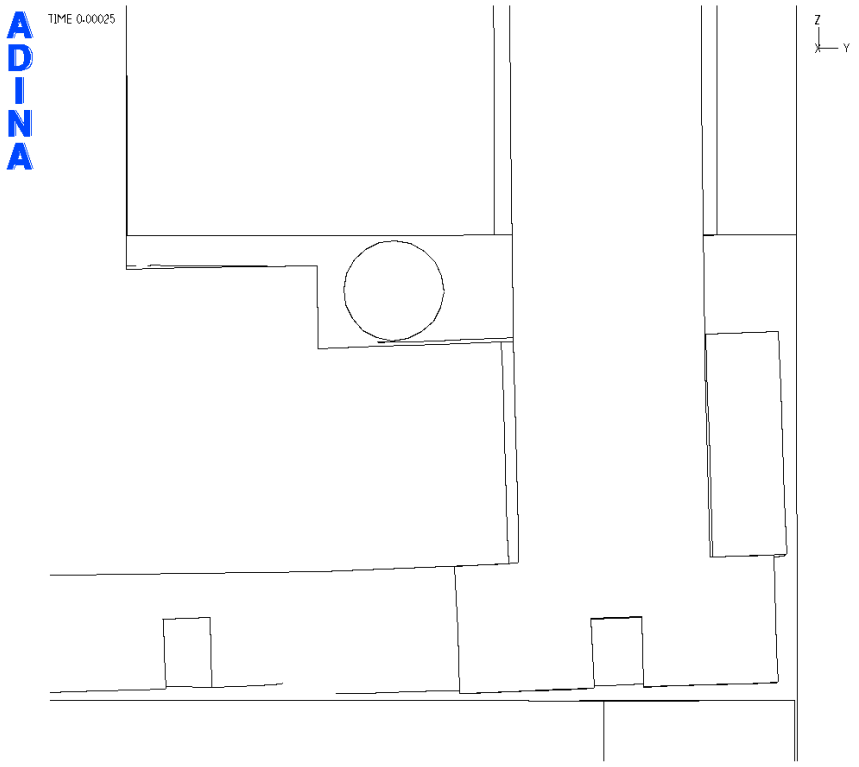

Fig. 3. The gasket release status detail

4. Conclusion

The use of the finite element fall test simulation allows the analysis of the behavior of the structure without the need for its manufacturing and experimental tests at the design stage of the transport container. Simulations allow identification of critical points of the structure and their modification in order to remove them. The use of fall simulations makes it possible to significantly reduce the cost of design and experimental verification.

Acknowledgements

This work has been supported by grant agency KEGA project No. 015ŽU-4/2017 and grant agency VEGA project No. 1/0073/19

References

[1] Bathe, K.J., Finite element procedures, New Persey, Prentice Hall, 1996.
[2] Bathe, K.J., Wilson, E.L., Numerical methods in finite element analysis, New Jersey, Prentice-Hill, 1976.
[3] Haftka, R.T., Gürdal, Z., Elements of structural optimization, Kluwer Academic Publisher, 1992.
[4] Jakubovičová, L., Kopas, P., Contribution to stress and residual strain analyse of the welded specimen, Transactions of the University of Košice, No. 3, Research reports from the universities of Košice, pp. 57-64.
[5] Kwon, Y.W., Bang, H., The finite element method using MATLAB, CRC Press University of Minnesota, 1996.
[6] Vaško, M., Ardeshir, G., Jakubovičová, L., Kopas, P., Effects of the loading rate on contact stresses of a roller bearing: A computational study, Fourth Serbian Congress on Theoretical and Applied Mechanics, Vrnjačka Banja, Serbia, 2013, pp. 547-553.

COMPUTATIONAL MECHANICS 2019
35th conference with international participation
Srní
November 4 - 6, 2019

Planar and spatial active resonator absorbers for robotics

Z. Šika[a], K. Kraus[a], J. Krivošej[a], P. Denk[a]

[a] *Faculty of Mechanical Engineering, Czech Technical University in Prague, Technická 4, Praha 6, 160 00 Prague, Czech republic*

Vibrations have negative effect in many engineering applications. In robotics, there are types of machines such as serial robots or cable manipulators, that are typically able to cover large workspace, which usually implies high mass/stiffness ratio. Such robots are not capable of high accuracy while performing operations with high dynamic of the end-effector tool or external excitations. During last decades, there has been an intensive development of serial robots in order to increase their production efficiency, including their non-traditional usage e.g. for drilling [1].

The open problem is what can be achieved through the accurate measurement of the absolute end-effector motion and its subsequent use to compensate for control loop errors between robot drives and the end-effector. Such measurement, considering large workspace in complex industrial environment, is typically very problematic. Second problem is, that the drives of robots typically are not capable to operate in frequency range of vibrations induced by disturbances. Consequently, some other robust concept of vibration suppression is desirable. The usage of dynamic absorbers with active elements is one of the promising ways [2], [3]. The important reason for usage of active resonator absorbers is the strong change of eigenfrequencies and eigenmodes of serial robots operating in large workspaces. In order to perform active vibration suppression effectively, it is important to begin with absorber (Fig. 1) optimized properly passively with respect to dynamic properties of the robot mechanical structure. The reasonable way is to tune absorber mechanically close to the average value of the robot lowest eigenfrequency. During the robot end-effector motion along the trajectory (Fig. 2 a)), however, not only the first eigenfrequency value (Fig. 2 b)) changes, but also the geometric shape of the corresponding first eigenmode. From this fact came the idea to tune the resonator passively and subsequently also actively along trajectory as uni-frequency. Concerning planar absorber (Fig. 1 a)) the goal is to tune all three absorber's working eigenfrequencies to one value. The analogous goal for the spatial absorber (Fig. 1 b)) would be to tune all its six eigenfrequencies to one value. However, this goal is unattainable for passive mechanical tuning of structure from Fig. 1 b), maximum 5 of its eigenfrequencies can be the same. The control law algorithm for vibration absorption of moving flexible robot has been firstly developed for planar robot (Fig. 2 a)) equipped by planar 3DOF uni-frequency absorber (Fig. 1 a)). The aim is to prepare the control law as simple as possible.

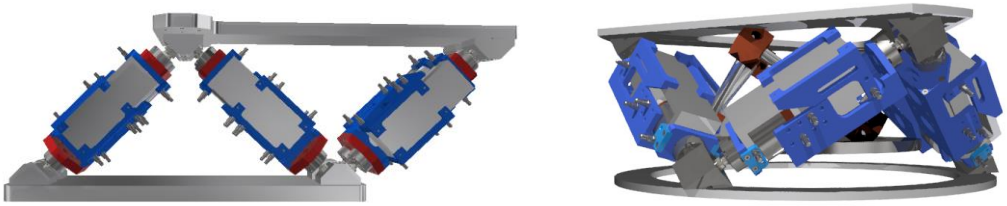

a) planar 3 DOF version b) spatial 6 DOF version

Fig. 1. Experimental demonstrators of active absorbers with mutually perpendicular voice-coil actuators

The basic concept of the control law is to evaluate the active voice-coils forces in order to change absorber tuning according to the first eigenfrequency in given position of robot (Fig. 2 b)). The active force in each voice-coil has two components, component modifying the efficient stiffness and component evaluated from the delayed acceleration. The example of effect of this control along some trajectory is shown in Fig. 3. The efficiency of this simple law with respect to other concepts (e.g. LQR with observer) is continuously evaluated.

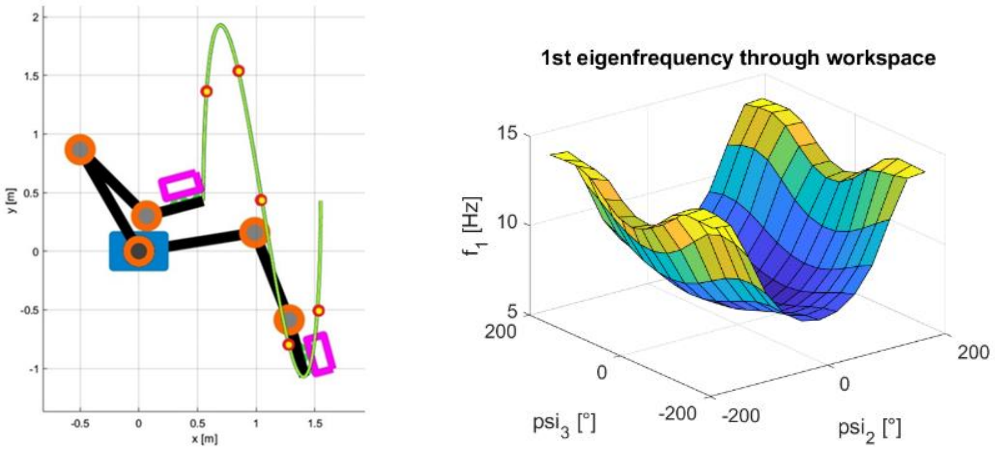

a) trajectory with points of impulse disturbance b) map of first eigenfrequency in workspace

Fig. 2. Model of flexible planar robot with planar absorbers

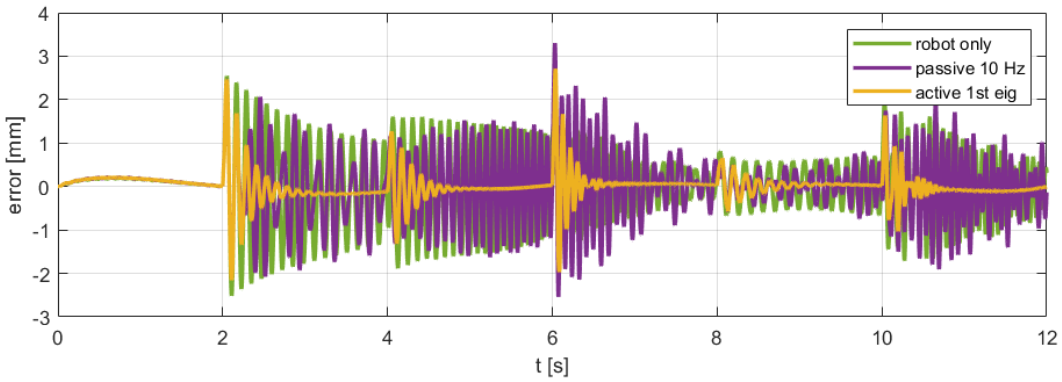

Fig. 3. Vibrational response of end-effector to force impulses on trajectory

Acknowledgements

The work has been supported by the Czech Science Foundation project GA17-20943S "Active multidimensional vibration absorbers for complex mechanical structures based on delayed resonator method".

References

[1] Olsson, T., Haage, M.. Kihlman, H., Cost-efficient drilling using industrial robots with high-bandwidth force feedback, Robotics and Computer-Integrating Manufacturing 26 (1) (2010) 24-38.
[2] Šika, Z., Kraus, K., Beneš, P., Vyhlídal, T., Valášek, M., Active multidimensional vibration absorbers for light robots, Proceedings of the 5th Joint International Conference on Multibody System Dynamics, Lisbon, Portugal, 2018, pp. 1-12.
[3] Verbaan, C., Rosielle, P. Steinbuch, M., Broadband damping of non-rigid-body resonances of planar positioning stages by tuned mass dampers", Mechatronics 24 (6) (2014) 712-723.

COMPUTATIONAL MECHANICS 2019
35th conference with international participation
Srní
November 4 - 6, 2019

Lifetime estimation of polyoxymethelene under mixed-mode loading conditions

O. Slávik[a, b], P. Hutař[a,c], A. Gosch[d], M. Berer[e], T. Vojtek[a], F. Arbeiter[d], G. Pinter[d], L. Náhlík[a,c]

[a] *Institute of Physics of Materials, AS CR, Žižkova 22, 616 62 Brno, Czech Republic*
[b] *Institute of Solid Mechanics, Mechatronics and Biomechanics, BUT Faculty of Mechanical Engineering, Technická 2, 616 69 Brno, Czech Republic*
[c] *CEITEC IPM, Žižkova 22, 616 62 Brno, Czech Republic*
[d] *Material Science and Testing of Polymers, Montanuniversitaet Leoben, Otto Gloeckel-Straße 2, 8700 Leoben, Austria*
[e] *Polymer Competence Center Leoben GmbH, Roseggerstr. 12, 8700 Leoben, Austria*

Roller bearing elements made of polymer materials started to become more frequently used in the recent past, thanks to their specific advantages. Such as good noise reduction or their suitability for smaller-sized parts. Though the application of such bearings is limited by number of the load cycles and possible load levels. As a result of manufacture process, they contain small voids and additional internal stresses. Fatigue cracks are mostly initiating from these defects, while it is important to note, that the cracks in bearing elements are exposed to mixed-mode loading conditions. However, studies of the mixed-mode conditions are a bit problematic, namely because these conditions are often times difficult to achieve and also cracks tend to deviate from the original trajectory. This fact brought an idea of trying to observe, if the mode I data are applicable for mixed-mode conditions, or if there is any relation between these scenarios. Therefore, the main focus of this study was to compare lifetimes – experimentally measured under mixed-mode conditions with numerically predicted ones, that has been based on the data, produced on mode I conditions. Also FEM model was implemented in this study.

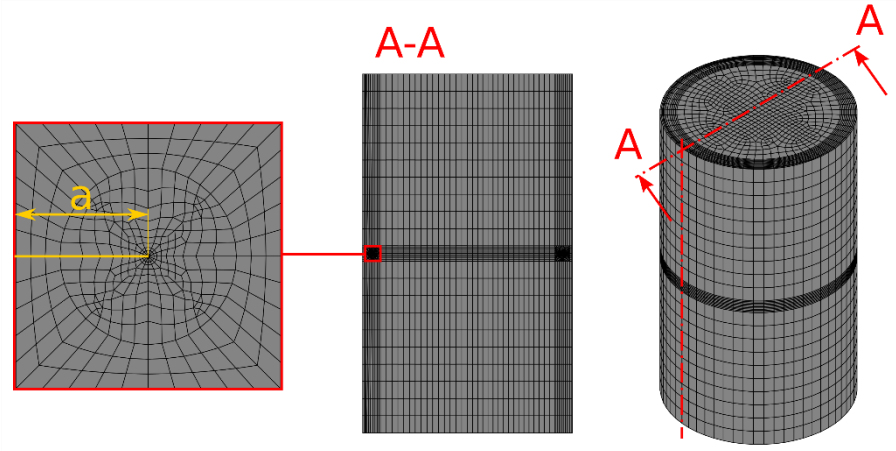

Fig. 1. Meshed specimen geometry

Cracked round bar (CRB) specimens were used for experimental purposes, as this type of specimen provides clear combination of loading modes I + III, when loaded by tension + torsion. However, knowledge of the crack growth rates is necessary for further lifetime predictions. Usually it is very difficult to obtain usable crack growth rates under mixed-mode

loading conditions. Therefore, this is how mode I data were implemented in this study. Because the crack growth rates were measured on the tension-only loaded CRB specimens – mode I loading conditions. Crack growth rates were also measured on compact tension (CT) specimens, since these are easier to experiment with and linear part of the v-K curves is much more significant.

FEM numerical simulations were carried out in ANSYS APDL software. Fatigue crack propagation was described by small scale yielding conditions, therefore LEFM approach was applied. Linear elastic material model was used with elastic constants of the polyoxymethelene, more specifically Young's moduli was 4600 MPa and Poisson's ratio was 0,45. Meshed specimen with detailed cross section of the crack front area is displayed in Fig. 1. Boundary conditions were set according to experiment – bottom surface was fixed, while upper surface was loaded by tension and torsion. Main focus of the numerical simulations was the calculation of the stress intensity factors K_I and K_{III}. Thanks to knowledge of the stress intensity factors, the K-calibration was carried out for different crack lengths in range of the experimental data. Based on this data, effective stress intensity factor range was evaluated. Finally, comparison of the experimentally measured lifetimes of the mixed-mode CRB specimens with numerically predicted ones, that were based on crack growth rates, measured on tension loaded CRB specimens and CT specimens was carried out, see Fig.2.

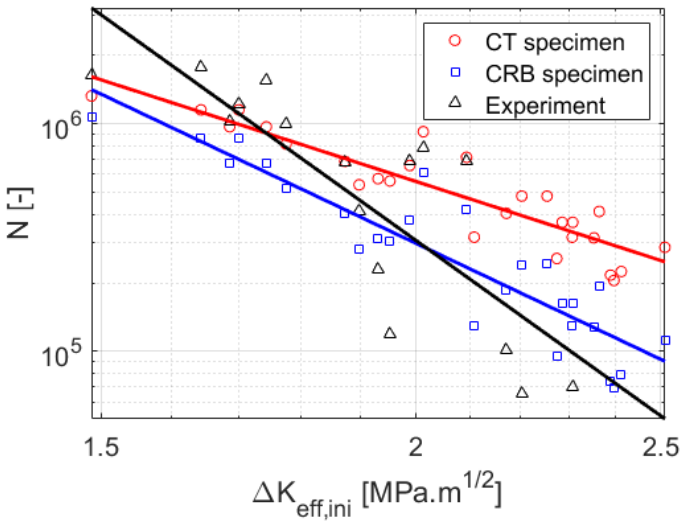

Fig. 2. Dependence of the lifetimes on the initial effective stress intensity factor

In order to do that, additional parameter had to be implemented, against which the lifetimes could be plotted. For these purposes the initial effective stress intensity factor was used, as it is best reflecting the initial loading conditions, which have the highest impact on lifetimes themselves.

Acknowledgements

This research has been supported by Polymer Competence Center Leoben GmbH (PCCL, Austria) and the Ministry of Education, Youth and Sports of the Czech Republic under the project m-IPMinfra (CZ.02.1.01/0.0/0.0/16_013/0001823) and the equipment and the base of research infrastructure IPMinfra were used during the research activities. Also, thanks are due to the specific research project FSI-S-17-4386 of the Faculty of Mechanical Engineering, BUT.

COMPUTATIONAL MECHANICS 2019
35th conference with international participation
Srní
November 4 - 6, 2019

The most dangerous factors for child passenger collisions in the interior of a rail vehicle

S. Spirk[a], J. Vychytil[b]

[a] Faculty of Mechanical Engineering, University of West Bohemia in Pilsen, Univerzitní 8, 306 14 Plzeň, Czech Republic
[b] New Technologies - Research Centre , University of West Bohemia in Pilsen, Univerzitní 8, 306 14 Plzeň, Czech Republic

This contribution is focused on the most dangerous factors for child passenger collisions in the interior of a rail vehicle. The actual legislation deals only with an injury of an average adult male, but the evaluation for the wider population (5 and 95 percentile) will be other logical steps in the near future. It is possible to overtake the current trends and to carry out an rail interior safety assessment for children due to the excellent scalability of the VIRTHUMAN model. The virtual assessment of passive safety continues to increase its role in transport. Hence finite element method and multibody simulations are used for the safety risk assessment. The injury criteria are used for probability of injury evaluation. The vehicles, which are used in this research, were developed recently and they are currently in operation.

The simulation of the rail vehicle collision scenario is provided according to the acceleration pulse by the GMRT 2100 standard. Only 50-percentile adult male is considered in current standards, [2]. The developers of rail vehicles are usually inspired by the European Standard EN 1176-6:2017 "European Safety Standard for playground equipment and impact absorbing playground surfacing„, when a new vehicle with compartments intended for child passengers is designed. Although requirements in this standard are not connected with rail transportation, it is possible to overtake the current trends and to carry out a rail interior safety assessment for children. For these simulations, an interior model consisting of seats with seat tables was created. Interesting part of the modelled interior is the seat padding foam material, which was validated experimentally in previous work, [3]. Part of the description is a chosen geometry, material constants, and a finite element calculation network. In addition, the report describes the scaling of the VIRTHUMAN human body model to represent a child passenger. For the explicit simulations the commercial SW VPS was used, [1]. The scaled child model is seated in the seat. Two variants representing the actual seating of the child on the seat are considered. The standard simulations themselves are presented in two configurations, with a folded and unfolded table. The simulations results are significantly influenced by the passenger initial position. It is obvious that this position is difficult to predict. Therefore the two standard initial positions (observed by experiment) and more non-standard positions are considered. The results are evaluated in terms of kinematics and prediction of injury to the passenger. Based on these, a general recommendation is made to improve the safety of the selected interior type. Some recommendations for rail interior design safe for children are provided at the end of this paper.

The final consideration is based on the results of the simulations. The rail transportation is very different in the contrast with automotive industry. The requirement for special child restraint system in rail vehicle is unreal. Although the safety performance of standard interior (not designed for child passenger) is not as bad, there exist significantly worst scenarios. The most significant safety risk for child passenger is connected wit the table in the open position

(see Fig. 1 right). This part represents significant safety risk for child passenger which is amplified significantly if the child passenger is sitting on the knee of adult passenger. The table can be partially closed after collision, what is also prohibited by standard GM/RT2100. It can be shown that this collision scenario can be still dangerous even during emergency barking (statistically more often). The considered table design is reason of significant head injury even in the closed position. This result is caused by one design of table and cannot predict result for very different design, but the change is highly recommended. For example very simple step will be to omit the tables in the departments intended for child passengers.

Another simulations has as the aim to show safety risk of standing passenger. It this type of simulations exist real risk of non-precious results (in longer time). Therefore the simulation time was significantly reduced. After the fall over the next seat the model is able to show very different results for very small changes in initial conditions (see Fig. 1 left). This problem must be studied in the next research to exclude the influence of possible chaotic behavior.

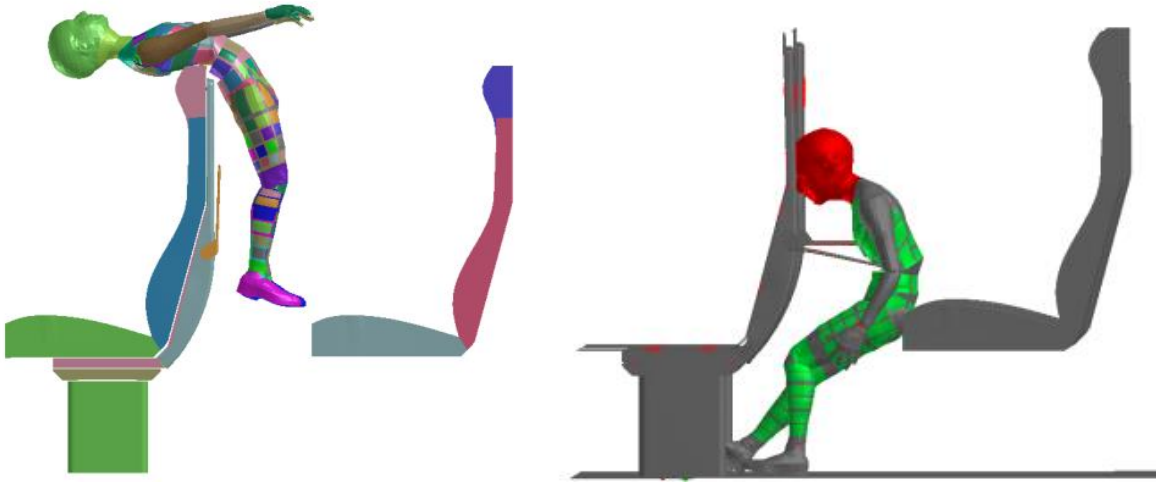

Fig. 1. The example of two results of collision simulations with 6 years old child

Acknowledgements

This paper was created with the support of Technology Agency of the Czech Republic, project No TE01020038 “Competence Centre of Railway Vehicles”.

References

[1] Hyncik, L., Manas, J., Spicka, J., Kovar, L., Development of 6 years old child virtual model by automatic scaling, SAE Technical Papers, SAE 10th International Conference on Automotive Engineering, Vol. 2, 2014.

[2] Severson, K., Research and development of a safety Standard for workstation tables in the United States, Proceedings of the 9th International Symposium on PASSIVE SAFETY of Rail Vehicles, 2013, pp. 107-121.

[3] Spirk, S., Krizek, M., Jenicek, S. Polyurethane foam behaviour during impact, MATEC Web of Conferences, 2018, 157, Art. No. 02050.

COMPUTATIONAL MECHANICS 2019
35th conference with international participation
Srní
November 4 - 6, 2019

Vibration-based health monitoring of lighting poles

P. Steinbauer[a], Z. Neusser[a], I. Bukovský[a]

[a] *Faculty of Mechanical Engineering, Czech Technical University in Prague, Technická 4, 160 00, Praha 6, Czech Republic*

The health and integrity of lighting poles must be ensured as they are often installed at public places and as they must withstand severe conditions. Corrosive deterioration of lighting poles is dangerous and difficult to forecast due to their varying operating conditions of the poles. The Roch's study on structural stability of pole systems "Infrastrukturprojekt Straßenbeleuchtung 2000" (Infrastructure Project: Street Lighting 2000), which is representative on a Germany-wide scale, found that 3.3% of all poles pose a hazard [2]. To prevent pole collapse, the poles are regularly replaced, e.g. every 15 years. Such solution is expensive, workforce demanding and unreliable. Some poles are damaged sooner due to more sever conditions, but some poles may withstand much longer.

The corrosive damage of the pole occurs usually at the pole base, often under the surface. The corrosion on the top of the pole is less frequent. In any case, the damage is not apparent and localizable (Fig. 1).

Fig. 1. Damaged lighting poles

Due to the amazing number of lighting poles already installed, it is not feasible to regularly monitor and measure the pole conditions manually, esp. using complicated devices and tools. The automatic monitoring of pole health may enable engineers to concentrate maintenance effort only to damaged poles. Even though some specialized devices were proposed [1,2], their implementation into daily routine is quite limited and costly.

The paper deals with possibilities and feasibility of vibration based lighting pole monitoring. The modal properties of the structure are global values that aggregate all the local structure properties. The relation between pole deterioration and modal properties change is analysed.

The modal properties (eigen frequencies, modal damping and shapes) are studied as a tool for structural damage or structural change identification [3, 4, 5]. The published results and recommendations are quite broadly scattered. Either only a very small change of eigen

frequency or damping is reported to be caused by quite significant structural damage of structure [3], or a quite large change of eigen frequency is used as the damage measure [4,5].

The lighting pole is of a specific construction. On one hand, it is quite simple welded beam with few moving parts or screw connections that often introduce nonlinearities. On the other hand, the poles are usually fixed into the ground using the sand bed. The sand is a material with excellent damping properties; however, the properties are related to the humidity of the sand. So the modal damping is not stationary and also the damping measurement has low accuracy; thus, damping cannot be used as a measure of the pole health. The pole eigen frequencies and shapes were initially analysed based on FEM modelling. The FEM model of healthy pole fixed into the frame and the pole destroyed (one third hole of the diameter) were compared. Eigen frequency change was very small for lower frequency range up to 40Hz (Δf cca 0.02-0.4 Hz). The change of eigen frequencies in higher frequency range (up to 250Hz) was more promising, although some differences were very small, some almost 3 Hz. But the pole deterioration cannot be judged based on observation of only one eigen frequency.

Fig. 2. Measurement setup for experimental modal analysis of lighting poles

The promising modelling results had to be verified experimentally. The two sets of existing, installed poles with same design, dimensions and arrangement, but quite different health, were selected. The complete experimental modal analyses were carried out for each pole in the investigated set. The first set was laboratory installation, fixed into the concrete bed, the second pole set consisted of regularly installed poles (same dimensions), i.e. in the sand bed. The excitation force was introduced by electromechanical shaker connected through load cell mounted on the pole in the height 3m. The pole response was measured by scanning laser vibrometer at several points on the pole (Fig. 2). The setup was same for all poles in the set.

The results in the form of frequency response functions (FRF) that were measured at the point 10 (see Fig. 2) are demonstrated in Fig. 4.

The concrete bed set has very low damping and eigen frequencies can be clearly visible. The frequency shift is almost negligible in the lower frequency range, but the frequency shift can be easily distinguished in higher frequency range. The regular set (sand bed poles) was heavily damped in all cases and some of pole eigen frequencies were not detectable due to high damping or position of measurement. But still, the higher frequency range of eigen frequencies exhibited a detectable frequency shift.

Pole health can be determined based on the pole vibration measurement. The complete experimental modal analyses requiring many measured transfer functions is not necessary.

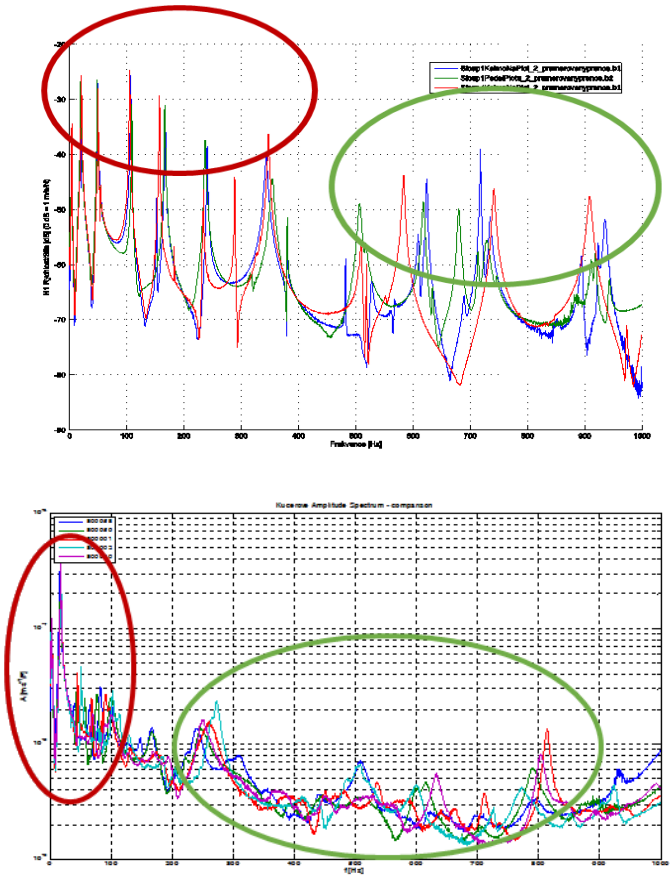

Fig. 3. Frequency transfer function of the lighting pole (a) in the concrete bed (b) in the sand bed

Many eigen frequencies, especially in higher frequency range must be taken into evaluation of the pole damage, which makes the evaluation more robust against the influence of soil, sand damping, pole damage location and the location of selected excitation and response measurement point. A single frequency, especially the first eigen frequency, does not provide us with solid information about structural damage of the pole.

The development of automatic pole inspection methods based on vibration measurement is thus feasible.

Acknowledgements

The support of TACR Epsilon project #TH02010770 INDIVO and TACR project #TN01000071 National Competence Centre of Mechatronics and Smart Technologies for Mechanical Engineering (MESTEC) are greatly acknowledged.

References

[1] Adams, R.D., Cawley, P., Pye, C.J., Stone, B.J., A vibration technique for non-destructively assessing the integrity of structures, Journal of Mechanical Engineering Science 20 (2) (1978) 93-100.

[2] Roch Services GmbH, Roch Test Method. [cited 30.9. 2019] https://www.roch-services.co.uk/standsicherheit/rochverfahren

[3] Salawu, O.S., Detection of structural damage through changes in frequency: a review, Engineering structures 19 (9) (1997) 718-723.

[4] Steinbauer, P., Valášek, M., Mechatronic lighting pole testing device. In recent advances in mechatronics, Springer, Berlin, Heidelberg, 2010, pp. 127-132.

[5] Wang, Z., Lin, R. M., Lim, M.K., Structural damage detection using measured FRF data, Computer methods in applied mechanics and engineering 147 (1-2) (1997) 187-197.

COMPUTATIONAL MECHANICS 2019
35th conference with international participation
Srní
November 4 - 6, 2019

Modelling of swelling and deformations of homogeneous hydrogel

J. Štorkán[a], T. Vampola[a], M. Dušková-Smrčková[b], K. Dušek[b]

[a] Faculty of Mechanical Engineering, Czech Technical University in Prague, Technická 4, 160 00 Praha, Czech Republic
[b] Institute of Macromolecular Chemistry, Czech Academy of Sciences, Heyrovského nám. 2, 162 06 Praha, Czech Republic

1. Introduction

The work deals with the analysis of mechanical behavior of swelling materials and numerical problems that arise in solving them. Any material capable of absorbing or dissolving a fluid can swell. Most often, osmosis enters liquid into the mass, increasing the body volume. Elastic forces try to maintain volume, and create pressure in the liquid. The pressure from the elastic forces must be in equilibrium with the osmotic pressure. On larger scales, the osmotic pressure can be replaced by the surface tension of the liquid that holds the liquid in the pores of the material. The liquid pressure causes a volume increase. If the pore structure is sufficiently fine (compared to the overall model size), the swelling material can be modeled as a continuum. In the case of osmotic pressure swelling, the conditions for the continuum are always met.

Our team develops materials for biological use. A suitable medium is required for the cultivation of cells, fungi or other materials. The environment must be humid. In the environment there must be solid matter on which the cells grow and multiply. Polymer hydrogels are used as this medium. They are materials made up of long polymer chains. Swells on contact with solvent [2]. Both homogeneous and porous can be produced. The size, amount and topology of the pores can be well influenced during manufacture. One method of pore formation is to mix crystals into the gel, which are then allowed to dissolve. Representative of such gels is silica gel, which is used as a moisture absorber.

2. Mechanical properties

Modeling of material swelling using the finite element method goes in several ways. Volume change can be forced by boundary conditions, by analogy to thermal expansion, or by inclusion in the material description. The last option is closest to reality. Material experts describe swelling by changing Gibbs' free energy. Neglecting the difference between Gibbs and Helmholtz free energy (hereinafter referred to as potential), this energy can be used directly as a material description. Most large FEM packages allow you to use any hyperelastic description of material behavior.

The potential for swelling materials has 2 parts. One part describes the specific work performed by osmotic pressure Δg_{mix}, see [4]. The second part presents the normal hyperelastic material description $\Delta g_{el,n}$, see [3]. These energies are additive.

$$\Delta g = \Delta g_{mix} + \Delta g_{el,n}\,, \tag{1}$$

$$\Delta g_{mix} = RT\frac{\phi_2^0}{V_{1mol}}\frac{\phi_1}{\phi_2}(\ln\phi_1 + g(\phi_2)\phi_2) - RT\frac{f_e-2}{f_e}v_e\phi_2^0\ln\phi_2\,, \tag{2}$$

$$g(\phi_2) = g_0 + g_1\phi_2 + g_2{\phi_2}^2, \tag{3}$$

$$\Delta g_{el,n} = \Delta\psi_{el}(\boldsymbol{\lambda}) - \upsilon_e RT\phi_2^0 \ln\frac{V}{V_0}, \tag{4}$$

$$\Delta\psi_{el}(\boldsymbol{\lambda}) = -RT\upsilon_e\phi_2^0\frac{n-1}{2}\left(\ln\left(1-\frac{\lambda_1^2}{n-1}\right)+\ln\left(1-\frac{\lambda_2^2}{n-1}\right)+\ln\left(1-\frac{\lambda_3^2}{n-1}\right)-3\ln\left(1-\frac{1}{n-1}\right)\right), \tag{5}$$

$$\phi_1 + \phi_2 = 1\,, \tag{6}$$

$$\frac{\phi_2^0}{\phi_2} = \frac{V}{V_0} = \lambda_1\lambda_2\lambda_3\,. \tag{7}$$

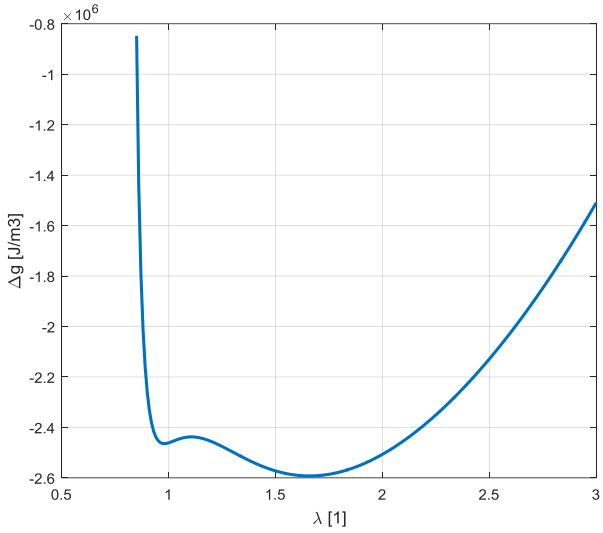

Fig. 1. Potential for isotropic stretch

Parameters λ_i are the main encounters, parameters ϕ_1, ϕ_2 are volume fractions of gel and solvent. The other parameters are constants of different physical meaning. Only the constants g_0-g_2 have no direct physical meaning. In substitution, the potential of functions is only deformation and is therefore well applicable to finite element calculations.

Swelling modeling can be a problem for the stability of the finite element calculation. FEM is a numerical method that requires an initial estimate to find a solution. This estimate is zero shifts. If the actual solution is far from the estimate used, the calculation may not converge. The solution is simple parameters that enforce the magnitude of feeds (typically boundary conditions) do not set straight to the final magnitude, but increase gradually. The calculation is incremental. After each increment, the calculation iterates, finds the solution, and uses it as a new estimate. The incremental scheme ensures small changes to the solution from the estimate and thus ensures convergence. If the material description itself induces the shifts, FEM does not have parameters that it can incrementally control. Therefore, the entire swelling process takes place in a single increment. If the displacements since swelling are large, the calculation may not converge.

The second problem of the material description used is the uniqueness of the solution. Depending on the constants used, the potential may not be convex. The potential may show more extremes. The only way to choose one of many solutions is to initially estimate the displacements. This choice is very problematic. It can be done on simple tasks, but on complicated tasks it may not be realistic.

Our solution procedure allows to solve both problems simultaneously. The whole principle is to apply the incremental scheme not only to boundary conditions and other external influences, but also to the material model itself. It is necessary to find a parameter in the material description that controls the amount of swelling. From non-swelling material to fully swelling. There is no such parameter. But it is possible to create it artificially. We can use non-swelling material description in addition to swelling. This sum may be supplemented by a weighting

coefficient. This coefficient folds as a switch between material descriptions. Switching the description can be both step and continuous. If the weight coefficient is incrementally controlled, the swelling will be controlled to ensure convergence.

It still does not solve the case of non-convex potential. The choice of solution is not determined. We use three potentials instead of two. The first description is still non-swelling, the second can be swelling convex, where the minimum is equal to the minimum of the non-convex potential to which the calculation will converge. The last third description is the material description of the equation (1).

$$\Delta g = (1-\alpha)\Delta g_1 + \alpha\big((1-\beta)\Delta g_2 + \beta\Delta g_3\big)\,. \tag{8}$$

Equation (8) shows the composition of the total potential from three parts coefficient α serves as a switch between potential 1 and 2, coefficient β switches between potential 2 and 3. The calculation is divided into two steps in the first is β = 0 and α is incrementally controlled from 0 to 1. In the second step, α = 1 and β is controlled from 0 to 1. In such a case, the calculation should reliably converge and it is possible to choose the solution to which the calculation converges.

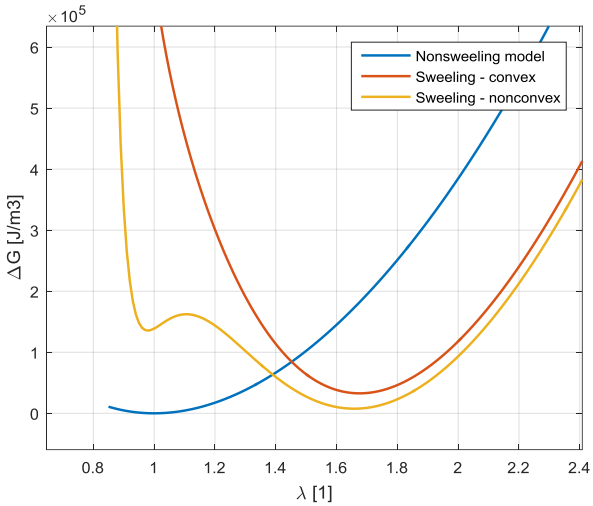

Fig. 2. Potential for models Δg_1 – blue, Δg_2 – red, Δg_3 – yellow

There are 3 possible solutions for the potential from the Fig. 1 is the local maximum potential. This is an unstable solution. The remaining 2 are stable. The choice of solution for use is arbitrary. One way is based on Maxwell's construction. It is based on the calculation of the chemical potential. The sign of the chemical potential integral between stable roots determines a more stable root [1]. A simpler procedure is to select the root with the lowest potential. This is the most stable solution.

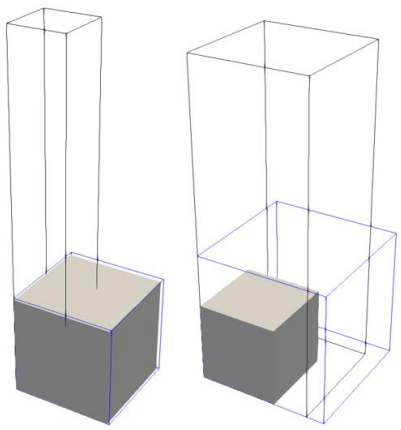

Fig. 3. Initial, swollen and tense shape of cubes

The calculation can be demonstrated on a cube model. If we select the constants in the potential, we get the waveform according to Fig. 1. There are 2 sizes of swelling. For the first root, the material swells only a little less than the original. The second root swells to about 50% larger than the original. Fig. 2 shows the waveforms of potentials when we want to find a solution to the second root. The first step starts with the first potential (blue curve) and gradually switches to the second potential (red curve). In the second step, the second potential is switched to the third potential in the same way. The figure shows that the first potential does not swell and the second potential has a minimum equal to the second minimum of the final potential. If we were to find a solution at the first root, we would use a different second potential. Let the cube swell to both roots and then try to stretch it in one direction (1D stress).

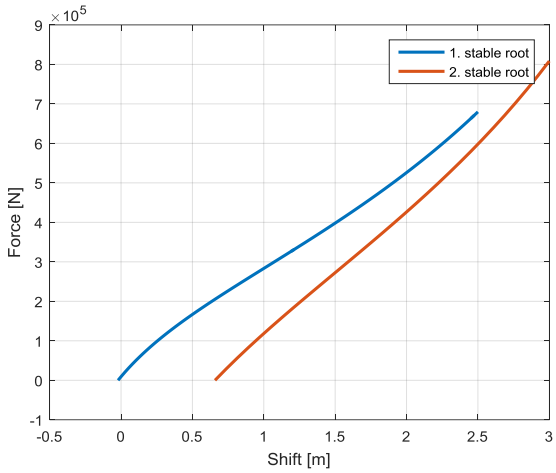

Fig. 4. Tensile curves

3. Conclusion

The test procedure showed how to find multiple solutions for one task, if exists. An example is a cube model with a material description allowing 2 swellings. One will swell to a smaller volume and the other to a larger volume. In both cases the geometry, boundary conditions and material description were identical. The results are shown in Fig. 3. The original configuration, the swollen state, and the stretched state are shown. Fig. 4 shows the tensile curves. In case of greater swelling, the model is stiffer. Without the described procedure, the calculation would probably not find any solution. If he converged, then he would find only one and the other could not be found.

Acknowledgements

The research is supported by Grant agency of Czech Republic by project No 17-08531S Computationally designed hydrogel cell supports. Additional support provider is Student Grant Competition by project No SGS19/157/OHK2/3T/12 Modelling, control and design of mechanical system 2019.

References

[1] Barra, A., Moro, A., Exact solution of the van der Waals model in the critical region, Annals of Physics 359 (2015) 290-299.
[2] Dušek, K., Dušková-Smrčková, M., Šomvársky, J., Effect of constraints on swelling of polymer networks, Macromol, Symposia 358 (2015) 120-127.
[3] Gent, A.N., A new constitutive relation for rubber, Rubber Chemistry and Technology 69 (1) (1996) 59-61.
[4] Nakamoto, C., Kitada, T., Kato, E., Pressure dependence on the Flory-Huggins interaction parameter of poly (N-isopropylacrylamide) gels, Polymer Gels and Networks 4 (1) (1996) 17-31.

COMPUTATIONAL MECHANICS 2019
35th conference with international participation
Srní
November 4 - 6, 2019

Numerical simulation of the one-and-half axial turbine stage properties

P. Straka [a]

[a] Czech aerospace research centre, Beranových 130, 199 05 Prague, Czech Republic

Aerodynamic and energy properties of the axial turbine stages may be different in case of the single-stage configuration and in case of the multi-stage configuration. Effect of foregoing stage has an impact particularly on the secondary flows in peripheral parts of the blade span. Effect of the following stage lies particularly in redistribution of the pressure along the blade span, it consequently leads to changes in distribution of the degree of reaction along the blade span. These effects don't exist in the single-stage configuration.

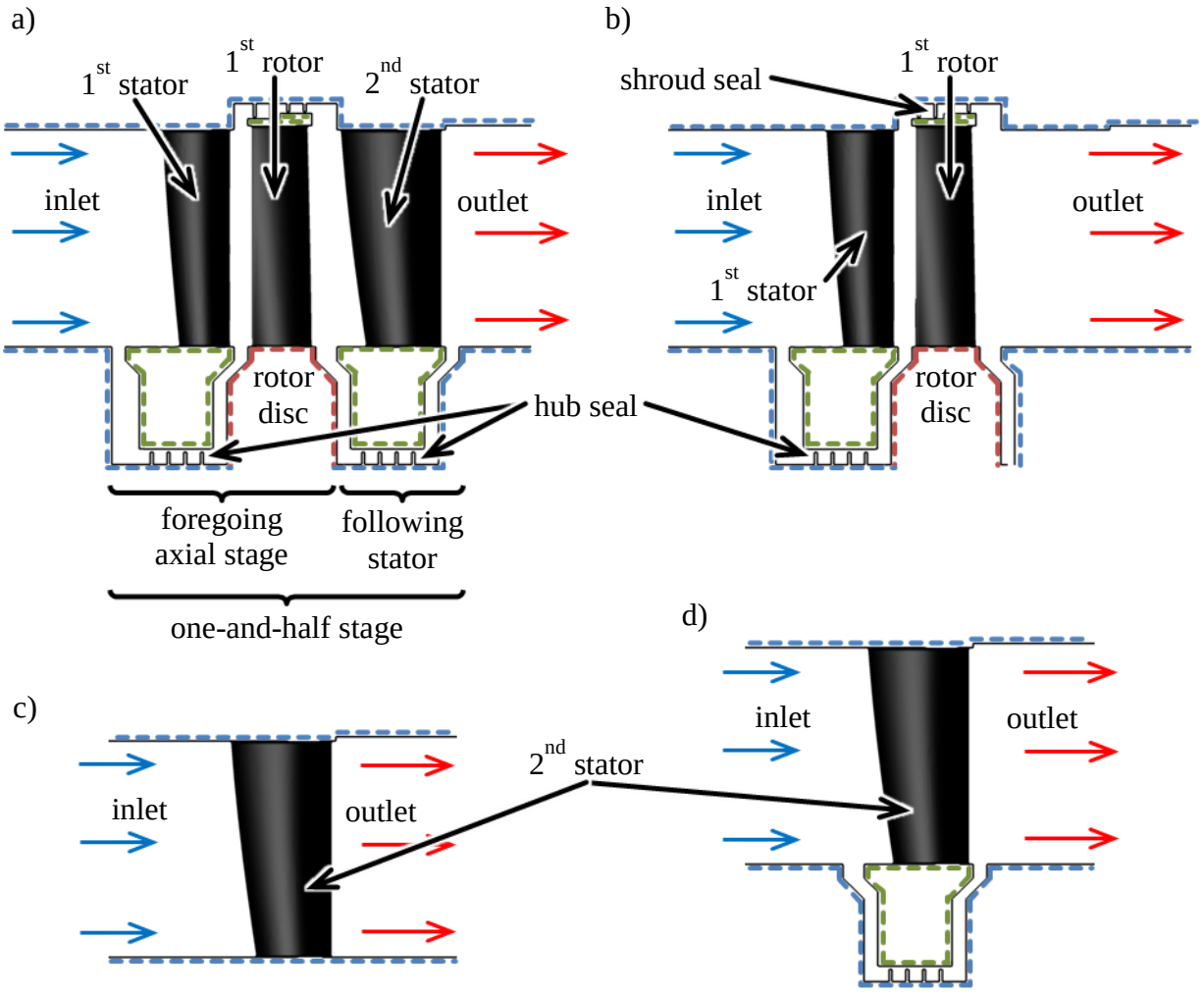

Fig. 1. Schemes of the computational domains: a) one-and-half stage configuration, b) separated single stage configuration, c) separated following stator without the hub seal, d) separated following stator with the hub seal

One way how to induce a state similar to the multi-stage configuration in an experimental investigation is to use so-called one-and-half stage configuration [1, 5]. The axial turbine stage is composed of the stator blades wheel and the rotor blades wheel. In the one-and-half stage configuration the single-stage is complemented by additional following stator blades wheel.

In research of the one-and-half stage configuration it can be investigated the effect of the following stator blades wheel on properties of the foregoing axial stage as well as an impact of the foregoing stage on flow through the following stator blades wheel.

This contribution deals with numerical simulation of flow through the one-and-half stage configuration of the experimental axial turbine as is installed in the test stand [2 - 4]. A special attention is paid to the influence of a secondary leakage flows from the hub- and shroud-seals.

The effect of mutual interaction between foregoing axial stage and following stator wheel is determined by comparison of computational results of full one-and-half stage with results of separated axial stage and separated subsequent stator wheel (see fig. 1).

Simulation was done using in-house numerical software [6] based on solution of the RANS equation closed with the $k - \omega$ turbulence model. The computational domain was covered with the multi-block structured mesh of hexahedral cells. The computational mesh is refined close to the walls to ensure that the viscous sub-layer is covered at least by five cells. At the inlet boundaries (to the axial stage as well as to the hub-seal) there were prescribed the total temperature T_{T0}, the total pressure p_T, the inlet turbulence intensity Tu_0, ratio of the turbulent and the molecular viscosity μ_t / μ and axial flow direction. At the outlet boundary there was prescribed the static pressure p_{S2} at the hub diameter together with the radial equilibrium assumption. At all walls the no-slip condition (zero relative velocity) together with the zero heat flux in normal direction were prescribed. For connection of the stationary stator domain and the moving rotor domain the sliding-mesh interface based on interpolation (with respect to current relative displacement and the rotational speed) was used.

In fig. 2a there is shown the span wise distribution of the degree of reaction R which is defined as $R = \Delta h_{is,\ rotor} / \Delta h_{is,\ stage}$ where $\Delta h_{is,\ rotor/stage}$ is the isentropic enthalpy change in rotor/stage respectively. We can see that the following stator in the one-and-half stage

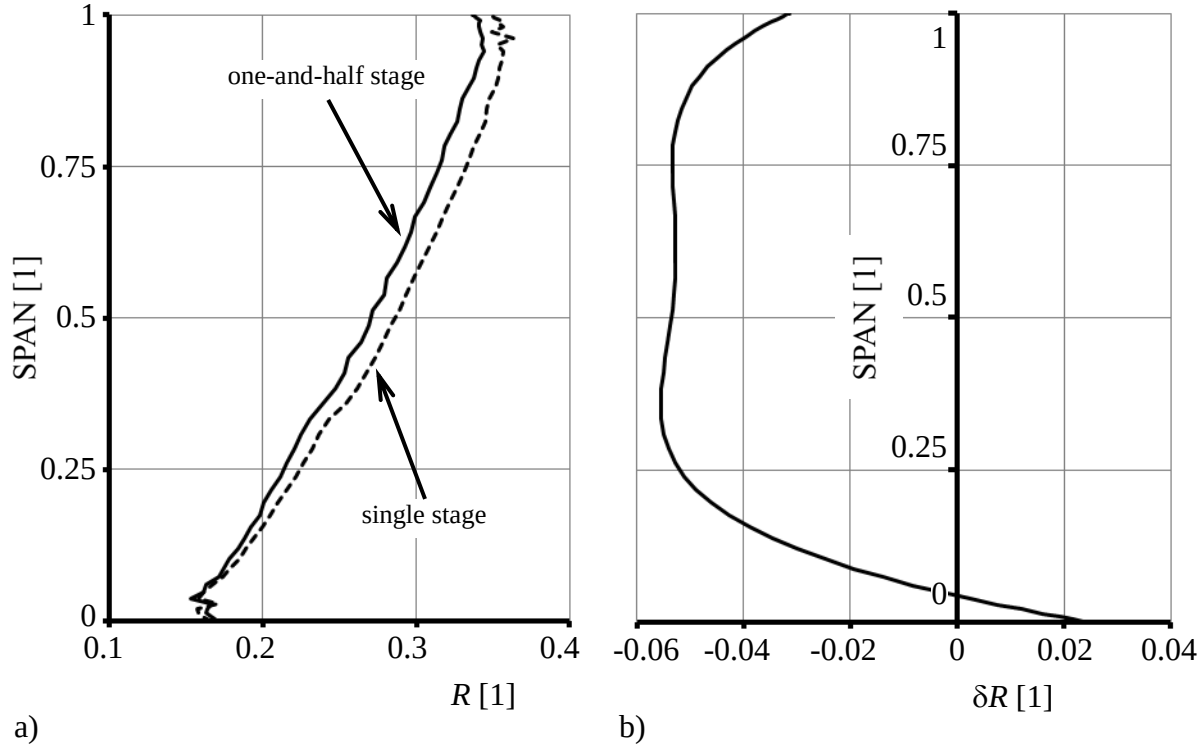

Fig. 2. Span wise distribution of the degree of reaction (a), relative change of the degree of reaction (b)

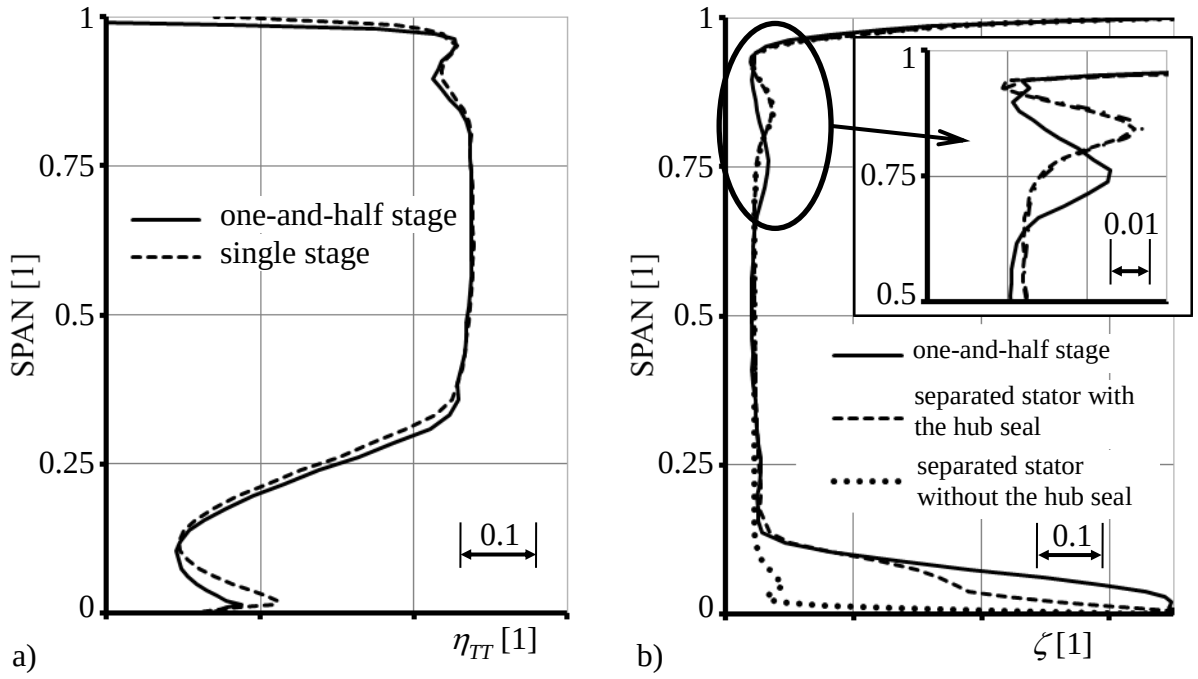

Fig. 3. Span wise distribution of the total-total efficiency (a), span wise distribution of the kinetic energy losses (b)

configuration influences decreasing the degree of reaction of more than five percent. The relative change of the degree of reaction shown in fig. 2b is defined as $\delta R = 1 - (R_{one\text{-}and\text{-}half} / R_{single\ stage})$. A value of the degree of reaction of about 0.26 at the middle diameter indicates that this is a low reaction axial turbine stage.

Fig. 3a shows the total-total efficiency defined as $\eta_{TT} = (T_{Tin} - T_T) / (T_{Tin} - T_{Tis})$, where T_{Tin} is the total inlet temperature, T_T is local total temperature, T_{Tis} is local isentropic total temperature. The effect of the following stator has only minor impact on the stage efficiency particularly in the hub region.

The effect of the foregoing axial stage on the flow through the following stator is characterized via comparison of the kinetic energy losses distribution in fig. 3b. The kinetic energy loss coefficient ζ is defined as $\zeta = 1 - (v / v_{is})^2$ where v is local velocity magnitude and v_{is} is local isentropic velocity. The effect of the leakage flow from the hub seal leads to dramatically increasing the kinetic energy losses in the hub region. On the other hand, the effect of the leakage flow from the shroud seal does not lies in increasing of the kinetic energy losses in the tip region, but the local maximum is shifted to lower diameter from around 85 percent to 75 percent of the blade span (see fig. 3b).

In fig. 4 we can compare distribution of the normalized entropy index in the meridian plane for all four considered cases. The normalized entropy index is defined as $s = p_{norm} / \rho_{norm}$ where p_{norm} is normalized pressure and ρ_{norm} is the normalized density. The entropy index highlights the dissipative regions which relate, as we can see, with the leakage flows from the hub seals and the shroud seal.

Finally, let's summarize that the effect of the following stator lies in influence on the degree of reaction of the foregoing axial stage, whereas the foregoing axial stage has impact on the secondary flows in peripheral parts of the following stator.

Acknowledgements

This work has been supported by the project TH02020086 of the Technology Agency of the Czech Republic.

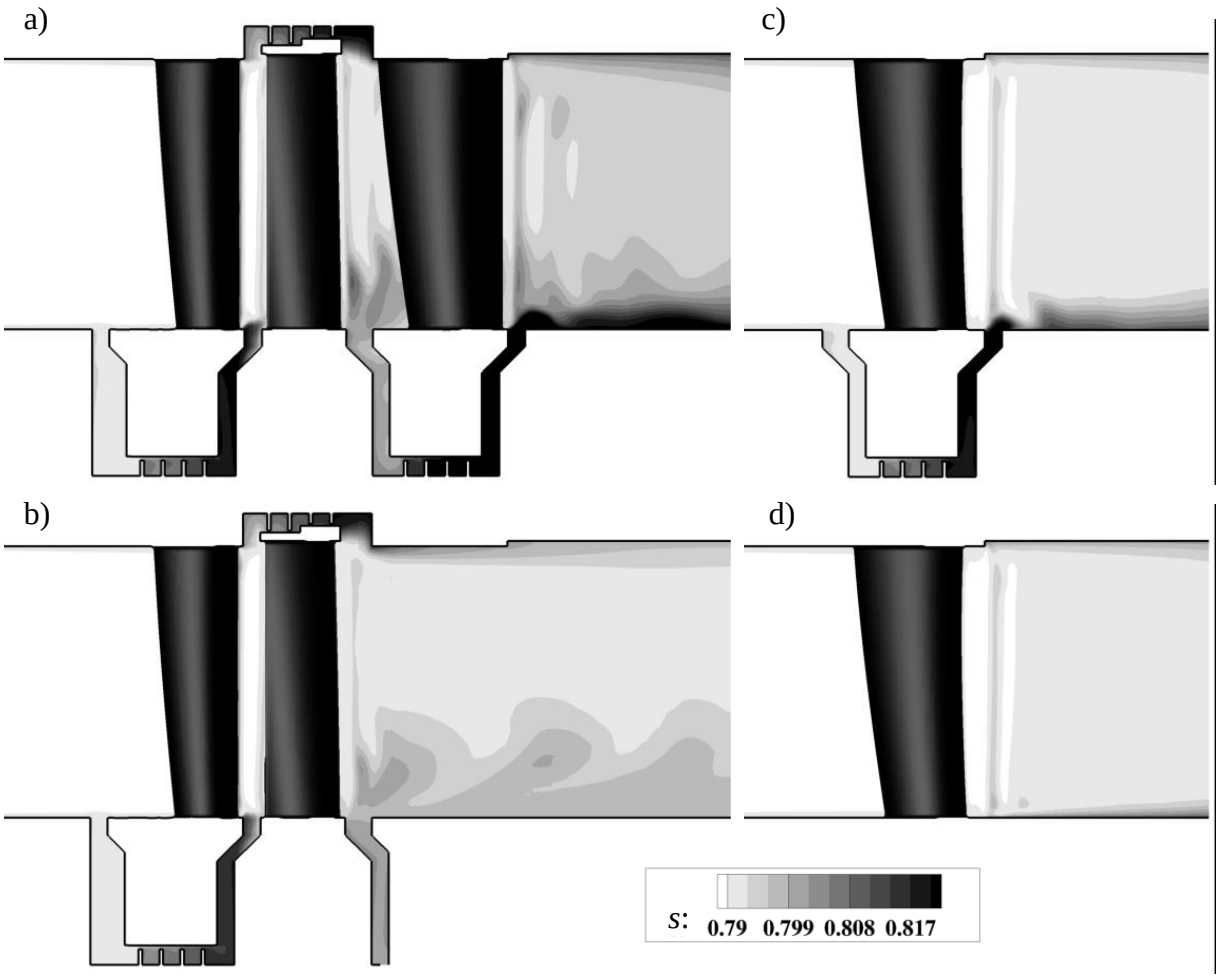

Fig. 4. Distribution of the normalized entropy index in the meridian plane: a) one-and-half stage configuration, b) separated single stage configuration, c) separated following stator without the hub seal, d) separated following stator with the hub seal

References

[1] Clark, J.P., Stetson, G.M., Magge, S.S., The effect of airfoil scaling on the predicted unsteady loading on the blade of a 1 and 1 / 2 stage transonic turbine and a comparison with experimental results, ASME Paper No. 2000-GT-0446.

[2] Jelínek, T., Němec, M., Comparison of total pressure fluctuations in steam turbine stages with different degree of reaction, Acta Polytechnica CTU Proceedings 20, 2018, pp. 51–55.

[3] Němec, M., Jelínek, T., Milčák, P., An investigation of aflow field in a one and half axial turbine stage. AIP Conference Proceedings 1889, 2017, 020025.

[4] Němec, M., Jelínek, T., Milčák, P., Clocking of stators in one and half stage of axial steam turbine, EPJ Web of conferences 180, 2018, 02071.

[5] Reinmöller, U., Stephan, B., Schmidt, S., Clocking effects in a 1.5 stage axial turbine - steady and unsteady experimental investigations supported by numerical simulations, ASME Paper No. 2001-GT-0304.

[6] Straka, P., Software for calculation of turbulent unsteady flow using the nonlinear turbulence model, Report VZLÚ R-6381, 2016. (in Czech)

COMPUTATIONAL MECHANICS 2019
35th conference with international participation
Srní
November 4 - 6, 2019

On modelling and simulation of flow in the vocal tract with consideration of the glottis closure

P. Sváček[a]

[a] *Faculty of Mechanical Engineering, Czech Technical University in Prague, Department of Technical Mathematics, Karlovo nám 13, 121 35 Praha 2, Czech Republic*

1. Introduction

In this paper the problem mathematical modelling of voice creation is addressed. The voice production mechanism is a complex process consisting of fluid-structure-acoustic interaction problem, where the coupling between fluid flow, viscoelastic tissue deformation and acoustics is crucial, see [6]. The so-called phonation onset (flutter instability) for certain airflow rate and a certain prephonatory position leads to the vocal folds to oscillation. The important aspect of the phenomena is the glottis closure (glottis is the narrowest part between the vibrating vocal folds). The problem is mathematically characterized as a problem of fluid-structure interaction with the (periodical) contact problem of the vocal folds involved. In order to include the interactions of the fluid flow with solid body deformation as well as the contact problem, a simplified model problem is considered. This model is similar to the simplified twomass model of the vocal folds of [4], see also the aeroelastic model in [3]. Here, the mathematical model is introduced and the numerical approximation of the problem is described using the residual based stabilization The simplified lumped vocal fold model with the Hertz impact forces is considered. The model is based on a suitable modification of the inlet boundary condition and the arbitrary Lagrangian-Eulerian method with a remeshing algorithm. Two strategies are suggested for treatment of the gap closure. Numerical tests are presented.

2. Flow model

First, the air flow is modelled by the system of the Navier-Stokes equations (cf. [2]) written in the ALE form (cf. [5])

$$\rho\frac{D^{\mathcal{A}}\boldsymbol{u}}{Dt}+\rho((\boldsymbol{u}-\boldsymbol{w}_D)\cdot\nabla)\boldsymbol{u}=\operatorname{div}\boldsymbol{\tau}^f,\qquad \nabla\cdot\boldsymbol{u}=0, \tag{1}$$

where $\boldsymbol{u}=(v_1,v_2)$ is the fluid velocity vector, ρ is the constant fluid density, $\boldsymbol{w}_D$ is the domain velocity, $\frac{D^{\mathcal{A}}\boldsymbol{u}}{Dt}$ denotes the ALE derivative and $\boldsymbol{\tau}^f=(\tau_{ij}^f)$ is the fluid stress tensor given by $\boldsymbol{\tau}^f=-p\mathbb{I}+\mu(\nabla\boldsymbol{u}+\nabla^T\boldsymbol{u})$. Here p is the pressure and $\mu>0$ is the constant fluid viscosity. For the system (1) the initial and boundary conditions are prescribed. The boundary conditions are prescribed on the boundary $\partial\Omega_t^f$ of the computational domain formed by mutually disjoint parts $\partial\Omega_t^f=\Gamma_I\cup\Gamma_S\cup\Gamma_O\cup\Gamma_{Wt}$, where Γ_I denotes the inlet, Γ_O the outlet, Γ_S the axis of symmetry and Γ_{Wt} denotes either fixed or deformable wall. Except the standard boundary conditions used at the fixed or moving walss, the following combination of boundary conditions was used at the

inlet and outlet

$$\begin{aligned} &\text{a)} \quad -\boldsymbol{n}\cdot\boldsymbol{\tau}^f + \frac{1}{2}\rho(\boldsymbol{u}\cdot\boldsymbol{n})^-\boldsymbol{u} = p_I\boldsymbol{n} + \frac{1}{\varepsilon}(\boldsymbol{u}-\boldsymbol{u}_I) \qquad \text{on } \Gamma_I, \\ &\text{b)} \quad -\boldsymbol{n}\cdot\boldsymbol{\tau}^f + \frac{1}{2}\rho(\boldsymbol{u}\cdot\boldsymbol{n})^-\boldsymbol{u} = 0 \qquad \text{on } \Gamma_O, \end{aligned} \tag{2}$$

where $\boldsymbol{n}$ denotes the unit outward normal vector to $\partial\Omega_t^f$, $\boldsymbol{u}_I$ is the inlet velocity, p_I is a reference pressure value at the inlet, $\varepsilon > 0$ is a penalization parameter, $p_{ref} = 0$ is a reference pressure value at the outlet and α^- denotes the negative part of a real number α.

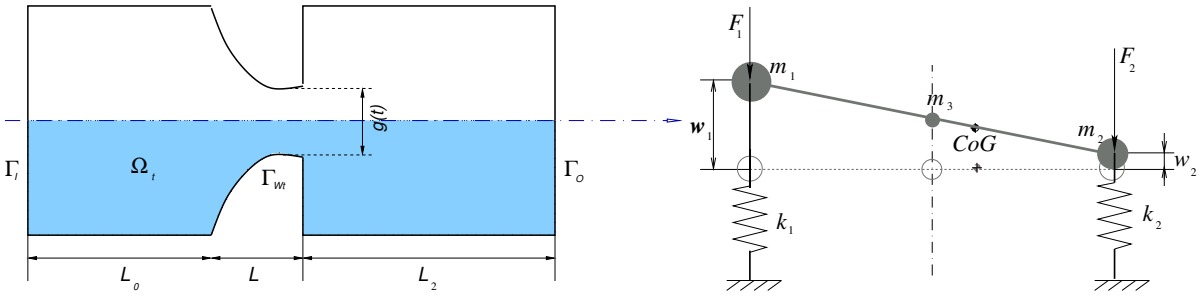

Fig. 1. The 2D computational domain Ω_t and the boundary parts (on the left). Aeroelastic two degrees of freedom model (with masses m_1, m_2, m_3) in displaced position (displacements w_1 and w_2) and resulting aerodynamic forces F_1 and F_2 (on the right).

3. Structure model

The motion of the vocal fold model is governed by the displacements $w_1(t)$ and $w_2(t)$ of the two masses m_1 and m_2, respectively (see Fig. 1). The displacement vector $\boldsymbol{w} = (w_1, w_2)^T$ is obtained by the solution of the following equations (see [3] for details)

$$\mathbb{M}\ddot{\boldsymbol{w}} + \mathbb{B}\dot{\boldsymbol{w}} + \mathbb{K}\boldsymbol{w} = -\boldsymbol{F}, \tag{3}$$

where $\mathbb{M}$ is the mass matrix, $\mathbb{K}$ is the diagonal stiffness matrix with spring constants c_1, c_2 on its diagonal and $\mathbb{B}$ is the matrix of the proportional structural damping. The mass matrix is given by

$$\mathbb{M} = \begin{pmatrix} m_1 + \frac{m_3}{4} & \frac{m_3}{4} \\ \frac{m_3}{4} & m_2 + \frac{m_3}{4} \end{pmatrix}, \tag{4}$$

where m_1, m_2, m_3 are the masses shown in Fig. 1. The components of $\boldsymbol{F} = (F_1, F_2)^T$ are the aerodynamical forces (downward positive). The proportional damping matrix is chosen as $\mathbb{B} = \varepsilon_1\mathbb{M} + \varepsilon_2\mathbb{K}$.

4. Finite element and stabilized finite element methods

In order to describe the details of the application of the finite element method for solution of (stationary) boundary value flow problem, the space $\mathcal{X} \subset \boldsymbol{H}^1(\Omega_t^f)$ for velocity including the Dirichlet boundary conditions is used and the pressure space $\mathcal{Q}$ is chosen as $\mathcal{Q} = L_2(\Omega_t^f)$. The finite element approximation is then sought in the finite element spaces $\mathcal{V}_h = \mathcal{X}_h \times \mathcal{Q}_h$ constructed over an admissble triangulation τ_h of the computational domain Ω_t^f: Find an approximate solution $U_h = (\boldsymbol{u}, p) \in \mathcal{V}_h$ such that at time t holds

$$\left(\frac{D^{\mathcal{A}}\boldsymbol{u}}{Dt} + \overline{\boldsymbol{w}}\cdot\nabla\boldsymbol{u}, \boldsymbol{v}\right) + (\nu\nabla\boldsymbol{u} - p\mathbb{I}, \nabla\boldsymbol{v}) + (q, \nabla\cdot\boldsymbol{u}) + \mathcal{L}(U, V) \;=\; 0$$

for all test functions $\boldsymbol{v}$ and q. ($\overline{\boldsymbol{w}} = (\boldsymbol{u} - \boldsymbol{w}_D)$). Here, the SUPG/PSPG stabilization terms together with the div-div stabilization terms are given as

$$\mathcal{L}(U,V) = \sum_{K\in\tau_h} \delta_K \left[\left(\frac{D^{\mathcal{A}}}{Dt}\boldsymbol{u} - \nu\triangle\boldsymbol{u} + (\overline{\boldsymbol{w}}\cdot\nabla)\,\boldsymbol{u} + \nabla p, (\overline{\boldsymbol{w}}\cdot\nabla)\boldsymbol{v} + \nabla q \right)_K + \tau_K \Big(\nabla\cdot\boldsymbol{u}, \nabla\cdot\boldsymbol{v} \Big)_K \right].$$

5. Numerical analysis of Oseen problem

First, the Oseen problem is considered

$$-\nu\triangle\boldsymbol{u} + \boldsymbol{b}\cdot\nabla\boldsymbol{u} + \nabla p + \sigma\boldsymbol{u} = \boldsymbol{f}, \qquad \nabla\cdot\boldsymbol{u} = 0$$

in the computational domain $\Omega = (0,1)^2$. The problem is equipped with the Dirichlet boundary condition $\boldsymbol{u} = \boldsymbol{b}$ prescribed at $\partial\Omega$. Here we set $\sigma = 0$ is used, $\boldsymbol{b} = (\sin(\pi x), -\pi y\cos(\pi x))$ and the right hand side $\boldsymbol{f}$ is chosen in such a way, that $\boldsymbol{b}$ is solution of the Oseen problem, i.e.,

$$\boldsymbol{f}(x,y) = \nu\pi^2\sin(\pi x) + \pi\cos(\pi x)(\sin(\pi x) + \cos(\pi y)), -\nu\pi^3 y\cos(\pi x) + \pi^2 y - \pi\sin(\pi x)\sin(\pi y)).$$

The computations were performed for different values of the viscosity coefficient nu. First convergence of the Galerkin finite element approximations $\boldsymbol{u}_h^G$ to the exact solution $\boldsymbol{u} = \boldsymbol{b}$ is investigated, $p(x,y) = \sin(\pi x)\cos(\pi y)$ for $\nu = 0.05$ (here, relatively high viscosity was chosen in order to obtain stable Galerkin approximations even on coarser meshes). For approximation of flow problem the Taylor Hood finite elements were used. The errors in H^1 norm are shown in Table 1. These results are compared to the results of stabilized formulation of the same problem, which shows that the used residual based stabilization does not polute the solution, see Table 2. The convergence orders in both cases agreee well with the theoretical estimate. For the stabilized method such a convergence rates are well preserved for the values $\nu = 10^{-3}, \ldots, 10^{-6}$ with a slow down observed only for coarse grid configuration. Let us emphasize, that as the convection $\boldsymbol{b}$ equals the exact solution $\boldsymbol{u}$, the Dirichlet problem for Navier-Stokes equations can be formulated with the same analytical solution. Similar convergence analysis was performed with analogous results.

6. Gap closure treatment, remeshing and remaping

In order to treat the gap closure, the large deformation of the mesh needs to be addressed. This can lead to the high distortion of the mesh mainly in the region of the glottis. Here, the two possible solution are discussed. The first one based on the restriction of the applied model at the part of the domain which corresponds to the closed area. This is realized using the solution of an artificial problem at this part of the mesh in combination with a modified definition of mesh deformation (ALE mapping).

The other possibility is the use of the remeshing algorithm together with conservative remapping of the flow variables. First, the remeshing algorithm is avoided here with the consideration of several

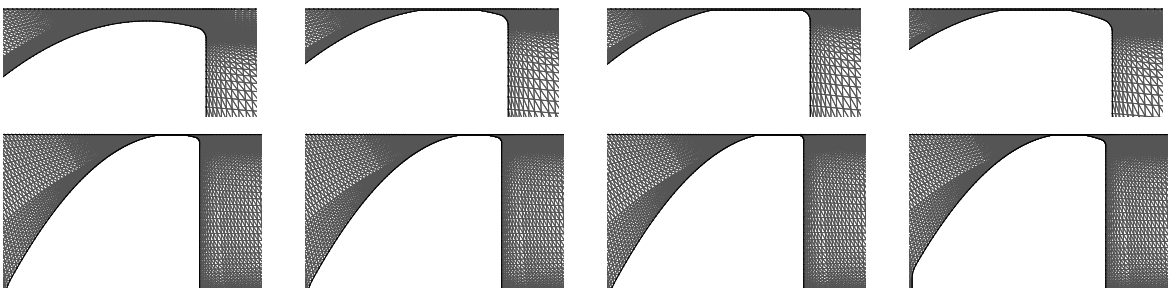

Fig. 2. Remeshing of the mesh for the (almost) closed glottal part

Table 1. Convergence of Galerkin FE method to the solution of the Oseen problem

h_{max}	$H^1(u)$	$H^1(v)$	$H^1(p)$	q_{H1u}	q_{H1v}	q_{H1p}
0.333174	0.148971	0.278814	0.824015			
0.166358	0.0294769	0.0389521	0.306831	2.33	2.83	1.42
0.0881204	0.00751673	0.00970303	0.155735	2.15	2.19	1.07
0.0449673	0.00178417	0.00225841	0.0781441	2.14	2.17	1.03
0.0230627	0.000444434	0.00055994	0.038375	2.08	2.09	1.07
0.0118955	0.000107972	0.000139096	0.0192135	2.14	2.1	1.04

Table 2. Convergence of Stabilized FE method to the solution of the Oseen problem

h_{max}	$H^1(u)$	$H^1(v)$	$H^1(p)$	q_{H1u}	q_{H1v}	q_{H1p}
0.333174	0.148971	0.278814	0.824015			
0.158053	0.0385103	0.0479786	0.332202	1.81	2.36	1.22
0.0877183	0.00912475	0.0113478	0.162359	2.45	2.45	1.22
0.0451748	0.00239609	0.00279304	0.0821471	2.02	2.11	1.03
0.0235271	0.000593443	0.000695859	0.0402822	2.14	2.13	1.09
0.0119951	0.000148245	0.000174687	0.0201917	2.06	2.05	1.03

meshes suitable for different cases of glottis closure or opening. Here, four configurations are considered characterized by their displacement in terms of w_1 and w_2. In dependence on the current displacement $w_1(t)$ and $w_2(t)$ of the vocal fold either the current underlying mesh is deformed or a remeshing step is used. For the remeshing step the conservative remapping of the flow quantities is applied. The algorithms with the conservative remapping of momentum(velocity) components followed by the projection on the divergence-free space was tested. Fig. 2 shows the mesh in the deformed positions for the case of the closed gap.

In order to treat such a gap closing several modifications of two algorithms were tested. The first algorithm is based on artificial fluid formulation, where part of the flow in the computational domain is modelled with the aid of the artificial porous media flow, see [1]. The second algorithm considers the relaxad contact formulation with a combination with the well tuned inlet boundary conditions.

Acknowledgment

This work was supported by the *Czech Science Foundation* under the *Grant No. 19 - 07744S*.

References

[1] Burman, E., Fernández, M. A., Frei, S., A Nitsche-based formulation for fluid-structure interactions with contact, 2018, arXiv:1808.08758.

[2] Feistauer, M., Mathematical methods in fluid dynamics, Longman Scientific & Technical, Harlow, 1993.

[3] Horáček, J., Šidlof, P., Švec, J. G., Numerical simulation of self-oscillations of human vocal folds with Hertz model of impact forces, Journal of Fluids and Structures 20 (6) (2005) 853-869.

[4] Ishizaka, K., Flanagan, J. L., Synthesis of voiced sounds from a two-mass model of the vocal cords, The Bell System Technical Journal 51 (1972) 1233-1268.

[5] Nomura, T., Hughes, T. J. R., An arbitrary Lagrangian-Eulerian finite element method for interaction of fluid and a rigid body, Computer Methods in Applied Mechanics and Engineering 95 (1992) 115-138.

[6] Titze, I. R., The myoelastic aerodynamic theory of phonation, National Center for Voice and Speech, U.S.A., 2006.

COMPUTATIONAL MECHANICS 2019
35th conference with international participation
Srní
November 4 - 6, 2019

Loading condition monitoring on trusses applying a machine learning approach with training data of a finite element model: A study case

H. A. Tinoco[a,b,c], C. I. Cardona[a]

[a] *Experimental and Computational Mechanics Laboratory, Universidad Autónoma de Manizales. C.P. 170001. Manizales-Caldas. Colombia.*
[b] *Institute of Physics of Materials, Czech Academy of Sciences. Brno, Czech Republic*
[c] *Central European Institute of Technology - Brno University of Technology, Technická 3058/10, 61600 Brno, Czech*

Structural health monitoring (SHM) techniques deal with the changes in the dynamic or static characteristics of the structures that affect its performance during the service [2]. Mainly, these techniques are based on vibrations, and their implementation includes complex integrated systems not addressed from the structural design. Despite the numerous applications of SHM, loading condition monitoring (application place, direction, and magnitude) is not a very implemented strategy in this engineering field. This paper presents a methodology to monitor the application of external forces on structures using a learning machine process and finite element analysis (FEA). In Fig. 1a is described the proposed monitoring methodology, which is applied to a truss structure to validate this study. The truss contains nine structural elements, and each one presents a piezoelectric transducer to measure the forces in their links, as illustrated in Fig. 1b. The real truss was modeled by means of a FEA (implemented in Matlab with truss elements) considering their mechanical properties and loading conditions, as observed in Fig. 1c. To simulate different loading conditions, a force F_s is applied in node 3 varying two parameters, angle β, and magnitude. This is carried out to establish a database using the internal forces (in each bar) obtained by FEA.

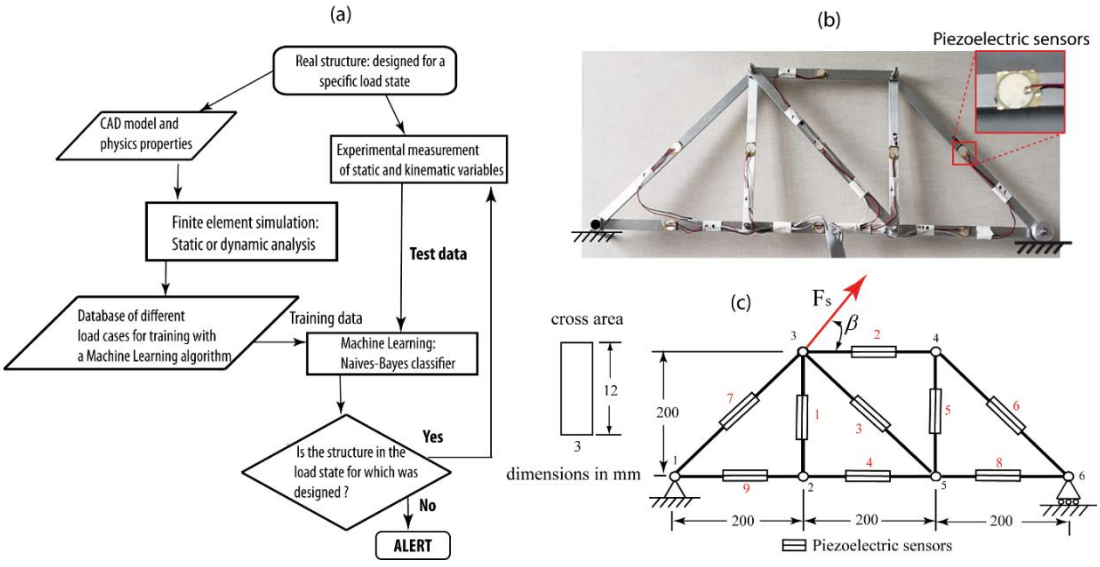

Fig. 1. (a) Methodology for SHM based on FEA and machine learning; (b) Experimental truss with piezoelectric sensors; (c) Real truss scheme for the finite element model

The applied force magnitude (F_s) was constrained to the limit state of the truss; it means that its maximum load produces an elastic behaviour in the simulation. In the experimental implementation, and before monitoring tasks, compensation values of forces were computed to normalize the electrical measurements with the finite element solutions; the results are evidenced in Fig. 2a. Naive Bayes classifier [1] was implemented for the machine learning process to monitor the force direction (known state) using the FEA solutions as a training database in the classifier. Several monitoring tests were performed with the experimental setup illustrated in Fig. 2b, but two only are reported in this study ($\beta = 150°$ and $\beta = 90°$). Fig. 2c shows the results obtained during the monitoring process (in real-time) when a force of 2.45 N was applied at the test directions. The training data means the number of simulations calculated corresponding with the divisions of β angle. For example; for $\beta = 150°$, the algorithm determined the correct β direction after 1600 training data, and for $\beta = 90°$ were necessary more than 3600 training data. This shows the importance of the database creation by FEA; however, β direction was monitored correctly in all done experiments. In a real context, the structures are designed for a known loading condition; it implies that not undesirable states could be monitored to emit early alerts. This is possible with the presented methodology since any loading state could be simulated and monitored during the service of the structure.

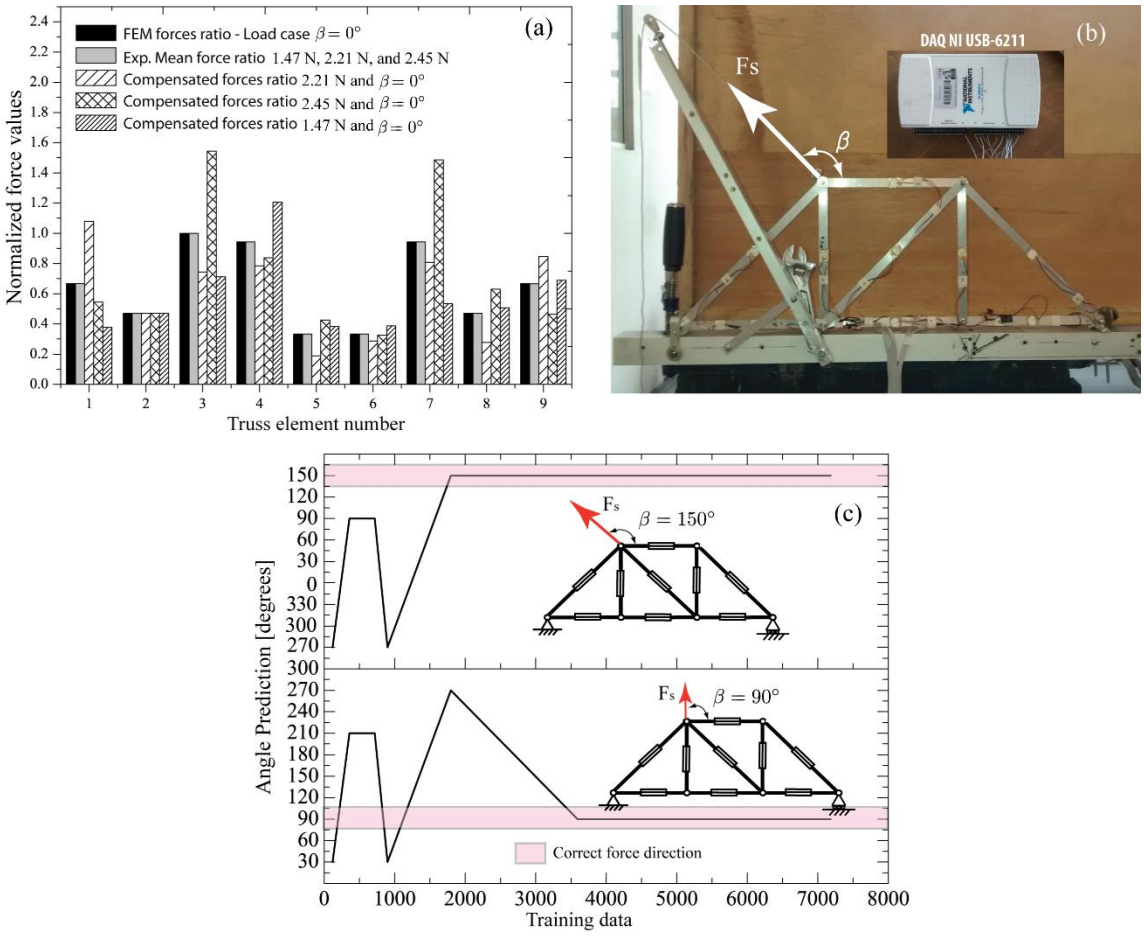

Fig. 2. (a) Electrical force normalization with FEA data; (b) Experimental application of the force in β direction; (c) Angle prediction for two experimental cases

References

[1] Friedman, N., Geiger, D., Goldszmidt, M., Bayesian network classifiers, *Machine learning* 29 (2-3) (1997) 131-163.

[2] Goyal, D., Pabla, B.S., The vibration monitoring methods and signal processing techniques for structural health monitoring: a review, *Archives of Computational Methods in Engineering* 23 (4) (2016) 585-594.

COMPUTATIONAL MECHANICS 2019
35th conference with international participation
Srní
November 4 - 6, 2019

Fatigue crack propagation in a component produced by additive manufacturing of polymer materials

L. Trávníček[a,b], F. Arbeiter[c], P. Dlhý[a,b], M. Spoerk[d], L. Náhlík[a,b], P. Hutař[a,b]

[a] CEITEC BUT, Purkyňova 123, 621 00 Brno, Czech Republic
[b] Institute of Physics of Materials, Academy of Science of the Czech Republic, Žižkova 22, 616 62 Brno, Czech Republic
[c] Polymer Competence Center Leoben, Roseggerstrasse 12, A-8700 Leoben, Austria
[d] Montanuniversität Leoben, Otto Glöckel-Strasse 2/II, A-8700 Leoben, Austria

1. Introduction

Additive manufacturing is a layer-based manufacturing process which allows automatic fabrication of products of complex shape at optimized cost with reduced time. In the last decade, the application of additive manufacturing has grown significantly, mainly due to the availability of comparatively inexpensive 3D-printing devices [3]. As the relatively inexpensive process is definitely the advantage, on the other hand, it has been widely believed that components produced by this method have slightly worse mechanical properties in comparison with conventionally produced homogenous components, due to existence of weld lines [4]. However, recent studies proved, that the negative effect of weld lines can be reduced by choosing appropriate welding conditions during the printing process [2].

Fracture properties and crack growth kinetics of PLA (polylactic acid) were studied by Arbeiter [1] in a series of measurement on CT specimens with different line orientations. The results showed that regardless of the orientation of the lines, the cycles to fracture and to initiation as well as the crack initiation and propagation law appear to be almost identical. Based on these results, a Paris' crack propagation law was used for the crack propagation description, and the material constants were determined: $A = 10^{-3.78}$ and $m = 2.87$ [1]. In order to verify the validity of the obtained material constants, a study of crack growth in a real mechanical component – a wrench – made of PLA material has been in progress. The main aim of presented study is to create a 3D numerical model containing a crack that will allow calculation of the stress intensity factor along the crack front and estimate a residual fatigue lifetime of the modeled wrench with consideration of a growing crack from given initial size to the final one. Finally, the comparison between estimated fatigue lifetime value and experimentally obtained one was done.

Fatigue tests were carried out on the plastic wrench mounted to a steel nut, which was fixed. The wrench was cyclically loaded by force in a range of 24 N to 40 N with a loading ratio R of 0.1 at room temperature. A scheme of the experiment with basic dimensions of both components is shown in Fig. 1. Tests were aborted when maximum displacement of the machine was reached. Fatigue experiments were carried out at Polymer Competence Center Leoben, Austria.

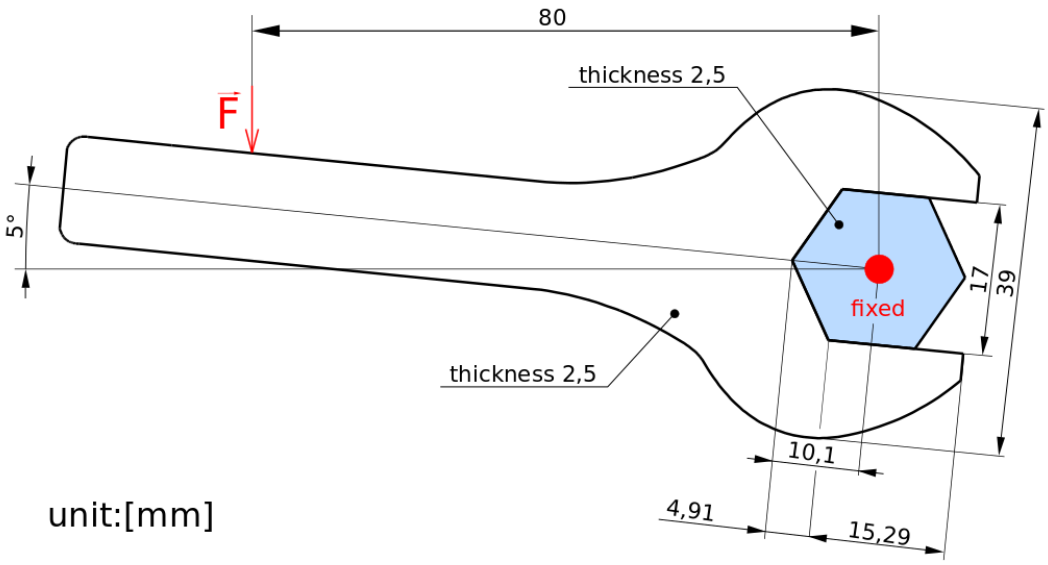

Fig. 1. A scheme of the experiment with basic dimensions of both components

2. Numerical modeling

The numerical modeling was chosen due to the complicated stress field near the crack front, that is influenced by contact stresses and by the stress concentration caused by sharp edge, where the crack initiated. During the crack propagation modeling, the assumption that the crack propagates as semielliptical was taken into account. A typical 3D numerical model contained between 5×10^6 and 9×10^6 isoparametric elements depending on the crack size. The finite element mesh was prepared very fine near the crack front to describe the singular stress field near the crack front properly (see detail in Fig. 2). Keeping both parts in contact during the simulation was secured by COMBIN element (highlighted by purple color) and by using contact elements between both models (highlighted by green color), see Fig. 2.

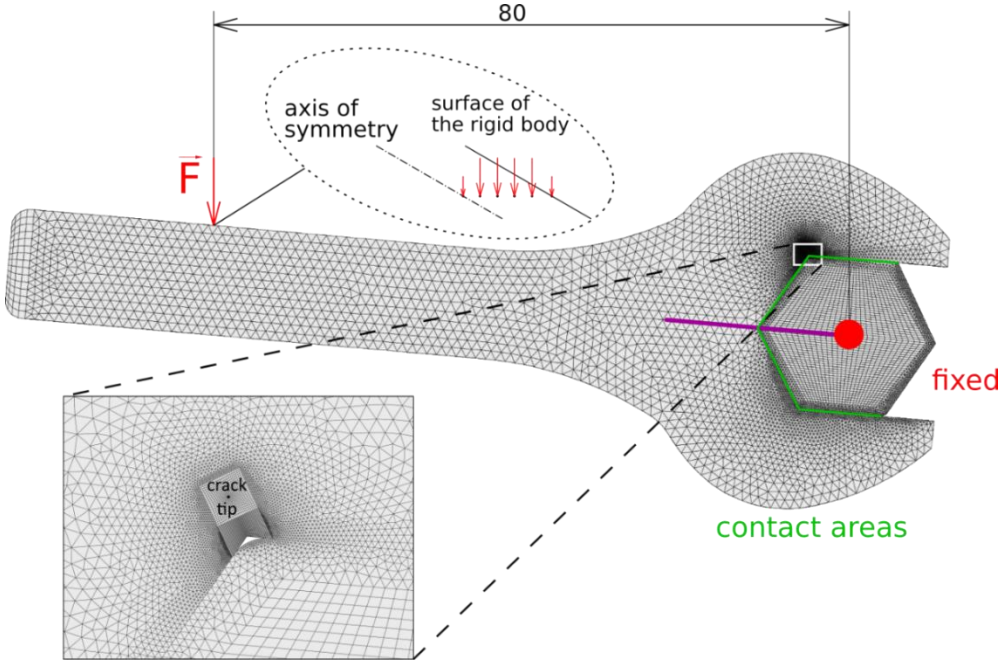

Fig. 2. 3D Finite element model containing a crack. Very fine mesh around the crack tip is shown in the detail

The loading force was distributed symmetrically on the width of the wrench, see detail in Fig. 2. The elastic properties of both materials taken in the optimization are shown in Table 1.

Table 1. Basic elastic properties of both materials

Material properties:	**Young's modulus [GPa]**	**Poisson's ratio [-]**
Plastic wrench	3.4	0.37
Metal bolt	210	0.33

The crack propagation was modelled by crack increments, i.e. number of steps (numerical calculations with extended crack by chosen crack increment) were performed during numerical simulation of crack growth from initial to the final size. The size of initial defects from the printing pattern was between 50 and 100 μm according to the fracture surface. Therefore, the crack length for the first numerical step was chosen 50 μm and the initial crack was of semicircle shape. As the crack was growing the crack front shape was continuously changing to a semielliptical one. The semielliptical crack was modeled up to crack length when the crack front reached surface of the wrench. Therefore, approximately to 2 mm due to very fine mesh in the crack surrounding. For higher values of the crack lengths, the straight crack front shape was considered.

3. Conclusion

This numerical model allows calculation of the stress intensity factor along the crack front, where the crack growth is simulated in steps and two models of cracks are considered. The first one covers the short crack lengths up to 2 mm, where the semielliptical crack front shape is assumed. The second model can be used for crack lengths values from 2 mm and the crack front shape is considered as straight – as the crack grew through all the thickness of the model. The obtained stress intensity factor values were used for numerical estimation of residual fatigue lifetime of the wrench. The comparison with experimental date was done and good agreement has been found. The work presented contributes to the better understanding of fatigue crack behavior in 3D-printed PLA materials.

Acknowledgements

This research has been supported by Polymer Competence Center Leoben GmbH (PCCL, Austria) and the Ministry of Education, Youth and Sports of the Czech Republic under the project m- IPMinfra (CZ.02.1.01/0.0/0.0/16_013/0001823) and the equipment and the base of research infrastructure IPMinfra were used during the research activities.

References

[1] Arbeiter, F., Spoerk, M., Wiener, J., Gosch, A., Pinter, G., Fracture mechanical characterization and lifetime estimation of near-homogeneous components produced by fused filament fabrication, Polymer Testing 66 (2018) [online].

[2] Spoerk, M., Arbeiter, F., Cajner, H., Sapkota, J., Holzer, C., Parametric optimization of intra- and inter-layer strengths in parts produced by extrusion-based additive manufacturing of poly(lactic acid), Journal of Applied Polymer Science **134** (41) (2017) [online].

[3] Song, Y., Li, Y., Song, W., Yee, K., Lee, K.-Y., Tagarielli, V.L., Measurements of the mechanical response of unidirectional 3D-printed PLA, Materials & Design 123 (2017) [online].

[4] Ziemian, S., Okwara, M., Ziemian, C.W., Tensile and fatigue behavior of layered acrylonitrile butadiene styrene, Rapid Prototyping Journal 21 (3) (2015) [online].

COMPUTATIONAL MECHANICS 2019
35th conference with international participation
Srní
November 4 - 6, 2019

On 3D dynamical structure of the wake behind circular cylinder

V. Uruba[a,b], P. Procházka[a], V. Skála[a]

[a] *Institute of Thermomechanics of the Czech Academy of Sciences, Dolejškova 5, 182 00 Praha 8, Czech*
[b] *Faculty of Mechanical Engineering, University of West Bohemia in Pilsen, Univerzitní 22, 306 14 Plzeň, Czech Republic*

The wake behind a cylinder with circular cross-section will be explored experimentally using Stereo PIV time-resolved method. Dynamics of the wake is to be analysed using the OPD method. Variation of the flow-field in spanwise direction are to be studied in detail. Presence of streamwise vorticity in the wake is to be shown in instantaneous snapshots, however absent completely in the time-mean flow-field.

Both external and internal flows could be characterized by 2D boundary conditions in practical cases very often. Typical example could be the case of cross-flow around a prismatic body. In spite of inherent dynamical nature of the flow-field, this case could be considered as a plane flow, invariant along the body (excluding the ends). Such a case is also mathematically modelled as a 2D flow very often, taking into account only a single section, supposing the same flow picture for any other cross-section along the body.

The case of circular cylinder in cross-flow belongs to so called canonical cases. We could find extensive information on this case in literature – theoretical, experimental and numerical studies. Most of available studies treat the prismatic cylinder as forced 2D case, no 3D structures are detected, of course. The 3D structure of the wake behind a body of 2D geometry has been already addressed e.g. in [2]. The paper [1] deals with the d'Alembert paradox (zero forces) for inviscid flow and shows that this paradox is due to forcing 2D stationary flow pattern. In the real 3D nonstationary flow the forces are generated even in the inviscid case and the the d'Alembert paradox is thus resolved.

It is known that the wake behind circular cylinder exhibits several types of flow patterns: steady, unsteady periodical and chaotic, the control parameter is Reynolds number. Description of the wake topology including its dynamics could be find in any good book on fluid mechanics, more information on the details are in numerous papers, see e.g. [4].

In the presented paper flow-fields in the cylinder wake are to be shown. The cylinder is placed in the low turbulent regular flow, Reynolds number is about 5 thousands. The measurements are performed in the plane perpendicular to the flow and parallel to the cylinder axis in the distance 8 cylinder diameters. Time resolved PIV stereo technique is used evaluating all 3 velocity components within the plane of measurement with repetition frequency 1 kHz.

The figures are to be presented in dimensionless form, references are cylinder diameter for lengths and incoming velocity for velocities.

The mean velocity field is shown in Fig. 1. The variations of the mean velocity along the cylinder axis are due to perspective view of the cameras, which are placed symmetrically in x direction. The in-plane velocity field is shown by vectors with vector lines, the third out-of-plane velocity component W is represented by colour.

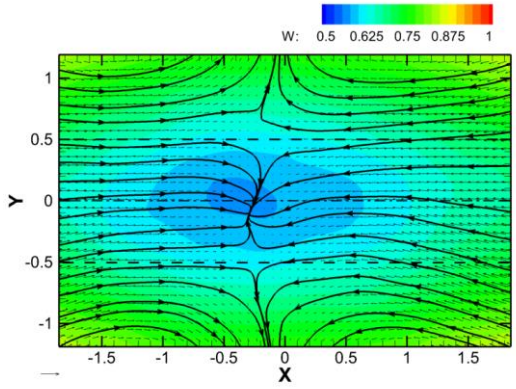

Fig. 1. Mean velocity field

To study the dynamical properties of the flow-field the Oscillation Pattern Decomposition method (OPD) was adopted resulting in series of OPD modes. Each OPD mode is characterized by its topology in complex form (consisting of real and imaginary parts), frequency and attenuation of the pseudo-periodic (oscillating) behaviour. The details on OPD method could be found in [3].

For presentation the dominant oscillating mode has been chosen corresponding to the vortex shedding process.

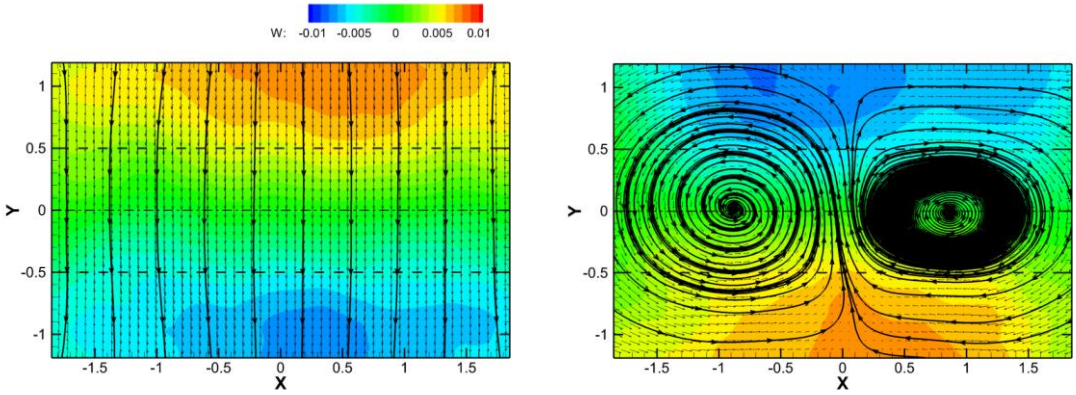

Fig. 2. The vortex shedding OPD mode, real part left, imaginary part right

The real part of the OPD mode is shown in left part of Fig. 2 and documents 2D structure of the fluctuation flow-field. On the other hand the imaginary part in the right Fig. 2 part contains a contra-rotating pair of streamwise vortices with spacing 2 cylinder diameters.

Acknowledgements

This work was supported by the Grant Agency of the Czech Republic, project Nos. 17-01088S and 19-04695S.

References

[1] Hoffman J., Johnson C., Resolution of d'Alembert's paradox, Journal of Mathematical Fluid Mechanics 12 (3) (2010) 321-334.
[2] Uruba V., On 3D instability of wake behind a cylinder, AIP Conference Proceedings, Vol 1745, 2016, Art. no. 020062.
[3] Uruba V., Near wake dynamics around a vibrating airfoil by means of PIV and oscillation pattern decomposition at Reynolds number of 65 000, Journal of Fluids and Structures 55 (2015) 372-383.
[4] Williamson, C.H.K., Vortex dynamics in the cylinder wake, Annual Review of Fluid Mechanics 28 (1996) 477-539.

COMPUTATIONAL MECHANICS 2019
35th conference with international participation
Srní
November 4 - 6, 2019

The influence of penalization inlet boundary condition on the stability boundary

J. Valášek[a], P. Sváček[a], J. Horáček[b]

[a] *Faculty of Mechanical Engineering, Czech Technical University in Prague, Karlovo nám. 13, Praha 2, 121 35*
[b] *Institute of Thermomechanics, Czech Academy of Sciences, Dolejškova 5, Praha 8, 182 00*

The flow-induced vibrations of human vocal folds (VFs) are interesting and complex phenomenon with number of possible practical applications, see e.g. [2, 3]. Mathematically it represents the fluid-structure interaction (FSI) problem which in this specific case poses many difficulties for numerical realization. One of the major difficulty is need to consider the flow domain time evolution especially during the closing phase, see [5], followed by the question of a suitable inlet boundary condition, see [4] etc. We present here the two-dimensional FSI model, see Fig. 1, where linear elastic problem is coupled to the incompressible Navier-Stokes equations in the arbitrary Lagrangian-Eulerian (ALE) form. The special attention is paid to the flow inlet boundary conditions (BCs), where the penalization boundary condition is introduced as a promising alternative to the usually used Dirichlet boundary condition or to the prescribed pressure drop between inlet and outlet.

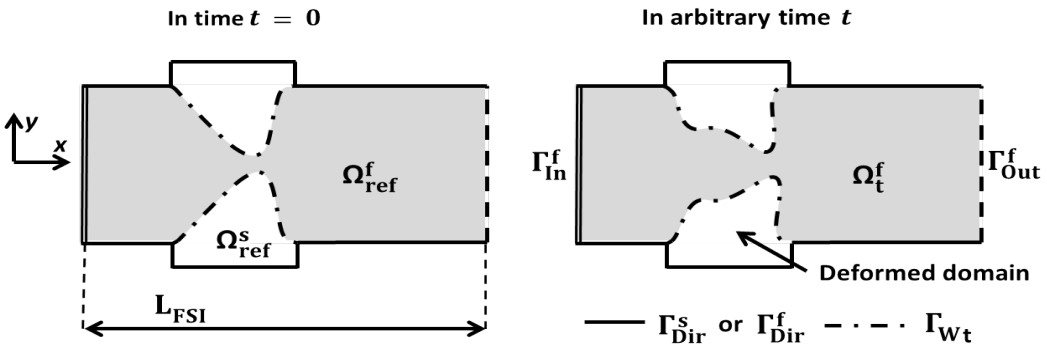

Fig. 1. The scheme of FSI domain composed of fluid domain Ω_t^f and the elastic body domain Ω^s

Structure. The motion of structure with density ρ^s is given by partial differential equations

$$\rho^s \frac{\partial^2 u_i}{\partial t^2} - \frac{\partial \tau_{ij}^s}{\partial x_j} = 0 \qquad \text{in } \Omega^s \times (0,T), \tag{1}$$

where $\mathbf{u}(x,t) = (u_1, u_2)$ is sought displacement and τ_{ij}^s are the components of the Cauchy stress tensor [1]. The small displacements are assumed and the elastic body is modelled as isotropic.

Fluid flow. In order to incorporate the effects of the fluid computational domain, the ALE method is used. The motion of the viscous incompressible fluid in a time dependent domain Ω_t^f is modelled by the Navier-Stokes equations written in the ALE form

$$\frac{D^A \mathbf{v}}{Dt} + ((\mathbf{v} - \mathbf{w}_D) \cdot \nabla)\mathbf{v} - \nu^f \Delta \mathbf{v} + \nabla p = \mathbf{0}, \quad \text{div } \mathbf{v} = 0 \quad \text{in } \Omega_t^f, \tag{2}$$

where $\mathbf{v}(x,t)$ denotes the fluid velocity, p is the kinematic pressure and ν^f is the kinematic fluid viscosity, further the term $\frac{D^A}{Dt}$ denotes so called ALE derivative and the term $\mathbf{w}_D$ is domain deformation velocity, see e.g. [1].

The system of equations (2) is equipped with the zero initial condition and appropriate BC, see [6]. Especially, on the inlet Γ^f_{In} the three different inlet BC are considered

$$\begin{aligned}
&\text{a)} && \mathbf{v}(x,t) = \mathbf{v}_{\mathrm{Dir}}(x,t) && \text{for } x \in \Gamma^f_{\mathrm{In}},\\
&\text{b)} && (p(x,t) - p_{\mathrm{in}})\vec{n}^f - \nu^f \frac{\partial \mathbf{v}}{\partial \vec{n}^f}(x,t) = -\frac{1}{2}\mathbf{v}(\mathbf{v}\cdot\vec{n}^f)^- && \text{for } x \in \Gamma^f_{\mathrm{In}}, \quad (3)\\
&\text{c)} && p(x,t)\vec{n}^f - \nu^f \frac{\partial \mathbf{v}}{\partial \vec{n}^f}(x,t) = -\frac{1}{2}\mathbf{v}(\mathbf{v}\cdot\vec{n}^f)^- + \frac{1}{\epsilon}(\mathbf{v} - \mathbf{v}_{\mathrm{Dir}}) && \text{for } x \in \Gamma^f_{\mathrm{In}},
\end{aligned}$$

where the vector $\mathbf{n}^f = (n^f_j)$ denotes the outward unit normal to the boundary $\partial\Omega^f$ and $\alpha^+ = \max\{0,\alpha\}$, $\alpha^- = \min\{0,\alpha\}$, see [6]. The condition (3 c) is weakly imposed Dirichlet boundary condition, which fulfilment is enforced with the aid of penalization coefficient ϵ.

Numerical model. The FSI problem given by Eqs. (1) and (2) together with appropriate initial and boundary conditions are discretized in space by the finite element method and in time by the Newmark method. The partitioned approach with strong coupling is chosen. Especially, the modified streamline-upwind/Petrov-Galerkin method is used for stabilization of flow solver. For implementation details, see [6].

Numerical results. Numerical results of flow-induced vibration of vocal folds (VFs) with the full channel configuration are presented. The VF geometry is based on articles [4] and [6]. The constant time step Δt is chosen as $2.5 \times 10^{-5}\,\mathrm{s}$, the densities are set to $\rho^s = 1000\,\mathrm{kg/m^3}$ and $\rho^f = 1.185\,\mathrm{kg/m^3}$, the kinematic fluid viscosity is $\nu^f = 1.47 \times 10^{-5}\,\mathrm{m^2/s}$. The elastic parameters are chosen as follows: Young modulus $E^s = 8\,\mathrm{kPa}$ and Poisson ratio $\sigma = 0.4$.

Comparison of different inlet boundary conditions. The following four simulations with different inlet boundary conditions are compared, namely:

a) Case *VEL* with prescribed Dirichlet BC (3 a) with $\mathbf{v}_{\mathrm{dir}} = (2.1, 0.0)\,\mathrm{m/s}$,
b) Case *PEN-S* with penalization BC (3 c), where velocity $\mathbf{v}_{\mathrm{dir}}$ is imposed by $\epsilon = 10^{-5}$,
c) Case *PEN-W* with penalization BC (3 c), where velocity $\mathbf{v}_{\mathrm{dir}}$ is imposed by $\epsilon = 5 \times 10^{-4}$,
d) Case *PRES* with given pressure drop $\Delta p = p_{\mathrm{in}} - p_{ref} = 400\,\mathrm{Pa}$ in (3 b).

The inlet flow velocity and the pressure drop are displayed in Fig. 2. While the inlet velocity is for Dirichlet BC constant and for the prescribed pressure drop highly oscillating, in cases *PEN-S* and *PEN-W* we see the moderately oscillation behaviour of inlet velocity. The amplitude of oscillation increases with the higher values of penalization parameter ϵ ($\frac{1}{\epsilon}$ is decreasing).

The pressure drop in the case *PRES* is constant, see Fig. 2 (right), whereas in cases *VEL*, *PEN-S* and *PEN-W* it oscillates with exponentially increasing amplitude. This can be expected because the inlet velocity $\mathbf{v}_{\mathrm{Dir}}$ exceeds critical velocity of flutter instability $\mathbf{v}_{flutter}$. Then the VF oscillation amplitude gradually grows and the airflow pressure increases as the channel cross-section becomes smaller. The increase of pressure drop is most rapid for case *VEL*, the cases *PEN-S* and *PEN-W* are time delayed. The simulations in all four cases end by the fluid flow solver failure caused by too distorted fluid computational mesh near the top of the VFs.

The gap denoting the distance between vocal folds is plotted in Fig. 3. The gradually closing gap corresponds well with pressure drop behaviour in cases *VEL*, *PEN-S* and *PEN-W*. In the case *PRES* the VF oscillation develops despite constant pressure drop nevertheless the development of large VF oscillation took longer time. We found explanation in the fact, that prescribed Δp lays more closer to stability boundary contrary to given inlet velocity $\mathbf{v}_{\mathrm{Dir}}$, which substantially exceeds the stability boundary.

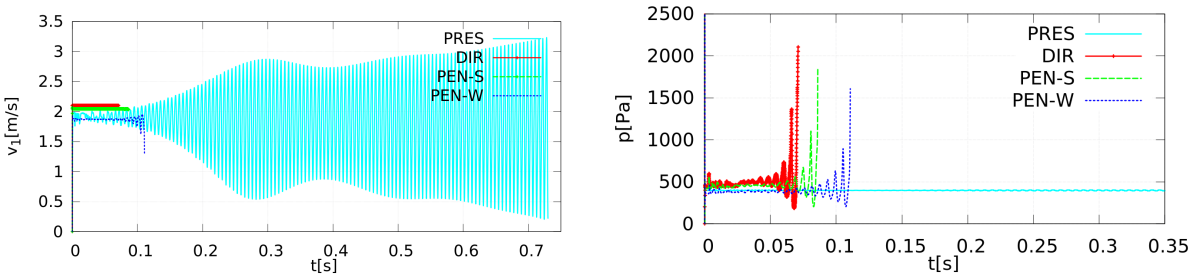

Fig. 2. The numerically simulated inlet airflow velocity and pressure difference between inlet and outlet of the channel are shown on the left and on the right, respectively. The simulation cases *VEL*, *PEN-S*, *PEN-W* and *PRES* are compared.

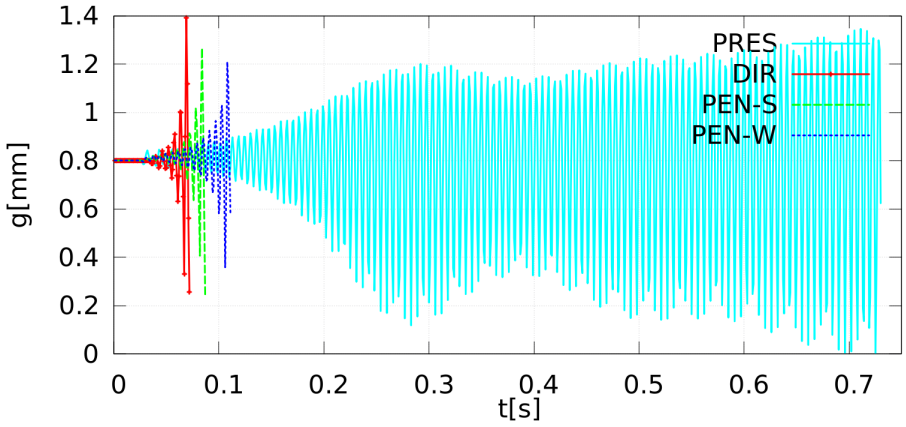

Fig. 3. Time development of the gap numerically simulated for cases *VEL*, *PEN-S*, *PEN-W* and *PRES* (The graph envelope is undulated due to too low sampling rate for saving the data for drawings.)

Comparison of simulations with hemi-larynx and full larynx configuration. The simulations with the full larynx geometry are compared with the hemi-larynx geometry as performed in [6], where the flow symmetry along x-axis is assumed in order to considerably reduce computational time. The numerical approximation of FSI problem for both configurations at one time instant are shown in Fig. 4.

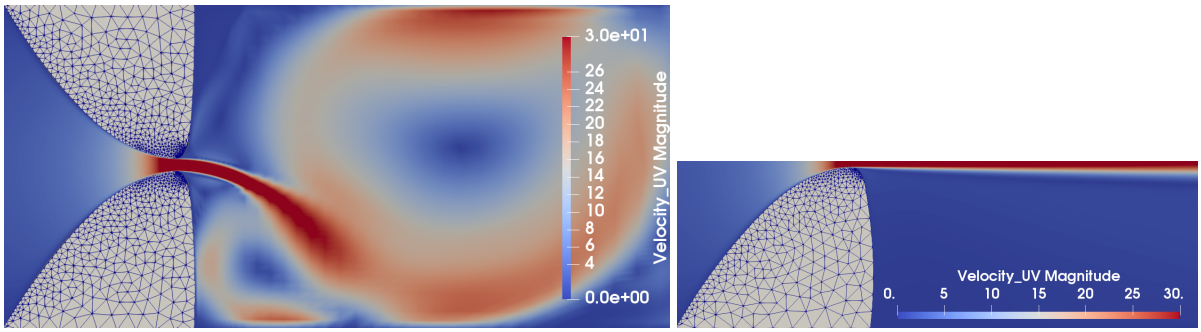

Fig. 4. The airflow velocity magnitude shown in similar time instant during closing phase of VF oscillation cycle. The simulation case *PEN-W* (full larynx configuration) is shown left, the simulation with hemi-larynx configuration is also computed with prescribed penalization BC (3 c) enforced with the aid of $\epsilon = 5 \times 10^4$.

Finally, the critical velocity of flutter instability $v_{flutter}$ is determined by the successively increasing the prescribed airflow inlet velocity until the unstable VF vibration regime occurs. Further, we studied the dependence of the determined critical velocity on the penalization parameter, see Fig. 5. The dependency of velocity $v_{flutter}$ on the parameter ϵ in the range $1 \times 10^{-10} < \epsilon < 5 \times 10^{4}$ is compared for both configurations, i.e., the geometry of full larynx and hemi-larynx. The both dependencies show the similar behaviour however exact values slightly differs. Nevertheless the computationally cheaper simulation of the hemi-larynx configuration can be used to estimate quite well the critical velocity of the full larynx configuration.

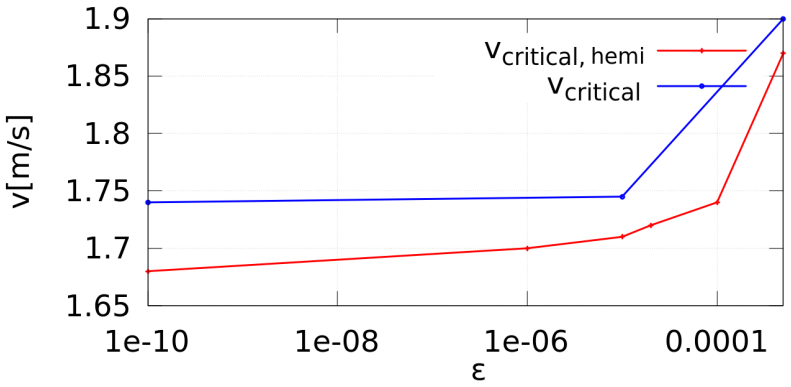

Fig. 5. The dependencies of critical velocity of flutter instability on the penalization parameter. The dependency of simulations with the full larynx configuration is plotted by blue curve, while the dependency of simulations with the hemi-larynx configuration is denoted as $v_{critical,hemi}$.

Acknowledgments

Authors are grateful for support provided by *Grant No. GA19-04477S* of Czech Science Foundation and by *Grant No. SGS19/154/OHK2/3T/12* of the CTU in Prague.

References

[1] Feistauer, M., Sváček, P., Horáček, J., Numerical simulation of fluid-structure interaction problems with applications to flow in vocal folds, In: T. Bodnár, G. P. Galdi, S. Nečasová (eds.), Fluid-structure interaction and biomedical applications, Birkhauser, 2014, pp. 312-393.

[2] Horáček, J., Radolf, V., Laukkanen, A. M., Experimental and computational modeling of the effects of voice therapy using tubes, Journal of Speech, Language, and Hearing Research 62 (7) (2019) 2227-2244.

[3] Mittal, R., Zheng, X., Bhardwaj, R., Seo, J. H., Xue, Q., Bielamowicz, S., Toward a simulation-based tool for the treatment of vocal fold paralysis, Frontiers in Physiology 2 (19) (2011) 1-15.

[4] Sváček, P., Horáček, J., Finite element approximation of flow induced vibrations of human vocal folds model: Effects of inflow boundary conditions and the length of subglottal and supraglottal channel on phonation onset, Applied Mathematics and Computation 319 (2018) 178-194.

[5] Sváček, P., Valášek, J., Mathematical modelling and numerical simulation of flow induced vibrations of vocal folds model with collisions, AIP Conference Proceedings 2116 (2019) No. 030003, doi: 10.1063/1.5113987.

[6] Valášek, J., Sváček, P., Horáček, J., On suitable inlet boundary conditions for fluid-structure interaction problems in a channel, Applications of Mathematics 64 (2) (2019) 225-251.

COMPUTATIONAL MECHANICS 2019
35th conference with international participation
Srní
November 4 - 6, 2019

Methodology of prediction of dilatation gap between aluminum segments of vulcanization molds based on thermal-stress analysis

M. Vaško[a], M. Ságа[a], M. Handrik[a], Z. Ságová[b]

[a] *Department of Applied Mechanics, Faculty of Mechanical Engineering, University of Žilina, Univerzitná 1, 010 26 Žilina, Slovakia*
[b] *Department of Automation and Production Systems, Faculty of Mechanical Engineering, University of Žilina, Univerzitná 1, 010 26 Žilina, Slovakia*

1. Introduction

The paper presents the application of numerical methods in order to improve tire production. The study of the possibility of minimizing finishing by manual trimming of excess material was carried out. A computational methodology is proposed to simulate the prediction of the dilatation gap between vulcanization mold segments with the aim of minimizing the flow of rubber from the mold when heated to 165°C.

The solution of the problem is important especially from the point of view of increasing the mentioned production efficiency. The analysis was carried out on finite element models of the Al segment, its carrier and the tightening ring. Based on the obtained results, a methodology was developed to predict the dilatation gap needed to zero the gap between the Al segment and its support at 165°C [2].

2. Determination of radial displacement and dilatation gap

The finite-element models of segment carriers and tightening rings were created for four types of containers - K1 to K4 (Fig. 1) [1, 3]. Individual members of the analyzed system were connected to a state that corresponds to the system in the pre-heating state. The calculation has been done using the FE method and using the ANSYS and MATLAB [4, 5].

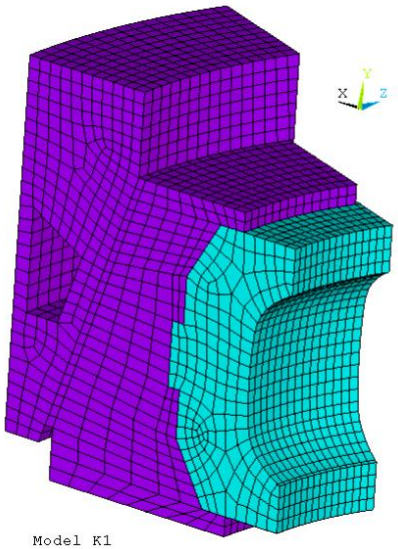

Fig. 1 Computational model of Al segment, carrier and tightening ring (K1 container)

The difficulty of analyzes has been simplified by the possibility of prescribing symmetry conditions. The boundary conditions are prescribed on the surfaces and correspond to the state when the container is closed but not compressed to the operating state.

Places on the surfaces that come into contact with the upper or lower plate of a given container type have been designed to evaluate radial displacements. The values at eight points were analyzed. This method was chosen primarily because the radial displacements of the monitored areas did not have a constant value. Analyzes were processed for realized prescribed dilatation gaps of half of one segment, i.e. for 0.1 and 0.5 mm. The resulting radial displacements for the individual containers at the prescribed tangential displacement of the Al segment are shown in Figs. 2 and 3.

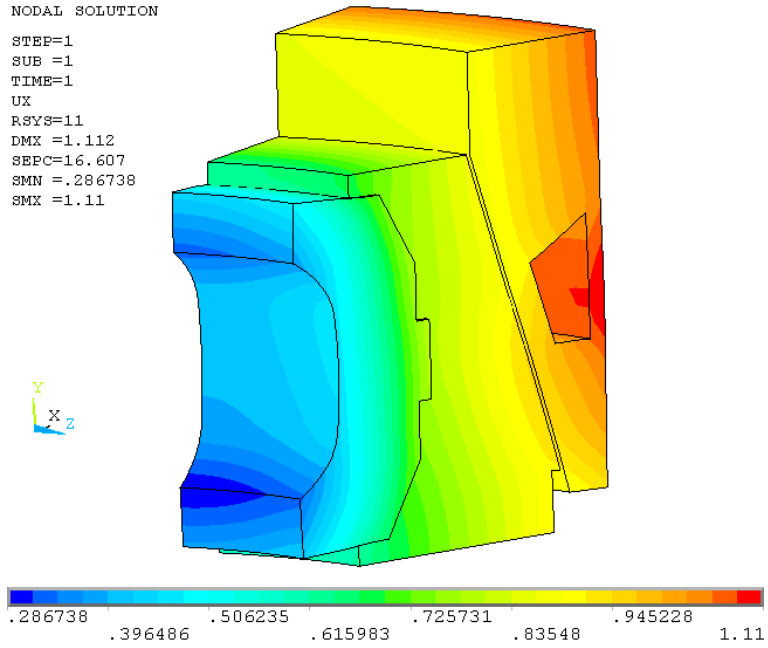

Fig. 2 Radial displacement of K1 container segment for prescribed displacements of 0.1 mm

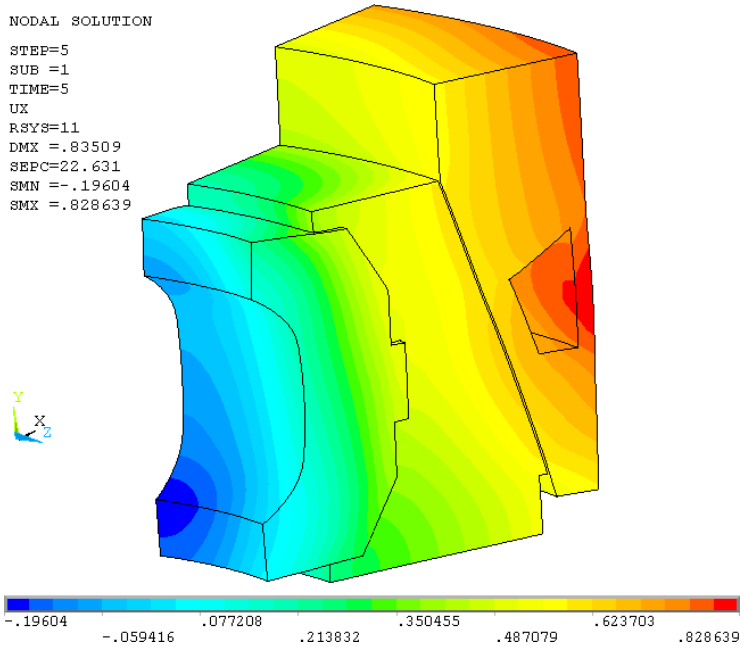

Fig. 3 Radial displacement of K1 container segment for prescribed displacements of 0.5 mm

To determine the expansion gap, it was also necessary to calculate the radial displacements of the upper and lower plates for the individual containers as they come into contact with the Al segment surface. The boundary conditions correspond to the storage in a closed container. The finite element models (Fig. 4) were generated for the purpose of calculations in the ANSYS program package and the radial displacements were subsequently analyzed.

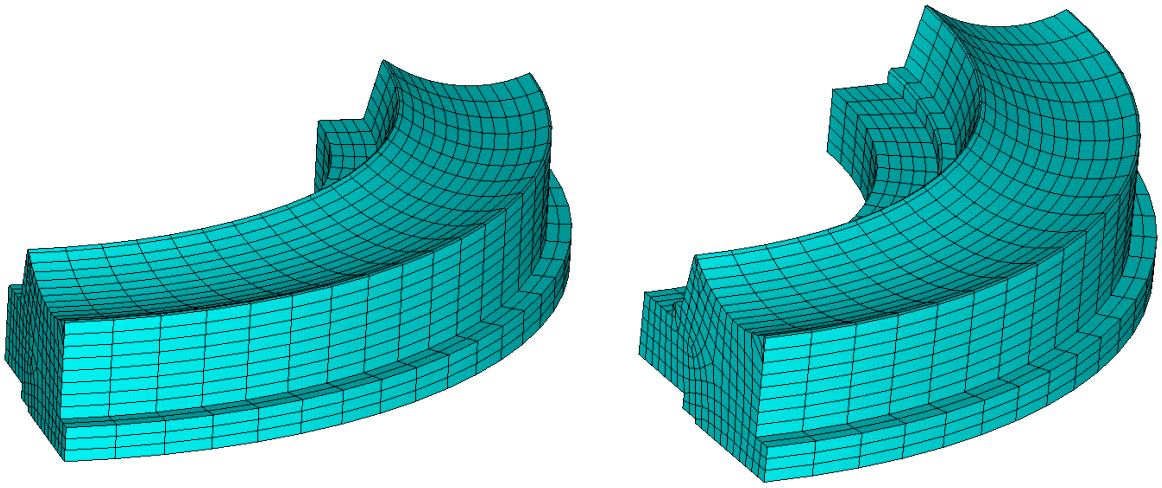

Fig. 4 Finite element mesh on upper (left) and lower (right) plate models of the K1 container

The resulting average values of the radial displacement of the upper and lower plates of the monitored contact surface are shown in Table 1.

Table 1 The radial displacements of the upper and lower pressure plate

Container type	Average value of the radial displacement (upper plate) [mm]	Average value of the radial displacement (lower plate) [mm]	Used average radial displacement of plates [mm]
K1	0.39432	0.39925	0.3968
K2	0.44828	0.44876	0.4485
K3	0.49672	0.49690	0.4968
K4	0.49661	0.49660	0.4966

The main idea of the methodology for determining the dilatation gap between Al segments was based on a series of simulations to determine the value of the prescribed tangential displacement of the Al segment so that the resulting radial displacements of the Al segment contact surface and the upper (or lower) plate are equal when heated to 165°C. This modeled the state where gaps in contact between individual system members should be zero.

Proposal of the methodology for determining the dilatation gap:

- analysis of the resulting radial displacements of Al segments (due to a temperature gradient of 145°C),
- analysis of radial displacements of the upper and lower plates (due to a temperature gradient of 145°C),
- analysis of dependence of radial displacements of Al segments on prescribed dilatation gap defined in the range of 0.1 to 0.5 mm in half of the segment (corresponded to the total prescribed gap in the range of 1.6 mm to 8 mm),

- linear extrapolation of the observed functional dependence to a point with the same radial displacement value as in the case of a plate (resets the gap between the Al segment and the plate),
- determination of the resulting dilatation gaps for individual types of containers.

When calculating the resulting dilatation gap, the average values of the investigated variables on the monitored areas were considered. By extrapolating the functional dependence of the radial displacement of the Al segment to the size of the dilatation gap, the size of the dilatation gap per half of the segment was determined. By multiplying the obtained value by 16, the resulting value of the dilatation gap required to zeroing the radial gap between the Al segments and the upper or lower plate when heated to 165°C was obtained (Table 2).

Table 2 The resulting value of the dilatation gap

Container type	Average radial displacement of horizontal plates [mm]	Extrapolated average value of radial displacement of Al segment [mm]	Resulting extrapolated value of the dilatation gap between Al segments [mm]
K1	0.3968	0.3968	16 x 0.0852 = **1.36**
K2	0.4485	0.4485	16 x 0.1151 = **1.84**
K3	0.4968	0.4968	16 x 0.1739 = **2.58**
K4	0.4966	0.4966	16 x 0.1225 = **1.96**

3. Conclusion

The presented contribution is of great application importance and its aim is to present the methodology and possibilities of using a series of suitably controlled calculations using the FEM for computer prediction of the dilatation gap between Al segments of the vulcanization mold with the aim of zeroing at 165°C.

The obtained results have the character of an initial study. In order to obtain reliable results, it is necessary to describe the technological process more precisely, control measurements to refine the input data and modify the model, to define more precisely the thermal interaction between individual system members and to carry out subsequent verification under real conditions.

Acknowledgements

The work has been supported by grant agency KEGA, project No. 037ŽU-4/2018 and grant agency VEGA, project No. 1/0073/19.

References

[1] Bathe, K.J., Finite Element Procedures, Prentice Hall, 1996.
[2] Vaško, M., Blatnický, M., Kopas, P., Sága, M., Research of weld joint fatigue life of the AlMgSi07.F25 aluminium alloy under bending-torsion cyclic loading, Metalurgija 56 (1-2) (2017) 94-98.
[3] Zienkiewicz, O.C., Taylor, R.L., The Finite Element Method, Oxford, 2000.
[4] ANSYS, Theory and Modelling guide [help manual], 2017, https://www.ansys.com/
[5] MATLAB, 2018, https://www.mathworks.com/

COMPUTATIONAL MECHANICS 2019
35th conference with international participation
Srní
November 4 - 6, 2019

Hydrodynamically lubricated contact between axial rings of the pinion and the wheel of a high-speed gearbox: Contribution to numerical assessment

J. Voldřich[a,b], Š. Morávka[a]

[a] *New Technologies – Research Centre, University of West Bohemia in Pilsen, Univerzitní 8, 301 00 Plzeň, Czech Republic*
[b] *Faculty of Mechanical Engineering, University of West Bohemia in Pilsen, Univerzitní 8, 301 00 Plzeň, Czech Republic*

1. Introduction

Main application field for high-speed gearboxes is the power sector, particularly gas and steam turbine drives, turbo compressors and auxiliary starting drives. A present-day requirement for such gearboxes is their mechanical efficiency to achieve at least to 99%. This topicality is emphasized by the fact that transmitted power reaches to tens of MW. The high efficiency mentioned above is achieved by optimizing gear design comprising also the reduction of friction loss in bearings. At the same time, low-speed shaft bearings prove the lesser loss than the high-speed ones. In this case, therefore, the axial bearing of a pinion shaft is replaced by axial rings for transmission of axial forces from the high-speed shaft to a low-speed one. Both the gear force and an outside force, e.g. from a turbine or a compressor, are involved. Nevertheless, it is necessary to consider friction loss even between axial rings. Actually, in addition to rolling, slipping of rings occurs due to the shift of their contact centre out of the pitch circles (see Fig. 1).

Nomenclature

F	the contact axial force of rings
h	film thickness, $h = h_a + h_b$
h_a	distance between a pinion ring point and the reference plane
h_b	distance between a wheel ring point and the reference plane
p	pressure
x,y,z	coordinates in global coordinate system
x	direction in the plane of shaft axes
z	the pinion shaft axial direction in global coordinate system
ξ, χ, ψ	the Cartesian coordinates relative to the contact reference plane
ξ	direction perpendicular to the contact reference plane
χ	direction of the intersection of shaft axes with the contact reference plane
u	fluid velocity in the χ direction
v	fluid velocity in the ψ direction
w	fluid velocity in the ξ direction
η	oil dynamic viscosity
μ_0	oil kinematic viscosity for atmospheric pressure
μ	oil kinematic viscosity
α	parametr in the Barus equation
ρ	oil density
$\pi/2 - \varphi$	bevel of the pinion ring
$\pi/2 - \phi$	bevel of the wheel ring
ω	the angular frequency of the pinion shaft
Ω	the angular frequency of the wheel shaft

Subscripts

a	surface of the pinion
b	surface of the wheel

It seems, no convincing research paper dealing with behaviour of axial rings has been published yet. That is why design offices use the over-simplifying computations of the oil film load capacity between the rings. For example, their conicalness and other geometric and operational parameters are not included. Similarly, an assessment based on the Hertz dry contact theory is acceptable only for the case of gearbox run-up. The insufficient knowledge entails a stumbling block in next rings developments and in the increasing of gearbox transmitted power keeping high efficiency.

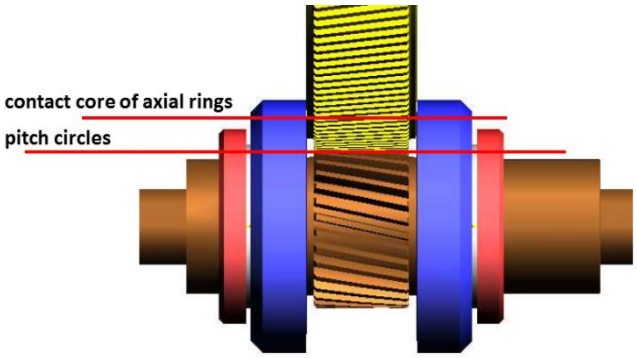

Fig. 1. Pinion and the part of wheel with axial rings

In this study, the hydrodynamically lubricated contact between axial rings considering their steady state operating mode is studied. Perfect geometry of rings and isothermal oil condition are next simplifying assumptions. The assumption that the contact of rings is hydrodynamically lubricated is suitable as the ratio between the minimal oil film thickness, $h_{\min}$, and roughness, σ, fulfils the precondition $h_{\min}/\sigma \gg 3$ (see e.g. [2]) for the operating mode. The general Reynolds equation for 2D situation is then convenient to use for the determination of the oil pressure field and of the oil flow rate. It is remarked in the third section. Before it, in the second section, our focus is payed to the geometry of film thickness, i.e. to the gap between rings. Results for an example with a geometry of rings and with an operating mode are presented in the fourth section. Important dependence between the nominal film thickness and the value of transmitted axial force is brought out here for the considered lubricated contact. An attention is also devoted to friction losses.

2. Clearance between cones

Fig. 2 shows the overall situation with parameters of axial rings depicted in the plane of both parallel shaft axes. The directions ξ and χ of the global coordinate system considered lie in the plane. Further, the reference plane of the lubricated contact of rings, α, is defined so that it is orthogonal to the direction ξ and it touches the pinion cone surface. Points of the reference plane, just as perpendicular projections of points of cone surfaces into the plane, are then uniquely determined by the coordinates χ and ψ. The clearance $h = h(\chi, \psi)$ is the function of these coordinates and is measured in the direction of ξ. Isolines of the film thickness h are depicted in Fig. 3 for the considered parameters.

3. Theory

Oil is considered as a Newtonian fluid. Its inertial effects can be neglected in our case. With the boundary conditions u_a, v_a, u_b, v_b, prescribed on surfaces of rings, the velocity components are

$$u(\xi,\chi,\psi) = \frac{1}{2\eta}\frac{\partial p}{\partial \chi}\{\xi^2 - \xi(h_b - h_a) - h_a h_b\} + u_b\frac{\xi + h_a}{h} + u_a\frac{h_b - \xi}{h}\ , -h_a \le \xi \le h_b\ ,$$

$$v(\xi,\chi,\psi)=\frac{1}{2\eta}\frac{\partial p}{\partial \psi}\{\xi^2-\xi(h_\mathrm{b}-h_\mathrm{a})-h_\mathrm{a}h_\mathrm{b}\}+v_\mathrm{b}\frac{\xi+h_\mathrm{a}}{h}+v_\mathrm{a}\frac{h_\mathrm{b}-\xi}{h}\ ,-h_\mathrm{a}\le\xi\le h_\mathrm{b}\ ,$$

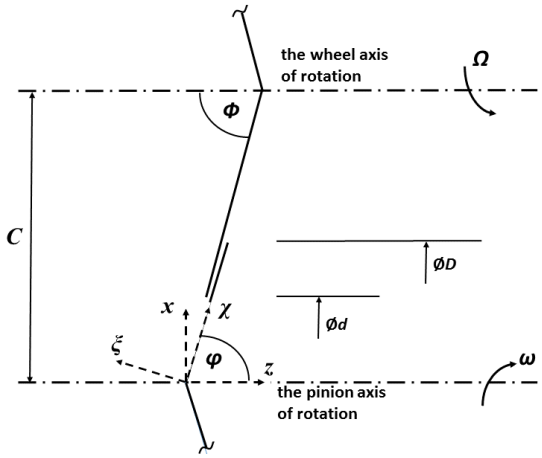

Fig. 2. The plane of shaft axes with depicted Cartesian coordinate systems and with parameters of axial rings

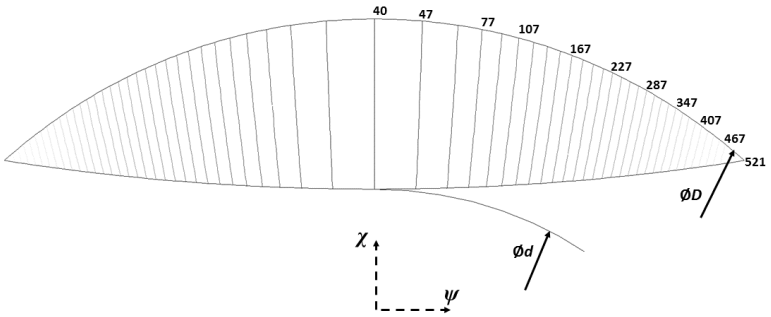

Fig. 3. Film thickness, h, in μm for the nominal thickness 40 μm and parameters d = 125 mm, D = 180 mm, C = 450 mm, $\varphi = \Phi = 89^\mathrm{o}$

where quantities h, h_a, h_b and p with the boundary velocities are functions dependent on coordinates χ, ψ. Integrating the continuity equation over the thickness h yields, after some algebra near to of [1], the general Reynolds equation

$$\frac{\partial}{\partial\chi}\left(\frac{\rho h^3}{12\eta}\frac{\partial p}{\partial\chi}\right)+\frac{\partial}{\partial\psi}\left(\frac{\rho h^3}{12\eta}\frac{\partial p}{\partial\psi}\right)=\frac{\partial}{\partial\chi}\left(\frac{\rho h(u_\mathrm{a}+u_\mathrm{b})}{2}\right)+\frac{\partial}{\partial\psi}\left(\frac{\rho h(v_\mathrm{a}+v_\mathrm{b})}{2}\right)+$$
$$+\rho(w_\mathrm{a}-w_\mathrm{b})+\rho u_\mathrm{b}\frac{\partial h_\mathrm{b}}{\partial\chi}-\rho u_\mathrm{a}\frac{\partial h_\mathrm{a}}{\partial\chi}+\rho v_\mathrm{b}\frac{\partial h_\mathrm{b}}{\partial\psi}-\rho v_\mathrm{a}\frac{\partial h_\mathrm{a}}{\partial\psi}$$

for unknown pressure, p. The viscosity, η, and the density, ρ, change with oil temperature and pressure, but, for the sake of brevity, only isothermal situation is considered here. Furthermore, the Barus empirical equation $\ln\frac{\mu}{\mu_0}=\alpha p$ (see [3]) is used to express the dependence of viscosity on pressure. Besides, the mathematical model described is necessary to complete by some condition for a cavitation region. Here, the simple approach taken by Kapitza that ignores the negative pressures, i.e. $p\ge 0$, is considered [1].

4. Results

Before starting computational simulations, an in-house program based on the theory described above was created by the first author. As an illustrative example, rings with the geometry parameters h_min = 0.04 mm, d = 125 mm, D = 180 mm, C = 450 mm, $\varphi = \Phi = 89^\mathrm{o}$ (see Fig. 3)

are considered below. Their contact is lubricated by oil of ISO VG 46 at temperature 40°C, the value α = 0.0215xMPa^{-1} is given from [3]. Angular frequencies are ω = 10791 rpm, Ω = 1490 rpm. Fig. 4 shows the oil pressure field calculated under boundary conditions with atmospheric pressure. In accordance with the inequality $p \geq 0$, the field is zero in the right hand part of the contact as opposite points of cone surfaces are receding. The most important result is the dependence of the total contact axial force on the minimal thickness, $h_{min} - F$, (see Fig. 5). That the force increases steeply for h_{min} below the value 0.05 mm is apparent. It was also worked out that friction losses increases simultaneously with the contact force.

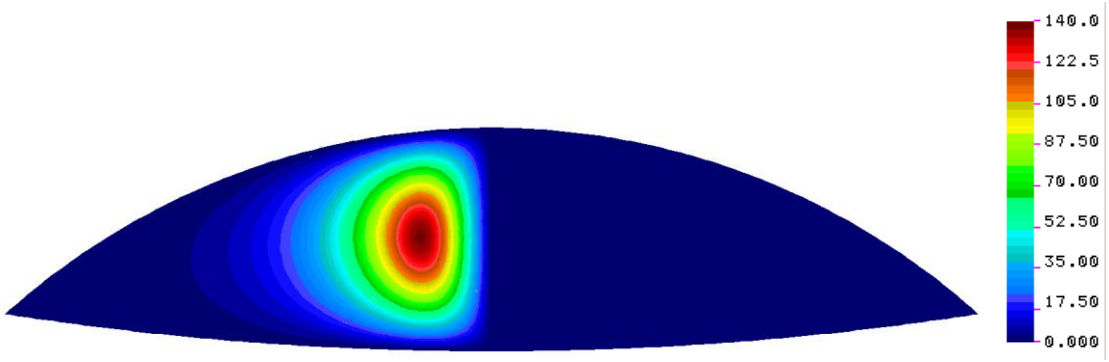

Fig. 4. Oil pressure field, p, in MPa for geometry of rings from Fig. 3, for angular frequencies ω = 10791 rpm, Ω = 1490 rpm, and for the mineral oil ISO VG 46

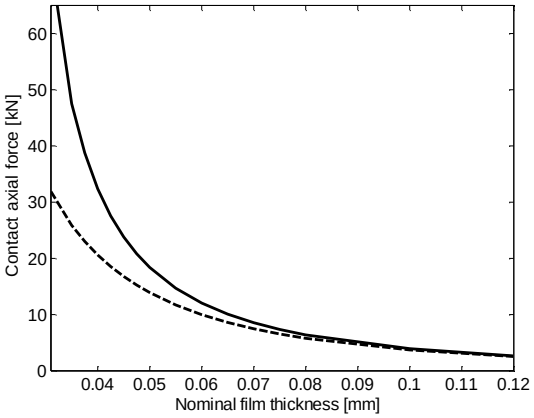

Fig. 5. Dependence of the contact axial force on the minimal thickness, $h_{min} - F$, for the parameters from Fig. 3 and 4. Solid line: α = 0.0215xMPa^{-1}; dashed line: α = 0

Acknowledgements

This study is supported by the The Technology Agency of the Czech Republic under the project "National Centre of Competence for Machinary Engineering" no. TN01000015. Authors also thank workers of Wikov Gear Ltd. company for constructive discussions.

References

[1] Hamrock, B.J., Schmid, S.R., Jacobson B.O., Fundamentals of fluid film lubrication, Second Edition, Marcel Dekker, Inc., New York, Basel, 2004.
[2] Patir, N., Cheng, H.S., An average flow model for determining effects of three-dimensional roughness on partial hydrodynamic lubrication, ASME Journal of Lubrication Technology 100 (1978) 12-17.
[3] So, B.Y.C., Klaus, E.E., Viscosity-pressure correlation of liquids, ASLE Transactions 23 (4) (1980) 409-421.

COMPUTATIONAL MECHANICS 2019
35th conference with international participation
Srní
November 4 - 6, 2019

Vibration suppression and shape change of thin plate by clusters of actuators

J. Volech[a], Z. Šika[a], M. Hromčík[b], F. Svoboda[b], J. Zavřel[a]

[a] *Faculty of Mechanical Engineering, Czech Technical University in Prague, Technická 4, 166 27 Prague 6, Czech Republic*
[b] *Faculty of Electrical Engineering, Czech Technical University in Prague, Karlovo náměstí 13, 121 35 Prague 2, Czech Republic*

Presented field in this paper is vibration suppression of the plate with heavily distributed grid of the piezo actuators and sensors. Such mechatronic smart materials have potential in many different field of use. For example, morphing wing of the plane [3]. The classic wing of the aircraft uses flaps, which are mechanically positioned. The morphing wing, on the other hand, is a single element that has the ability to change its shape. This eliminates the need for gears, rods and other mechanical components. Its advantage is uniformity, which gives the wing better aerodynamic properties. There are several possibilities how to shape the wing into the desired shape. One possibility is to use smart material with active elements to clad the pliable internal structure of the wing. Another advantage of such material is the possibility of active vibration damping in the wing. One of the vibration cases studied is flutter. Flutter phenomena are seen when vibrations occurring in an aircraft match the natural frequency of the structure. If they aren't properly damped, the oscillations can increase in amplitude, leading to structural damage or even failure. Work focuses on the research of creating such a smart material that is able to suppress vibration or even change its shape. Studied way is that the base material is equipped with a uniform network of piezo sensors and actuators [4] Fig. **1**, which are divided into individual units (clusters Fig. 3). It is then possible to design a single cluster control and apply it to a large structure, such as the wing of aircraft.

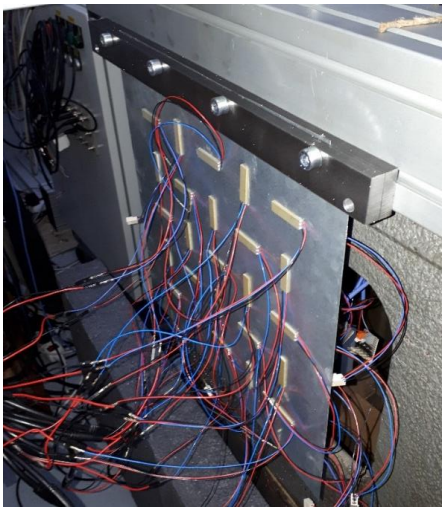

Fig. 1. Experimental structure

Simulation model (delivered by black box identification) of the plate equipped with 8 actuators (control inputs u_i) and 20 sensors (measured outputs y_i) is used for design and

validation of control law. Which is designed using the H infinity structured optimization methodology [1, 2] to attenuate resonant modes of this flexible structure Fig. 2.

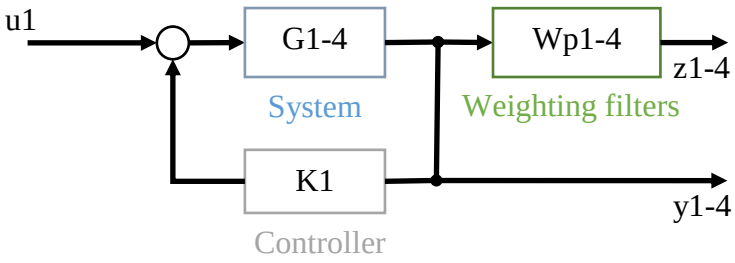

Fig. 2. Design of the controller with weighting filters

For purpose of simplify control, the clusters of sensors were used Fig. 3. For actuator 1 (ACT 1) are relevant 4 sensors (sensor 1, 2, 7, 9) with labeling cluster 1 (cl1). For another example for actuator 4 (ACT 4) are relevant sensors (sensor 4, 5, 12, 13) with labeling cluster 4 (cl4).

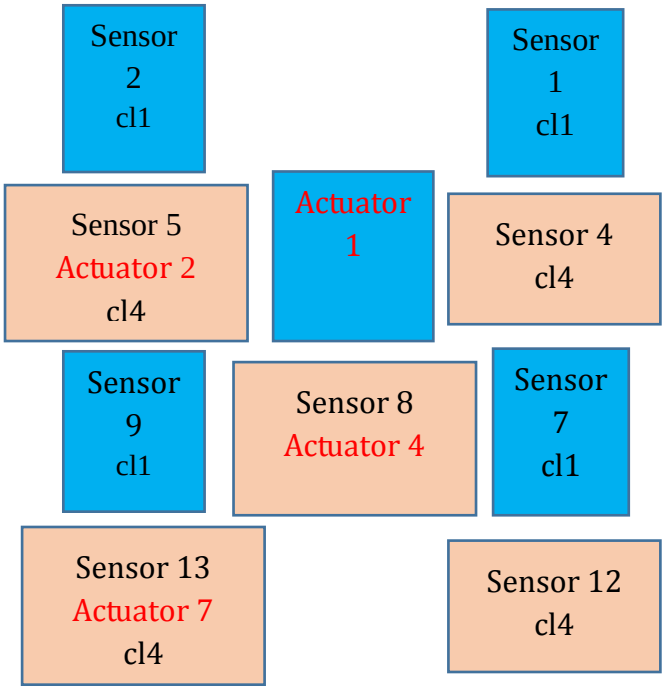

Fig. 3. Clusters

More specificaly we deal with distributed control law where the control action applied to each node depends on measured outputs at the neighboring nodes Fig. 3,

$$u_i = -k_i(y_{i-1} - y_i) - k_i(y_{i+1} - y_i). \quad (1)$$

The scenarios with constant gains throughout the structure is studied. The control system is described as a generalized LTI system with tunable components and weighting filters (Fig. 2). The *hinfstruct* function tunes those components by minimizing the closed-loop H infinity gain from the system inputs $(u_1, u_2, \dots, u_i)$ to outputs $(z_1, z_2, \dots, z_i)$. Weighting filters $(W_1, W_2, \dots, W_i)$ are included for resonant frequencies penalization. The results, in the form of a transfer function, with the structure described above are satisfactory and can be seen that it dampen penalized natural frequencies well, Fig. 4.

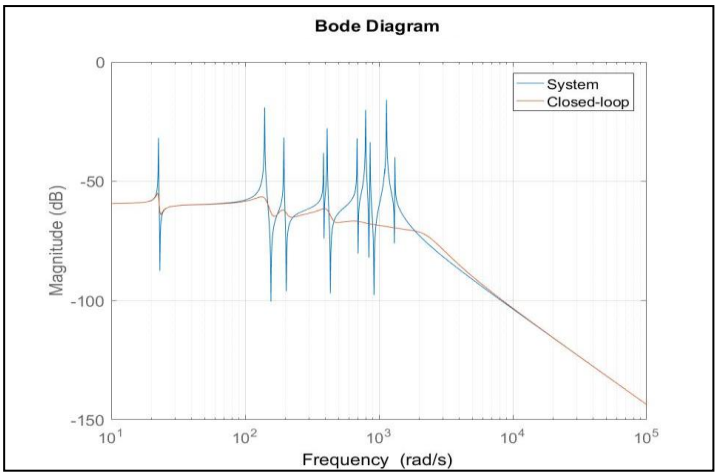

Fig. 4. Result of Hinf regulator

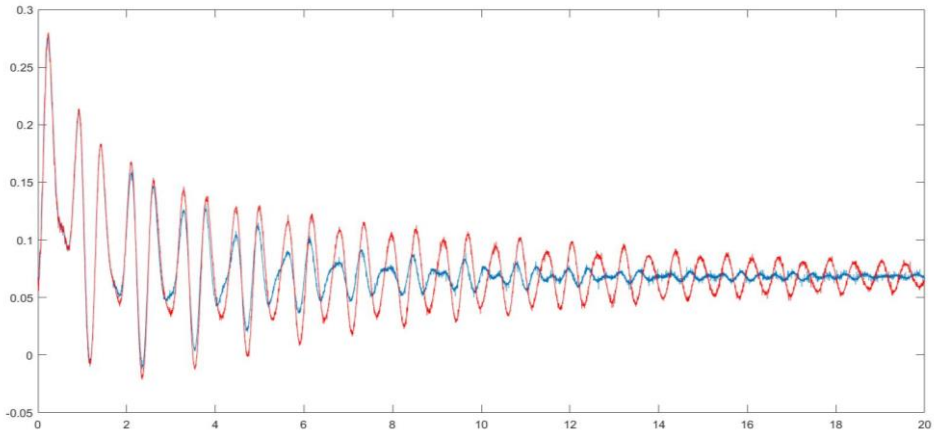

Fig. 5. Result of demonstrator

The Fig. 5 shows the results on a real demonstrator. As we can see the attenuation proceeds much faster, but the first oscillations are not damped at all. This is due to the disproportionately high excitation force that was applied to the demonstrator and the piezoelements were getting saturated. The use of proportional excitation force is the object of further study. Also simulate the form of a flatter that appears on the wings of aircraft as excitation force.

Acknowledgements

The work has been supported by the Czech Science Foundation project Aerodynamic bodies with actively controlled morphing, 19-16772S and the grant SGS19/156/OHK2/3T/12 "Mechatronics and adaptronics 2019" of Czech Technical University in Prague.

References

[1] Apkarian, P., Noll, D., Nonsmooth H-infinity synthesis, IEEE Transactions on Automatic Control (2006) 71-86.
[2] Burke, J.V., Henrion, D., Lewis, A.S. Overton, M.L., HIFOO - A MATLAB package for fixed-order controller design and H-infinity optimization, IFAC Symposium on Robust Control Design, Toulouse, 2006.
[3] Kozek, M., Schirrer, A., Modeling and control for a blended wing body aircraft, Springer, 2015.
[4] Preumont, A., Mechatronics. Dynamics of electromechanical and piezoelectric systems, Springer, 2006.

COMPUTATIONAL MECHANICS 2019
35th conference with international participation
Srní
November 4 - 6, 2019

Use of dynamic damper in hydromechanics

J. Vrána[a], F. Pochylý[a]

[a] *Brno University of Technology, Faculty of Mechanical Engineering, Victor Kaplan Department of Fluids Engineering, Technická 2896/2, 61669 Brno, Czech Republic*

1. Introduction

The transmission of energy from active fluid elements in the hydraulic systems leads to pressure and flow pulsations. If the excitation frequency coincides with natural fluid frequency of the system, resonance occurs similar to the mechanical systems, which can reduce the system life, affect the control and monitoring elements, increase the noise and possibility system crashes.This study explores the possibilities of using a dynamic damper to suppress pulsations and stabilize the system.

2. Computation of pulsation in tube

Continuity and equilibrium equations for flexible tube were used to calculate pressure and flow pulsations [2]

$$\frac{\partial \mathbf{w}}{\partial t} + \mathbf{B}\mathbf{w} + \mathbf{K}\frac{\partial \mathbf{w}}{\partial \mathrm{x}} = 0\,, \tag{1}$$

$$\mathbf{B} = \begin{bmatrix} \frac{b}{\rho} & 0 \\ 0 & 0 \end{bmatrix}, \quad \mathbf{K} = \begin{bmatrix} 0 & \frac{S}{\rho} \\ \frac{K}{S} & 0 \end{bmatrix}, \quad \mathbf{w} = \begin{bmatrix} q \\ \sigma \end{bmatrix}.$$

Eq. (1) is solved by transfer matrices method in state space using Laplace transformation, where ρ – the fluid density, b – the fluid internal attenuation, K – the bulk modulus elasticity, S – the flow cross-section area, q – the unsteady flow and σ – the unsteady pressure.

The finite difference method is used to find eigenvalues [1, 3]. Label $\Delta(s)$ the function of a complex variable and whose zero values are the searched eigenvalues. Let the field O of complex numbers $s = a + i\omega$ be given in the Gaussian plane. If every s is assigned to exactly one complex number $\Delta(s)$, we can say that in O the function of two variables α, ω is defined as

$$\Delta(s) = u(\alpha, \omega) + i\, v(\alpha, \omega), \qquad u, v \in \mathbb{R}. \tag{2}$$

This function is based on relation $\Delta(s) = det(\mathbf{A} + \lambda\mathbf{E})$, where $\mathbf{A}$ is the system's transfer matrix and $\mathbf{E}$ is the identity matrix.

The theory of the function of complex variable states that the real and imaginary part $u(\alpha, \omega)$, $v(\alpha, \omega)$ of each holomorphic function is a harmonic function and therefore satisfies the Laplace equation (3) for boundary conditions (4)

$$\frac{\partial^2 u}{\partial \alpha^2} + \frac{\partial^2 u}{\partial \omega^2} = 0 \quad \wedge \quad \frac{\partial^2 v}{\partial \alpha^2} + \frac{\partial^2 v}{\partial \omega^2} = 0 \qquad \forall \alpha, \omega \in O, \tag{3}$$

$$u(\alpha,\omega) = u_\Gamma \qquad v(\alpha,\omega) = v_\Gamma \qquad \forall \alpha,\omega \in \Gamma. \tag{4}$$

The result is determined by the set of points obtained by solving the Laplace equation, for which $u = 0$, $v = 0$. In the geometric representation, the solution is a surface (see Fig. 1) that creates the isocurves at the point where it intersects the plane $u = 0$ or $v = 0$. The roots s_k are located at the intersections of these isocurves (see Fig. 2).

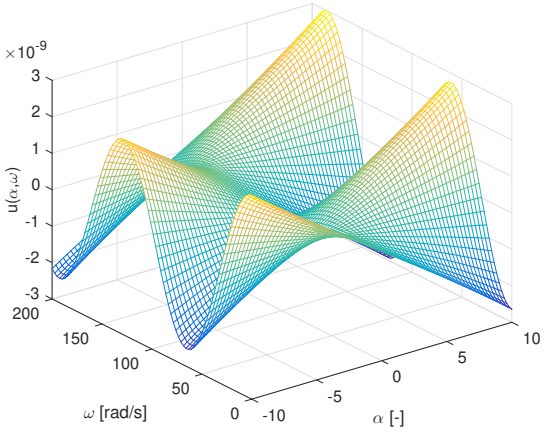

Fig. 1. Example of surface $u(\alpha,\omega)$

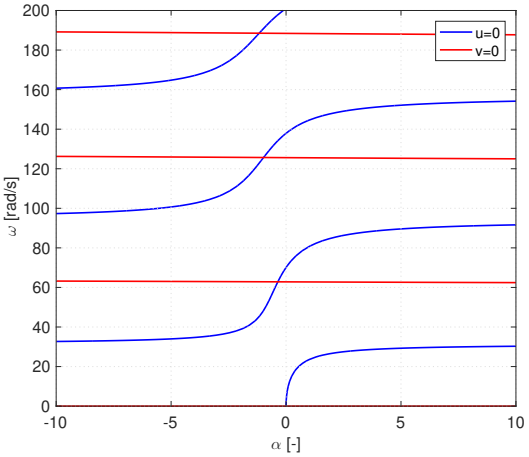

Fig. 2. Plot of isocurves

3. 1–D hydrodynamic system with dynamic damper

The influence of the damper on pressure and flow pulsations is assessed on a one-dimensional system consisting of a pulsator, two local resistors and the dynamic damper (see Fig. 3) with parameters listed in Table 1. Dynamic instability is created by a negative value of dynamic resistance b_1. The location of the damper affects its function in the system (see Fig. 4).

Table 1. Input parameters

branch length	L	50	[m]
tube diameter	ϕd	80	[mm]
speed of sound in fluid	a	1000	[m s^{-1}]
fluid density	ρ	1000	[kg m^{-3}]
fluid internal attenuation	b	12.8	[kg s^{-1} m^{-3}]
flow amplitude	Q_0	0.01	[m^3 s^{-1}]
excitation frequency	ω	63	[m^3 s^{-1}]

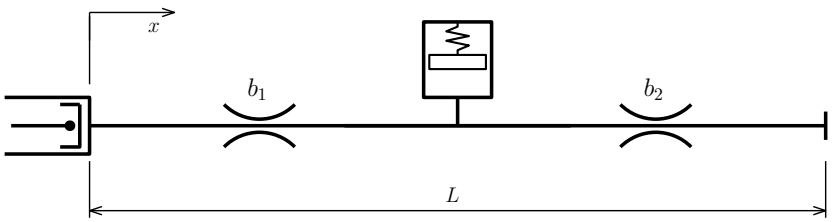

Fig. 3. Scheme of hydrodynamic system

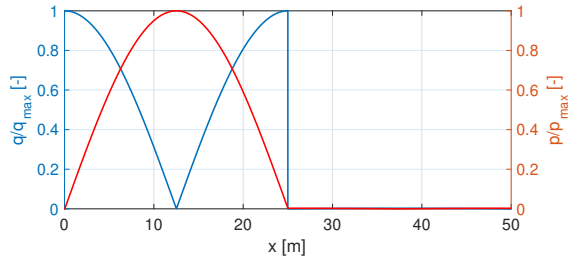

(a)

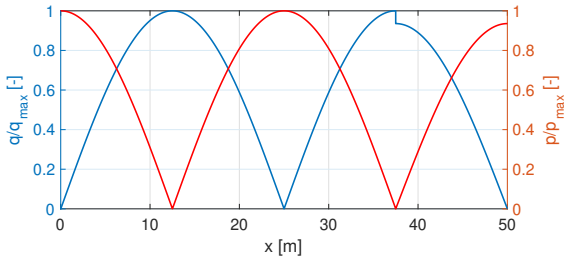

(b)

Fig. 4. Modes of 2nd eigenfrequency if damper is placed in: (a) flow node, (b) pressure node

System's boundary conditions are $q(0,t) = Q_0 \cdot \cos(\omega t)$ and $q(L,t) = 0$. Local resistance values are $b_1(x = 1\,\mathrm{m}) = -9.8 \times 10^8$ and $b_2(x = 40\,\mathrm{m}) = 9.0 \times 10^6$. The 1-DOF dynamic damper is described by mass m and stiffness k. Its natural frequency and location have impact on system stability (see Figs. 5 and 6).

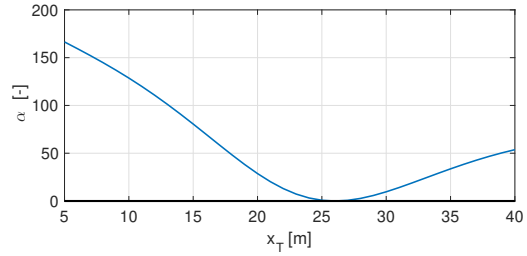

Fig. 5. α – damper location dependence

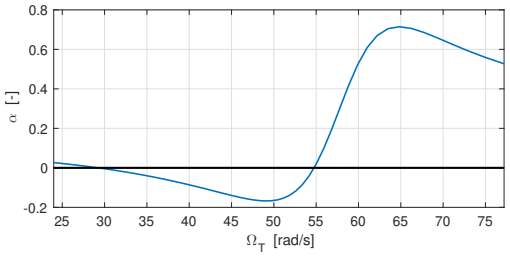

Fig. 6. α – damper eigenfrequency dependence

In order to dampen the system, it is advisable to place the damper at the point of the flow node. If the dynamic stability problem is examined, it is advisable to place the damper in the pressure node position. However, the damper does not perform the damping function at this point (see Fig. 7). The influence of the dynamic damper on the stability of the system can be best seen from the plot of the time response to the excitation of the resonant frequency (see Fig. 8). All results have been published in [4].

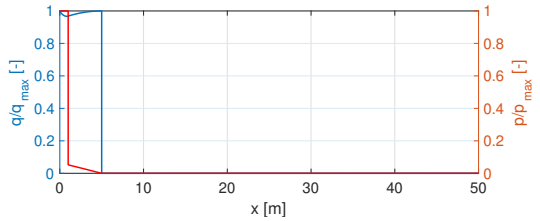

(a)

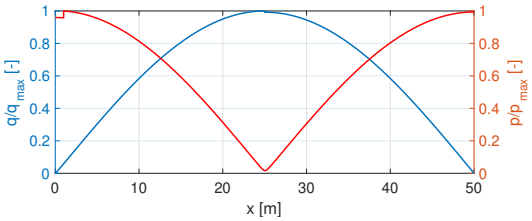

(b)

Fig. 7. Eigenmodes the damper is located: (a) close to the flow node ($x = 5$ m), (b) in the pressure node ($x = 25$ m)

4. Conclusion

In this study, the possibility of use of the dynamic damper to stabilize the dynamic system was investigated. The aim was to use a mathematical model describing dynamic behaviour in a

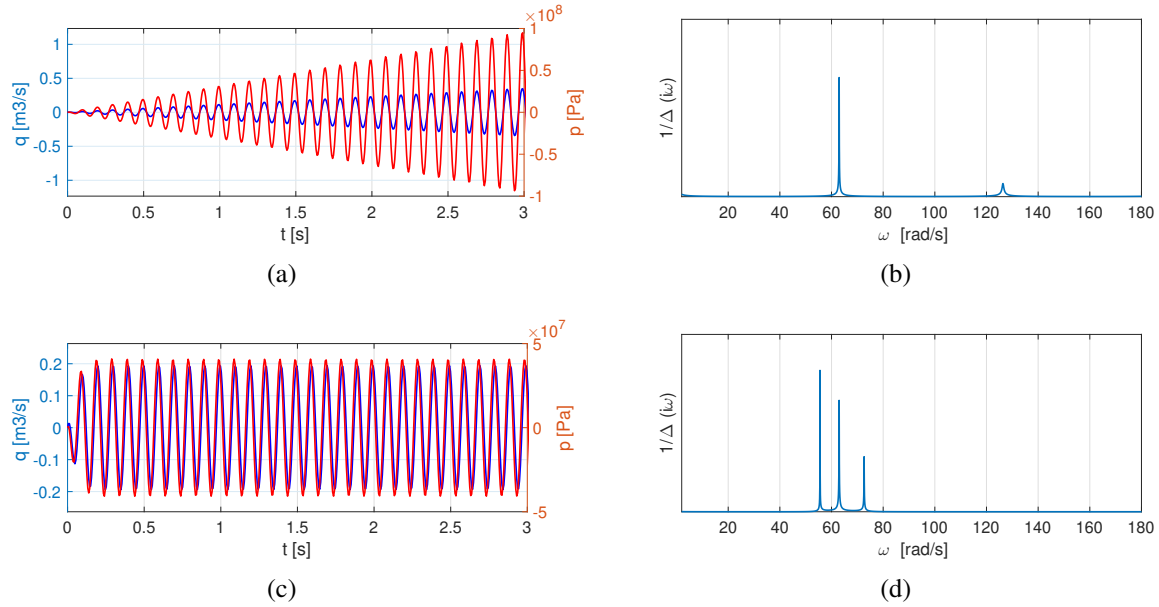

Fig. 8. Response to excitation in resonance (a) without damper and (c) with damper; and dynamic amplification of system (b) without damper and (d) with damper

flexible tube to solve a system with the dynamic damper. Using this model it was possible to assess the impact of the damper on the system.

It has been found that the damper can be used to stabilize the dynamic system. It depends on the damper tuning and its location in the tube. The damper should be placed in the node location of pressure eigenmode of given resonant frequency. In this case, the damper does not perform the damping function of the system.

Acknowledgement

Grant Agency of the Czech Republic (project no. GA 17-19444S) and Faculty of Mechanical Engineering (project no. BD13701003) are gratefully acknowledged for support of this work.

References

[1] Elsherbeni, A. Z., Demir, V., Finite-difference time-domain method for electromagnetics with MATLAB® simulations, Institution of Engineering and Technology, 2016.

[2] Pochylý, F., Dynamics of fluid systems, Československá redakce VN MON, Prague, 1990. (in Czech)

[3] Pochylý, F., Proposal on characteristic matrix values method of calculation, Journal of Mechanical Engineering 39 (1) (1988) 51-58.

[4] Vrána, J., Use of dynamic damper in hydrodynamics, Thesis, Brno University of Technology, Brno, 2019.

COMPUTATIONAL MECHANICS 2019
35th conference with international participation
Srní
November 4 - 6, 2019

Numerical analysis of a passenger safety during a railway vehicle collision: The effect of safety belts

J. Vychytil[a], S. Špirk[a]

[a]Regional Technological Institute, University of West Bohemia, Univerzitní 8, 301 00 Plzeň, Czech Republic

In automotive industry, safety belts are with no doubts established and inherent part of passive safety elements [1]. They keep the occupant at his or her seated position during the impact scenario. However, application of such safety elements in railway vehicles is questionable. There is an important aspect of the passenger comfort in railway vehicles which might be affected. Also, application of safety belts represents additional cost for manufacturer. Hence, the crucial question is related to the potential benefit of safety belts. Would their application increase passenger safety in a collision scenario of a railway vehicle? The study presented here aims to answer that question using numerical simulations.

As a representative of a passenger, the Virthuman model is used in the Virtual Performance Solution (VPS) software. It is based on multi-body structure with deformable segments. It is easy to position, it requires low computational time and it includes automatic algorithm for injury criteria evaluation, see e.g. [3]. In this case we evaluate the criteria described in the GMRT2100 regulation for railway vehicles such as HIC15, neck axial force and moment, thorax deflection, etc [2]. An important feature of the Virthuman model is the scaling algorithm that enables to represent any passenger of given age, height, weight and gender. For this particular study, 25-year-old male of a 50th percentile is considered, that is, an average male with the height of 178 cm and the weight of 76 kg.

An open coach type interior is considered. Its FE model is developed in the VPS software. It includes the passenger's seat and the seat in front of the passenger with folding table. Two-points or three-points belts are fixed to the passenger's seat in a common sense including retractors and sliprings. The collision scenario is considered in a configuration with no belt, two-points belt and the three-points belt. Each of these cases is considered in a configuration with folded and unfolded table at the backrest in front of the passenger. It means, 6 configurations of numerical simulations are considered in total. The acceleration pulse is prescribed for the vehicle interior as defined in GMRT2100 regulation. It corresponds to a frontal collision scenario of a railway vehicle. The simulation time is 300 ms.

The results are evaluated in terms of passenger's kinematics and injury risk. As an example, kinematics of the passenger at 150 ms for each belting option is provided in Fig. 1. The case with unfolded table is illustrated here. In case with no belt, knees impact the backrest possibly causing the injury of both femurs at approximate time of 95 ms. At the approximate time of 150 ms, the head hits the headrest causing the possible neck injury. In case with unfolded table, the thorax and abdomen hit the backrest just in the location of the table at approximate time of 185 ms. Since the table is made of steel, the impact causes higher injury risk of these two body parts. In case of folded table, no impact of the thorax and abdomen with the backseat occurs.

In case with two-points belt, no primary impact of lower limbs and the backrest occur. Hence, no injury risk of the lower limbs is indicated. The body of the passenger is fixed by the two-point belt at the abdomen area. However, the torso and lower limbs are thrown against the backrest. The abdomen is compressed by the belt causing higher injury risk of this body part. At the approximate time of 150 ms, the head hits the backrest. In the configuration with unfolded table the head hits right the table causing serious risk of head injury. In the configuration with folded table the had hits the plastic part of the backrest which does not increase the head injury risk.

In case with three-points belt, whole upper part of the body is fixed with the belt, hence it does not impact the backrest in front of the passenger. Slightly increased injury risk of abdomen and thorax only is predicted due to their compression with the belt.

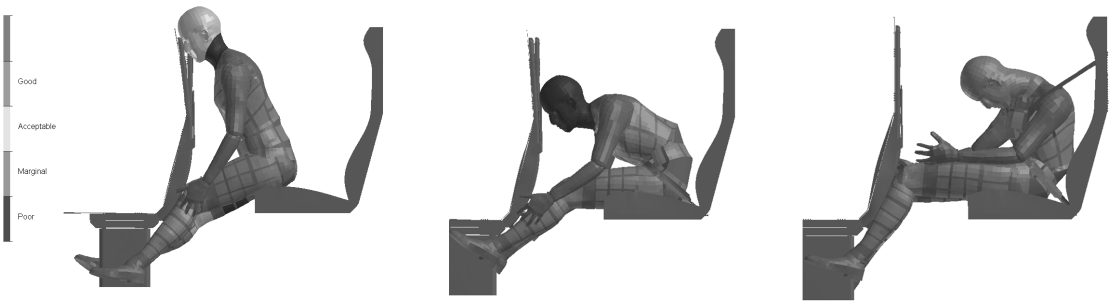

Fig. 1. Passenger's kinematics during collision scenario at 150 ms; configuration with no belt (*left*), the two-points belt (*middle*) and the three-points belt (*right*)

With respect to the results obtained, following conclusions can be formulated. With no seatbelt, high injury risk of lower limbs is predicted as a result of the impact with steel profiles. The head impact with the headrest leads to increased head injury risk. Injury risk of lower limbs is completely reduced in case of a two-point belt. However, this type of belt significantly increases the head injury risk in case of unfolded table. Also, significant neck injury risk is predicted in case of a two-point belt for both folded and unfolded table. Application of a three-point belt minimizes injury risk of both head and neck. Therefore, in case of mounting setabelts in the railway vehicle interior of an open coach type, three-point belts should be preferred to two-point belts. In case of a frontal collission scenario as defined by the GMRT2100 regulation, the overall injury risk of a passenger is lower for the three-point belt when compared to a two-point belt.

Acknowledgement

This paper was created with the support of Technology Agency of the Czech Republic, project No TE01020038 "Competence Centre of Railway Vehicles".

References

[1] EuroNCAP, Assessment protocol – Adult occupant protection, Version 8.0.2, 2017.

[2] RSSB, Requirements for rail vehicle structures, GMRT2100, 2012.

[3] Vychytil, J., Manas, J., Cechova, H., Spirk, S., Hyncik, L., Kovar, L., Scalable multi-purpose virtual human model for future safety assessment, SAE Technical Paper 2014-01-0534, 2014, doi: 10.4271/2014-01-0534.

COMPUTATIONAL MECHANICS 2019
35th conference with international participation
Srní
November 4 - 6, 2019

Numerical approximation of fluid flow problems by discontinuous Galerkin method

O. Winter, P. Sváček

Department of Technical Mathematics, Faculty of Mechanical Engineering, Czech Technical University, Charles Square 13, Praha 2, Czech Republic

The discontinuous Galerkin methods (DGM) are gaining popularity in solving partial differential equations arising from modeling scientific and engineering problems, see e.g. [1]. Amongst other, the DGM was successfully applied for the numerical solution of incompressible fluid flows, i.e., Navier-Stokes equations, see e.g. [2, 3, 5]. This contribution focus on the verification of the high order discontinuous Galerkin method implementation for the solution of the Navier-Stokes equations in two dimensions. The numerical method was implemented within the Julia programming language.

The fluid flow of an incompressible viscous fluid in the domain Ω is described by the system of the Navier-Stokes equations (see e.g. [3]), i.e.,

$$\frac{\partial \boldsymbol{u}}{\partial t} + \boldsymbol{\nabla}\cdot(\boldsymbol{u}\otimes\boldsymbol{u}) = -\boldsymbol{\nabla} p + \nu\,\boldsymbol{\nabla}^2\boldsymbol{u}, \quad \boldsymbol{\nabla}\cdot\boldsymbol{u} = 0, \tag{1}$$

where $\boldsymbol{u}$ is the fluid velocity vector, p is the pressure divided by the constant fluid density ϱ and ν is the constant kinematic viscosity of the fluid. The boundary of the computational domain Ω, see Fig. 1 (left), is divided into three distinct parts, i.e., $\partial\Omega = \Gamma_I \cup \Gamma_W \cup \Gamma_O$, where Γ_I and Γ_O are inlet, and outlet parts of the computational domain, respectively and Γ_W denotes the impenetrable wall. The system (1) is supplemented by suitable initial conditions $\boldsymbol{u}(\boldsymbol{x},0) = \boldsymbol{u}_0(\boldsymbol{x})$, $p(\boldsymbol{x},0) = p_0(\boldsymbol{x})$, and boundary conditions $\boldsymbol{u} = \boldsymbol{u}_I$ on Γ_I, $\boldsymbol{u} = \boldsymbol{0}$ on Γ_W and $p = p_O$ on Γ_O.

In order to solve the problem (1) the computational domain $\Omega_h(\approx \Omega)$ is discretized using a triangulation $\mathcal{T}_h$, where the higher order isoparametric elements were used on curved boundary, see e.g. [3]. The numerical solution is represented by piecewise polynomials of degree $N \geq 1$

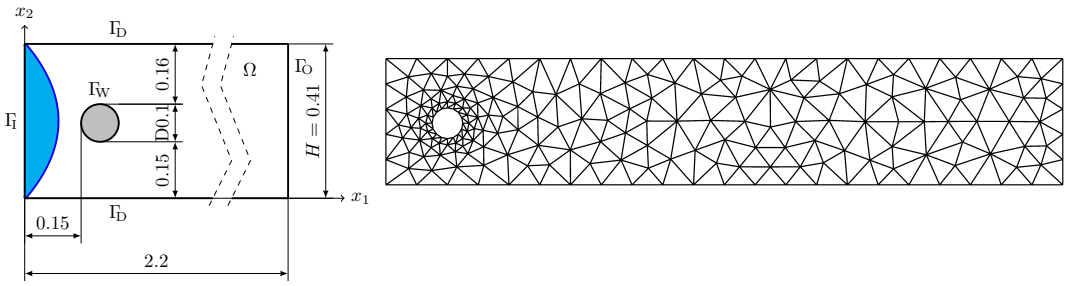

Fig. 1. (*Left*) Sketch of the computational domain. (*Right*) Computational grid consisting of 356 elements.

on each triangle $k \in \mathcal{T}_h$. The time integration is done by splitting scheme with three stages which takes into account the mixed nature of equations (1), see [3].

The implemented numerical method was tested on the benchmarks of laminar flow around a cylinder [4], so-called DFG benchmarks. Simulations were done on the very coarse grid consisting of 356 elements (see Fig. 1 (right)) and the different degrees of polynomials N were considered. Table 1 shows obtained reference values. One can see that values obtained by DGM corresponds well for higher orders of polynomials both for $\mathrm{Re} = 20$ (steady) and $\mathrm{Re} = 100$ (periodic) with DFG data. Fig. 2 shows vorticity contours for $N = 5$ and $N = 9$. Fig. 3 shows lift coefficient c_l during the computation.

Table 1. Overview of obtained reference values for the cases $\mathrm{Re} = 20,\ 100$; $*$ values from [4]

	$\mathrm{Re} = 20$			$\mathrm{Re} = 100$		
N	c_d	c_l	Δp	$\max(c_d)$	$\max(c_l)$	$\Delta p(t = 8)$
1	6.511912	0.816498	0.159512	7.811225	2.939393	0.140196
5	5.579752	0.012096	0.117506	2.958082	0.475532	0.110243
9	5.579598	0.010619	0.117532	2.943942	0.477448	0.111623
$*$	5.579535	0.010619	0.117520	2.943764	0.477488	0.111541

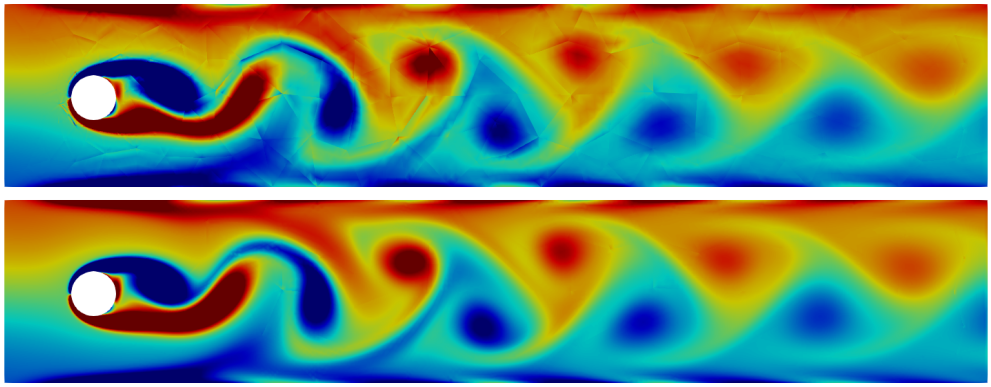

Fig. 2. Contours of vorticity for different N, $\mathrm{Re} = 100$ at 8 s: (*top*) $N = 5$, (*bottom*) $N = 9$

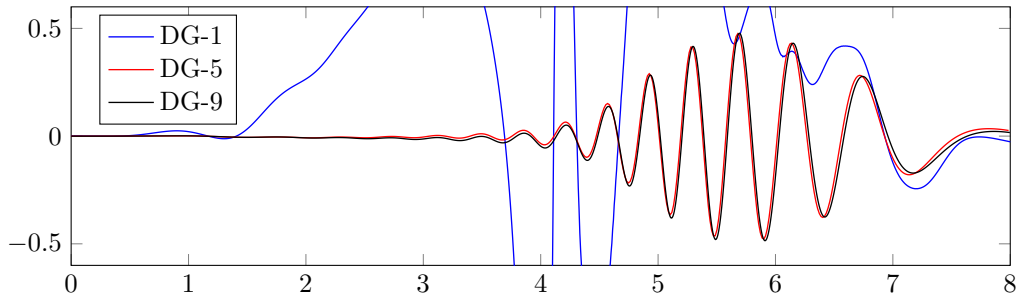

Fig. 3. Lift coefficient $c_l(t)$, $\mathrm{Re} = 100$

Conclusions. In this contribution the in-house implementation of the high-order discontinuous Galerkin method is used to compute flow past the cylinder. Obtain results correspond very well with DFG benchmarks reference values.

Acknowledgements

This work was supported by the Grant Agency of the Czech Technical University in Prague, grant SGS19/154/OHK2/3T/12. Authors acknowledge support from the EU Operational Programme Research, Development and Education, and from the Center of Advanced Aerospace Technology (CZ.02.1.01/0.0/0.0/16019/0000826), Faculty of Mechanical Engineering, Czech Technical University in Prague.

References

[1] Dolejší, V., Feistauer, M., Discontinuous Galerkin method: Analysis and applications to compressible flow, Springer Series in Computational Mathematics Vol. 48, Springer, 2015.

[2] Dumbser, M., Fambri, F., Furci, I., Mazza, M., Serra-Capizzano, S., Tavelli, M., Staggered discontinuous Galerkin methods for the incompressible Navier-Stokes equations: Spectral analysis and computational results, Numerical Linear Algebra with Applications 25 (2018) No. 2151, doi: 10.1002/nla.2151.

[3] Hesthaven, J. S., Warburton, T., Nodal discontinuous Galerkin methods: Algorithms, analysis, and applications, Springer, 2008.

[4] Schäfer, M., Turek, S., Benchmark computations of laminar flow around a cylinder, In: E. H. Hirschel (ed.), Flow simulation with high-performance computers II, Notes on Numerical Fluid Mechanics, Verlag, 1996, pp. 547-566.

[5] Shu, C.-W., IMEX time marching for discontinuous Galerkin methods, AIP Conference Proceedings 1863 (2017) No. 020006, doi: 10.1063/1.4992152.

COMPUTATIONAL MECHANICS 2019
35th conference with international participation
Srní
November 4 - 6, 2019

Clinical gait analysis of a 16 years old patient with walking difficulties after surgery

B. Yousefghahari[b,c], A. Vahidi-Shams[a,c], D. Sekoyan[d], A. Guran[a,c],

[a] *Institute of Structronics, Montreal, Canada*
[b] *Rheumatology ward, Babol University of Medical Sciences, Iran*
[c] *Rheumatology Clinic Atieh Medical Complex, 47166-88977, Babol, Iran,*
[d] *Wigmore Clininc, Yerevan, Armenia*

In this paper we present a procedure to improve the gait disorder in sixteen years old boy after the surgery due to mild CP.

A male patient 16 y/o has CP, spastic diplegia. In 2018 JUN was operated, B-Femur distal extension osteotomy, patellar tendon shortening Before the operation, he was walking so cold crouch gait with flexed knees 60 degrees, excessive dorsiflexion and hip flexion, early heel rises on the left side. And as result, he has pathological moments in knees.

Treatment Surgery: 2010 B-s/c hell cord lengthening

2016 Ulzibad fibrotomys quadriceps, biceps, gracilise, AD.

2018 JUN B-Femur distal 3rd extension osteotomy, patellar tendon shortening

Time series of the movement of patient were produced and a pair of shoes and orthoses were designed based on numerical computations to optimized the movement of the patient.

The gait of the patient after the surgery was studied by a group of orthopaedic surgeons, rheumatologists and biomechanicians (Fig. 1).

Fig. 1. Gait analysis of the patient with bare foot

Based on analysis of numerical results, the lower limb orthoses were designed manufactured and used (Fig. 2).

Fig. 2. Gait analysis of the patient with orthoses and shoes

Tables 1 and 2 are the results of the motions captured by 8 cameras during the gait of the patient

Table 1. Spatial temporal parameter of gait after surgery (bare foot)

SPATIAL-TEMPORAL PARAMETERS 06/04/2018

	LEFT	RIGHT	NORM~
Cadence	121 steps/min	125 steps/min	116.06 ± 3.13
Stride Time	0.99 s	0.96 s	1.04 ± 0.03
Walking Speed	0.83 m/s	0.83 m/s	1.34 ± 0.06
Stride Length	0.83 m	0.80m	1.38 ± 0.05
Step Length	0.42 m	0.39 m	0.71 ± 0.07
Step Time	0.48 s	0.48 s	0.6 ± 0.05
Single Support	0.29 s	0.30 s	0.42 ± 0.01
Double Support	0.40s	0.37 s	0.21 ± 0.01
Foot Off	69.8 %	70.1 %	60.21 ± 0.72
Opposite Foot Contact	51.6 %	50.0 %	49.92 ± 2.39

Table 2. Spatial temporal parameter of gait after surgery (with orthoses and shoes)

SPATIAL-TEMPORAL PARAMETERS

	LEFT	RIGHT	NORM~
Cadence	115 steps/min	117 steps/min	116.06 ± 3.13
Stride Time	1.04 s	1.02 s	1.04 ± 0.03
Walking Speed	0.91 m/s	0.92 m/s	1.34 ± 0.06
Stride Length	0.95 m	0.94m	1.38 ± 0.05
Step Length	0.50 m	0.42 m	0.71 ± 0.07
Step Time	0.50 s	0.53 s	0.6 ± 0.05
Single Support	0.40 s	0.28 s	0.42 ± 0.01
Double Support	0.36s	0.36 s	0.21 ± 0.01
Foot Off	73.5 %	61.8 %	60.21 ± 0.72
Opposite Foot Contact	52.1 %	48.7 %	49.92 ± 2.39

Fig. 3 (a) shows the pelvic oblequilty in left and right foot. Fig. 3 (a) shows the pelvic oblequilty in left and right foot. We can see the improvment by comparing the curve with normal gait Left and right foot.

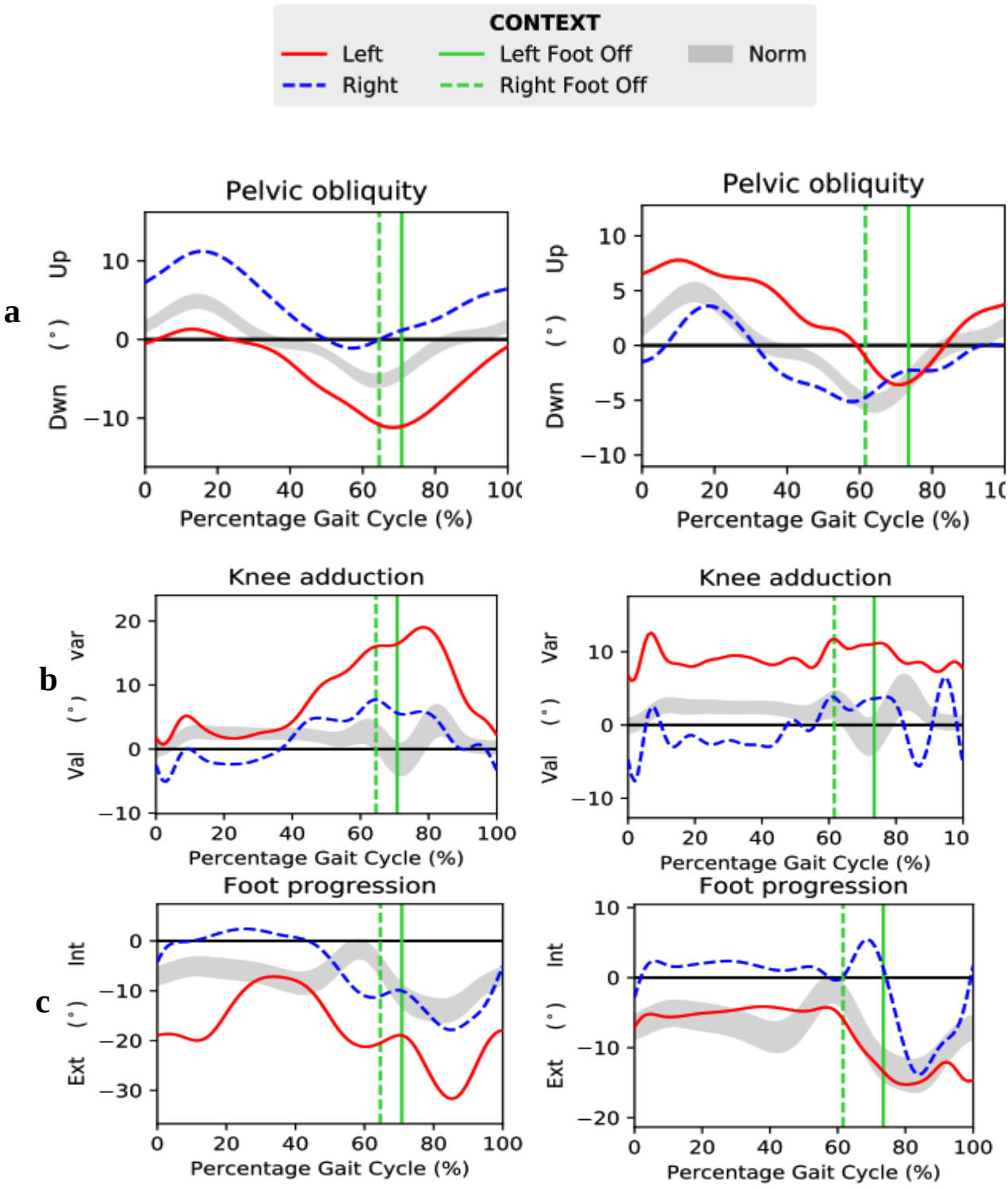

Fig. 3. Gait analysis of the patient with bare foot (Left) and with orthoses and shoes (Right)

Conclusion

After the operation, The patient has improvement in all levels: 20-30 degrees in knees, 10 degrees in ankles, heel-toe gait restored on both sides. Also, he has improvement in step length: The patient still needs feet stabilization. We see that with more stable feet which orthoses provide, he walks faster and better with them. So he is much better after the operation, but he needs rehabilitation and second stage operation for feet stabilization.

Acknowledgements

This research project was conducted in "STEP" Motion Research Laboratory, Wigmore Clinic, Yerevan, the Republic of Armenia.

References

[1] Frankel, V.H, Nordin, M., Basic biomechanics of the musculoskeletal system, Lippincott Williams & Wilkins, Philadelphia, 2001.
[2] Haddas, R., Belanger, T.., Clinical gait analysis on a patient undergoing surgical correction of kyphosis from severe ankylosing spondylitis, International Journal of Spine Surgery 11 (3) (2017) 138-144.
[3] Khouri, N., Desailly, E., Contribution of clinical gait analysis to single-event multi-level surgery in children with cerebral palsy. Orthopaedics and Traumatolgy: Surgery and Research 103 (1) (2017) 105-111.
[4] Yousefghahari, B., Vahidi-Shams, A., Guran, A., diagnostic and treatment procedure for motion disorder in a 3 years old girl with mild CP, 3rd national Congress on neural mosklescletal Disorder babol, iran, 2018.
[5] Yousefghahari, B., Vahidi-Shams, A., Guran, A., Treatment of gait disorder in a child with mild cerebral palsy, Proceedings of the conference Computational mechanics, Srní, 2018, pp. 131-132.

COMPUTATIONAL MECHANICS 2019
35th conference with international participation
Srní
November 4 - 6, 2019

Problematics of large batch winding of technical fabrics

J. Žák[a]

[a] *VÚTS, a.s., Svárovská 619, 460 01 Liberec, Czech Republic*

When weaving technical textiles we often encounter problems that are not known from weaving ordinary textiles. This is due to the significantly different mechanical properties of the fibres forming the fabrics. At the same time, productivity pressures cause additional complications, especially in the marginal areas of weaving, whether snipping or just wrapping the resulting product. As the resulting pack becomes larger, it becomes corrugated and consequently damages the fabric. This problem has increased in our case when weaving 3D fabric with higher thickness and lower transversal stiffness. We were therefore faced with the task of solving the problem of behaviours of such a batch. Due to the complexity of the problem we had to use finite elements method. It allowed us to cope with the anisotropic character of the bath and with the non linearities of mechanical properties.

Fabric large batch is essentially a strip of fabric spirally wound onto a rigid central tube (mandrel), Fig. 1. It can be produced in two fundamentally different ways, namely by winding on the driven central mandrel or by rolling the perimeter of the batch on two driven rolls. In the second method, the driving torque is exerted by friction between the fabric surface layer and the driving roll, whereby the contact force can be exerted by the actual weight of the wrap or by the controlled roller pressure against the central non driven tube. In both cases, the controlled variable is the tension in the wound fabric. During winding, only the surface layer has the

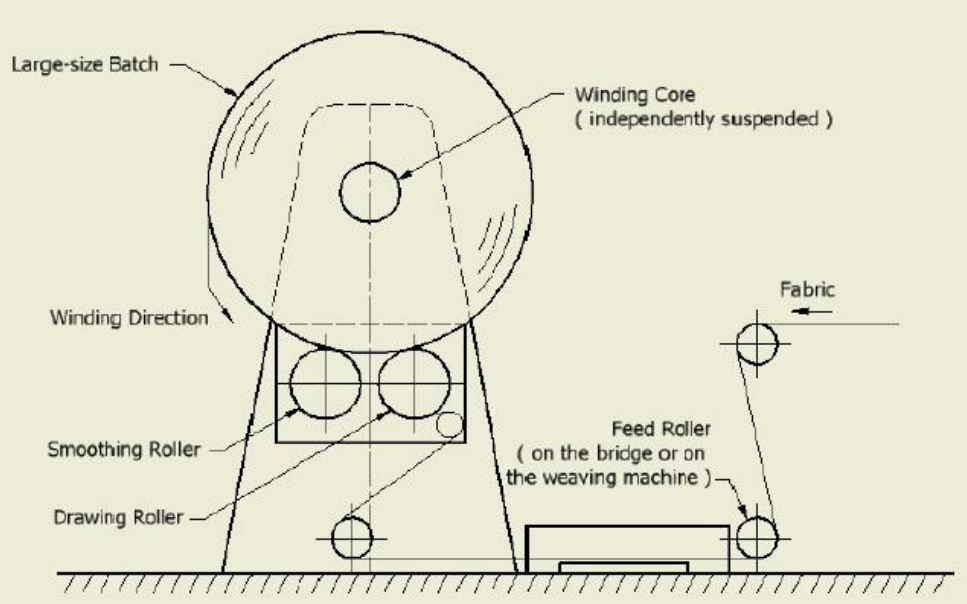

Figure 1. Schema of a large batch winder; courtesy of CEDIMA

required tension, in the inner layers, this pre-stressing decreases due to their suppleness. This phenomenon is the stronger the more supple the individual layers are in the radial direction. When the inner layers are compressed by the outer layers, this tangential stress may even vanish. These layers then become wavy in a certain radius range of batch. This is frequent especially in the gravity package, where the winding tension is limited to a certain extent by the weight of the wound fabric. Due to the three-dimensional nature of the batch, this phenomenon occurs differently in the middle of its width, where the state of stress has the character of a plane deformation, and near its free ends, where the state approaches the plane stresses. Together with the inherently different properties of the fabric in the middle of the woven width and at its edges, this leads to a double twist of the batch and a shear deformation of the wound fabric.

The first step, which is the subject of this work, was to determine the properties of batch as a rotationally symmetrical body and compare them with the experiment. The strongly anisotropic character given by the structure of the fabric layers was taken into account, but neither the varying load on the circumference of the batch from the driving rolls, nor the different properties along the rotation axis, were taken into account.

The basic equation describing the behaviour of such an object has the following form:

$$Q \cdot \frac{d}{dr}\left(r \cdot \left(\frac{du}{dr} + \nu_{tr} \cdot \frac{u}{r}\right)\right) - \left(Q \cdot \nu_{tr} \cdot \frac{du}{dr} + \frac{u}{r}\right) = f_t \cdot \frac{(1 - \nu_{tr}^2 \cdot Q)}{E_t} \,,$$

where $Q = \frac{E_r}{E_t} = \frac{\nu_{rt}}{\nu_{tr}}$ is the ratio between elastic modulus in the radial and tangential direction and right hand side member of the governing differential equation is a function of f_t – force per unit of width and per unit of radius (or better, unit of thickness) applied on the fabric during the winding (essentially a tangential stress; for the purposes of this work we consider it constant).

The analytic solution of this problem is possible for linear material behaviour and for $Q \neq 1$:

$$u = C_1 \cdot r^{\frac{1}{\sqrt{Q}}} + C_2 \cdot r^{-\frac{1}{\sqrt{Q}}} - f_t \cdot \frac{r}{E_t} \cdot \frac{1 - \nu_{tr}^2 \cdot Q}{1 - Q} \,.$$

While loosely wound batches satisfy well this equation, batches with higher tension of winding are beginning to show non-linearity in the material properties of the batch if perceived as a continuum. This is caused by the compression of the individual layers of the fabric, which increases the contact area between the layers and together, the overall batch compacting grows. While the properties in the tangential direction change minimally, the modulus of elasticity in the radial direction starts to increase strongly. This in turn increases the value of the Q ratio.

There may be several models for expressing the dependence of the elastic modulus on radial compression, but with the exception of the simplest models, expressing the function $Q = f(\varepsilon_r)$ prevents any analytical solution of the fundamental differential equation.

To cope with this problem we had to use finite elements method. One-dimensional finite elements with cubic approximation of radial displacements were chosen for modelling the batch as a rotationally symmetric continuum. Nodal variables are radial displacements and the first derivative of these displacements (essentially the value of ε_r strain). Consequently, their continuity ensures the continuity of tangential and radial stresses too.

When deriving the stiffness matrix, we chose the standard procedure of FEM method [1]

$$\mathbf{K_e} = \int_{V_e} |\mathbf{B}|^T \times |\mathbf{E}| \times |\mathbf{B}| \cdot dV \,,$$

where the matrix $\mathbf{B}$ takes the form

$$\mathbf{B} = \left| \begin{array}{c} \frac{d\mathbf{N}}{dr} \\ \frac{1}{r} \cdot \mathbf{N} \end{array} \right|$$

and $\mathbf{E}$ has the following form

$$\mathbf{E} = \frac{E_t}{1 - Q \cdot \nu_{tr}^2} \cdot \begin{vmatrix} Q & Q \cdot \nu_{tr} \\ Q \cdot \nu_{tr} & 1 \end{vmatrix} .$$

Although the resulting functions can be integrated analytically, the presence of $\ln\left(\frac{r_i + L_e}{r_i}\right)$ terms in the resulting functions, which tend to zero, makes them numerically difficult to evaluate. Therefore, a four-point Gaussian numerical integration was chosen, which proved to be faster than the repeated enumeration of logarithms. Moreover, for sake of simplicity integration on real elements was carried out instead of reference elements.

In the absence of other loads, the nodal forces are calculated from the tangent stress values f_t using functions of approximation

$$[F_e] = \int_{L_e} f_t \cdot \frac{1}{\rho} \cdot |N| \cdot \rho \cdot d\rho \, .$$

Seemingly, f_t has a character of volumetric forces but actually it is that of surface stress on the symmetry planes, hence the use of $(f_t \cdot \varepsilon_t \cdot dV)$ specific energy integration. The boundary conditions were expressed both by the prescribed displacement at the inner batch radius (i.e., at one free edge of the discretization) and by the prescribed radial stress at the free surface, i.e., at the other free end of the discretization. It is therefore a problem with mixed boundary conditions. While the expression of Dirichlet's type BC on the inner radius is obvious, the free surface condition

$$\sigma_r|_{r=R_{ext}} = \frac{Q \cdot E_t}{1 - Q \cdot \nu_{tr}^2} \cdot (\varepsilon_r + \nu \cdot \varepsilon_t) = f(Q) \cdot \left(u_{n-1} + \frac{\nu_{tr}}{r_N} \cdot u_n \right) = 0 \, ,$$

where u_i, u_{i-1} and r_N are corresponding nodal values and $f(Q) > 0$ may be expressed as transformation of nodal variables on the concerned element in the form [1]

$$\begin{array}{ll} \mathbf{K'_e} = \mathbf{R}^T \times \mathbf{K_e} \times \mathbf{R} & \ldots \text{ for transformation of matrix of rigidity,} \\ \mathbf{F'_e} = \mathbf{R}^T \times \mathbf{F_e} & \ldots \text{ for transformation of generalized nodal forces.} \end{array}$$

The transformation matrix $\mathbf{R}$ takes the form (for $\sigma_r|_{r=R_{ext}} = 0$):

$$\mathbf{R} = \begin{vmatrix} 1 & 0 & 0 & 0 \\ 0 & 1 & 0 & 0 \\ 0 & 0 & 1 & 0 \\ 0 & 0 & -\frac{\rho_4}{\nu_{tr}} & \frac{\rho_4}{\nu_{tr}} \end{vmatrix} .$$

Of course, the calculated nodal values of displacements must be re-transformed using R backwards into the natural displacements after calculation.

With regard to the assumed cause of the mechanical properties evolution, the dependence of the elasticity modulus in the radial direction (in terms of our approach, the values of the parameter Q, as the properties in the tangent direction are assumed constant) is chosen so as to simulate a normal distribution of contact surface size evolution between layers. Since its distribution function is not explicitly described, we have chosen a replacement model in the form:

$$\frac{dQ}{d\varepsilon_r}(\varepsilon_{r,0}, A) = \frac{2 \cdot A}{\pi \cdot \left(A^2 \cdot (\varepsilon_r - \varepsilon_{r,0})^2 + 1 \right)^2} \, (= f(\mu, \sigma)) \ ,$$

where $A = \sqrt{\frac{\pi}{8}} \cdot \frac{1}{\sigma}$. Values of $\varepsilon_{r,0}$ and σ correspond to mean value and standard deviation, respectively, of a normal distribution. This function satisfies condition $\int_{-\infty}^{\infty} f = 1$. Its integral form takes the following form

$$Q\left(\varepsilon_r\right) = \frac{1}{2} + \frac{A}{\pi} \cdot \left(\frac{\operatorname{atan}\left(\left(\varepsilon_r - \varepsilon_{r,0}\right) \cdot A\right)}{A} + \frac{\left(\varepsilon_r - \varepsilon_{r,0}\right)}{A^2 \cdot \left(\varepsilon_r - \varepsilon_{r,0}\right)^2 + 1} \right)$$

with A defined above.

The solution of the system of non-linear equations was carried out using the substitution method, where $\{X^i\}$ are i-th approximation of column-vectors of residua R, nodal dsiplacements U and nodal forces F, respectively, [1]

$$\begin{aligned} \left\{R^i\right\} = \left\{R\left(U^{i-1}\right)\right\} &= \{F\} - \mathbf{K}\left(U^{i-1}\right)\left\{U^{i-1}\right\} \ , \\ \mathbf{K}\left(U^{i-1}\right)\left\{\Delta U^i\right\} &= \left\{R^i\right\} \ , \\ \left\{U^i\right\} &= \left\{U^{i-1}\right\} + \left\{\Delta U^i\right\} \ . \end{aligned}$$

Fig. 2 shows an example of the solution for radial stresses for a relatively small batch. A batch of this size was subject of our experiments; even here the difference is notable and it grows with the batch size.

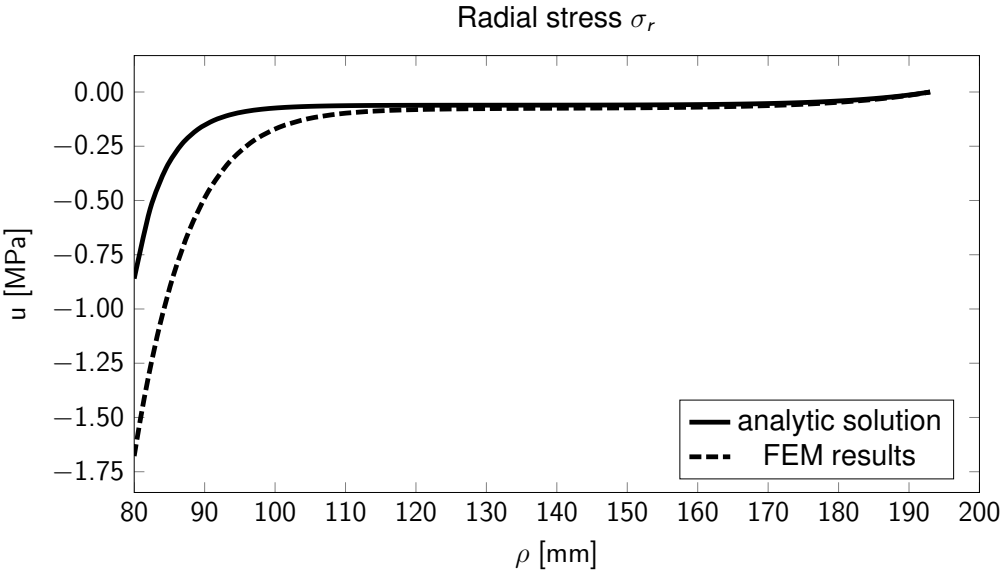

Figure 2. Difference between linear material and FEM solution using non-linear material

The use of FEM has allowed us to explain some of the discrepancies in the behaviour of large batches identified in experiments. In the future we expect to use the same material model for 2-D and 3-D FEM modelling of the batch.

References

[1] Dhatt, G., Touzot, G., A presentation of the finite element method, Maloine S.A., Paris, 1984. (in French)

COMPUTATIONAL MECHANICS 2019
35th conference with international participation
Srní
November 4 - 6, 2019

Design concepts of controllable hydrodynamic bearings lubricated by magnetically sensitive oils for the vibration control of rotors

J. Zapoměl [a,b], P. Ferfecki [a,c]

[a] Faculty of Mechanical Engineering, VŠB-Technical university of Ostrava, 17. Listopadu 15, 708 00 Ostrava, Czech Republic
[b] Institute of Thermomechanics, Czech Academy of Sciences, 182 00 Praha, Dolejškova 5, Czech Republic
[c] IT4Innovations National Supercomputing Center, VŠB-Technical university of Ostrava, 17. Listopadu 15, 708 00 Ostrava, Czech Republic

The rotors are often mounted in hydrodynamic bearings. To achieve their optimum performance in a wide range of running velocities, their stiffness and damping parameters must be adaptable to the current operating conditions. This is offered by application of magnetically sensitive lubricating oils.

Application of magnetorheological fluids to lubricate the hydrodynamic bearings is reported by Wang et al. [3]. The study on lubricating a floating ring bearing by magnetorheological fluid to design a controllable support element can be found in [4].

Several design concepts of hydrodynamic bearings lubricated by ferromagnetic fluids were introduced in literature. Nevertheless, the detailed analysis shows that their practical application for the vibration control of rotors is not technologically feasible. It implies the ferrofluids cannot be used as tunable lubricants to get an active journal bearing, because its rheological change is very low [2].

This paper deals with a design concept of a hydrodynamic bearing lubricated by ferromagnetic fluid-based magnetorheological oil and its applicability for controlling the rotor vibration. Addition of the micrometer-sized iron particles to a concentrated ferrofluid represents a simple way to control its magnetorheological and magnetoviscous behavior, which is sufficient to change the stiffness and damping in a hydrodynamic bearing [1].

The housing of the proposed bearing consists of a cylindrical part that forms a bushing and of a cylindrical pin (Fig. 1). The rotor journal is hollow, made of non-ferromagnetic material, and is inserted into the hole of the bearing bushing. The gap between the bushing and the rotor journal is filled with the magnetically sensitive oil. The electric coil mounted on the pin generates magnetic flux passing through the pin, the cylindrical part of the bearing, the oil layer, and returns back to the pin through the rotor journal. Because the rotor journal is not magnetic, it is not attracted to the bearing bushing.

The pressure distribution in the bearing gap is described by the modified Reynolds equation, which has been derived on the following assumptions: (i) the oil layer is divided in the sublayers in the radial direction, (ii) the liquid in each sublayer behaves as Newtonian, (iii) the applied boundary conditions require that the velocity and the shear stress at location of the contact of two neighboring sublayers are the same, and (iv) the apparent viscosity in the individual sublayers is constant in the radial direction and is determined from the flow curve for the average sublayer velocity rate in dependence of the circumferential position.

The bearing housing is considered to be consisted of a set of meridian segments and each segment as a divided core of an electromagnet. Magnetic induction in the lubricating layer is calculated by application of the Hopkinson law. The reluctance of the ferromagnetic parts of the magnetic circuit was neglected.

The influence of the hydrodynamic bearing lubricated by the ferrofluid based magnetorheological oil on vibration of a rigid rotor (Fig. 2) was examined by means of computational simulations. The rotor (mass 430 kg) was rotating at speed of 300 rad/s. It was loaded by its weight, by a stationary force (15 kN) acting in the vertical direction, and by the disc imbalance. The diameter of the rotor journal was 60 mm. The electric coil was formed by 900 turns. Relations for the determination of the yielding shear stress of the lubricating oil and the appopriate material parameters were taken from [1].

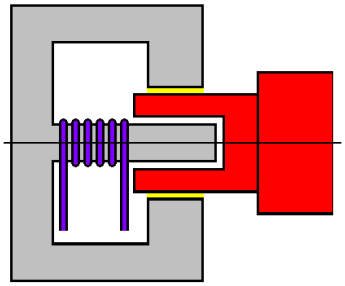

Fig. 1 The proposed bearing design

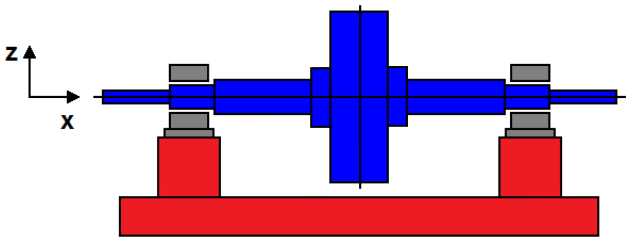

Fig. 2 The studied rotor system

Fig. 3 and 4 show dependence of magnetic induction in bearing gap and the yielding shear stress of the applied current. In Fig. 5 there are depicted the steady state orbits of the rotor journal for three magnitudes of the current. It is evident that increasing current shifts the orbits towards the bearing centre, which means the bearing load capacity rises.

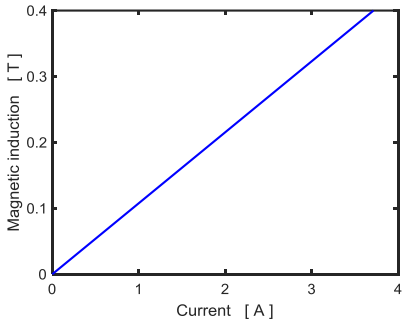

Fig. 3 Magnetic induction in bearing gap

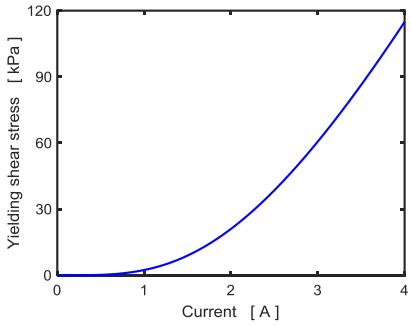

Fig. 4 The lubricant yield shear stress

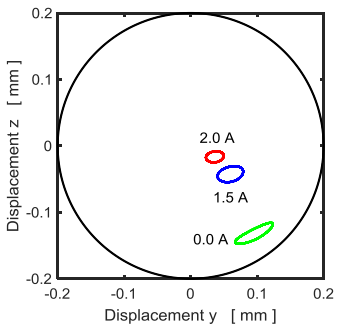

Fig. 5 The orbits position

The carried out research demonstrated that the appropriate control of hydrodynamic bearings lubricated by ferrofluid based magnetorheological oils can change dynamical parameters of rotors in sufficinently large extent and thus to adapt their performance to the current operating conditions.

Acknowledgements

This work was supported by the grant projects 19-06666S and LQ1602 (NPU II).

References

[1] Susan-Resiga, D., Vékás, L. Yield stress and flow behavior of concentrated ferrofluid-based magnetorheological fluids: the influence of composition, Rheologica Acta 53 (2014) 645-653.
[2] Urreta, H., Leicht, Z., Sanchez, A., Agirre, A., Kuzhir, P., Magnac, G. Hydrodynamic bearing lubricated with magnetic fluids, Journal of Intelligent Material Systems and Structures 21 (2010).
[3] Wang, X., Li, H., Li, M., Bai, H., Meng, G., Zhang, H., Dynamic characteristics of magnetorheological fluid lubricated journal bearing and its application to rotor vibration control, Journal of Vibroengineering 17 (2015) 1912-1927.
[4] Wang, X., Li, H., Meng, G. Rotordynamic coefficients of a controllable magnetorheological fluid lubricated floating ring bearing, Tribology International 114 (2017) 1-14.

COMPUTATIONAL MECHANICS 2019
35th conference with international participation
Srní
November 4 - 6, 2019

3D printer modification for printing of HEMA hydrogel

J. Zavřel[a], M. Michalák[a], T. Vampola[a]

[a] *Faculty of Mechanical Engineering, Czech Technical University in Prague, Technická 4, 166 07 Praha, Czech Republic*

Hydrogels are widely used materials. We can met them in products wherever there is a need to absorb liquids. Contact lenses are also made of hydrogel as it is a well biocompatible material [3]. Tissue cell population experiments are also conducted with this material. However, cell growth is dependent on the underlying object's geometry. Because the objects are very diverse in shape, 3D printing can be used to create them.

Hydrogel, based on HEMA, is composed of three basic ingredients. The basic component is HEMA (2-hydroxyethyl methacrylate), followed by crosslinker (about 0,5 % of ethylen dimetacrylate - EDMA) and initiator (activator) in appropriate proportions. Other ingredients, such as water, can be added to obtain different properties of the hydrogel. If water is added, it affects the swelling ability. A very important part is the initiator, which starts crosslinking. The initiator may initiate crosslinking based on mechanical pressure, temperature, UV radiation or other conditions. Depending on the amount of initiator and crosslinker, an appropriate crosslinking rate can be achieved. The speed of crosslinking parameter is an essential for successful printing of the hydrogel.

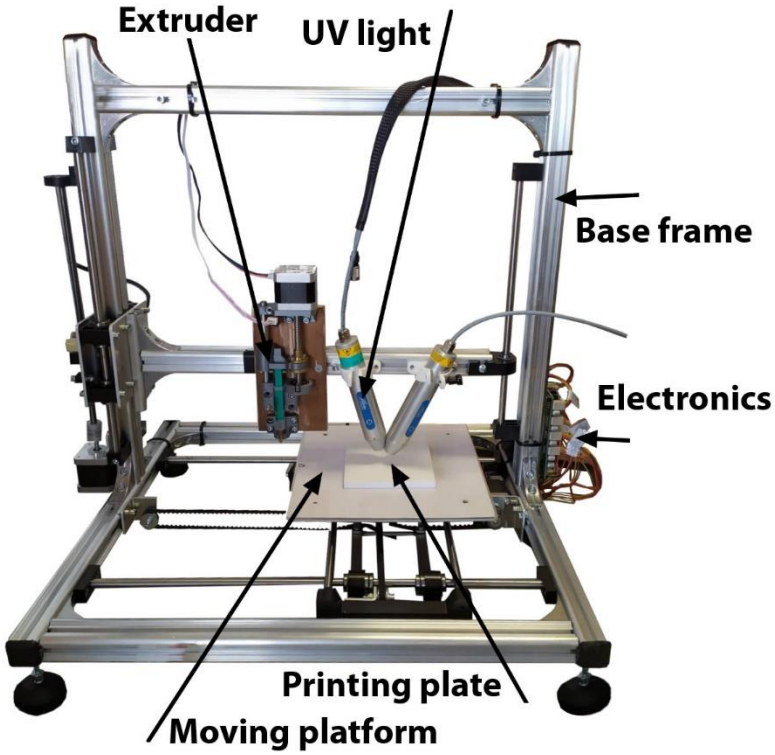

Fig. 1. Modified printer Velleman K8200

After crosslinking, the resulting polymer is blended as an anhydrous, solid, and relatively hard polymer. If water is also added to the mixture, the crosslinking properties are than affected. Such a polymer is then softer and it seems like an already swollen hydrogel. Depending on the composition of the hydrogel, the polymer is then able to absorb from 10 % to 600 % water relative to the dry weight. These properties are crucial to successful 3D printing.

Various methods of 3D hydrogel printing can be encountered [1]. The most common method is to extrude the hydrogel through a nozzle, often to the support material. Depending on the nozzle size, model details can be obtained. Depending on the method of initiating crosslinking, a printing method is also selected. Most often, crosslinking occurs after exposure of the hydrogel to UV radiation. Typically it is used a wavelength from 200 nm to 405 nm. The exposure time of the hydrogel is from a few seconds to several tens of seconds. It also depends on the thickness of the layer to be crosslinked. Another method is based on freezing the hydrogel during printing [2]. It is printed on a sheet of steel sheet. Dry ice is placed under the pad, keeping the steel pad at very low temperatures. Subsequently, the gel is applied to a cooled plate using a needle extruder. The high water content of the gel causes immediate freezing. When printing complex structures, a small amount of water is added to support the printing structure. Upon completion, the object thaws gradually until the ice is thawed and leaves only printed structure from the hydrogel. The last type is a method of applying a hydrogel similar to an inkjet printhead, as is the case with an office printer. This last method is suitable for small and detailed objects.

The design of the 3D hydrogel printer is based on the Velleman K8200 (Fig. 1). This printer is equipped with three feeds in the X, Y and Z axes and an extruder drive. The printer software is based on Marlin firmware. Since the design was not sufficient for printing the hydrogel, a hardware modification was necessary. A major change was the replacement of the filament extruder with other construction of the extruder. Due to the addition of the UV light source and the need to switch it on, it was also necessary to change the firmware and modify it. The printer operates via the Repetier-Host. For the initial tests, this application was sufficient, but with the gradual addition of functionality the work was lengthy. For this reason, MATLAB's control software was created, including preview and online modification of the generated G-code (Fig. 2).

A classic thin-needle syringe is used for the hydrogel extrusion. After it has been filled with hydrogel, the volume of the hydrogel is inserted into the control software and the extruder is brought into the correct position to allow its insertion. The printing of the hydrogel is based on the extrusion of droplets, which are subsequently cured by UV light. The printed object model is based on the solid model, which is exported to STL format using the Slic3r software. Since the printing is based on droplets, the G-code from the slicer must be modified. For these modifications of the G-code, the converting software "přechroupátor" is created. This software is written in MATLAB and modifies the G-code of lines, arcs, and other entities into the same objects from droplets. The software can adjust droplet sizes, retracting and spacing to fine tune print quality.

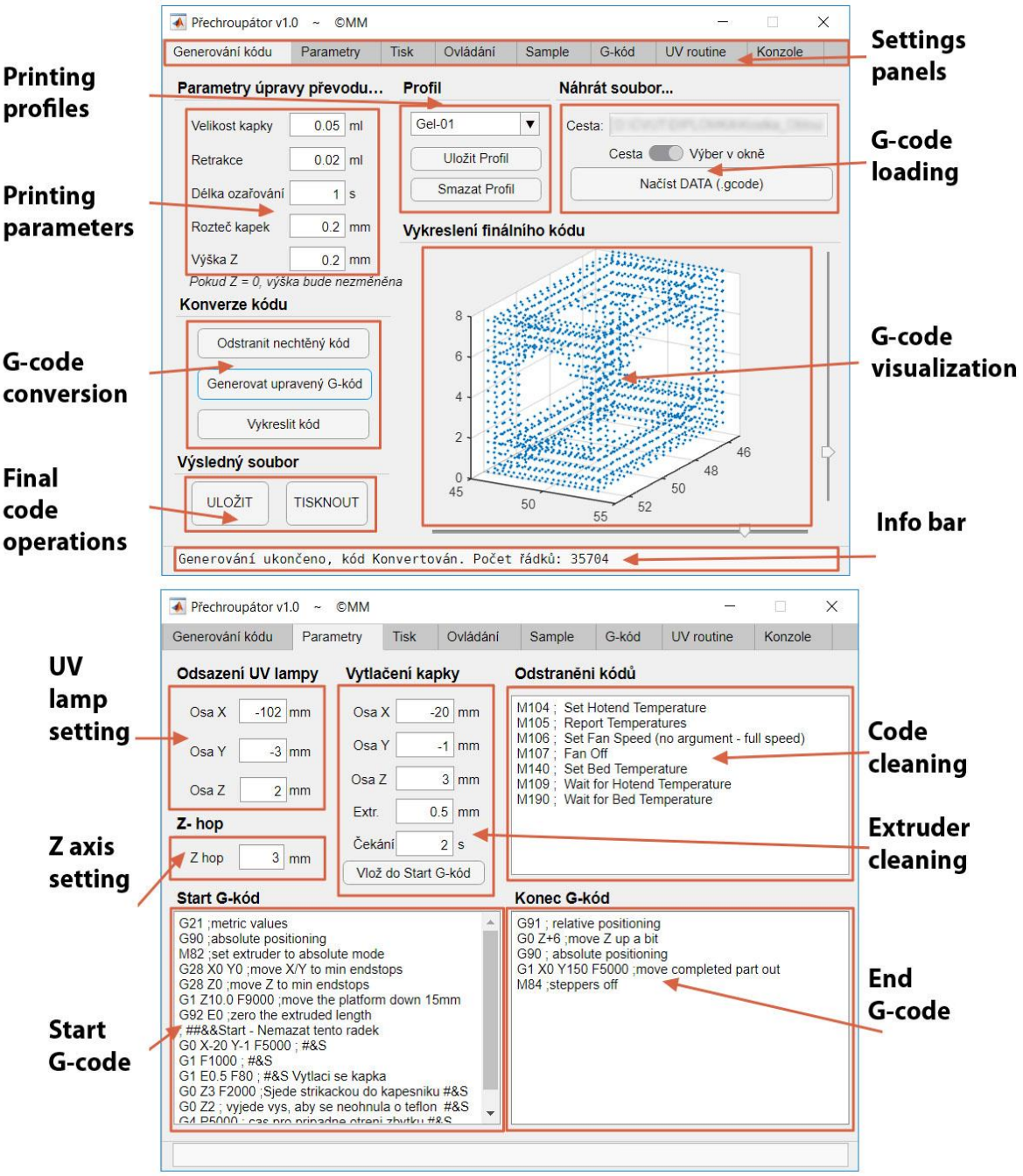

Fig. 2. The print control environment

Replacing a line with an object of droplets (Fig. 3) is based on the slope of the line k and the even distribution of the droplets along the trajectory

$$y = k \cdot x \;\Rightarrow k = \frac{y}{x}, \qquad \text{and after substituting} \qquad k = \frac{Y_{\text{Curr}} - Y_{\text{Last}}}{X_{\text{Curr}} - X_{\text{Last}}}.$$

The droplet pitch r is then given by the number n of droplets, from which the increment in the X axis can be calculated

$$r^2 = X_{\text{Incr}}^2 + X_{\text{Incr}}^2 \cdot k^2 \;\Rightarrow\; X_{\text{Incr}} = \sqrt{\frac{r^2}{(1+k^2)}}.$$

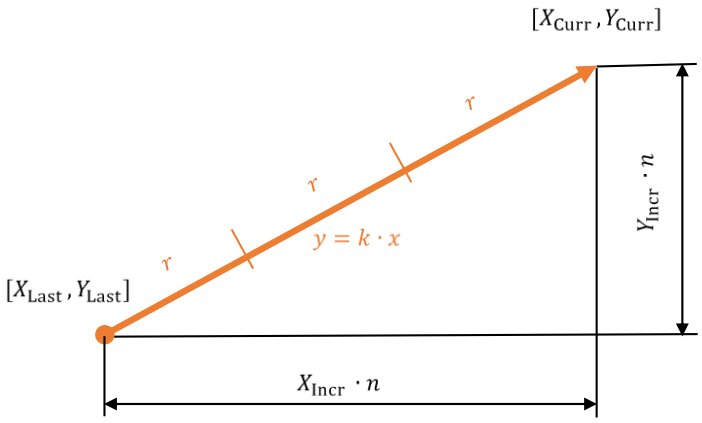

Fig. 3. Replacing a straight line with droplets

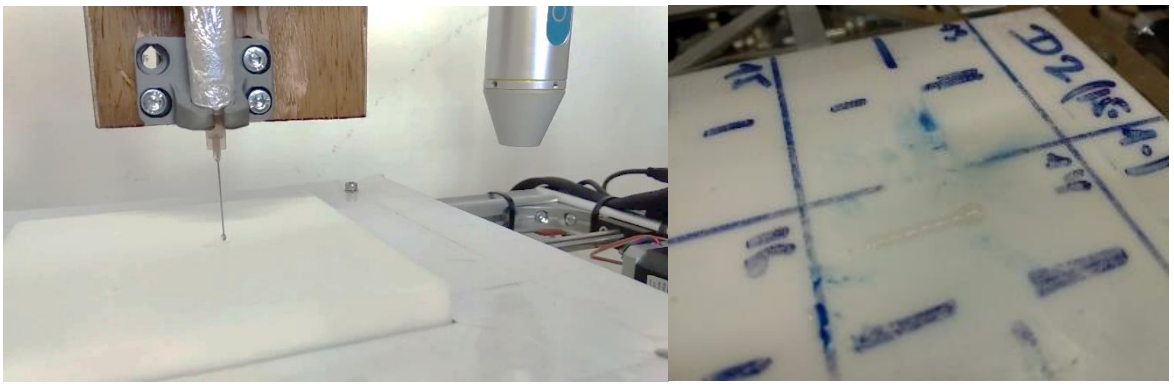

Fig. 4. Printing the droplet at the end of the needle (left) and demonstrating the printing of the line from the droplets (right)

A simple object was chosen to test the functionality of the hydrogel printer. Fig. 4 shows the droplet formation at the end of the needle as well as the printed line. This type of printer is suitable for printing larger objects that do not require high printing accuracy. The resolution is dependent on the size of the droplet and thus the inner diameter of the needle. However, this dimension is closely related to the need to accurately meter the amount of extruded hydrogel that limits the use for detail printing.

Acknowledgements

The research is supported by the Grant Agency of the Czech Republic by project No GA17-08531S – "Computational design of hydrogel cell scaffolds".

References

[1] Bittner, S.M., Guo, J.L., Melchiorri, A., Mikos, A.G., Three-dimensional printing of multilayered tissue engineering scaffolds, Materials Today 21 (8) (2018) 861-874.
[2] Tan, Z., Parisi, C., Di Silvio, L., Dini, D., Forte A.L., Cryogenic 3D printing of super soft hydrogels, Scientific Reports [online] 7(1) (2017).
[3] Wichterle, O., Lím, D., Hydrophilic gels for biological use, Nature 185 (4706) (1960) 117-118.

COMPUTATIONAL MECHANICS 2019
35th conference with international participation
Srní
November 4 - 6, 2019

Generalized modal reduction method in dynamics of mechanical systems

V. Zeman[a], Z. Hlaváč[a]

[a] NTIS – New Technologies for the Information Society, Faculty of Applied Sciences, University of West Bohemia, Univerzitní 8, 301 00 Plzeň, Czech Republic

The rotating mechanical systems (e.g., high-speed gearboxes, bladed disks, rotors, turbochargers) are composed of many flexible and rigid bodies (below subsystems) mutually joined by flexible nonlinear discrete couplings. The mathematical models of these subsystems are non-conservative with nonsymmetrical matrices and after discretization by the finite element method have large number of degrees of freedom (DOF number). The standard numerical methods of dynamic analyses of the rotating systems with nonlinear couplings are very hardly applicable. A suitable and established methods for DOF number reduction of the large multi-body systems is the modal synthesis method [2, 3, 6, 7]. The classical approach of the modal synthesis method is based on the reduction of the natural modes of subsystems conservative models respected in dynamic response. Rotatig mechanical systems contain gyroscopic effects and additional influences of rotation and dissipation [1, 2, 4, 5]. On this account the eigenvalues and right and left eigenvectors of rotating subsystems are complex. The main aim of this contribution is to present the generalized modal reduction method with reduction DOF number of the whole system or individual subsystems for modelling of the multi-body systems with strong gyroscopic effects, damping and friction in couplings.

Let us consider the mechanical system (rotor, blade packet, rings) which can be decomposed into N linearized rotating or nonrotating subsystems. The first step of modelling using modal synthesis method consists in the first-order formulation of the equations of motion [1] in the form

$$\boldsymbol{N}_j\dot{\boldsymbol{u}}_j + \boldsymbol{P}_j\boldsymbol{u}_j = \boldsymbol{p}_j\,,\ \boldsymbol{p}_j = \begin{bmatrix} \boldsymbol{0} \\ \boldsymbol{f}_j^C + \boldsymbol{f}_j^E(t) \end{bmatrix}\,,\ j = 1,\ldots,N \tag{1}$$

in the state space defined by the state vector of subsystem j , $\boldsymbol{u}_j = [\dot{\boldsymbol{q}}_j^T, \boldsymbol{q}_j^T]^T$, where $\boldsymbol{q}_j$ is the vector of the generalized coordinates of dimension n_j. Vector $\boldsymbol{p}_j$ expresses effect of internal couplings $\boldsymbol{f}_j^C$ of the subsystem j with surrouding subsystems and excitation forces $\boldsymbol{f}_j^E(t)$.

Let all modal values $\lambda_\nu^{(j)}$, $\nu = 1,\ldots,n_j$, of each mutually uncoupled subsystem j (for $\boldsymbol{f}_j^C = \boldsymbol{0}$) satisfy the stability conditions $\mathrm{Re}[\lambda_\nu^{(j)}] < 0$. Modal properties of subsystem j are expressed by the complex diagonal spectral matrix $\boldsymbol{\Lambda}_j \in C^{2n_j,2n_j}$ and complex couple right and left modal matrices $\boldsymbol{U}_j \in C^{2n_j,2n_j}$, $\boldsymbol{W}_j \in C^{2n_j,2n_j}$ satisfying the biorthonormality conditions [1]

$$\boldsymbol{W}_j^T\boldsymbol{N}_j\boldsymbol{U}_j = \boldsymbol{E}_j\,,\ \boldsymbol{W}_j^T\boldsymbol{P}_j\boldsymbol{U}_j = -\boldsymbol{\Lambda}_j\,,\ j = 1,\ldots,N\,, \tag{2}$$

where $\boldsymbol{E}_j$ is the identity matrix of the $2n_j$-th order. We chose for each subsystem j two sets of $2m_j$ $(m_j \le n_j)$ so called master right and left natural modes corresponding to m_j pairs of complex conjugate eigenvalues (diagonal elements of $\boldsymbol{\Lambda}_j$) $\lambda_\nu^{(j)} = \alpha_\nu^{(j)} + \mathrm{i}\beta_\nu^{(j)}$, $\lambda_\nu^{(j)*} = \alpha_\nu^{(j)} - \mathrm{i}\beta_\nu^{(j)}$

ordered according to the size of the imaginary parts $\beta_1^{(j)} \leq \beta_2^{(j)} \leq \cdots \leq \beta_{m_j}^{(j)}$. Corresponding natural modes are represented by pairs of the complex conjugate right $\boldsymbol{u}_\nu^{(j)}$, $\boldsymbol{u}_\nu^{(j)*}$ and left $\boldsymbol{w}_\nu^{(j)}$, $\boldsymbol{w}_\nu^{(j)*}$ eigenvectors ordered in the master (subscript m) right and left modal submatrices

$$
{}^m\boldsymbol{U}_j = [\boldsymbol{u}_1^{(j)}, \ldots, \boldsymbol{u}_{m_j}^{(j)}, \boldsymbol{u}_1^{(j)*}, \ldots, \boldsymbol{u}_{m_j}^{(j)*}] \in C^{2n_j,2m_j},
$$

$$
{}^m\boldsymbol{W}_j = [\boldsymbol{w}_1^{(j)}, \ldots, \boldsymbol{w}_{m_j}^{(j)}, \boldsymbol{w}_1^{(j)*}, \ldots, \boldsymbol{w}_{m_j}^{(j)*}] \in C^{2n_j,2m_j},\ j = 1, \ldots, N\,, \tag{3}
$$

corresponding to master spectral submatrix

$$
{}^m\boldsymbol{\Lambda}_j = \mathrm{diag}[\lambda_1^{(j)}, \ldots, \lambda_{m_j}^{(j)}, \lambda_1^{(j)*}, \ldots, \lambda_{m_j}^{(j)*}] \in C^{2m_j,2m_j},\ j = 1, \ldots, N\,. \tag{4}
$$

State vectors $\boldsymbol{u}_j$ in model (1) are transformed by the master right modal submatrices ${}^m\boldsymbol{U}^{(j)} \in$ $\in C^{2n_j,2m_j}$ mutually uncoupled subsystems into the modal coordinates as

$$
\boldsymbol{u}_j = {}^m\boldsymbol{U}_j\boldsymbol{x}_j = \sum_{\nu=1}^{m_j} \left(\boldsymbol{u}_\nu^{(j)} x_\nu^{(j)} + \boldsymbol{u}_\nu^{(j)*} x_\nu^{(j)*}\right),\ j = 1, \ldots, N\,. \tag{5}
$$

After modal transformation (5) and premultiplaying of Eqs. (1) by the transposed left master modal submatrices ${}^m\boldsymbol{W}_j^T$ with regard to the biorthonormality conditions (2), Eqs. (1) become

$$
\dot{\boldsymbol{x}}_j - {}^m\boldsymbol{\Lambda}_j\boldsymbol{x}_j = {}^m\boldsymbol{W}_j^T\boldsymbol{p}_j,\ j = 1, \ldots, N\,. \tag{6}
$$

Taking into account structure of state vectors $\boldsymbol{u}_j$, the eigenvectors of the subsystems can be written in the form

$$
\boldsymbol{u}_\nu^{(j)} = \begin{bmatrix} \lambda_\nu^{(j)}\boldsymbol{q}_\nu^{(j)} \\ \boldsymbol{q}_\nu^{(j)} \end{bmatrix},\ \boldsymbol{w}_\nu^{(j)} = \begin{bmatrix} \lambda_\nu^{(j)}\boldsymbol{r}_\nu^{(j)} \\ \boldsymbol{r}_\nu^{(j)} \end{bmatrix},\ \nu = 1, \ldots, n_j,\ j = 1, \ldots, N\,. \tag{7}
$$

The modal submatrices defined in (3) can be written as

$$
{}^m\boldsymbol{U}_j = \begin{bmatrix} {}^m\boldsymbol{Q}_j\,{}^m\boldsymbol{\Lambda}_j \\ {}^m\boldsymbol{Q}_j \end{bmatrix},\ {}^m\boldsymbol{W}_j = \begin{bmatrix} {}^m\boldsymbol{R}_j\,{}^m\boldsymbol{\Lambda}_j \\ {}^m\boldsymbol{R}_j \end{bmatrix},\ j = 1, \ldots, N\,, \tag{8}
$$

where

$$
\begin{aligned}
{}^m\boldsymbol{Q}_j &= [\boldsymbol{q}_1^{(j)}, \ldots, \boldsymbol{q}_{m_j}^{(j)}, \boldsymbol{q}_1^{(j)*}, \ldots, \boldsymbol{q}_{m_j}^{(j)*}] \in C^{n_j,2m_j}\,, \\
{}^m\boldsymbol{R}_j &= [\boldsymbol{r}_1^{(j)}, \ldots, \boldsymbol{r}_{m_j}^{(j)}, \boldsymbol{r}_1^{(j)*}, \ldots, \boldsymbol{r}_{m_j}^{(j)*}] \in C^{n_j,2m_j}
\end{aligned} \tag{9}
$$

are the right and left master modal submatrices of uncoupled subsystems in the original configuration space of generalized coordinates $\boldsymbol{q}_j$. Eqs. (6) can be rewritten in the form

$$
\dot{\boldsymbol{x}}_j - {}^m\boldsymbol{\Lambda}_j\boldsymbol{x}_j = {}^m\boldsymbol{R}_j^T(\boldsymbol{f}_j^C + \boldsymbol{f}_j^E(t)),\ j = 1, \ldots, N\,. \tag{10}
$$

The global form is

$$
\dot{\boldsymbol{x}} - {}^m\boldsymbol{\Lambda}\boldsymbol{x} = {}^m\boldsymbol{R}^T[\boldsymbol{f}_C(\boldsymbol{q}, \dot{\boldsymbol{q}}) + \boldsymbol{f}_E(t)]\,, \tag{11}
$$

where

$$
\boldsymbol{x} = \begin{bmatrix} \boldsymbol{x}_1 \\ \vdots \\ \boldsymbol{x}_N \end{bmatrix},\ \boldsymbol{q} = \begin{bmatrix} \boldsymbol{q}_1 \\ \vdots \\ \boldsymbol{q}_N \end{bmatrix},\ \boldsymbol{f}_C(\boldsymbol{q}, \dot{\boldsymbol{q}}) = \begin{bmatrix} \boldsymbol{f}_1^C \\ \vdots \\ \boldsymbol{f}_N^C \end{bmatrix},\ \boldsymbol{f}_E(t) = \begin{bmatrix} \boldsymbol{f}_1^E(t) \\ \vdots \\ \boldsymbol{f}_N^E(t) \end{bmatrix},
$$

$$ {}^{m}\boldsymbol{\Lambda} = \mathrm{diag}[{}^{m}\boldsymbol{\Lambda}_1, \ldots, {}^{m}\boldsymbol{\Lambda}_N] \in C^{2m,2m},\ {}^{m}\boldsymbol{R}^T = \mathrm{diag}[{}^{m}\boldsymbol{R}_1^T, \ldots, {}^{m}\boldsymbol{R}_N^T] \in C^{2m,n}\,. \tag{12} $$

Matrices ${}^{m}\boldsymbol{\Lambda}$, ${}^{m}\boldsymbol{R}$ and vector $\boldsymbol{x}$ in (11) can be rewritten in the form

$$ {}^{m}\boldsymbol{\Lambda} = \mathrm{diag}[{}^{m}\overline{\boldsymbol{\Lambda}}, {}^{m}\overline{\boldsymbol{\Lambda}}^*],\ {}^{m}\boldsymbol{R} = [{}^{m}\overline{\boldsymbol{R}}, {}^{m}\overline{\boldsymbol{R}}^*],\ \boldsymbol{x} = \begin{bmatrix} \overline{\boldsymbol{x}} \\ \overline{\boldsymbol{x}}^* \end{bmatrix}, \tag{13} $$

where spectral submatrix ${}^{m}\overline{\boldsymbol{\Lambda}}$ includes the chosen eigenvalues $\lambda_\nu^{(j)} = \alpha_\nu^{(j)} + \mathrm{i}\beta_\nu^{(j)}$ of the all subsystems with positive imaginary part and left master modal submatrix ${}^{m}\overline{\boldsymbol{R}}$ includes corresponding eigenvectors $\boldsymbol{r}_\nu^{(j)}$. The complex conjugate eigenvalues are arranged in matrices ${}^{m}\overline{\boldsymbol{\Lambda}}^*$, ${}^{m}\overline{\boldsymbol{R}}^*$ and the complex conjugate modal coordinates are arranged in vector $\overline{\boldsymbol{x}}^*$. We can use the MATLAB built in `ode45` solver for the integration of the submodel

$$ \dot{\overline{\boldsymbol{x}}} - {}^{m}\overline{\boldsymbol{\Lambda}}\overline{\boldsymbol{x}} = {}^{m}\overline{\boldsymbol{R}}^T[\boldsymbol{f}_C(\boldsymbol{q}, \dot{\boldsymbol{q}}) + \boldsymbol{f}_E(t)]\,, \tag{14} $$

where

$$ {}^{m}\overline{\boldsymbol{\Lambda}} = \mathrm{diag}[{}^{m}\overline{\boldsymbol{\Lambda}}_1, \ldots, {}^{m}\overline{\boldsymbol{\Lambda}}_N] \in C^{m,m},\ {}^{m}\overline{\boldsymbol{R}}^T = [{}^{m}\overline{\boldsymbol{R}}_1^T, \ldots, {}^{m}\overline{\boldsymbol{R}}_N^T] \in C^{m,n}\,. $$

According to (5) and (8) the vector $\boldsymbol{q}$ of generalized coordinates can be expressed as

$$ \boldsymbol{q} = {}^{m}\overline{\boldsymbol{Q}}\overline{\boldsymbol{x}} + {}^{m}\overline{\boldsymbol{Q}}^*\overline{\boldsymbol{x}}^*,\ \dot{\boldsymbol{q}} = {}^{m}\overline{\boldsymbol{Q}}\,{}^{m}\overline{\boldsymbol{\Lambda}}\overline{\boldsymbol{x}} + {}^{m}\overline{\boldsymbol{Q}}^*\,{}^{m}\overline{\boldsymbol{\Lambda}}^*\overline{\boldsymbol{x}}^*\,, \tag{15} $$

where right master modal submatrix ${}^{m}\overline{\boldsymbol{Q}}$ corresponds to ${}^{m}\overline{\boldsymbol{\Lambda}}$. Model (14) of the coupled system in space of modal coordinates $x_\nu^{(j)}$ uncoupled subsystems has $m = \sum_{j=1}^{N} m_j$ DOF number and for $\sum_{j=1}^{N} m_j < \sum_{j=1}^{N} n_j$ is reduced.

If the linear part of elastic and viscous forces in couplings between subsystems can be excluded from the nonlinear couplings, vector $\boldsymbol{f}_C(\boldsymbol{q}, \dot{\boldsymbol{q}})$ in (11) can be written in the form

$$ \boldsymbol{f}_C(\boldsymbol{q}, \dot{\boldsymbol{q}}) = -\boldsymbol{K}_C\boldsymbol{q} - \boldsymbol{B}_C\dot{\boldsymbol{q}} + \boldsymbol{f}_N(\boldsymbol{q}, \dot{\boldsymbol{q}})\,, \tag{16} $$

where $\boldsymbol{K}_C$ and $\boldsymbol{B}_C$ are the global stiffness and damping matrices corresponding to the linearized forces in couplings, vector $\boldsymbol{f}_N(\boldsymbol{q}, \dot{\boldsymbol{q}})$ expresses the nonlinear coupling forces and $\boldsymbol{q} = [\boldsymbol{q}_1^T, \ldots, \boldsymbol{q}_N^T]^T$ is the global vector of the generalized coordinates. All equations of motion (1) can be expressed in the state space $\boldsymbol{u} = [\dot{\boldsymbol{q}}^T, \boldsymbol{q}^T]^T$ in the global form

$$ \boldsymbol{N}\dot{\boldsymbol{u}} + \boldsymbol{P}\boldsymbol{u} = \boldsymbol{p}\,, \quad \boldsymbol{p} = \begin{bmatrix} \boldsymbol{0} \\ \boldsymbol{f}_N(\boldsymbol{q}, \dot{\boldsymbol{q}}) + \boldsymbol{f}_E(t) \end{bmatrix}, \tag{17} $$

where linearized forces in couplings are included in matrices $\boldsymbol{N}$ and $\boldsymbol{P}$. Similarly as in the modal synthesis method, only the following global submodel with m DOF number can be integrated

$$ \dot{\overline{\boldsymbol{x}}} - {}^{m}\overline{\boldsymbol{\Lambda}}\overline{\boldsymbol{x}} = {}^{m}\overline{\boldsymbol{R}}^T[\boldsymbol{f}_N(\boldsymbol{q}, \dot{\boldsymbol{q}}) + \boldsymbol{f}_E(t)]\,, \tag{18} $$

where $\overline{\boldsymbol{x}}$ and ${}^{m}\overline{\boldsymbol{R}}$ correspond to spectral submatrix ${}^{m}\overline{\boldsymbol{\Lambda}} = \mathrm{diag}[\lambda_1, \ldots, \lambda_m]$ including chosen eigenvalues $\lambda_\nu = \alpha_\nu + \mathrm{i}\beta_\nu$ of model (17) for $\boldsymbol{p} = \boldsymbol{0}$ with the positive imaginary part.

From the high computational costs point of view, an application of this method is suitable especially for dynamic analysis of the large rotating systems with nonlinear couplings. The method enables dynamic analyses of the damped rotating systems including all rotation effects

and nonlinear contact forces in internal couplings between subsystems. Contrary on the classical approach characterized by transformation of the generalized coordinates using the real modal submatrix of the linear part of the undamped and nonrotating system, the new approach is based on the transformation by the complex modal submatrix of the nonconservative linear part of the rotating system including all rotating and dissipative effects. The dynamic response in master modal coordinates is investigated by integration of the first order nonlinear equations, whose number corresponds to identical number of the second order nonlinear equations, using a classical approach. Consideration of the chosen master complex mode shapes improves approximation of the damped gyroscopic structures behaviour in comparison with classical modal reduction in the basis of the real mode shapes of the undamped and nonrotating structures.

Acknowledgement

This work was supported by the project LO1506 of the Ministry of Education, Youth and Sports of the Czech Republic.

References

[1] Byrtus, M., Hajžman, M., Zeman, V., Dynamics of rotating systems, University of West Bohemia, Pilsen, 2010. (in Czech)

[2] Genta, G., Dynamics of rotating systems, Springer Science and Business Media, New York, 2005.

[3] Irretier, H., Modal synthesis method with free interfaces and residual flexibility matrices for frame structures, Building Journal 37 (9) (1989) 601-610.

[4] Sui, Y., Zhong, W., Eigenvalue problem of a large scale indefinite gyroscopic dynamic system, Applied Mathematics and Mechanics 27 (1) (2006) 15-22.

[5] Yamamoto, T., Ishida, Y., Linear and nonlinear rotordynamics: A modern treatment with applications, John Wiley and Sons, Inc., New York, 2001.

[6] Zeman, V., Vibration of mechanical systems by the modal synthesis method, ZAMM – Journal of applied mathematics and mechanics: Zeitschrift für angewandte Mathematik und Mechanik. 74 (4) (1994) 99-101.

[7] Zeman, V., Hlaváč, Z., Condensed dynamical models in optimization of mechanical systems, ZAMM – Journal of applied mathematics and mechanics: Zeitschrift für angewandte Mathematik und Mechanik 75 (1995) 71-72.

COMPUTATIONAL MECHANICS 2019
35th conference with international participation
Srní
November 4 - 6, 2019

Local tilings informed synthesis of micro-mechanical fields by means of Wang tiles

L. Zrůbek[a], M. Doškář[a], A. Kučerová[a]

[a] *Department of Mechanics, Faculty of Civil Engineering, CTU in Prague, Thákurova 7, 166 29 Prague 6, Czech Republic*

In this paper, we present our work based on Wang tiles method and its utilisation on synthesis of micro-mechanical fields extended by local tilings information.

The very basic concept of the Wang tiles method [5] can be compared to jigsaw puzzle or classic board game domino. The fundamental pieces are positioned next to each other according to corresponding edge information like fitting edge shape, number of dots or in case of Wang tiles for example colours, patterns and others. Tiles are modelled visually as squares and by rotating or mirroring existing tile a new tile is created.

Group of tiles is called set and specially designed tile set in combination with particular tiling algorithm can construct planar domain of arbitrary size.

In contrast with other methods modelling heterogeneous materials like periodic unit cell method (PUC) or statistically equivalent periodic unit cell method (SEPUC) (used for example for homogenisation) the main advantage of Wang tiles method is the ability to preserve stochastic layout of original micro-structure. This is achieved by the tiling algorithm that in addition requires specifically defined tile set and tile design.

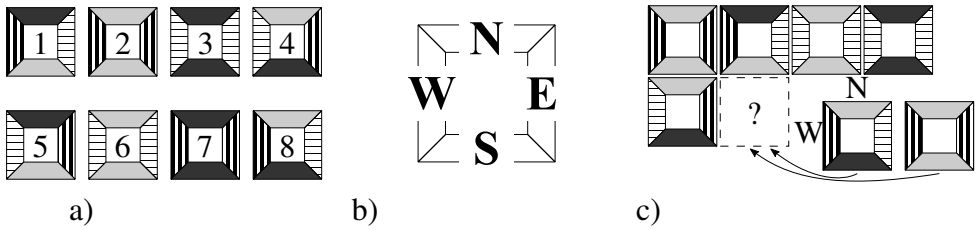

Fig. 1. a) Wang tiles set W8/2-2 (eight tiles with two different codes on vertical and horizontal edges), b) Tile edge labels, c) North-West corner position

As a tiling algorithm, we use algorithm presented in [1] (further called CSHD) which specifies one simple rule. Every time the tile is positioned in the *NW* corner position (Fig. 1c) the set must comprise at least two valid tiles. From these tiles one is randomly selected and the process is repeated. Algorithm can be also modified to prevent occurrence of group of same tile in the tiling by allowing to repeat the tile selection n-times. The minimal Wang tile set that fulfils the requirements of CSHD algorithm is presented in Fig. 1a.

Tiles can be designed with various methods. One method is similar to generating SEPUC where the original micro-structure is analysed and the tiles are optimised in such way the resulting micro-structure holds the same spatial characteristics. This approach is very robust but also extremely slow.

Next method to create tiles is based on samples from the original micro-structure where the number of extracted samples is equal to number of different edge information in set. For each tile the respective samples are arranged in to rhombus shape with overlap and stitched together by means of image quilting algorithm [1]. This method gives almost instant results, but struggles with fine details of micro-structures. Then other methods based on particle dynamics [4] and level set [2] can be also used, but these methods have limited control over spatial statistics.

To obtain micro-mechanical fields (e.g. stresses, strains or displacements) the whole micro-structural domain can be discretized by very fine FEM mesh and evaluated. Unfortunately according to domain size and fineness of the mesh the computational requirements and evaluation time can be very demanding. These can be reduced by utilising the Wang tiles method as the process of micro-structure reconstruction can be applied to micro-mechanical field synthesis.

Each tile is discretised by fine FEM mesh in such way that the meshes are still edge compatible. Then the required mechanical response is evaluated on each tile separately and synthesised back according to underlying map of tiles. However, because of the non-local character of mechanical quantities the results contains discontinuities on tile edges and therefore the underlying grid of tiles is recognisable [3]. That is because of the mechanical response of each tile is affected by a different combination of surrounding tiles.

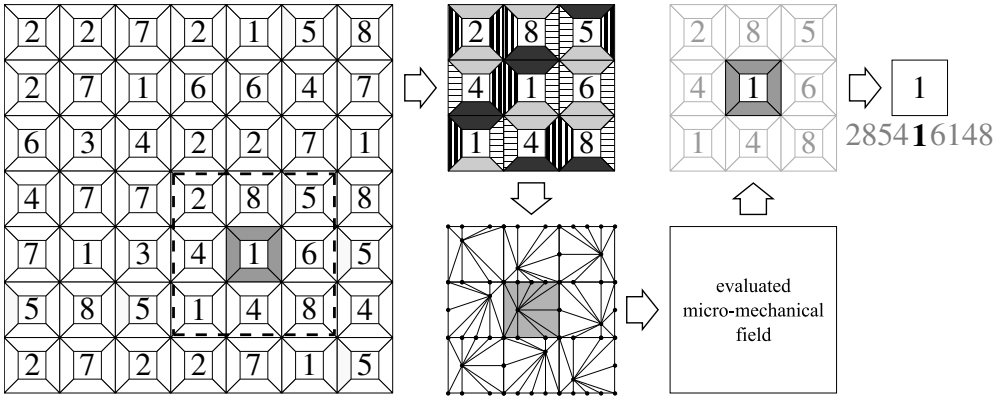

Fig. 2. Local tiling evaluation process

To solve this problem we create so-called local tiling for each tile T_i from underlying tiling map by including surrounding tiles into the evaluation of the mechanical response. This process is demonstrated on the Fig. 2 where on left is part of the reconstructed domain illustrated as grid of tiles. For currently solved tile T_1 (highlighted by grey colour) the small sub-domain of this centre tile and first layer of surrounding tiles is created. This sub-domain is discretised by FEM mesh and required micro–mechanical response is evaluated. Results for tiles in surrounding layer are discarded and only results for centre tile T_1 are saved under label $T_{28541\mathbf{1}6148}$. This process is repeated for every tile in the domain until results for each tile in the domain are obtained. Then the micro-mechanical field for the whole domain can be synthesised or these results can be used as fluctuation fields in Partition of Unity methods.

Acknowledgements

The authors gratefully acknowledge the financial support from the Grant Agency of the CTU in Prague, the grant No. SGS19/033/OHK1/1T/11 - Design toolchain for modular structures: Accelerated optimization and stochastic analysis (L. Zrůbek, M. Doškář and A. Kučerová).

References

[1] Cohen, M. F., Shade, J., Hiller, S., Deussen, O., Wang tiles for image and texture generation, ACM Transactions on Graphics 22 (3) (2003) 287-294.

[2] Doškář, M., Zeman, J., Rypl, D., Novák, J., Level-set based design of Wang tiles for modelling complex microstructures, 2019, arXiv:1904.07657. (preprint)

[3] Novák, J., Kučerová, A., Zeman, J., Microstructural enrichment functions based on stochastic Wang tilings, Modelling and Simulation in Materials Science and Engineering 21 (2) (2013) No. 025014, doi: 10.1088/0965-0393/21/2/025014.

[4] Šedlbauer, D., Lepš, M., Wang tiling for particle heterogeneous materials: Algorithms for generation of tiles/cubes via molecular dynamics, Applied and Computational Mechanics 13 (1) (2019) 53-76.

[5] Wang, H., Proving theorems by pattern recognition – II, Bell System Technical Journal 40 (1) (1961) 1-41.